Faculty of Science and Engineering
School of Earth and Planetary Sciences

UHT metamorphism. Can integrated thermobarometry and geochronology quantify lower crustal processes?

Ruairidh J. Mitchell

This thesis is presented for the Degree of
Doctor of Philosophy (Applied Geology)
of
Curtin University

December 2019

Declaration

To the best of my knowledge and belief this thesis contains no material previously published by any other person except where due acknowledgment has been made. This thesis contains no material which has been accepted for the award of any other degree or diploma in any university.

Signature:_____ Date: 12/12/2019

Ruairidh J. Mitchell

Acknowledgements

Firstly, I would like to thank my supervisors: Tim Johnson, Chris Clark, Katy Evans of Curtin University and Saibal Gupta of IIT Kharagpur for over three years of support, discussion and diligent feedback. Thanks go to Tim and Chris, who I approached about starting this project and made it happen. I extend this gratitude to co-authors – Michael Brown, Simon Harley, Chris Kirkaland and Richard Taylor – with which I have enjoyed lively back-and-forths about all things granulites, crustal melting and geochronology over the past three years. The staff of the John de Laeter centre, Curtin University have gone above and beyond to help me with analytical work, without which the work in this thesis would have been impossible.

Many thanks again to Saibal and my fellow research scholars at the Department of Geology and Geophysics at IIT Kharagpur for making me feel so welcome, and helping me to settle in during my time there. It was a great experience and I hope that I get the opportunity to return in the future. Tim, Chris C., Mike and Saibal are all thanked for two very enjoyable field trips to the Eastern Ghats!

Notably, I owe Simon for introducing me to metamorphic petrology. He had the patience to bear with my initial forays into what I learned to be a fascinating discipline.

All of my friends in Perth have made the last three and a bit years fly by, and have always been there to sneak away for a swift half when things got rough! There are too many to mention by name, but thanks for making life down-under so easy. Particular thanks go to my fellow HDR students at the School of Earth and Planetary Sciences, Curtin University. Their solidarity throughout the whole process is greatly appreciated, and everyone provided welcome distractions, from pub outings to futsal games!

Finally, thanks to my family – Mum, Dad and Eilidh, for always being available for a chat and giving every bit of support needed over the past few years.

Abstract

The timescales and pressure–temperature (*P–T*) conditions recorded by granulite facies metamorphic rocks permit inferences about the geodynamic regime in which they formed. Phase equilibrium modelling and genochronology of accessory phases – often U–Pb isotopes in zircon and monazite – are most commonly employed to constrain the *P–T–t* evolution of granulite facies rocks. The intricacies of these methods were investigated, and lead to a robust method and tectonic interpretation of an ultra-high temperature (UHT) terrane – the Eastern Ghats Province (EGP), India.

Defining a suitable equilibrium volume is vital for phase equilibrium modelling. However, in granulites it can be non-trivial due to heterogeneities in protolith composition and open system behaviour, including melt loss or gain and deformation. Consequently, equilibrium volumes and the mineral assemblages they contain may vary both temporally and spatially. Additionally, despite the extreme temperatures they attained, granulites commonly contain microtextures indicative of local equilibrium, developed after the metamorphic peak. Firstly, in order to establish how local equilibrium at two scales influences thermobarometric interpritation of UHT rocks, this thesis presents a combined approach of phase equilibrium forward modelling and chemical potential diagrams to simulate the suprasolidus evolution of a compositionally hetergoeneous granulite. Assuming equilibrium within adjacent compositional domains, evolving granulite facies assemblages vary significantly along a modelled high *T/P* (125 °C/kbar) clockwise *P–T* path. Most retrograde microtextures in metapelitic rocks can be reproduced by considering chemical potential (μ) gradients in μ_{MgO}, μ_{FeO} and μ_{CaO} between pre-existing phases, assuming the presence of melt on grain boundaries, that Al_2O_3 is perfectly immobile and that K_2O, Na_2O and H_2O are perfectly mobile. Additionally, documented microstructures in granulites imply SiO_2-undersaturation locally; requiring that μ_{SiO_2} is not superimposed on these microstructures by matrix quartz. Preserving such chemical potential gradients requires that solid phases are chemically and physically isolated from melt after their formation. Efficient melt loss along a high *T/P P–T* path to > 900 °C leads to an order of magnitude increase in melt viscosity. This may isolate solid phases in granulites from melt, allowing element mobility to be controlled by solid state diffusion. The reaction textures form when isolated pockets of melt allows intergranular reaction

microtextures to form.

Using the rationale established above, the petrology of two compositionally heterogeneous cordierite–spinel–quartz -bearing granulites from Vizianagaram, Eastern Ghats Province (EGP), India, was investigated. To provide *P–T* constraints, detailed petrography and phase equilibrium modelling were applied. These ultrahigh temperature (UHT) granulites preserve discrete compositional layering in which different inferred peak assemblages are developed, including layers bearing garnet–sillimanite–spinel–quartz and others bearing orthopyroxene–sillimanite–spinel–quartz. These mineral associations cannot be reproduced by phase equilibrium modelling of whole rock compositions, indicating that the samples became domainal on a scale less than that of a thin section, even at UHT conditions. Calculation of the *P–T* stability fields for six compositional domains within which the main rock-forming minerals are considered to have attained equilibrium suggests peak metamorphic conditions of ~6.8–8.3 kbar at ~1000 °C. In most of these domains, the subsequent evolution resulted in the growth of cordierite and final crystallization of melt at an elevated (residual) H_2O-undersaturated solidus, consistent with <1 kbar of decompression and ~25 °C cooling.

To investigate further the tectonic precursors and the duration of granulite facies metamorphism, U–Pb isotopes, rare earth element (REE), and trace element compositions of detrital and metamorphic zircon from the Vizianagaram granulites and six additional metasedimentary samples were investigated. The EGP has a complex detrital history and experienced more than one granulite facies metamorphic event. A new workflow for interpreting granulite facies metasedimentary zircon was implemented, including the use of a clustering algorithm based on trace element chemistry. Three zircon populations were identified – inherited igneous zircon, metamorphic zircon and hydrothermally altered zircon. Based on the age of inherited igneous zircons, the EGP samples define populations at >2500 Ma, c. 1600–1350 and c. 1220–1080 Ma that relate to the ages of the source rocks for the metasedimentary protoliths, in which the age of the oldest components are recognised based on Pb loss trends towards younger metamorphic events. Analyses of zircon grains with c. 1650–1350 Ma concordant ages have elevated positive Ce/Ce* anomalies and U/Yb ratios, suggesting that their magmatic source was relatively oxidised. By contrast, the c. 1220–1080 Ma grains have elevated Nb/Yb ratios, low Ce/Ce*

anomalies and high Ti concentrations, which likely reflect derivation from high-temperature, reduced, A-type magmas formed by low degree melting of the mantle in an extensional regime, marking the onset of rifting in the EGP depocentre.

Following the input of sediment to the EGP, two anatectic metamorphic events occurred at *c.* 1000–880 Ma (M1) and *c.* 600–500 Ma (M2), corroborated by concordant (within uncertainty) U–Pb zircon (spread *c.* 1050-800Ma, concordia age of 511 ± 6) and monazite (spread *c.* 950-800Ma) data collected by SHRIMP from the Vizianagaram Granulites. Ti-in-zircon concentrations and concordant ages reveal that during M1, the EGP samples cooled from >950 °C to below ~900 °C at a rate of 0.34 ± 0.09 °C/Ma, and were then reheated to ~920 °C during M2.

Overall, the results suggest that, in the interval 1050 to 800 Ma, the evolution of the EGP culminated with UHT conditions during the M1 event. From c.1000 Ma to c. 880 Ma, minor decompression occurred at Vizianagaram, before further zircon crystallization at c. 880–800 Ma during cooling to the solidus at this locality. However, these rocks are adjacent to the Paderu–Anantagiri–Salur crustal block to the NW that experienced counterclockwise *P–T–t* paths, and records similar UHT peak metamorphic conditions (7–8 kbar, ~950°C) followed by near-isobaric cooling, and has a similar chronology during the Neoproterozoic. The limited decompression inferred at Vizianagaram may be explained by partial exhumation due to thrusting of this crustal block over the adjacent Paderu–Anantagiri–Salur crustal block. The residual granulites in both blocks have high concentrations of heat producing elements and likely remained hot at mid-crustal depths throughout a period of relative tectonic quiescence in the interval 800–550 Ma. The later M2 event is recorded by zircon crystallization at temperatures of >900 °C. Slow cooling and reheating at >900 °C was facilitated by a sustained period of burial in the deep crust, reflecting high radiogenic heat production and very slow rates of erosion. During the Cambrian Period the EGP was located in the hinterland of the Denman–Pinjarra–Prydz orogen. The M2 age may record a low-degree of melting due to limited influx of fluid into hot, weak crust in response to convergence of the Crohn craton with a composite orogenic hinterland comprising the Rayner terrane, Eastern Ghats Province and cratonic India.

Contents

List of figures

List of tables

Chapter 1 | Introduction

The tectonics of hot orogens through geological time

Throughout the evolution of Earth, mountain building events – orogens – have formed in variety of different tectonic settings. As a result, rocks in the lower crust preserve evidence of a wide range of metamorphic conditions reflecting changes in pressure–temperature (*P–T*) and composition, which can occur over a durations of a few hundred thousand to several tens of millions of years or more (Harley, 2016; Harley and Nandakumar, 2016; Kelsey and Hand, 2015).

Regional metamorphism of rocks is commonly classified based on the peak *P–T* conditions and the post-peak evolution they record. Peak conditions can be subdivided based on the apparent prograde geothermal gradient they record (Figure 1.1a) into low *T/P* (<375 °C/GPa), high *T/P* (375-775 °C/GPa) and high *T/P* (>775 °C/GPa). A global metamorphic dataset shows a bimodal distribution of *T/P* since 2.2 Ga (Brown, 2007; Brown and Johnson, 2018), comprising discrete populations of higher *T/P* and lower *T/P* that is argued to mostly reflect paired metamorphism that develops due to accretionary and, ultimately, collisional orogenesis. This study focuses on the development of granulite facies lower crustal rocks that record high *T/P* conditions (Figure 1.1a) (Fyfe and Turner, 1966). The post-peak *P–T* path of high *T/P* granulites generally follow either clockwise (CW) or counter-clockwise (CCW) trajectories (Harley, 1989, 1998a, 2008; Kelsey, 2008; Kelsey and Hand,

Figure 1.1 | Global metamorphic dataset after Brown and Johnson (2018). High *T/P* datapoints in red, intermediate *T/P* in yellow and low *T/P* in blue and data from the Eastern Ghats Province are indicated by white circles. a) *P–T* diagram of peak metamorphic conditions, b) Moving average time series for High *T/P* (red), medium *T/P* (yellow) and low *T/P* (blue), including 1σ envelopes.

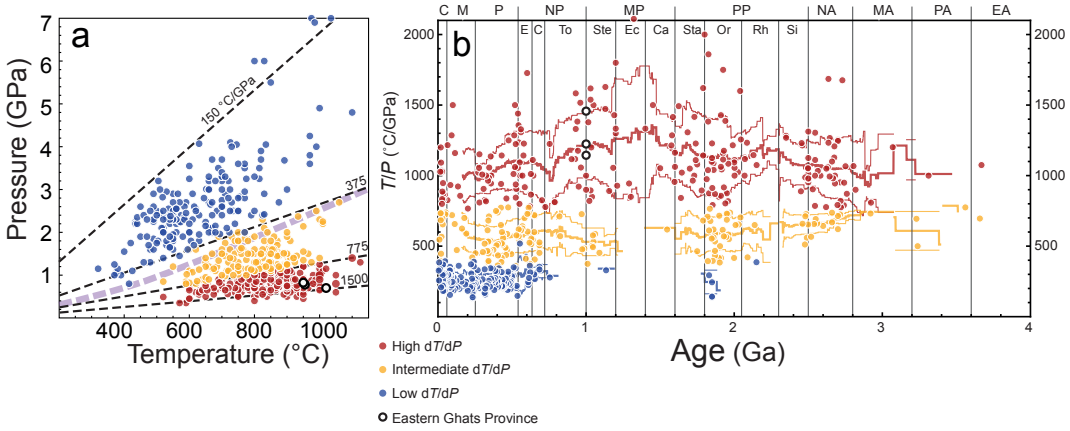

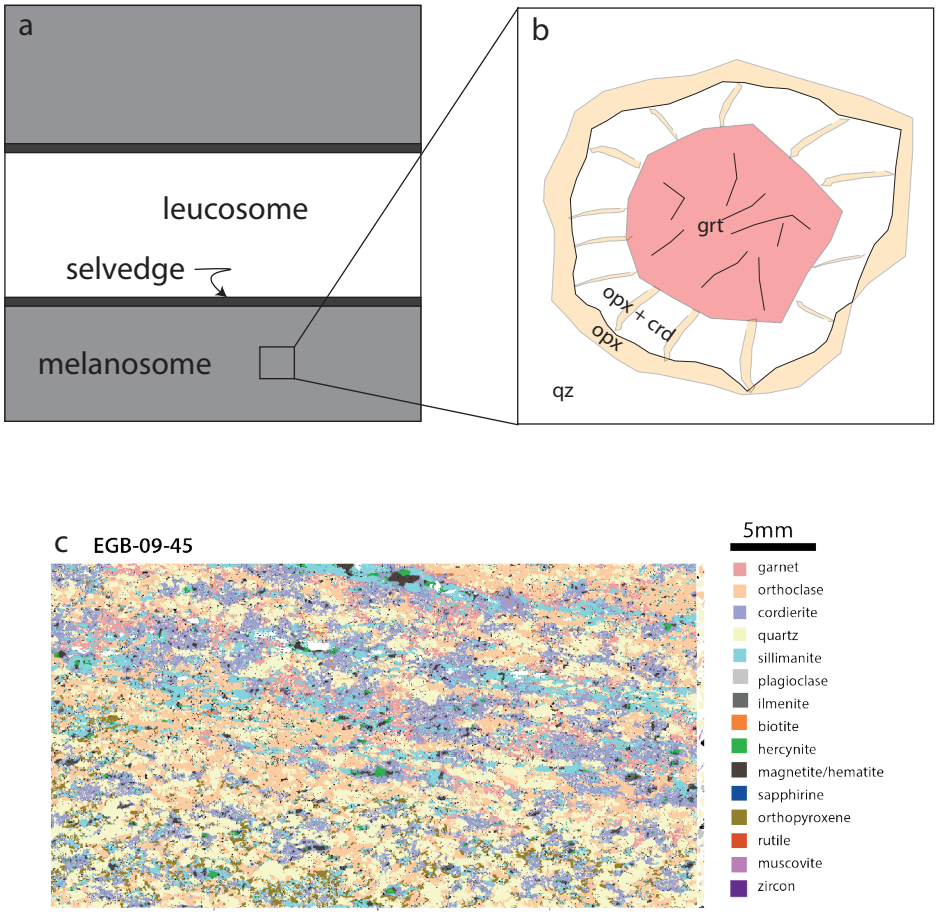

Figure 1.2 | Textural features in granulites. (a) Spatial arrangement of leucosome, melanosome and selvedge, after White and Powell (2010). (b) Corona texture of garnet|orthopyroxene + cordierite|orthopyroxene|quartz, interpreted using local equilibrium by Doukkari et al. (2018). (c) Heterogenous metamorphic peak assemblages, bearing orthopyroxene–sillimanite and garnet –sillimanite, on the centimetre scale, as documented by Mitchell et al. (2019).

2015), which are dominated by segments of near-isobaric cooling (IBC) and near-isothermal decompression (ITD), respectively.

The post peak *P–T* trajectory of granulites depends on the mechanism of exhumation. Post-peak decompression (CW trajectories) reflects tectonic environments that partially exhume portions of the lower crust after burial. Such settings include those in which regions of the orogeny or orogenic hinterland are subject to a high rates of erosion. For example, partially molten regions of the lower crust can be extruded through rheologically-weak channels, where rock packages are brought to the surface as an isostatic response to erosion (Beaumont et al., 2004; Beaumont et al.,

2006). Additionally, where back-arc extension occurs, the upwelling of asthenospheric mantle causes partial exhumation of parts of the lower crust. Alternatively, post-peak *P–T* paths dominated by IBC reflect tectonic environments in which the crust remains close to isostatic equilibrium, with extremely low erosion rates and slow exhumation (Bohlen, 1991; Korhonen et al., 2013a; Sandiford and Powell, 1986; Sizova et al., 2014).

The duration of regional metamorphism varies depending on the tectonic setting; even the rate of cooling from peak metamorphic conditions depends on the manner in which exhumation occurs. For example, the cooling rate of rocks recording high-pressure metamorphism associated with subduction relates to rapid exhumation that is broadly equivalent to plate velocities (Hermann et al., 2001; Rubatto and Hermann, 2001; Rubatto et al., 2001). Granulite facies metamorphic rocks formed in metamorphic core complexes that are exhumed during transpression typically have rapid cooling rates of 20-30 °C/Ma due to their short thermal length scales (Brown and Dallmeyer, 1996; Scibiorski et al., 2015; Spear and Parrish, 1996). By contrast, rocks subject to regional high *T/P* metamorphism can be subject to slow cooling, on time integrated rates of <5 °C/Ma (Ashwal et al., 1999; Clark et al., 2018; Korhonen et al., 2013b; Mezger et al., 1991; Möller et al., 2000; Vry and Baker, 2006) over durations that can exceed 100 Ma (Korhonen et al. 2013b).

Global datasets of metamorphic and detrital zircon ages have peaks around c. 2700 Ma, 2500 Ma, c. 2000–1800 Ma, c. 1000 Ma and c. 500 Ma (Brown, 2007; Brown and Johnson, 2018; Roberts and Spencer, 2015). This age spectrum seemingly coincides with supercontinent or supercraton amalgamation. As shown in Figure 1.1b, the maximum average geothermal gradient for high *T/P* metamorphism occurred in the time span from 2300 to 850 Ma. Furthermore, Brown and Johnson (2018) outlined three cycles of geodynamic activity; the first prior to c. 2300 Ma, a second from c. 2300–1000 Ma and a third after c. 1000 Ma. The first cycle is thought to coincide with decreasing mantle heat production and the amalgamation of blocks of continental lithosphere into supercratons through paired metamorphic belts. The second cycle relates to the prevalence of high *T/P* intracontinental orogens, when the mantle became insulated beneath the supercontinent Columbia. Finally, the third cycle signifies the emergence of low *T/P* metamorphism at c. 1000 Ma, coinciding with the breakup of Rodinia.

Crustal rocks can undergo melting through a range of processes that are

either fluid-fluxed or fluid-absent (Brown et al., 1995; Clarke et al., 2005; Sawyer, 1996, 2010; Stevens and Clemens, 1993). The peak *P–T* conditions reached by granulite facies, high *T/P* metamorphic terranes mean that all but the most anhydrous rocks cross incongruent melting reactions that produce silicate melt and peritectic minerals (Green et al., 2016; Holland and Powell, 2001; White et al., 2007; White et al., 2014). Partial melting has implications for the thermal and tectonic behaviour of Earth's middle-to-lower crust. Consistent with observations in nature (Sawyer, 1996), experiments show that below some connectivity threshold, melt is present in isolated pockets along grain boundaries, above which an interconnected melt network can be formed. When melt volumes exceed ~40 vol.%, the rheology approaches that of a magma (Rosenberg and Handy, 2005). While episodic partial melting and melt-loss can weaken the continental lithosphere (Cavalcante et al., 2016; Vanderhaeghe and Teyssier, 2001), long term melt loss can ultimately increase the strength of residual metasediments by 50–400% (Diener and Fagereng, 2014). Incongruent melting reactions are endothermic (Connolly and Thompson, 1989); meaning that melt production can buffer crustal temperatures (Schorn et al., 2018; Stüwe, 1995), potentially making extreme thermal conditions in the lower crust more difficult to attain, especially if heat producing elements (HPE) are removed from the middle to lower crust (Rudnick and Fountain, 1995).

The preservation of granulite facies assemblages is also affected by melting and melt segregation. Gradients in the chemical potential (μ) of H_2O (White and Powell, 2010), for example between melt and residuum, can lead to anhydrous leucosomes and melanosomes, with interstitial selvedges containing almost exclusively hydrous phases (Figure 1.1a). Furthermore, the degree of melt loss required to preserve pristine granulite facies assemblages can vary with the bulk composition (White and Powell, 2002), and can modify the bulk composition such that some diagnostic mineral assemblages of ultra-high temperature (UHT) metamorphism become stable at lower temperatures (Diener et al., 2008).

For the reasons outlined above, the timing and duration of anatexis, the thermobaric gradient (*T/P)* and the post peak *P–T* path all provide key constraints on the geodynamic conditions responsible for partial melting and UHT metamorphism in the lower crust. Consequently, it is imperative, therefore, that these parameters are determined as accurately as possible.

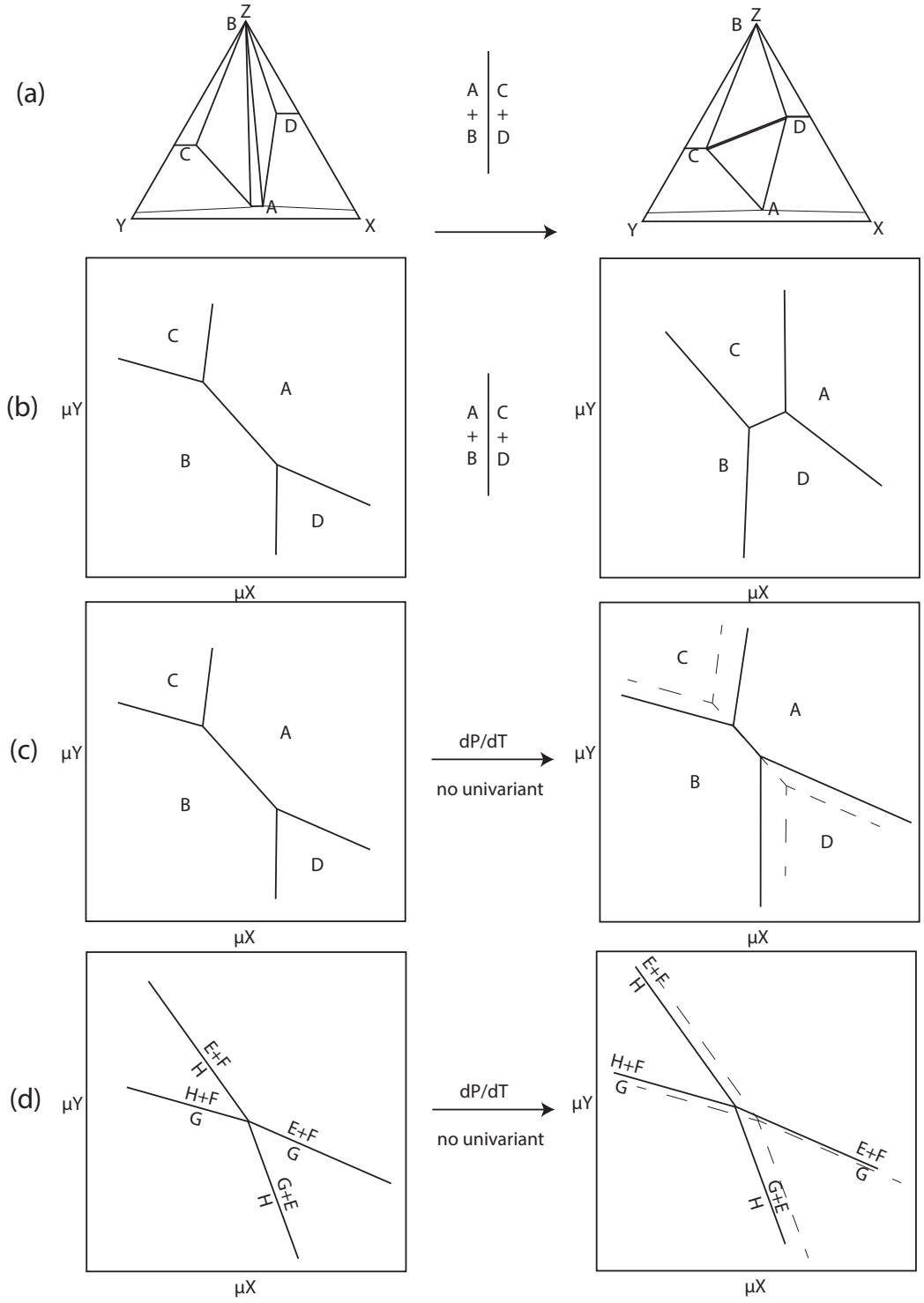

Figure 1.3 | Chemical potential topology and their effect on reaction textures. (a) A ternary plot of hypothetical chemical components X, Y and Z, showing a hypothetical univariant reaction A + B = C + D. (b) The change of chemical potential topology on each side of the reaction A + B = C + D. Assemblages A + B + C and A + B + D are replaced by A + C + D and B + C + D. (c) Two phase trivariants change position with a change in *P–T* without crossing a univariant reaction; phases C and D replace A and B. (d) Three phase trivariants change position with a change in *P–T* without crossing a univariant reaction; phases E + F replace H and G + E replaces H. In this case, it is possible to have two phase symplectites of E + F or G + E replacing phase H.

Thermodynamic equilibrium in granulites

A common method used to infer the *P–T* conditions of equilibrium mineral assemblages in granulites is phase equilibrium, or pseudosection modelling. Pseudosections show the stability fields of phase assemblages, either for a fixed bulk composition over a *P–T* range (*P–T* pseudosections), or for a linear range of bulk compositions between two end-member compositions at a fixed *P–T* (*T–X* or *P–X* pseudosections, respectively). The diagrams are calculated using internally consistent thermodynamic datasets that contain the thermodynamic properties of pure endmembers and activity–composition models to account for the thermodynamics of mixing in solid solution phases (Diener and Powell, 2012; Green et al., 2016; Holland and Powell, 2003; Holland and Powell, 1990, 2011; White et al., 2014). Pseudosection modelling assumes equilibrium on the scale of the bulk composition(s) used. Major element compositions are mostly derived either from X-ray fluorescence (XRF) whole rock (WR) analyses, perhaps including Fe^{2+}/Fe^{3+} titration, or by using phase maps and quantitative mineral chemistry, in particular when the interpreted equilibrium volue is considered to be smaller than the size of a standard thin section block (i.e. a few centimetres).

Although somewhat counterintuitive, it is clear that granulites do not always equilibrate on volumes sufficiently large that the composition of such a volume can be analysed by XRF (Figure 1.2). Peak mineral assemblages and/or mineral compositions may vary over much smaller length scales of (< or << 10 mm; Dorfler et al., 2015; Harley, 1998b; Johnson et al., 2003; Mitchell et al. 2019). This results from the fact that there are heterogeneities in primary protolith compositions, such as sedimentary or igneous layering (primary features), or that the sample records mass transfer due to melt or fluid migration or deformation that may occur during its prograde evolution. (secondary features). Either may lead to variations in chemical composition that influence phase equilibria on a centimetre or smaller scale (Ague, 1994, 1997; Hobbs et al., 2011). Regardless of the processes that lead to compositional heterogeneities and/or the establishment of transient chemical potential gradients, isochemical phase diagrams (pseudosections) based, for example, on whole-rock compositions may fail to reproduce one or more of the stable assemblages (Mitchell et al., 2019) if local equilibrium persists at a scale smaller than the measured bulk composition.

Smaller scale petrological relationships such as symplectites and coronae, characteristic retrograde textural features (i.e. Figure 1.2b), are also

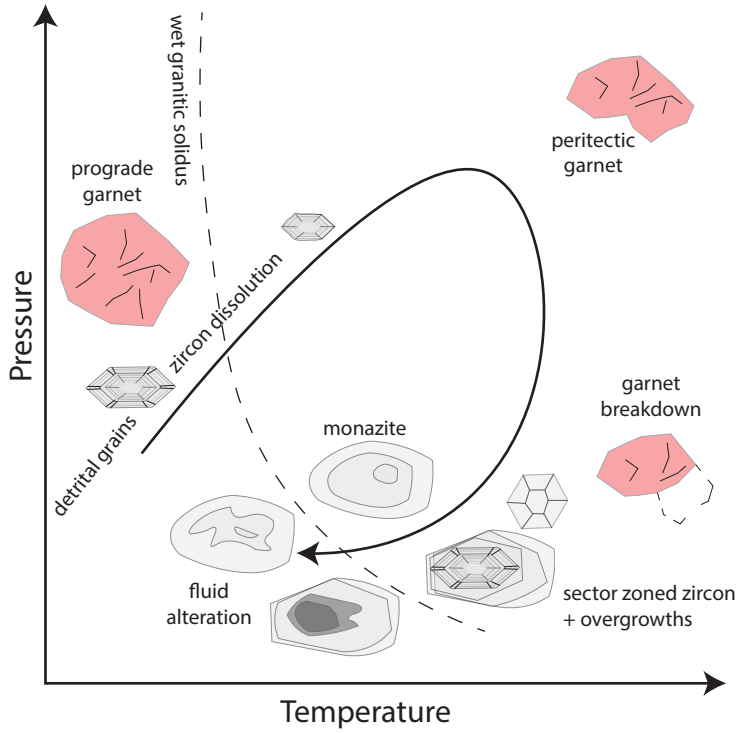

Figure 1.4 | Typical textural features of zircon and monazite on a typical granulite *P–T* path, including subsolidus and supersolidus features, after Taylor et al. (2016).

indicative of local equilibrium volumes, where the effective bulk composition can vary on a scale down to the unit cell (Korzhinskiĭ, 1959; Powell et al., 2018). There is empirical petrological evidence for local equilibrium in granulites in the preservation of reaction microtextures, explained by modelled chemical potential relationships (Figure 1.3; Baldwin et al., 2015; Doukkari et al., 2018; Schorn and Diener, 2017; Štípská et al., 2010; White and Powell, 2011; White et al., 2008).

Geochronology in granulite terranes

As peak temperatures of granulite facies metamorphism commonly exceed the closure temperatures of some geochronometers, such as U–Pb in rutile and apatite (Cherniak, 2000; Cochrane et al., 2014; Watson et al., 1985), the U–Pb isotope system in zircon and monazite are most commonly used to constrain the timing and duration of high-grade metamorphism (Cherniak, 2010; Cherniak and Watson, 2001; Harley and Kelly, 2007; Harley et al., 2007; Kusiak et al., 2013). Zircon and monazite are present in minor quantities in many protoliths (Kelsey et al., 2008; Kelsey and Powell, 2011; Yakymchuk and Brown, 2014). Both are thought to dissolve in anatectic melt along the prograde metamorphic *P–T* path, depending on melt composition. As most crustal melts are felsic and silica saturated, during

melt crystallization, zircon and monazite will grow if the melt is saturated in Zr and SiO2 – for zircon – or light rare earth elements (LREE) and P – for monazite (Kelsey et al., 2008; Kelsey and Powell, 2011; Yakymchuk and Brown, 2014). Correlating metamorphic zircon and monazite growth with processes such as melt crystallization and phase growth and dissolution (see Figure 1.4) is used to constrain the timing and duration of metamorphism in granulites (Clark et al., 2018; Taylor et al., 2017).

As the parameters of rare-earth element partitioning between zircon or monazite and garnet, fluid or melt have been constrained, it is possible to correlate zones of zircon and monazite growth to the growth of garnet or the presence of fluid or melt (Rubatto, 2002; Rubatto and Hermann, 2007; Taylor et al., 2015). However, zircon and monazite in high grade metamorphic systems preserve evidence for both open or closed system behaviour (Hokada and Harley, 2004; Kelly and Harley, 2005; Yakymchuk and Brown, 2014). Recovering detrital information from granulite facies zircon is often challenging, as large proportions of zircon dissolved during partial melting at granulite facies conditions (Kelsey et al., 2008; Yakymchuk and Brown, 2014). Therefore, unmodified, inherited (detrital) zircon cores are rare (Taylor et al., 2016). Furthermore, pervasive Pb loss can result in any record of zircon crystallisation preceding high grade metamorphic events being cryptic (Collins et al., 2012; Collins et al., 2003; Collins et al., 2007; Plavsa et al., 2012; Plavsa et al., 2014). The problem is amplified when considering multiple detrital age populations and inhomogeneous analytical volumes, where the time of resetting cannot easily be determined, or where more than one episode of Pb-loss event occurred (Clark et al., 2015; Plavsa et al., 2014).

1.1 | Research Aims

Our understanding of the scale of thermodynamic equilibrium in granulites in the lower crust, and the spatial variation of the duration and *P–T* evolution of metamorphism within hot orogens remains incomplete. Other poorly constrained parameters include the cooling rate of long-lived hot orogens and their common tectonic precursors. A set of research aims and methodologies were devised to show how thermometry and geochronology can address these unknowns.

1.1.1 | Assess the scales of equilibrium in granulites

1. Investigate how prograde local equilibrium can be maintained with respect to element mobility between pelitic granulites with contrasting compositions
2. Demonstrate the role of chemical potential relationships on the development of reaction microtextures (Figure 1.3)
3. Discuss how different scales of equilibrium volumes and local equilibrium can be established during the prograde and retrograde evolution of granulites
4. Postulate how centimetre to micron scales of local equilibrium in granulites may be preserved

1.1.2 | *P–T–time* evolution of granulties from Vizianagaram, Eastern Ghats Province

1. Accurately constrain the *P–T* evolution of granulites with heterogeneous peak assemblages
2. Find the timing and duration of anatexis by using U–Pb zircon and monazite geocrhonology
3. Ti-in-zircon thermometry to calculate the average cooling rate of the UHT metamorphic event
4. Devise a tectonic model for the duration and *P–T* evolution of this region of the EGP

1.1.3 | Terrane scale zircon geochronology in the Eastern Ghats Province

1. Develop an algorithm to categorise zircon laser ablation split-stream analyses based on trace element chemistry
2. Use zircon trace element discrimination plots to find viable igneous protoliths for inherited zircon grains
3. Apply Ti-in-zircon thermometry to concordant metamorphic data to retrieve peak metamorphic temperatures and cooling rates
4. Discriminate between concordia and discordia trends of metamorphic U–Pb data
5. Develop a tectonic model for the EGP that matches the detrital and metamorphic zircon information

1.2 | Research Methodology

1.2.1 | Assessing the scales of equilibrium in granulites

In order to assess the scales of equilibrium in granulite facies rocks, a detailed

petrological investigation was carried out as a precursor to a series of phase equilibrium methods. Samples with diagnostic UHT assemblages were analysed using optical and electron microscopy, automated phase mapping and analysis of quantitative mineral chemistry. Key reaction textures and interpreted equilibrium volumes were observed and noted.
To test how domains in granulites with different bulk chemistry can equilibrate, the main driver of diffusion, chemical potential values of components were calculated on a model *P–T* path. The model *P–T* path used is one typical of a Proterozoic orogen; a high *T/P* (125 °C/GPa) prograde geothermal gradient followed by post peak decompression of 1 kbar. Melt extraction events were simulated and melt compositions were also calculated along the model *P–T* path.

Chemical potential diagrams were calculated at several post-peak points on the model *P–T* path. The topology of chemical potential diagrams, each calculated at a fixed *P–T*, depends on the position of that point relative to invariant points and univariant reactions in that chemical system. In turn, the phases that can be in equilibrium with each other at that *P–T* point will be stable at a point in chemical potential space (Figure 1.3). With a change in *P–T* the position of equilibria in chemical potential space changes, certain phases becoming stable at the expense of others, if diffusion is allowed to flatten chemical potneital gradients. In this manner, the changing position of equilibria in chemical potential space was used to predict the reaction textures that could grow as a result of local equilibrium along the model granulite *P–T* path.

1.2.2 | *P–T–time* evolution of granulties from Vizianagaram, Eastern Ghats Province

The petrological techniques described in section 1.2.1 were applied to two samples from a locality in the north-western region of the study area – Vizianagaram. The peak assemblages appear to vary on the centimetre scale. After detailed petrography, phase maps and quantitative mineral chemistry were used to calculate domainal bulk compositions for *P–T* pseudosections. Additionally, zircon and monazite U–Pb data from SHRIMP analyses were used to constrain the duration and timing of melt crystallization in the Vizianagaram granuliutes.

Combining the *P–T* and geochronological constraints, a tectonic model was found to match recent plate tectonic reconstructions from 1100-500 Ma.

1.2.3 | Terrane scale zircon geochronology in the Eastern Ghats Province

Metasedimentary samples from the Eastern Ghats Province were collected on a broad NE-SW section, known to have variable a variable detrital record and to have been subjected to at least one long lived metamorphic event with peak temperatures exceeding 900 °C.

Zircon grains were separated from the metasediments so that U–Pb isotopes and trace elements could be analysed using laser ablation split-stream (LASS) analysis. A clustering algorithm was applied to the dataset as an attempt to differentiate between populations of metamorphic, inherited igneous and modified zircon based on trace element chemistry.

The duration and temperature of metamorphism was constrained using U–Pb zircon ages and Ti-in-zircon thermometry respectively. An activity correction ($aTiO_2$) was calculated using the bulk composition of a representative khondalite from the EGP. The correction was applied as the analysed pelites do not always contain an accessory TiO_2 phase, in this case, rutile.

Using discrimination plots based on elemental ratios, as outlined by Grimes et al. (2012), inferences were made on the igneous protolith that crystallised inherited zircon before the first metamorphic event in the EGP. In conjunction with zircon U–Pb concordia and regression ages, feasible detrital sources for the EGP metasediments were assessed along with a likely tectonic precursor to UHT metamorphism.

1.3 | References

Ague, J. J., 1994, Mass transfer during Barrovian metamorphism of pelites, south-central Connecticut; I, Evidence for changes in composition and volume: American Journal of Science, v. 294, no. 8, p. 989-1057.

-, 1997, Crustal mass transfer and index mineral growth in Barrow's garnet zone, northeast Scotland: Geology, v. 25, no. 1, p. 73-76.

Ashwal, L. D., Tucker, R. D., and Zinner, E. K., 1999, Slow cooling of deep crustal granulites and Pb-loss in zircon: Geochimica et Cosmochimica

Acta, v. 63, no. 18, p. 2839-2851.

Baldwin, J., Powell, R., White, R., and Štípská, P., 2015, Using calculated chemical potential relationships to account for replacement of kyanite by symplectite in high pressure granulites: Journal of Metamorphic Geology, v. 33, no. 3, p. 311-330.

Beaumont, C., Jamieson, R. A., Nguyen, M. H., and Medvedev, S., 2004, Crustal channel flows: 1. Numerical models with applications to the tectonics of the Himalayan-Tibetan orogen: Journal of Geophysical Research B: Solid Earth, v. 109, no. 6, p. B06406 06401-06429.

Beaumont, C., Nguyen, M. H., Jamieson, R. A., and Ellis, S., 2006, Crustal flow modes in large hot orogens, in Law, R. D., Searle, M. P., and Godin, L., eds., Geological Society Special Publication, Volume 268, p. 91-145.

Bohlen, S. R., 1991, On the formation of granulites: Journal of Metamorphic Geology, v. 9, no. 3, p. 223-229.

Brown, M., 2007, Metamorphism, Plate Tectonics, and the Supercontinent Cycle: Earth Science Frontiers, v. 14, no. 1, p. 1-18.

Brown, M., Averkin, Y. A., McLellan, E. L., and Sawyer, E. W., 1995, Melt segregation in migmatites: Journal of Geophysical Research: Solid Earth, v. 100, no. B8, p. 15655-15679.

Brown, M., and Dallmeyer, R. D., 1996, Rapid Variscan exhumation and the role of magma in core complex formation: southern Brittany metamorphic belt, France: Journal of metamorphic Geology, v. 14, no. 3, p. 361-379.

Brown, M., and Johnson, T. E., 2018, Secular change in metamorphism and the onset of global plate tectonics: American Mineralogist.

Cavalcante, G. C. G., Viegas, G., Archanjo, C. J., and da Silva, M. E., 2016, The influence of partial melting and melt migration on the rheology of the continental crust: Journal of Geodynamics, v. 101, p. 186-199.

Cherniak, D., 2010, Diffusion in accessory minerals: zircon, titanite, apatite, monazite and xenotime: Reviews in Mineralogy and Geochemistry, v. 72, no. 1, p. 827-869.

Cherniak, D., and Watson, E., 2001, Pb diffusion in zircon: Chemical Geology, v. 172, no. 1-2, p. 5-24.

Cherniak, D. J., 2000, Pb diffusion in rutile: Contributions to Mineralogy and Petrology, v. 139, no. 2, p. 198-207.

Clark, C., Healy, D., Johnson, T., Collins, A. S., Taylor, R. J., Santosh, M., and Timms, N. E., 2015, Hot orogens and supercontinent amalgamation: A Gondwanan example from southern India: Gondwana Research, v. 28, no. 4, p. 1310-1328.

Clark, C., Taylor, R. J. M., Kylander-Clark, A. R. C., and Hacker, Bradley R., 2018, Prolonged (>100 Ma) ultra-high temperature metamorphism in the Napier Complex, East Antarctica: A petrochronological investigation of Earth's hottest crust: Journal of Metamorphic Geology, v. 36, no. 9, p. 1117-1139.

Clarke, G. L., Daczko, N., Klepeis, K., and Rushmer, T., 2005, Roles for fluid and/or melt advection in forming high-P mafic migmatites, Fiordland, New Zealand: Journal of Metamorphic Geology, v. 23, no. 7, p. 557-567.

Cochrane, R., Spikings, R. A., Chew, D., Wotzlaw, J.-F., Chiaradia, M., Tyrrell, S., Schaltegger, U., and Van der Lelij, R., 2014, High temperature (> 350 C) thermochronology and mechanisms of Pb loss in apatite: Geochimica et Cosmochimica Acta, v. 127, p. 39-56.

Collins, A. S., Kinny, P. D., and Razakamanana, T., 2012, Depositional age, provenance and metamorphic age of metasedimentary rocks from southern Madagascar: Gondwana Research, v. 21, no. 2-3, p. 353-361.

Collins, A. S., Kröner, A., Fitzsimons, I. C. W., and Razakamanana, T., 2003, Detrital footprint of the Mozambique ocean: U-Pb SHRIMP and Pb evaporation zircon geochronology of metasedimentary gneisses in eastern Madagascar: Tectonophysics, v. 375, no. 1-4, p. 77-99.

Collins, A. S., Santosh, M., Braun, I., and Clark, C., 2007, Age and sedimentary provenance of the Southern Granulites, South India: U-Th-Pb SHRIMP secondary ion mass spectrometry: Precambrian Research, v. 155, no. 1-2, p. 125-138.

Connolly, J. A. D., and Thompson, A. B., 1989, Fluid and enthalpy production during regional metamorphism: Contributions to Mineralogy and Petrology, v. 102, no. 3, p. 347-366.

Diener, J. F., and Powell, R., 2012, Revised activity-composition medels for clinopyroxene and amphibole: Journal of Metamorphic Geology, v. 30, no. 2, p. 131-142.

Diener, J. F., and Fagereng, Å., 2014, The influence of melting and melt drainage on crustal rheology during orogenesis: Journal of Geophysical Research: Solid Earth, v. 119, no. 8, p. 6193-6210.

Diener, J. F. A., White, R. W., and Powell, R., 2008, Granulite facies metamorphism and subsolidus fluid-absent reworking, Strangways Range, Arunta Block, central Australia: Journal of Metamorphic Geology, v. 26, no. 6, p. 603-622.

Dorfler, K. M., Caddick, M. J., and Tracy, R. J., 2015, Thermodynamic modeling of crustal melting using xenolith analogs from the Cortlandt Complex, New York, USA: Journal of Petrology, v. 56, no. 2, p. 389-408.

Doukkari, S. A., Diener, J. F. A., Ouzegane, K., Arab, A., Kienast, J. R., 2018, Mineral equilibrium modelling and calculated chemical potential relations of reaction textures in the ultrahigh temperature In Ouzzal terrane (In Hihaou area, Western Hoggar, Algeria): Journal of Metamorphic Geology, v. 36, no. 9, p. 276-286.

Fyfe, W. S., and Turner, F. J., 1966, Reappraisal of the metamorphic facies concept: Contributions to Mineralogy and Petrology, v. 12, no. 4, p. 354-364.

Green, E., White, R., Diener, J., Powell, R., Holland, T., and Palin, R., 2016, Activity–composition relations for the calculation of partial melting equilibria in metabasic rocks: Journal of Metamorphic Geology, v. 34, no. 9, p. 845-869.

Harley, S. L., 1989, The origins of granulites: A metamorphic perspective: Geological Magazine, v. 126, no. 3, p. 215-247.

-, 1998a, On the occurrence and characterization of ultrahigh-temperature crustal metamorphism, Geological Society Special Publication, Volume 138, p. 81-107.

-, 1998b, Ultra-high temperature granulite metamorphism (1050°C, 12 kbar) and decompression in garnet (Mg70) - orthopyroxene-sillimanite gneisses from the Rauer Group, East Antarctica: Journal of Metamorphic Geology, v. 16, no. 4, p. 541-562.

-, 2008, Refining the P-T records of UHT crustal metamorphism: Journal of Metamorphic Geology, v. 26, no. 2, p. 125-154.

-, 2016, A matter of time: The importance of the duration of UHT

metamorphism: Journal of Mineralogical and Petrological Sciences, v. 111, no. 2, p. 50-72.

Harley, S. L., and Kelly, N. M., 2007, Zircon: Tiny but timely: Elements, v. 3, no. 1, p. 13-18.

Harley, S. L., Kelly, N. M., and Möller, A., 2007, Zircon behaviour and the thermal histories of moutain chains: Elements, v. 3, no. 1, p. 25-30.

Harley, S. L., and Nandakumar, V., 2016, New evidence for Palaeoproterozoic high grade metamorphism in the Trivandrum Block, Southern India: Precambrian Research, v. 280, p. 120-138.

Hermann, J., Rubatto, D., Korsakov, A., and Shatsky, V. S., 2001, Multiple zircon growth during fast exhumation of diamondiferous, deeply subducted continental crust (Kokchetav Massif, Kazakhstan): Contributions to Mineralogy and Petrology, v. 141, no. 1, p. 66-82.

Hobbs, B. E., Ord, A., and Regenauer-Lieb, K., 2011, The thermodynamics of deformed metamorphic rocks: a review: Journal of Structural Geology, v. 33, no. 5, p. 758-818.

Hokada, T., and Harley, S. L., 2004, Zircon growth in UHT leucosome: Constraints from zircon-garnet rare earth elements (REE) relations in Napier Complex, East Antarctica: Journal of Mineralogical and Petrological Sciences, v. 99, no. 4, p. 180-190.

Holland, T. J. B., and Powell, R., 1990, An enlarged and updated internally consistent thermodynamic dataset with uncertainties and correlations: the system K2O–Na2O–CaO–MgO–MnO–FeO–Fe2O3–Al2O3–TiO2–SiO2–C–H2–O2: Journal of Metamorphic Geology, v. 8, no. 1, p. 89-124.

-, 1990, An enlarged and updated internally consistent thermodynamic dataset with uncertainties and correlations: the system K2O–Na2O–CaO–MgO–MnO–FeO–Fe2O3–Al2O3–TiO2–SiO2–C–H2–O2: Journal of Metamorphic Geology, v. 8, no. 1, p. 89-124.

-, 2001, Calculation of phase relations involving haplogranitic melts using an internally consistent thermodynamic dataset: Journal of Petrology, v. 42, no. 4, p. 673-683.

-, 2003, Activity–composition relations for phases in petrological calculations: an asymmetric multicomponent formulation: Contributions to

Mineralogy and Petrology, v. 145, no. 4, p. 492-501.

-, 2011, An improved and extended internally consistent thermodynamic dataset for phases of petrological interest, involving a new equation of state for solids: Journal of Metamorphic Geology, v. 29, no. 3, p. 333-383.

Johnson, T. E., Gibson, R. L., Brown, M., Buick, I. S., and Cartwright, I., 2003, Partial melting of metapelitic rocks beneath the Bushveld Complex, South Africa: Journal of Petrology, v. 44, no. 5, p. 789-813.

Kelly, N. M., and Harley, S. L., 2005, An integrated microtextural and chemical approach to zircon geochronology: Refining the Archaean history of the Napier Complex, east Antarctica: Contributions to Mineralogy and Petrology, v. 149, no. 1, p. 57-84.

Kelsey, D. E., 2008, On ultrahigh-temperature crustal metamorphism: Gondwana Research, v. 13, no. 1, p. 1-29.

Kelsey, D. E., Clark, C., and Hand, M., 2008, Thermobarometric modelling of zircon and monazite growth in melt-bearing systems: Examples using model metapelitic and metapsammitic granulites: Journal of Metamorphic Geology, v. 26, no. 2, p. 199-212.

Kelsey, D. E., and Hand, M., 2015, On ultra-high temperature crustal metamorphism: Phase equilibria, trace element thermometry, bulk composition, heat sources, timescales and tectonic settings: Geoscience Frontiers, v. 6, no. 3, p. 311-356.

Kelsey, D. E., and Powell, R., 2011, Progress in linking accessory mineral growth and breakdown to major mineral evolution in metamorphic rocks: A thermodynamic approach in the Na 2O-CaO-K 2O-FeO-MgO-Al 2O 3-SiO 2-H 2O-TiO 2-ZrO 2 system: Journal of Metamorphic Geology, v. 29, no. 1, p. 151-166.

Korhonen, F. J., Brown, M., Clark, C., and Bhattacharya, S., 2013a, Osumilite-melt interactions in ultra-high temperature granulites: Phase equilibria modelling and implications for the P-T-t evolution of the eastern ghats province, india: Journal of Metamorphic Geology, v. 31, no. 8, p. 881-907.

Korhonen, F. J., Clark, C., Brown, M., Bhattacharya, S., and Taylor, R., 2013b, How long-lived is ultra-high temperature (UHT) metamorphism? Constraints from zircon and monazite geochronology in the Eastern Ghats orogenic belt, India: Precambrian Research, v. 234, p. 322-350.

Korzhinskiĭ, D. S., 1959, Physicochemical basis of the analysis of the paragenesis of minerals, Consultants Bureau.

Kusiak, M. A., Whitehouse, M. J., Wilde, S. A., Dunkley, D. J., Menneken, M., Nemchin, A. A., and Clark, C., 2013, Changes in zircon chemistry during archean UHT metamorphism in the Napier Complex, Antarctica: American Journal of Science, v. 313, no. 9, p. 933-967.

Mezger, K., Rawnsley, C., Bohlen, S., and Hanson, G., 1991, U-Pb garnet, sphene, monazite, and rutile ages: implications for the duration of high-grade metamorphism and cooling histories, Adirondack Mts., New York: The Journal of Geology, v. 99, no. 3, p. 415-428.

Mitchell, R. J., Johnson, T. E., Clark, C., Gupta, S., Brown, M., Harley, S. L., and Taylor, R., 2019, Neoproterozoic evolution and Cambrian reworking of ultra-high temperature granulites in the Eastern Ghats Province, India: Journal of Metamorphic Geology.

Möller, A., Mezger, K., and Schenk, V., 2000, U-Pb dating of metamorphic minerals: Pan-African metamorphism and prolonged slow cooling of high pressure granulites in Tanzania, East Africa: Precambrian Research, v. 104, no. 3-4, p. 123-146.

Plavsa, D., Collins, A. S., Foden, J. F., Kropinski, L., Santosh, M., Chetty, T. R. K., and Clark, C., 2012, Delineating crustal domains in Peninsular India: Age and chemistry of orthopyroxene-bearing felsic gneisses in the Madurai Block: Precambrian Research, v. 198-199, p. 77-93.

Plavsa, D., Collins, A. S., Payne, J. L., Foden, J. D., Clark, C., and Santosh, M., 2014, Detrital zircons in basement metasedimentary protoliths unveil the origins of southern India: Bulletin of the Geological Society of America, v. 126, no. 5-6, p. 791-812.

Powell, R., Evans, K., Green, E., and White, R., 2018, On equilibrium in non-hydrostatic metamorphic systems: Journal of Metamorphic Geology, v. 36, no. 4, p. 419-438.

Roberts, N. M., and Spencer, C. J., 2015, The zircon archive of continent formation through time: Geological Society, London, Special Publications, v. 389, no. 1, p. 197-225.

Rosenberg, C., and Handy, M., 2005, Experimental deformation of partially melted granite revisited: implications for the continental crust: Journal of metamorphic Geology, v. 23, no. 1, p. 19-28.

Rubatto, D., 2002, Zircon trace element geochemistry: Partitioning with garnet and the link between U-Pb ages and metamorphism: Chemical Geology, v. 184, no. 1-2, p. 123-138.

Rubatto, D., and Hermann, J., 2007, Experimental zircon/melt and zircon/garnet trace element partitioning and implications for the geochronology of crustal rocks: Chemical Geology, v. 241, no. 1-2, p. 38-61.

Rubatto, D., and Hermann, J. r., 2001, Exhumation as fast as subduction?: Geology, v. 29, no. 1, p. 3-6.

Rubatto, D., Williams, I. S., and Buick, I. S., 2001, Zircon and monazite response to prograde metamorphism in the Reynolds Range, central Australia: Contributions to Mineralogy and Petrology, v. 140, no. 4, p. 458-468.

Rudnick, R. L., and Fountain, D. M., 1995, Nature and composition of the continental crust: A lower crustal perspective: Reviews of Geophysics, v. 33, no. 3, p. 267-309.

Sandiford, M., and Powell, R., 1986, Deep crustal metamorphism during continental extension: modern and ancient examples: Earth and Planetary Science Letters, v. 79, no. 1-2, p. 151-158.

Sawyer, E., 1996, Melt segregation and magma flow in migmatites: implications for the generation of granite magmas: Earth and Environmental Science Transactions of the Royal Society of Edinburgh, v. 87, no. 1-2, p. 85-94.

-, 2010, Migmatites formed by water-fluxed partial melting of a leucogranodiorite protolith: Microstructures in the residual rocks and source of the fluid: Lithos, v. 116, no. 3-4, p. 273-286.

Schorn, S., and Diener, J., 2017, Details of the gabbro-to-eclogite transition determined from microtextures and calculated chemical potential relationships: Journal of Metamorphic Geology, v. 35, no. 1, p. 55-75.

Schorn, S., Diener, J. F., Powell, R., and Stüwe, K., 2018, Thermal buffering in the orogenic crust: Geology, v. 46, no. 7, p. 643-646.

Scibiorski, E., Tohver, E., and Jourdan, F., 2015, Rapid cooling and exhumation in the western part of the Mesoproterozoic Albany-Fraser Orogen, Western Australia: Precambrian Research, v. 265, p. 232-248.

Sizova, E., Gerya, T., and Brown, M., 2014, Contrasting styles of

Phanerozoic and Precambrian continental collision: Gondwana Research, v. 25, no. 2, p. 522-545.

Spear, F. S., and Parrish, R. R., 1996, Petrology and cooling rates of the Valhalla complex, British Columbia, Canada: Journal of Petrology, v. 37, no. 4, p. 733-765.

Stevens, G., and Clemens, J., 1993, Fluid-absent melting and the roles of fluids in the lithosphere: a slanted summary?: Chemical Geology, v. 108, no. 1-4, p. 1-17.

Štípská, P., Powell, R., White, R., and Baldwin, J., 2010, Using calculated chemical potential relationships to account for coronas around kyanite: an example from the Bohemian Massif: Journal of Metamorphic Geology, v. 28, no. 1, p. 97-116.

Stüwe, K., 1995, Thermal buffering effects at the solidus. Implications for the equilibration of partially melted metamorphic rocks: Tectonophysics, v. 248, no. 1-2, p. 39-51.

Taylor, R. J. M., Clark, C., Harley, S. L., Kylander-Clark, A. R. C., Hacker, B. R., and Kinny, P. D., 2017, Interpreting granulite facies events through rare earth element partitioning arrays: Journal of Metamorphic Geology, v. 35, no. 7, p. 759-775.

Taylor, R. J. M., Harley, S. L., Hinton, R. W., Elphick, S., Clark, C., and Kelly, N. M., 2015, Experimental determination of REE partition coefficients between zircon, garnet and melt: A key to understanding high-T crustal processes: Journal of Metamorphic Geology, v. 33, no. 3, p. 231-248.

Taylor, R. J. M., Kirkland, C. L., and Clark, C., 2016, Accessories after the facts: Constraining the timing, duration and conditions of high-temperature metamorphic processes: Lithos, v. 264, p. 239-257.

Vanderhaeghe, O., and Teyssier, C., 2001, Partial melting and flow of orogens: Tectonophysics, v. 342, no. 3-4, p. 451-472.

Vry, J. K., and Baker, J. A., 2006, LA-MC-ICPMS Pb-Pb dating of rutile from slowly cooled granulites: Confirmation of the high closure temperature for Pb diffusion in rutile: Geochimica et Cosmochimica Acta, v. 70, no. 7, p. 1807-1820.

Watson, E. B., Harrison, T. M., and Ryerson, F. J., 1985, Diffusion of Sm, Sr, and Pb in fluorapatite: Geochimica et Cosmochimica Acta, v. 49, no.

8, p. 1813-1823.

White, R. W., and Powell, R., 2002, Melt loss and the preservation of granulite facies mineral assemblages: Journal of Metamorphic Geology, v. 20, no. 7, p. 621-632.

-, 2010, Retrograde melt-residue interaction and the formation of near-anhydrous leucosomes in migmatites: Journal of Metamorphic Geology, v. 28, no. 6, p. 579-597.

-, 2011, On the interpretation of retrograde reaction textures in granulite facies rocks: Journal of Metamorphic Geology, v. 29, no. 1, p. 131-149.

White, R. W., Powell, R., and Baldwin, J. A., 2008, Calculated phase equilibria involving chemical potentials to investigate the textural evolution of metamorphic rocks: Journal of Metamorphic Geology, v. 26, no. 2, p. 181-198.

White, R. W., Powell, R., and Holland, T. J. B., 2007, Progress relating to calculation of partial melting equilibria for metapelites: Journal of Metamorphic Geology, v. 25, no. 5, p. 511-527.

White, R. W., Powell, R., Holland, T. J. B., Johnson, T. E., and Green, E. C. R., 2014, New mineral activity-composition relations for thermodynamic calculations in metapelitic systems: Journal of Metamorphic Geology, v. 32, no. 3, p. 261-286.

Yakymchuk, C., and Brown, M., 2014, Behaviour of zircon and monazite during crustal melting: Journal of the Geological Society, v. 171, no. 4, p. 465-479.

Chapter 2 | Controls on the scales of equilibrium during granulite facies metamorphism

Ruairidh J. Mitchell[1,2], Tim E. Johnson[1,3], Katy Evans[1], Saibal Gupta[2], Chris Clark[1]

[1]School of Earth and Planetary Sciences, The Institute for Geoscience Research, Curtin University, Perth, WA 6102, Australia.

[2]Department of Geology and Geophysics, Indian Institute of Technology Kharagpur, Kharagpur, India.

[3]State Key Laboratory for Geological Processes and Mineral Resources and Center for Global Tectonics, School of Earth Sciences, China University of Geosciences, Wuhan 430074, China.

Abstract

Phase equilibrium modelling is commonly employed to constrain the pressure–temperature (*P–T*) evolution of granulite facies rocks, from which their geodynamic setting may be inferred. However, defining a suitable equilibrium volume in such rocks is non-trivial due to heterogeneities in protolith composition and open system behaviour, including melt loss or gain and deformation. Consequently, equilibrium volumes and the mineral assemblages they contain may vary both temporally and spatially within a single rock. Additionally, despite the extreme temperatures they attained, granulites commonly contain microtextures indicative gradients in chemical potential after the metamorphic peak. This study assesses the processes that control compositional heterogeneity between equilibrium volumes in a suprasolidus granulite and the consequences for the development of a range of microstructures. An approach combining phase equilibrium forward modelling and chemical potential diagrams is used to simulate the suprasolidus evolution of two adjacent equilibrium volumes in an Mg-rich metapelite. Assuming equilibrium within the two compositional domains, evolving granulite facies assemblages vary along a high *T/P* (125 °C/kbar) clockwise *P–T* path representative of a high *T/P* metamorphic terrane. Many retrograde microtextures in metapelitic rocks can be reproduced by considering chemical potential (μ) gradients in μ_{MgO}, μ_{FeO} and μ_{CaO} between phases, assuming (i) the presence of melt on grain boundaries, (ii) that Al_2O_3 is perfectly immobile and (iii) that K_2O and Na_2O are perfectly mobile. Additionally, documented microtextures in granulites imply local SiO_2-undersaturation, despite the presence of matrix quartz in the rock. Preserving such chemical potential gradients requires that solid phases are chemically and physically isolated from melt. Efficient prograde melt drainage may lead to a loss in melt interconnectivity at high–*T*

(>900 °C), meaning that equilibration of cm-scale compositional domains is controlled by solid-state diffusion. The presence of isolated pockets of viscous melt allows the formation of discontinuous intergranular reaction microtextures.

2.1 | Introduction

Phase equilibrium modelling has become the tool of choice in constraining the pressure-–temperature (*P–T*) conditions of metamorphism. This method uses calculated phase equilibria based on the composition of a fixed volume of rock assumed to have attained equilibrium. In granulite facies rocks, most of which reached peak temperatures in excess of 750 °C, equilibrium volumes are commonly assumed to be large, and the effective bulk composition is taken to be the measured bulk rock composition of an entire hand specimen or thin section. However, the presence of peak phase assemblages (Figure 2.1) and/or mineral compositions that vary over much smaller length scales (Dorfler, Caddick, & Tracy, 2015; Harley, 1998; Johnson, Gibson, Brown, Buick, & Cartwright, 2003; Mitchell et al., 2019), and the existence of reaction microstructures such as coronae or symplectites (Figure 2.2) (Doukkari, Diener, Ouzegane, & Kienast, 2018; Droop & Bucher-Nurminen, 1984; Harley, 1989; Kelsey et al., 2017; Štípská, Powell, White, & Baldwin, 2010; White & Powell, 2011; White, Powell, & Baldwin, 2008), suggest that a simple assumption of equilibrium over large length scales may be misplaced.

The existence of chemical potential gradients is not necessarily incompatible with an assumption of equilibrium. Equilibrium typically applies over some

Figure 2.1 | Phase map of sample EGB-09-47a (Mitchell et al., 2019) showing domains 47-a (X(Mg)=0.54) and 47-b (X(Mg)=0.61), each with a different inferred peak assemblage despite reaching UHT conditions.

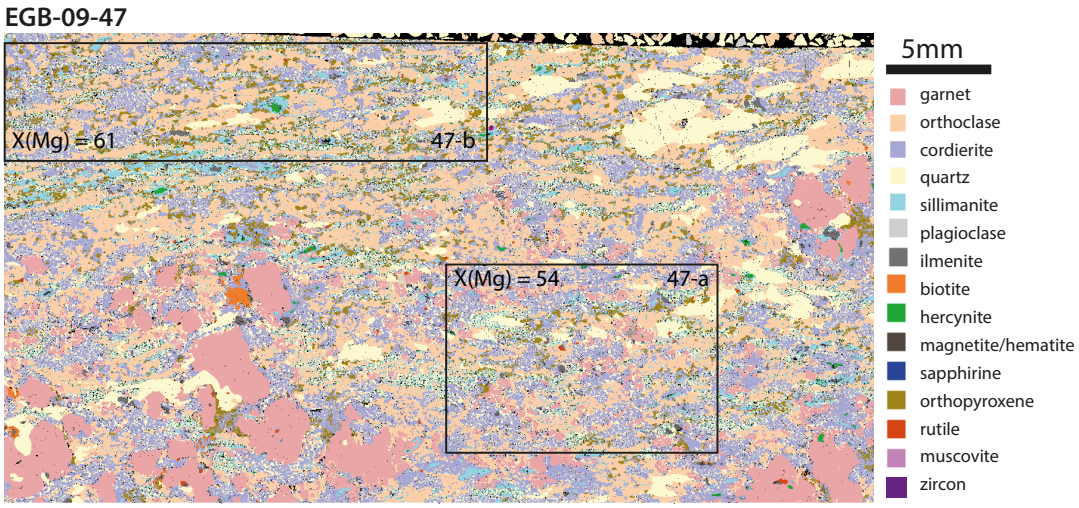

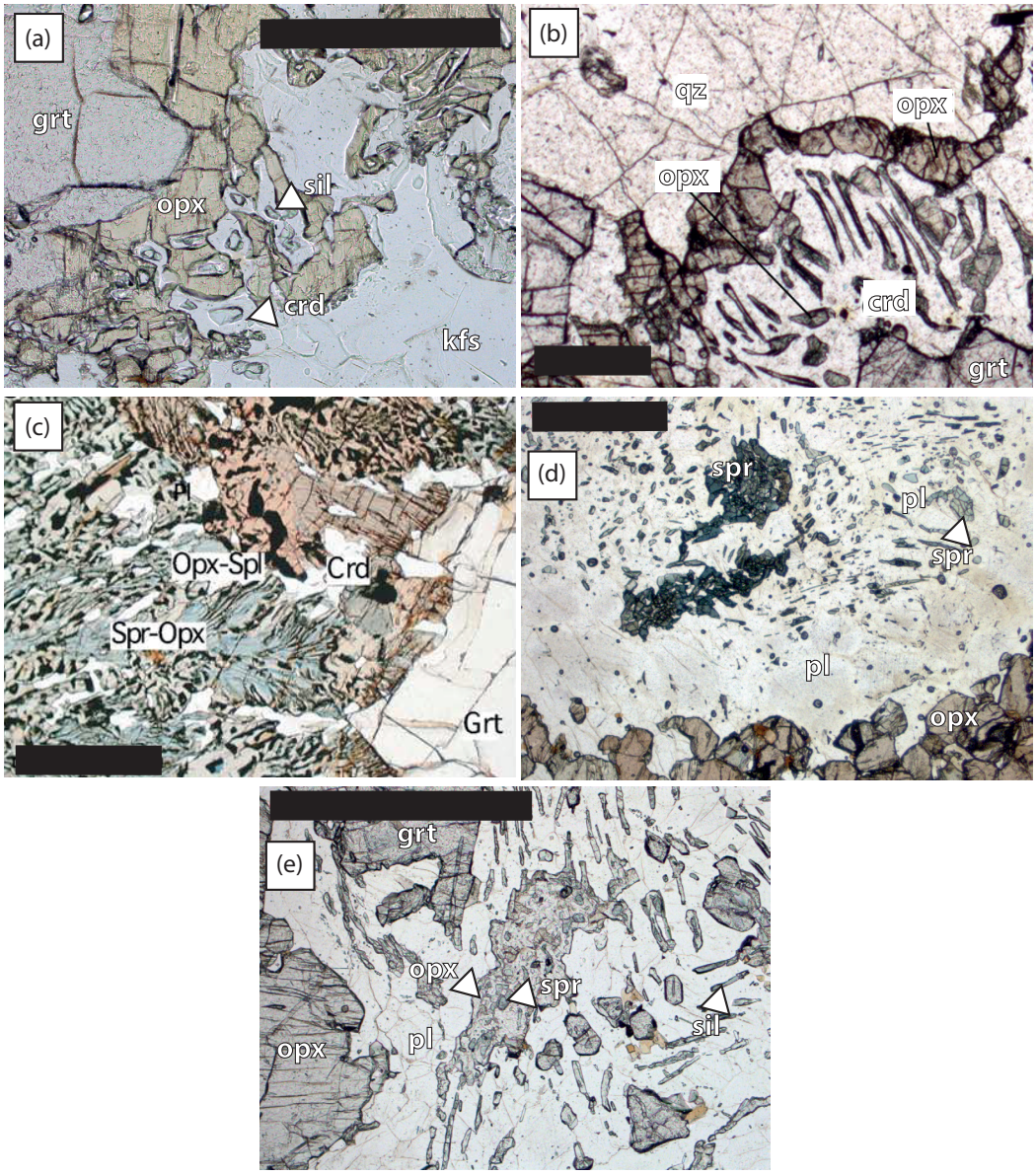

Figure 2.2 | Representative post-peak decompression reaction microtextures in pelites. Photomicrographs taken from the literature (a-f) or of samples from the Eastern Ghats Province, India; (d-e). All scale bars are 1mm. (a) Garnet replaced by orthopyroxene, sillimanite and cordierite in the absence of quartz (Mitchell et al., 2019). (b) Orthopyroxene-cordierite symplectite replacing garnet, surrounded by an orthopyroxene moat in equilibrium with a quartz matrix (Doukkari et al., 2018). (c) Sapphirine-orthopyroxene and spinel orthopyroxene intergrowths replacing garnet, absent from quartz (Sajeev et al., 2004). (d) Sapphirine-plagioclase intergrowths which have replaced garnet, surrounded by a moat of orthopyroxene. (e) Garnet replaced by a complex texture comprising orthopyroxene, sapphirine, plagioclase and sillimanite. A plagioclase and orthopyroxene moat isolates the texture from the quartz matrix (outside the field of view).

length scale that will vary based on the diffusivity of the component in question, no matter if it is part of a larger overall chemical potential profile. This is the core tenet of the local (mosaic) equilibrium principle (Korzhinskiĭ,

1959), in that a phase or phase assemblage that appears to reflect a gradient in chemical potential can be assumed to be in equilibrium at a scale where the chemical potential profile is flat (Powell, Evans, Green, & White, 2018).

This concept of local equilibrium can be usefully applied to investigate granulites that contain compositional heterogeneities that are primary, such as sedimentary or igneous layering, or secondary, due to mass transfer resulting from melt loss or deformation, and which influence phase equilibria on a centimetre or smaller scale (Ague, 1994, 1997; Hobbs, Ord, & Regenauer-Lieb, 2011). Regardless of the processes responsible for the heterogeneities, isochemical phase diagrams (pseudosections) based on whole-rock compositions may to fail to reproduce one or more of the stable assemblages (Mitchell et al., 2019).

An assumption of local equilibrium can also be used to predict stable phases in the complex reaction microtextures that are common in granulite facies rocks (Korzhinskiĭ, 1959; Powell et al., 2018; Štípská et al., 2010; White & Powell, 2011; White et al., 2008). This approach considers the phase assemblages stabilised by transient chemical potential gradients between neighbouring phases with a change in *P* and/or *T*. Several studies have attempted to model the development of reaction textures in high-grade metamorphic rocks using calculated chemical potential (μ) relationships based on crossing of univariant equilibria (discontinuous reactions) in simplified chemical systems (Baldwin, Powell, White, & Štípská, 2015; Doukkari et al., 2018; Schorn & Diener, 2017; Štípská et al., 2010; White & Powell, 2011; White et al., 2008).

In this study, we investigate a sample of UHT granulite preserving small-scale compositional heterogeneities using an assumption of local equilibrium (Figure 2.1) to understand the chemical potential profiles, and the consequences of exchange of chemical species as a function of P, T, composition and availability of melt. We calculate how mineral modes evolve in two discrete compositional domains within a UHT granulite (Table 1) along a representative high T/P clockwise *P–T* path (Brown & Johnson, 2018). The model simulates partial melting and melt loss for the two protolith compositions, for which chemical potentials of all chemical components were calculated along the model *P–T* path. Using calculated melt compositions along the *P–T* path, melt viscosities were calculated using the calibration of Holtz et al. (1999). The differences were then used to assess variations in the

exchange of chemical species and melt availability.

Next, we use an assumption of local equilibrium on a smaller (>1 mm) scale to model the development of common microtextures in metapelitic granulites (Figure 2.2) related to garnet breakdown. We use calculated chemical potential diagrams appropriate to the post-peak supersolidus portion of the model *P–T* path. The topology and predicted phase assemblages of the chemical potential diagrams are compared to microtextures observed in a range of residual granulites inferred to have followed a similar *P–T* trajectory (Harley, 1989, 2008; Kelsey, 2008; Kelsey & Hand, 2015), with implication for processes related to their preservation.

This aims of this work are twofold. Firstly, to build on the principles and observations of local equilibrium stated above that are widely understood (Baldwin et al., 2015; Doukkari et al., 2018; Powell et al., 2018; Schorn & Diener, 2017; Štípská et al., 2010; White & Powell, 2011; White et al., 2008) by providing specific chemical potential constraints on the development of cm-scale compositional heteregoneities and retrograde reaction microtextures in UHT granulite. Secondly, informed by melt viscosity calculations, this paper aims to propose a mechanism that allows the preservation of local equilibrium on the centimetre scale and reaction microtextures.

2.2 | Methods

2.2.1 | Phase equilibrium forward modelling

Phase equilibria were calculated in the chemical system NCKFMASHTO using THERMOCALC 3.45 and the internally consistent thermodynamic dataset ds62 (Holland & Powell, 2011) using the solution models for biotite, garnet, cordierite, orthopyroxene, silicate melt, ternary feldspar, ilmenite from White, Powell, Holland, Johnson, and Green (2014), sapphirine from Wheller and Powell (2014) and spinel from White, Powell, and Clarke (2002). In order to simulate the suprasolidus evolution of adjacent compositional domains within an Mg-rich metapelite (sample EGB-09-47; Figure 2.1) from the Eastern Ghats, India, the phase diagrams are based on an average amphibolite facies metapelite (Ague, 1994) with an adjusted X(Mg) (atomic MgO/(MgO + FeO)) and a constant A/AFM (atomic Al2O3/(Al2O3+MgO + FeO)). An X(Mg) of 0.54 corresponds to domain 47-a within sample EGB-09-47 (Figure 2.1), and a higher X(Mg) of 0.61 corresponds to domain

47-b (Figure 2.1, Table 2.1). For both compositions, H_2O concentrations were initially set to produce minimal H_2O-saturated melt on crossing the solidus along the modelled *P–T* path. The modelled *P–T* path (Figure 2.3) is clockwise, for which the prograde path follows a thermal gradient of 125 °C/kbar, typical of Proterozoic UHT metamorphic terranes (Brown & Johnson, 2018), reaching peak *P–T* conditions of 1000 °C, 7.6 kbar. The evolution from peak *P–T* comprises a segment of isothermal decompression to 7 kbar, followed by decompression and cooling to 950 °C, 6.5 kbar, or until the residual solidus (not shown here) is crossed (Figure 2.3).

Along this path, a melt extraction (ME) event is imposed whenever the melt mode reaches 7 mol.% (~7 vol.%, the percolation threshold of Rosenburg & Handy, 2005), at which point 6 mol.% is extracted and a new (residual) bulk composition is calculated. To investigate which components must be mobile to achieve equilibrium between the two bulk rock compositions, chemical potential values for all of the components of the system NCKFMASHTO were calculated along the modelled *P–T* path (Figure 2.3).

2.2.2 | Chemical potential diagrams

Chemical potential diagrams are a means of investigating the phase assemblages that make up the microstructures that develop in metamorphic rocks due to stranded chemical potential gradients (Baldwin et al., 2015; Doukkari et al., 2018; Schorn & Diener, 2017; Štípská et al., 2010; White & Powell, 2011; White et al., 2008). Like petrogenetic grids and pseudosections, quantitative chemical potential diagrams can be calculated, and provide a powerful means of visualising the effects of chemical potential gradients between, for example, grain boundaries, triple junctions or between porphyroblasts and matrix. A series of *P–T* petrogenetic grids were drawn in the same chemical systems and using the same fixed variables as the chemical potential diagrams to show which univariant reactions are crossed along the model *P–T* path (Figures S1 and S2).

Visualisation of phase relations in chemical potential space practically

Table 2.1 | Starting compositions for the forward modelling of 47-a (X(Mg)=0.54) and 47-b (X(Mg)=0.61) over the *P–T* path shown in Figure 2.3.

mol %	H2O	SiO2	Al2O3	CaO	MgO	FeO	K2O	Na2O	TiO2	O	X(Mg)
47-a	5.81	60.76	12.84	1.50	6.88	5.86	2.77	1.89	0.85	0.83	54
47-b	5.82	61.00	12.89	1.50	7.66	4.90	2.78	1.89	0.86	0.70	61

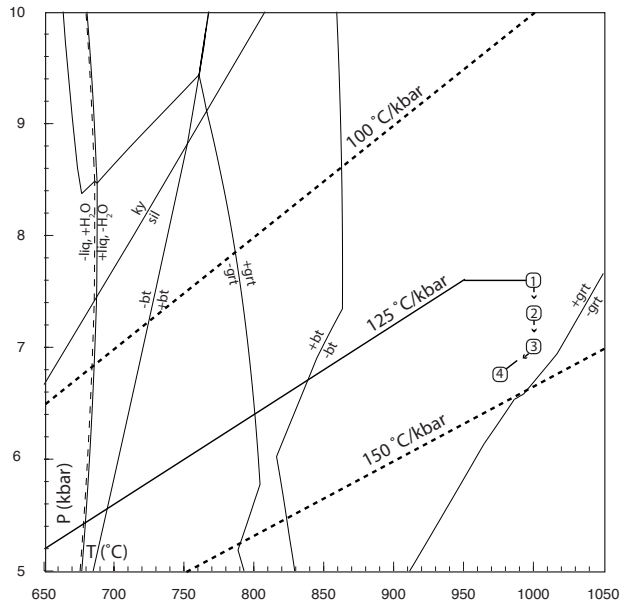

Figure 2.3 | *P–T* path with a 125 °C/kbar thermal gradient used for phase equilibrium forward modelling. Major phase boundaries and H2O saturated solidus for an average metapelite (Ague, 1991) are labelled. Chemical potential diagrams were calculated at points 1-3. Point 4 and 5 represent the residual solidus on the retrograde *P–T* path for 47-a and 47-b starting compositions

requires a simplification of the model system under consideration (here NCKFMASHTO), so that effectively univariant lines in μ–μ space (which are divariant equilibria in the system of interest) may be calculated that are appropriate to the development of the mineral associations and microstructures under consideration. Further, it is convenient to further reduce the simplified system to two 'controlling' components whose chemical potentials are allowed to vary (White et al., 2008) by considering the other components as either perfectly mobile (i.e. with diffusion rates that are effectively infinitely fast), or perfectly immobile (i.e. with diffusion rates that are effectively zero). Although clearly a simplification, examples of perfectly mobile components might be H_2O and K_2O whereas, in many instances, Al_2O_3 may be considered to be perfectly immobile. The basis of the construction and interpretation of chemical potential phase diagrams is provided by White et al. (2008) and references therein. We describe below the approach specific to this study.

In all chemical potential diagrams, the calcmu and setmu scripts in THERMOCALC 3.45 were used to calculate chemical potential diagrams at *P–T* points 1 to 3 in Figure 2.3 to simulate the development of reaction microstructures along a path from the *P–T* peak at 1000 °C, 7.6 kbar along

an isothermal decompression path to 1000 °C, 7.0 kbar (points 1 to 3), then along a path involving cooling and decompression to 950 °C, 6.5 kbar (points 3 to 4), thereafter cooling until encountering an elevated (residual) solidus. The chemical potential diagrams were calculated for corundum-absent equilibria in the NCKFMASH chemical system for textures involving plagioclase, and in the NKFMASH system for those not involving plagioclase. In both systems, K_2O and Na_2O are considered to be perfectly mobile, with values of μ_{K2O} and μ_{Na2O} fixed at the values calculated for the appropriate composition at the given *P–T* conditions. Silicate melt is assumed to be in excess to simulate the local availability of melt on grain boundaries.

In NKFMASH, assuming quartz and silicate melt to be in excess, the system is reduced to three components Al_2O_3, FeO and MgO. Considering Al_2O_3 to be perfectly immobile leaves μ_{MgO} and μ_{FeO} as the variables to be plotted (the 'controlling' components). In order to model SiO_2-undersaturated systems, for example where a reaction texture is interpreted to have become chemically isolated from a quartzofeldspathic matrix, quartz can no longer be considered in excess. In these cases, calculated divariant and trivariant equilibria below the SiO_2-saturation surface (White & Powell, 2008) contain an additional phase in place of quartz. In the NKFMASH diagrams, phases are always in equilibrium with silicate melt at the fixed μK2O and μ_{Na2O} values. In addition to excess melt, a point represents four phases in equilibrium, a line three and a field only two. For SiO_2-saturated equilibria (black lines in all diagrams), one of the phases is always quartz. For SiO2-undersaturated equilibria (red lines in all diagrams), another phase is stable instead of quartz.

In NCKFMASH, the chemical system used to examine reaction textures that contain plagioclase, μ_{K2O} and μ_{Na2O} are fixed. In these scenarios, with quartz and silicate liquid in excess, μCaO and μMgO are chosen the controlling components. Quartz-absent equilibria were calculated using the same method as described previously. In the NCKFMASH diagrams, phases are assumed to exist in equilibrium with silicate melt at the fixed μ_{K2O} and μ_{Na2O} values. In addition to excess melt, a point represents five phases in equilibrium, a line four and a field three. For SiO_2-saturated equilibria (black lines in all diagrams), one of the phases is always quartz. For SiO_2-undersaturated equilibria (red lines in all diagrams), another phase is stable instead of quartz.

In both the NKFMASH and NCKFMASH diagrams, the SiO_2-undersaturated equilibria project onto different values of μSiO_2. Therefore, in all diagrams, a SiO2-undersaturated assemblage stable in a field in μ_{MgO}–μ_{FeO} or μ_{MgO}–μ_{CaO} space may be in equilibrium with the SiO_2-saturated assemblage it shares the field with.

2.3 | Results

2.3.1 | Forward modelling

Modelled phase assemblages for 47-a and –b starting compositions

For the starting composition with X(Mg) = 0.54 (47-a) at temperatures above the H2O-saturated (wet) solidus, melt is mostly generated via the breakdown of hydrous phases biotite, muscovite and cordierite. Melt extraction (ME) events are modelled where melt modes reach 7 mol.%, at which point 6 mol.% melt is extracted (Figure 2.4a). Melt extraction (ME) events ME1 and ME2 occur as free H_2O vapour and muscovite are consumed at ~680 °C. Thereafter, the mode of biotite decreases – related to its breakdown to garnet, K-feldspar and melt – between ~800 and 855 °C. Sufficient melt is

Figure 2.4 | Modeboxes calculated over the *P–T* path shown in Figure 2.1. Mineral and melt modes calculated using starting compisitions based on (a) domains 47-a (X(Mg)=0.54) and (b) 47-b (X(Mg)=0.61); see Table 1. Melt extraction events are labelled ME1-8 for each calculation, along with *P–T* points 1-4.

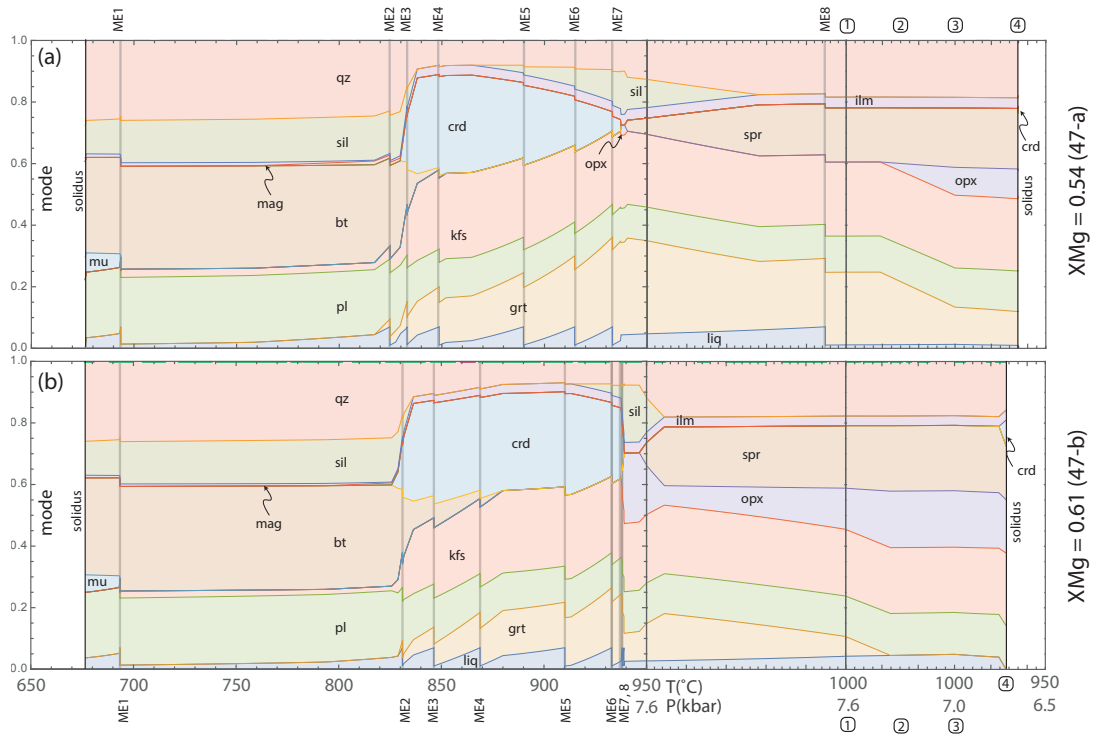

produced by biotite breakdown to reach the extraction threshold three times (ME2–4). Cordierite (>30 mode %) is produced as biotite is lost at ~850 °C. Cordierite mode decreases after ME4, replaced by sillimanite, garnet and melt up to ~930 °C, and by orthopyroxene at ~940 °C. Melt extraction events ME5–7 are modelled between ~890 °C and ~930 °C concurrent with cordierite breakdown. Above ~940 °C, orthopyroxene and sillimanite are replaced by sapphirine and quartz. Orthopyroxene is not stable above ~940 °C on the prograde path, however sillimanite persists to near-peak conditions of 980 °C, 7.6 kbar. The final melt extraction event occurs at ~995 °C, at which point the metamorphic assemblage of melt–garnet–sapphirine–K–feldspar–plagioclase–quartz–ilmenite does not change further until peak conditions of 1000 °C, 7.6 kbar are attained. During retrograde isothermal decompression, the modes of garnet decrease, to be replaced by sapphirine and orthopyroxene. Late cordierite stabilizes as the final vestiges of melt crystallise just above the solidus, to produce the assemblage garnet–sapphirine–orthopyroxene–cordierite–K-feldspar–plagioclase–quartz–ilmenite at 965 °C and 6.65 kbar.

There are several differences in the evolution of the X(Mg) = 0.61 (47-b; Figure 2.4b) composition compared to the less magnesian composition based on 47-a (Figure 2.4a). ME1 is modelled at ~690 °C as a result of the breakdown of muscovite. Thereafter, the breakdown of biotite and sillimanite produce garnet, cordierite, K-feldspar and melt between ~830 °C and ~880 °C that give rise to ME2–4. Four further melt extraction events, ME5–8, result from the breakdown of cordierite and garnet to form orthopyroxene and sillimanite at ~910–940 °C. Sillimanite becomes unstable at ~955 °C, 7.6 kbar, with the formation of sapphirine, and the assemblage melt–garnet–orthopyroxene–sapphirine–K-feldspar–plagioclase–quartz–ilmenite persists until peak conditions at 1000 °C, 7.6 kbar. Isobaric decompression leads to the disappearance of garnet and formation of additional orthopyroxene at 1000 °C, 7.3 kbar. Immediately before crossing of the elevated solidus, at 971 °C, 6.71 kbar, the assemblage is melt–orthopyroxene–sapphirine–cordierite–K-feldspar–plagioclase–quartz–ilmenite.

The 47-a and 47-b starting compositions produce different assemblages that are diagnostic of UHT conditions (Harley, 1989, 2008; Kelsey, 2008; Kelsey & Hand, 2015). Melt–garnet–sapphirine–K-feldspar–plagioclase–ilmenite–quartz in 47-a and melt–garnet–sapphirine–orthopyroxene–K-feldspar–plagioclase–ilmenite–quartz in 47-b are the peak assemblages at 1000 °C

and 7.6 kbar. Garnet only breaks down completely during the decompression segment of the *P–T* path in 47-b. Sapphirine–quartz and spinel–quartz are produced along the *P–T* path for both compositions above ~950 °C. Sillimanite–orthopyroxene–quartz is stable between ~940 °C and ~955 °C for 47-b and at ~940 °C for 47a. Above ~945 °C, sapphirine–quartz assemblages remain stable, until the elevated solidus is reached.

Modelled chemical potential of components for 47-a and –b starting compositions

The chemical potential of SiO_2, Al_2O_3, MgO and FeO should decrease with an increase in pressure and temperature on the prograde path, and during decompression, then increase again with cooling (Figure 2.4). This is caused by the pressure and temperature dependency of the pure end-member chemical potential and the activity term in the Henry's law expression for the chemical potential of a mixture. There are, however, significant differences between the chemical potential of these components in calculated mineral equilibria for the evolution of the X(Mg) = 54 and X(Mg) = 0.61 protoliths, relating to their bulk composition and consequent modal mineralogy (Figure 2.5).

The difference in μ_{SiO_2} ($\delta\mu_{SiO_2}$) between the two hypothetical bulk compositions is negligible, as both are SiO2-saturated (quartz-present) throughout the *P–T* path (Figure 2.5a). However, $\delta\mu_{Al_2O_3}$ (Figure 2.5b) increases at ~830 °C along this *P–T* path, due to differences in the predicted modes of prograde cordierite and garnet and the introduction of K-feldspar between the 47-a and 47-b model systems. A decrease in $\delta\mu_{Al_2O_3}$ occurs towards ~910 °C because of a sharp increase in the modes of garnet and K-feldspar in the 47-b bulk composition (Figure 2.4b) after ME5. Further increases in $\delta\mu_{Al_2O_3}$ occur during the decompression segment, where garnet is eliminated from the 47-b bulk composition at ~7.4 kbar, 1000 °C but is present in 47-a throughout.

A difference in μ_{MgO} and μ_{FeO} between the 47-a and 47-b bulk compositions is present throughout the modelled path (Figure 2.5c, d). Initially, lower μ_{MgO} and higher μ_{FeO} values are calculated for 47-a relative to 47-b. However, this difference disappears when the bulk compositions stabilize identical divariant assemblage of melt–garnet–cordierite–biotite–sillimanite–K-feldspar–plagioclase–ilmenite–magnetite–quartz at 835 °C and garnet–

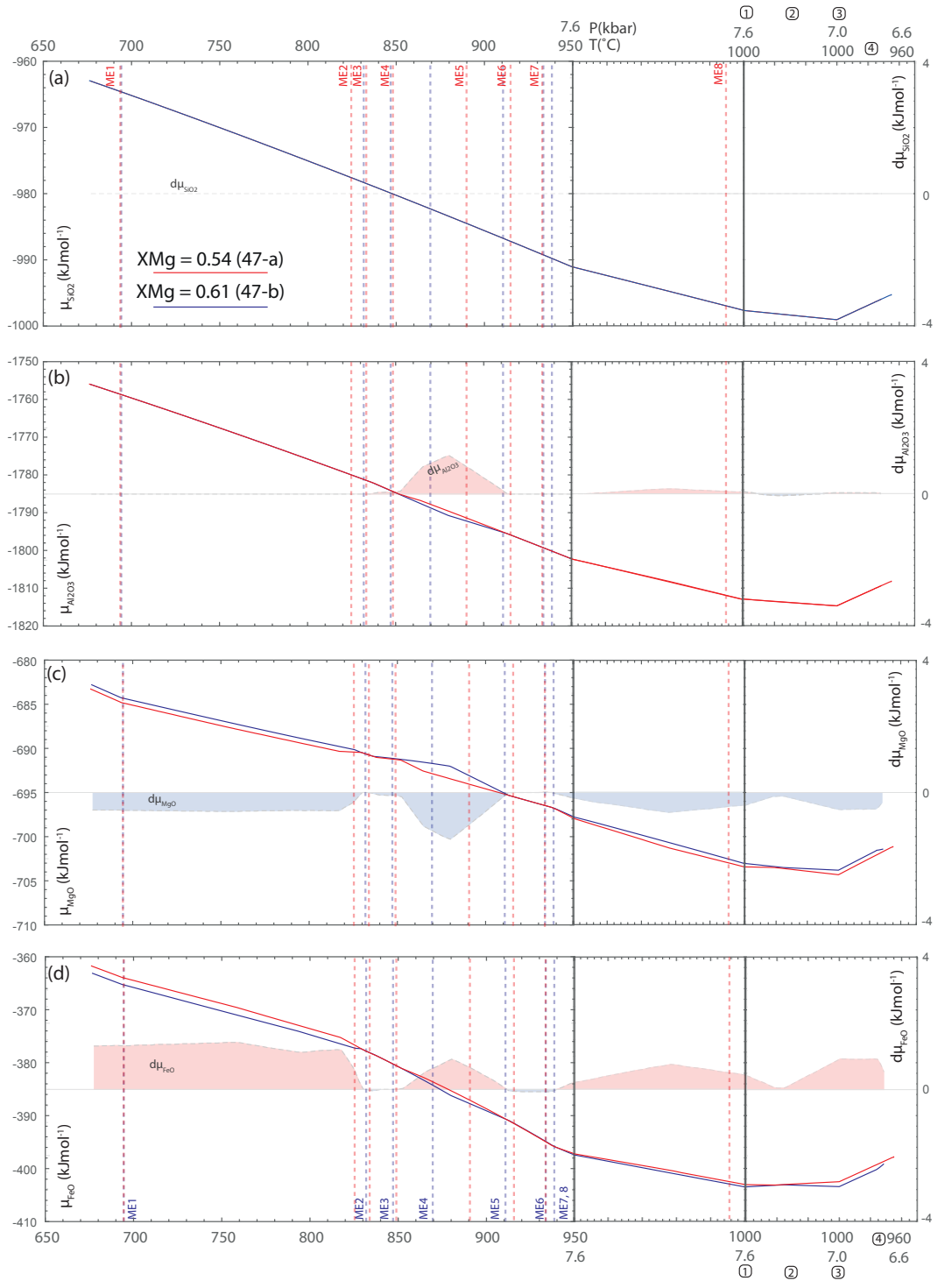

Figure 2.5 | Chemical potential values of equilibria calculated to be stable in 47-a (X(Mg)=0.54) (red) and 47-b (X(Mg)=0.61) (blue) starting compositions over the hypothetical *P–T* path shown in Figure 2.1. Difference in chemical potential in each component is shown by a red shaded area if it is higher in 47-a or a blue shaded area if higher in 47-b. The horizontal line represents dμ=0. (a) μ_{SiO_2}, (b) $\mu_{Al_2O_3}$, (c) μ_{MgO} and (d) μ_{FeO}.

melt–cordierite–K-feldspar–plagioclase–ilmenite–sillimanite–quartz at 920 °C along the prescribed *P–T* path. Garnet and cordierite form in response to biotite and sillimanite breakdown in the two bulk compositions, leading to a sharp increase in absolute $\delta\mu_{MgO}$ and $\delta\mu_{FeO}$. The difference is further exacerbated by the development of substantial quantities of orthopyroxene and sillimanite via the breakdown of garnet and cordierite in 47-b at ~940 °C (Figure 2.4b). Absolute values of $\delta\mu_{MgO}$ and $\delta\mu_{FeO}$ remain high, because peak and retrograde assemblages continue to have different modal proportions and mineral chemistry.

Modelled melt viscosity for 47-a and -b starting compositions

Changes in the calculated melt viscosity of 47-a and 47-b occur in conjunction with a change in *P–T*, the breakdown of hydrous phases and/or modelled melt extraction (ME) events. For example, the gradient of viscosity increase is lower in both starting compositions after ME1, and there are significant increases that coincide with ME3 in 47-a (Figure 2.6a), and ME2, 7 and 8 in 47-b (Figure 2.6b). The viscosity increases are related to an abrupt change in melt composition that is controlled by the incongruent breakdown of

Figure 2.6 | H_2O concentration and viscosity of melt along the *P–T* path shown in Figure 2.1. Melt viscosity (η; thick solid line) and H2O concentration (c; thick dashed line) and melt mode (thin line) were calculated using starting compisitions based on (a) domains 47-a (X(Mg)=0.54) and (b) 47-b (X(Mg)=0.61); see Table 1. Melt extraction events are labelled ME1-7/8 for each calculation, along with *P–T* points 1-5.

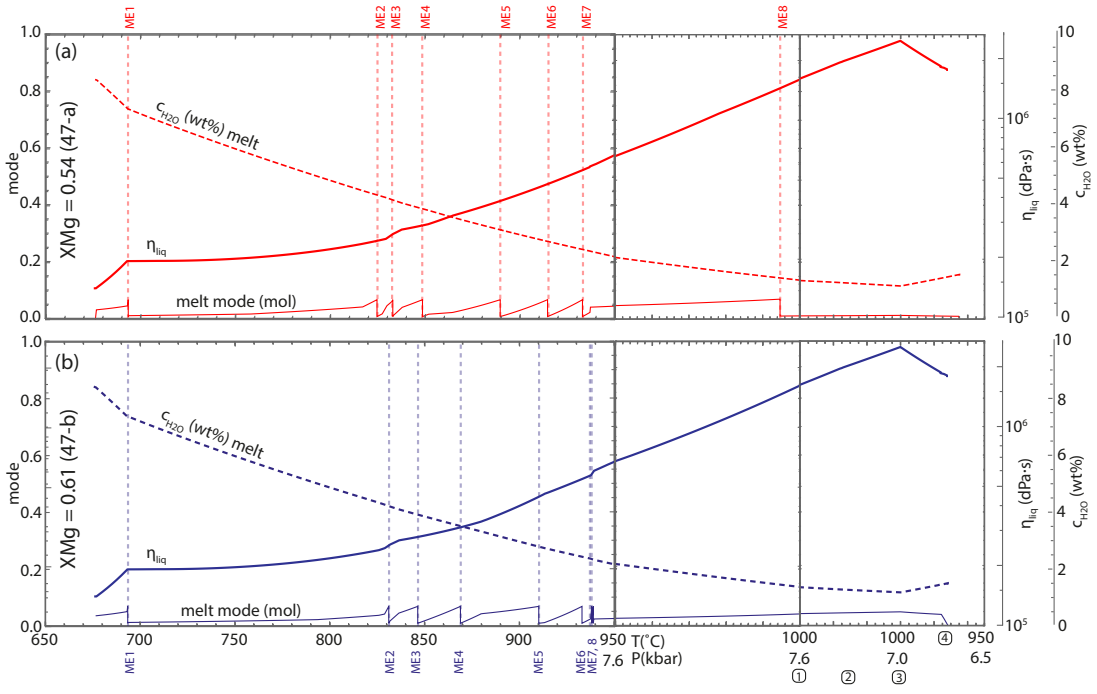

reactants, as these changes coincide with the loss of biotite and sillimanite to produce garnet, cordierite, K-feldspar and melt beginning at ~830 °C (Figure 2.4a, b), and cordierite, garnet and K–feldspar to orthopyroxene, sillimanite and melt at ~935 °C (Figure 2.4b).

Along the modelled *P–T* path with melt extraction, H2O concentration in melt decreases with increasing temperature and decreasing pressure for both 47-a and 47-b starting compositions. As the melt produced becomes less hydrous towards the highest T and lowest P (i.e. after decompression but before cooling), the calculated viscosity increases to a maximum of 1.86×10^6 dPa•s at 7.0 kbar, 1000 °C (Figure 2.6), an order of magnitude greater than that of melt produced at the solidus in both starting compositions.

2.3.2 | Chemical potential calculations

Chemical potential relationships and reaction microtextures at UHT in NKFMASH

Using the petrogenetic grid shown in Appendix B.1, NKFMASH divariant points and trivariant lines in μ_{MgO}-μ_{FeO} space were calculated for *P–T* points 1 to 3 and *P–T* (Figure 2.3). The topology in chemical potential space changes when a univariant reaction is crossed in *P–T* space, and the μ_{MgO}–μ_{FeO} coordinates of points and lines change with any change in *P–T*. Although many other reaction microtextures can be explained by migrating stability fields in these chemical potential diagrams, as garnet is common in peak metamorphic assemblages at UHT, only reaction textures involving the breakdown of peak metamorphic garnet are discussed here.

For the *P–T* segment after *P–T* point 1, equilibria were calculated at 7.60 kbar, 1000 °C (Figure 2.7a(i)) and 7.56 kbar, 1000 °C (Figure 2.7a(ii)) with silicate melt and quartz in excess and at $\mu_{K2O} = -992.00$ kJmol^{-1}, $\mu_{Na2O} = -929.81$ kJmol^{-1} and $\mu_{K2O} = -992.18$ kJmol^{-1}, $\mu_{Na2O} = -929.94$ kJmol^{-1}, respectively. For SiO_2 saturated (quartz present) conditions, μ_{MgO}–μ_{FeO} fields with orthopyroxene stable converge on garnet and sillimanite stability fields. Decompression at these conditions causes μ_{MgO}–μ_{FeO} fields in which orthopyroxene–sillimanite, orthopyroxene–sapphirine and orthopyroxene–spinel are stable to migrate towards fields in which garnet is stable, if conditions are SiO_2-undersaturated. These SiO_2-undersaturated fields overlap with the orthopyroxene + quartz stability field in μ_{MgO}–μ_{FeO} space.

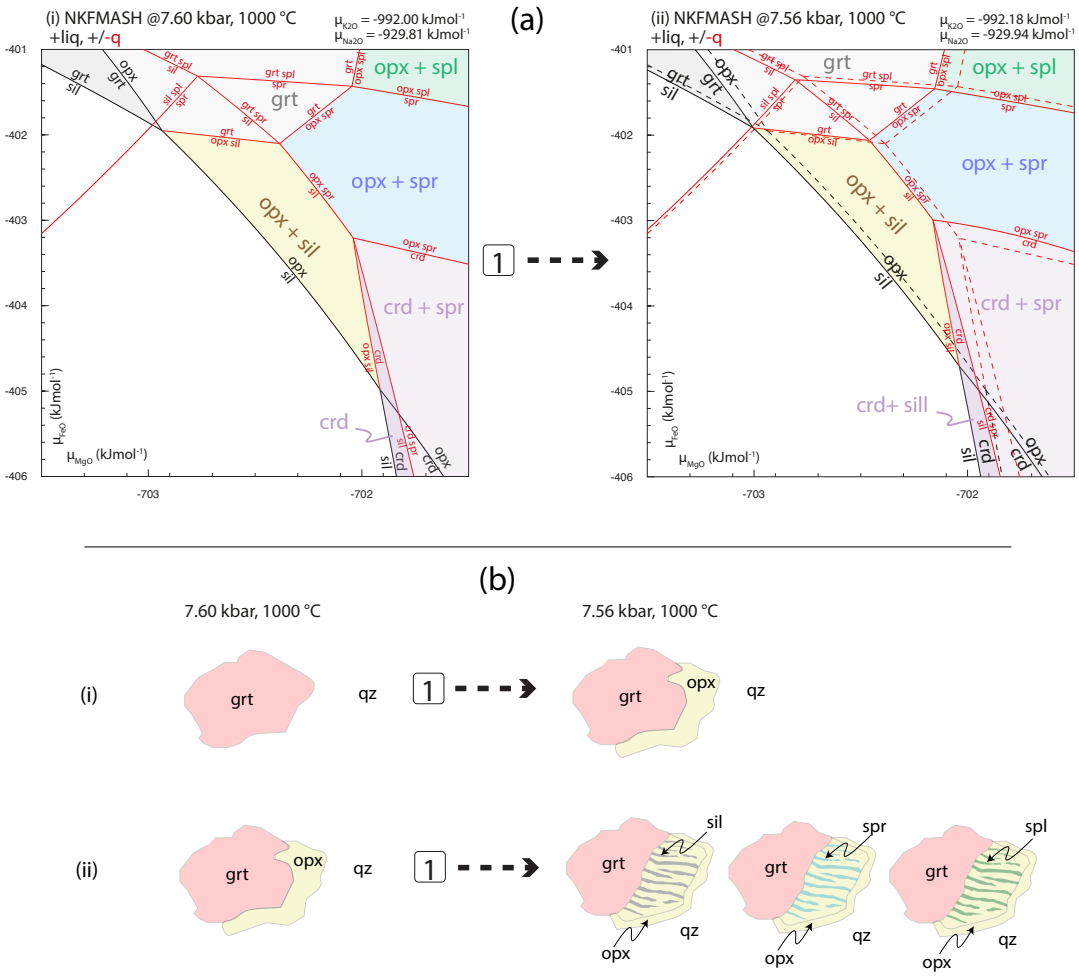

Figure 2.7 | : (a) Chemical potential diagrams of μ_{MgO} vs μ_{FeO} at *P*–*T* point 1 in the system NKFMASH. Equilibria with excess quartz (SiO_2-saturated) are plotted in black. Equilibria without quartz (SiO_2-undersaturated) are plotted in red. (i) Stable equilibria at *P*–*T* point 1 (1000 °C, 7.6 kbar), (ii) stable equilibria after point 1 on the P–T path (1000 °C, 7.56 kbar) and stable equilibria point 1 for comparison (dashed). (b) Reaction textures inferred from (a). (i) orthopyroxene replacing garnet in SiO_2 saturated conditions. (ii) SiO_2 undersaturated orthopyroxene–sillimanite, orthopyroxene–sapphirine and orthopyroxene–spinel replacing garnet, rimmed by orthopyroxene.

A range of reaction microtextures are consistent with the above migration of divariant and trivariant equilibria in μ_{MgO}–μ_{FeO} space after *P*–*T* point 1. If garnet is in equilibrium with a quartz matrix and melt, garnet will break down to form orthopyroxene (Figure 2.7b(i)) when pressure decreases. If a grain boundary between garnet and orthopyroxene becomes SiO_2-undersaturated, then symplectites containing orthopyroxene–sillimanite, orthopyroxene–sapphirine or orthopyroxene–spinel can form, replacing garnet (Figure 2.7b(ii)). Orthopyroxene–sillimanite, orthopyroxene–

sapphirine and orthopyroxene–spinel SiO_2-undersaturated equilibria overlap with the orthopyroxene + quartz stability field, so these symplectites will be surrounded by orthopyroxene if they occur in a quartz matrix (Figure 2.7b(ii)).

For the *P–T* segment after *P–T* point 2, equilibria were calculated at 7.30 kbar, 1000 °C (Figure 2.8a(i)) and 7.26 kbar, 1000 °C (Figure 2.8a(ii)) with silicate melt and quartz in excess and at μ_{K2O} = −993.37 kJmol^{-1}, μ_{Na2O}

Figure 2.8 | (a) Chemical potential diagrams of μ_{MgO} vs μ_{FeO} at *P–T* point 2 in the system NKFMASH. Equilibria with excess quartz (SiO_2-saturated) are plotted in black. Equilibria without quartz (SiO_2-undersaturated) are plotted in red. (i) Stable equilibria at *P–T* point 1 (1000 °C, 7.3 kbar), (ii) stable equilibria after point 2 on the *P–T* path (1000 °C, 7.26 kbar) and stable equilibria point 2 for comparison (dashed). (b) Reaction textures inferred from (a). (i) orthopyroxene replacing garnet in SiO_2 saturated conditions. (ii) SiO_2 undersaturated orthopyroxene–sillimanite, orthopyroxene–sapphirine, orthopyroxene–spinel and orthopyroxene–cordierite replacing garnet, rimmed by orthopyroxene.

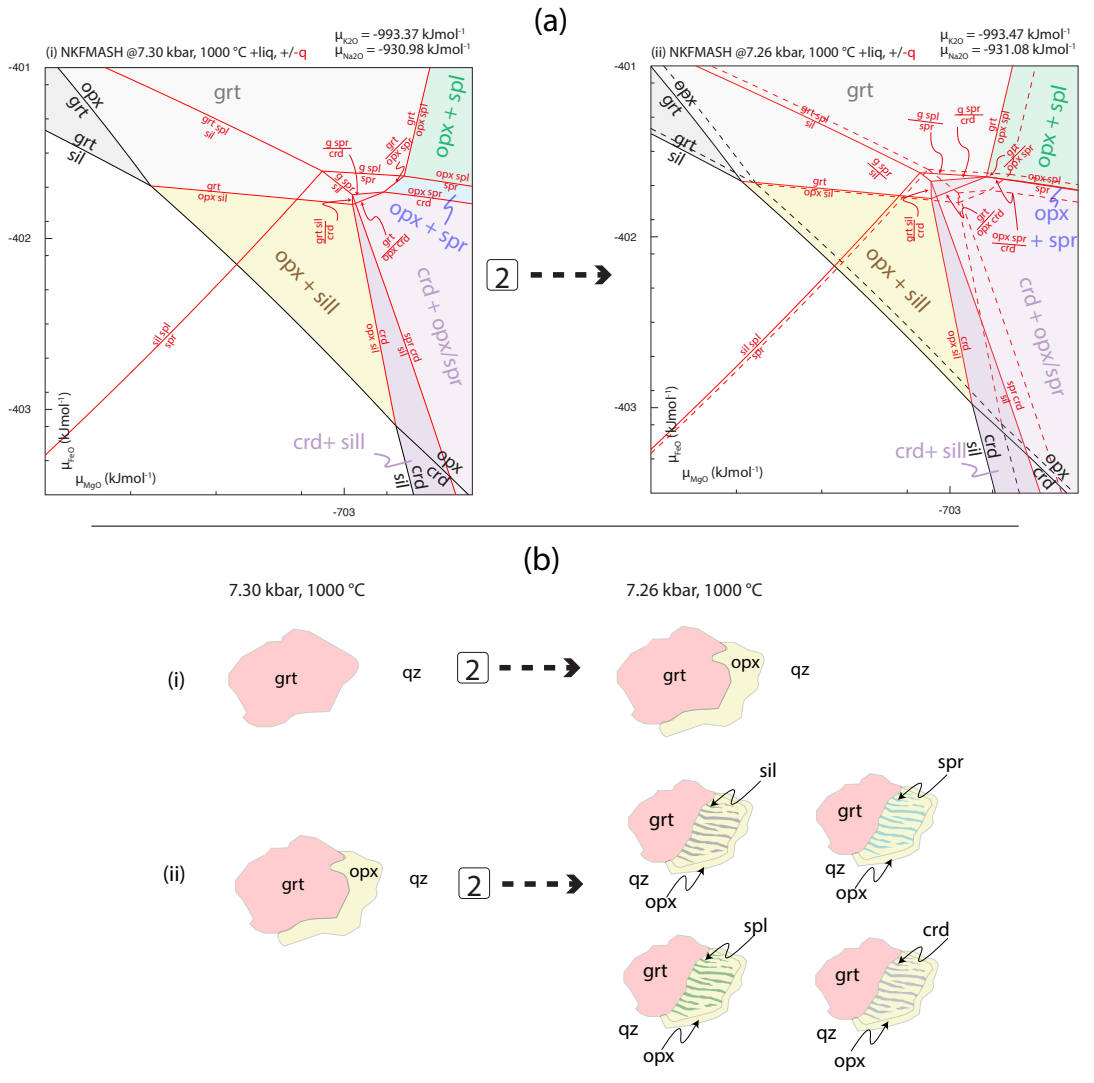

= −930.98 kJmol^{-1} and μ_{K2O} = −993.47 kJmol^{-1}, μ_{Na2O} = −931.08 kJmol^{-1}. The migration of divariant and trivariant equilibria proceeds in the same direction as after point 1, consistent with development of the same reaction microtextures, with the addition of the orthopyroxene–cordierite stability field that advances into fields where garnet is stable, if conditions are SiO2-undersaturated. These SiO_2-undersaturated fields overlap with the orthopyroxene + quartz stability field in μ_{MgO}–μ_{FeO} space.

The same reaction microtextures are consistent with the above migration of divariant and trivariant equilibria in μ_{MgO}–μ_{FeO} space after *P*–*T* point 2

Figure 2.9 | (a) Chemical potential diagrams of μ_{MgO} vs μ_{FeO} at *P*–*T* point 3 in the system NKFMASH. Equilibria with excess quartz (SiO_2-saturated) are plotted in black. Equilibria without quartz (SiO_2-undersaturated) are plotted in red. (i) Stable equilibria at *P*–*T* point 3 (1000 °C, 7.0 kbar), (ii) stable equilibria after point 3 on the *P*–*T* path (998 °C, 6.98 kbar) and stable equilibria point 3 for comparison (dashed). (b) Reaction textures inferred from (a). (i) orthopyroxene replacing garnet in SiO_2 saturated conditions. (i) SiO2 undersaturated orthopyroxene–cordierite replacing garnet. (ii) $Garnet_2$ replacing an orthopyroxene–spinel symplectite.

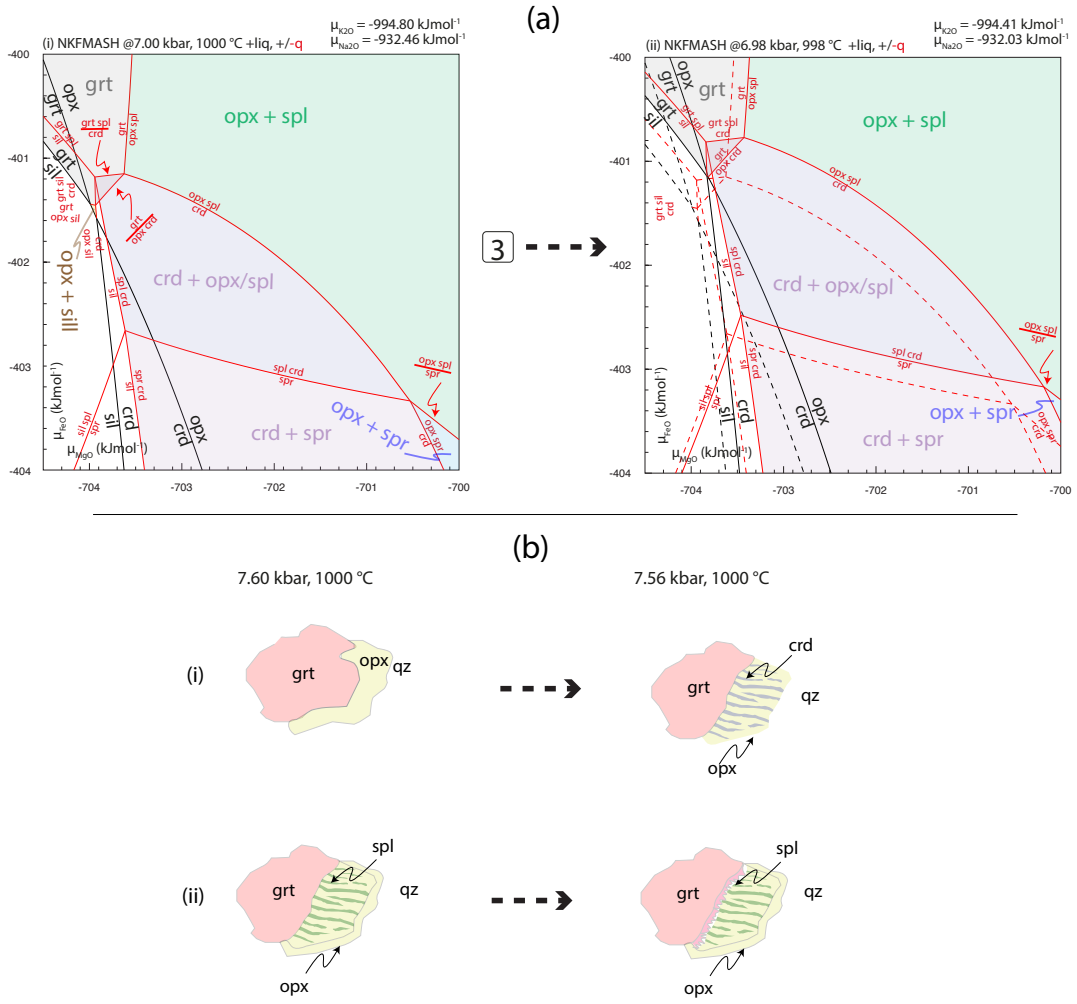

as after *P–T* point 1 with one addition (Figure 2.8b). If a grain boundary between garnet and orthopyroxene becomes SiO2-undersaturated, then orthopyroxene–cordierite may now form to replace garnet (Figure 2.8b(ii)). Orthopyroxene–cordierite symplectites can occur with either cordierite or orthopyroxene in contact with quartz as the orthopyroxene–cordierite field overlaps with cordierite and orthopyroxene quartz saturated fields.

For the *P–T* segment after *P–T* point 3, equilibria were calculated at 7.00 kbar, 1000 °C (Figure 2.9a(i)) and 6.98 kbar, 998 °C (Figure 2.9a(ii)) with silicate melt and quartz in excess and at μ_{K2O} = −994.80 kJmol^{-1}, μ_{Na2O} = −932.46 kJmol^{-1} and μ_{K2O} = −994.41 kJmol^{-1}, μ_{Na2O} = −932.03 kJmol$_{-1}$. For SiO_2 saturated (quartz present) conditions, μ_{MgO}–μ_{FeO} fields with garnet stable converge on the orthopyroxene stability field. Decompression and cooling at these conditions causes the μ_{MgO}–μ_{FeO} field in which orthopyroxene–cordierite is stable to converge on fields where garnet is stable, if conditions are SiO_2-undersaturated, in addition the garnet stability field converges on the orthopyroxene–spinel field. Garnet and orthopyroxene–spinel and SiO_2-undersaturated fields overlap with the orthopyroxene + quartz stability field in μ_{MgO}–μ_{FeO} space, and orthopyroxene–cordierite overlaps with both orthopyroxene + quartz and cordierite + quartz field.

Several reaction microtextures are consistent with the above migration of divariant and trivariant equilibria in μ_{MgO}–μ_{FeO} space after *P–T* point 3. If garnet and orthopyroxene are in equilibrium with a quartz matrix and melt, it will break down, forming garnet (Figure 2.9b(i)), observed as a secondary generation of garnet (grt2). If a grain boundary between garnet and orthopyroxene becomes SiO2-undersaturated, then a symplectite containing orthopyroxene–cordierite forms to replace garnet (Figure 2.9b(ii)) with either cordierite or orthopyroxene in contact with quartz. As the garnet stability fields converges on orthopyroxene–spinel, a secondary generation of garnet will form in place of orthopyroxene–spinel.

Chemical potential relationships and reaction microtextures at UHT in NCKFMASH

Using the petrogenetic grid shown in Appendix B.2, NCKFMASH divariant points and trivariant lines in μ_{MgO}–μ_{CaO} space were calculated for *P–T* points 1 to 3 and the *P–T* segments that immediately follow (Figure 2.3). As with the NKFMASH examples, only reaction textures involving the breakdown of peak

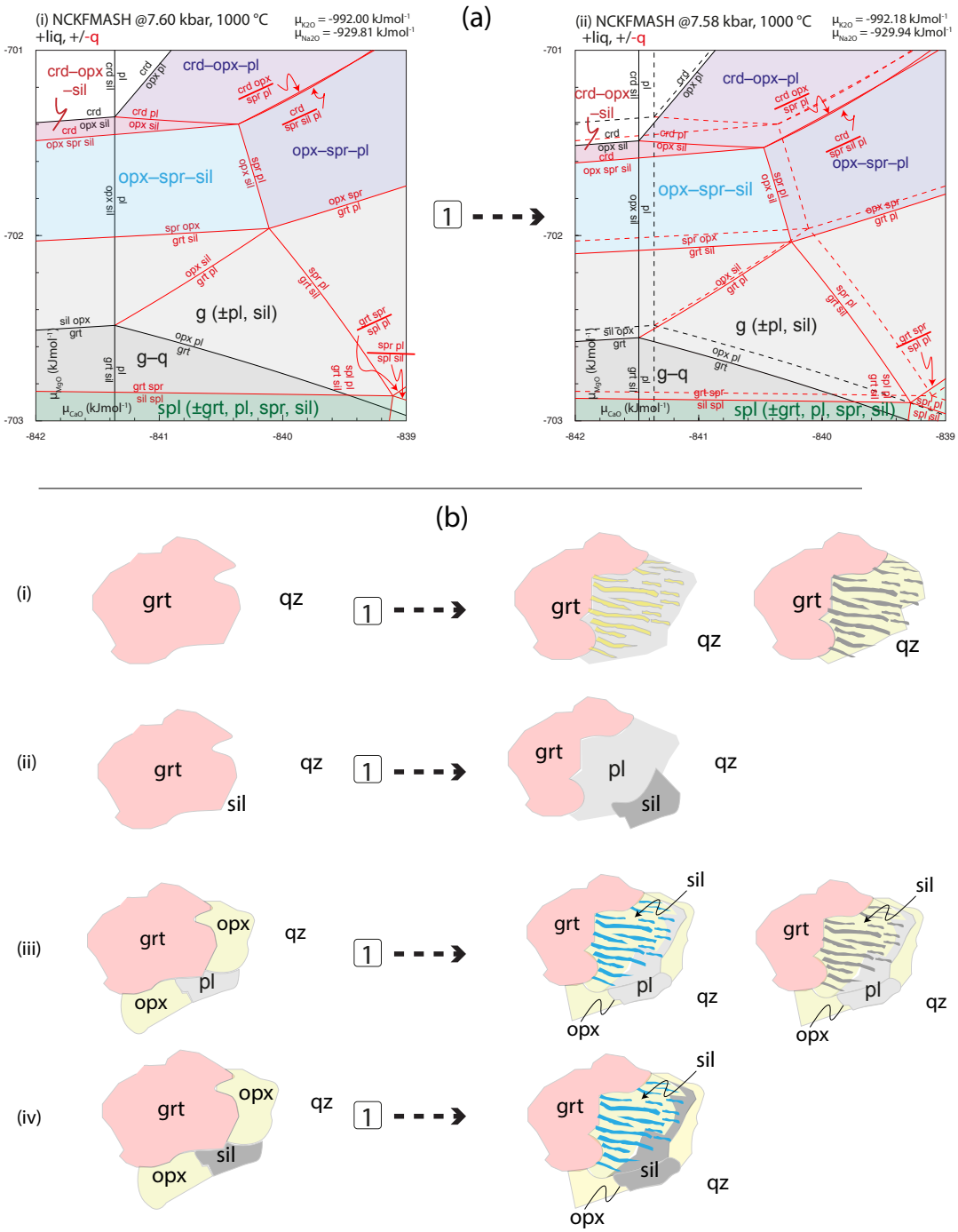

Figure 2.10 | (a) Chemical potential diagrams of μ_{MgO} vs μ_{CaO} at *P*–*T* point 1 in the system NCKFMASH. Equilibria with excess quartz (SiO_2-saturated) are plotted in black. Equilibria without quartz (SiO_2-undersaturated) are plotted in red. (i) Stable equilibria at *P*–*T* point 1 (1000 °C, 7.6 kbar), (ii) stable equilibria after point 1 on the *P*–*T* path (1000 °C, 7.56 kbar) and stable equilibria point 1 for comparison (dashed). (b) Reaction textures inferred from (a). (i) orthopyroxene–sillimanite and orthopyroxene–plagioclase replacing garnet in SiO_2-saturated conditions. (ii) Plagioclase replacing garnet–sapphirine in SiO_2-saturated conditions. (iii) SiO_2-undersaturated orthopyroxene–sillimanite, orthopyroxene–sapphirine and replacing garnet, rimmed by orthopyroxene and plagioclase. (iv) SiO_2-undersaturated orthopyroxene–sapphirine and replacing garnet, rimmed by orthopyroxene and sillimanite.

metamorphic garnet will be discussed henceforth.

For the *P–T* segment after *P–T* point 1, equilibria were calculated at 7.60 kbar, 1000 °C (Figure 2.10a(i)) and 7.56 kbar, 1000 °C (Figure 2.10a(ii)) with silicate melt and quartz in excess and at μ_{K2O} = –992.00 kJmol^{-1}, μ_{Na2O} = –929.81 kJmol^{-1} and μ_{K2O} = –992.18 kJmol^{-1}, μ_{Na2O} = –929.94 kJmol^{-1}. For SiO_2 saturated (quartz present) conditions, μ_{MgO}–μ_{CaO} fields with orthopyroxene–plagioclase and orthopyroxene–sillimanite stable converge on garnet stability fields. Decompression at these conditions causes μ_{MgO}–μ_{FeO} fields in which orthopyroxene–sapphirine is stable to converge on fields where garnet–sillimanite or garnet–plagioclase is stable. Orthopyroxene–sillimanite fields converge on garnet-plagioclase fields if conditions are SiO_2-undersaturated. These SiO_2-undersaturated fields overlap with the orthopyroxene–plagioclase–quartz stability field in μ_{MgO}–μ_{CaO} space.

A range of reaction microtextures are consistent with the above migration of divariant and trivariant equilibria in μ_{MgO}–μ_{CaO} space after *P–T* point 1. If garnet is in equilibrium with a quartz matrix and melt, garnet will break down to form orthopyroxene–plagioclase or orthopyroxene–sillimanite symplectites (Figure 2.10b(i)) or garnet–sillimanite to plagioclase. If a garnet–orthopyroxene–plagioclase assemblage becomes SiO_2-undersaturated, then symplectites containing orthopyroxene–sillimanite or orthopyroxene–sapphirine can form, replacing garnet (Figure 2.10b(ii)). As orthopyroxene–sillimanite and orthopyroxene–sapphirine SiO_2-undersaturated equilibria overlap with the orthopyroxene–plagioclase–quartz stability field, these symplectites will be surrounded by orthopyroxene and plagioclase if they occur in a quartz matrix (Figure 2.10b(iii and iv)).

After *P–T* point 2, equilibria were calculated at 7.60 kbar, 1000 °C (Figure 2.10a(i)) and 7.56 kbar, 1000 °C (Figure 2.11a(ii)) with silicate melt and quartz in excess and at μ_{K2O} = –992.00 kJmol^{-1}, μ_{Na2O} = –929.81 kJmol^{-1} and μ_{K2O} = –992.18 kJmol^{-1}, μ_{Na2O} = –929.94 kJmol^{-1}, respectively. For SiO_2-saturated (quartz present) and SiO_2-undersaturated conditions, μ_{MgO}–μ_{CaO} fields migrate in the same manner as after *P–T* point 1, resulting in the same reaction microtextures (Figure 2.11b).

For the *P–T* segment after *P–T* point 3, equilibria were calculated at 7.00 kbar, 1000 °C (Figure 2.12a(i)) and 6.98 kbar, 998 °C (Figure 2.12a(ii)) with silicate melt and quartz in excess and at μ_{K2O} = –994.80 kJmol^{-1}, μ_{Na2O}

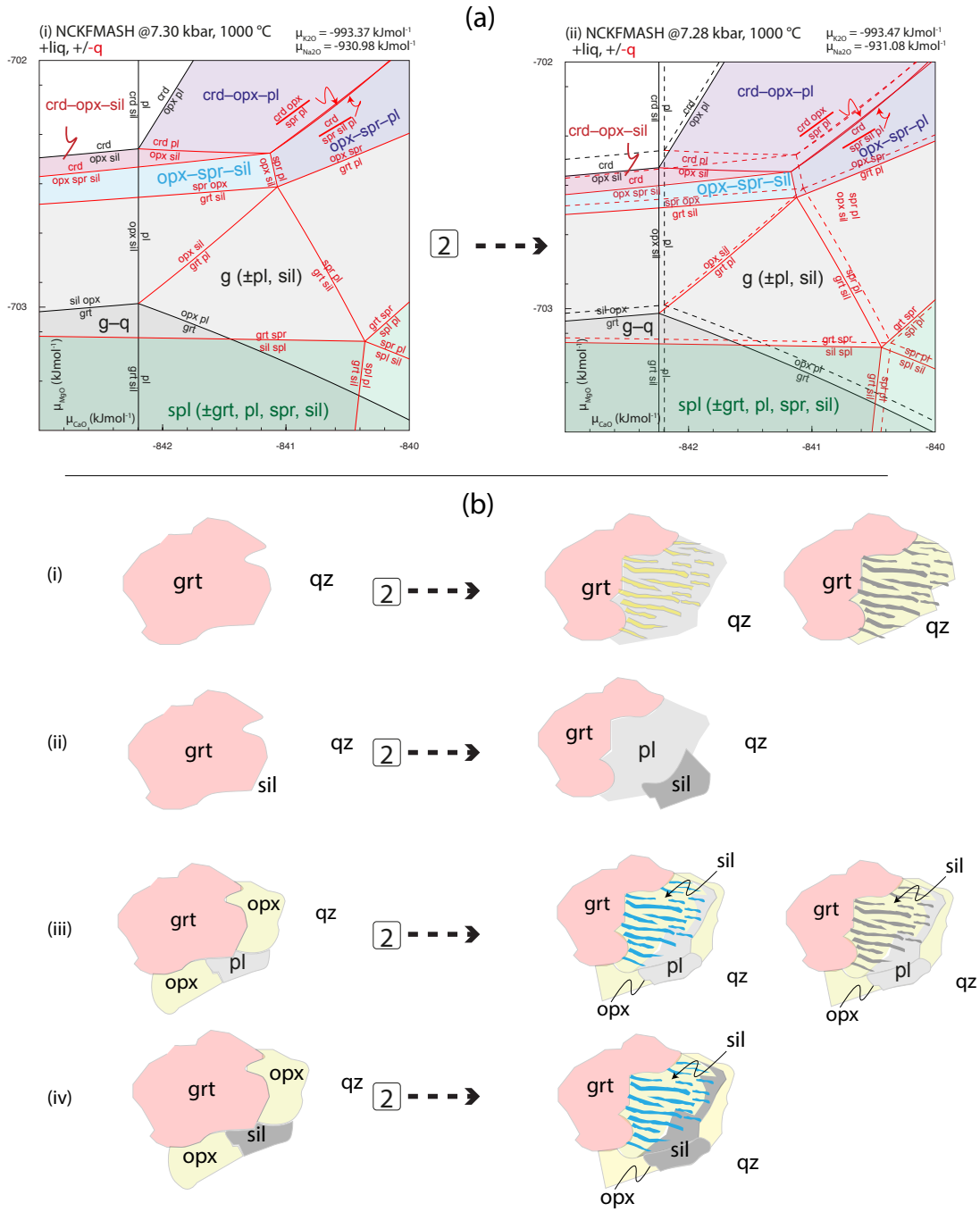

Figure 2.11: (a) Chemical potential diagrams of μ_{MgO} vs μ_{CaO} at *P*–*T* point 2 in the system NCKFMASH. Equilibria with excess quartz (SiO_2-saturated) are plotted in black. Equilibria without quartz (SiO_2-undersaturated) are plotted in red. (i) Stable equilibria at *P*–*T* point 2 (1000 °C, 7.3 kbar), (ii) stable equilibria after point 1 on the *P*–*T* path (1000 °C, 7.26 kbar) and stable equilibria point 2 for comparison (dashed). (b) Reaction textures inferred from (a). (i) orthopyroxene–sillimanite and orthopyroxene–plagioclase replacing garnet in SiO_2 saturated conditions. (ii) Plagioclase replacing garnet–sapphirine in SiO_2 saturated conditions. (iii) SiO_2 undersaturated orthopyroxene–sillimanite, orthopyroxene–sapphirine and replacing garnet, rimmed by orthopyroxene and plagioclase. (iv) SiO_2 undersaturated orthopyroxene–sapphirine and replacing garnet, rimmed by orthopyroxene and sillimanite.

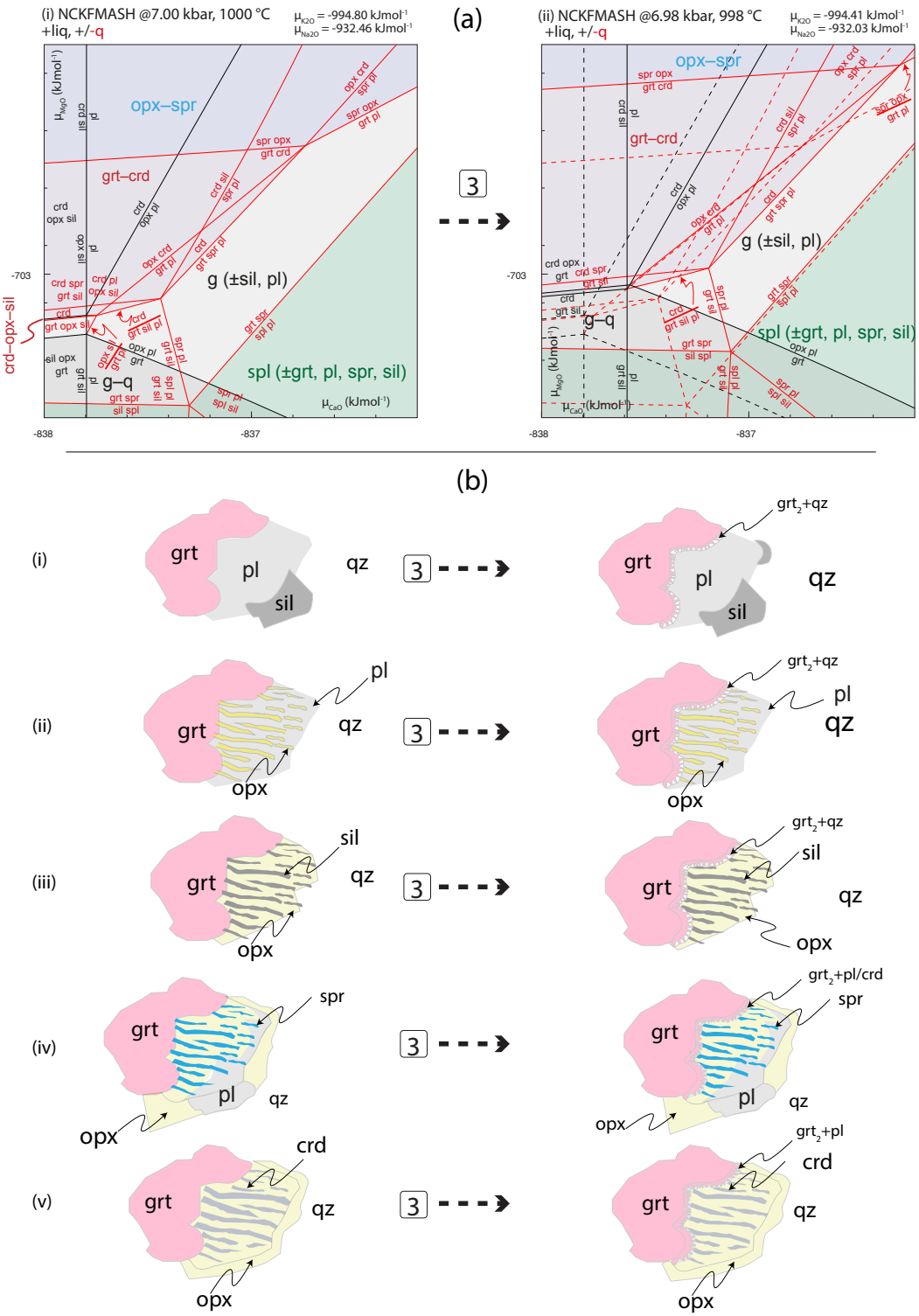

(a) Chemical potential diagrams of μMgO vs μCaO at *P*–*T* point 3 in the system NCKFMASH. Equilibria with excess quartz (SiO2-saturated) are plotted in black. Equilibria without quartz (SiO2-undersaturated) are plotted in red. (i) Stable equilibria at *P*–*T* point 3 (1000 °C, 7.3 kbar), (ii) stable equilibria after point 1 on the *P*–*T* path (1000 °C, 7.26 kbar) and stable equilibria point 3 for comparison (dashed). (b) Reaction textures inferred from (a). Garnet2–quartz overgrowing (i) plagioclase, (ii) orthopyroxene–plagioclase and (iii) orthopyroxene–sillimanite. Garnet2–plagioclase/cordierite overgrowing (i) orthopyroxene–sapphirine and (ii) orthopyroxene–cordierite.

= −932.46 kJmol^{-1} and μ_{K2O} = −994.41 kJmol$_{-1}$, μ_{Na2O} = −932.03 kJmol^{-1}. For SiO_2 saturated conditions, μ_{MgO}–μ_{CaO} fields with garnet + quartz stable converges on orthopyroxene–sillimanite, orthopyroxene–plagioclase, and garnet + sillimanite converges on plagioclase stability fields. Decompression and cooling at these conditions causes the μ_{MgO}–μ_{CaO} field in which garnet–cordierite or garnet–cordierite are stable to converge on fields where orthopyroxene–sapphirine is stable, if conditions are SiO_2-undersaturated. Garnet and orthopyroxene–spinel and SiO_2-undersaturated fields overlap with the orthopyroxene + quartz stability field in μ_{MgO}–μ_{CaO} space, and orthopyroxene–cordierite overlaps with both the orthopyroxene + quartz and cordierite + quartz fields.

Several reaction microtextures are consistent with the above migration of divariant and trivariant equilibria in μ_{MgO}–μ_{CaO} space after *P–T* point 3. Due to advancing garnet-forming trivariant lines (Figure 2.12b(i)), growth of a secondary generation of garnet (grt_2) intergrown with either plagioclase or cordierite are predicted if conditions are locally SiO_2-undersaturated. If the environment is SiO_2-saturated, secondary garnet will occur intergrown with quartz (Figure 2.12b).

2.4 | Discussion

Scales of local equilibrium at UHT

Granulite facies metasedimentary rocks can contain equilibrium mineral assemblages that vary on a millimetre to centimetre scale (Figures 1 and 2). Such assemblages may have equilibrated at a single *P–T*, implying the establishment of gradients in chemical potential during the prograde evolution. Evidence for the persistence of chemical potential gradients is provided by retrograde reaction textures that are also common in granulite facies metamorphic rocks (White & Powell, 2011; White et al., 2008). Post-peak reaction textures can be modelled by considering the migration of a series of trivariant lines in chemical potential space in an appropriate chemical system (Figures 7–12).

Textures in granulites of the type described here and elsewhere (Blereau et al., 2017; Doukkari et al., 2018; Harley, 1998; Harley, Hensen, & Sheraton, 1990; Kelsey et al., 2017; Mitchell et al., 2019; Ogilvie & Gibson, 2017; Rickers, Raith, & Dasgupta, 2001; Sajeev, Osanai, & Santosh, 2004; Štípská et al., 2010; White & Powell, 2011; White et al., 2008; White et al., 2002) can

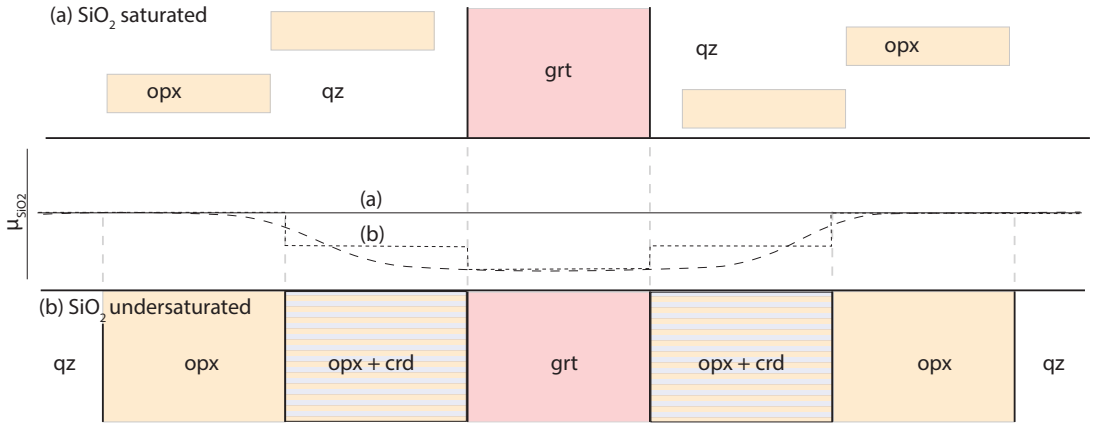

Figure 2.13 | Hypothetical μSiO2 profiles across an SiO_2-saturated (a) and locally SiO_2 unsaturated (b) microstructure (Figure 2.10d). (a) SiO_2-saturated microstructure with quartz in equilibrium with garnet and orthopyroxene, μ_{SiO_2} has a flat profile. (b) An SiO_2-undersaturated microstructure, where only orthopyroxene is equilibrium with quartz, μ_{SiO_2} may have a stepped (dotted line) or smoothed profile (dashed line). Other phases towards the centre of the corona texture are not in equilibrium with quartz and as such have lower μ_{SiO_2} values.

be ascribed to chemical potential gradients established due to, for example, the juxtaposition of different phases in a peak metamorphic assemblage. Grain boundaries and triple junctions permit local equilibria to develop between two or three phases, in which the number of components in the chemical system may effectively be reduced in the vicinity of the phases along with any grain boundary fluid/melt (Watson, 1982). Although two phases are likely to be in equilibrium along at a grain boundary, this is not necessarily the case towards the core of the two grains, which at each point will have their own discrete chemical potential values. As trivariant equilibria migrate in chemical potential space in the chemical subsystem established along the grain boundary in response to changes in *P* and *T*, reaction microtextures can develop.

Several documented reaction textures preserve phase relations that can only be stable under SiO2-undersaturated conditions (Figures 7–12). In these cases, or anywhere that chemical potential variations are preserved, an assumption of local equilibrium is important, because equilibrium assemblages vary spatially within a corona structure (Figures 13). For the SiO2-undersaturated example shown in Figure 2.13b, μSiO_2 may have a smoothed or stepped profile. Evidence of a smoothed profile may include gradual chemical zonation form margin to core of the symplectite (Baldwin et al., 2015). In the example shown in Figure 2.13b, μ_{SiO_2} is fixed at the boundary of the symplectite where it is SiO_2-saturated, but not imposed internally,

where local phase equilibria are SiO_2-understaturated; SiO_2 is internally buffered as it does not exchange freely between the symplectite and the quartz boundary. Consequently, μ_{SiO_2} values in the symplectite are a function of mineral mode, chemistry, and diffusion between phases in the symplectite. A smoothed profile reflects partial diffusional equilibration between spatially arranged, variable chemical potential values. Meanwhile, no gradual chemical zonation may exist within such a corona texture if there is a stepped chemical potential profile, as different chemical potential values of a given component are required to stabilise the local assemblages. In this case, minimal diffusion has occurred between rock volumes with local equilibria with variable chemical potential.

Reaction microtextures preserve evidence of chemical potential gradients on the millimetre scale that did not equilibrate on the available timescale. This visible evidence of local equilibrium is often preserved in granulite facies rock which have achieved supersolidus conditions for >10 Ma (Harley, 2016; Kelsey & Hand, 2015). The empirical petrological evidence suggests that chemical potential gradients are preserved both on the centimetre scale and at the scale of reaction microtextures (Figure 2.13).

Melt availability in granulites

The preservation versus formation of the reaction textures that represent stranded chemical potential gradients depends on the availability of melt to expedite diffusion. Partially molten rock analogue experiments show that intergranular melt films feed melt-bearing shear zones around which strain is localised, channelling overpressured melt into low pressure sites (Rosenberg & Handy, 2001, 2005; Takei, 2005), an observation consistent with natural observations in migmatites (Brown, Averkin, McLellan, & Sawyer, 1995; Waters, 2001). Depending on several factors, including intergranular dihedral angles, melt mode and melt viscosity (Walte, Bons, & Passchier, 2005), stress in partially molten rocks can be relaxed by either grain boundary diffusion or grain boundary wetting. In the latter case, an interconnected grain boundary fluid/melt network forms (Hier-Majumder, Leo, & Kohlstedt, 2004; Hier-Majumder, Ricard, & Bercovici, 2006).

As the effectiveness of grain boundary wetting to redistribute melt decreases with increasing melt viscosity (Hier-Majumder et al., 2006), it is possible that rock volumes may become chemically isolated from a viscous melt.

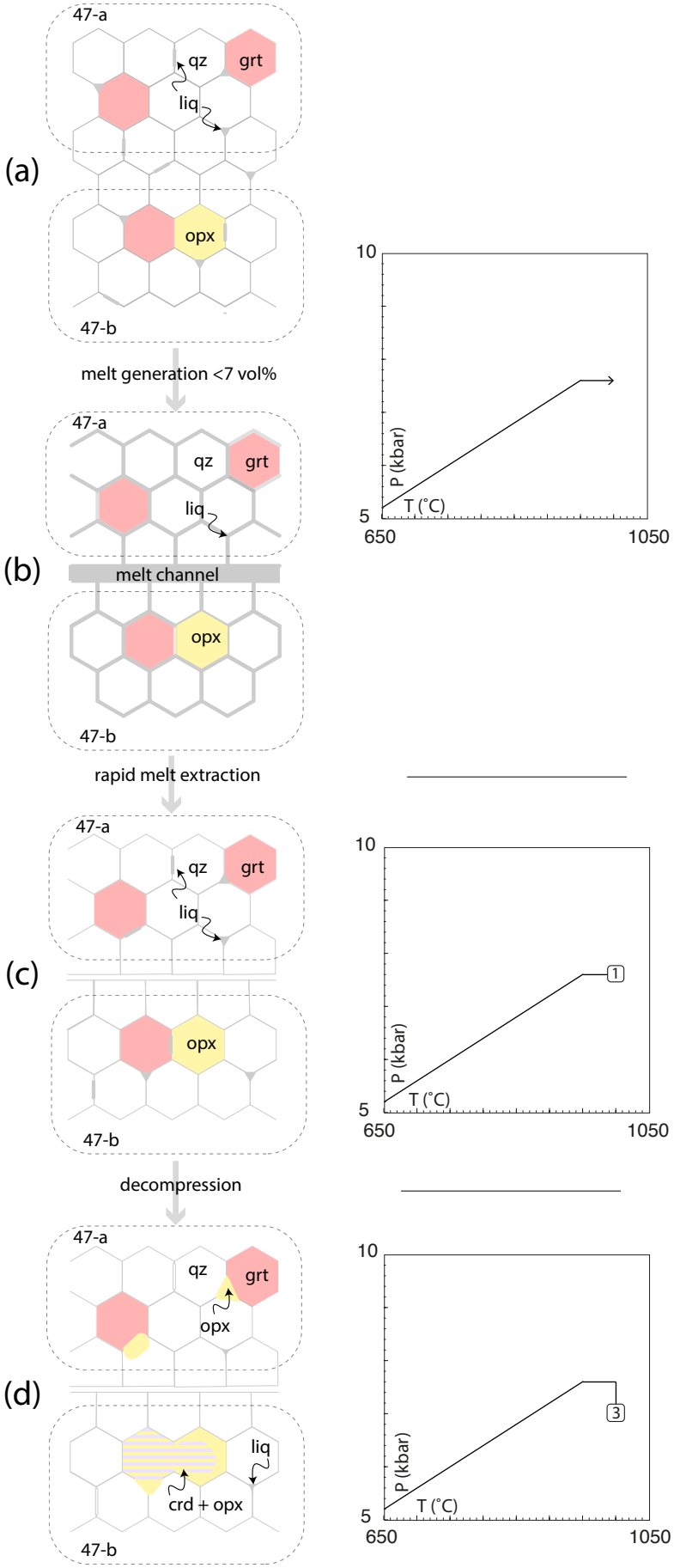
(a)
47-a
qz
grt
liq
opx
47-b
melt generation <7 vol%
(b)
47-a
qz
grt
liq
melt channel
opx
47-b
rapid melt extraction
(c)
47-a
qz
grt
liq
opx
47-b
decompression
(d)
47-a
qz
grt
opx
liq
crd + opx
47-b
10
5
P (kbar)
T (°C)
650
1050
1
3

Figure 2.14 | Theoretical model that preserves local equilibrium at both the centimetre scale (volumes 47-a and 47-b as indicated) and the scale of and reaction microtextures. (a) Melt is generated on the prograde *P–T* path and contained along grain boundaries and at triple junctions and does not migrate. (b) Melt is extracted faster than equilibration by fluid diffusion so a chemical potential gradient remains. (c) At peak conditions, more viscous melt is retained as discrete pockets within volumes 47-a and 47-b and does not migrate. (d) With decompression, the pockets of melt allow reaction microtextures to form along chemical potential gradients between peak phases.

According to the calibration of Holtz et al. (1999), the viscosity (η) of the melt increases by an order of magnitude on the *P–T* path from the solidus to the metamorphic peak (7.6 kbar, 1000 °C), and continues to increase to a maximum during decompression to 7.0 kbar, 1000 °C, viscosity then decreases with cooling (Figure 2.6). An order of magnitude increase in viscosity corresponds to <2 wt.% decrease in H_2O concentration (Hess & Dingwell, 1996; Holtz, Roux, Ohlhorst, Behrens, & Schulze, 1999; Schulze, Behrens, Holtz, Roux, & Johannes, 1996) – less than is modelled for both 47-a and 47-b on the high T/P *P–T* path. Small disparities in melt viscosity can be compositionally dependent (Figure 2.6), as the atomic ratio of (Si + Al)/(H + Na + K) in melt is a primary control on its viscosity (Holtz et al., 1999), and this may change when incongruent melting reactions occur.

The tectonic implications of the model shown in Figure 2.5 are that the increased melt viscosity at UHT can inhibit heat transfer caused by melt advection, and removal of the melt fraction can limit endothermic melting reactions (Stüwe, 1995). In addition, and more relevant to this study, as diffusion in melt or fluid species is faster than solid state diffusion (Brady, 1995; Chakraborty & Ganguly, 1992; Mungall, 2002), there are implications for the preservation of different scales of local equilibrium from the increasing melt viscosity and decreased melt migration.

Preserving local equilibrium at UHT

$FeO–MgO–Al_2O_3–SiO_2$ are the four components that, in most cases, control the major mineral mineralogy in metapelites (Thompson Jr, 1957). Therefore, the redistribution of these components is the rate-determining step for equilibrating chemical potential gradients at all scales. Both solid-state diffusion and diffusion through fluids (volatiles or melts) operate in natural metamorphic systems, and the diffusion coefficients of chemical components in phases stable along the prograde path control the rate at which chemical potential gradients will equilibrate. Experimentally-determined diffusion

coefficients for phases of interest vary with crystallographic orientation in anisotropic minerals (Brady, 1995), and with both the concentration of a given component and that of other components (Chakraborty & Ganguly, 1992). In general, the rate of diffusion of more immobile components can change that of those relevant to the considered equilibria, for example Fe2+ and Mg diffusion are coupled with Ca and Mn diffusion in garnet (Carlson, 2006). Diffusion coefficients in silicate melt, which is assumed to be present on grain boundaries in the scenarios modelled here, can be determined via tracer diffusion experiments (Mungall, 2002). Rates of diffusion of the relevant cations (e.g. Fe^{2+} and Mg) in fluids and melts are significantly faster than solid-state diffusion. For example, the diffusion coefficient of Mg in garnet is exceeded by that in silicate melt by more than three orders of magnitude (Brady, 1995; Chakraborty & Ganguly, 1992; Mungall, 2002).

The interactions between solid state and fluid diffusion in natural systems are complex, and diffusion modelling requires variations of Fick's law to be solved using a finite element setup (Chakraborty, 2008; Dohmen & Chakraborty, 2003; Spear, 2014). Calculations of hypothetical model systems including solid and fluid phases show that the behaviour of a system can be defined in terms of a series of dimensionless parameters calculated based on the diffusion coefficients in both the solid and the fluid, the surface area, the width of the fluid conduit and the radius of the solid phase (Dohmen & Chakraborty, 2003). Depending on the magnitude of these parameters, diffusion rates may be controlled either by either fluid diffusion, solid-state diffusion or by the interface (Chakraborty, 2008). Solid-state diffusion rates are slowest, and thus chemical potential gradients are most likely to be preserved when controlled by solid-state diffusion. Factors that allow solid-state diffusion to be the rate controlling process include a narrow fluid conduit (i.e. leucosome), a coarse grain size and a low surface area (Dohmen & Chakraborty, 2003). Therefore, the most likely processes to preserve chemical potential gradients are those that fulfil these criteria.

At low melt fractions, it is more likely that solid-state diffusion is the rate determining process for element redistribution in high-grade metamorphic rocks. In our model, along a prograde *P–T* path with an apparent thermal gradient of 125 °C/kbar, melt extraction events that are modelled once the melt connectivity threshold is exceeded (Rosenberg & Handy, 2005) lead to the development of chemical potential gradients between two different equilibrium domains (Figure 2.5). However, the chemical potential

differences of MgO, FeO, Al_2O_3 and SiO_2 are zero ($\delta\mu = 0$) where the two starting compositions stabilize the same assemblages; garnet–melt–cordierite–biotite–K-feldspar–plagioclase–magnetite–ilmenite–sillimanite–quartz at ~830 °C, and garnet–melt–cordierite–K-feldspar–plagioclase–ilmenite–sillimanite–quartz at ~920 °C. Melt-loss events do not perturb the chemical potential differences of MgO, FeO, Al_2O_3 and SiO_2 as they do not greatly alter the proportion of major phases (Figure 2.4). If a chemical potential gradient is subsequently reintroduced (Figure 2.5), slow, solid-state diffusion will continue to be the rate determining process until the metamorphic peak. Therefore, melt modes must be minimised throughout the prograde evolution if chemical potential gradients remain between the two lithologies in the model system at peak UHT conditions.

The most likely explanation for the formation and preservation of local equilibrium on the centimetre scale, and at the scale of a reaction microtexture, are episodes of efficient and inefficient melt migration (Figure 2.14). As melt is generated on the prograde *P–T* path, melt modes must be minimised so that the redistribution of Fe^{2+}, Mg, Ca and Si species between neighbouring rock volumes occurs at the rate of solid-state diffusion. This may occur because of efficient melt extraction due to grain boundary wetting and the formation of interconnected melt networks (Figure 2.14b). As the rock reaches peak *P–T* conditions (*P–T* point 1) and begins to decompress, melt viscosity will increase by an order of magnitude, and melt modes will continually decrease (Figure 2.6). In this scenario, grain boundary wetting does not occur and an interconnected melt network never forms, so low modes of physically and chemically isolated, viscous melt will form pockets along grain boundaries and at triple junctions (Figure 2.14c). The presence of melt will allow reaction microtextures to form locally during decompression to *P–T* point 3, within each neighbouring rock volume, as the mobility of Fe^{2+}, Mg, Ca and Si will increase because melt is locally present, until it is consumed by the reaction.

Incidentally, melt extraction on the prograde *P–T* path by an interconnected melt network must be faster than the flattening of chemical potential gradients by fluid diffusion if chemical potential gradients are to persist after melt extraction, as is required if chemical potential gradients on the cm-scale persist at peak UHT conditions – observed in EGB-09-47 (Figure 2.1). When a rock reaches the solidus on its retrograde path, solid-state diffusion, often an order of magnitude slower than fluid diffusion, must be the rate-

determining process if fluid is absent. When a rock volume approaches the solidus, melt can reach low enough modes for solid-state diffusion to become the rate determining process, and local equilibrium may persist on shorter length scales. Hence, the final chemical potential relationships at solidus conditions are more likely to be preserved as reaction textures than those at temperatures below the solidus, as solid state diffusion is much slower.

Considerations for thermodynamic modelling

Quantitative interpretation of textures and variable peak assemblages requires a departure from the norm of phase equilibrium modelling using whole-rock compositions (i.e. *P–T* pseudosections). Primarily, peak metamorphic assemblages commonly vary on a smaller scale than the volume ordinarily used for XRF whole rock analyses (Dorfler et al., 2015; Harley, 1998; Johnson et al., 2003; Mitchell et al., 2019), and are not in equilibrium on that scale. Consequently, where the interpreted peak assemblage is observed to differ across a previously analysed volume, the bulk composition of that equilibrium volume must be ascertained for the peak assemblage to be meaningfully modelled (Guevara and Caddick, 2016; Palin, Weller, Waters, & Dyck, 2016).

Post peak reaction textures often develop in response to chemical potential gradients and simplified chemical systems imposed by the juxtaposition of peak phases, as such the textures develop in conditions different to those simulated by assuming equilibrium and a single bulk rock composition. The implicit assumptions of the local equilibrium approach is that a rock can be in equilibrium at the scale of the unit cell of a considered mineral phase (Korzhinskiĭ, 1959) if it is part of a chemical potential gradient (White & Powell, 2011). It is therefore inappropriate to calculate pseudosections based on bulk compositions that are from analysed volumes within a chemical potential gradient. Therefore, the *P–T* range over which observed reaction microtextures evolve must be corroborated by calculated chemical potential diagrams in suitable reduced systems, to confirm that it is possible for them to develop at the postulated conditions.

2.5 | Conclusions

The research objectives of this chapter are described in section 1.1.1. Addressing objective 1; changes to the X(Mg) (ΔX(Mg) = 0.04) of pelitic

bulk compositions can produce different peak assemblages under granulite facies and UHT conditions. Different peak assemblages preserved in adjacent compositional domains at UHT lead to the establishment of gradients in chemical potential. Such compositional differences may be primary, such as sedimentary layering, or secondary, such as due to melt loss or the juxtaposition of grains of different minerals. In respect to objective 2; Formation of reaction microtextures during decompression at UHT due to stranded chemical potential gradients can be attributed to the migration of trivariant equilibria in chemical potential space.

Research objectives 3 and 4 are fulfilled as follows. Chemical isolation from matrix quartz can lead to SiO_2-undersaturated equilibria and reaction textures, for example, if a grain boundary between peak phases becomes chemically isolated from a SiO_2-saturated matrix. Chemical and physical isolation from melt may allow solid-state diffusion to become the rate determining factor in the preservation of local equilibrium. Isolation of solid phases from melt can occur if the melt becomes viscous, leading to ineffective grain boundary wetting. In order to prevent rapid fluid diffusion of SiO_2, Al_2O_3, MgO and FeO, the interconnected melt networks required for melt loss events must exist for less than the duration required for the rapid fluid diffusion of FMAS components to flatten chemical potential gradients. Melt loss along a typical granulite high *T/P P–T* path to 7.6 kbar, 1000 °C leads to an order of magnitude increase of melt viscosity in a model metapelite, meaning that melt migration is inhibited, restricting viscous melt to isolated pockets. In this scenario, chemical potential gradients may be preserved locally if melt modes are low enough to allow diffusion rate to be solid state controlled, or isolated melt pockets can allow reaction microtextures to form along locally intergranular chemical potential gradients.

2.6 | References

Ague, J. J. (1994). Mass transfer during Barrovian metamorphism of pelites, south-central Connecticut; I, Evidence for changes in composition and volume. American Journal of Science, 294(8), 989-1057.

Ague, J. J. (1997). Crustal mass transfer and index mineral growth in Barrow's garnet zone, northeast Scotland. Geology, 25(1), 73-76. doi:10.1130/0091-7613(1997)025<0073:CMTAIM>2.3.CO;2

Baldwin, J., Powell, R., White, R., & Štípská, P. (2015). Using calculated

chemical potential relationships to account for replacement of kyanite by symplectite in high pressure granulites. Journal of Metamorphic Geology, 33(3), 311-330.

Blereau, E., Johnson, T. E., Clark, C., Taylor, R. J. M., Kinny, P. D., & Hand, M. (2017). Reappraising the *P–T* evolution of the Rogaland–Vest Agder Sector, southwestern Norway. Geoscience Frontiers, 8(1), 1-14. doi:10.1016/j.gsf.2016.07.003

Brady, J. B. (1995). Diffusion data for silicate minerals, glasses, and liquids. Mineral Physics and Crystallography: A Handbook of Physical Constants, 2, 269-290.

Brown, M., Averkin, Y. A., McLellan, E. L., & Sawyer, E. W. (1995). Melt segregation in migmatites. Journal of Geophysical Research: Solid Earth, 100(B8), 15655-15679.

Brown, M., & Johnson, T. E. (2018). Secular change in metamorphism and the onset of global plate tectonics. American Mineralogist. doi:/10.2138/am-2018-6166

Carlson, W. D. (2006). Rates of Fe, Mg, Mn, and Ca diffusion in garnet. American Mineralogist, 91(1), 1-11.

Chakraborty, S. (2008). Diffusion in solid silicates: a tool to track timescales of processes comes of age. Annu. Rev. Earth Planet. Sci., 36, 153-190.

Chakraborty, S., & Ganguly, J. (1992). Cation diffusion in aluminosilicate garnets: experimental determination in spessartine-almandine diffusion couples, evaluation of effective binary diffusion coefficients, and applications. Contributions to Mineralogy and Petrology, 111(1), 74-86.

Dohmen, R., & Chakraborty, S. (2003). Mechanism and kinetics of element and isotopic exchange mediated by a fluid phase. American Mineralogist, 88(8-9), 1251-1270.

Dorfler, K. M., Caddick, M. J., & Tracy, R. J. (2015). Thermodynamic modeling of crustal melting using xenolith analogs from the Cortlandt Complex, New York, USA. Journal of Petrology, 56(2), 389-408.

Doukkari, S. A., Diener, J. F., Ouzegane, K., & Kienast, J. R. (2018). Mineral equilibrium modelling and calculated chemical potential relations of reaction textures in the ultrahigh-temperature In Ouzzal terrane (In Hihaou area, Western Hoggar, Algeria). Journal of Metamorphic Geology, 36(9), 1175-

1198.

Droop, G. R., & Bucher-Nurminen, K. (1984). Reaction textures and metamorphic evolution of sapphirine-bearing granulites from the Gruf Complex, Italian Central Alps. Journal of Petrology, 25(3), 766-803.

Guevara, V.E., Caddick, M.J. (2016). Shooting at a moving target. Phase equilibrium modelling of high temperature metamorphism. Journal of Metamorphic Petrology, 34(3), 209-235.

Harley, S. L. (1989). The origins of granulites: A metamorphic perspective. Geological Magazine, 126(3), 215-247. doi:10.1017/S0016756800022330

Harley, S. L. (1998). Ultrahigh temperature granulite metamorphism (1050°C, 12 kbar) and decompression in garnet (Mg70) - orthopyroxene-sillimanite gneisses from the Rauer Group, East Antarctica. Journal of Metamorphic Geology, 16(4), 541-562.

Harley, S. L. (2008). Refining the P-T records of UHT crustal metamorphism. Journal of Metamorphic Geology, 26(2), 125-154. doi:10.1111/j.1525-1314.2008.00765.x

Harley, S. L. (2016). A matter of time: The importance of the duration of UHT metamorphism. Journal of Mineralogical and Petrological Sciences, 111(2), 50-72. doi:10.2465/jmps.160128

Harley, S. L., Hensen, B. J., & Sheraton, J. W. (1990). Two-stage decompression in orthopyroxene–sillimanite granulites from Forefinger Point, Enderby Land, Antarctica: implications for the evolution of the Archaean Napier Complex. Journal of Metamorphic Geology, 8(6), 591-613. doi:10.1111/j.1525-1314.1990.tb00490.x

Hess, K., & Dingwell, D. B. (1996). Viscosities of hydrous leucogranitic melts: A non-Arrhenian model. American Mineralogist: Journal of Earth and Planetary Materials, 81(9-10), 1297-1300.

Hier-Majumder, S., Leo, P. H., & Kohlstedt, D. L. (2004). On grain boundary wetting during deformation. Acta materialia, 52(12), 3425-3433.

Hier-Majumder, S., Ricard, Y., & Bercovici, D. (2006). Role of grain boundaries in magma migration and storage. Earth and Planetary Science Letters, 248(3-4), 735-749.

Hobbs, B. E., Ord, A., & Regenauer-Lieb, K. (2011). The thermodynamics of deformed metamorphic rocks: a review. Journal of Structural Geology, 33(5),

758-818.

Holland, T. J. B., & Powell, R. (2011). An improved and extended internally consistent thermodynamic dataset for phases of petrological interest, involving a new equation of state for solids. Journal of Metamorphic Geology, 29(3), 333-383. doi:10.1111/j.1525-1314.2010.00923.x

Holtz, F., Roux, J., Ohlhorst, S., Behrens, H., & Schulze, F. (1999). The effects of silica and water on the viscosity of hydrous quartzofeldspathic melts. American Mineralogist, 84(1-2), 27-36.

Johnson, T. E., Gibson, R. L., Brown, M., Buick, I. S., & Cartwright, I. (2003). Partial melting of metapelitic rocks beneath the Bushveld Complex, South Africa. Journal of Petrology, 44(5), 789-813.

Kelsey, D. E. (2008). On ultrahigh-temperature crustal metamorphism. Gondwana Research, 13(1), 1-29. doi:10.1016/j.gr.2007.06.001

Kelsey, D. E., & Hand, M. (2015). On ultrahigh temperature crustal metamorphism: Phase equilibria, trace element thermometry, bulk composition, heat sources, timescales and tectonic settings. Geoscience Frontiers, 6(3), 311-356. doi:10.1016/j.gsf.2014.09.006

Kelsey, D. E., Morrissey, L. J., Hand, M., Clark, C., Tamblyn, R., Gaehl, A. A., & Marshall, S. (2017). Significance of post-peak metamorphic reaction microstructures in the ultrahigh temperature Eastern Ghats Province, India. Journal of Metamorphic Geology, 35(9), 1081-1109. doi:10.1111/jmg.12277

Korzhinskiĭ, D. S. (1959). Physicochemical basis of the analysis of the paragenesis of minerals: Consultants Bureau.

Mitchell, R. J., Johnson, T. E., Clark, C., Gupta, S., Brown, M., Harley, S. L., & Taylor, R. (2019). Neoproterozoic evolution and Cambrian reworking of ultrahigh temperature granulites in the Eastern Ghats Province, India. Journal of Metamorphic Geology, 37(7), 977-1006.

Mungall, J. E. (2002). Empirical models relating viscosity and tracer diffusion in magmatic silicate melts. Geochimica et Cosmochimica Acta, 66(1), 125-143.

Ogilvie, P., & Gibson, R. L. (2017). Arrested development-a comparative analysis of multilayer corona textures in high-grade metamorphic rocks. Solid Earth, 8(1), 93.

Palin, R. M., Weller, O. M., Waters, D. J., & Dyck, B. (2016). Quantifying

geological uncertainty in metamorphic phase equilibria modelling; a Monte Carlo assessment and implications for tectonic interpretations. Geoscience Frontiers, 7(4), 591-607.

Powell, R., Evans, K., Green, E., & White, R. (2018). On equilibrium in non-hydrostatic metamorphic systems. Journal of Metamorphic Geology, 36(4), 419-438.

Rickers, K., Raith, M., & Dasgupta, S. (2001). Multistage reaction textures in xenolithic high-MgAl granulites at Anakapalle, Eastern Ghats Belt, India: Examples of contact polymetamorphism and infiltration-driven metasomatism. Journal of Metamorphic Geology, 19(5), 561-580. doi:10.1046/j.0263-4929.2001.00329.x

Rosenberg, C., & Handy, M. (2001). Mechanisms and orientation of melt segregation paths during pure shearing of a partially molten rock analog (norcamphor–benzamide). Journal of Structural Geology, 23(12), 1917-1932.

Rosenberg, C., & Handy, M. (2005). Experimental deformation of partially melted granite revisited: implications for the continental crust. Journal of Metamorphic Geology, 23(1), 19-28.

Sajeev, K., Osanai, Y., & Santosh, M. (2004). Ultrahigh-temperature metamorphism followed by two-stage decompression of garnet-orthopyroxene-sillimanite granulites from Ganguvarpatti, Madurai block, southern India. Contributions to Mineralogy and Petrology, 148(1), 29-46. doi:10.1007/s00410-004-0592-0

Schorn, S., & Diener, J. (2017). Details of the gabbro-to-eclogite transition determined from microtextures and calculated chemical potential relationships. Journal of Metamorphic Geology, 35(1), 55-75.

Schulze, F., Behrens, H., Holtz, F., Roux, J., & Johannes, W. (1996). The influence of H2O on the viscosity of a haplogranitic melt. American Mineralogist, 81(9-10), 1155-1165.

Spear, F. (2014). The duration of near-peak metamorphism from diffusion modelling of garnet zoning. Journal of Metamorphic Geology, 32(8), 903-914.

Štípská, P., Powell, R., White, R., & Baldwin, J. (2010). Using calculated chemical potential relationships to account for coronas around kyanite: an example from the Bohemian Massif. Journal of Metamorphic Geology, 28(1), 97-116.

Stüwe, K. (1995). Thermal buffering effects at the solidus. Implications for the equilibration of partially melted metamorphic rocks. Tectonophysics, 248(1-2), 39-51.

Takei, Y. (2005). Deformation-induced grain boundary wetting and its effects on the acoustic and rheological properties of partially molten rock analogue. Journal of Geophysical Research: Solid Earth, 110(B12).

Thompson Jr, J. B. (1957). The graphical analysis of mineral assemblages in pelitic schists. American Mineralogist: Journal of Earth and Planetary Materials, 42(11-12), 842-858.

Walte, N. P., Bons, P. D., & Passchier, C. W. (2005). Deformation of melt-bearing systems—insight from in situ grain-scale analogue experiments. Journal of Structural Geology, 27(9), 1666-1679.

Waters, D. J. (2001). The significance of prograde and retrograde quartz-bearing intergrowth microstructures in partially melted granulite-facies rocks. Lithos, 56(1), 108-110.

Watson, E. B. (1982). Melt infiltration and magma evolution. Geology, 10(5), 236-240.

Wheller, C. J., & Powell, R. (2014). A new thermodynamic model for sapphirine: Calculated phase equilibria in K2O-FeO-MgO-Al2O3-SiO2-H2O-TiO2-Fe2O3. Journal of Metamorphic Geology, 32(3), 287-299. doi:10.1111/jmg.12067

White, R. W., & Powell, R. (2011). On the interpretation of retrograde reaction textures in granulite facies rocks. Journal of Metamorphic Geology, 29(1), 131-149. doi:10.1111/j.1525-1314.2010.00905.x

White, R. W., Powell, R., & Baldwin, J. A. (2008). Calculated phase equilibria involving chemical potentials to investigate the textural evolution of metamorphic rocks. Journal of Metamorphic Geology, 26(2), 181-198. doi:10.1111/j.1525-1314.2008.00764.x

White, R. W., Powell, R., & Clarke, G. L. (2002). The interpretation of reaction textures in Fe-rich metapelitic granulites of the Musgrave Block, Central Australia: Constraints from mineral equilibria calculations in the system. Journal of Metamorphic Geology, 20(1), 41-55. doi:10.1046/j.0263-4929.2001.00349.x

White, R. W., Powell, R., Holland, T. J. B., Johnson, T. E., & Green, E. C.

R. (2014). New mineral activity-composition relations for thermodynamic calculations in metapelitic systems. Journal of Metamorphic Geology, 32(3), 261-286. doi:10.1111/jmg.12071

Chapter 3 | Neoproterozoic evolution and Cambrian reworking of granulites from Vizianagaram, Eastern Ghats Province

Ruairidh J. Mitchell[1,2], Tim E. Johnson[1,3], Chris Clark[1], Saibal Gupta[2], Michael Brown[4], Simon L. Harley[5], Richard Taylor[6]

1. School of Earth and Planetary Sciences, The Institute for Geoscience Research, Curtin University, Perth, WA 6102, Australia
2. Department of Geology and Geophysics, Indian Institute of Technology, Kharagpur, India
3. State Key Laboratory for Geological Processes and Mineral Resources and Center for Global Tectonics, School of Earth Sciences, China University of Geosciences, Wuhan 430074, China.
4. Laboratory for Crustal Petrology, Department of Geology, University of Maryland, College Park, MD 20742-4211, USA
5. School of Geosciences, University of Edinburgh, Edinburgh, EH9 3FE, UK
6. Department of Earth Sciences, University of Cambridge, Cambridge, CB2 3EQ, UK

Abstract

The timescales and pressure–temperature (*P–T*) conditions recorded by granulite facies metamorphic rocks permit inferences about the geodynamic regime in which they formed. Two compositionally heterogeneous cordierite–spinel-bearing granulites from Vizianagaram, Eastern Ghats Province (EGP), India, were investigated to provide *P–T–time* constraints using petrography, phase equilibrium modelling, U–Pb geochronology, the rare earth element (REE) composition of zircon and monazite, and Ti-in-zircon thermometry. These ultra-high temperature (UHT) granulites preserve discrete compositional layering in which different inferred peak assemblages are developed, including layers bearing garnet–sillimanite–spinel and others bearing orthopyroxene–sillimanite–spinel. These mineral associations cannot be reproduced by phase equilibrium modelling of whole rock compositions, indicating that the samples became domainal on a scale less than that of a thin section, even at UHT conditions. Calculation of the *P–T* stability fields for six compositional domains within which the main rock-forming minerals are considered to have attained equilibrium suggests peak metamorphic conditions of ~6.8–8.3 kbar at ~1000°C. In most of these domains, the subsequent evolution resulted in the growth of cordierite and final crystallization of melt at an elevated (residual) H_2O-undersaturated solidus, consistent with <1 kbar of decompression. Concordant U–Pb ages obtained by SHRIMP from zircon (spread 1050-800Ma) and monazite (spread 950-800Ma) suggest that crystallization of these minerals occurred during an interval of c. 250 Ma. By combining LA-ICPMS U–Pb

zircon ages with Ti-in-zircon temperatures from the same analysis sites, we show that the crust may have remained above 900°C for a minimum of c. 120 Ma between c. 1000 and c. 880 Ma. Overall, the results suggest that, in the interval 1050 to 800 Ma, the evolution of the Vizianagaram granulites culminated with UHT conditions from c.1000 Ma to c. 880 Ma, associated with minor decompression, before further zircon crystallization at c. 880–800 Ma during cooling to the solidus. However, these rocks are adjacent to the Paderu–Anantagiri–Salur crustal block to the NW that experienced counterclockwise *P–T–t* paths, and records similar UHT peak metamorphic conditions (7–8 kbar, ~950°C) followed by near-isobaric cooling, and has a similar chronology during the Neoproterozoic. The limited decompression inferred at Vizianagaram may be explained by partial exhumation due to thrusting of this crustal block over the adjacent Paderu–Anantagiri–Salur crustal block. The residual granulites in both blocks have high concentrations of heat producing elements and likely remained hot at mid-crustal depths throughout a period of relative tectonic quiescence in the interval 800–550 Ma. During the Cambrian Period the EGP was located in the hinterland of the Denman–Pinjarra–Prydz orogen. A later concordant population of zircon dated at 511 ± 6 Ma records crystallization at temperatures of ~810°C. This age may record a low-degree of melting due to limited influx of fluid into hot, weak crust in response to convergence of the Crohn craton with a composite orogenic hinterland comprising the Rayner terrane, Eastern Ghats Province and cratonic India.

Figure 3.1 | Map of the Eastern Ghats Mobile Belt (EGMB) to show domains defined by different characteristic lithologies (after Rickers et al., 2001, Korhonen, Clark et al., 2013). The samples were collected from north of Vizianagaram: GR: 18° 09' 17.7" N, 83° 25' 07.3" E (EGB-09-45), 18° 09' 17.3" N, 83° 25' 24.6" E (EGB-09-47), 18° 08' 46.7" N, 83° 26' 27.4" E (EGB-09-55).

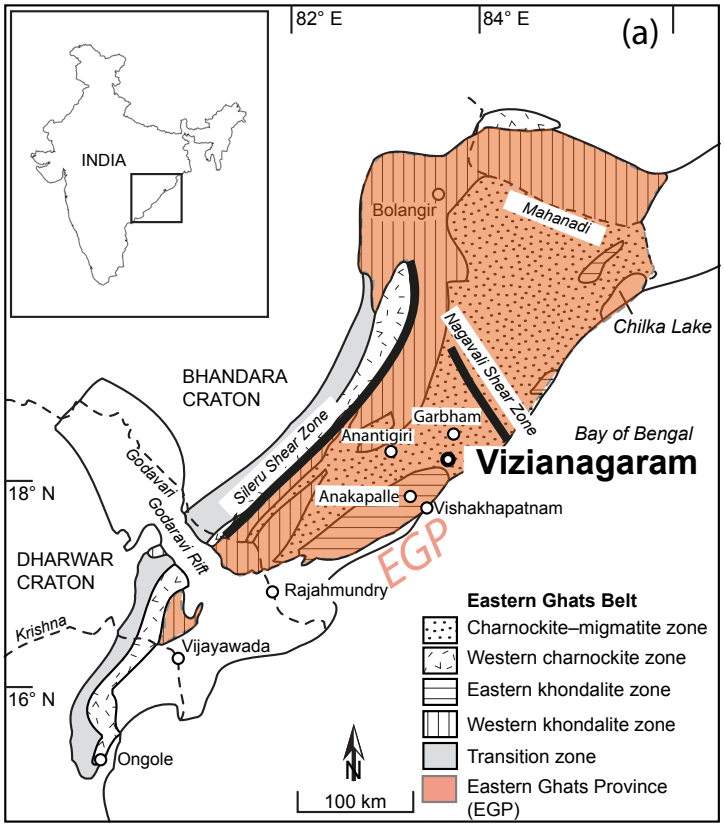

3.1 | Introduction

Exhumed granulite facies metamorphic rocks are witnesses to the evolving thermal and rheological conditions in the mid-to-lower crust during orogenesis (Brown and Johnson, 2018; Harley, 2008; Kelsey and Hand, 2015). The widespread occurrence of high temperatures in the deep crust throughout Earth's history is inferred from the presence of granulites with metamorphic ages ranging from the Archean to the present day (Brown, 2007; Harley, 1998; Kelsey, 2008; Kelsey and Hand, 2015). The suggested duration of high and ultra-high temperature metamorphic events vary from < or <<20 Ma (Dragovic et al., 2016; Galli et al., 2011; Pownall, 2015) to in excess of 100 Ma (Blereau et al., 2017; Harley, 2016; Holder et al., 2018; Korhonen et al., 2013b).

Granulites form across a range of apparent thermal gradients to reach high and ultra-high temperatures (UHT, where T > 900°C), conditions under which widespread partial melting, melt migration and melt loss are inevitable for almost all crustal protoliths (e.g. Brown, 2013; Johnson, White, & Powell, 2008; Rushmer, 1991; White, Powell, Holland, Johnson, & Green, 2014). In addition, granulites may record a range of retrograde pressure–temperature (*P–T*) paths associated with cooling rates that vary from fast to slow (Harley, 2016; Kelsey and Hand, 2015). Metamorphic conditions recovered from peak metamorphic mineral assemblages typically yield apparent thermal gradients ranging from ~77.5 °C/kbar to >150 °C/kbar (Brown and Johnson, 2018). Several 1D thermal models predict that UHT conditions may be sustained for 60 Ma or more at crustal depths of ~20–50 km, if there was a favourable combination of high mantle heat flow, elevated radiogenic heat production from heat producing elements (HPE), net removal of melt, and low erosion rates (Clark et al., 2011; Horton et al., 2016).

Many granulite terranes are temporally linked to supercontinent assembly (Brown, 2007; Brown and Johnson, 2018; Clark et al., 2015; Sizova et al., 2014). Extension in backarc regions within accretionary orogens may result in high advectively-driven thermal gradients, leading to UHT metamorphism as a precursor to thickening and formation of mobile belts during collision (Brown, 2007b) in rocks containing high concentrations of HPE (Clark et al., 2011). This hypothesis may provide a robust explanation for granulite facies metamorphism in modern backarcs (Currie and Hyndman, 2006; Hyndman, 2015; Hyndman and Currie, 2011). Alternatively, granulite facies metamorphism may occur in the deep crust of thickened orogenic

plateaux (Clark et al., 2015; Harley, 2016; Jamieson and Beaumont, 2011; Jamieson et al., 2010), particularly where radiogenic heat production and low erosion rates may be sustained for >60 Ma (Clark et al., 2011). Examples of such settings include the modern Tibetan plateau (Hacker et al., 2000; McKenzie and Priestley, 2008), where granulite facies metamorphism is still occurring (Hacker et al., 2014), and the East African Orogen (Collins et al., 2003; Fritz et al., 2013), in which late Neoproterozoic and early Palaeozoic metamorphism lasted for up to 100 Ma (Boger et al., 2015; Clark et al., 2015; Clark et al., 2014; Plavsa et al., 2015).

In order to evaluate the tectonic evolution of a terrane with similarly long lived granulite facies conditions, we present further *P–T–time* constraints; data from metapelitic rocks from Vizianagaram, Eastern Ghats Province (EGP), India (Figure 3.1). We use petrographic observations combined with phase equilibrium modelling, U-Pb geochronology of zircon and monazite, coupled with the REE concentrations of zircon, and Ti-in-zircon thermometry to suggest that these rocks experienced long-lived UHT conditions in the interval 1000–880 Ma, associated with decompression of <1 kbar. These rocks may have remained melt bearing for a total of c. 250 million years in the interval 1050–800 Ma. Further, there is evidence for suprasolidus neocrystallization of zircon at temperatures of ~810°C at c. 510 Ma. Our results from Vizianagaram contrast with published results from the adjacent Paderu–Anantagiri–Salur crustal block to the NW, which experienced counterclockwise *P–T–t* paths at UHT conditions followed by near-isobaric cooling (Das et al., 2011; Korhonen et al., 2013a; Korhonen et al., 2014; Korhonen et al., 2011). This contrast suggests a tectonic model in which two crustal blocks were juxtaposed by thrusting.

3.2 | Regional Geology

The Eastern Ghats Mobile Belt is a polymetamorphic terrane located in the east of the Indian peninsula (Figure 3.1). The rocks preserve a varied and complex history spanning the period from the late Paleoproterozoic to the early Palaeozoic (Dasgupta et al., 2013; Kelsey et al., 2017; Sarkar and Schenk, 2014; Simmat and Raith, 2008). Discrete crustal blocks (terranes) bounded by large-scale shear zone systems have previously been invoked based on the isotopic, metamorphic and lithological characteristics of the rocks (Rickers et al., 2001a). One such terrane, the Eastern Ghats Province (EGP; Figure 3.1), lies between the Godaravi rift to the south, the Kerajang

shear zone to the north and the Sileru shear zone system to the west (Dobmeier and Raith, 2003).

Multiple localities within the EGP preserve evidence for UHT conditions (Das et al., 2011; Korhonen et al., 2013a; Korhonen et al., 2013b; Korhonen et al., 2014; Korhonen et al., 2011; Prakash et al., 2015), suggesting that UHT metamorphism was regional in extent. The *P–T* evolution of rocks within the EGP has been constrained using a variety of methods at different localities. Phase equilibrium studies from various localities constrain peak conditions to >950°C and ~8 kbar followed by near-isobaric cooling (Korhonen et al., 2013a; Korhonen et al., 2011). In addition, high Al–Mg granulites at Anantagiri are inferred to record peak metamorphic temperatures that exceeded 1000°C (Korhonen et al., 2014).

The duration of granulite facies conditions in the EGP has been estimated from U–Pb zircon and monazite geochronology at multiple localities (Korhonen et al., 2015; Korhonen et al., 2013b). Korhonen et al. (2013b) report protracted growth of metamorphic zircon throughout the EGP over durations of up to 300 Ma between c. 1100 and c. 800 Ma. Their samples yield discrete clusters of concordant zircon and monazite ages within this broader temporal range, implying partial melt crystallization above different elevated (H2O-undersaturated) solidii following some drainage of melt. Near-concordant ages of 613 Ma and 566 Ma may record new zircon growth or else be related to Pb loss from older zircon due to lower temperature fluid-mediated processes (Korhonen et al., 2013b). Although there are no *P–T* constraints linked to these Pan African ages, to the west Mahato & Bhattacharya (2010) report *P–T* conditions of 6.5 ± 1.5 kbar and 730 ± 30 °C related to a Pan African metamorphic overprint which may have been developed close to the Eastern Ghats Frontal Thrust at c. 525-510 Ma (Chatterjee, Das, Bose, Ganguly & Hidaka, 2017). Additionally c. 700 Ma zircon U-Pb and 724-698 Ma titanite U-Pb ages (Nanda, Gupta & Hacker, 2018) have been recovered close to the Sileru Shear Zone (Figure 3.1).

The EGP samples analysed in this study are garnet–cordierite–sillimanite granulites from Vizianagaram (samples EGB-09-45 from 18° 09’ 17.7” N, 83° 25’ 07.3” E; EGB-09-47 from 18° 09’ 17.3” N, 83° 25’ 24.6” E; and EGB-09-55 from 18° 08’ 46.7” N, 83° 26’ 27.4” E; Figure 3.1). Published *P–T* constraints for this locality are peak conditions of 8-10 kbar at >1000 °C, followed by near isobaric cooling to 750-800 °C and then near isothermal

decompression to 4-5 kbar (Kamineni and Rao, 1988; Sarkar et al., 2003). These *P–T* estimates were inferred from univariant equilibria in petrogenetic grids in the simplified FMAS and KFMASH chemical systems, which neglect the complexity of natural rocks.

3.3 | Methods

3.3.1 | Phase equilibrium modelling

Pressure–temperature pseudosections were calculated using THERMOCALC 3.40 and the ds6 internally consistent thermodynamic dataset (Holland and Powell, 2011); tc–ds62.txt, updated 6 February 2012). Pseudosections were calculated in the Na_2O–CaO–K_2O–FeO–MgO–Al_2O_3–SiO_2–H_2O–TiO_2–Fe_2O_3 (NCKFMASHTO) chemical system using the following solution models: biotite, garnet, cordierite, orthopyroxene, silicate melt, ilmenite (White et al., 2014); sapphirine (Wheller and Powell, 2014), ternary feldspar from Holland & Powell (2003) and spinel–magnetite from White, Powell & Clarke (2002). Whole rock compositions for initial *P–T* pseudosections are based on whole rock XRF analyses for which loss-on-ignition (LOI) and Fe titration were used to constrain maximum H_2O and Fe_2O_3 concentrations, respectively. However, since these initial *P–T* pseudosections do not reproduce the inferred peak assemblages, domainal compositions were calculated based on the abundance and composition of minerals in selected areas in polished thin sections. The areas are inferred to have different mineral assemblages stable at the metamorphic peak. In order to conform to the rationale for interpreting granulite peak assemblages described in Chapter 2, the following method was applied. proportion of minerals (Table 3.1) in each domain was measured using the TESCAN TIMA FEG–SEM at Curtin University (analytical procedures are given in Appendix C.1), whereas representative mineral compositions were determined by EPMA using a Cameca SX51 at the University of Adelaide, for which the analytical protocol is can be found in Kelsey et al. (2017). The mineral compositions are provided in Appendix C.2. In principle, this method returns comparable results to using mass-balance calculations on mineral proportions calculated from X-ray maps or BSE images, but is automated so larger datasets can be collected. Volatile concentrations in cordierite were measured in cordierite grain-separates by SIMS using a Cameca IMS–4f ion microprobe at the University of Edinburgh (Harley, 1994); see Appendix C.3. Measured H2O concentrations in cordierite and ideal H_2O concentrations in biotite were used, together with the measured abundance of these minerals, to estimate H2O concentrations

within domains. Mineral abbreviations follow Whitney and Evans (2010). *P–T* uncertainties for zero-mode isopleths bounding inferred prograde, peak and retrograde mineral assemblage fields were calculated using the calcsdnle script in THERMOCALC 3.40.

3.3.2 | Zircon geochronology and thermometry

SHRIMP analysis of zircon was undertaken using the method detailed in Korhonen et al. (2013b). Zircon grains from samples EGB–09–45, –47 and –55 were separated from crushed rock using standard magnetic and heavy liquid methods. Grains were hand-picked and mounted on epoxy resin discs, polished to approximate half grain thickness then carbon coated. Zircon grains were imaged by cathodoluminescence (CL) with a Phillips XL30 scanning electron microscope located in the John de Laeter Centre, Curtin University using an acceleration voltage of 12 kV and a working distance of 15 mm. Cathodoluminescence imaging highlights distortions in the crystal lattice related to trace element distribution and radiation damage (Nasdala et al., 2003; Rubatto and Gebauer, 2000). After imaging, the grain mounts were then cleaned ultrasonically with ethanol, petroleum ether and detergent (Decon), before being rinsed in distilled and deionized water, and dried in an oven at 60°C. The mount was coated with a thin membrane of gold producing a resistivity of 10–20 Ωm across the disk.

Zircon U–Th–Pb isotope ratios were measured using the SHRIMP II in the John de Laeter Centre, Curtin University. Analysis spots on zircon are shown in Appendix C.4. The sensitivity for Pb isotope measurements in zircon was 21 cps/pp/nA, the primary beam current was 2.5–3.0 nA and mass resolution was ~5000. Measured isotope ratios were corrected for common Pb based on the measured 204Pb, in most cases resulting in a <1% correction to the 206Pb counts. The Stacey and Kramers (1975) correction for common lead was used to correct U–Pb ages. Pb/U isotope ratios were corrected for instrumental inter-element discrimination using the observed co-variation between Pb+/U+ and UO+/U+ (Compston et al., 1984; Hinthorne et al., 1979) determined from interspersed analyses of zircon standard BR266. Standard BR266 is a single zircon megacryst from Sri Lanka with an age of 559 ± 0.3 Ma, $^{206}Pb/^{238}U$ = 0.09059, U and Th concentrations of 909 and 201 ppm respectively (Stern, 2001). Raw data are presented in Appendix C.5.

For laser ablation inductively coupled mass spectrometry (LA–ICP–MS) analyses, eleven zircon grains from three garnet–cordierite gneisses

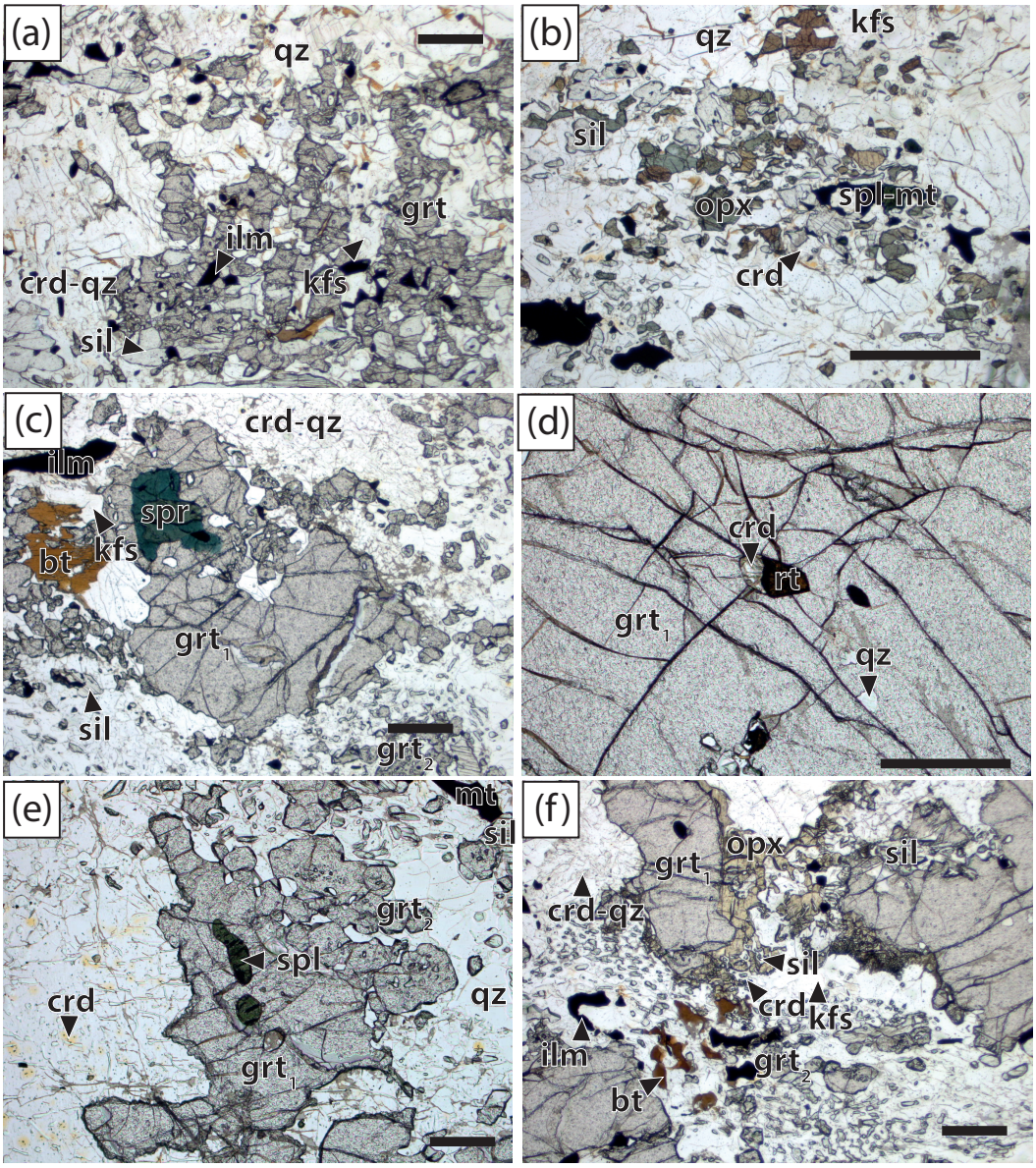

Figure 3.2 | Plane polarized light photomicrographs of samples EGB–09–45 (a, b) and EGB–09–47 (c–i); scale bars are 500 μm. (a) Grt and sill porphyroblasts with adjacent crd–qz intergrowths in kfs + qz matrix. (b) Opx–sil–spl intergrowths; thin seams of crd separate opx and sil. (c) Grt_1 with spr inclusions wrapped by fine-grained sil–crd–qz intergrowths. Euhedral grt2 occurs with coarse bt laths and kfs. (d) Crd, rt and qz inclusions in grt1. (e) Spl inclusions in grt_1. (f) Grt_1 in contact with prismatic sil and opx, mantled by crd and grt_2.

from Vizianagaram (samples EGB–09–45, 47 and 55) were texturally characterized in thin section using CL imaging on a Tescan Mira3 XMU VP–FESEM at Curtin University. Concentrations of selected REEs and Ti, along with isotope ratios of U, Th and Pb, to monitor the age of the analysed zircon zone, were determined using the LA–ICP–MS facility at the John de Laeter Center, Curtin University. The analysis time included 15–20 s of background

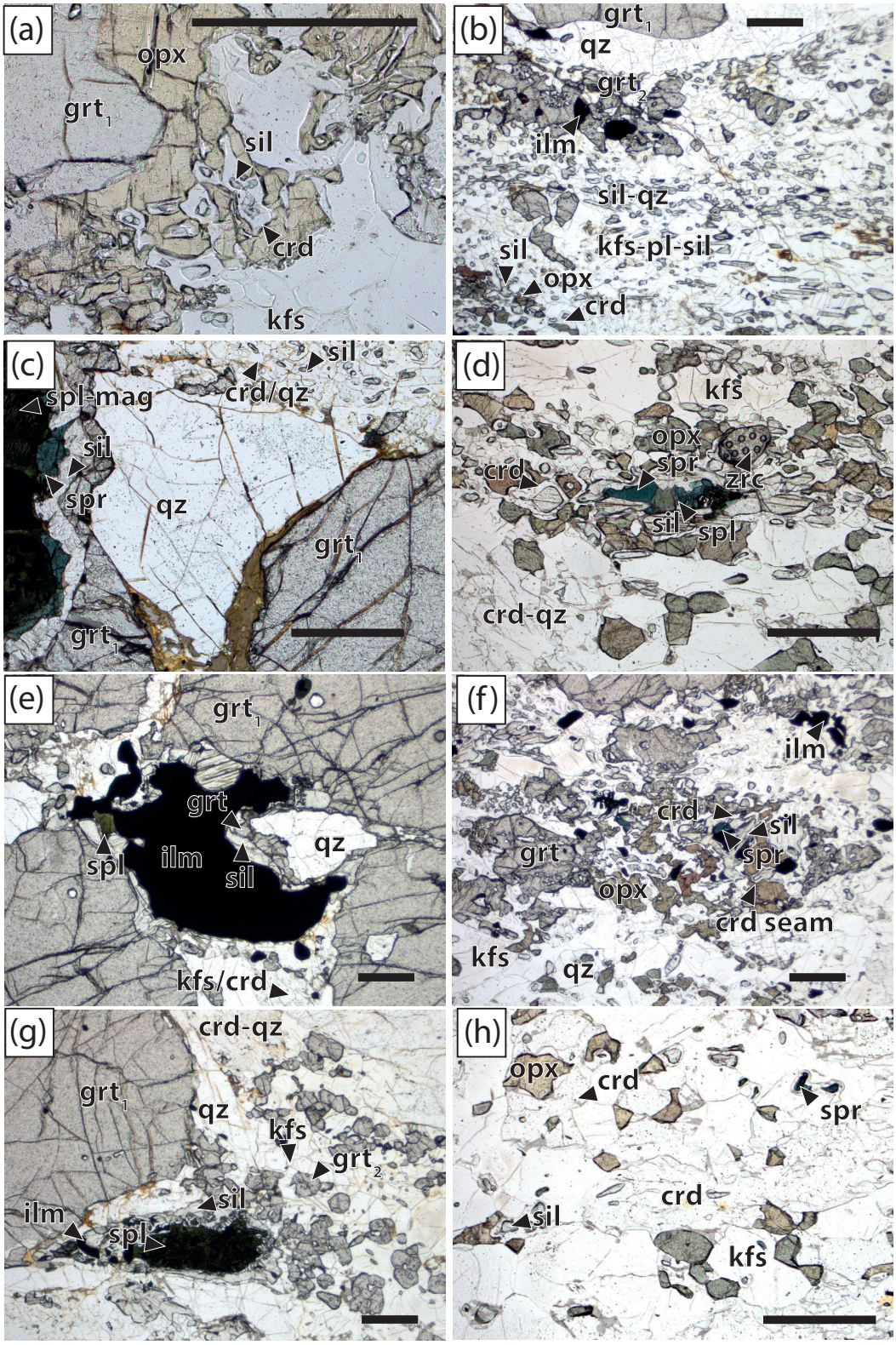
(a)
opx
grt1
sil
crd
kfs
(b)
grt1
qz
grt2
ilm
sil-qz
sil
kfs-pl-sil
opx
crd
(c)
sil
spl-mag
crd/qz
sil
spr
qz
grt1
grt1
(d)
kfs
opx
spr
crd
zrc
sil
spl
crd-qz
(e)
grt1
grt
spl
ilm
sil
qz
kfs/crd
(f)
ilm
crd
sil
grt
spr
opx
crd seam
kfs
qz
(g)
crd-qz
grt1
qz
kfs
grt2
sil
ilm
spl
(h)
opx
crd
spr
crd
sil
kfs

Figure 3.3 | Plane polarized light photomicrographs of sample EGB–09–47. (a) Grt1 porphyroblasts mantled by opx–sil intergrowth (NB opx and sil now separated by crd). (b) Domains in EGB–09–47: grt2–ilm–kfs, finer grained sil–crd–qz, coarser opx–sil intergrowths. (c) Rare spr–spl mantled by sil. Opx–sil intergrowths, in which opx and sil are separated by crd; NB large zrc grain shown in Fig 6c. (d) Spl with spr|sil|grt|qz corona. (e) Ilm with sil|grt|qz corona. (f) Setting of opx|crd|sil coronae. (g) Setting of grt¬2-kfs relict leucosomes, grt1, and spl|sil|grt corona; NB distinctive euhedral habit of grt2. (h) Porphyroblastic crd, grain diameter >500μm, in contact with opx. NB retrograde crd seam between opx and sill to the left of the Figure for comparison.

and most analyses used spot sizes of 25 μm (33 μm for larger grains). Grains were ablated using a 193 nm wavelength Resonetics RESOlution M–50A–LR, incorporating a ComplexPro 102 coherent excimerlaser with a 1.7 J/cm2 energy density at the sample surface and a 7 Hz repetition rate. Isotope ratios were measured with an Agilent 7700x ICP–MS system with high purity Ar plasma gas with a 0.98 l/min flow rate. Isotopes were monitored for 0.01 s, except ^{204}Pb, ^{206}Pb, ^{207}Pb (0.03 s), ^{232}Th and ^{238}U (0.0125 s). Data reduction was undertaken using the Iolite v.3 software (Paton et al., 2011). Reduction of U–Th–Pb isotopic compositions used natural zircon standard 91500 (1062 ± 0.4 Ma; (Wiedenbeck et al., 1995) as an external reference material and 238U/235U = 137.82 as an internal standard. For zircon trace element analysis, glass standard NIST 612 was used as an external reference material and stoichiometric 49.00 wt% ^{91}Zr as an internal standard (Liu et al., 2010); analyses returning anomalous (non–stoichometric) Si concentrations were discarded. The calibration of (Ferry and Watson, 2007) at 10 kbar was used for Ti-in-zircon thermometry, as there is no published calibration of the pressure dependence for this thermometer (Ferry & Watson, 2007; Tomkins, Powell, & Ellis, 2007). Analytical data are provided – U-Pb data in Appendix C.6 and REE/Ti concentrations in Appendix C.7.

3.3.3 | Monazite geochronology

Thin section fragments from samples EGB–09–45, –47 and –55 containing monazite grains were mounted along with chips of monazite standard ind–1 [509 Ma, 2–6Pb/238U = 0.082133; (Korhonen et al., 2011)] and prepared using a similar procedure to the zircon mounts. Monazite was imaged using a backscatter electron (BSE) detector on a Philips XL30 SEM located at the John de Laeter Centre, Curtin University using a working distance of 5mm and an accelerating voltage of 20 kV. U–Pb isotope measurements on the SHRIMP II used a ~0.5nA O^{2-} primary beam, 10 μm spots, a 5-scan duty cycle and a mass resolution of ~5000. Additional details regarding the Curtin SHRIMP procedures for measurement of monazite are outlined by (Foster

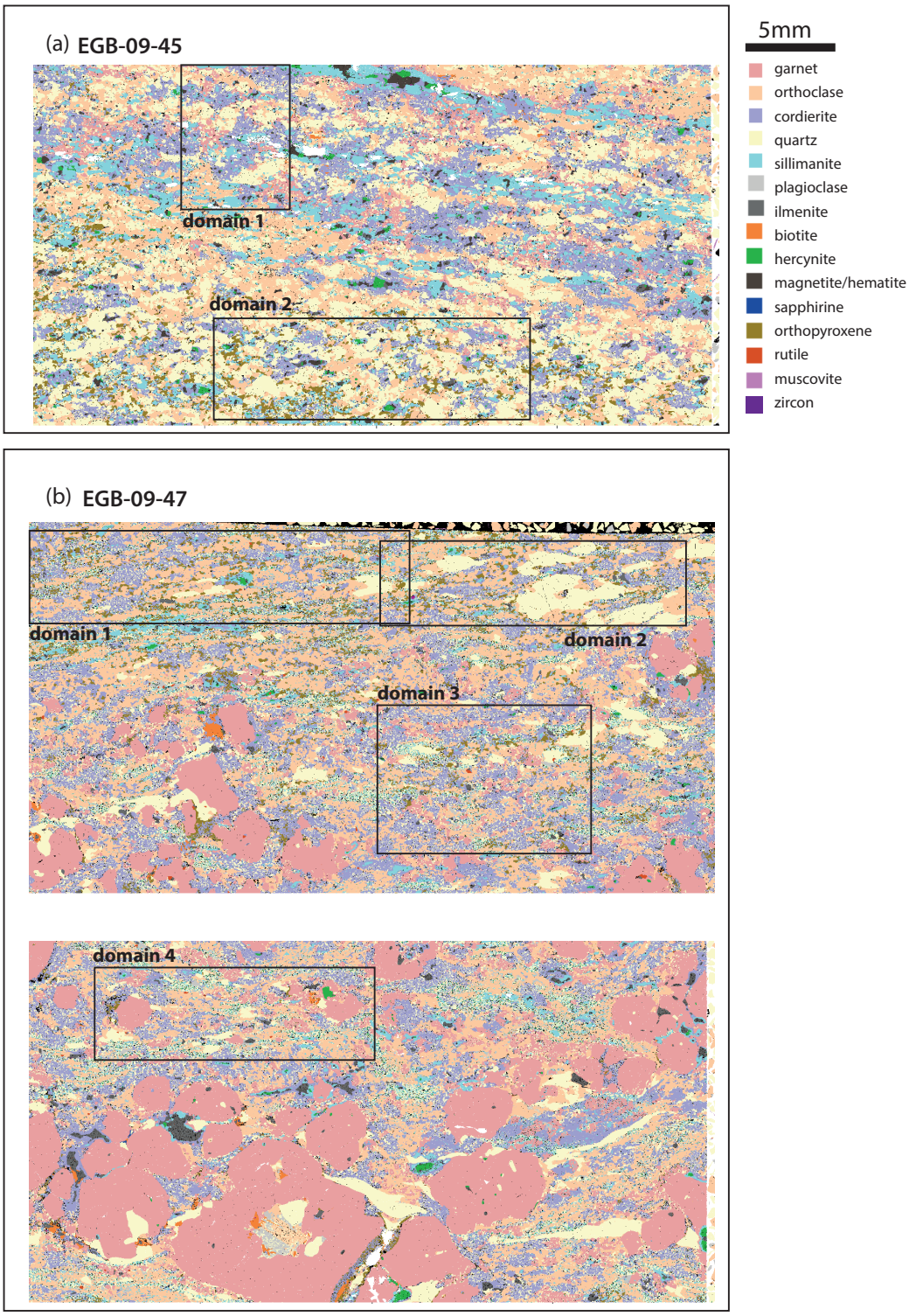

Figure 3.4 | Tescan Integrated Mineral Analyser (TIMA) mineral maps for samples EGB–09–45 and -47 with petrological domains used for phase equilibrium modelling outlined. Compositions were calculated from mineral abundances (Table 1) for each area shown (Table 2).

	domain	quartz	K-feldspar	cordierite	garnet	sillimanite	orthopyroxene	sapphirine	magnetite	plagioclase	ilmenite	spinel	biotite	rutile
EGB-09-45	1.	44.24	14.81	16.24	0.00	10.23	11.17	0.01	1.80	0.09	0.48	0.82	0.01	0.10
	2.	28.51	16.59	26.05	11.26	14.34	0.00	0.02	1.89	0.07	0.78	0.31	0.16	0.02
EGB-09-47	1.	15.75	35.72	26.25	0.00	8.26	10.63	0.17	0.07	1.87	0.85	0.01	0.37	0.06
	2.	33.94	30.84	19.24	0.00	5.50	7.90	0.13	0.03	1.39	0.89	0.01	0.02	0.11
	3.	21.91	24.79	31.26	9.07	4.63	3.95	0.00	0.16	2.86	1.06	0.09	0.01	0.22
	4.	23.00	24.80	20.57	19.96	5.84	0.60	0.39	0.16	3.47	0.73	0.01	0.28	0.18

Table 3.1 | Mineral area proportions for petrological domains in samples EGB-09-45 and -47 (see Figure 3.3) from Tescan-Integrated-Mineral-Analyser (TIMA) phase maps.

		mol %											
	domain	H2O	SiO2	Al2O3	CaO	MgO	FeO	K2O	Na2O	TiO2	O	XMg	A/AFM
EGB-09-45	1.	0.04	82.29	8.67	0.08	2.06	4.31	0.72	0.20	0.41	1.22	0.32	0.58
	2.	0.01	86.93	4.93	0.02	2.89	3.49	0.46	0.14	0.35	0.78	0.45	0.44
EGB-09-47	1.	0.06	77.46	9.24	0.20	5.64	3.60	2.04	0.50	1.17	0.09	0.61	0.50
	2.	0.02	87.54	4.84	0.11	2.92	2.06	1.22	0.30	0.95	0.05	0.59	0.49
	3.	0.04	81.66	7.02	0.26	4.06	3.50	1.28	0.39	1.58	0.21	0.54	0.48
	4.	0.04	82.10	7.44	0.35	3.48	3.57	1.28	0.44	1.13	0.16	0.49	0.51

Table 3.2 | Calculated bulk compositions for petrological domains in samples EGB-09-45 and -47 (see Figure 3.3).

et al., 2000). BSE images of monazite grains are given in Appendix C.8, and U-Pb data tables for monazite analyses are given in Appendix C.6.

3.4 | Results

3.4.1 | Petrography

The petrological features of samples EGB–09–45 and –47 are illustrated in Figure 3.2a, b (EGB–09–45), and Figures 3.2c–f and 3.3 (EGB–09–47). EGB–09–45 was likely sampled accross lithological layering, as observed in the field photos of EGB–09–45 and –47 (Appendix C.9).

Sample EGB–09–45 is a granulite with discrete compositional layers ~5 mm thick. Individual layers are dominated either by garnet–sillimanite–spinel–cordierite (domain 1; Figure 3.2a) or orthopyroxene–sillimanite–cordierite–spinel (domain 2; Figure 3.2b), in which a weak foliation is defined by prismatic sillimanite. K-feldspar, plagioclase and quartz are present in all domains. Accessory minerals include ilmenite, composite grains of spinel–magnetite, zircon and monazite. Garnet contains abundant inclusions of quartz, K-feldspar and, rarely, spinel–magnetite mantled by sillimanite. Cordierite in domain 1 occurs as ~5 mm poikiloblasts containing quartz and K-feldspar inclusions, and as thin seams separating sillimanite from garnet (Figure 3.2a). Prismatic sillimanite commonly surrounds spinel and ilmenite.

Orthopyroxene and sillimanite occur throughout domain 2, but are always separated by a thin layer of cordierite (Figure 3.2b). Cordierite also occurs as patchy intergrowths with K-feldspar and quartz.

We interpret the peak assemblages in domains 1 and 2 to be garnet–sillimanite–spinel (Figure 2a; domain 1 in Figure 3.4a) and orthopyroxene–sillimanite–spinel (Figure 3.2b; domain 2 in Figure 3.4a), respectively, each with K-feldspar, quartz and ilmenite. Fine-grained interstitial cordierite–quartz intergrowths are considered to be a retrograde feature.

Sample EGB–09–47 is a garnet–sillimanite–orthopyroxene–cordierite–sapphirine–spinel-bearing metapelitic granulite. Large grains (~3 cm) of garnet, interpreted to record an early prograde growth stage ($garnet_1$), have inclusions of cordierite, isolated sapphirine, quartz, spinel, magnetite, ilmenite, rutile and zircon (Figure 3.2c–e). Rarely, euhedral sillimanite is observed in direct contact with $garnet_1$ (Figure 3.2f). A second generation of garnet ($garnet_2$) occurs as euhedral grains ~200 μm across containing abundant lobate inclusions of quartz. Garnet2 commonly coexists with granoblastic K-feldspar and quartz, consistent with it forming in the presence of partial melt ((Waters, 2001); Figures 3.2c, f and 3.3b, g). Orthopyroxene grains up to ~500 μm across occur in layers dominated by cordierite and sillimanite (Figure 3.3b, d). Commonly, domains containing garnet2 and K-feldspar contain coarse biotite (Figure 3.2c). Sillimanite, orthopyroxene and spinel, which are separated by thin seams of cordierite, occur in clearly defined layers, similar to those in EGB–09–45 (Figure 3.3b, d). Sapphirine porphyroblasts occur within the K-feldspar-quartz dominated matrix and are mantled by cordierite or sillimanite, separating it from quartz (Figure 3.3d, f). Quartz is present throughout the matrix and as inclusions in $garnet_1$, so is inferred to have been present throughout the metamorphic evolution of EGB-09-47.

$Garnet_1$ grains are commonly replaced at their margins by symplectites comprising fine intergrowths of orthopyroxene and cordierite with or without sillimanite (Figures 3.2f and 3.3a). In some cases, the symplectites occur in close proximity to biotite (Figure 3.2f). A fabric defined by compositional layering wraps the garnet1 porphyroblasts. The layering comprises three garnet-bearing associations: (i) a granoblastic areas comprising euhedral garnet2 and K-feldspar, (ii) areas with garnet2 and cordierite, and (iii) fine intergrowths of garnet–sillimanite–cordierite–K-feldspar–quartz

(Figure 3.2c; 3.3b). In addition, there are aluminous layers dominated by orthopyroxene and sillimanite (Figure 3.3b), which lack garnet and are separated from garnet-bearing domains by K-feldspar–cordierite–quartz horizons. Furthermore, several corona textures occur throughout the sample. These are (from core to rim): spinel|sapphirine|sillimanite|garnet2|qz (Figure 3.3c) and ilmenite|sillimanite|garnet2|quartz (Figure 3.3e) coronae, both of which are developed at the margins of garnet1, and spinel|sillimanite|K-feldspar and orthopyroxene|cordierite|sillimanite coronae that occur in garnet-absent orthopyroxene–sillimanite layers (Figure 3.3d). Garnet2 never exhibits symplectic intergrowths at its margins, regardless of textural association.

The textural development of EGB–09–47 is complex. However, we interpret the that prograde growth of garnet1 occurred in equilibrium with cordierite, sapphirine and quartz. Inferred domainal peak assemblages include: garnet–sapphirine–sillimanite (Figure 3.2c; Figure 4b, domain 4), garnet–orthopyroxene–sillimanite (Figures 3.2f and 3.3a; Figure 4b, domain 3) and orthopyroxene–sapphirine–sillimanite–spinel–(porphyroblastic) cordierite (Figure 3.3d, h; Figure 3.4b, domains 1 and 2), each with K-feldspar and quartz. The retrograde breakdown of peak phases has led to the development of fine-grained cordierite–sillimanite–quartz intergrowths (Figures 3.2e, f, h and 3.4b) within the orthopyroxene–sillimanite–spinel bearing layers. However, coarse inclusion-poor cordierite distinct to that between orthopyroxene and sillimanite is interpreted to be part of the domainal peak assemblage (i.e. Figure 3.3h; Figure 3.4b, domains 1 and 2). Domains containing euhedral garnet2 and rich in K-feldspar (Figure 3.3g) are interpreted as relict leucosomes formed with cooling through garnet stability fields.

3.4.2 | Phase equilibrium modelling

Whole rock compositions

For samples EGB–09–45 and –47, orthopyroxene and sillimanite are interpreted to have stably coexisted at the metamorphic peak in some petrographic domains (Figures 3.2b and 3.3a, d, f), but orthopyroxene is not predicted to be stable with sillimanite anywhere in the *P–T* pseudosection based on the whole rock composition for either sample (Appendix C.10). Furthermore, as these interpreted peak assemblages vary on a centimetre scale in each sample (Figure 3.4), the rocks are inferred to have become domainal at UHT conditions.

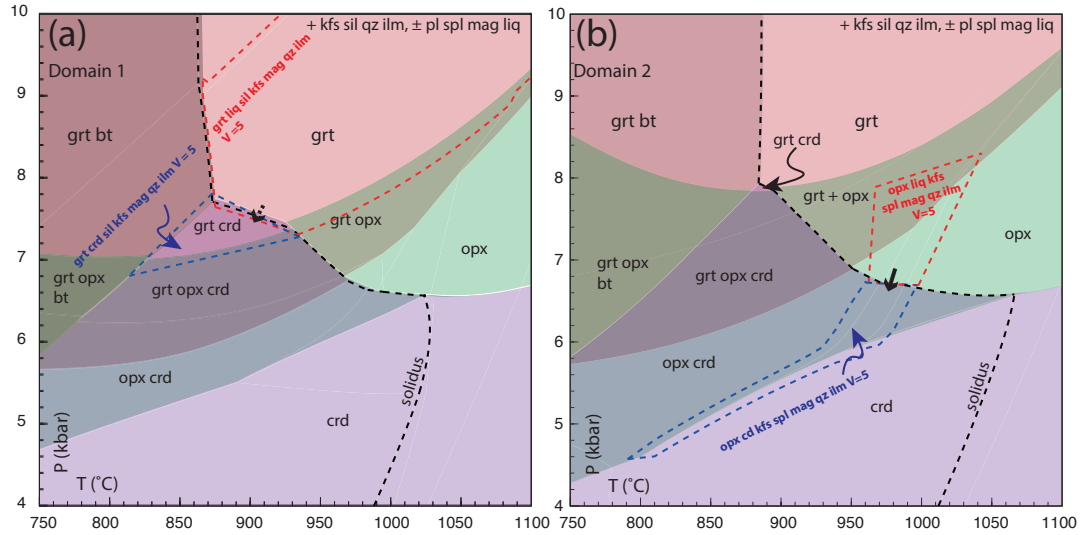

Figure 3.5 | Simplified *P–T* phase diagrams for domains 1 (a) and 2 (b) for sample EGB–09–45. Fully labeled *P–T* phase diagrams are given in Figure S4. Interpreted peak (red) and retrograde (blue) stability fields for each domain are outlined by dashed lines that include the 2σ uncertainties on the peak and retrograde fields. Black arrows connect peak and retrograde fields, across the solidus, and indicate the simplest post peak *P—T* vector in each case.

To investigate these different domains, *P–T* pseudosections were calculated using bulk compositions derived from selected areas within the thin sections (shown as domains in Figure 3.4). Simplified *P–T* phase diagrams for these areas that highlight the stability fields for the main silicate minerals from 4–10 kbar and 750–1050°C are shown in Figures 3.5 (sample EGB–09–45) and 3.6 (sample EGB–09–47). The full phase diagrams on which these simplified diagrams are based are given in Appendix C.11 and C12 respectively.

3.4.3 | Domainal compositions

Sample EGB–09–45

A *P–T* phase diagram calculated for the composition (Table 3.2) of a garnet–sillimanite–spinel–cordierite-bearing domain (domain 1 in Figure 4a; Table 3.2), with X(Mg) = 0.32 and A/AFM = 0.58, is shown in Figure 5a. The presence of ~25 vol.% cordierite and <1 vol.% biotite corresponds to 0.04 mol.% H2O in the bulk composition of this domain (Figure 4a). For this H2O content, at P > 7.5 kbar the calculated solidus occurs at temperatures of 860–870°C, stepping up to ~1000°C at P < 6.5 kbar. For the X(Fe3+) of the domain 1, which is based on mineral stoichiometry, spinel is predicted to be stable at ultrahigh-temperatures at pressures up to 9 kbar. Magnetite with or without spinel is stable except at the highest temperatures and pressures below ~9 kbar. Including the calculated 2σ errors on the end-

member thermodynamic data, the interpreted peak assemblage of garnet–melt–sillimanite–K-feldspar–magnetite–ilmenite–quartz for domain 1 in sample EGB–09–45 occurs at >7 kbar and >850°C (area outlined by the red dashed line in Figure 3.5a). This field is limited to lower *P–T* by cordierite-in, biotite-in and orthopyroxene-in equilibria. The development of retrograde cordierite is consistent with decompression with or without cooling into fields at pressures of ~7–8 kbar and temperatures of ~800–950°C, and final crystallization of melt at the elevated (residual) H2O-undersaturated solidus (area outlined by the blue dashed line in Figure 3.5a).

A *P–T* phase diagram for the composition of an orthopyroxene–sillimanite–spinel–cordierite-bearing domain (domain 2 in Figure 3.4a; Table 3.2) is shown in Figure 3.5b. This composition has X(Mg) = 0.45 and A/AFM = 0.44; H2O content is estimated to be ~0.01 mol % based on the mode of cordierite and biotite. The solidus is located at a temperature of ~885°C above ~8 kbar and steps up to T > 1000°C at P < 6.5 kbar. The solidus is at a higher temperature than the solidus for domain 1 due to a lower H2O content, which is a consequence of the lower mode of cordierite and absence of biotite. Compared to domain 1, spinel is stable to lower temperatures (~775°C) at P ~4 .5 kbar, extending to 1100°C and higher at P > 9 kbar. The inferred peak assemblage of orthopyroxene–melt–sillimanite–ilmenite–spinel–magnetite–K-feldspar–quartz occurs in a field at *P–T* conditions of 6.7–7.9 kbar and 970–1020°C (area outlined by the red dashed line, Figure 3.5c). This peak field is limited by spinel out to lower T, garnet in to higher P, magnetite out to higher T and cordierite in to lower P. The development of retrograde cordierite is consistent with minor decompression with or without cooling, and crystallization of all melt at the H2O-undersaturated solidus (area outlined by the blue dashed line, Figure 3.5b).

Sample EGB–09–47

Four *P–T* phase diagrams were calculated using bulk compositions (Table 3.2) derived from the areas shown in Figure 3.4b. Domains 1 and 2 are orthopyroxene–sapphirine–sillimanite–spinel–cordierite-bearing areas that contain sparse and abundant quartz, respectively (Figure 3.4b). Domain 1 has X(Mg) = 0.61 and A/AFM = 0.50, whereas domain 2 has X(Mg) = 0.59 and A/AFM = 0.49. In both cases, H2O contents are estimated to be <0.07 mol.% based on the mode of cordierite. Within the *P–T* range of interest for both domains (Figure 3.6a, b), quartz is predicted in all fields and the solidus occurs at temperatures of ~900°C for pressures >8 kbar, stepping up

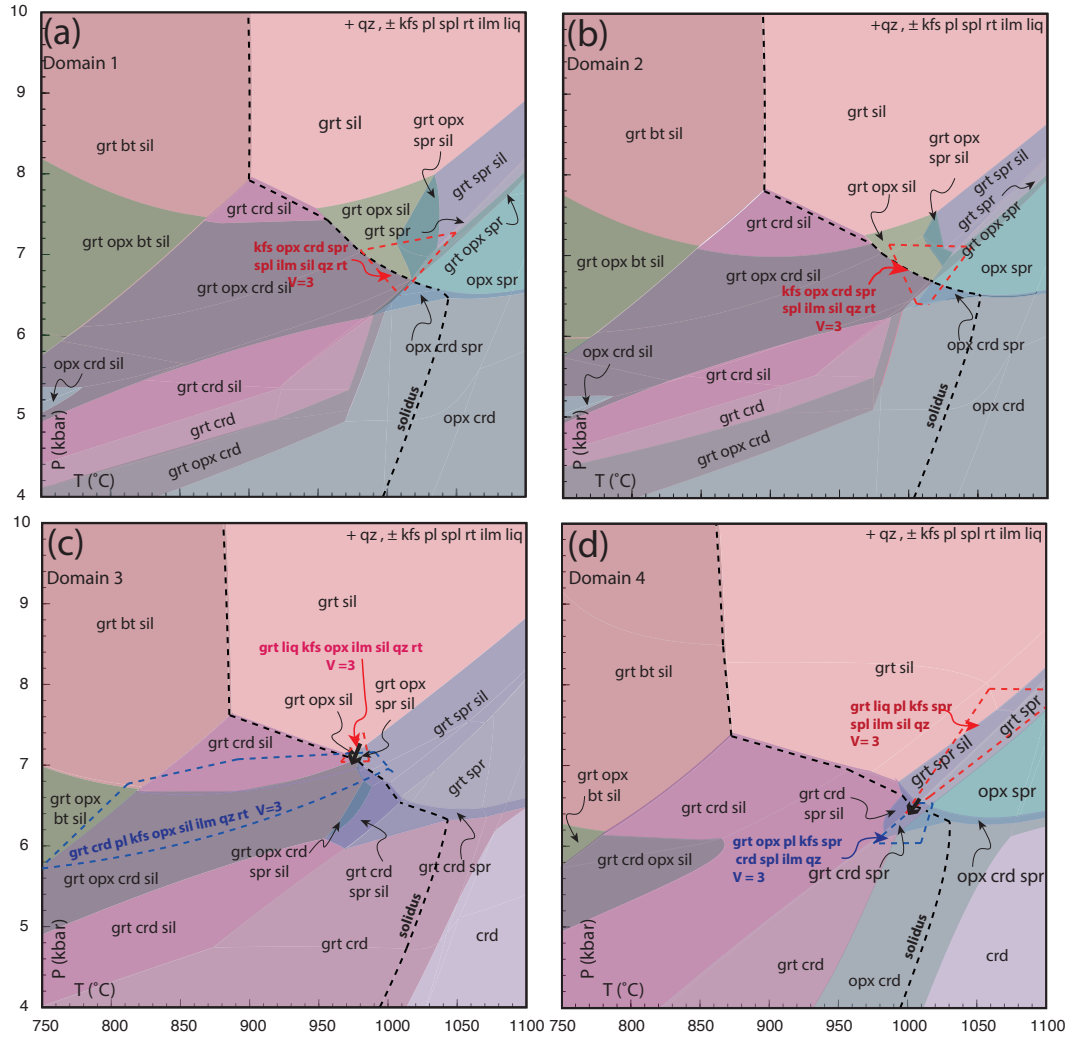

Figure 3.6 | Simplified *P–T* phase diagrams for domains 1 (a), 2 (b), 3 (c) and 4 (d) for sample EGB–09–47. Fully labeled *P–T* phase diagrams are given in Figure S5. Interpreted peak (red) and retrograde (blue) stability fields for each domain are outlined by dashed lines that include the 2σ uncertainties on the peak and retrograde fields. Black arrows connect peak and retrograde fields, across the solidus, and indicate the simplest post peak *P—T* vector in each case.

to temperatures of ~1000°C or more at P < 6.5 kbar. In both cases, garnet is present above a P of ~4kbar at low T and above, extending to ~8 kbar or above at the extreme T of 1100°C. Cordierite is predicted to be stable below pressures of between ~8 and 6.5 kbar at temperatures of ~900–1050°C, respectively. Sapphirine is stable at temperatures above ~1000°C at intermediate pressures in both domains; the decreased stability of sapphirine compared to sample EGB-09-45 likely reflects the relatively low X(Fe3+). The peak assemblage for both domains is inferred to be orthopyroxene–sapphirine–sillimanite–spinel–cordierite–K-feldspar–quartz–rutile–ilmenite (cordierite occurs as coarse porphyroblasts; domains 1 and 2, Figures 3.3h and 3.4b). The assemblage occurs in overlapping *P–T* fields

(taking into account the 2σ uncertainties) at ~6.4–7.2 kbar and 975–1025°C (area outlined by the red dashed line, Figure 3.6a, b). The boundaries of the peak field are garnet-in at high-P, sillimanite-out at low-T, rutile-out at low P and T, and for domain 2, sapphirine-out at low-P.

A *P–T* phase diagram for domain 3, which contains garnet–orthopyroxene–sillimanite–cordierite (Figure 3.4b, Table 3.2), is shown in Figure 6c. Domain 3 has X(Mg) = 0.54 and A/AFM = 0.48; H2O content is estimated to be ~0.04 mol.% based on the mode of cordierite. Quartz is present in all assemblage fields, while orthopyroxene is only predicted at intermediate pressures of ~5–7 kbar and at 750°C and ~6–7 kbar at 950°C, and up to a maximum temperature of 990°C. Sapphirine is stable at temperatures above 950°C at intermediate pressures. The peak assemblage of garnet–melt–orthopyroxene–sillimanite–K-feldspar–quartz–ilmenite–rutile is stable in a small *P–T* field at ~7.2 kbar and ~975°C (the area outlined by the red dashed line, Figure 3.6c). This field is constrained by orthopyroxene-out to higher P, sapphirine-in to higher T and cordierite-in to lower P and T. The retrograde assemblage with additional cordierite and plagioclase occurs at between P of ~6–7 kbar and T of 750–960°C. The retrograde field, which is subsolidus and based on the appearance of cordierite, is restricted by plagioclase-out and orthopyroxene-in at high-P, biotite-in at low-T, rutile-out at low-P and sapphirine-in at high–T (area outlined by the blue dashed line, Figure 3.6c).

Within domain 4 (Figure 3.4b), symplectites of cordierite–orthopyroxene–sillimanite–K-feldspar (e.g. Figures 3.2f and 3.3a) partially replace garnet in the garnet1–melt–sapphirine–sillimanite–K-feldspar–plagioclase–spinel–ilmenite–rutile–quartz assemblage. This is interpreted to record the breakdown of peak garnet in the presence of melt. For this domain, X(Mg) = 0.49 and A/AFM = 0.44; H_2O content is estimated to be ~0.04 mol.% based on the mode of cordierite. In the phase diagram for domain 4 (Figure 3.6d) within the *P–T* range considered, the solidus occurs at ~875°C at pressures greater than ~7.4 kbar stepping up to 1000–1050°C at pressures below 6–6.5 kbar. Orthopyroxene-bearing equilibria occur in the high-T and low-P quadrant, above ~930°C from ~4 to ~8 kbar, and in a small window below ~870°C between ~5 and ~6.3 kbar. The inferred peak assemblage field of $garnet_1$–melt–sapphirine–sillimanite–K-feldspar–plagioclase–spinel–ilmenite–rutile–quartz field is consistent with pressures of ~6–8 kbar and temperatures in excess of 1000°C (area outlined by the red dashed line in Figure 3.6d). The cordierite-bearing $garnet_1$–cordierite–sapphirine–

sillimanite–K-feldspar–plagioclase–spinel–ilmenite–rutile–quartz field indicates that the interpreted retrograde evolution for this domain is consistent with minor decompression across the solidus (area outlined by the blue dashed line in Figure 3.6d).

3.4.4 | Zircon geochronology and thermometry

Zircon morphology and petrography

The characteristic morphology of zircon grains in CL is shown in Figure 3.7. Grains that show clear oscillatory zoning patterns characteristic of magmatic zircon are rare; most grains have textures consistent with crystallization of zircon from anatectic melt generated during UHT metamorphism and/or recrystallization during fluid mediated processes (Taylor et al., 2016). Core domains in zircon from samples EGB–09–45, –47 and –55 are variable, with sector-zoned, 'fir-tree' and 'soccer ball' textures all present (Figure 3.7a, b, c, d). Other examples have inclusion-rich cores with low CL responses characterised by convolute zoning; where overgrowths are present, they have cuspate boundaries with the cores (Figure 3.7e, f). Cores with low CL

Figure 3.7 | Cathodoluminescence (CL) images of representative zircon morphologies in EGB–09–45 (e), –47 (b, c, d) and –55 (a, f). In-situ LA–ICP–MS analysis spots highlighted: green – U-Pb age (Ma, discordant analyses scored); red, Ti-in-zircon temperature (°C). (a) Bright CL sector zoned core with dark CL sector zoned overgrowths. (b) Zircon with a soccer ball morphology. (c) Large, high CL resoponse, sector zoned zircon. (d) Coarse sector zoned grain in ilm|sil|grt|qz corona. (e, f) Grains with convolute zoning in cores and bright CL rims.

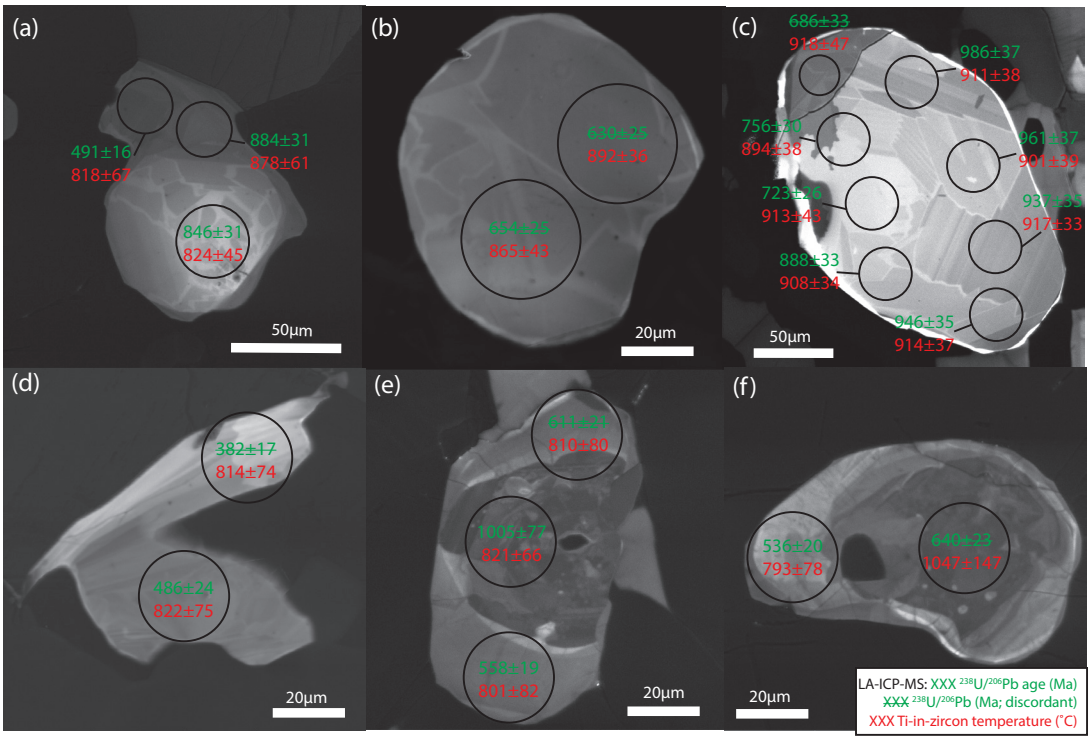

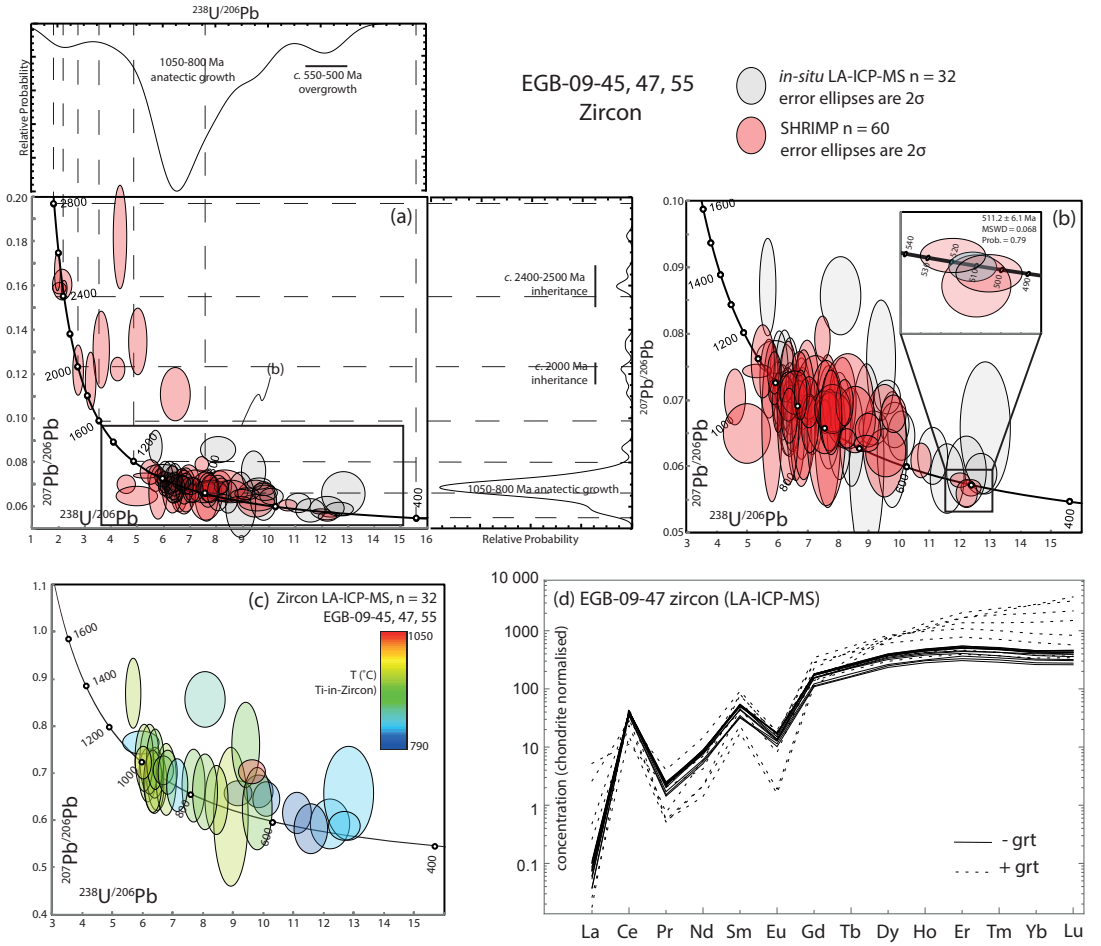

Figure 3.8 | (a) Tera–Wasserburg plot of LA–ICP–MS and SHRIMP U-Pb isotope ratios for all analysed spots on zircon from samples EGB–09–45, –47 and –55. Probability density functions for 207Pb/206Pb and 238U/206Pb are also shown. The data shown in Figure (b) are outlined by the box. (b) Tera–Wasserburg plot of LA–ICP–MS and SHRIMP U-Pb isotope ratios for Neoproterozoic–Cambrian zircon data from samples EGB–09–45, –47 and –55. Note the gap in concordant SHRIMP data in the interval 800–550 Ma, and Concordia age of 511.2 ± 6.1 Ma. (c) Tera–Wasseberg plot of LA–ICP–MS U-Pb isotope ratios for zircon from EGB–09–45, –47 and –55, with error ellipses shaded for Ti–in–zircon temperature. (d) Chondrite-normalised rare earth element plot for zircon in EGB–09–47. Dark lines indicate grains in garnet-absent domains, whereas the dotted lines represent grains in garnet bearing domains.

response are interpreted as inherited grains.

Overgrowths are common; the outermost layers generally have a lower CL response and are texturally homogenous, rarely showing parallel sector zoning that is discontinuous with high CL response ‘fir–tree’ and ‘soccer ball’ sector-zoned regions closer to grain cores (EGB–09–55; Figure 3.7a). In sample EGB–09–45, analysed grains occur adjacent to ilmenite and sillimanite, and occur in both orthopyroxene–sillimanite–cordierite- and

garnet–sillimanite–cordierite–spinel-bearing domains. However, zircon grains in direct contact with garnet are not observed in this study. Zircon grains in sample EGB–09–47 occur in several domains. Large, sector-zoned grains (e.g. Figure 3.7c) are found in orthopyroxene–sillimanite-bearing domains and within the interstitial K-feldspar–cordierite–quartz matrix. A variety of 'soccer ball' and oscillatory-zoned zircons are found in garnet1 and garnet2-bearing domains and in contact with spinel–ilmenite–sillimanite–garnet2 coronae. Additionally, zircon grains in garnet$_2$-bearing domains within sample EGB–09–47 commonly show sector zoning, accompanied with fine-scale zoning patterns (Figure 3.7d).

U–Pb geochronology

High precision SHRIMP analyses (n = 60) from samples EGB–09–45, –47 and –55 provide timing constraints (Appendix C.5; Figure 3.8a, b; red ellipses) on the metamorphic events recorded in these rocks. Dark-CL inherited cores (Appendix C.4) return three concordant ages c. 2500–2400 Ma, and a single concordant age of c. 2000 Ma. The 238U/206Pb ages define a probability density function (PDF) with a primary peak at c. 950 Ma and secondary peak at c. 550–500 Ma (Figure 3.8a). Analyses from sector-zoned grains yield concordant ages of c. 1050–800 Ma, with an age span of c. 200 Ma often apparent within single sector zoned grains (Figure 3.7c). A further group of analyses return ages between c. 800 and 600 Ma that are discordant and define a broadly Pan-African lower intercept. Three analyses from zircon overgrowths return a weighted mean Concordia age of 511 ± 6 Ma (MSWD = 0.068, Prob. = 0.79).

Trace element patterns

Chondrite-normalised rare earth element (REE) patterns of zircon within the garnet-bearing sample EGB–09–47 are plotted in Figure 3.8d. Notably, sector-zoned zircon grains in garnet-absent, orthopyroxene–sillimanite-bearing domains in this sample have depleted heavy REE (HREE) patterns (Figure 3.8d, solid lines) relative to grains in garnet-bearing domains. Zircon grains in garnet1 or garnet2-bearing domains show a wider spread of REE patterns, may have a more pronounced Eu anomaly, and exhibit a wider range of HREE concentrations – often enriched by up to an order of magnitude. In this sample, there is no clear correlation between normalized REE patterns and internal zircon morphology. The only apparent REE trend with age is HREE enrichment associated with spot analyses from some zircon rims in EGB–09–45 and –55 (Appendices 3.6 and 3.7). However, a range of

higher Yb/Gd ratios is apparent for zircon spots across all age populations from grains coexisting with garnet (Figure 3.8d).

Ti-in-zircon thermometry

For zircon with concordant ages determined by LA–ICP–MS (Figures 3.8c and 3.9a), Ti-in-zircon thermometry was used to assess crystallization temperatures for the same spots. The Ti-in-zircon temperatures yield a bimodal PDF (Figure 3.9a) corresponding to the age peaks, with Ti-in-zircon temperatures of ~905°C and ~810°C. The data forms three clusters (Figure 3.9b): the first at around 940–880°C in the age range c. 1000–880 Ma, which are interpreted to represent the peak of UHT metamorphism and which correspond to sector zoned domains in zircon; the second at ~900°C between c. 800 and 600 Ma, although the ages in this interval determined by SHRIMP are discordant, suggesting that the temperatures do not record a discrete metamorphic event; and; the third at ~820–800°C and c. 550–500 Ma corresponding to low-response CL zircon rims. The assumption used here that $aTiO_2$=1 leads to an underestimate of temperature for rutile-absent domains by up to ~70 °C (Ferry & Watson, 2007). The peak pressure of ~7 kbar here, compared to the 10kbar calibration of this thermometer may result in a further underestimation of ~15 °C, hence the Ti-in-zircon temperatures should be regarded as minima. An orthogonal regression technique (Krystek & Anton, 2007) was used to obtain an average cooling rate of 0.13 ± 0.08°C/Ma from concordant LA-ICP-MS $^{238}U/^{206}Pb$ ages and Ti-in-zircon temperatures associated with the c.1000-880 Ma UHT event (Figure 3.9a). This result is consistent with very slow cooling towards the elevated solidus.

3.4.5 | Monazite geochronology

Monazite morphology and petrography

Monazite grains in samples EGB–09–47 and –55 vary between 20 and 200 μm in diameter and have a variety of textures. Core domains may exhibit planar features with varying BSE response, similar to sector zoned zircon grains (Figure 3.9a, b). Several show mottled, patchy zoning (Figure 3.9b) or lobate inclusions that cut across features in inner domains. Almost all grains have overgrowths ~20 μm thick, with a darker BSE response, that cross-cut internal zoning (Figure 3.10b)

Monazite U–Pb geochronology

Monazite U, Th and Pb isotope ratios for samples EGB–09–47 and –55 are given in Appendix C.5 and displayed in Tera–Wasserburg concordia plots in

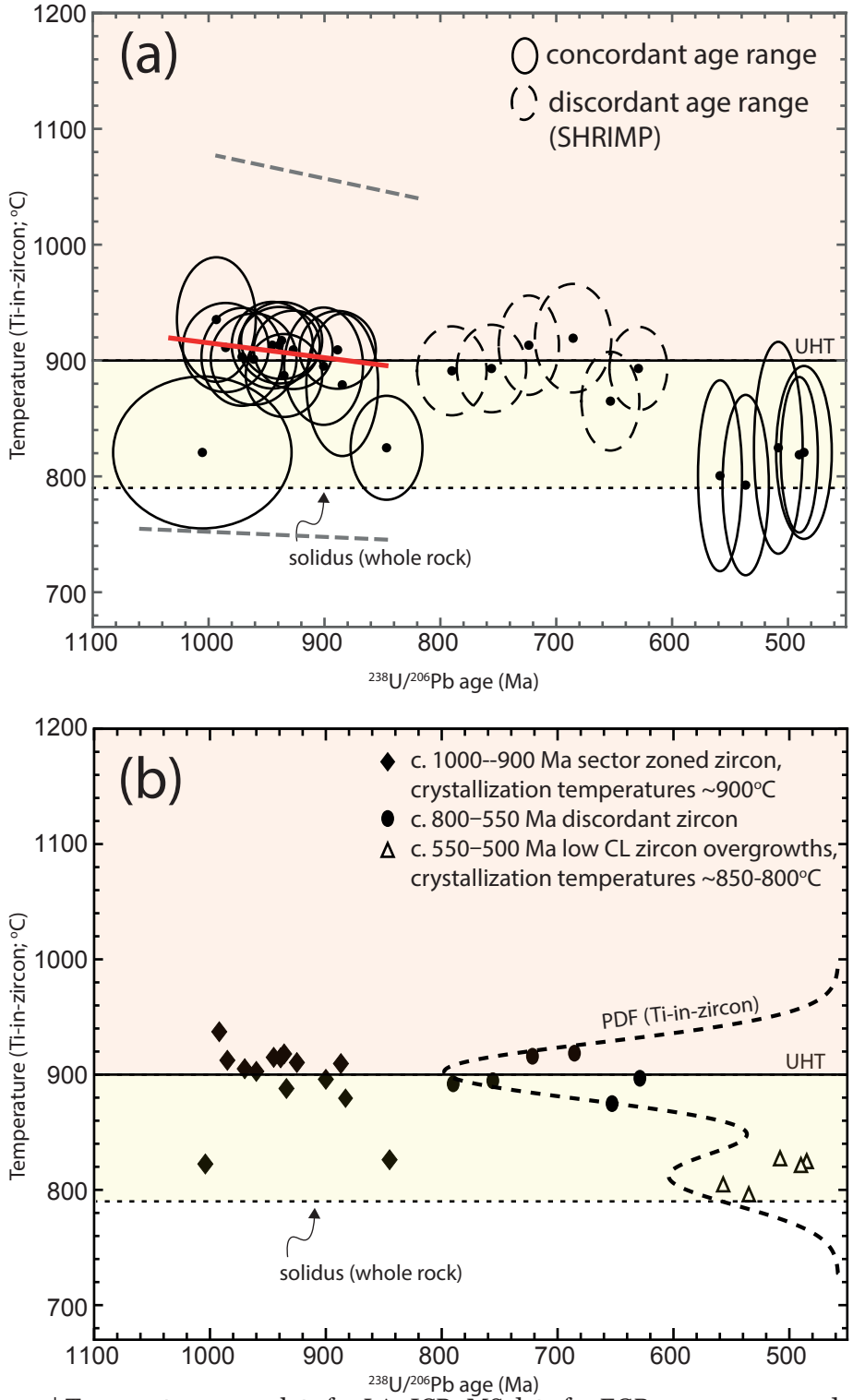

Figure 3.9 | Temperature–age plots for LA–ICP–MS data for EGB–09–45, –47 and –55. (a) Solid ellipses are LA–ICP–MS data from the age ranges of concordant SHRIMP data (see Figure 3.7). Dashed ellipses are analyses in the age range of discordant SHRIMP analyses; the red line indicates the regression line for average cooling rate (0.13 ± 0.08°C/Ma), during UHT, with the minimum and maximum shown with grey dashed lines. (b) Temperature–age plot labelled with textural features seen in CL images of zircon. Probability Density Functions (PDFs) emphasize the population of zircon with crystallization temperatures around 900 °C between c. 1000 and 880 Ma, and a second population of zircon with crystallization temperatures around 810 °C at c. 550–500 Ma.

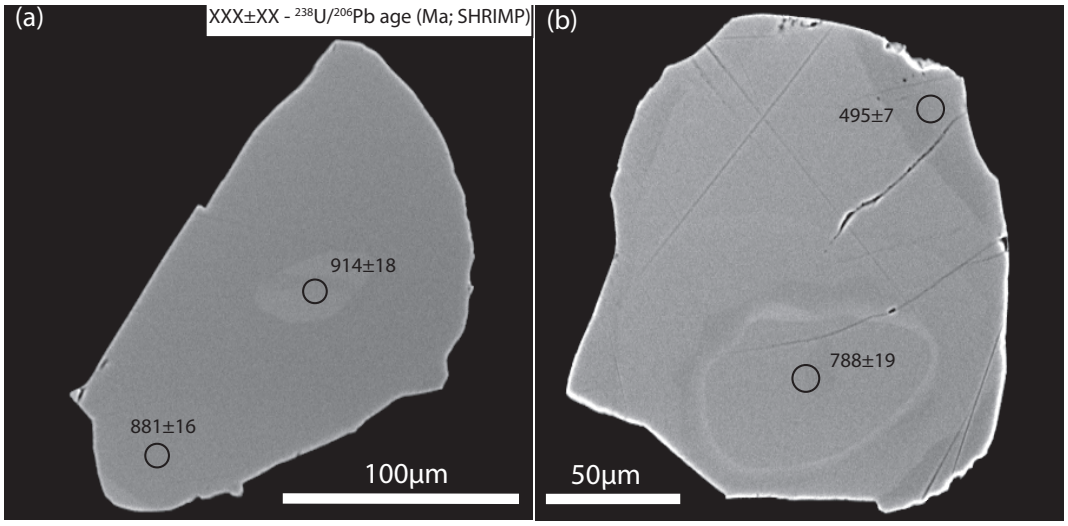

Figure 3.10 | Backscatter electron (BSE) images of monazite to show the typical morphology of grains from EGB–09–47 and –55, including SHRIMP analysis spots (ages in Ma).

Figure 3.11. Monazite in sample EGB–09–47 (Figure 3.11a) yields concordant ages of c. 950–850 Ma. A single analysis with an age of 550 ± 43 Ma is within 2σ error of the concordia. Monazite grains in sample EGB–09–55 yield ages that spread along Concordia from c. 950 to c. 800 Ma. Three data plot on Concordia within error and yield ages between c. 595 Ma and c. 485 Ma.

3.5 | Discussion

3.5.1 | Evidence for domainal equilibration volumes during UHT metamorphism

Samples EGB–09–45 and –47 are high-grade metamorphic rocks with mineral assemblages that are variable over length scales as small as ~5 mm. Compositional layers preserved on a centimetre scale (Figure 3.3b)

Figure 3.11 | Tera–Wasserburg plot of SHRIMP U–Pb monazite data from samples EGB–09–47 and –55.

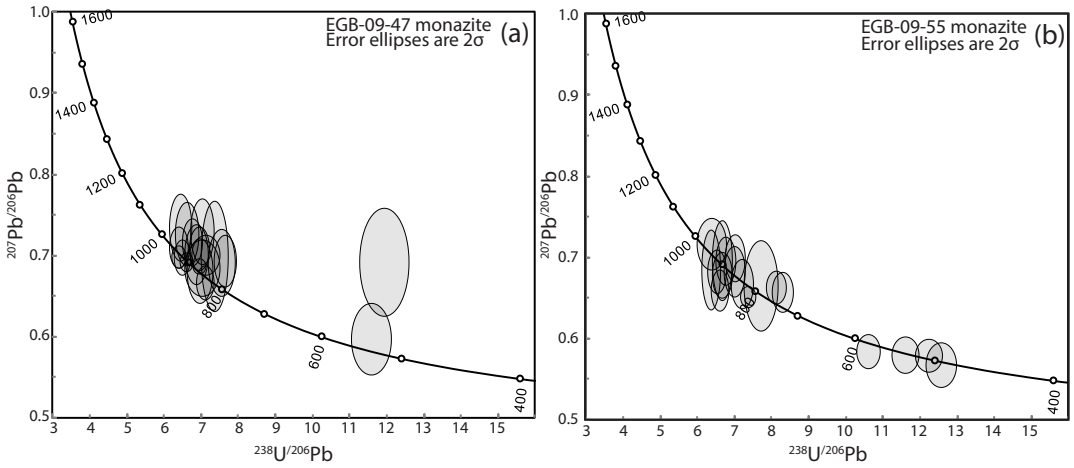

suggest the possibility of preservation of primary compositional layering in the sedimentary protoliths. Peak mineral associations (all of which include matrix K-feldspar and quartz) in the different layers include garnet–sillimanite–ilmenite (Figure 3.2a), orthopyroxene–sillimanite–spinel±cordierite (Figure 3.2b), garnet–sapphirine–sillimanite (Figure 3.2c), garnet–orthopyroxene–sillimanite (Figure 3.2g) and orthopyroxene–sillimanite–sapphirine–spinel±cordierite (Figure 3.3d, h). In sample EGB–09–45, garnet–sillimanite–ilmenite-bearing domains have an X(Mg) that is significantly lower (by 0.13) than the orthopyroxene–sillimanite–spinel-bearing domains, but an A/AFM that is higher by 0.14. Similarly, in sample EGB–09–47, the garnet–sapphirine–sillimanite-bearing domain 4 has an X(Mg) that is lower by 0.12 than the orthopyroxene–sillimanite–sapphirine–spinel-bearing domain 1 but, in this case, is less aluminous with an A/AFM by 0.06. These observations demonstrate that the rocks preserved significant differences in two compositional parameters critical to metapelitic phase equilibria —X(Mg) [molar MgO/(MgO+FeO)] and A/AFM [molar Al_2O_3/(Al_2O_3+MgO+FeO)] (Thompson Jr, 1957) —on a centimetre scale. Similarly small domains occur in various granulite facies xenoliths that record temperatures of ~1000°C, for example in the northern limb of the Bushveld Complex (Johnson et al., 2010) and the Cortlandt Complex (Dorfler et al., 2015).

Felsic domains dominated by coarse-grained K-feldspar and quartz are interpreted as leucosome; these are interspersed between garnet–sillimanite–spinel- and orthopyroxene–sillimanite–spinel-bearing layers in EGB–09–45, and commonly surround $garnet_1$ porphyroblasts in EGB–09–47 (Figures 3.2h and 3.3g). In both samples, cordierite, which is interpreted to have grown variably as part of the peak assemblage (Figures 3.3h and 3.6a, b) or during the high-T retrograde evolution (Figures 3.5 and 3.6c, d), is the only primary hydrous mineral. Consequently, the H_2O content of the domains may be determined based on the measured abundance and volatile content of cordierite, providing cordierite was part of the close-to-peak assemblage.

In sample EGB–09–47, small millimetre scale leucosome domains consist of inclusion-rich euhedral garnet grains ($garnet_2$) in a granoblastic K-feldspar–quartz matrix (Figure 3.3g) with rare large biotite laths (Figure 3.2c, g). These domains are commonly juxtaposed against cordierite–quartz intergrowths. The orthopyroxene–cordierite–sillimanite symplectites that surround garnet1 are not found associated with $garnet_2$, which suggests the

formation of such symplectites records melt crystallization. Late biotite and the preservation of pristine cordierite potentially may be due to an increase in a(H_2O) due to the preferential crystallization of CO_2-bearing cordierite, as DCO_2(liq)/CO2(cordierite) << DH_2O(liq)/H_2O(cordierite) (Thompson et al., 2001). However, a–X models incorporating CO_2 into melt and cordierite are required to construct appropriate pseudosections to test this proposal.

3.5.2 | *P–T* evolution

In some cases, constraints on the prograde path followed by rocks may be made by using inclusions within prograde to peak minerals. For example, sample EGB-09-47 contains garnet prophyroblasts with inclusions of cordierite, sillimanite, sapphirine and spinel (Figure 3.2c–e). However, along the prograde evolution at temperatures above the wet solidus (~650 °C), the composition of these granulites would have been constantly evolving due to the production and loss of melt regardless of the scale of equilibration. Consequently, the bulk composition of the prograde equilibration domain is often unknown, and phase equilibrium modelling based on these inclusion suites is not appropriate for quantitatively evaluating *P–T* conditions, unless prograde processes that modify the bulk composition – such as melt loss – are well understood (Korhonen et al. 2013a).

A *P–T* path for the peak and retrograde evolution of the granulites of this study is proposed based on mineral assemblages and microstructures inferred to have developed during the peak and retrograde evolution using phase diagrams constructed for selected domains within samples EGB–09–45 and –47. *P–T* pseudosections for the composition of selected areas in thin sections reproduce the interpreted domainal peak assemblages. Peak metamorphic mineral associations include coexisting orthopyroxene and sillimanite in domain 2 in sample EGB–09–45 (Figure 3.5c) and domain 1 in sample EGB-09-47 (Figure 3.6b). Cordierite is inferred to have been stable at peak conditions in domains 1 and 2 of sample EGB-09-47, where it occurs as coarse porphyroblasts (Figures 3.3g and 3.6b, c), in addition to its occurrence as poikiloblastic grains with quartz and sillimanite inclusions and as seams separating orthopyroxene and sillimanite (Figure 3.3d). Coexisting garnet and sillimanite without cordierite are inferred in the peak assemblage for domain 1 in sample EGB-09-45 (Figure 3.5b), garnet–sillimanite–orthopyroxene for domain 3 of sample EGB-09-47 (Figure 3.6d) and garnet–sillimanite–sapphirine for domain 4 in sample EGB-09-47 (Figure 3.6e). Peak fields for these various domains record similar conditions. Peak stability

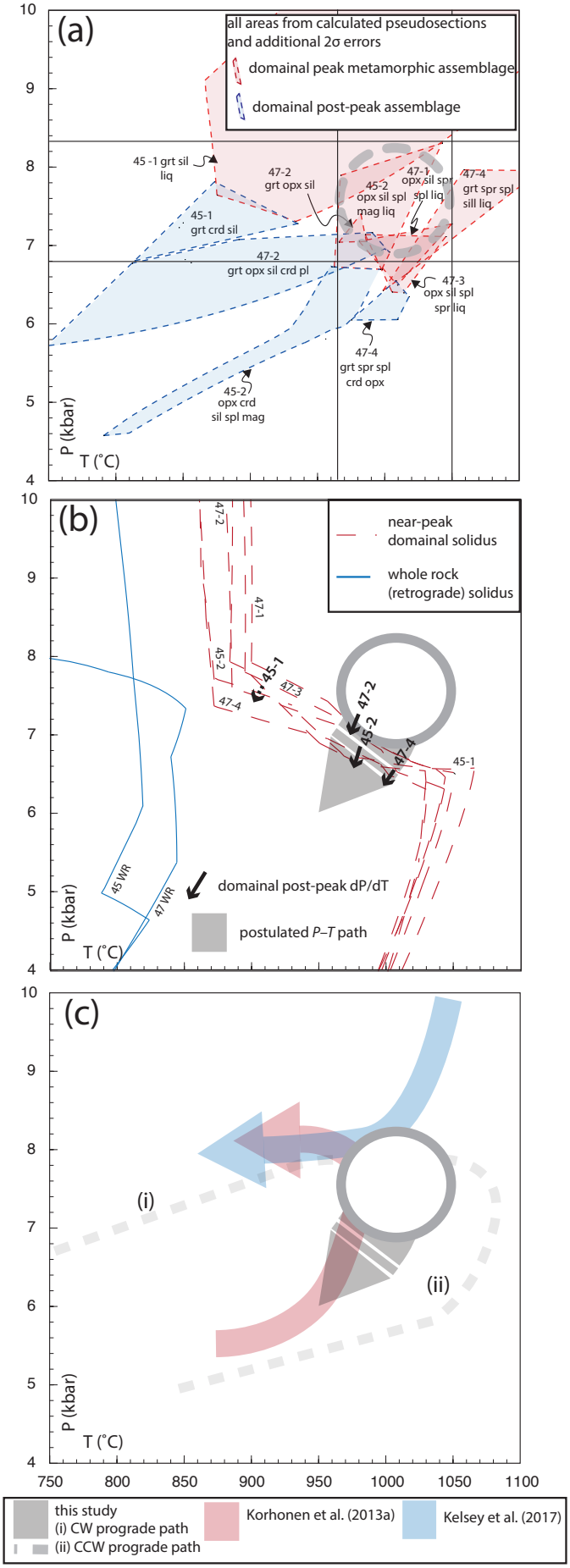
(a)
all areas from calculated pseudosections and additional 2σ errors
domainal peak metamorphic assemblage
domainal post-peak assemblage
45 -1 grt sil liq
47-2 grt opx sil
45-2 opx sil spl mag liq
47-1 opx sil spr spl liq
47-4 grt spr spl sill liq
45-1 grt crd sil
47-2 grt opx sil crd pl
47-3 opx sil spl spr liq
47-4 grt spr spl crd opx
45-2 opx crd sil spl mag
P (kbar)
T (°C)
(b)
near-peak domainal solidus
whole rock (retrograde) solidus
47-2
47-1
45-2
45-1
47-3
47-4
45 WR
47 WR
domainal post-peak dP/dT
postulated P–T path
(c)
(i)
(ii)
750
800
850
900
950
1000
1050
1100
this study
(i) CW prograde path
(ii) CCW prograde path
Korhonen et al. (2013a)
Kelsey et al. (2017)

Figure | 3.12 (a) *P–T* plot of peak (red) and retrograde (blue) stability fields (+ kfs, qz, ilm ± rt) from various domains in EGB–09–45 and –47 (see Figures 4, 5 and 6). (b) Domainal near peak (red) and whole-rock retrograde (blue) solidi. Black arrows indicate the simplest post peak *P–T* vector for domains 45-1, 45-2, 47-2 and 47-4. The overall inferred *P–T* trajectory is marked with a grey arrow. C) Inferred *P–T* paths for this study (grey), Korhonen et al. (2013) (red) and Kelsey et al. (2017) (blue). (i) A potential prograde path for a clockwise *P–T* evolution. (ii) A potential prograde path for a counterclockwise *P–T* evolution.

fields overlap implying temperatures of 965–1050°C, and pressures must extend to ~6.8–8.3 kbar where peak stability fields of EGB-09-45 domains 1 and 2 overlap, as summarised in Figure 3.12a.

For most domains, the stability fields for post-peak assemblages that record the breakdown of peak minerals are constrained by cordierite-bearing equilibria. These retrograde fields generally overlap the peak assemblage stability fields, but consistently extend down temperature, always at a lower pressure (Figure 3.12a). For every pair of modelled peak and retrograde assemblage, the inferred retrograde assemblages are consistent with minor decompression (on the order of <1 kbar). In all modelled compositions, the elevated solidus is characterised by a sharp increase in temperature (100–200°C) from higher to lower pressure, which occurs between 8.0 and 6.5 kbar (Figure 3.12b). Post peak *P—T* vectors for each domain indicate minor decompression and cooling from their respective peak field. Consequently, the majority of P—T vectors coincide with <1 kbar of decompression from the inferred metamorphic peak conditions (~6.8–8.3 kbar at 965–1050°C), leading to the H_2O-undersaturated solidus (Figure 3.12b), with final crystallization of melt and growth of cordierite. Symplectic replacement of garnet by orthopyroxene, sillimanite and cordierite, fine grained cordierite-sillimanite-quartz intergrowths (Figure 3.2f), and cordierite seams between orthopyroxene and sillimanite can all be achieved in the presence of melt by crossing the garnet + cordierite + K-feldspar + quartz = orthopyroxene + sillimanite + melt univariant KFMASH reaction from high to low *P—T* (Harley, 2008). Similar textures around this univariant have been ascribed to chemical potential gradients of MgO and FeO, decompression of <<1 kbar and the local presence of melt (Doukkari et al., 2018). However, pressure variations on the order of 1 kbar are probably within the uncertainties associated with phase equilibrium modelling (Doukkari et al., 2018), Increasing CO_2 concentration in the system would enlarge the cordierite stability field to higher pressure, as CO_2 partitions preferentially into cordierite rather than melt under granulite facies conditions (Harley, 2008;

Thompson et al., 2001). As such, systems which include CO_2 tend to stabilise cordierite at higher P (Harley, 2008). In spite of these considerations; the simplest explanation of numerous lines of petrological evidence and post-peak *P—T* vectors is decompression of <1 kbar with cooling, in the presence of local melt towards the solidus at ~6.5-7.0 kbar, 950-1000 °C (Figure 3.12b).

$Garnet_2$ poikiloblasts commonly form aggregates that are rounded and contain numerous quartz inclusions, consistent with crystallization with melt (Waters, 2001). Garnet is stable in adjacent fields down-T from post peak assemblages in garnet absent domains (Figure 3.6a, b). Thus, domains containing entrained aggregates of euhedral, garnet2 poikiloblasts (Figures 3.2c and 3.3g) and K-feldspar (e.g. EGB–09–47; domains 3 and 4) are interpreted as relict leucosomes that formed by cooling immediately before crossing the elevated domainal solidi along the retrograde *P–T* path. Despite a lack of explicit *P–T* evidence preceding peak conditions, the presence of lower-pressure phases (e.g. spinel, sapphirine cordierite) as garnet1 inclusions and in coronae with $garnet_2$ may be consistent with either a clockwise (Figure 3.12c(i)) or a counterclockwise (Figure 3.12c(ii)) *P–T* evolution. A clockwise *P–T* path with a high prograde dT/dP gradient (Figure 3.12c(i)) can reach peak conditions of ~7.6 kbar at ~1000 °C where garnet—sapphirine—spinel assemblages are stable (Figure 5c, d), after stabilising garnet—cordierite assemblages on the prograde path. A counterclockwise *P–T* path (Figure 3.12 c(ii)) would pass through cordierite, sapphirine and spinel (+ quartz) stability fields at >900 °C before forming peritectic garnet at UHT around peak conditions of ~7.6 kbar at ~1000 °C. However, our results do not allow us to discriminate between these alternatives, and the prograde *P–T* path at Vizianagarma remains unresolved.

3.5.3 | Timescales of metamorphism

The petrological evolution of samples EGB–09–45, –47 and –55 is summarized and compared to the inferred *P–T* path in Figure 3.13. The spread of concordant SHRIMP zircon ages from c.1050 to c. 800 Ma likely represents zircon growth from crystallising melt during this interval, supported by the Ti-in-zircon temperatures almost all of which exceed 880°C (Figure 3.9). Ti-in-zircon temperatures exceed 900 °C for LA-ICPMS zircon ages in the range c.1000–880 Ma; the time interval with the most numerous SHRIMP U-Pb zircon ages (see PDFs, Figure 3.8a). We interpret this data to record a protracted suprasolidus evolution between c. 1050 and

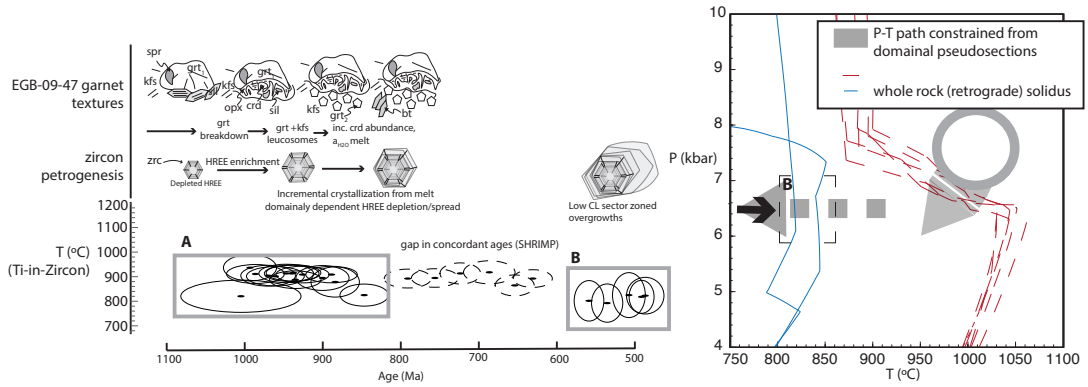

Figure 3.13 | Sketches depicting the timescale of the integrated petrological (a) and *P–T* (b) evolution of samples EGB–09–45, –47 and –55. A) The UHT peak was followed by crystallization of melt during slight decompression and slow cooling to form leucosomes in the interval from c. 1050 to c. 800 Ma, marked by sector zoned anatectic zircon. B) Neocrystallization of zircon at 550–500 Ma and >800 ºC due to minor fluid influx.

800 Ma, where UHT conditions were sustained for a minimum period of 120 Ma between c. 1000 and c. 900 Ma. In the majority of the rock volume, zircon likely crystallized from melt c.1000–900 Ma until reaching a H_2O undersaturated residuum solidus at T >900°C. An average cooling rate of 0.13 ± 0.08°C/Ma for the c.1000-880 Ma duration of UHT metamorphism is derived from a orthogonal regression of the Ti-in-zircon temperatures within error of 900 °C and the LA-ICPMS 238U/206Pb ages and errors (Figure 3.9a).

There are alternative explanations possible for the spread in near-concordant U-Pb zircon ages from c. 1050 to c. 800 Ma. Firstly, the ages could represent prolonged crystallization related to periodic melt influx (Harley et al., 2007; Harley and Nandakumar, 2016; Kelsey et al., 2008; Kelsey and Powell, 2011). Secondly, one or more Pb-loss episodes could have occurred, leading to analyses within error of Concordia between 1050 Ma and 800 Ma (e.g. Whitehouse et al., 1999).

Despite their growth in garnet absent domains, the presence of HREE-depleted, sector-zoned zircon is consistent with equilibration of the growing zircon with garnet and melt, the major repositories of HREE at these *P–T* conditions. Zircon grains with a spread between equally depleted, or more HREE-enriched signatures occur in garnet1 and $garnet_2$ -bearing domains (Figure 3.8d). During the post-peak evolution in the interval c. 1000-880 Ma, enrichment of HREE in zircon should occur due to garnet-consuming

reactions in those domains that form, for example, orthopyroxene–cordierite intergrowths at the margins of garnet1 (Figure 3.2d) in the presence of melt. However, HREE re-equilibration of zircon with $garnet_2$ must occur when euhedral $garnet_2$ crystallizes with melt. A plausible reason for the disparity in zircon HREE signatures between garnet absent and garnet bearing assemblages is an interplay between open and closed system behaviour. During the growth of large HREE-depleted zircons in garnet absent domains, the equilibration volume for the zircon–garnet–melt HREE system must be such that zircon throughout the rock volume could equilibrate with garnet and melt. However, during the post-peak evolution involving decompression and garnet breakdown, melt could have been locally isolated if melt volume remained below the melt connectivity threshold. In this scenario, zircon and garnet would only re-equilibrate in garnet bearing domains. Slow incremental growth of sector-zoned zircon in the age range is further diagnostic evidence of zircon growth in crystallising melt pockets under granulite facies conditions (Figure 3.7c; Harley et al. (2007); Taylor et al., (2016)).

The U–Pb data from zircon rims project onto Concordia between c. 550 and 500 Ma (Figures 3.7e, f and 3.8a, b). A weighted mean age of 511.2 ± 6.1 Ma is calculated from three concordant dates, suggesting a discrete phase of new zircon growth at this time. The enriched HREE signatures in zircon rims from samples EGB–09–45, 55 reflect the absence of garnet2 in these samples.

Monazite U–Pb ages are interpreted to reflect more-or-less continuous growth between c. 950 and 800 Ma in both samples EGB–09–47 and –55. The few concordant Pan-African ages (c. 550–500 Ma) are not associated with discordant Pb loss trends. In combination with Ti-in-zircon temperatures of ~810°C, this provides robust evidence for some, albeit limited, crystallization of monazite and zircon at c. 550–500 Ma.

The process responsible for limited neocrystallization of zircon and monazite at c. 550–500 Ma is unclear. Given that the new zircon rims record Ti-in-zircon temperatures in excess of 800°C (Figures 3.7c, 3.8 and 3.9), this new growth is unlikely to reflect subsolidus fluid-mediated dissolution–reprecipitation (Geisler et al., 2007; Harley et al., 2007). There are two plausible alternative processes that could have been responsible for zircon growth at this time: (i) final crystallization of the last vestiges of melt on cooling to the temperature of the elevated (residual) H_2O-undersaturated solidus as part of a protracted metamorphic event lasting in excess of 500

Ma; (ii) limited melting due to a minor influx of fluids, with or without any temperature increase. Both processes are consistent with crystallization of sparse biotite laths within leucosome domains in sample EGB–09–47 (Figure 3.2c). Preserving trapped melt pockets at long lived suprasolidus conditions may seem feasible, given the average cooling rate of 0.13 ± 0.08°C/Ma. However, if melt had remained in these rocks throughout the c. 1050–500 Ma tectonothermal history, the occurrence of concordant zircon ages throughout this period might be expected, in contrast with the observed c. 300 Ma gap in the zircon record (Figure 3.8a, b). The leucosome domains that host the younger zircon contain more H2O in the bulk composition (~2 mol.%) than the (nominally anhydrous) domains with peak mineral assemblages. An influx of ~2 mol.% H2O shifts the solidus down temperature to between ~800–850°C at 6.2 kbar for samples EGB–09–45 and –47 (Figure 3.12b), consistent with Ti-in-zircon temperatures >800°C recorded by the c. 550–500 Ma neocrystallized zircon rims. Fluid infiltration into cordierite-bearing granulites commonly results in pinitisation of cordierite. However, at temperatures in excess of 800°C cordierite is stable, whereas white mica, a principal constituent of pinite, is not. Thus, a process involving limited influx of H2O during the Pan-African event (e.g. Mezger & Cosca, 1999) is more consistent with observations than retention of residual melt in pockets.

3.5.4 | Regional geological context

In the EGP, the metamorphic evolution of the UHT granulites along the coastal belt differs from those located on the plateau. At Anakapalle, ~60km to the southwest along strike from Vizianagaram, based on evidence of >2 kbar decompression, a clockwise *P–T* path has been inferred for UHT granulites (Kelsey et al., 2017; Rickers et al., 2001b). By contrast, the inferred *P–T* evolution from several highland localities in the Paderu–Anantagiri–Salur block is inferred to have been counterclockwise (Figure 3.14c; (Korhonen et al., 2013a). However, peak *P–T* conditions of ~ 7–8 kbar and >950°C are recorded in both cases. At the highland localities, incremental growth of anatectic zircon occurred from c. 1050 Ma reaching peak UHT conditions between c. 1000 and c. 900 Ma (Korhonen et al., 2013b). However, continuous growth of anatectic zircon until c. 800 Ma, as inferred for the rocks at Vizianagaram, has not been recorded at the highland localities. In addition, a Pan-African population of zircon at c. 550–500 Ma is most clearly defined at Vizianagaram and at Garbham, another lowland locality (Korhonen et al., 2015).

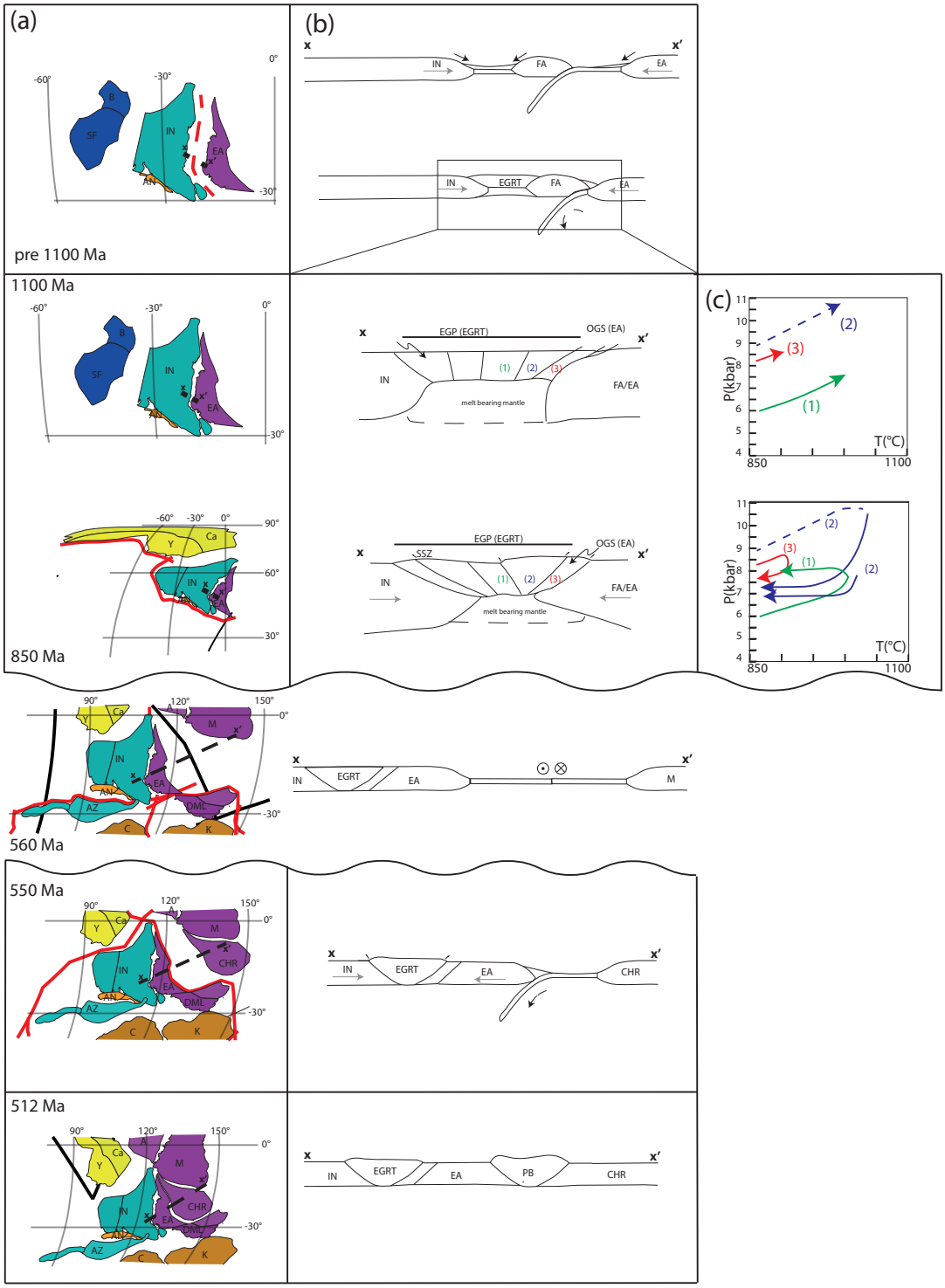
(a)
(b)
(c)
pre 1100 Ma
1100 Ma
850 Ma
560 Ma
550 Ma
512 Ma
B
SF
IN
EA
AN
AZ
Y
Ca
M
CHR
DML
C
K
PB
EGRT
FA
FA/EA
OGS (EA)
EGP (EGRT)
SSZ
melt bearing mantle
P(kbar)
T(°C)
850
1100

Figure 3.14 | A series of sketches to depict the possible tectonic evolution of the EGP between c.1100 Ma and 512 Ma from available geochronological evidence. (a) the Merdith et al. (2017) plate reconstructions in the Robinson projection, drawn using GPlates (Williams, Dietmar Müller, Landgrebe, & Whittaker, 2012). Red boundaries – destructive plate boundaries, bold black boundaries – transform and constructive plate boundaries. (b) Cross section sketch x'—x as illustrated in (a). (c) P—T paths for tectonic blocks labelled 1 (green; Korhonen, Brown, et al., 2013), 2 (blue; this study and Kelsey et al., 2017 with a postulated prograde path) and 3 (red; Halpin, Clarke, et al., 2007; Harley & Hensen, 1990; Kelly & Harley, 2004) in column (b). Abbreviations: A – South Australian Craton, AN – Antongil Block, AZ – Azania, B – Borborema Craton, BC – Bastar Craton, C – Congo Craton, Ca – South China Craton, CHR – Crohn Craton, DML – Dronning Maud Land, EA – East Antarctic cratons, EGP – Eastern Ghats Province, EGRT – Eastern Ghats Rayner Terrane, FA – Fisher Arc, K – Kalahari Craton, IN – Indian cratons, M – Mawson Block, NC – Napier Complex, OGS – Oygarden Group/Stilwell Hills, PB – Prydz Belt, SF – San Francisco Craton, Y – Yilgarn Craton.

A correlation between the EGP and Rayner Complex (RC) during the Proterozoic is well documented (Dasgupta et al., 2013; Fitzsimons, 2000; Harley, 2003; Mezger and Cosca, 1999), and is reflected here in several facets of the zircon geochronology and metamorphic evolution. Prolonged growth of concordant zircon between c. 1050 and c. 800 Ma, and suprasolidus granulite facies reworking of the EGP at Vizianagaram at 550–500 Ma is similar to the sequence of events recorded by monazite U–Pb ages in the RC in the Northern Prince Charles Mountains (NPCM; (Morrissey et al., 2016). Meanwhile, Mesoproterozoic to Neoproterozoic metamorphism and magmatism during the interval 1050–900 Ma is recorded throughout the RC within rocks cropping out along the Mawson Coast (Halpin et al., 2005) and from the reworked Archean crust of the Oygarden Group and Stillwell Hills (Halpin et al., 2005; Morrissey et al., 2016). The Beaver Terrane of the Rayner Complex records peak *P–T* conditions of ~6.0 kbar and 850–900°C and post peak near-isobaric cooling (Halpin et al., 2007a; Morrissey et al., 2016). However a decompression dominated post-peak history is evident in clockwise evolution through peak *P–T* conditions of ~8.5 kbar and 900–950°C, associated with Neoproterozoic reworking of the Oygarden Group and the Stillwell Hills (Halpin et al., 2007a; Halpin et al., 2007b).

Inherited zircon ages in the EGP record a series of concordant clusters and discordant trends associated with ages at c. 1650–1600 Ma and c. 1900–1800 Ma throughout the highland localities (Das et al., 2011; Korhonen et al., 2015; Korhonen et al., 2013b). Ages between c.1650–1600 Ma seemingly coincide

with ages for granite and charnockite emplacement in the Ongole Domain (Dharma Rao et al., 2012b; Kovach et al., 2001). Similar inherited ages from arc-related magmatism (Figure 3.14b) are found in zircon cores from the RC, with felsic magmatism c. 1600 Ma in the Oygarden group, and charnockite emplacement at c. 2100–1800 Ma along the Mawson Coast (Halpin et al., 2005) and NPCM (Zhao et al., 1997).

Interestingly, the granulites from Vizianagaram have inherited concordant zircon with ages of c. 2500–2400 Ma, which is seemingly unique to the EGP, but lies within the range of Sm–Nd whole-rock protolith ages of c. 2900–2200 Ma from the EGB (Rickers et al., 2001a). These inherited cores could have originated from several adjacent terranes. Granitic magmatism occurred in the Bastar Craton at c. 2500–2450 Ma (Sarkar et al., 1993), which is now adjacent to the Singhbhum and Rengali Provinces at the northern margin of the EGB. Granulite facies metamorphism occurred in the Vestfold Hills terrane at c. 2520–2450 Ma (Clark et al., 2012), which was likely situated around the northern margin of the EGB. Further from the study area, on the other side of the EGP–RC depocentre, c. 2500 Ma detrital zircon in the Ruker Terrane and granitoids emplaced in the Lambert Terrane at c. 2400 Ma (Boger et al., 2001; Mikhalsky et al., 2006) are further possibilities for the source of this Archean to Paleoproterozoic detritus.

Despite these potential sources, inheritance of c. 2500–2400 Ma is lacking in granulites from the northern EGP (Bhattacharya et al., 2016; Bose et al., 2016; Sawant et al., 2017), a region that is in close proximity to the Rengali Orogen (Bhattacharya et al., 2016), and potentially accessible from the Vestfold, Ruker and Lambert Terranes based on recent Proterozoic plate tectonic reconstructions (Merdith et al., 2017). However, the Archean Napier Complex records a high volume of anatectic zircon growth in the age range c. 2500–2400 Ma (Carson et al., 2002; Hokada et al., 2004; Horie et al., 2012), similar to the neighbouring reworked Archean basement of the Oygarden Group of islands, which also record high-grade recrystallization at c. 1000–900 Ma (Halpin et al., 2005; Kelly et al., 2002). In addition, granites were emplaced in the northern Napier Complex c. 2410 Ma (Black et al., 1986). This Archean basement was probably closer to the EGP during the Proterozoic (Merdith et al., 2017), and the inherited zircon in this study may have been derived from sediment sourced from this crust. If the c. 2500–2400 Ma zircon was sourced from the Napier Complex granulites, non-oscillatory, weakly-zoned zircon textures with flattened HREE

signatures might be expected (Kelly and Harley, 2005). However, to properly discriminate between potential sources of inherited zircon in the EGP would require a separate study involving a larger sample size, appropriate textural analysis, higher resolution U–Pb zircon geochronology, and determination of REE and Lu–Hf isotopic signatures. The detrital zircon record in the EGP will be explored further in Chapter 4.

3.5.5 | Development of a hot orogen

A polymetamorphic evolution at UHT conditions has commonly been inferred for the EGP (Dasgupta, 1995; Dasgupta et al., 2013; Rickers et al., 2001b; Simmat and Raith, 2008). Many models propose a Grenvillian counterclockwise *P–T* evolution to an UHT peak at c. 1130–930 Ma, followed by near isobaric cooling ('M1') followed by decompression during a separate ('M2') metamorphic event (Das et al., 2011; Dharma Rao et al., 2012a; Mohan et al., 1997). At Vizianagaram, there is scant evidence for an earlier counterclockwise metamorphic event or for a distribution of concordant U–Pb zircon ages to identify multiple separate tectonothermal events. The simplest explanation for the spread of concordant zircon ages from c. 1050 to c. 800 Ma determined in this study (Figure 3.8) is a single long-lived event in which temperature remained above ~800°C, appropriate to suprasolidus conditions in most rocks.

Any tectonic model for the evolution of the EGP must explain the UHT metamorphism, the crustal shortening related to the collision of EGP with the Indian craton (Gupta, 2012), and also explain juxtaposition of crustal blocks that experienced contemporaneous decompression and near-isobaric cooling dominated post-peak *P–T* histories. The granulites at Vizianagaram which record decompression of <1 kbar during long-lived cooling from UHT (Figure 3.10) are separated by ~50 km from the granulites in the Paderu–Anantagiri–Salur block which record a counterclockwise evolution (Korhonen et al., 2013a; Korhonen et al., 2013b; Korhonen et al., 2011). A model of truncated hot orogenesis has previously been suggested to explain the evolution of the region (Korhonen et al., 2013a; Sizova et al., 2014). These models ascribe metamorphism at UHT and moderate pressures to slab breakoff, crustal extension and replacement of the sub-continental lithospheric mantle with melt-bearing asthenospheric mantle. In these models, counterclockwise *P–T* paths at UHT conditions could have been produced via renewed shortening, which would return the crust to a 'normal' thickness and allow long–lived near-isobaric cooling (Figure 3.14b, c). Gupta (2012) suggested that: 1) the

available structural, metamorphic and geochronological evidence supports shortening of the EGP under granulite facies conditions shortly after the Neoproterozoic UHT peak; and, 2) a tectonic contact may exist between the domains experiencing decompression and those recording near-isobaric cooling after a counterclockwise *P–T* evolution at UHT, with the former being thrust westward over the latter. This model predicts loading with a counterclockwise *P–T* path in the footwall and exhumation with a decompression dominated *P–T* path in the hanging wall, consistent with observations (Figure 3.14c). Furthermore, post–peak decompression could represent partial exhumation via thrusting of hot crust over an adjacent cratonic indentor, such as the Napier Complex (Figure 3.14b). This possibility is supported by c. 2500–2400 Ma zircon inheritance at Vizianagaram and comparable post-peak *P–T* paths between Vizianagaram and granulites from western Kemp Land, where post-peak decompression is more pronounced (Halpin et al., 2007a; Harley et al., 1990; Kelly and Harley, 2004).

A decompression-dominated *P–T* path from >10 kbar to ~8 kbar at >1000°C has been proposed (Kelsey et al., 2017; Rickers et al., 2001b) for granulites from Anakapalle ~60 km to the southwest along strike from Vizianagaram in the Eastern Ghats. Kelsey et al. (2017) argue that the decompression could have occurred towards the end of a long-lived counterclockwise *P–T* loop, an evolution postulated to be typical of the EGP as a whole. Such an evolution would have been characterized by a near uniform >150°C/kbar prograde apparent geotherm. To account for the lack of evidence elsewhere in the terrane, they argue that the refractory compositions of other Al–Mg granulites in the EGP would not have recorded the late-stage decompression. However, this explanation contradicts evidence from UHT localities in other metamorphic belts that garnet-bearing high Al–Mg granulites in particular commonly do record post-peak decompression (Harley, 1998). We contend that this is also true for the garnet-bearing high Al–Mg granulites from the EGP. If high-T decompression had occurred at the localities studied by Korhonen et al. (2013a) and Korhonen et al., (2014), it is likely that reaction microstructures involving garnet breakdown would have developed, but these are absent. Mafic rocks at Anakapalle were emplaced at 1580 Ma (Kelsey et al., 2017), far earlier than at many other localities, where emplacement occurred at c. 950 Ma (Korhonen et al., 2013b). Therefore, a higher apparent thermal gradient [>150°C/kbar; (Korhonen et al., 2013a)] may have been induced in parts of the EGP during the UHT event by elevated mantle heat flow. Furthermore, in modern collisional belts, rocks exhumed closer to

a thrust tend to be exhumed from higher pressures (Harris et al., 2004; Jamieson et al., 2004; Yakymchuk and Godin, 2012), which may be the case at Anakapalle.

A higher spatial distribution of reliably constrained *P–T* paths and zircon provenance studies are required to better discriminate between the potential tectonic models, and satisfactorily explain sustained UHT metamorphism for c. 100 Ma in thinned crust in the hinterland of a collisional orogen. Possible solutions to this conundrum include prolonged focused radiogenic heat production (Horton et al., 2016), high mantle heat flux, anomalously strengthened residual crust, low erosion rates and/or re–activated convergence at c. 900 Ma (Dasgupta et al., 2013; Mezger and Cosca, 1999). Merdith et al. (2017) place a passive plate margin outboard of the Eastern Ghats/Rayner terrane (EGRT) after subduction/accretion ended at c. 850 Ma. This remained a passive margin until the EGRT was within close proximity to the Mawson and South Australian cratons due to subduction from c.1050 to c. 650 Ma in the Mawson Sea outboard of Australia (Figure 3.14a). Radiogenic heat production from dominant khondalite and charnockite lithologies were ~3 μWm^{-3} at 550 Ma in the EGP (Kumar et al., 2007). Low erosion rates in the heat producing element (HPE) enriched backarc region of this system could have led to prolonged high–T conditions. Few inherited zircon data in the Prydz orogen are younger than c. 900 Ma (Grew et al., 2012; Hokada et al., 2016; Kinny et al., 1993; Wang et al., 2016), inhibiting reliable tectonic inferences based on the geochronological data for the period c. 900–550 Ma. However maximum detrital zircon ages for passive margins are commonly >100 Ma older than sedimentation ages (Cawood et al., 2012). These regions are often tectonically stable with low uplift and sedimentation rates induced on the inboard craton, while contemporaneous magmatism is also sparse (Cawood et al., 2012; Cawood and Nemchin, 2001; Cawood et al., 2007). Thus, focused radiogenic heat production over a long period may be the explanation for the long-lived UHT metamorphism in the EGP–RC.

Pan African reworking in the EGP recorded by zircon and monazite was previously interpreted as a mid-amphibolite facies overprint localized along regional scale shear zones or around pegmatites found throughout the EGP. Granulite facies conditions (>810°C) at c. 550–500 Ma, as reported in this study based on in–situ Ti-in-zircon thermometry on samples from Vizianagaram, refute these claims. Neosomes in granulites from Garbham, to

the north of Vizianagaram, similarly contain zircon overgrowths of c. 550 Ma age. Additionally, U–Pb rutile ages of c. 450 Ma from the EGP record a lower closure temperature (~600°C for 100μm grain size) than zircon and monazite (Cherniak, 2000; Taylor et al., 2012). Therefore, the inference can be drawn that the EGP terrane had cooled to ~ 600°C by c. 450 Ma. Simmat and Raith (2008) report pronounced hydrous retrogression occurring near shear zones due to fluid flux, but temperatures >800°C are unlikely to be recorded by their mineral assemblages. Pan African zircon and monazite age populations are sparse in southern regions of the EGP.

Preferential reheating may occur in residual granulites that were formed during the 1050–800 Ma granulite facies event, with reworking being determined by the geographic distribution of these residual granulites. The removal of partial melt from the crust leaves dry residual assemblages and removes the buffering effect that partial melting has on crustal heating (Stüwe, 1995). Burial of rocks with high HPE concentrations for >40 Ma means HPE are an important heat source. Khondalite and charnockite lithologies in the Eastern Ghats terrane typically produce ~3 μWm–3 heat from HPE; a value that is high compared to other Archean and Proterozoic terranes (Kumar et al., 2007). It is feasible that dry, residual rock volumes with high HPE values remained buried at ~20 km after the 1050–800 Ma granulite event (Figure 3.14), during a period of regional tectonic quiescence until c. 550 Ma (Li et al., 2008).

The EGRT is placed to the west of a passive margin during the time period until c.550 Ma in some tectonic plate reconstructions (Merdith et al., 2017). (Merdith et al., 2017) suggest that subduction was initiated on the eastern margin of the EGRT by 550 Ma (Figure 3.14a, b), instigating collision between the EGRT and Australia leading to the development of the Prydz Belt, an orogenic belt traced through the Southern Prince Charles Mountains (Li et al., 2008). It is possible that the Vizianagaram granulites––already residual, HPE enriched and at ~20 km depth––were in a widened orogenic backarc region inboard of the Prydz orogeny and subject to elevated mantle heat flow to enable minimal reheating to granulite facies conditions (Figure 3.14). Reworking and melt generation in hot orogens is most likely to occur around regional scale shear zone systems (Perchuk et al., 2016), such as the Nagavali Shear Zone. Reworking of the Vizianagaram granulites at c. 550 Ma could have been a result of an influx of some H2O into the residual granulites, lowering their solidus temperatures to ~800°C, leading to remelting and

neocrystallized zircon rims at these temperatures. Final concordant zircon crystallization at c. 510 Ma (Figure 3.8b) and U–Pb rutile ages of c. 450 Ma (Taylor et al., 2012) are consistent with slow cooling of the EGRT to ~ 600°C in the lower crust in the aftermath of the assembly of Gondwana.

3.6 | Conclusions

A list of research objectives for Chapter 3 can be found in section 1.1.2 of the introduction. Objectives 1-3 are addressed in conclusions 1 and 2 and objective 4 in conclusion 5:

1. Granulites at Vizianagaram, Eastern Ghats Province, India, record petrologically robust evidence for suprasolidus zircon crystallization from c. 1050–800 Ma. In–situ Ti-in-zircon thermometry suggests UHT conditions (>900°C) persisted for a minimum of c. 120 Ma between c.1000 and c. 880 Ma. Post peak metamorphic conditions are characterized by <1 kbar of decompression at ~1000°C before cooling to ~800°C. However, the UHT granulites at Vizianagaram may not have followed a conterclockwise *P–T* path similar to highland localities in the EGP (Korhonen, Brown, et al., 2013).

2. Based on Ti-in-zircon thermometry, neocrystallization of zircon and monazite rims at c. 550–510 Ma occurred at ~810°C. Neocrystallization was likely due to reheating of the Vizianagaram granulites at c. 550 Ma assisted by an influx of ~2 mol.% H_2O.

3.Vizianagaram granulites share events at c.1050–800 and c. 550–500 Ma with several localities in the Rayner Complex. Sources for inherited c. 2500–2400 Ma zircon populations include the Napier Complex, Ruker Terrane and Bastar Craton.

4. A tectonic model has been proposed for the EGP that accounts for the long-lived juxtaposition of crustal blocks experiencing near-isobaric cooling or decompression dominated post-peak *P–T* paths at granulite facies conditions. A truncated hot orogen (Korhonen et al., 2013a; Sizova et al., 2014) may be adequate to generate UHT metamorphism. After crustal thinning, renewed convergence may have led to post-peak decompression, representing partial exhumation via thrusting of hot crust over adjacent granulites with counterclockwise *P–T* paths and the cratonic indentor.

5. Localised suprasolidus reworking of the EGP occurred in susceptible, preconditioned rocks. Prolonged residence of residual granulites with high HPE concentrations between c. 800 and c. 550 Ma preceded the initiation of subduction outboard of the EGRT at c. 550 and formation of the Prydz Belt. Increased mantle heat flow in a widened back-arc comprising the amalgamated EGRT may have preferentially heated susceptible, residual, HPE rich crustal material to suprasolidus (>800°C) temperatures in proximity to regional shear zone systems.

3.7 | References

Bhattacharya, A., Das, H. H., Bell, E., Bhattacharya, A., Chatterjee, N., Saha, L., and Dutt, A., 2016, Restoration of Late Neoarchean–Early Cambrian tectonics in the Rengali orogen and its environs (eastern India): The Antarctic connection: Lithos, v. 263, p. 190-212.

Black, L. P., Sheraton, J. W., and James, P. R., 1986, Late Archaean granites of the Napier Complex, Enderby Land, Antarctica: A comparison of Rb-Sr, Sm-Nd and U-Pb isotopic systematics in a complex terrain: Precambrian Research, v. 32, no. 4, p. 343-368.

Blereau, E., Johnson, T. E., Clark, C., Taylor, R. J. M., Kinny, P. D., and Hand, M., 2017, Reappraising the P–T evolution of the Rogaland–Vest Agder Sector, southwestern Norway: Geoscience Frontiers, v. 8, no. 1, p. 1-14.

Boger, S. D., Hirdes, W., Ferreira, C. A. M., Jenett, T., Dallwig, R., and Fanning, C. M., 2015, The 580-520Ma Gondwana suture of Madagascar and its continuation into Antarctica and Africa: Gondwana Research, v. 28, no. 3, p. 1048-1060.

Boger, S. D., Wilson, C. J. L., and Fanning, C. M., 2001, Early Paleozoic tectonism within the East Antarctic craton: The final suture between east and west Gondwana?: Geology, v. 29, no. 5, p. 463-466.

Bose, S., Das, K., Torimoto, J., Arima, M., and Dunkley, D. J., 2016, Evolution of the Chilka Lake granulite complex, northern Eastern Ghats Belt, India: First evidence of ~ 780 Ma decompression of the deep crust and its implication on the India–Antarctica correlation: Lithos, v. 263, p. 161-189.

Brown, M., 2007, Metamorphism, Plate Tectonics, and the Supercontinent Cycle: Earth Science Frontiers, v. 14, no. 1, p. 1-18.

Brown, M., and Johnson, T. E., 2018, Secular change in metamorphism and the onset of global plate tectonics: American Mineralogist.

Carson, C. J., Ague, J. J., and Coath, C. D., 2002, U-Pb geochronology from Tonagh Island, East Antarctica: Implications for the timing of ultra-high temperature metamorphism of the Napier Complex: Precambrian Research, v. 116, no. 3-4, p. 237-263.

Cawood, P. A., Hawkesworth, C. J., and Dhuime, B., 2012, Detrital zircon record and tectonic setting: Geology, v. 40, no. 10, p. 875-878.

Cawood, P. A., and Nemchin, A. A., 2001, Paleogeographic development of the east Laurentian margin: Constraints from U-Pb dating of detrital zircons in the Newfoundland Appalachians: Geological Society of America Bulletin, v. 113, no. 9, p. 1234-1246.

Cawood, P. A., Nemchin, A. A., and Strachan, R., 2007, Provenance record of Laurentian passive-margin strata in the northern Caledonides: Implications for paleodrainage and paleogeography: Bulletin of the Geological Society of America, v. 119, no. 7-8, p. 993-1003.

Cherniak, D. J., 2000, Pb diffusion in rutile: Contributions to Mineralogy and Petrology, v. 139, no. 2, p. 198-207.

Clark, C., Fitzsimons, I. C. W., Healy, D., and Harley, S. L., 2011, How does the continental crust get really hot?: Elements, v. 7, no. 4, p. 235-240.

Clark, C., Healy, D., Johnson, T., Collins, A. S., Taylor, R. J., Santosh, M., and Timms, N. E., 2015, Hot orogens and supercontinent amalgamation: A Gondwanan example from southern India: Gondwana Research, v. 28, no. 4, p. 1310-1328.

Clark, C., Kinny, P. D., and Harley, S. L., 2012, Sedimentary provenance and age of metamorphism of the Vestfold Hills, East Antarctica: Evidence for a piece of Chinese Antarctica?: Precambrian Research, v. 196-197, p. 23-45.

Clark, C., Kirkland, C. L., Spaggiari, C. V., Oorschot, C., Wingate, M. T. D., and Taylor, R. J., 2014, Proterozoic granulite formation driven by mafic magmatism: An example from the Fraser Range Metamorphics, Western Australia: Precambrian Research, v. 240, p. 1-21.

Collins, A. S., Fitzsimons, I. C. W., Hulscher, B., and Razakamanana, T., 2003, Structure of the eastern margin of the East African Orogen in central Madagascar: Precambrian Research, v. 123, no. 2-4, p. 111-133.

Compston, W., Williams, I., and Meyer, C., 1984, U–Pb geochronology of zircons from lunar breccia 73217 using a sensitive high mass-resolution ion microprobe: Journal of Geophysical Research: Solid Earth, v. 89, no. S02.

Currie, C. A., and Hyndman, R. D., 2006, The thermal structure of subduction zone back arcs: Journal of Geophysical Research: Solid Earth, v. 111, no. B8, p. n/a-n/a.

Das, K., Bose, S., Karmakar, S., Dunkley, D. J., and Dasgupta, S., 2011, Multiple tectonometamorphic imprints in the lower crust: First evidence of ca. 950Ma (zircon U-Pb SHRIMP) compressional reworking of UHT aluminous granulites from the Eastern Ghats Belt, India: Geological Journal, v. 46, no. 2-3, p. 217-239.

Dasgupta, S., 1995, Pressure-temperature evolutionary history of the Eastern Ghats granulite province: recent advances and some thoughts: Memoirs - Geological Society of India, v. 34, p. 101-110.

Dasgupta, S., Bose, S., and Das, K., 2013, Tectonic evolution of the Eastern Ghats Belt, India: Precambrian Research, v. 227, p. 247-258.

Dharma Rao, C. V., Santosh, M., and Chmielowski, R. M., 2012a, Sapphirine granulites from Panasapattu, Eastern Ghats belt, India: Ultrahigh-temperature metamorphism in a Proterozoic convergent plate margin: Geoscience Frontiers, v. 3, no. 1, p. 9-31.

Dharma Rao, C. V., Santosh, M., and Dong, Y., 2012b, U-Pb zircon chronology of the Pangidi-Kondapalle layered intrusion, Eastern Ghats belt, India: Constraints on Mesoproterozoic arc magmatism in a convergent margin setting: Journal of Asian Earth Sciences, v. 49, p. 362-375.

Dobmeier, C. J., and Raith, M. M., 2003, Crustal architecture and evolution of the Eastern Ghats Belt and adjacent regions of India, Geological Society Special Publication, Volume 206, p. 145-168.

Dorfler, K. M., Caddick, M. J., and Tracy, R. J., 2015, Thermodynamic modeling of crustal melting using xenolith analogs from the Cortlandt Complex, New York, USA: Journal of Petrology, v. 56, no. 2, p. 389-408.

Doukkari, S. A., Diener, J. F., Ouzegane, K., and Kienast, J. R., 2018, Mineral equilibrium modelling and calculated chemical potential relations of reaction textures in the ultrahigh□temperature In Ouzzal terrane (In Hihaou area, Western Hoggar, Algeria): Journal of Metamorphic Geology, v. 36, no. 9, p. 1175-1198.

Dragovic, B., Guevara, V. E., Caddick, M. J., Baxter, E. F., and Kylander-Clark, A. R. C., 2016, A pulse of cryptic granulite-facies metamorphism in the Archean Wyoming Craton revealed by Sm–Nd garnet and U–Pb monazite geochronology: Precambrian Research, v. 283, p. 24-49.

Ferry, J. M., and Watson, E. B., 2007, New thermodynamic models and revised calibrations for the Ti-in-zircon and Zr-in-rutile thermometers: Contributions to Mineralogy and Petrology, v. 154, no. 4, p. 429-437.

Fitzsimons, I. C. W., 2000, A review of tectonic events in the east antarctic shield and their implications for gondwana and earlier supercontinents: Journal of African Earth Sciences, v. 31, no. 1, p. 3-23.

Foster, G., Kinny, P., Vance, D., Prince, C., and Harris, N., 2000, The significance of monazite U–Th–Pb age data in metamorphic assemblages; a combined study of monazite and garnet chronometry: Earth and Planetary Science Letters, v. 181, no. 3, p. 327-340.

Fritz, H., Abdelsalam, M., Ali, K. A., Bingen, B., Collins, A. S., Fowler, A. R., Ghebreab, W., Hauzenberger, C. A., Johnson, P. R., Kusky, T. M., Macey, P., Muhongo, S., Stern, R. J., and Viola, G., 2013, Orogen styles in the East African Orogen: A review of the Neoproterozoic to Cambrian tectonic evolution: Journal of African Earth Sciences, v. 86, p. 65-106.

Galli, A., Le Bayon, B., Schmidt, M. W., Burg, J. P., Caddick, M. J., and Reusser, E., 2011, Granulites and charnockites of the Gruf Complex: Evidence for Permian ultra-high temperature metamorphism in the Central Alps: Lithos, v. 124, no. 1-2, p. 17-45.

Geisler, T., Schaltegger, U., and Tomaschek, F., 2007, Re-equilibration of zircon in aqueous fluids and melts: Elements, v. 3, no. 1, p. 43-50.

Grew, E. S., Carson, C. J., Christy, A. G., Maas, R., Yaxley, G. M., Boger, S. D., and Fanning, C. M., 2012, New constraints from U–Pb, Lu–Hf and Sm–Nd isotopic data on the timing of sedimentation and felsic magmatism in the Larsemann Hills, Prydz Bay, East Antarctica: Precambrian Research, v. 206, p. 87-108.

Gupta, S., 2012, Strain localization, granulite formation and geodynamic setting of 'hot orogens': A case study from the Eastern Ghats Province, India: Geological Journal, v. 47, no. 2-3, p. 334-351.

Hacker, B. R., Gnos, E., Ratschbacher, L., Grove, M., McWilliams, M., Sobolev, S. V., Wan, J., and Wu, Z., 2000, Hot and dry deep crustal xenoliths

from Tibet: Science, v. 287, no. 5462, p. 2463-2466.

Hacker, B. R., Ritzwoller, M. H., and Xie, J., 2014, Partially melted, mica-bearing crust in central tibet: Tectonics, v. 33, no. 7, p. 1408-1424.

Halpin, J. A., Clarke, G. L., White, R. W., and Kelsey, D. E., 2007a, Contrasting P-T-t paths for Neoproterozoic metamorphism in MacRobertson and Kemp Lands, east Antarctica: Journal of Metamorphic Geology, v. 25, no. 6, p. 683-701.

Halpin, J. A., Gerakiteys, C., Clarke, G., Belousova, E., and Griffin, W., 2005, In-situ U–Pb geochronology and Hf isotope analyses of the Rayner Complex, east Antarctica: Contributions to Mineralogy and Petrology, v. 148, no. 6, p. 689-706.

Halpin, J. A., White, R. W., Clarke, G. L., and Kelsey, D. E., 2007b, The Proterozoic P-T-t evolution of the Kemp Land Coast, East Antarctica; constraints from Si-saturated and Si-undersaturated metapelites: Journal of Petrology, v. 48, no. 7, p. 1321-1349.

Harley, S. L., 1994, Cordierite as a sensor of fluid and melt distribution in crustal metamorphism: Mineralogical Magazine, v. 58, no. 1, p. 374-375.

-, 1998, On the occurrence and characterization of ultrahigh-temperature crustal metamorphism, Geological Society Special Publication, Volume 138, p. 81-107.

-, 2003, Archaean-Cambrian crustal development of East Antarctica: Metamorphic characteristics and tectonic implications, Geological Society Special Publication, Volume 206, p. 203-230.

-, 2008, Refining the P-T records of UHT crustal metamorphism: Journal of Metamorphic Geology, v. 26, no. 2, p. 125-154.

-, 2016, A matter of time: The importance of the duration of UHT metamorphism: Journal of Mineralogical and Petrological Sciences, v. 111, no. 2, p. 50-72.

Harley, S. L., Hensen, B. J., and Sheraton, J. W., 1990, Two□stage decompression in orthopyroxene–sillimanite granulites from Forefinger Point, Enderby Land, Antarctica: implications for the evolution of the Archaean Napier Complex: Journal of Metamorphic Geology, v. 8, no. 6, p. 591-613.

Harley, S. L., Kelly, N. M., and Möller, A., 2007, Zircon behaviour and

the thermal histories of moutain chains: Elements, v. 3, no. 1, p. 25-30.

Harley, S. L., and Nandakumar, V., 2016, New evidence for Palaeoproterozoic high grade metamorphism in the Trivandrum Block, Southern India: Precambrian Research, v. 280, p. 120-138.

Harris, N., Caddick, M., Kosler, J., Goswami, S., Vance, D., and Tindle, A., 2004, The pressure–temperature–time path of migmatites from the Sikkim Himalaya: Journal of Metamorphic Geology, v. 22, no. 3, p. 249-264.

Hinthorne, J., Andersen, C., Conrad, R., and Lovering, J., 1979, Single-grain 207Pb206Pb and U/Pb age determinations with a 10-μm spatial resolution using the ion microprobe mass analyzer (IMMA): Chemical Geology, v. 25, no. 4, p. 271-303.

Hokada, T., Harley, S. L., Dunkley, D. J., Kelly, N. M., and Yokoyama, K., 2016, Peak and post-peak development of UHT metamorphism at Mather Peninsula, Rauer Islands: Zircon and monazite U-Th-Pb and REE chemistry constraints: Journal of Mineralogical and Petrological Sciences, v. 111, no. 2, p. 89-103.

Hokada, T., Misawa, K., Yokoyama, K., Shiraishi, K., and Yamaguchi, A., 2004, SHRIMP and electron micropobe chronology of UHT metamorphism in the Napier Complex, East Antarctica: Implications for zircon growth at >1,000 °C: Contributions to Mineralogy and Petrology, v. 147, no. 1, p. 1-20.

Holder, R. M., Hacker, B. R., Horton, F., and Rakotondrazafy, A. M., 2018, Ultrahigh–temperature osumilite gneisses in southern Madagascar record combined heat advection and high rates of radiogenic heat production in a long-lived high-T orogen: Journal of Metamorphic Geology, v. 36, no. 7, p. 855-880.

Holland, T. J. B., and Powell, R., 2011, An improved and extended internally consistent thermodynamic dataset for phases of petrological interest, involving a new equation of state for solids: Journal of Metamorphic Geology, v. 29, no. 3, p. 333-383.

Horie, K., Hokada, T., Hiroi, Y., Motoyoshi, Y., and Shiraishi, K., 2012, Contrasting Archaean crustal records in western part of the Napier Complex, East Antarctica: New constraints from SHRIMP geochronology: Gondwana Research, v. 21, no. 4, p. 829-837.

Horton, F., Hacker, B., Kylander-Clark, A., Holder, R., and Jöns, N., 2016, Focused radiogenic heating of middle crust caused ultra-high

temperatures in southern Madagascar: Tectonics, v. 35, no. 2, p. 293-314.

Hyndman, R. D., 2015, Tectonic consequences of a uniformly hot backarc and why is the cordilleran mountain belt high?: Geoscience Canada, v. 42, no. 4, p. 383-402.

Hyndman, R. D., and Currie, C. A., 2011, Why is the North America Cordillera high? Hot backarcs, thermal isostasy, and mountain belts: Geology, v. 39, no. 8, p. 783-786.

Jamieson, R. A., and Beaumont, C., 2011, Coeval thrusting and extension during lower crustal ductile flow - implications for exhumation of high-grade metamorphic rocks: Journal of Metamorphic Geology, v. 29, no. 1, p. 33-51.

Jamieson, R. A., Beaumont, C., Medvedev, S., and Nguyen, M. H., 2004, Crustal channel flows: 2. Numerical models with implications for metamorphism in the Himalayan-Tibetan orogen: Journal of Geophysical Research B: Solid Earth, v. 109, no. 6, p. B06407 06401-06424.

Jamieson, R. A., Beaumont, C., Warren, C. J., and Nguyen, M. H., 2010, The Grenville Orogen explained? Applications and limitations of integrating numerical models with geological and geophysical data: Canadian Journal of Earth Sciences, v. 47, no. 4, p. 517-539.

Johnson, T., Brown, M., and White, R., 2010, Petrogenetic modelling of strongly residual metapelitic xenoliths within the southern Platreef, Bushveld Complex, South Africa: Journal of Metamorphic Geology, v. 28, no. 3, p. 269-291.

Kamineni, D. C., and Rao, A. T., 1988, Sapphirine-Bearing Quartzite from the Eastern Ghats Granulite Terrain, Vizianagaram, India: The Journal of Geology, v. 96, no. 2, p. 209-220.

Kelly, N. M., Clarke, G. L., and Fanning, C. M., 2002, A two-stage evolution of the Neoproterozoic Rayner Structural Episode: New U-Pb sensitive high resolution ion microprobe constraints from the Oygarden Group, Kemp Land, East Antarctica: Precambrian Research, v. 116, no. 3-4, p. 307-330.

Kelly, N. M., and Harley, S. L., 2004, Orthopyroxene-corundum in Mg-Al-rich granulites from the Oygarden islands, East Antarctica: Journal of Petrology, v. 45, no. 7, p. 1481-1512.

-, 2005, An integrated microtextural and chemical approach to zircon geochronology: Refining the Archaean history of the Napier Complex, east Antarctica: Contributions to Mineralogy and Petrology, v. 149, no. 1, p. 57-84.

Kelsey, D. E., 2008, On ultrahigh-temperature crustal metamorphism: Gondwana Research, v. 13, no. 1, p. 1-29.

Kelsey, D. E., Clark, C., and Hand, M., 2008, Thermobarometric modelling of zircon and monazite growth in melt-bearing systems: Examples using model metapelitic and metapsammitic granulites: Journal of Metamorphic Geology, v. 26, no. 2, p. 199-212.

Kelsey, D. E., and Hand, M., 2015, On ultra-high temperature crustal metamorphism: Phase equilibria, trace element thermometry, bulk composition, heat sources, timescales and tectonic settings: Geoscience Frontiers, v. 6, no. 3, p. 311-356.

Kelsey, D. E., Morrissey, L. J., Hand, M., Clark, C., Tamblyn, R., Gaehl, A. A., and Marshall, S., 2017, Significance of post-peak metamorphic reaction microstructures in the ultra-high temperature Eastern Ghats Province, India: Journal of Metamorphic Geology, v. 35, no. 9, p. 1081-1109.

Kelsey, D. E., and Powell, R., 2011, Progress in linking accessory mineral growth and breakdown to major mineral evolution in metamorphic rocks: A thermodynamic approach in the Na 2O-CaO-K 2O-FeO-MgO-Al 2O 3-SiO 2-H 2O-TiO 2-ZrO 2 system: Journal of Metamorphic Geology, v. 29, no. 1, p. 151-166.

Kinny, P. D., Black, L. P., and Sheraton, J. W., 1993, Zircon ages and the distribution of Archaean and Proterozoic rocks in the Rauer Islands: Antarctic Science, v. 5, no. 2, p. 193-206.

Korhonen, F. J., Brown, M., Clark, C., and Bhattacharya, S., 2013a, Osumilite-melt interactions in ultra-high temperature granulites: Phase equilibria modelling and implications for the P-T-t evolution of the eastern ghats province, india: Journal of Metamorphic Geology, v. 31, no. 8, p. 881-907.

Korhonen, F. J., Brown, M., Clark, C., Foden, J. D., and Taylor, R., 2015, Are granites and granulites consanguineous?: Geology, v. 43, no. 11, p. 991-994.

Korhonen, F. J., Clark, C., Brown, M., Bhattacharya, S., and Taylor, R., 2013b, How long-lived is ultra-high temperature (UHT) metamorphism?

Constraints from zircon and monazite geochronology in the Eastern Ghats orogenic belt, India: Precambrian Research, v. 234, p. 322-350.

Korhonen, F. J., Clark, C., Brown, M., and Taylor, R. J. M., 2014, Taking the temperature of Earth's hottest crust: Earth and Planetary Science Letters, v. 408, p. 341-354.

Korhonen, F. J., Saw, A. K., Clark, C., Brown, M., and Bhattacharya, S., 2011, New constraints on UHT metamorphism in the Eastern Ghats Province through the application of phase equilibria modelling and in situ geochronology: Gondwana Research, v. 20, no. 4, p. 764-781.

Kovach, V. P., Simmat, R., Rickers, K., Berezhnaya, N. G., Salnikova, E. B., Dobmeier, C., Raith, M. M., Yakovleva, S. Z., and Kotov, A. B., 2001, The Western Charnockite Zone of the Eastern Ghats Belt, India - An Independent Crustal Province of Late Archaean (2.8 Ga) and Palaeoproterozoic (1.7-1.6 Ga) Terrains: Gondwana Research, v. 4, no. 4, p. 666-667.

Kumar, P. S., Menon, R., and Reddy, G. K., 2007, The role of radiogenic heat production in the thermal evolution of a Proterozoic granulite-facies orogenic belt: Eastern Ghats, Indian Shield: Earth and Planetary Science Letters, v. 254, no. 1-2, p. 39-54.

Li, Z.-X., Bogdanova, S., Collins, A., Davidson, A., De Waele, B., Ernst, R., Fitzsimons, I., Fuck, R., Gladkochub, D., and Jacobs, J., 2008, Assembly, configuration, and break-up history of Rodinia: a synthesis: Precambrian research, v. 160, no. 1-2, p. 179-210.

Liu, Y., Hu, Z., Zong, K., Gao, C., Gao, S., Xu, J., and Chen, H., 2010, Reappraisement and refinement of zircon U-Pb isotope and trace element analyses by LA-ICP-MS: Chinese Science Bulletin, v. 55, no. 15, p. 1535-1546.

McKenzie, D., and Priestley, K., 2008, The influence of lithospheric thickness variations on continental evolution: Lithos, v. 102, no. 1-2, p. 1-11.

Merdith, A. S., Collins, A. S., Williams, S. E., Pisarevsky, S., Foden, J. D., Archibald, D. B., Blades, M. L., Alessio, B. L., Armistead, S., and Plavsa, D., 2017, A full-plate global reconstruction of the Neoproterozoic: Gondwana Research, v. 50, p. 84-134.

Mezger, K., and Cosca, M. A., 1999, The thermal history of the Eastern Ghats Belt (India) as revealed by U-Pb and 40Ar/39Ar dating of metamorphic and magmatic minerals: Implications for the SWEAT correlation: Precambrian Research, v. 94, no. 3-4, p. 251-271.

Mikhalsky, E. V., Beliatsky, B. V., Sheraton, J. W., and Roland, N. W., 2006, Two distinct Precambrian terranes in the Southern Prince Charles Mountains, East Antarctica: SHRIMP dating and geochemical constraints: Gondwana Research, v. 9, no. 3, p. 291-309.

Mohan, A., Tripathi, P., and Motoyoshi, Y., 1997, Reaction history of sapphirine granulites and a decompressional P-T path in a granulite complex from the Eastern Ghats: Proceedings of the Indian Academy of Sciences, Earth and Planetary Sciences, v. 106, no. 3, p. 115-129.

Morrissey, L. J., Hand, M., Kelsey, D. E., and Wade, B. P., 2016, Cambrian high-temperature reworking of the Rayner-Eastern ghats terrane: Constraints from the Northern Prince Charles Mountains region, East Antarctica: Journal of Petrology, v. 57, no. 1, p. 53-91.

Nasdala, L., Zhang, M., Kempe, U., Panczer, G., Gaft, M., Andrut, M., and Plötze, M., 2003, Spectroscopic methods applied to zircon: Reviews in Mineralogy and Geochemistry, v. 53, no. 1, p. 427-467.

Paton, C., Hellstrom, J., Paul, B., Woodhead, J., and Hergt, J., 2011, Iolite: Freeware for the visualisation and processing of mass spectrometric data: Journal of Analytical Atomic Spectrometry, v. 26, no. 12, p. 2508-2518.

Perchuk, A., Safonov, O., Smit, C., Van Reenen, D., Zakharov, V., and Gerya, T., 2016, Precambrian ultra-hot orogenic factory: Making and reworking of continental crust: Tectonophysics.

Plavsa, D., Collins, A. S., Foden, J. D., and Clark, C., 2015, The evolution of a Gondwanan collisional orogen: A structural and geochronological appraisal from the Southern Granulite Terrane, South India: Tectonics, v. 34, no. 5, p. 820-857.

Pownall, J. M., 2015, UHT metamorphism on Seram, eastern Indonesia: Reaction microstructures and P-T evolution of spinel-bearing garnet-sillimanite granulites from the Kobipoto Complex: Journal of Metamorphic Geology, v. 33, no. 9, p. 909-935.

Prakash, D., Singh, P. C., Singh, C. K., Tewari, S., Arima, M., and Frimmel, H. E., 2015, Reaction textures and metamorphic evolution of sapphirine-spinel-bearing and associated granulites from Diguva Sonaba, Eastern Ghats Mobile Belt, India: Geological Magazine, v. 152, no. 2, p. 316-340.

Rickers, K., Mezger, K., and Raith, M. M., 2001a, Evolution of the

continental crust in the Proterozoic Eastern Ghats Belt, India and new constraints for Rodinia reconstruction: Implications from Sm-Nd, Rb-Sr and Pb-Pb isotopes: Precambrian Research, v. 112, no. 3-4, p. 183-210.

Rickers, K., Raith, M., and Dasgupta, S., 2001b, Multistage reaction textures in xenolithic high-MgAl granulites at Anakapalle, Eastern Ghats Belt, India: Examples of contact polymetamorphism and infiltration-driven metasomatism: Journal of Metamorphic Geology, v. 19, no. 5, p. 561-580.

Rubatto, D., and Gebauer, D., 2000, Use of cathodoluminescence for U-Pb zircon dating by ion microprobe: some examples from the Western Alps, Cathodoluminescence in geosciences, Springer, p. 373-400.

Sarkar, G., Corfu, F., Paul, D., McNaughton, N., Gupta, S., and Bishui, P., 1993, Early Archean crust in Bastar Craton, Central India—a geochemical and isotopic study: Precambrian Research, v. 62, no. 1-2, p. 127-137.

Sarkar, S., Dasgupta, S., and Fukuoka, M., 2003, Petrological evolution of a suite of spinel granulites from Vizianagram, Eastern Ghats Belt, India, and genesis of sapphirine-bearing assemblages: Journal of Metamorphic Geology, v. 21, no. 9, p. 899-913.

Sarkar, T., and Schenk, V., 2014, Two-stage granulite formation in a Proterozoic magmatic arc (Ongole domain of the Eastern Ghats Belt, India): Part 1. Petrology and pressure-temperature evolution: Precambrian Research, v. 255, no. P1, p. 485-509.

Sawant, A. D., Gupta, S., Clark, C., and Misra, S., 2017, The Rauer-Rengali connection in the Indo-Antarctica amalgam: Evidence from structure, metamorphism and geochronology, Geological Society Special Publication, Volume 457, Geological Society of London, p. 171-196.

Simmat, R., and Raith, M. M., 2008, U-Th-Pb monazite geochronometry of the Eastern Ghats Belt, India: Timing and spatial disposition of poly-metamorphism: Precambrian Research, v. 162, no. 1-2, p. 16-39.

Sizova, E., Gerya, T., and Brown, M., 2014, Contrasting styles of Phanerozoic and Precambrian continental collision: Gondwana Research, v. 25, no. 2, p. 522-545.

Stacey, J. S., and Kramers, J. D., 1975, Approximation of terrestrial lead isotope evolution by a two-stage model: Earth and planetary science letters, v. 26, no. 2, p. 207-221.

Stern, R. A., 2001, A new isotopic and trace-element standard for the ion microprobe: preliminary thermal ionization mass spectrometry (TIMS) U-Pb and electron-microprobe data, Ressources naturelles Canada.

Stüwe, K., 1995, Thermal buffering effects at the solidus. Implications for the equilibration of partially melted metamorphic rocks: Tectonophysics, v. 248, no. 1-2, p. 39-51.

Taylor, R., Clark, C., and Reddy, S. M., 2012, The effect of grain orientation on secondary ion mass spectrometry (SIMS) analysis of rutile: Chemical Geology, v. 300-301, p. 81-87.

Taylor, R. J. M., Kirkland, C. L., and Clark, C., 2016, Accessories after the facts: Constraining the timing, duration and conditions of high-temperature metamorphic processes: Lithos, v. 264, p. 239-257.

Thompson Jr, J. B., 1957, The graphical analysis of mineral assemblages in pelitic schists: Am. Mineral., v. 42, p. 842–858.

Thompson, P., Harley, S. L., and Carrington, D. P., 2001, The distribution of H 2 O–CO 2 between cordierite and granitic melt under fluid-saturated conditions at 5ákbar and 900°C: Contributions to Mineralogy and Petrology, v. 142, no. 1, p. 107-118.

Wang, W., Liu, X., Zhao, Y., Zheng, G., and Chen, L., 2016, U-Pb zircon ages and Hf isotopic compositions of metasedimentary rocks from the Grove Subglacial Highlands, East Antarctica: Constraints on the provenance of protoliths and timing of sedimentation and metamorphism: Precambrian Research, v. 275, p. 135-150.

Waters, D. J., 2001, The significance of prograde and retrograde quartz-bearing intergrowth microstructures in partially melted granulite-facies rocks: Lithos, v. 56, no. 1, p. 108-110.

Wheller, C. J., and Powell, R., 2014, A new thermodynamic model for sapphirine: Calculated phase equilibria in K2O-FeO-MgO-Al2O3-SiO2-H2O-TiO2-Fe2O3: Journal of Metamorphic Geology, v. 32, no. 3, p. 287-299.

White, R. W., Powell, R., Holland, T. J. B., Johnson, T. E., and Green, E. C. R., 2014, New mineral activity-composition relations for thermodynamic calculations in metapelitic systems: Journal of Metamorphic Geology, v. 32, no. 3, p. 261-286.

Whitney, D. L., and Evans, B. W., 2010, Abbreviations for names of

rock-forming minerals: American Mineralogist, v. 95, no. 1, p. 185-187.

Wiedenbeck, M., Alle, P., Corfu, F., Griffin, W., Meier, M., Oberli, F. v., Quadt, A. v., Roddick, J., and Spiegel, W., 1995, Three natural zircon standards for U–Th–Pb, Lu–Hf, trace element and REE analyses: Geostandards and Geoanalytical Research, v. 19, no. 1, p. 1-23.

Yakymchuk, C., and Godin, L., 2012, Coupled role of deformation and metamorphism in the construction of inverted metamorphic sequences: an example from far-northwest Nepal: Journal of Metamorphic Geology, v. 30, no. 5, p. 513-535.

Zhao, J. X., Ellis, D. J., Kilpatrick, J. A., and McCulloch, M. T., 1997, Geochemical and Sr-Nd isotopic study of charnockites and related rocks in the northern Prince Charles Mountains, East Antarctica: Implications for charnockite petrogenesis and proterozoic crustal evolution: Precambrian Research, v. 81, no. 1-2, p. 37-66.

Chapter 4 | Deciphering the zircon record in a long-lived granulite terrane

Ruairidh J. Mitchell[1,2], Tim E. Johnson[1,3], Chris Clark[1], Michael Brown[4], Chris L. Kirkland[1], Saibal Gupta[2]

1. School of Earth and Planetary Sciences, The Institute for Geoscience Research, Curtin University, Perth, WA 6102, Australia
2. Department of Geology and Geophysics, Indian Institute of Technology, Kharagpur, India
3. State Key Laboratory for Geological Processes and Mineral Resources and Center for Global Tectonics, School of Earth Sciences, China University of Geosciences, Wuhan 430074, China.
4. Laboratory for Crustal Petrology, Department of Geology, University of Maryland, College Park, MD 20742-4211, USA

Abstract

Interpreting zircon U–Pb geochronological data from metasedimentary rocks in high-grade terranes is commonly challenging due to the potential for pervasive and sometimes cryptic resetting of the U–Pb isotopic system. Such modification may be manifest in complex internal textures reflecting variable rates of diffusion and dissolution–reprecipitation, and in heterogeneous isotope and trace element compositions. As a result, disentangling meaningful information relating to the age, composition and provenance of the source rocks that provided the sedimentary protoliths may be difficult. Rocks from the Eastern Ghats Province (EGP), India, have a complex detrital zircon record and experienced more than one granulite facies metamorphic event. Here we propose a new workflow for interpreting U–Pb geochronological data from granulite facies metasedimentary zircon. Using a clustering algorithm based on trace element chemistry, we identified three zircon populations–inherited igneous zircon, metamorphic zircon and hydrothermally altered zircon—in six metasedimentary granulites. Based on a combination of U–Pb ages of inherited igneous zircon grains and Pb loss trends towards younger metamorphic events to identify the age of the oldest components, we identify three populations of dates at >2500 Ma, c. 1650–1350 Ma and c. 1220–1080 Ma that relate to the ages of the source rocks for the sedimentary protoliths. Zircon grains with c. 1650–1350 Ma concordant ages have elevated positive Ce anomalies (Ce/Ce*) and U/Yb ratios, suggesting that their magmatic source was relatively oxidised. By contrast, the c. 1220–1080 Ma grains have elevated Nb/Yb ratios, low Ce anomalies and high Ti concentrations, which likely reflect derivation from high-temperature, reduced, A-type magmas formed by low degree melting of the mantle in an extensional regime. Following input of sediment to the EGP depocentre, two anatectic metamorphic events occurred at c. 990–890 Ma (M1) and c. 600–500 Ma (M2). During M1, the EGP granulites cooled from >950 °C to below ~900 °C at a rate of 0.34 ± 0.09 °C/Ma. Subsequently, the EGP granulites were reheated to ~920 °C during M2. Slow cooling at and reheating to ultrahigh temperatures was facilitated by a sustained period of burial in the deep crust, reflecting high radiogenic heat production and low rates of erosion.

4.1 | Introduction

4.1.1 | Zircon geochronology in high grade terranes

Zircon ($ZrSiO_4$) is an accessory mineral that occurs in a wide range of crustal rocks (Corfu et al., 2003; Harley et al., 2007; Taylor et al., 2016). Zircon incorporates trace concentrations of uranium (U^{4+}) but almost no Pb, and solid state diffusion of U, Th and Pb are generally slow, making zircon a robust geochronometer in most high temperature igneous and metamorphic environments (Cherniak, 2010; Cherniak and Watson, 2001; Harley and Kelly, 2007; Harley et al., 2007; Kusiak et al., 2013). Zircon also contains relatively high abundances of heavy rare-earth elements (HREE), the concentrations of which can be used to link its growth and/or breakdown to other HREE-bearing phases (Rubatto, 2002; Rubatto and Hermann, 2007; Taylor et al., 2015). In addition, substitution of trace concentrations of Ti^{4+} into zircon permits the direct estimation of zircon crystallisation temperatures in SiO_2- and TiO_2-saturated (quartz- and rutile-bearing) igneous and metamorphic rocks (Ferry and Watson, 2007; Fu et al., 2008; Yakymchuk et al., 2017).

Experiments show that the solubility of zirconium in silicate melt is a function of the SiO_2, Al_2O_3 and MgO contents of the melt (Boehnke et al., 2013). Consequently, the proportion of zircon dissolved during partial melting at granulite facies metamorphic conditions depends on the protolith composition and the composition and volume of melt (Kelsey et al., 2008; Kelsey and Powell, 2011; Yakymchuk and Brown, 2014). In addition, loss of melt elevates the temperature at which solidification occurs during subsequent cooling (i.e. raises the temperature of the solidus), thereby restricting the temporal range over which melt crystallization (and zircon growth) can occur (Korhonen et al., 2013b; Korhonen et al., 2014). Assuming that zircon U–Pb ages record melt crystallization, the timing and duration of a metamorphic event can appear to vary greatly over an apparently uniformly cooling terrane (Clark et al., 2018; Korhonen et al., 2013b). Garnet and rutile, which are common in rocks metamorphosed at deep crustal levels, also contain trace concentrations of Zr, and may break down to form zircon (Fraser et al., 1997). However, the degree to which trace elements (including isotopes) equilibrate within zircon may vary between small-scale petrological domains, with evidence for both open and closed system behaviour (Hokada and Harley, 2004; Kelly and Harley, 2005; Yakymchuk and Brown, 2014). As such, constraining the timing of zircon dissolution and growth is non-trivial.

Advances in laser ablation split-stream (LASS) techniques have enabled simultaneous collection of large numbers of U–Pb and trace element analyses of zircon. Combining REE and Ti concentrations with U–Pb ages permits more detailed inferences on the conditions of zircon crystallisation in formerly suprasolidus rocks. Lattice strain models based on experimental studies predict that at >900 °C zircon/garnet partition coefficients for light REE ($D_{LREE}^{Zrc/Grt}$) decrease sharply with atomic number, for example by two orders of magnitude between La and Nd, whereas for HREE, there is only a small increase in ($D_{HREE}^{Zrc/Grt}$) with atomic number (e.g. Taylor et al. 2015). For most of the experimental runs of Taylor et al. (2015; experiments at7 kbar) $D_{HREE}^{Zrc/Grt}$ was >1, which is larger by an order of magnitude than values based on the experiments of Rubatto and Hermann (2007; experiments at 20 kbar). These experimentally-determined partition coefficients are commonly applied to metamorphic rocks, for which partitioning arrays may be plotted to ascertain whether zircon growth occurred in equilibrium with garnet (Clark et al., 2018; Taylor et al., 2017). The partitioning arrays reconcile the two experimental datasets—in both cases $D_{HREE}^{Zrc/Grt}$ decreases with increasing temperature, with the offset between the two datasets relating to the difference in pressure between the experimental runs. The Ti-in-zircon thermometer (Ferry and Watson, 2007) can be applied in conjunction with the partitioning data, although Ti may become decoupled from HREE at high temperatures (Kunz et al., 2018).

At lower temperatures, the trace element composition of zircon may change due to interaction with hydrothermal fluids, in particular with respect to the Th/U ratios, and the LREE, total REE and Hf concentrations (Ayers and Peters, 2018; Geisler et al., 2003; Geisler et al., 2007). Experiments investigating the partitioning of REE^{3+} between non-metamict (not radiation damaged) zircon and fluid (Fl) at 800–1000 °C and 15 kbar show that zircon will develop small positive Ce anomalies (Ce/Ce*), and that $D^{Zrc/Fl}$ between Lu and La decreases by only one order of magnitude (Ayers and Peters, 2018).

Due to the proportionally large volume of zircon that is dissolved as a protolith undergoes partial melting under granulite facies conditions (Kelsey et al., 2008; Yakymchuk and Brown, 2014), unmodified, inherited (detrital) zircon cores are rare (Taylor et al., 2016). As such, any record of zircon provenance before the high-grade metamorphic event tends to be cryptic and is generally represented by discordant zircon, reflecting Pb loss that extends

from the crystallisation age of the detrital source rocks to a lower intercept corresponding to the timing of the high-grade metamorphic event. As a result, a common approach to identify the age of the source rocks is to regress the data interpreted to result from a Pb loss event by anchoring the discordia on a single age of resetting (Collins et al., 2012; Collins et al., 2003; Collins et al., 2007; Gehrels, 2011; Gehrels, 2014; Harley and Kelly, 2007; Mezger and Krogstad, 1997; Plavsa et al., 2012; Plavsa et al., 2014; Wetherill, 1956). However, the problem becomes more complex when: (i) considering multiple detrital age populations and inhomogeneous analytical volumes, where the time of resetting cannot easily be determined; (ii) the data are within uncertainty of Concordia; or, (iii) the rocks record more than one high-grade metamorphic event leading to more than one episode of Pb-loss (Ashwal et al., 1999; Clark et al., 2015; Corfu et al., 1994; Plavsa et al., 2014; Vavra et al., 1996; Vavra et al., 1999).

The metasedimentary granulites analysed in this study are from the Eastern Ghats Province (EGP), India. The EGP was subject to multiple high-temperature metamorphic events (Das et al., 2011; Korhonen et al., 2013a; Korhonen et al., 2013b; Korhonen et al., 2014; Korhonen et al., 2011; Prakash et al., 2015), and the detritus that constituted the sedimentary protoliths may have had various sources (Korhonen et al., 2013b; Mitchell et al., 2019). The confluence of a varied detrital history and more than one high-grade metamorphic event makes these samples ideal to investigate methods for extracting detrital and metamorphic information from a complex geochronological dataset, and to tackle the objectives set out in section 1.1.3 of the introduction.

4.1.2 | Geological evolution of the Eastern Ghats Province

The EGP, part of the Eastern Ghats Mobile Belt, is situated on the eastern coast of India (Figure 4.1). It is a discrete crustal block defined on the basis of its isotopic, metamorphic and lithological characteristics (Rickers et al., 2001), which is bounded by the Godaravi Rift to the south, the Kerajang shear zone to the north and the Sileru shear zone system to the west (Dobmeier and Raith, 2003). As discussed in Chapter 3, the geological record of the EGP is complex, with evidence for several magmatic and metamorphic events ranging from the late Neoarchean, through the Proterozoic, to the early Palaeozoic (Dasgupta et al., 2013; Kelsey et al., 2017; Rickers et al., 2001; Sarkar and Schenk, 2016; Simmat and Raith, 2008; Upadhyay et al., 2009).

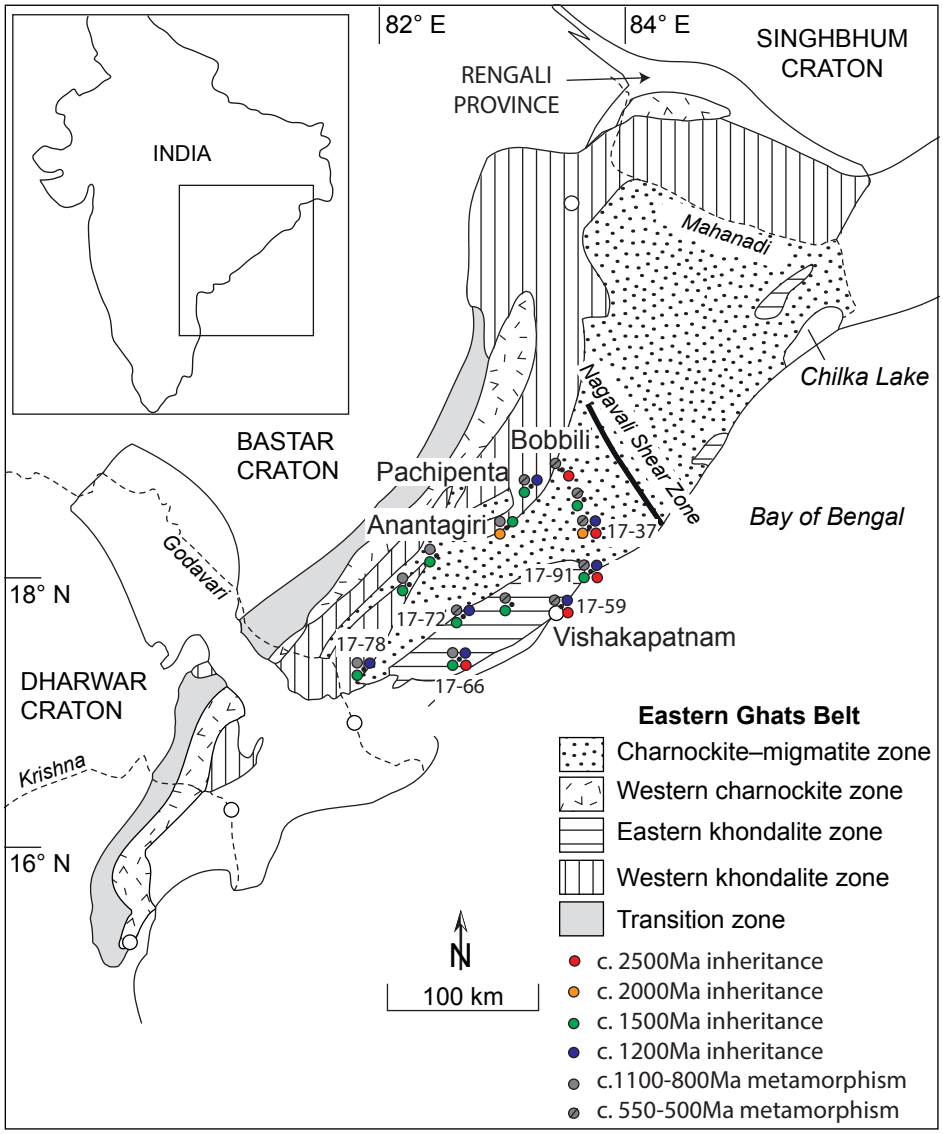

Figure 4.1 | Lithological map of the Eastern Ghats Province, India, map of India is inset. Localities with inherited zircon ages from Korhonen et al. (2013) and Mitchell et al. (2019), as well as the localities for samples 17-37 (18° 11' 25.3" N, 83° 27' 49.5" E), -91 (17° 53' 19.67" N, 83° 26' 59.28" E), -59 (17° 44' 50.20" N, 83° 20' 57.90" E), -72 (17° 38' 33.58" N, 82° 37' 50.27" E), -66 (17° 22' 30.82" N, 82° 32' 41" E) and -78 (17° 20' 15.48" N, 81° 48' 50.35" E).

Rare concordant c.2450–2400 Ma ages from SIMS (SHRIMP) analyses of zircon in metapelitic rocks from Vizianagaram (Mitchell et al., 2019) and Bobbili (Korhonen et al., 2015) provide evidence for Neoarchean inheritance, although the nature of this event is poorly constrained. A gap in the EGP zircon record likely occurs between c. 2400 Ma and c. 2000 Ma, since only a small number of concordant U–Pb analyses of this age have been identified from zircon in metapelitic rocks (Mitchell et al., 2019). A major Mesoproterozoic event adjacent EGP was the intrusion of alkaline complexes that occur along its margins against the Bastar or Singhbhum cratons (Figure

4.1). A zircon U–Pb upper intercept age of 1500 ± 18 Ma (Nanda et al., 2018) from the Koraput alkaline complex marks the oldest preserved igneous age for this event. However, crystallisation ages from other alkaline complexes along the craton margin may be as young as 1350 ± 14 Ma (Hippe et al., 2016). The trace element signatures of zircon formed during this event are mixed, but typically display positive HREE slopes and pronounced positive Ce anomalies (Nanda et al., 2018). This event seems to be ubiquitous, based on analysis of detrital zircon grains in metapelitic rocks across the EGP (Korhonen et al., 2013b). Another discrete event at c. 1200 Ma (Korhonen et al., 2013b) is marked by concordant U–Pb zircon populations in some metapelitic rocks from Pachipenta (Figure 4.1).

Multiple localities within the EGP preserve evidence for ultrahigh temperature (UHT; >900°C) metamorphic conditions (Das et al., 2011; Korhonen et al., 2013a; Korhonen et al., 2013b; Korhonen et al., 2014; Korhonen et al., 2011; Prakash et al., 2015), suggesting that UHT metamorphism was regional in extent. Phase equilibrium studies from various localities constrain peak conditions to >950°C and ~0.8 GPa followed by near-isobaric cooling (Korhonen et al., 2013a; Korhonen et al., 2011). In addition, high Al–Mg granulites at Anantagiri are inferred to record peak metamorphic temperatures >1000°C (Korhonen et al., 2014).

The duration of granulite facies conditions in the EGP has been estimated from U–Pb zircon and monazite geochronology at multiple localities. Korhonen et al. (2013b) report protracted growth of metamorphic zircon throughout the EGP over durations of up to 300 Ma (between c. 1100 and c. 800 Ma). The samples studied by these authors yield discrete clusters of concordant zircon and monazite ages within this broader temporal range, implying melt crystallization above different elevated (H_2O-undersaturated) solidi following some drainage of melt. Near-concordant ages of c. 613 Ma and c. 566 Ma may record new zircon growth or else be related to Pb loss from older zircon due to lower-temperature fluid-mediated processes (Korhonen et al., 2013b). Average cooling rates from the thermal peak are slow, with estimates from ~1°C/Ma (Korhonen et al., 2013a) to 0.13 ± 0.08 °C/Ma (Mitchell et al., 2019).

To investigate the varied metamorphic and detrital record within the EGP, six metasedimentary granulites were collected broadly along an orogen-parallel transect (Figure 4.1), but further from the craton margin

than metasedimentary rocks previously investigated for U–Pb zircon geochronology (Korhonen et al., 2013b).

4.2 | Methods

4.2.1 | Laser ablation split stream analysis

LASS analysis was performed at the GeoHistory Facility in the John de Laeter Centre (JdL), Curtin University, Perth, Australia. Zircon grains from samples 17-37, -59, -66, -72, -78 and -91 were separated using standard methods, mounted and polished in one-inch epoxy round blocks. The location of analytical spots was selected based on cathodoluminescence (CL) images obtained using a TESCAN MIRA3 VP-FESEM scanning electron microscope (SEM) at the Microscopy and Microanalysis Facility in the JdL. Zircon zones with a morphology indicative of inherited components, metamorphic overgrowths and homogeneous 'soccer ball' grains characteristic of anatectic growth (Corfu et al., 2003; Harley et al., 2007; Taylor et al., 2016) were targeted for LASS analyses. After two cleaning pulses, grains were ablated using a RESOlution M-50A-LR, incorporating a Compex 102 excimer laser equipped with a Laurin Technic S155 cell. Analyses used a beam diameter of 22 μm and repetition rate of 10 Hz with a measured laser energy of 2 J cm^{-2} at the sample surface. The sample cell was flushed with ultrahigh purity He (350 mL min-1 and N2 (3.8 mL min^{-1}). Each analysis consisted of 35 s of baseline acquisition followed by 30 s of data acquisition and another 20 s of background counting. Unknowns were bracketed by a suite of standard zircons, with the standard block analysed after every 25 unknown analyses. Isotopic intensities were split to facilitate simultaneous measurement of U–Pb isotope ratios using a Nu Plasma II multicollector ICP–MS, and trace element concentrations using an Agilent 8900 QQQ MS, with high purity Ar as the carrier gas.

U–Pb isotope ratio analysis of zircon rims used the following setup over a 0.8 s integration time (detector in brackets: H or L – Faraday Cup; IC – Ion Counter): ^{238}U (H10), ^{232}Th (H8), ^{208}Pb (IC0), ^{207}Pb (IC1), ^{206}Pb (IC2), ^{204}Pb (IC3), and ^{202}Hg (IC4). The primary reference material used for rims was 91500 zircon (1062.4 ± 0.4 Ma; Wiedenbeck et al., 1995); Plesovice (337.13 ± 0.37 Ma; (Sláma et al., 2008) and GJ-1 (601.7 ± 1.4 Ma; Jackson et al., 2004) zircons were used as secondary age standards. $^{206}Pb/^{238}U$ ages calculated for all zircon age standards, treated as unknowns, are within 2% of the accepted value. U–Pb isotope ratio analysis of zircon cores used the following

setup over a 0.8 s integration time: ^{238}U (H10), ^{208}Pb (L2), ^{207}Pb (L3), ^{206}Pb (L4), ^{204}Pb (IC0), and ^{202}Hg (IC2) and ^{200}Hg (IC3). The primary reference material used for cores was zircon GJ-1 with Plesovice and 91500 zircon used as secondary age standards. $^{206}Pb/^{238}U$ ages calculated for all zircon age standards, treated as unknowns, were found to be within 3% of the accepted value. Time-resolved mass spectra were reduced using the U–Pb_Geochron4 data reduction scheme in Iolite3.5 (Paton et al., 2011) and in-house Microsoft Excel macros.

Analyses of the following trace elements were monitored for 0.01–0.02 s each (^{29}Si , ^{49}Ti, ^{89}Y, ^{90}Zr, ^{91}Zr, ^{93}Nb, ^{139}La, ^{140}Ce, ^{146}Nd, ^{147}Sm, ^{151}Eu, ^{157}Gd, ^{163}Dy, ^{165}Ho, ^{166}Er, ^{169}Tm, ^{175}Lu, ^{178}Hf, ^{204}Pb, ^{206}Pb, ^{207}Pb, ^{208}Pb, ^{232}Th, ^{238}U). The in-house zircon standard PL-1 (fully characterized megacryst of Penglai zircon (Li et al., 2010)) was used as the primary standard to calculate elemental concentrations (using ^{91}Zr as the internal standard element and assuming 43.14% Zr in the unknowns). During the time-resolved analysis, contamination from inclusions and compositional zoning was monitored and only the relevant part of the signal was integrated. The trace element results for NIST 612 (secondary standard), using NIST 610 as the reference material and assuming 33.6% Si, indicate that the accuracy was better than 3% for most elements with the exception of P (5%) and Fe (10%). The analytical precision was <7% for most elements. The time-resolved mass spectra were reduced using the Trace Elements data reduction scheme in Iolite3.5 (Paton et al., 2011).

4.2.3 | Ti-in-zircon thermometry

For Ti-in-zircon thermometry we used the calibration of Ferry and Watson (2007). This calibration requires values for the activity of silica ($aSiO_2$) and titanium oxide ($aTiO_2$). All six samples are quartz-bearing garnet–sillimanite gneisses, in which the activity of silica ($aSiO_2$) was assumed to be unity. However, the analysed rocks do not contain rutile (i.e. $aTiO_2 < 1$). For metamorphic zircon, the $aTiO_2$ during cooling was corrected through calculation of a *P–T* phase diagram based on the whole-rock composition of a representative garnet–sillimanite gneiss, from which aTiO2 was calculated along an isobaric cooling path starting at 1000 °C, 7.6 kbar. The isobaric cooling path is similar to a *P–T* path previously inferred for the EGP (Korhonen et al., 2013a). A polynomial line of best fit was plotted between the Ti-in-zircon concentration required to maintain the $aTiO_2$ at 0.5 and the Ti-in-zircon concentration corresponding to the $aTiO_2$ values in the

reference garnet–sillimanite gneiss at a range of temperatures along the cooling path. This polynomial fit was used to correct the analyzed Ti-in-zircon concentration to a value assuming an $aTiO_2$ of 0.5, as shown in Appendix C.1

4.2.4 | Cluster analysis

Using the trace element compositions of the zircon grains from the six granulites, we developed a procedure to separate zircon into compositionally distinct populations. The resulting petrogenetic groups are based on Eu and Ce anomalies, Y concentrations and intermediate to light REE concentrations

Figure 4.2 | Cluster analysis of 548 zircon analyses using selected trace elements of allows separation between igneous detrital (green), metamorphic (blue) and hydrothermally altered (red) zircon. (a) Ce/Ce* versus Eu/Eu* contour plot; metamorphic zircon is characterized by both low Ce/Ce* and Eu/Eu*, detrital analyses by high Ce*/Ce and hydrothermally altered zircon by high Eu/Eu*. (b) Eu/Eu* versus I-LREE contour plot. Metamorphic analyses are distinguished from igneous and modified analyses by low I-LREE and Eu*/Eu values. Metamorphic zircon is further characterized by a low Lu/Gd ratio which leads to a flatter Heavy Rare Earth Element (HREE) profile than detrital or altered zircon (c).

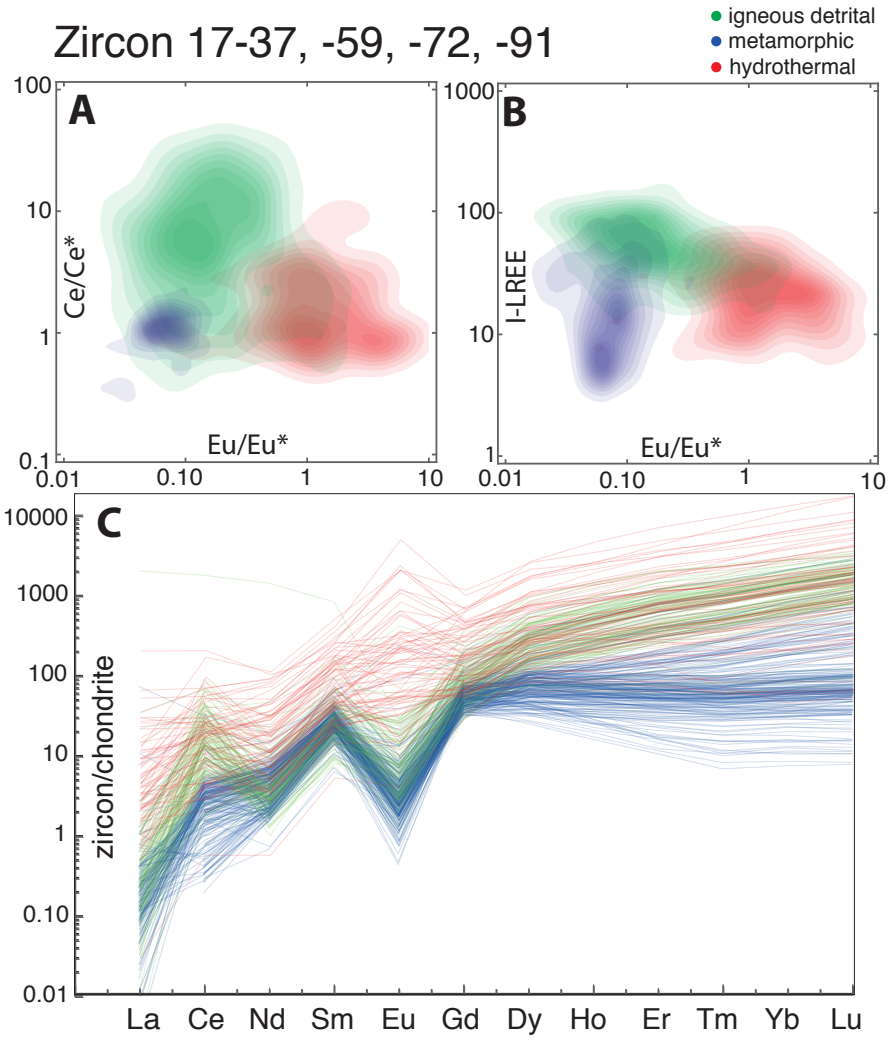

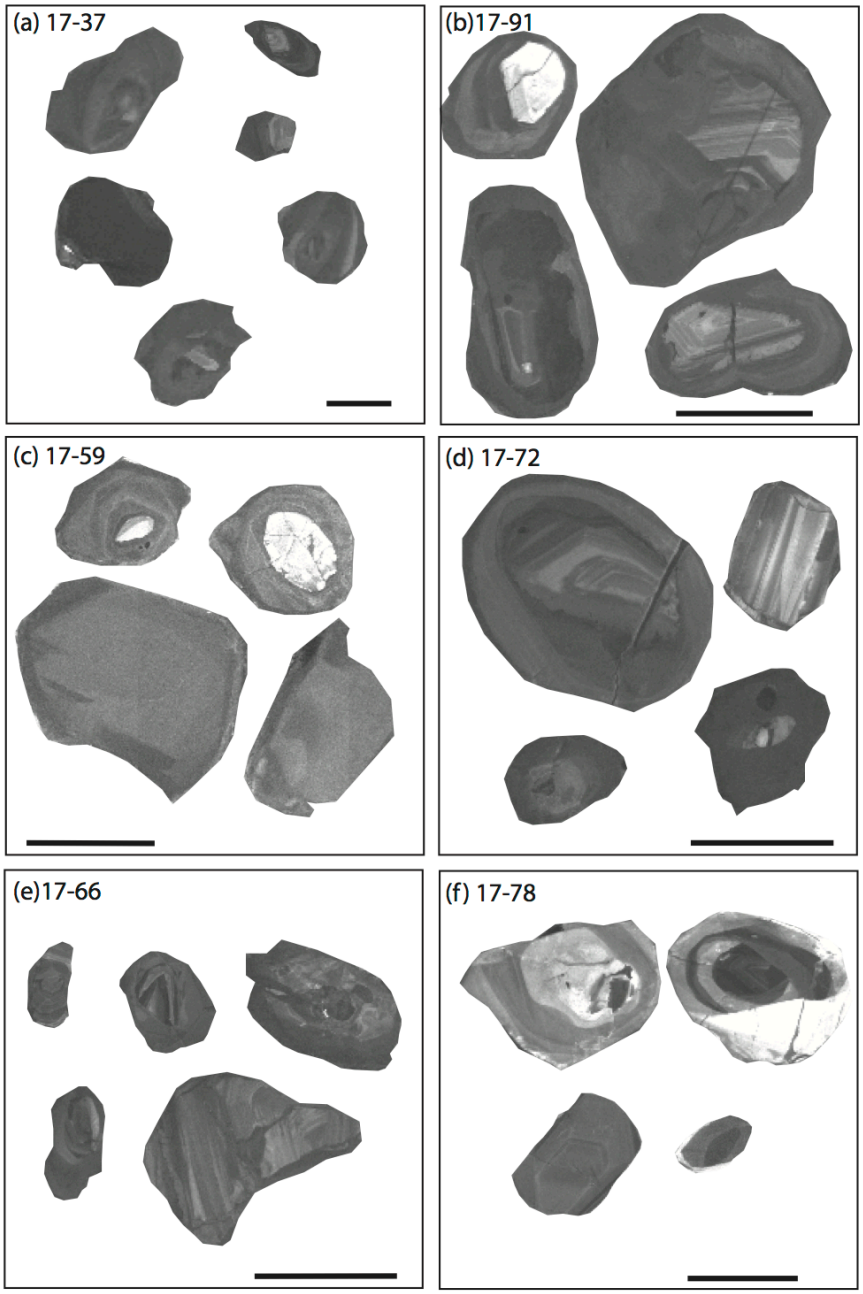

Figure 4.3 | Cathodoluminescence (CL) images of representative zircon grains in samples 17-37 (a), 17-91 (b), 17-59 (c), 17-72 (d), 17-66 (e), 17-78 (f). Scale bars are all 100 μm.

(I-LREE; Bell et al., 2019) using a k-means clustering algorithm (MacQueen, 1967). K-means clustering is a relatively simple unsupervised machine learning algorithm that identifies a number (k) of centroids then allocates every data point to the nearest cluster, while keeping the centroids as small as possible. Eu and Ce anomalies were calculated using the geometric mean of the chondrite-normalized concentrations of their neighboring elements, such that $Eu^* = Eu_N/\sqrt{(Sm_N^2 \bullet Gd_N^2)}$ and $Ce^* = CeN/\sqrt{(La_N^2 \bullet Nd_N^2)}$. Values of I–LREE were calculated as $I\text{-}LREE = Dy_N \bullet 0.254/(Nd_N \bullet 0.467) + Dy_N \bullet 0.254/$

(Sm_N•0.167) using chondrite-normalized concentrations. The k-means clustering was carried out using Wolfra Mathematica 11.0 using the built-in Wolfram "FindClusters" symbol and the "KMeans" method. The script (see Appendix C.2) was built to output the analyses that corresponded to the resulting clusters.

The results of cluster analyses for the granulites, in which the three distinct zircon populations were recognised (samples 17-37, -59, -72, -91), are shown in Figure 4.2. The zircon population characterized by large positive Ce anomalies, negative Eu anomalies and strongly fractionated HREE (YbN/GdN) signatures is interpreted as comprising inherited igneous grains – green in Figure 4.2 (Belousova et al., 2002; Grimes et al., 2015). The population characterized by small positive Ce anomalies, large negative Eu anomalies and a range of moderately positive to negatively sloping HREE patterns is interpreted as granulite facies metamorphic zircon – blue in Figure 4.2 (Taylor et al., 2017; Taylor et al., 2015). The population characterized by high concentrations of light and middle REE, high I-LREE, and small negative to positive Eu anomalies, is interpreted as zircon that was modified by hydrothermal alteration – red in Fig. 2 (Bell et al., 2019; Hoskin, 2005). CL images of representative zircon grains are shown in Figure 4 3. The U–Pb isotope and trace element data, and a summary of Ti-in-zircon temperatures for samples 17-37, -59, -72 and -91 are shown in Figures 4–7. Distinct populations of zircon composition could not be recognised in samples 17-66 and -78 (Figures 8 and 9).

4.3 | Results

Cathodoluminescence (CL) images of all analysed zircon grains are provided in Appendix C.3. The U–Pb and trace element data for all samples is provided in Appendix C.4.

4.3.1 | Sample 17-37

Zircon morphology and textures

Zircon grains in sample 17-37 are small (most <100 μm in diameter) and rounded (Figure 4.3a). Core domains are <20 μm in diameter and show either a low-CL response and convolute zonation or a high-CL response and diffuse sector zoning. Overgrowths and zircon grains lacking inherited cores have diffuse sector zoning and a low-CL response (Figure 4.3a).

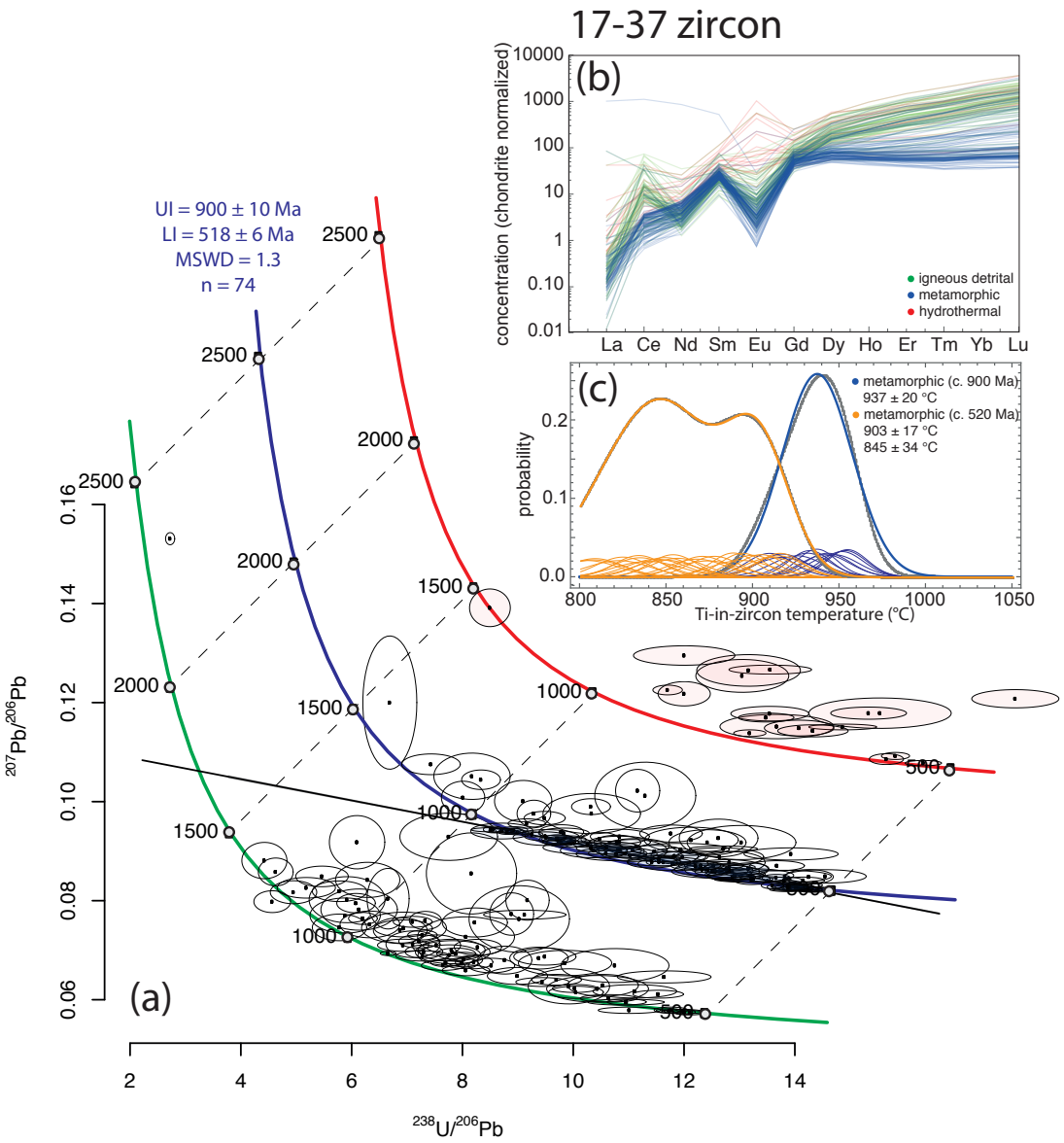

Figure 4.4 | Tera-Wasserburg concordia diagrams (a), chondrite normalized REE concentrations (b) and metamorphic Ti-in-zircon thermometry results (c) for sample 17-37. Igneous detrital/recrystallized zircon is green, metamorphic zircon in blue and hydrothermally altered zircon in red. UI: upper intercept of discord, LI: lower intercept of discord, CA: concordia age. Datapoints used in dicordia and concordia calculations are shaded.

Zircon U–Pb and trace element data

Three zircon grains with igneous REE patterns yield data that overlap Concordia within 2 sigma uncertainty at c. 1230 Ma; in addition, a single discordant zircon is significantly older (Figure 4.4a). Zircon grains with metamorphic trace element compositions are spread along a discord with a lower intercept age of 518 ± 6 Ma (n = 72; MSWD = 1.3). Zircon with a hydrothermal signature is mostly discordant, yielding dates within the

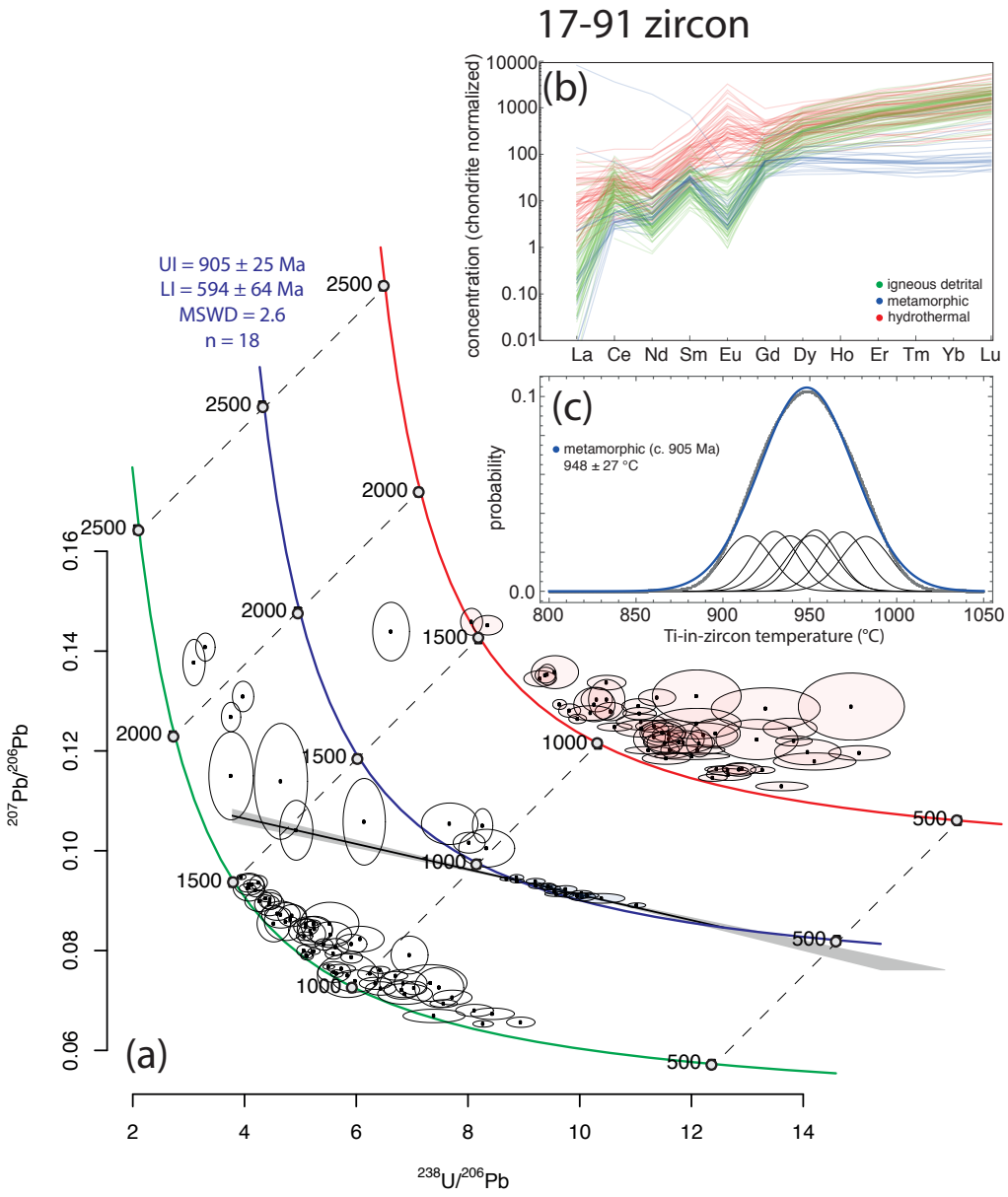

Figure 4.5 | Tera-Wasserburg concordia diagrams (a), chondrite normalized REE concentrations (b) and metamorphic Ti-in-zircon thermometry results (c) for sample 17-91. Igneous detrital/recrystallized zircon is green, metamorphic zircon in blue and hydrothermally altered zircon in red. Zircon analyses used for average age or discordia recessions are shaded. UI: upper intercept of discord, LI: lower intercept of discord, CA: concordia age. Datapoints used in dicordia and concordia calculations are shaded.

range of igneous and metamorphic ages. Activity corrected Ti-in-zircon temperatures retrieved from concordant metamorphic zircon around 900 Ma forms a normal distribution around 937 ± 20 °C (Figure 4.4c). By contrast, temperatures for concordant metamorphic zircon around 520 Ma are more variable and comprise a bimodal distribution with maxima at 903 ± 17 °C and 845 ± 34 °C (Figure 4.4c).

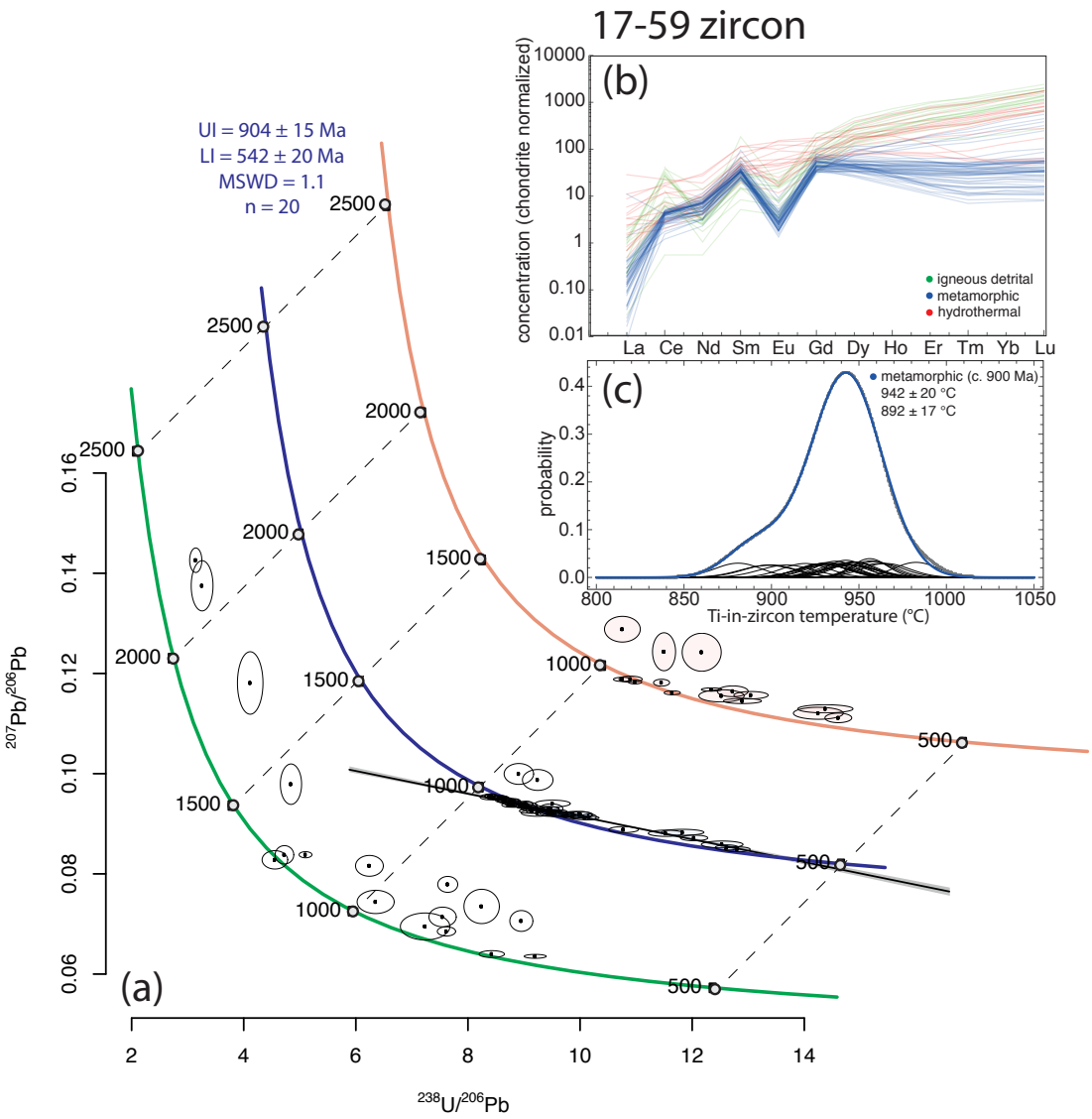

Figure 4.6 | Tera-Wasserburg concordia diagrams (a), chondrite normalized REE concentrations (b) and metamorphic Ti-in-zircon thermometry results (c) for sample 17-59. Igneous detrital/recrystallized zircon is green, metamorphic zircon in blue and hydrothermally altered zircon in red. UI: upper intercept of discord, LI: lower intercept of discord, CA: concordia age. Datapoints used in dicordia and concordia calculations are shaded.

4.3.2 | Sample 17-91

Zircon morphology and textures

Zircon grains from sample 17-91 are rounded and up to ~350 µm across (Figure 4.3b). Several varieties of inherited cores occur: diffuse sector-zoned with a bright-CL response, featureless with a bright CL response, sector-zoned with a moderate to bright-CL response and convolutely zoned with a low to moderate CL response. Inner (primary) metamorphic overgrowths and zircon grains without inherited cores typically have a low to moderate CL response and diffuse sector zonation. Some outer (secondary) overgrowths

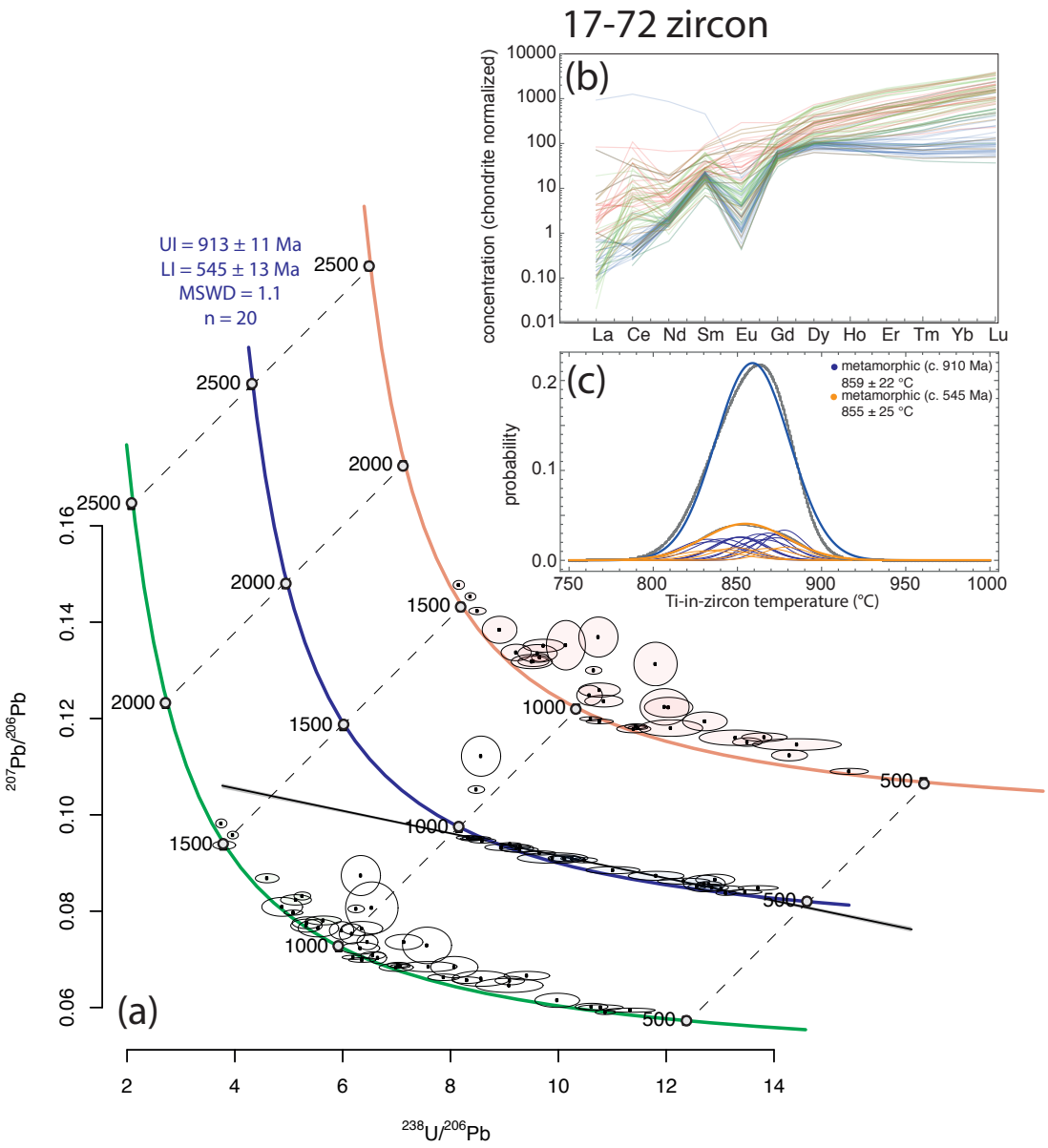

Figure 4.7 | Tera-Wasserburg concordia diagrams (a), chondrite normalized REE concentrations (b) and metamorphic Ti-in-zircon thermometry results (c) for sample 17-72. Igneous detrital/recrystallized zircon is green, metamorphic zircon in blue and hydrothermally altered zircon in red. UI: upper intercept of discord, LI: lower intercept of discord, CA: concordia age. Datapoints used in dicordia and concordia calculations are shaded.

have moderate CL response and preserve sharp sector zoning. Commonly, core and overgrowth domains are cross-cut by linear features with a low CL response.

Zircon U–Pb and trace element data

U–Pb data from zircon with igneous REE characteristics define a series of apparent discordia, with trends from c. 2500 Ma, c. 1500 Ma and c. 1200 Ma

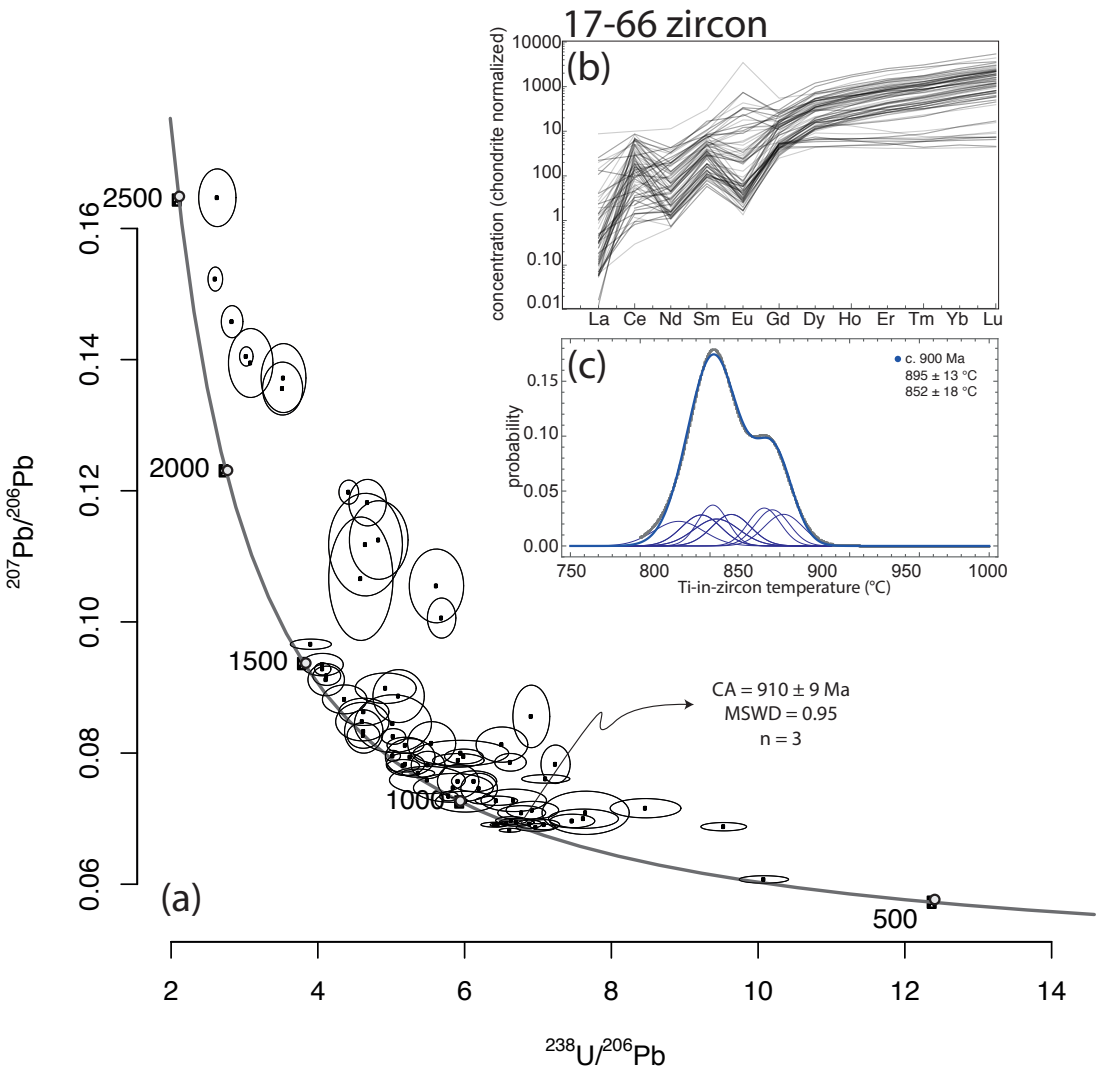

Figure 4.8 | Tera-Wasserburg concordia diagram (a), chondrite normalized REE concentrations (b) and metamorphic Ti-in-zircon thermometry results (c) for sample 17-66. UI: upper intercept of discord, LI: lower intercept of discord, CA: concordia age. Datapoints used in dicordia and concordia calculations are shaded.

(see green Concordia diagram; Figure 4.5a, b). Three near concordant data yield an age of c. 1150 Ma (Figure 4.5a). Dates of zircon with metamorphic REE characteristics define a separate discord with an upper intercept age of 903 ± 25 Ma and a lower intercept age of 594 ± 64 (n = 18; MSWD = 2.4; Figure 4.5a, b). Activity-corrected Ti-in-zircon temperatures for concordant metamorphic zircon with ages of c. 905 Ma define a normal distribution about 948 ± 27 °C (Figure 4.5c).

4.3.3 | Sample 17-59

Zircon morphology and textures

In sample 17-59, zircon grains are mostly <100 µm across and rounded (Figure 4.3c). Inherited cores have a bright CL response and are unzoned.

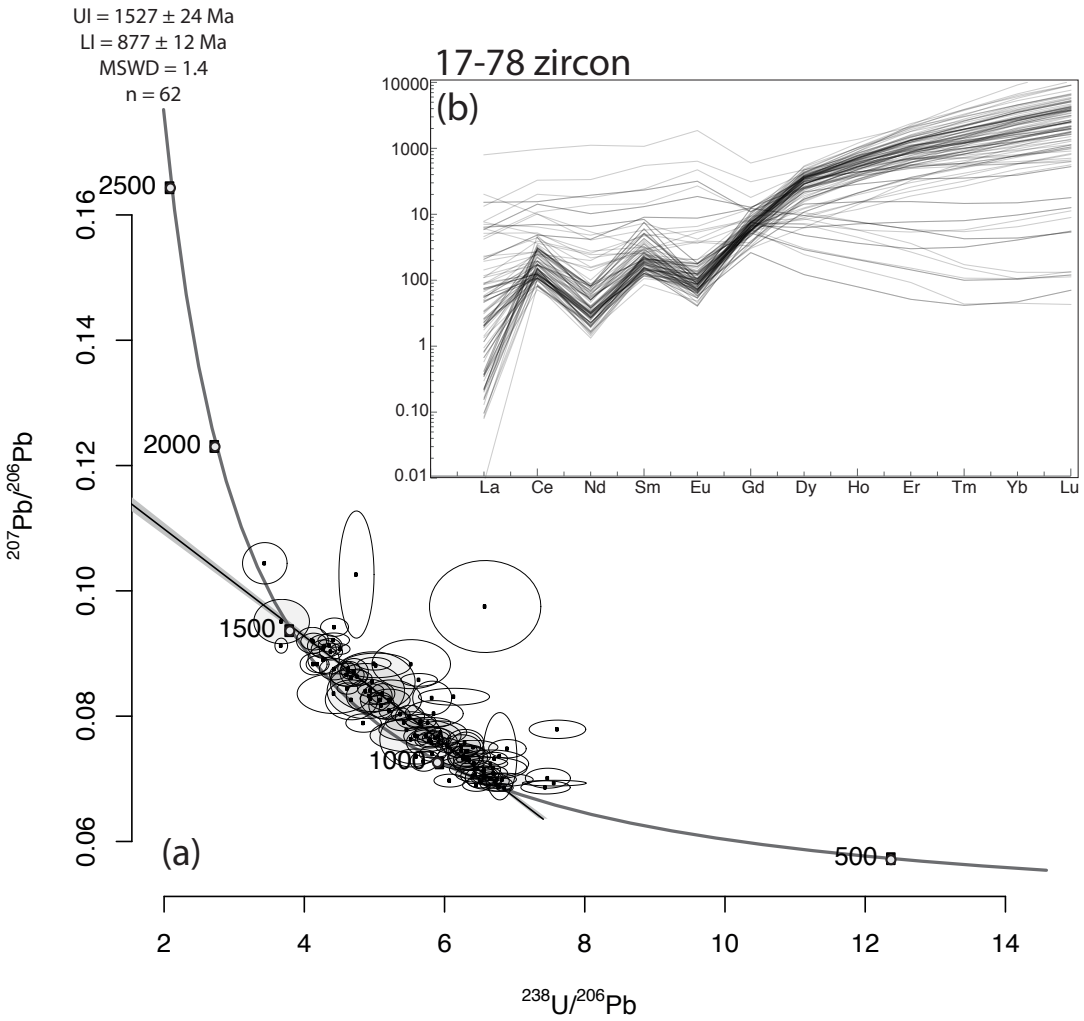

Figure 4.9 | Tera-Wasserburg concordia diagram (a), chondrite normalized REE concentrations (b) for sample 17-78. UI: upper intercept of discord, LI: lower intercept of discord, CA: concordia age. Datapoints used in dicordia and concordia calculations are shaded.

Overgrowths show a low to moderate CL response and diffuse sector zoning. Most commonly, zircon grains lack inherited cores and show diffuse sector zoning or have a 'soccer ball' morphology with a low to moderate CL response (Corfu et al., 2003; Harley et al., 2007; Taylor et al., 2016).

Zircon U–Pb and trace element data

Two zircon grains with igneous REE characteristics plot within error of Concordia at c. 1260 Ma. Older data may define a discordant trend with an upper intercept between c. 2600 Ma and c. 2450 Ma. Metamorphic zircon yields a spread of data along Concordia from c. 950 to 900 Ma. In addition, the data define a discord with intercept ages of 904 ± 15 to 542 ± 20 (n = 20; MSWD = 1.1). Activity-corrected Ti-in-zircon temperatures from concordant analyses at c. 900 Ma yield a bimodal distribution with peaks at 942 ± 20 °C and 892 ± 17 °C (Figure 4.6c).

4.3.4 | Sample 17-72

Zircon morphology and textures

Zircon grains are <200 μm across and rounded (Figure 4.3d). Cores of zircon typically have a moderate CL response and are either sector- or oscillatory-zoned. Cores are overgrown by CL-dark, diffuse sector-zoned domains, a morphology shared by grains that do not contain inherited cores or rarely by grains with a high CL response. Thin rims ~10 μm wide are unzoned and have a moderate CL response.

Zircon U–Pb and trace element data

Zircon with igneous REE characteristics yields one near-concordant datum at c. 1500 Ma and another cluster of data at c. 1200 Ma (Figure 4.7a, b). Two data may lie on a discordia trend with an upper intercept older than c. 1500 Ma. Metamorphic zircon follows a Pb-loss trend with an upper intercept at 913 ± 11 Ma and a lower intercept at 545 ± 13 Ma (n = 20; MSWD = 1.1). Activity-corrected Ti-in-zircon temperatures from concordant metamorphic zircon with ages of c. 900 Ma define a normal distribution about 859 ± 22 °C, while those with ages of c. 545 Ma define a normal distribution about 855 ± 25 °C (Figure 4.7c).

4.3.5 | Sample 17-66

Zircon morphology and textures

Zircon grains are 50–300 μm across and rounded (Figure 4.3e). The cores of zircon preserve either diffuse sector zones with a high CL response or sharp oscillatory zones with a moderate CL response or have convoluted zoning patterns and a low CL response. Otherwise, zircon grains tend to have dark to moderate CL response with diffuse sector zones, features shared with overgrowths of core domains, and/or a ‘soccer ball’ morphology.

Zircon U–Pb and trace element data

Cluster analysis based on REE compositions failed to identify distinct groups in this sample. Zircon shows a wide variation in REE contents, Ce anomalies are positive but variable in magnitude, and Eu anomalies are both negative and positive. HREE slopes are either flat or, more commonly, have a steep positive slope (Figure 4.8b). The U–Pb data fall into distinct groups. Some of the data form a discord with an upper intercept of c. 2400 Ma, and two discordant data have older $^{207}Pb/^{206}Pb$ dates, likely reflecting inheritance that is older than c. 2500 Ma (Figure 4.8a). Between c. 1500 Ma and c. 1000

Ma, a significant cluster of data plot within uncertainty of Concordia around c. 1200 Ma. Three grains define a Concordia intercept age of 910 ± 9 Ma (n = 3; MSWD = 0.95). Activity-corrected Ti-in-zircon temperatures from concordant metamorphic zircon with ages of c. 910 Ma define a bimodal distribution, with a higher probability peak at 852 ± 18 °C and a lower probability peak at 895 ± 13 °C.

4.3.6 | Sample 17-78

Zircon morphology and textures

Zircon grains are typically 50–200 μm across, rounded and anhedral (Figure 4.3f), and exhibit a variety of CL responses. Cores with a dark CL response commonly show sharp sector zoning, although grains showing moderate CL response with more diffuse sector zoning are also common. Rarely, dark CL cores preserve convoluted zoning patterns. Overgrowth rims 10–20 μm wide with high CL response are common, many of which preserve sharp sector zoning.

Zircon U–Pb and trace element data

Cluster analysis based on REE compositions failed to identify distinct groups in this sample. Nevertheless, distinct REE patterns are recognised, including zircon with elevated LREE concentrations, and others with small negative Ce and Eu anomalies. Additionally, some zircon shows variable HREE concentrations with both shallow and steep slopes (Figure 4.9b). A subset of the data define a discordia trend with an upper intercept age of 1527 ± 24 Ma and a lower intercept age of 877 ± 12 Ma (n = 62; MSWD = 1.4). Compared to the other samples, the absence of younger dates as evidence of the c. 550–500 Ma metamorphic event in this sample is striking. This suggests the regression to find the detrital age of 1527 ± 24 Ma may be robust.

4.4 | Discussion

4.4.1 | Clustering algorithms applied to zircon trace element compositions

An inherent limitation in cluster analysis is a requirement to define the number of clusters. Bias may be introduced, as the primary interpretation of the compositional data determines the number (k) of centroids that are used for clustering. Furthermore, it is unlikely that k-means clustering alone is sufficient to describe the full variation in composition within the dataset or to fully differentiate between populations. As exemplified by samples 17-66

and -78, the trace element composition of zircon can present as a more-or-less continuous array of several parameters otherwise used for clustering, such as I–LREE, and Eu and Ce anomlies (as can be observed on REE plots; Figures 8b, 9b), for which the k-means algorithm does not return geologically meaningful clusters (Appendix C.2).

Nevertheless, for four of the six granulite samples, each with a varied and complex zircon dataset, the k-means clustering algorithm successfully grouped the zircon data geologically meaningful populations (Figure 4.2). In turn, this allowed us to target specific zircon data for interpretation in terms of their detrital or metamorphic history.

4.4.2 | Detrital ages and trace element patterns

For detrital grains, we applied a 10% discordance threshold to eliminate potential interference due to loss of radiogenic Pb or due to analyses that mixed older with younger zircon. Despite exceeding the 10% discordance threshold, there is evidence for a late Neoarchean (> 2300 Ma) detrital component in samples 17-37, -59, -66 and -91, as discussed above, but not in the most south-westerly samples (17-72 and 17-78). For five of the six samples (excluding sample 19-78), zircon records evidence for more than one high temperature metamorphic event. Accordingly, the $^{207}Pb/^{206}Pb$ ages of igneous zircon grains are likely to provide the best representation of detrital age populations derived from Proterozoic sources (Nemchin and Cawood, 2005). For Proterozoic detrital zircon grains characterised by an igneous trace element composition and <10% discordance, to define statistically

Figure 4.10 | Kernal density estimates (KDEs; green) and probability density functions (PDFs; black) for zircon with an igneous detrital signature from samples 17-37 (a), -91(b), -59 (c), and -72 (d) calculated using DensityPlotter (Vermeesch, 2012) . A concordance threshold of 10% has been applied to all four samples.

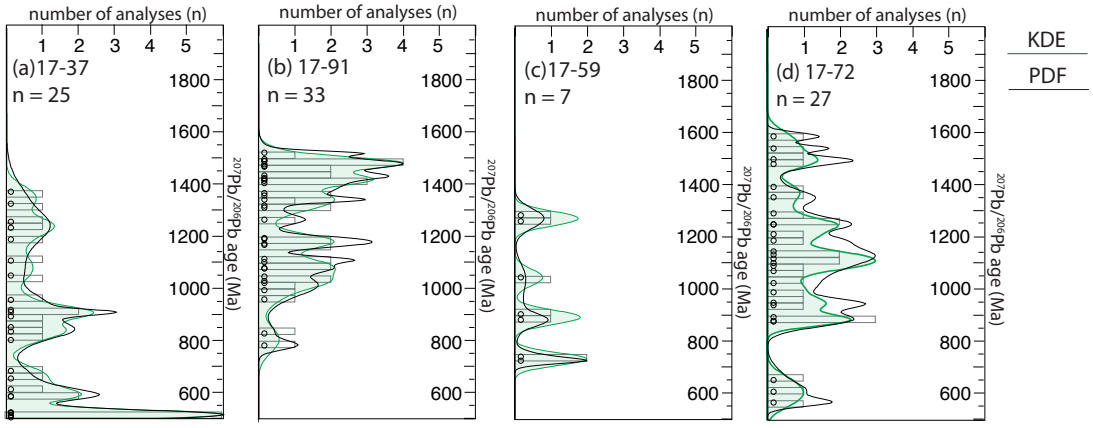

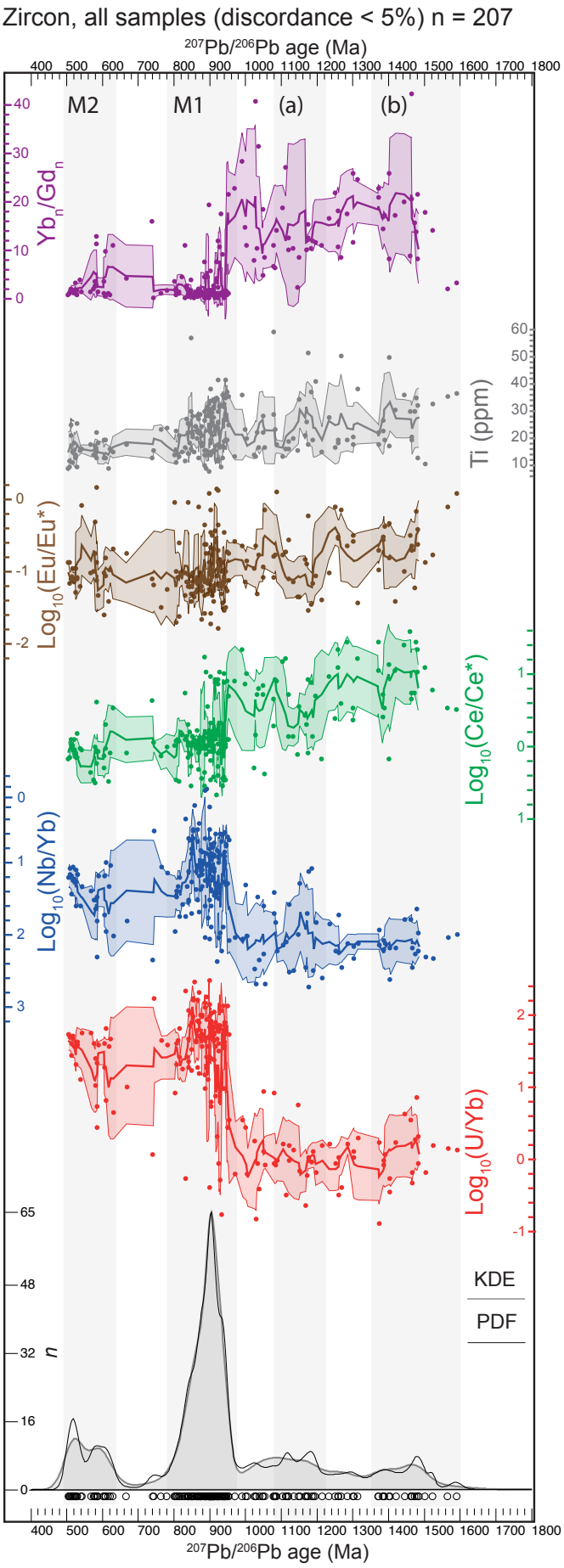
Zircon, all samples (discordance < 5%) n = 207
207Pb/206Pb age (Ma)
400 500 600 700 800 900 1000 1100 1200 1300 1400 1500 1600 1700 1800
M2
M1
(a)
(b)
Yb$_n$/Gd$_n$
Ti (ppm)
Log$_{10}$(Eu/Eu*)
Log$_{10}$(Ce/Ce*)
Log$_{10}$(Nb/Yb)
Log$_{10}$(U/Yb)
KDE
PDF
n

Figure 4.11 | Time resolved concordant (< 5% discordance) zircon data from all samples. A Kernal density Estimate (KDE) and Probability Density Function (PDF) for $^{207}Pb/^{206}Pb$ age is shown for reference. For all moving average time series, the coloured envelope is is 1σ; Red – $\log_{10}(U/Yb)$, Blue – $\log_{10}(Nb/Yb)$, Green– $\log_{10}(Ce/Ce^*)$, Brown – $\log_{10}(Eu/Eu^*)$, Grey – Ti (ppm), Pink – Yb_N/Gd_N. Age envelopes for further analysis are chosen based on KDE minima: (a) c. 1220–1080 Ma, (b) c. 1350–1600 Ma.

robust populations of ages we calculated kernel density estimates (KDEs) and probability density functions (PDFs) of $^{207}Pb/^{206}Pb$ ages from samples 17-37, -59, -72 and -91 (Fig. 10; (Vermeesch, 2012)).

Using a combination of the KDEs and PDFs, Mesoproterozoic detrital igneous zircon defines two broad groups of data—early and late Mesoproterozoic—with distinct but smaller populations of data within each group (Fig. 10). Within the early Mesoproterozoic group (1600–1350 Ma), zircon with an age around 1500 Ma is present in samples 17-66, -72, -78 and -91, but not in the two samples from the north-east (17-37 and -59). The KDEs for both samples 17-91 and -72 show peaks at c. 1500 Ma, and sample 17-72 has two older dates between c.1500 and c.1600 Ma. Furthermore, zircon in sample 17-78 defines a discordant trend that yields a regression age of 1527 ± 24 (Figure 4.9a). Within the late Mesoproterozoic group (<1350 Ma; Fig. 10), zircon in samples 17-91 and -59 defines peaks between 1300 and 1250 Ma, whereas zircon in samples 17-37 and -72 defines peaks at c. 1250 Ma. Two samples have peaks at c. 1100 Ma (17-72 and -91).

The zircon separated from the six granulites records detrital ages that are older than the recrystallized or new metamorphic zircon. To evaluate how the trace element composition of the detrital zircon relates to the wide range of primary crystallisation ages, we calculated a probability density function (PDF) of age for all samples using a 5% concordance filter. The PDF has probability peaks at c. 1480 Ma, c. 1250–1200 Ma and c. 1120 Ma (Figure 4.11), similar to the age distributions observed in samples 17-37, -59, -72 and -91. Then we calculated moving averages of Ti and various elemental ratios (Yb_N/Gd_N, Eu/Eu*, Ce/Ce*, Nb/Yb and U/Yb) from the time series of data from concordant zircon in all samples show the temporal variation of these parameters in zircon (Figure 4.11).

Early Mesoproterozoic zircon (1600–1350 Ma has elevated U/Yb and YbN/GdN ratios, and elevated Ce/Ce* and Ti concentrations compared with the late Mesoproterozoic zircon (Figure 4.11b). By contrast, within the latter

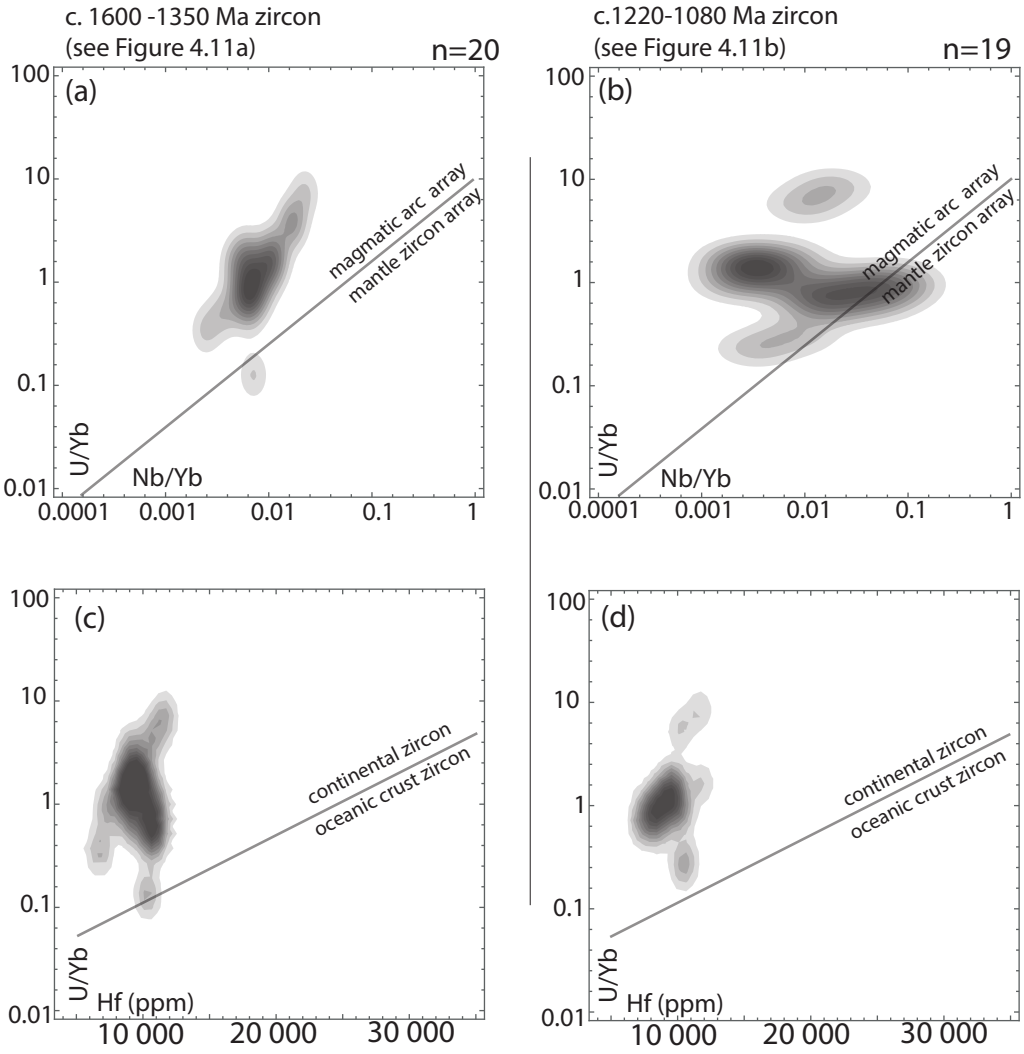

Figure 4.12 | Discrimination plots of Grimes et al. (2012), with the line dividing the magmatic arc and mantle zircon arrays. Concordant data from all samples. (a, b) U/Yb vs Nb/Yb plots, (c, d) U/Yb vs Hf concentration.

group, zircon between c. 1220 and c. 1080 Ma has elevated Nb/Yb ratios and Ti concentrations, but Ce/Ce* and Eu/Eu* both show pronounced minima between c. 1200 and c. 1120 Ma (Figure 4.11a).

Information about the composition and tectonic setting of the igneous sources of the detrital zircons may be inferred from their trace element signatures (Belousova et al., 2002; Grimes et al., 2015; Grimes et al., 2007). For large global datasets, discrimination plots based on U/Yb and Nb/Yb ratios, and Hf concentrations have been used to discriminate between zircons crystallised from magmas derived from mantle and/or crustal sources, and to provide constraints on the possible tectonic settings of these magmas (Grimes et al., 2015; Grimes et al., 2007). Accordingly, we calculated two-dimensional

KDE distributions for U/Yb and Nb/Yb ratios, and Hf concentrations in both early and late Mesoproterozoic groups of zircon.

For zircon in the age range c. 1600–1350 Ma, the overlapping two-dimensional KDE distributions in the U/Yb vs Nb/Yb plot (Figure 4.12a) lie along an array similar to zircons that define the continental arc array (Grimes et al., 2015). In the U/Yb vs Hf plot (Figure 4.12c), the overlapping two-dimensional KDE distributions of the early Mesoproterozoic zircons define a steep trend above the oceanic crust array, which is inconsistent with the trend for fractional crystallization (Grimes et al., 2015). This zircon likely crystallised from a magma that had either an enriched mantle source or a MORB source mixed with some crustal input. A plausible tectonic setting is an arc.

Similar to the early Mesoproterozoic zircon data, for zircon in the age range c. 1220–1080 Ma the overlapping two-dimensional KDE distributions of U/Yb vs Nb/Yb define a field that overlaps the magmatic arc array, but in this case the field shows an enrichment trend in Nb that extends into the ocean-island (OI) sector of the mantle array (Figure 4.12b). Although similar to zircon crystallized in continental arc systems, the wider range of Nb/Yb ratios may suggest rifting, perhaps related to a mantle plume (Grimes et al., 2015). In addition, in the U/Yb vs Hf plot (Figure 4.12d), the two-dimensional KDE distributions define a steep trend above the mantle array and do not follow a fractional crystallization trend (Grimes et al., 2015). Thus, this zircon more likely crystallised from a magma that had an enriched mantle source, or possibly a MORB source mixed with some crustal input. A plausible tectonic setting is a rifted continental arc.

In summary, early Mesoproterozoic zircon has elevated Yb_N/Gd_N ratios, indicating that it did not grow in equilibrium with garnet, while the elevated Eu and Ce anomalies suggest the magmas were relatively oxidised (Trail et al., 2012). These features are consistent with an arc setting. By contrast, late Mesoproterozoic zircon has depressed Ce and Eu anomalies, consistent with crystallisation from a reduced magma. These zircons have a wide range of Nb/Yb ratios that extend to high values; elevated Nb concentrations are a feature of within-plate felsic igneous rocks and alkaline magmas in general (Grimes et al., 2015; Grimes et al., 2007). Coupled with the high Ti concentrations, the data indicate that zircon likely crystallised from a high-temperature alkaline magma, possibly related to rifting of a continental arc.

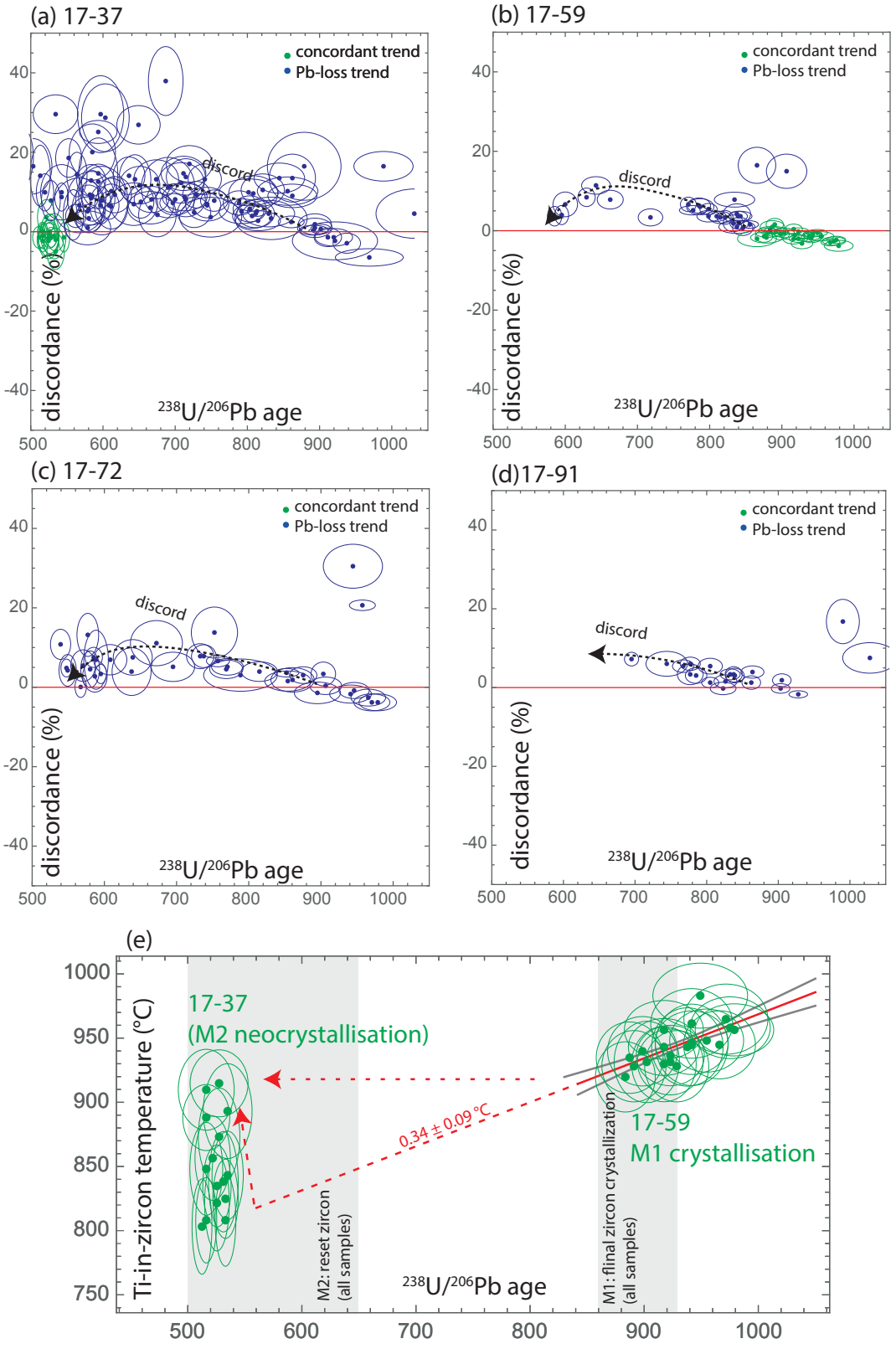
(a) 17-37
concordant trend
Pb-loss trend
discord
discordance (%)
$^{238}U/^{206}Pb$ age
(b) 17-59
concordant trend
Pb-loss trend
discord
discordance (%)
$^{238}U/^{206}Pb$ age
(c) 17-72
concordant trend
Pb-loss trend
discord
discordance (%)
$^{238}U/^{206}Pb$ age
(d)17-91
concordant trend
Pb-loss trend
discord
discordance (%)
$^{238}U/^{206}Pb$ age
(e)
Ti-in-zircon temperature (°C)
17-37
(M2 neocrystallisation)
0.34 ± 0.09 °C
17-59
M1 crystallisation
M2: reset zircon
(all samples)
M1: flinal zircon crystallization
(all samples)
$^{238}U/^{206}Pb$ age

Figure 4.13 | Discordance vs age plots (a-d) and Ti-in-zircon vs $^{238}U/^{206}Pb$ age plot (e) for metamorphic zircon in 17-37, -59, -72 and -91. Data which trend along concordia (discordance = 0) are coloured green and those which are discordant, following a Pb-loss trend are coloured blue for all samples. The Ti-in- zircon vs $^{238}U/^{206}Pb$ age plot (e) shows only the data from 17-37 and 17-59 that trend along concordia with age. Note the positive correlation between age and Ti-in-zircon temperature for M1 (an average cooling rate of 0.34 ± 0.09 °C/Ma), and that the temperature recorded for M2 exceeds that of the extrapolated cooling trend.

4.4.3 | Metamorphic ages and conditions

Excluding the southernmost samples 17-66 and 17-78, the other four granulites show evidence for two metamorphic events; M1 at around 900 Ma and M2 with ages between c. 600 and c. 500 Ma. In samples 17-37, -59, -72, -91, metamorphic zircon is identified to have shallow Yb_N/Gd_N slopes, small positive Ce*/Ce and large negative Eu*/Eu (Figure 4.2c). For these four samples, there is no correlation between α-dose events and age (Appendix C.5), and the majority fulfil the crystalline 'stage 1' criteria of Murakami et al. (1991). This suggests that any Pb loss was not facilitated by radiation damage to the zircon crystal lattice.

In this study, U–Pb data for metamorphic zircon (Figure 4.13a–d) either spread along Concordia (i.e. trend along discordance = 0) over a given timespan (Figure 4.13a, b) or define discordant arrays (i.e. an ancient radiogenic Pb loss trend). Data that spread along Concordia are interpreted as primary (re)crystallised zircon. However, data that define discordant arrays plot as arcs on age vs. discordance plots (Figure 4.13a–d), which we interpret as Pb loss from zircon crystallised during M1 triggered by M2. M1 ages are the youngest in the northernmost (sample 17-37, 900 ± 10 Ma) and southernmost (sample 17-78, 877 ± 12 Ma) granulites. Sample 17-59 is the only granulite to preserve clear evidence for protracted crystallisation of primary metamorphic zircon, between c. 990 and c. 880 Ma (Figure 4.13b). Regression ages for M2 range from 518 ± 6 Ma in sample 17-37 to 594 ± 64 Ma in sample 17-91.

For datasets with a Pb-loss trend, concordant zircon with M1 ages defines a normal distribution of Ti-in-zircon temperatures either around 937 ± 20 °C (sample 17-37) and 948 ± 27 °C (sample 17-91) or around 859 ± 22 °C (sample 17-72) and 852 ± 18 °C (sample 17-66). For primary metamorphic zircon that spreads along Concordia, it is possible to directly relate age and Ti-in-

zircon temperature (M1 in sample 17-59 and M2 in sample 17-37; Figure 4.13e). The data from sample 17-59 are consistent with a mean cooling rate of 0.34 ± 0.09 °C from c. 990 Ma until c. 890 Ma (Figure 4.13e). For samples 17-72 and 17-66, both located in the southwest of the EGB, the Ti-in-zircon temperatures for M1 are ~90 °C lower than in the other samples located to the northeast. This suggests either that these granulites were less residual (i.e. the solidii for these rocks were not as elevated) and/or they experienced lower peak metamorphic temperatures. This spatial disparity is also evident in the geochronology, with slightly older ages for M1 in the southwest (c. 910 Ma) than the northeast (c. 900 Ma).

Crystallisation temperatures for M2, as recorded in sample 17-37, range from ~920 °C to ~800 °C between c. 530 and c. 510 Ma. In addition, concordant data points for M2 in sample 17-72 have Ti-in-zircon temperatures that produce a normal distribution around 855 ± 25 °C.

4.4.4 | Tectonic implications for the Eastern Ghats Province

Neoarchean to Proterozoic detrital record in the EGP

Neoarchean to early Paleoproterozoic detrital zircon ages (>2300 Ma) have previously only been reported in samples from Vizianagaram (Mitchell et al., 2019). There are several potential sources for these inherited zircon grains. Detrital zircons with inherited ages >2500 Ma could have originated from any of the cratons surrounding the EGP, with the possible source materials including granitoids from the Bastar Craton (Bhattacharya et al., 2016) or the Lambert Terrane (Mikhalsky et al., 2006; Phillips et al., 2006), and granulites from the Vestfold Hills terrane (Clark et al., 2012) or the Napier Complex (Carson et al., 2002; Clark et al., 2018; Horie et al., 2012; Kelly and Harley, 2005). The Bastar Craton (Figure 4.1), adjacent to the EGP on the west, has abundant Neoarchean and Paleoproterozoic components, some of which could match the discordia trends shown in samples 17-59 and 17-66. In the north, in the Rengali Province (Figure 4.1), gneisses and granitoids yield zircon U–Pb ages spanning the range 1989 ± 34 Ma to 2840 ± 16 Ma, including events at 2377 ± 18 Ma and 2560 ± 10 Ma (Bhattacharya et al., 2016). These zircons have steep positive HREE slopes, suggesting they did not crystallise in equilibrium with garnet, consistent with an interpretation that the gneisses and granitoids represent a reworked slice of the Bastar Craton (Bhattacharya et al., 2016). Archean zircon in samples 17-59 and 17-66 also has steep positive HREE slopes, consistent with the Bastar craton and/or the gneisses and granitoids in the Rengali Province as the most likely

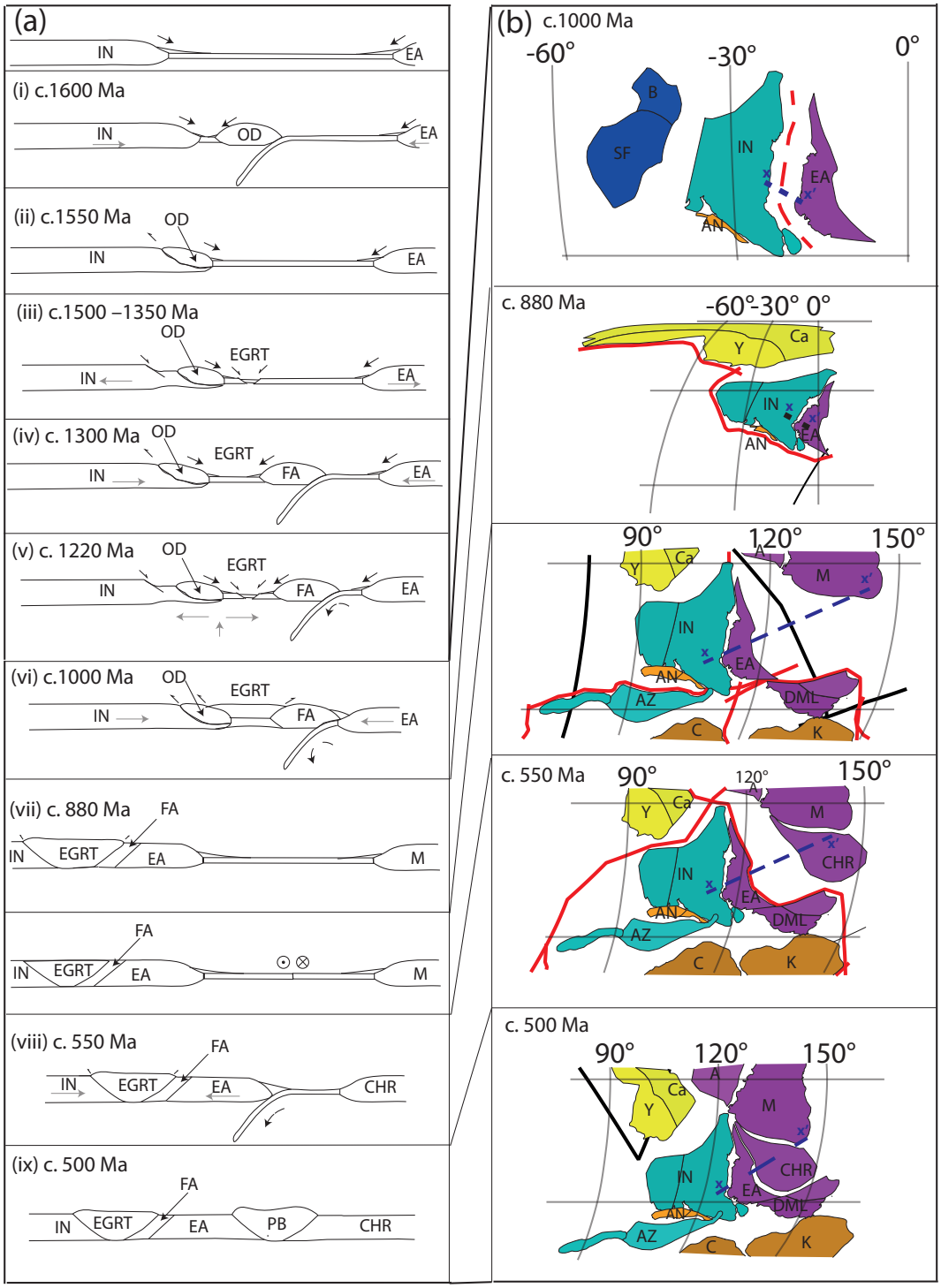
(a)
IN
EA
(i) c.1600 Ma
OD
(ii) c.1550 Ma
(iii) c.1500 –1350 Ma
EGRT
(iv) c. 1300 Ma
FA
(v) c. 1220 Ma
(vi) c.1000 Ma
(vii) c. 880 Ma
M
(viii) c. 550 Ma
CHR
(ix) c. 500 Ma
PB
(b) c.1000 Ma
-60°
-30°
0°
B
SF
AN
c. 880 Ma
Y
Ca
90°
120°
150°
A
AZ
C
K
c. 550 Ma
DML
c. 500 Ma
constructive/transform plate boundary
destructive plate boundary

Figure 4.14 | Cross section sketches (a) depicting the evolution of the Eastern Ghats/Rayner depoocentre from before c. 1500 Ma to c. 1000 Ma, then the tectonic environmnent for M1 (c.1000-900 Ma) and M2 (c. 550-500 Ma) metamorphic events [after Mitchell et al. (2018)]. For a detailed tectonic interpretation, see text. The black arrows signify sedimentary sources for the Eastern Ghats Province depocenter. (b) The Merdith et al. (2017) plate reconstructions in the Robinson projection, drawn using GPlates (Williams et al., 2012). Red boundaries – destructive plate boundaries, bold black boundaries – transform and constructive plate boundaries. Abbreviations: A – South Australian Craton, AN – Antongil Block, AZ – Azania, B – Borborema Craton, BC – Bastar Craton, C – Congo Craton, Ca – South China Craton, CHR – Crohn Craton, DML – Dronning Maud Land, EA – East Antarctic cratons, EGP – Eastern Ghats Province, EGRT – Eastern Ghats Rayner Terrane, FA – Fisher Arc, K – Kalahari Craton, IN – Indian cratons, M – Mawson Block, NC – Napier Complex, OGS – Oygarden Group/Stilwell Hills, PB – Prydz Belt, SF – San Francisco Craton, Y – Yilgarn Craton.

source terranes.

An early Mesoproterozoic group of concordant detrital zircons is present in samples 17-91, 17-72, 17-66 and 17-78, with a prominent population peak at c. 1500 Ma. Although some detrital input may have originated from charnockites and granites in the Ongole Domain (Figure 4.14a(i)) to the southwest, most of the arc-related igneous protoliths there are of late Paleoproterozoic age (Dharma Rao et al., 2012; Henderson et al., 2014; Kovach et al., 2001; Sarkar et al., 2015; Upadhyay et al., 2009). Early Mesoproterozoic felsic magmatic rocks are exposed in Enderby Land, in the Oygarden Islands, along the Mawson coast and in the Northern Prince Charles Mountains in East Antarctica (Halpin et al., 2005), which is a likely source terrane. Furthermore, charnockite along the Mawson coast and in the Northern Prince Charles Mountains have calc-alkaline geochemical signatures that are consistent with early Mesoproterozoic crustal growth along an active convergent plate margin (Young and Ellis, 1991; Zhao et al., 1997). Consistent with the hypothesis of a source terrane in East Antarctica, based on trace element discrimination diagrams for zircon, the early Mesoproterozoic group of concordant detrital zircons in the EGB is inferred to be derived from an arc environment, as discussed above.

Close to the cratonic margin of the EGP there are several alkaline complexes that are Mesoproterozoic in age, and although dating these complexes has proved to be contentious (Hippe et al., 2016; Nanda et al., 2018), most appear to be of mid Mesoproterozoic age (c. 1500–1350 Ma; Figure 4.14a(iii)). These complexes could have been the source of the c. 1350 Ma population peaks in samples 17-91 and 17-72 (Figure 4.10). Varied late Mesoproterozoic

arc-related mafic and felsic metavolcanics and I- and S-type granites in the Fisher Massif in the Northern Prince Charles Mountains (Kinny et al., 1997; Mikhalsky et al., 1996) indicate that arc formation began at c. 1300 Ma (Figure 4.14a(iv)). However, the late Mesoproterozoic group of concordant detrital zircons is present in samples 17-37, 17-91, 17-59 and 17-72, have prominent population peaks at c. 1250-1200 and c. 1100 Ma, and their U/Yb, Nb/Yb and Hf signatures are consistent with an extensional continental environment with mantle input. The 1250-1100 Ma age range may identify the onset of rifting between East Antarctica and cratonic India, providing an extensional environment for the sedimentary protoliths of the Eastern Ghats–Rayner Terrane (Figure 4.14a(v)), and is also consistent with younger alkaline complexes (Hippe et al., 2016). Basin inversion was consequent upon collision of the Rucker Terrane with the Fisher Arc and subsequent convergence of East Antarctica with cratonic India. Thickening associated with basin inversion initiated the first metamorphic event (M1) in the EGP (Figure 4.14a(vi and vii)).

Neoproterozoic to Cambrian metamorphism in the EGP

Ti-in-zircon temperatures for concordant zircons of M1 age either have distributions around ~940 °C (samples 17-37, -91 and -59) or ~850 °C (samples 17-72 and -66). However, it is possible that the Ti-in-zircon temperatures do not record peak thermal conditions, but conditions at which zircon crystallized near the solidus (Korhonen et al., 2014). The bulk-rock composition of these metapelites may be such that the residuum solidus occurs at a lower temperature, and the lower Ti-in-zircon temperatures merely record this feature and have no tectonic significance. Linear regression of Ti-in-zircon temperatures and $^{238}U/^{206}Pb$ ages in 17-59 gives an average cooling rate of 0.34 ± 0.09 °C/Ma. However, it is unclear if this cooling rate was sustained past the limit of zircon crystallisation in this sample.

The timing of M2 is constrained by regression along discords which signify Pb loss between M1 and M2 metamorphic events. M2 ages range from c. 600 to c. 515 Ma, the youngest age, 518 ± 6 Ma, coming from the northernmost sample 17-37. Ti-in-zircon temperatures range from ~920 °C to ~840 °C.

Sustaining >900 °C in the Earth's crust for 100 Ma

Partial melting and the volume and distribution of melt can significantly impact the thermal and mechanical properties of the lower crust; as such

precondition it in a way which retains heat. Melt-producing reactions may buffer heat flow, whereas melt crystallization buffers cooling (Schorn et al., 2018; Stüwe, 1995; Thompson and Connolly, 1995). The presence of even a low volume (< or <<10%) of melt reduces the shear strength of the crust (Rosenberg and Handy, 2005), and drainage of the melt has been thought to remove a significant proportion of the heat producing elements (HPEs) from metasedimentary protoliths (Rudnick and Fountain, 1995). However, recent field studies (Alessio et al., 2018) and thermodynamic modeling (Yakymchuk and Brown, 2019) argue for retention of high heat production under certain conditions. Metasedimentary rocks in the EGP have nominally high HPE concentrations (Kumar et al., 2007), similar to the granites postulated to have formed through their partial melting (Korhonen et al., 2015). It follows that the process of partial melting may not deplete the protoliths in their HPEs. In addition to high HPE concentrations, low erosion rates and high mantle heat flux may sustain suprasolidus temperatures in the lower crust on timescales approaching c. 100 Ma (Clark et al., 2011; Sizova et al., 2014).

The majority of metamorphic rocks of the Eastern Ghats Province followed a counter clockwise (CCW) *P–T* evolution, inferred to represent initial extension followed by moderate thickening, with the lower crust reaching ~7–8 kbar (Korhonen et al., 2013a). If the generation of topography is limited (Sizova et al., 2014), limiting erosion, and the crust likely remained close to isostatic equilibrium, with no gravitational driving force for exhumation. Any significant decrease in mantle heat flow would produce a cold lithospheric root, subsidence and formation of a sedimentary basin. By contrast, if mantle heat flow is sustained, both erosion and subsidence are minimal (Bohlen, 1991; Sandiford and Powell, 1986). Limited erosion and exhumation leads to retention of the heat source in the lower crust, and potentially enables terranes such as the EGP to retain heat and remain melt-present over long durations. However, rheologically weakened, melt-bearing lower crust will be susceptible to the localization of plate boundary stresses. Palaeogeographic reconstructions place the Eastern Ghats on the margin of the supercontinent Rodinia (Merdith et al., 2017). It is likely that significant compressive stress was not applied to the outboard margin of the Eastern Ghats and Rayner Provinces until the major plate reorganization that accompanied the amalgamation of Gondwana during the Pan-African orogenic event. At that time, the strain would have been localized in the weak lower crust of the EGP and would have allowed the thrust-driven exhumation (Figure 4.14(viii)) of the EGP over the Bastar Craton to the east (Biswal et al., 2007).

4.5 | Conclusions

The following conclusions were drawn, meeting the research objectives presented in section 1.1.3.

1. Using a k-means clustering algorithm with experimentally derived diagnostic trace element signatures to group igneous, metamorphic and hydrothermally modified zircon can return geologically meaningful populations.

2. Detrital sources for metasedimentary protoliths on the EGP may include: The Dharwar Craton or the Lambert Terrane for c. 2500 Ma inherited grains, the Ongole Terrane and continental rift-related alkaline complexes for grains aged c. 1650–1350 Ma. The concordant zircon aged c. 1220–1080 have a Nb/Yb ratio and high Ti concentration consistent with zircon crystallised from high temperature alkaline magma, and this age range represents the onset of rifting between cratonic East Antarctica and India.

3. Metamorphic zircon U–Pb isotopes in these EGP samples have two types of behaviour that can be differentiated by discordia vs age plots. The data either trends along concordia with age, or represent discordia, likely due to Pb-loss. Concordant populations are likely representative of crystallisation of zircon from anatectic melt over the age range of concordant data.

4. U–Pb analysis of metamorphic zircon follows a concordant trend during M1 in sample 17-59 and during M2 in sample 17-37. During M1, zircon crystallised from melt at >900 °C over >100 Ma between c. 990–890 Ma, cooling at a rate of 0.34 ± 0.09 °C/Ma. Between c. 540 Ma and c. 500 Ma, zircon crystallised at up to ~920 °C, exceeding the extrapolated cooling trend of M1

5. Cooling rates of <0.50 °C/Ma and temperatures >900 °C for >100 Ma can be maintained in Earth's lower crust when it is thickened, enriched in heat producing elements (HPE) and subject to minimal erosion. These conditions can allow melt to be present. Lower crust which has been preconditioned in this way will be more susceptible to reheating, in the case of the Eastern Ghats Province, those samples which have M2 U–Pb zircon ages.

4.6 | References

Alessio, K. L., Hand, M., Kelsey, D. E., Williams, M. A., Morrissey, L. J., and Barovich, K., 2018, Conservation of deep crustal heat production: Geology, v. 46, no. 4, p. 335-338.

Ashwal, L. D., Tucker, R. D., and Zinner, E. K., 1999, Slow cooling of deep crustal granulites and Pb-loss in zircon: Geochimica et Cosmochimica Acta, v. 63, no. 18, p. 2839-2851.

Ayers, J. C., and Peters, T. J., 2018, Zircon/fluid trace element partition coefficients measured by recrystallization of Mud Tank zircon at 1.5 GPa and 800–1000° C: Geochimica et Cosmochimica Acta, v. 223, p. 60-74.

Bell, E. A., Boehnke, P., Barboni, M., and Harrison, T. M., 2019, Tracking chemical alteration in magmatic zircon using rare earth element abundances: Chemical Geology.

Belousova, E., Griffin, W. L., O'Reilly, S. Y., and Fisher, N., 2002, Igneous zircon: trace element composition as an indicator of source rock type: Contributions to mineralogy and petrology, v. 143, no. 5, p. 602-622.

Bhattacharya, A., Das, H. H., Bell, E., Bhattacharya, A., Chatterjee, N., Saha, L., and Dutt, A., 2016, Restoration of Late Neoarchean–Early Cambrian tectonics in the Rengali orogen and its environs (eastern India): The Antarctic connection: Lithos, v. 263, p. 190-212.

Biswal, T. K., De Waele, B., and Ahuja, H., 2007, Timing and dynamics of the juxtaposition of the Eastern Ghats mobile belt against the Bhandara Craton, India: A structural and zircon U-Pb SHRIMP study of the fold-thrust belt and associated nepheline syenite plutons: Tectonics, v. 26, no. 4.

Boehnke, P., Watson, E. B., Trail, D., Harrison, T. M., and Schmitt, A. K., 2013, Zircon saturation re-revisited: Chemical Geology, v. 351, p. 324-334.

Bohlen, S. R., 1991, On the formation of granulites: Journal of Metamorphic Geology, v. 9, no. 3, p. 223-229.

Carson, C. J., Ague, J. J., and Coath, C. D., 2002, U-Pb geochronology from Tonagh Island, East Antarctica: Implications for the timing of ultra-high temperature metamorphism of the Napier Complex: Precambrian Research, v. 116, no. 3-4, p. 237-263.

Cherniak, D., 2010, Diffusion in accessory minerals: zircon, titanite, apatite, monazite and xenotime: Reviews in Mineralogy and Geochemistry, v. 72, no. 1, p. 827-869.

Cherniak, D., and Watson, E., 2001, Pb diffusion in zircon: Chemical Geology, v. 172, no. 1-2, p. 5-24.

Clark, C., Fitzsimons, I. C. W., Healy, D., and Harley, S. L., 2011, How does the continental crust get really hot?: Elements, v. 7, no. 4, p. 235-240.

Clark, C., Healy, D., Johnson, T., Collins, A. S., Taylor, R. J., Santosh, M., and Timms, N. E., 2015, Hot orogens and supercontinent amalgamation: A Gondwanan example from southern India: Gondwana Research, v. 28, no. 4, p. 1310-1328.

Clark, C., Kinny, P. D., and Harley, S. L., 2012, Sedimentary provenance and age of metamorphism of the Vestfold Hills, East Antarctica: Evidence for a piece of Chinese Antarctica?: Precambrian Research, v. 196-197, p. 23-45.

Clark, C., Taylor, R. J. M., Kylander-Clark, A. R. C., and Hacker, Bradley R., 2018, Prolonged (>100 Ma) ultrahigh temperature metamorphism in the Napier Complex, East Antarctica: A petrochronological investigation of Earth's hottest crust: Journal of Metamorphic Geology, v. 36, no. 9, p. 1117-1139.

Collins, A. S., Kinny, P. D., and Razakamanana, T., 2012, Depositional age, provenance and metamorphic age of metasedimentary rocks from southern Madagascar: Gondwana Research, v. 21, no. 2-3, p. 353-361.

Collins, A. S., Kröner, A., Fitzsimons, I. C. W., and Razakamanana, T., 2003, Detrital footprint of the Mozambique ocean: U-Pb SHRIMP and Pb evaporation zircon geochronology of metasedimentary gneisses in eastern Madagascar: Tectonophysics, v. 375, no. 1-4, p. 77-99.

Collins, A. S., Santosh, M., Braun, I., and Clark, C., 2007, Age and sedimentary provenance of the Southern Granulites, South India: U-Th-Pb SHRIMP secondary ion mass spectrometry: Precambrian Research, v. 155, no. 1-2, p. 125-138.

Corfu, F., Hanchar, J. M., Hoskin, P. W., and Kinny, P., 2003, Atlas of zircon textures: Reviews in mineralogy and geochemistry, v. 53, no. 1, p. 469-500.

Corfu, F., Heaman, L. M., and Rogers, G., 1994, Polymetamorphic

evolution of the Lewisian complex, NW Scotland, as recorded by U-Pb isotopic compositions of zircon, titanite and rutile: Contributions to Mineralogy and Petrology, v. 117, no. 3, p. 215-228.

Das, K., Bose, S., Karmakar, S., Dunkley, D. J., and Dasgupta, S., 2011, Multiple tectonometamorphic imprints in the lower crust: First evidence of ca. 950Ma (zircon U-Pb SHRIMP) compressional reworking of UHT aluminous granulites from the Eastern Ghats Belt, India: Geological Journal, v. 46, no. 2-3, p. 217-239.

Dasgupta, S., Bose, S., and Das, K., 2013, Tectonic evolution of the Eastern Ghats Belt, India: Precambrian Research, v. 227, p. 247-258.

Dharma Rao, C. V., Santosh, M., and Dong, Y., 2012, U-Pb zircon chronology of the Pangidi-Kondapalle layered intrusion, Eastern Ghats belt, India: Constraints on Mesoproterozoic arc magmatism in a convergent margin setting: Journal of Asian Earth Sciences, v. 49, p. 362-375.

Dobmeier, C. J., and Raith, M. M., 2003, Crustal architecture and evolution of the Eastern Ghats Belt and adjacent regions of India, Geological Society Special Publication, Volume 206, p. 145-168.

Ferry, J. M., and Watson, E. B., 2007, New thermodynamic models and revised calibrations for the Ti-in-zircon and Zr-in-rutile thermometers: Contributions to Mineralogy and Petrology, v. 154, no. 4, p. 429-437.

Fraser, G., Ellis, D., and Eggins, S., 1997, Zirconium abundance in granulite-facies minerals, with implications for zircon geochronology in high-grade rocks: Geology, v. 25, no. 7, p. 607-610.

Fu, B., Page, F. Z., Cavosie, A. J., Fournelle, J., Kita, N. T., Lackey, J. S., Wilde, S. A., and Valley, J. W., 2008, Ti-in-zircon thermometry: applications and limitations: Contributions to Mineralogy and Petrology, v. 156, no. 2, p. 197-215.

Gehrels, G., 2011, Detrital zircon U-Pb geochronology: Current methods and new opportunities: Tectonics of sedimentary basins: Recent advances, p. 45-62.

Gehrels, G., 2014, Detrital zircon U-Pb geochronology applied to tectonics, Annual Review of Earth and Planetary Sciences, Volume 42, Annual Reviews Inc., p. 127-149.

Geisler, T., Pidgeon, R. T., Kurtz, R., Van Bronswijk, W., and Schleicher,

H., 2003, Experimental hydrothermal alteration of partially metamict zircon: American Mineralogist, v. 88, no. 10, p. 1496-1513.

Geisler, T., Schaltegger, U., and Tomaschek, F., 2007, Re-equilibration of zircon in aqueous fluids and melts: Elements, v. 3, no. 1, p. 43-50.

Grimes, C., Wooden, J., Cheadle, M., and John, B., 2015, "Fingerprinting" tectono-magmatic provenance using trace elements in igneous zircon: Contributions to Mineralogy and Petrology, v. 170, no. 5-6, p. 46.

Grimes, C. B., John, B. E., Kelemen, P., Mazdab, F., Wooden, J., Cheadle, M. J., Hanghøj, K., and Schwartz, J., 2007, Trace element chemistry of zircons from oceanic crust: A method for distinguishing detrital zircon provenance: Geology, v. 35, no. 7, p. 643-646.

Halpin, J. A., Gerakiteys, C., Clarke, G., Belousova, E., and Griffin, W., 2005, In-situ U–Pb geochronology and Hf isotope analyses of the Rayner Complex, east Antarctica: Contributions to Mineralogy and Petrology, v. 148, no. 6, p. 689-706.

Harley, S. L., and Kelly, N. M., 2007, Zircon: Tiny but timely: Elements, v. 3, no. 1, p. 13-18.

Harley, S. L., Kelly, N. M., and Möller, A., 2007, Zircon behaviour and the thermal histories of moutain chains: Elements, v. 3, no. 1, p. 25-30.

Henderson, B., Collins, A. S., Payne, J., Forbes, C., and Saha, D., 2014, Geologically constraining India in Columbia: The age, isotopic provenance and geochemistry of the protoliths of the Ongole Domain, Southern Eastern Ghats, India: Gondwana Research, v. 26, no. 3-4, p. 888-906.

Hippe, K., Möller, A., von Quadt, A., Peytcheva, I., and Hammerschmidt, K., 2016, Zircon geochronology of the Koraput alkaline complex: Insights from combined geochemical and U-Pb-Hf isotope analyses, and implications for the timing of alkaline magmatism in the Eastern Ghats Belt, India: Gondwana Research, v. 34, p. 205-220.

Hokada, T., and Harley, S. L., 2004, Zircon growth in UHT leucosome: Constraints from zircon-garnet rare earth elements (REE) relations in Napier Complex, East Antarctica: Journal of Mineralogical and Petrological Sciences, v. 99, no. 4, p. 180-190.

Horie, K., Hokada, T., Hiroi, Y., Motoyoshi, Y., and Shiraishi, K., 2012,

Contrasting Archaean crustal records in western part of the Napier Complex, East Antarctica: New constraints from SHRIMP geochronology: Gondwana Research, v. 21, no. 4, p. 829-837.

Hoskin, P. W., 2005, Trace-element composition of hydrothermal zircon and the alteration of Hadean zircon from the Jack Hills, Australia: Geochimica et Cosmochimica Acta, v. 69, no. 3, p. 637-648.

Jackson, S. E., Pearson, N. J., Griffin, W. L., and Belousova, E. A., 2004, The application of laser ablation-inductively coupled plasma-mass spectrometry to in situ U–Pb zircon geochronology: Chemical Geology, v. 211, no. 1-2, p. 47-69.

Kelly, N. M., and Harley, S. L., 2005, An integrated microtextural and chemical approach to zircon geochronology: Refining the Archaean history of the Napier Complex, east Antarctica: Contributions to Mineralogy and Petrology, v. 149, no. 1, p. 57-84.

Kelsey, D. E., Clark, C., and Hand, M., 2008, Thermobarometric modelling of zircon and monazite growth in melt-bearing systems: Examples using model metapelitic and metapsammitic granulites: Journal of Metamorphic Geology, v. 26, no. 2, p. 199-212.

Kelsey, D. E., Morrissey, L. J., Hand, M., Clark, C., Tamblyn, R., Gaehl, A. A., and Marshall, S., 2017, Significance of post-peak metamorphic reaction microstructures in the ultrahigh temperature Eastern Ghats Province, India: Journal of Metamorphic Geology, v. 35, no. 9, p. 1081-1109.

Kelsey, D. E., and Powell, R., 2011, Progress in linking accessory mineral growth and breakdown to major mineral evolution in metamorphic rocks: A thermodynamic approach in the Na 2O-CaO-K 2O-FeO-MgO-Al 2O 3-SiO 2-H 2O-TiO 2-ZrO 2 system: Journal of Metamorphic Geology, v. 29, no. 1, p. 151-166.

Kinny, P., Black, L., and Sheraton, J., 1997, Zircon U-Pb ages and geochemistry of igneous and metamorphic rocks in the northern Prince Charles Mountains, Antarctica: AGSO Journal of Australian Geology and Geophysics, v. 16, no. 5, p. 637-654.

Korhonen, F. J., Brown, M., Clark, C., and Bhattacharya, S., 2013a, Osumilite-melt interactions in ultrahigh temperature granulites: Phase equilibria modelling and implications for the P-T-t evolution of the eastern ghats province, india: Journal of Metamorphic Geology, v. 31, no. 8, p. 881-

907.

Korhonen, F. J., Brown, M., Clark, C., Foden, J. D., and Taylor, R., 2015, Are granites and granulites consanguineous?: Geology, v. 43, no. 11, p. 991-994.

Korhonen, F. J., Clark, C., Brown, M., Bhattacharya, S., and Taylor, R., 2013b, How long-lived is ultrahigh temperature (UHT) metamorphism? Constraints from zircon and monazite geochronology in the Eastern Ghats orogenic belt, India: Precambrian Research, v. 234, p. 322-350.

Korhonen, F. J., Clark, C., Brown, M., and Taylor, R. J. M., 2014, Taking the temperature of Earth's hottest crust: Earth and Planetary Science Letters, v. 408, p. 341-354.

Korhonen, F. J., Saw, A. K., Clark, C., Brown, M., and Bhattacharya, S., 2011, New constraints on UHT metamorphism in the Eastern Ghats Province through the application of phase equilibria modelling and in situ geochronology: Gondwana Research, v. 20, no. 4, p. 764-781.

Kovach, V. P., Simmat, R., Rickers, K., Berezhnaya, N. G., Salnikova, E. B., Dobmeier, C., Raith, M. M., Yakovleva, S. Z., and Kotov, A. B., 2001, The Western Charnockite Zone of the Eastern Ghats Belt, India - An Independent Crustal Province of Late Archaean (2.8 Ga) and Palaeoproterozoic (1.7-1.6 Ga) Terrains: Gondwana Research, v. 4, no. 4, p. 666-667.

Kumar, P. S., Menon, R., and Reddy, G. K., 2007, The role of radiogenic heat production in the thermal evolution of a Proterozoic granulite-facies orogenic belt: Eastern Ghats, Indian Shield: Earth and Planetary Science Letters, v. 254, no. 1-2, p. 39-54.

Kunz, B. E., Regis, D., and Engi, M., 2018, Zircon ages in granulite facies rocks: decoupling from geochemistry above 850° C?: Contributions to Mineralogy and Petrology, v. 173, no. 3, p. 26.

Kusiak, M. A., Whitehouse, M. J., Wilde, S. A., Dunkley, D. J., Menneken, M., Nemchin, A. A., and Clark, C., 2013, Changes in zircon chemistry during archean UHT metamorphism in the Napier Complex, Antarctica: American Journal of Science, v. 313, no. 9, p. 933-967.

Li, X., Long, W., Li, Q., Liu, Y., Zheng, Y., Yang, Y., Chamberlain, K., Wan, D., Guo, C., and Wang, X., 2010, Penglai zircon megacryst: A potential new working reference for microbeam analysis of Hf-O isotopes and U-Pb age: Geostandard and Geoanalytical Research, v. 34: doi, v. 10, p. 117-134.

MacQueen, J., Some methods for classification and analysis of multivariate observations, in Proceedings Proceedings of the fifth Berkeley symposium on mathematical statistics and probability1967, Volume 1, Oakland, CA, USA, p. 281-297.

Merdith, A. S., Collins, A. S., Williams, S. E., Pisarevsky, S., Foden, J. D., Archibald, D. B., Blades, M. L., Alessio, B. L., Armistead, S., and Plavsa, D., 2017, A full-plate global reconstruction of the Neoproterozoic: Gondwana Research, v. 50, p. 84-134.

Mezger, K., and Krogstad, E., 1997, Interpretation of discordant U-Pb zircon ages: An evaluation: Journal of metamorphic Geology, v. 15, no. 1, p. 127-140.

Mikhalsky, E. V., Beliatsky, B. V., Sheraton, J. W., and Roland, N. W., 2006, Two distinct Precambrian terranes in the Southern Prince Charles Mountains, East Antarctica: SHRIMP dating and geochemical constraints: Gondwana Research, v. 9, no. 3, p. 291-309.

Mikhalsky, E. V., Sheraton, J. W., Laiba, A. A., and Beliatsky, B. V., 1996, Geochemistry and origin of Mesoproterozoic metavolcanic rocks from Fisher Massif, Prince Charles Mountains, East Antarctica: Antarctic Science, v. 8, no. 1, p. 85-104.

Mitchell, R. J., Johnson, T. E., Clark, C., Gupta, S., Brown, M., Harley, S. L., and Taylor, R., 2019, Neoproterozoic evolution and Cambrian reworking of ultrahigh temperature granulites in the Eastern Ghats Province, India: Journal of Metamorphic Geology, v. 37, no. 7, p. 977-1006.

Nanda, J., Gupta, S., and Hacker, B., 2018, U-Pb zircon and titanite ages from granulites of the Koraput area–evidence for Columbia, Rodinia and Gondwana from the Eastern Ghats Province, India: Precambrian Research, v. 314, p. 394-413.

Nemchin, A. A., and Cawood, P. A., 2005, Discordance of the U–Pb system in detrital zircons: implication for provenance studies of sedimentary rocks: Sedimentary Geology, v. 182, no. 1-4, p. 143-162.

Paton, C., Hellstrom, J., Paul, B., Woodhead, J., and Hergt, J., 2011, Iolite: Freeware for the visualisation and processing of mass spectrometric data: Journal of Analytical Atomic Spectrometry, v. 26, no. 12, p. 2508-2518.

Phillips, G., Wilson, C. J., Campbell, I., and Allen, C. M., 2006, U–Th–Pb detrital zircon geochronology from the southern Prince Charles

mountains, east Antarctica—defining the Archaean to Neoproterozoic Ruker province: Precambrian Research, v. 148, no. 3-4, p. 292-306.

Plavsa, D., Collins, A. S., Foden, J. F., Kropinski, L., Santosh, M., Chetty, T. R. K., and Clark, C., 2012, Delineating crustal domains in Peninsular India: Age and chemistry of orthopyroxene-bearing felsic gneisses in the Madurai Block: Precambrian Research, v. 198-199, p. 77-93.

Plavsa, D., Collins, A. S., Payne, J. L., Foden, J. D., Clark, C., and Santosh, M., 2014, Detrital zircons in basement metasedimentary protoliths unveil the origins of southern India: Bulletin of the Geological Society of America, v. 126, no. 5-6, p. 791-812.

Prakash, D., Singh, P. C., Singh, C. K., Tewari, S., Arima, M., and Frimmel, H. E., 2015, Reaction textures and metamorphic evolution of sapphirine-spinel-bearing and associated granulites from Diguva Sonaba, Eastern Ghats Mobile Belt, India: Geological Magazine, v. 152, no. 2, p. 316-340.

Rickers, K., Mezger, K., and Raith, M. M., 2001, Evolution of the continental crust in the Proterozoic Eastern Ghats Belt, India and new constraints for Rodinia reconstruction: Implications from Sm-Nd, Rb-Sr and Pb-Pb isotopes: Precambrian Research, v. 112, no. 3-4, p. 183-210.

Rosenberg, C., and Handy, M., 2005, Experimental deformation of partially melted granite revisited: implications for the continental crust: Journal of metamorphic Geology, v. 23, no. 1, p. 19-28.

Rubatto, D., 2002, Zircon trace element geochemistry: Partitioning with garnet and the link between U-Pb ages and metamorphism: Chemical Geology, v. 184, no. 1-2, p. 123-138.

Rubatto, D., and Hermann, J., 2007, Experimental zircon/melt and zircon/garnet trace element partitioning and implications for the geochronology of crustal rocks: Chemical Geology, v. 241, no. 1-2, p. 38-61.

Rudnick, R. L., and Fountain, D. M., 1995, Nature and composition of the continental crust: A lower crustal perspective: Reviews of Geophysics, v. 33, no. 3, p. 267-309.

Sandiford, M., and Powell, R., 1986, Deep crustal metamorphism during continental extension: modern and ancient examples: Earth and Planetary Science Letters, v. 79, no. 1-2, p. 151-158.

Sarkar, T., and Schenk, V., 2016, Early Mesoproterozoic (1.6–1.5 Ga) granulite facies events in the Ongole domain: geodynamic significance and global correlation: Journal of Metamorphic Geology, v. 34, no. 8, p. 765-784.

Sarkar, T., Schenk, V., and Berndt, J., 2015, Formation and evolution of a Proterozoic magmatic arc: geochemical and geochronological constraints from meta-igneous rocks of the Ongole domain, Eastern Ghats Belt, India: Contributions to Mineralogy and Petrology, v. 169, no. 1, p. 1-27.

Schorn, S., Diener, J. F., Powell, R., and Stüwe, K., 2018, Thermal buffering in the orogenic crust: Geology, v. 46, no. 7, p. 643-646.

Simmat, R., and Raith, M. M., 2008, U-Th-Pb monazite geochronometry of the Eastern Ghats Belt, India: Timing and spatial disposition of poly-metamorphism: Precambrian Research, v. 162, no. 1-2, p. 16-39.

Sizova, E., Gerya, T., and Brown, M., 2014, Contrasting styles of Phanerozoic and Precambrian continental collision: Gondwana Research, v. 25, no. 2, p. 522-545.

Sláma, J., Košler, J., Condon, D. J., Crowley, J. L., Gerdes, A., Hanchar, J. M., Horstwood, M. S. A., Morris, G. A., Nasdala, L., Norberg, N., Schaltegger, U., Schoene, B., Tubrett, M. N., and Whitehouse, M. J., 2008, Plešovice zircon - A new natural reference material for U-Pb and Hf isotopic microanalysis: Chemical Geology, v. 249, no. 1-2, p. 1-35.

Stüwe, K., 1995, Thermal buffering effects at the solidus. Implications for the equilibration of partially melted metamorphic rocks: Tectonophysics, v. 248, no. 1-2, p. 39-51.

Taylor, R. J. M., Clark, C., Harley, S. L., Kylander-Clark, A. R. C., Hacker, B. R., and Kinny, P. D., 2017, Interpreting granulite facies events through rare earth element partitioning arrays: Journal of Metamorphic Geology, v. 35, no. 7, p. 759-775.

Taylor, R. J. M., Harley, S. L., Hinton, R. W., Elphick, S., Clark, C., and Kelly, N. M., 2015, Experimental determination of REE partition coefficients between zircon, garnet and melt: A key to understanding high-T crustal processes: Journal of Metamorphic Geology, v. 33, no. 3, p. 231-248.

Taylor, R. J. M., Kirkland, C. L., and Clark, C., 2016, Accessories after the facts: Constraining the timing, duration and conditions of high-temperature metamorphic processes: Lithos, v. 264, p. 239-257.

Thompson, A. B., and Connolly, J. A., 1995, Melting of the continental crust: some thermal and petrological constraints on anatexis in continental collision zones and other tectonic settings: Journal of Geophysical Research: Solid Earth, v. 100, no. B8, p. 15565-15579.

Trail, D., Watson, E. B., and Tailby, N. D., 2012, Ce and Eu anomalies in zircon as proxies for the oxidation state of magmas: Geochimica et Cosmochimica Acta, v. 97, p. 70-87.

Upadhyay, D., Gerdes, A., and Raith, M. M., 2009, Unraveling sedimentary provenance and tectonothermal history of high-temperature metapelites, using zircon and monazite chemistry: A case study from the eastern ghats belt, India: Journal of Geology, v. 117, no. 6, p. 665-683.

Vavra, G., Gebauer, D., Schmid, R., and Compston, W., 1996, Multiple zircon growth and recrystallization during polyphase late carboniferous to triassic metamorphism in granulites of the Ivrea Zone (Southern Alps): An ion microprobe (SHRIMP) study: Contributions to Mineralogy and Petrology, v. 122, no. 4, p. 337-358.

Vavra, G., Schmid, R., and Gebauer, D., 1999, Internal morphology, habit and U-Th-Pb microanalysis of amphibolite-to-granulite facies zircons: Geochronology of the Ivrea Zone (Southern Alps): Contributions to Mineralogy and Petrology, v. 134, no. 4, p. 380-404.

Vermeesch, P., 2012, On the visualisation of detrital age distributions: Chemical Geology, v. 312, p. 190-194.

Wetherill, G. W., 1956, Discordant uranium-lead ages, I: Eos, Transactions American Geophysical Union, v. 37, no. 3, p. 320-326.

Wiedenbeck, M., Alle, P., Corfu, F., Griffin, W., Meier, M., Oberli, F. v., Quadt, A. v., Roddick, J., and Spiegel, W., 1995, Three natural zircon standards for U-Th-Pb, Lu-Hf, trace element and REE analyses: Geostandards and Geoanalytical Research, v. 19, no. 1, p. 1-23.

Williams, S. E., Dietmar Müller, R., Landgrebe, T. C. W., and Whittaker, J. M., 2012, An open-source software environment for visualizing and refining plate tectonic reconstructions using high-resolution geological and geophysical data sets: GSA Today, v. 22, no. 4-5, p. 4-9.

Yakymchuk, C., and Brown, M., Divergent behaviour of Th and U during anatexis: Implications for the thermal evolution of orogenic crust: Journal of Metamorphic Geology, v. 0, no. 0.

Yakymchuk, C., and Brown, M., 2014, Behaviour of zircon and monazite during crustal melting: Journal of the Geological Society, v. 171, no. 4, p. 465-479.

Yakymchuk, C., Clark, C., and White, R. W., 2017, Phase relations, reaction sequences and petrochronology: Reviews in Mineralogy and Geochemistry, v. 83, no. 1, p. 13-53.

Young, D., and Ellis, D., The intrusive Mawson charnockites: Evidence for a compressional plate margins of the Proterozoic mobile belt of East Antarctica, in Proceedings International symposium on Antarctic earth sciences. 51991, p. 25-31.

Zhao, J. X., Ellis, D. J., Kilpatrick, J. A., and McCulloch, M. T., 1997, Geochemical and Sr-Nd isotopic study of charnockites and related rocks in the northern Prince Charles Mountains, East Antarctica: Implications for charnockite petrogenesis and proterozoic crustal evolution: Precambrian Research, v. 81, no. 1-2, p. 37-66.

Chapter 5 | Conclusions

5.1 | Scales of thermodynamic equilibrium in granulites

5.1.1 | Observed scales of equilibrium

There is evidence for granulites attaining thermodynamic equilibrium over a range of scales; from local equilibrium on the centimeter scale down to the micron scale. Several granulites have peak assemblages that vary on the centimetre scale (Figure 2.1), with X(Mg) values that can differ by >0.6. Furthermore, reaction textures have mineral assemblages and/or mineral compositions that vary over much smaller length scales (Figure 2.2).

5.1.2 | Reaction textures and *P–T* interpretations

Reaction textures that are grown along the retrograde *P–T* path depend on the topology of equilibria in chemical potential space (Figure 1.1a). With a change in *P–T* conditions, the position of equilibria in chemical potential space changes, stabilising new phases at the expense of those at the original *P–T*. Consequently, the phases that make up reaction textures depend on the pre-existing phases and the *P–T* change (Figure 1.1b-d). The reaction textures that are preserved depends on the mobility of the components that are needed to make the symplectites, whether parts of a reaction microtexture can be chemically and physically isolated from the matrix, and whether melt can locally expedite diffusion.

For example, there is evidence from observed symplectites that chemical isolation from matrix quartz can lead to SiO_2 undersaturated equilibria and reaction textures (Figures 2.10 and 2.11), for example, if a grain boundary between peak phases becomes chemically isolated from a SiO_2 saturated matrix. In this case, symplectites become internally buffered, as μSiO_2 is not imposed on the symplectite by the matrix (Figure 2.12).

5.1.3 | Preserving local equilibrium

Chemical and physical isolation from melt may allow solid state diffusion to become the rate determining factor in the preservation of local equilibrium both on the prograde and retrograde path. As shown in Figure 2.14, on the prograde path, isolation of solid phases from melt can occur if the melt becomes viscous, leading to ineffective grain boundary wetting and

migration. In order to prevent rapid fluid diffusion of SiO2, Al2O3, MgO and FeO, the interconnected melt networks required for melt loss events (Figure 2.14b, c) must exist for less than the duration required for the rapid fluid diffusion of FMAS components to flatten chemical potential gradients. Melt loss along a typical prograde granulite high *T/P P–T* path to 7.6 kbar, 1000°C leads to an order of magnitude increase of melt viscosity in a model metapelite (Figure 2.6), meaning that melt migration is inhibited, restricting viscous melt to isolated pockets (Figure 2.14c). In this scenario, chemical potential gradients may be preserved locally if melt modes are low enough to allow diffusion rate to be solid state controlled, or isolated melt pockets can allow reaction microtextures to form along locally intergranular chemical potential gradients on a retrograde *P–T* path (Figure 2.14d).

5.2 | Metamorphic conditions in the Eastern Ghats Province

5.2.1 | *P–T* conditions of metamorphism

Peak and post-peak metamorphic conditions of granulites from the Eastern Ghats Province, India, vary between localities. Phase equilibrium studies from various highland localities constrain peak conditions to >950°C and ~8 kbar followed by near-isobaric cooling (Korhonen et al., 2013; Korhonen et al., 2011). In addition, high Al–Mg granulites at Anantagiri are inferred to record peak metamorphic temperatures that exceeded 1000°C (Korhonen et al., 2014). However, at Vizianagaram, further from the orogenic front than the highland localities, post peak metamorphic conditions are characterized by <1 kbar of decompression at ~1000°C before cooling to ~800°C (Figure 3.12). Additionally, the UHT granulites at Vizianagaram may not have followed a counterclockwise *P–T* path similar to highland localities in the EGP (Korhonen et al., 2013).

To account for the lack of evidence for decompression elsewhere in the terrane, Kelsey et al. (2017) argue that the refractory compositions of highland Al–Mg granulites in the EGP would not have recorded the late-stage decompression. However, this explanation contradicts evidence from UHT localities in other metamorphic belts that garnet-bearing high Al–Mg granulites in particular commonly do record post-peak decompression (Harley, 1998). This is also true for the garnet-bearing high Al–Mg granulites from the EGP. Had high-*T* decompression had occurred at the localities studied by (Korhonen et al., 2013; Korhonen et al., 2014), it is likely that

reaction microstructures involving garnet breakdown would have developed, but these are absent. Consequently, the post-peak *P–T* path inferred for both Vizianagaram and highland localities are tectonically significant.

5.2.2 | Duration of metamorphism

Metamorphic zircon was identified by shallow Yb_N/Gd_N slope, small positive Ce/Ce* anomaly and large negative Eu/Eu* anomaly (Figure 4.2). For samples where data defines either arrays that trend along concordia (zero discordance) over a given timespan, there is evidence for protracted crystallisation of primary metamorphic zircon, relating to an 'M1' event between c. 990–880 Ma. Regression zircon ages for an 'M2' event range from 518 ± 6 Ma to 594 ± 64 Ma.

For metamorphic zircon data points which follow a concordant trend, and because they can be interpreted as primary metamorphic grains, it is possible to directly relate age and Ti-in-zircon temperature for M1 and M2. Sample 17-59, for example, cools at a rate of 0.34 ± 0.09 °C from c. 990 Ma until c. 890 Ma. Zircon crystallisation temperatures for M2 range from ~920 °C to ~800 °C.

5.3 | Tectonics of a hot orogen

5.3.1 | Tectonic precursors to ultra-high-temperature metamorphism

In the EGP, the zircon population at c. 1600–1350 Ma, have elevated U/Yb and Yb_N/Gd_N ratios, Ce/Ce* anomaly and Ti concentration. On the other hand, the Ce/Ce* and Eu/Eu* anomalies have a negative spike between c. 1200 Ma and c. 1120 Ma. Furthermore, the zircon analyses between c. 1220 Ma and c. 1080 Ma have an elevated Nb/Yb ratio (Figure 5.2) and Ti concentration.

Therefore, the likely tectonic environment in which zircon crystallises, before being reworked and deposited into a basin, is as follows: The elevated U/Yb ratio of c. 1600–1350 Ma zircon indicates that it crystallised from a magma within an arc environment Elevated Yb_N/Gd_N ratios indicate that the magma was not in equilibrium with garnet, while the Ce/Ce* anomaly suggests that it was oxidised (Trail et al., 2012). Input to the EGRT basin was therefore provided by granitoids in the Ongole domain, or from continental rift related alkaline complexes near the cratonic margin of the EGP at this

time. The signature of c. 1220–1080 Ma zircon has low Ce/Ce* and Eu/Eu* anomalies, consistent with zircon crystallised from reduced melts. A high Nb/Yb ratio has been proposed as a proxy for low degree mantle melting and/or high alkalinity in magma. Therefore, the elevated Nb/Yb and high Ti concentration can be interpreted as indicators of zircon crystallised from an extensional setting. This age bracket can be taken as a constraint on the onset of rifting between cratonic India and East Antarctica. Renewed convergence of cratonic India and East Antarctica, after the onset of rifting, initiated the first metamorphic event (M1) in the EGP (Figure 5.2).

5.3.2 | Sustaining high-temperatures in the lower crust

The volume and distribution of melt can significantly impact the thermal and mechanical properties of the lower crust. Melt-producing reactions may buffer heat flow, whereas melt crystallization buffers cooling (Schorn et al., 2018; Stüwe, 1995; Thompson and Connolly, 1995). The presence of even a small volume (< or <<10%) of melt reduces the shear strength of the crust (Rosenberg and Handy, 2005), and drainage of the melt is commonly thought to remove a significant proportion of the heat producing elements (HPEs) from residual granulites (Rudnick and Fountain, 1995). However, recent field studies (Alessio et al., 2018) and thermodynamic modeling (Yakymchuk and Brown) argue that high heat production in a metapelitic residue can be maintained due to the retention of HPEs. Furthermore, along a prograde geothermal gradient of 0.125 °C/GPa (Figure 5.3a), it is possible to maintain a radiogenic heat production >3 $\mu W/m^{-3}$ if monazite, the main reservoir of Th and U in granulite facies rocks, remains unreactive with silicate melt (Figure 5.3b). However, if monazite is allowed to freely dissolve in, and exchange Th and U with silicate melt, then the radiogenic heat production in the residue will decrease significantly (Figure 5.3b). The metasedimentary rocks in the EGP have nominally high HPE concentrations of ~3 μWm^{-2} (Kumar et al., 2007), similar to the granites postulated to have formed through their partial melting (Korhonen et al., 2015). It follows that the process of partial melting may not deplete the melt residues, if monazite remains unreactive with silicate melt. In addition to high HPE concentrations, low erosion rates and high mantle heat flux may sustain suprasolidus temperatures in the lower crust on timescales approaching ~100 Ma (Clark et al., 2011; Sizova et al., 2014).

The majority of rocks in the EGP followed a counter clockwise (CCW) *P–T* evolution with initial extension followed by moderate thickening, during

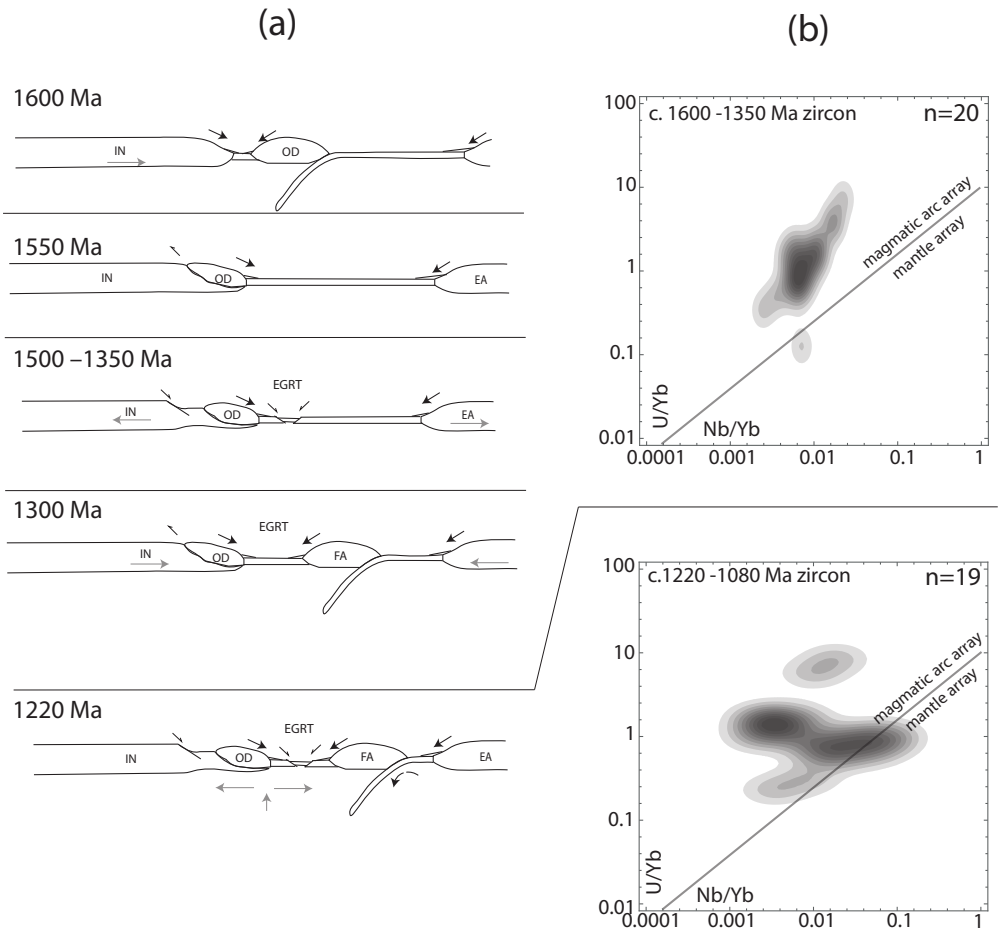

Figure 5.1 | Tectonic evolution of the Eastern Ghats Province preceding M1 and characteristic zircon chemistry. (a) Cross section sketches of the Eastern Ghats – Rayner Province before c.1000 Ma. (b) The c. 1600–1350 Ma population with an elevated U/Yb ratio and c. 1220–1080 Ma population with an elevated Nb/Yb ratio that plots within the mantle array of Grimes et al. (2015). Abbreviations: EA – East Antarctic cratons, EGP – Eastern Ghats Province, EGRT – Eastern Ghats Rayner Terrane, FA – Fisher Arc, IN – Indian cratons.

which the lower crust was at ~7–8 kbar (Korhonen et al., 2013). In these circumstances it is unlikely that significant topography was generated (Sizova et al., 2014), limiting erosion. Thus, the crust likely remained close to isostatic equilibrium, with no gravitational driving force for exhumation. Any significant decrease in mantle heat flow would produce a cold lithospheric root, subsidence and formation of a sedimentary basin. By contrast, if mantle heat flow is sustained, both erosion and subsidence are minimal, as implied for both the EGP (Bohlen, 1991; Sandiford and Powell, 1986). Limited erosion and exhumation leads to retention of heat in the lower crust, and potentially enable terranes such as the EGP to cool slowly, remaining melt-present over long durations. After crustal thinning, renewed convergence may have led to

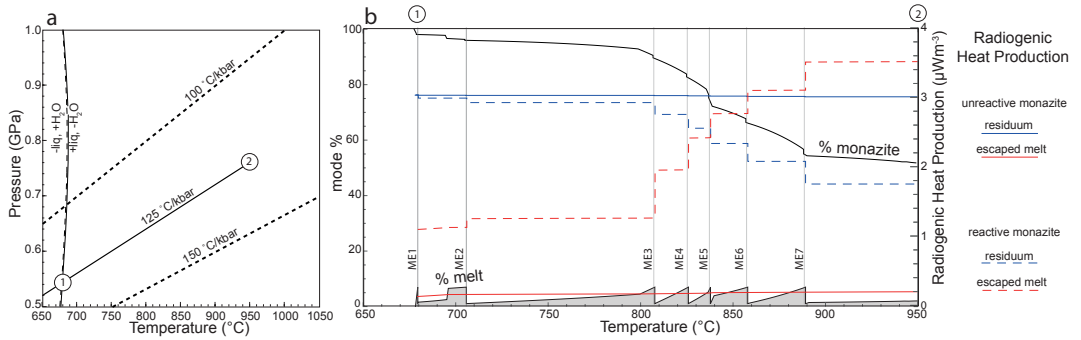

Figure 5.2 | Thermodynamic model of monazite solubility and radiogenic heat production of a metapelite over a prograde thermal gradient of 0.125 °C/GPa. A phase equilibrium model was calculated using modified average amphibolite facies metapelite composition (Ague, 1991) prograde thermal gradient of 125 °C/kbar, from the solidus (point 1) to peak conditions of 950 °C and 7.6 kbar (point 2), with melt extraction (see Figure 2.3). (b) Diagram showing how radiogenic heat production varies on the modelled prograde path in two model scenarios: Where monazite is completely unreactive in silicate melt (solid lines) and monazite reacts ideally with silicate melt (dashed lines). The radiogenic heat production of escaped melt is shown in red and the residuum in blue. Melt extraction (ME) events occur at each vertical grey line.

post-peak decompression, representing partial exhumation via thrusting of hot crust over adjacent granulites with counterclockwise *P–T* paths and the cratonic indentor.

5.3.3 | Reworking orogenic crust

Rheologically weakened melt-bearing lower crust will be susceptible to the localization of plate boundary stresses. It is likely that compressive stress was applied to the outboard margin of the Eastern Ghats and Rayner Provinces during major plate reorganization that accompanied the amalgamation of Gondwana during the Pan-African orogenic event around c. 540 Ma (Merdith et al., 2017). At that time, it is likely that the strain would have been localized in the weak lower crust of the EGP and would have allowed the thrust-driven exhumation of the EGP over the Bastar Craton to the east (Biswal et al., 2007), while reheating these preconditioned regions of the crust with high HPE concentrations to >800 °C. If the later reworking is of a high enough grade, earlier episodes of partial melting and melt loss that are a prerequisite may be similarly obscured in other high temperature metamorphic terranes.

Networks of mobile orogenic belts have led to the formation of supercontinents (Li et al., 2008; Merdith et al., 2017). Regions of continental crust, such as the EGP, that have been subject to high radiogenic heat production, high mantle heat flow and limited erosion before supercontinent assembly will be more likely to undergo deformation and reheating.

Therefore, the distribution of highly residual preconditioned crust may have determined the location of high temperature orogenic belts that formed during continental collision preceding the assembly of, for example, Gondwana and Rodinia.

5.4 | Areas for future research

Local equilibrium and reaction kinetics in granulites

A major aim for future research remains an accurate representation of mineral phases and reaction textures that can form on a granulite facies *P–T* path in a variety of rock compositions. In addition to the various scales of scale of local thermodynamic equilibrium addressed in this thesis, there are other processes related to reaction kinetics to consider (Carlson et al., 2015), especially in the context of the spatial evolution of reaction textures (Dégi et al., 2010).

A possible method for tackling reaction kinetics in granulties is by calculating the reaction affinity of the phases that comprise common reaction textures. For example, reaction overstepping can lead to reactants becoming stable after a reaction has been crossed, meaning that a certain phase is stable over a wider P–T range when reaction affinity is considered. The effect of reaction overstepping on stable assemblages has been calculated for diagnostic mineral isograds in Barrow Zone regional metamorphic rocks (Gaidies et al., 2011; Pattison and Spear, 2018; Pattison et al., 2011; Spear and Pattison, 2017) but this has not yet been expanded to granulite facies conditions. Furthermore, the spatial distribution and dimensions of reaction textures, and the time required to produce them, has been modelled using finite element methods (Dégi et al., 2010). A similar method may be applicable to the corona textures described in Chapter 2 to further constrain the metamorphic conditions of their formation.

What makes Earth's crust susceptible to orogenesis during the supercontinent cycle?

Tectonics on Earth is driven by the generation and destruction of continental crust in orogenic belts. The ability of regions of lower crust to attain and remain at high temperatures where they partially melt, and to undergo reheating during subsequent orogenesis, is of vital importance. In extreme cases, lower crustal rocks may even remain partially molten for >100 Myr, and reached these conditions more than once during their tectonothermal

evolution (Harley, 2016; Kelsey and Hand, 2015; Korhonen et al., 2013b). Networks of accretionary and then collisional orogens led to the mobile belts that formed supercontinents (Cawood et al., 2009; Li et al., 2008; Merdith et al., 2017). It is therefore important to evaluate the duration of orogenesis, and how this relates to key factors; including radiogenic heat production, mantle heat flow and erosion rate.

The rate of cooling of high-grade metamorphic rocks in an orogen provide a first-order constraint on how exhumation of the deep crust occurs. Exhumation of continental crust subducted to ultrahigh pressure conditions during collisional orogenesis is generally fast, at rates similar to plate velocities, and so cooling is also fast (Hermann et al., 2001; Rubatto and Hermann, 2001; Rubatto et al., 2001). Similarly, rates of cooling are commonly fast (generally ~20–30 °C/myr) during exhumation of metamorphic core complexes or due to exhumation by transpression (Brown and Dallmeyer, 1996; Scibiorski et al., 2015; Spear and Parrish, 1996), where the thermal length scale in some orogenic systems are comparatively small (Viete and Lister, 2017). By contrast, consistent with the findings o f Chapters 3 and 4 in this thesis, cooling in some granulite terranes may be slow and close-to-isobaric, leading to time-integrated rates of <5 °C/myr (Ashwal et al., 1999; Clark et al., 2018; Korhonen et al., 2013b; Mezger et al., 1991; Möller et al., 2000; Vry and Baker, 2006) over timescales approaching ~100 Ma (Clark et al., 2011; Sizova et al., 2014). The implication of such slow cooling rates is that these granulite terranes were never overthickened, thus limiting exhumation by erosion, but remained close to isostatic equilibrium with sustained high mantle heat flow and a high concentration of heat producing elements– HPEs (Bohlen, 1991; Sandiford and Powell, 1986).

The regions of continental crust associated with accretionary, collisional and additionally intraplate orogens all have different protoliths, a range of radiogenic heat production values, mantle heat flow and erosion rates. These factors determine the duration of orogenesis (Clark et al., 2011), a vital constraint on supercontinent assembly. Furthermore, the distribution of highly residual preconditioned crust may determine the regions of lower crust that are reworked during later continental collision.

Future studies may aim to constrain both the *Pressure–temperature–time* conditions and thermal drivers characteristic of accretionary, collisional and intraplate orogenesis and the role of each in the supercontinent cycle.

To achieve this, an analytical workflow of phase equilibrium modelling and geochronology could be applied to samples from preserved sections of the lower crust from accretionary, collisional and intraplate terranes.

5.5 | References

Ague, J. J., 1991, Evidence for major mass transfer and volume strain during regional metamorphism of pelites: Geology, v. 19, no. 8, p. 855-858.

Alessio, K. L., Hand, M., Kelsey, D. E., Williams, M. A., Morrissey, L. J., and Barovich, K., 2018, Conservation of deep crustal heat production: Geology, v. 46, no. 4, p. 335-338.

Ashwal, L. D., Tucker, R. D., and Zinner, E. K., 1999, Slow cooling of deep crustal granulites and Pb-loss in zircon: Geochimica et Cosmochimica Acta, v. 63, no. 18, p. 2839-2851.

Biswal, T. K., De Waele, B., and Ahuja, H., 2007, Timing and dynamics of the juxtaposition of the Eastern Ghats mobile belt against the Bhandara Craton, India: A structural and zircon U-Pb SHRIMP study of the fold-thrust belt and associated nepheline syenite plutons: Tectonics, v. 26, no. 4.

Bohlen, S. R., 1991, On the formation of granulites: Journal of Metamorphic Geology, v. 9, no. 3, p. 223-229.

Brown, M., and Dallmeyer, R. D., 1996, Rapid Variscan exhumation and the role of magma in core complex formation: southern Brittany metamorphic belt, France: Journal of metamorphic Geology, v. 14, no. 3, p. 361-379.

Carlson, W. D., Pattison, D. R., and Caddick, M. J., 2015, Beyond the equilibrium paradigm: How consideration of kinetics enhances metamorphic interpretation: American Mineralogist, v. 100, no. 8-9, p. 1659-1667.

Cawood, P. A., Kröner, A., Collins, W. J., Kusky, T. M., Mooney, W. D., and Windley, B. F., 2009, Accretionary orogens through Earth history: Geological Society, London, Special Publications, v. 318, no. 1, p. 1-36.

Clark, C., Fitzsimons, I. C. W., Healy, D., and Harley, S. L., 2011, How does the continental crust get really hot?: Elements, v. 7, no. 4, p. 235-240.

Clark, C., Taylor, R. J. M., Kylander-Clark, A. R. C., and Hacker, Bradley R., 2018, Prolonged (>100 Ma) ultrahigh temperature metamorphism in the Napier Complex, East Antarctica: A petrochronological

investigation of Earth's hottest crust: Journal of Metamorphic Geology, v. 36, no. 9, p. 1117-1139.

Dégi, J., Abart, R., Török, K., Bali, E., Wirth, R., and Rhede, D., 2010, Symplectite formation during decompression induced garnet breakdown in lower crustal mafic granulite xenoliths: mechanisms and rates: Contributions to Mineralogy and Petrology, v. 159, no. 3, p. 293-314.

Gaidies, F., Pattison, D., and De Capitani, C., 2011, Toward a quantitative model of metamorphic nucleation and growth: Contributions to Mineralogy and Petrology, v. 162, no. 5, p. 975.

Harley, S. L., 1998, On the occurrence and characterization of ultrahigh-temperature crustal metamorphism, Geological Society Special Publication, Volume 138, p. 81-107.

-, 2016, A matter of time: The importance of the duration of UHT metamorphism: Journal of Mineralogical and Petrological Sciences, v. 111, no. 2, p. 50-72.

Hermann, J., Rubatto, D., Korsakov, A., and Shatsky, V. S., 2001, Multiple zircon growth during fast exhumation of diamondiferous, deeply subducted continental crust (Kokchetav Massif, Kazakhstan): Contributions to Mineralogy and Petrology, v. 141, no. 1, p. 66-82.

Kelsey, D. E., and Hand, M., 2015, On ultrahigh temperature crustal metamorphism: Phase equilibria, trace element thermometry, bulk composition, heat sources, timescales and tectonic settings: Geoscience Frontiers, v. 6, no. 3, p. 311-356.

Korhonen, F. J., Brown, M., Clark, C., and Bhattacharya, S., 2013a, Osumilite-melt interactions in ultrahigh temperature granulites: Phase equilibria modelling and implications for the P-T-t evolution of the eastern ghats province, india: Journal of Metamorphic Geology, v. 31, no. 8, p. 881-907.

Korhonen, F. J., Brown, M., Clark, C., Foden, J. D., and Taylor, R., 2015, Are granites and granulites consanguineous?: Geology, v. 43, no. 11, p. 991-994.

Korhonen, F. J., Clark, C., Brown, M., Bhattacharya, S., and Taylor, R., 2013b, How long-lived is ultrahigh temperature (UHT) metamorphism? Constraints from zircon and monazite geochronology in the Eastern Ghats orogenic belt, India: Precambrian Research, v. 234, p. 322-350.

Korhonen, F. J., Clark, C., Brown, M., and Taylor, R. J. M., 2014, Taking the temperature of Earth's hottest crust: Earth and Planetary Science Letters, v. 408, p. 341-354.

Korhonen, F. J., Saw, A. K., Clark, C., Brown, M., and Bhattacharya, S., 2011, New constraints on UHT metamorphism in the Eastern Ghats Province through the application of phase equilibria modelling and in situ geochronology: Gondwana Research, v. 20, no. 4, p. 764-781.

Kumar, P. S., Menon, R., and Reddy, G. K., 2007, The role of radiogenic heat production in the thermal evolution of a Proterozoic granulite-facies orogenic belt: Eastern Ghats, Indian Shield: Earth and Planetary Science Letters, v. 254, no. 1-2, p. 39-54.

Li, Z.-X., Bogdanova, S., Collins, A., Davidson, A., De Waele, B., Ernst, R., Fitzsimons, I., Fuck, R., Gladkochub, D., and Jacobs, J., 2008, Assembly, configuration, and break-up history of Rodinia: a synthesis: Precambrian research, v. 160, no. 1-2, p. 179-210.

Merdith, A. S., Collins, A. S., Williams, S. E., Pisarevsky, S., Foden, J. D., Archibald, D. B., Blades, M. L., Alessio, B. L., Armistead, S., and Plavsa, D., 2017, A full-plate global reconstruction of the Neoproterozoic: Gondwana Research, v. 50, p. 84-134.

Mezger, K., Rawnsley, C., Bohlen, S., and Hanson, G., 1991, U-Pb garnet, sphene, monazite, and rutile ages: implications for the duration of high-grade metamorphism and cooling histories, Adirondack Mts., New York: The Journal of Geology, v. 99, no. 3, p. 415-428.

Möller, A., Mezger, K., and Schenk, V., 2000, U-Pb dating of metamorphic minerals: Pan-African metamorphism and prolonged slow cooling of high pressure granulites in Tanzania, East Africa: Precambrian Research, v. 104, no. 3-4, p. 123-146.

Pattison, D. R., and Spear, F. S., 2018, Kinetic control of staurolite–Al2SiO5 mineral assemblages: Implications for Barrovian and Buchan metamorphism: Journal of Metamorphic Geology, v. 36, no. 6, p. 667-690.

Pattison, D. R. M., de Capitani, C., and Gaidies, F., 2011, Petrological consequences of variations in metamorphic reaction affinity: Journal of Metamorphic Geology, v. 29, no. 9, p. 953-977.

Rosenberg, C., and Handy, M., 2005, Experimental deformation of partially melted granite revisited: implications for the continental crust:

Journal of metamorphic Geology, v. 23, no. 1, p. 19-28.

Rubatto, D., and Hermann, J. r., 2001, Exhumation as fast as subduction?: Geology, v. 29, no. 1, p. 3-6.

Rubatto, D., Williams, I. S., and Buick, I. S., 2001, Zircon and monazite response to prograde metamorphism in the Reynolds Range, central Australia: Contributions to Mineralogy and Petrology, v. 140, no. 4, p. 458-468.

Rudnick, R. L., and Fountain, D. M., 1995, Nature and composition of the continental crust: A lower crustal perspective: Reviews of Geophysics, v. 33, no. 3, p. 267-309.

Sandiford, M., and Powell, R., 1986, Deep crustal metamorphism during continental extension: modern and ancient examples: Earth and Planetary Science Letters, v. 79, no. 1-2, p. 151-158.

Schorn, S., Diener, J. F., Powell, R., and Stüwe, K., 2018, Thermal buffering in the orogenic crust: Geology, v. 46, no. 7, p. 643-646.

Scibiorski, E., Tohver, E., and Jourdan, F., 2015, Rapid cooling and exhumation in the western part of the Mesoproterozoic Albany-Fraser Orogen, Western Australia: Precambrian Research, v. 265, p. 232-248.

Sizova, E., Gerya, T., and Brown, M., 2014, Contrasting styles of Phanerozoic and Precambrian continental collision: Gondwana Research, v. 25, no. 2, p. 522-545.

Spear, F. S., and Parrish, R. R., 1996, Petrology and cooling rates of the Valhalla complex, British Columbia, Canada: Journal of Petrology, v. 37, no. 4, p. 733-765.

Spear, F. S., and Pattison, D. R., 2017, The implications of overstepping for metamorphic assemblage diagrams (MADs): Chemical Geology, v. 457, p. 38-46.

Stüwe, K., 1995, Thermal buffering effects at the solidus. Implications for the equilibration of partially melted metamorphic rocks: Tectonophysics, v. 248, no. 1-2, p. 39-51.

Thompson, A. B., and Connolly, J. A., 1995, Melting of the continental crust: some thermal and petrological constraints on anatexis in continental collision zones and other tectonic settings: Journal of Geophysical Research: Solid Earth, v. 100, no. B8, p. 15565-15579.

Trail, D., Watson, E. B., and Tailby, N. D., 2012, Ce and Eu anomalies in zircon as proxies for the oxidation state of magmas: Geochimica et Cosmochimica Acta, v. 97, p. 70-87.

Viete, D. R., and Lister, G. S., 2017, On the significance of short-duration regional metamorphism: Journal of the Geological Society, v. 174, no. 3, p. 377-392.

Vry, J. K., and Baker, J. A., 2006, LA-MC-ICPMS Pb-Pb dating of rutile from slowly cooled granulites: Confirmation of the high closure temperature for Pb diffusion in rutile: Geochimica et Cosmochimica Acta, v. 70, no. 7, p. 1807-1820.

Yakymchuk, C., and Brown, M., 2019, Divergent behaviour of Th and U during anatexis: Implications for the thermal evolution of orogenic crust: Journal of Metamorphic Geology, v. 37, no. 7, p. 899-916.

Bibliography

Ague, J. J., 1991, Evidence for major mass transfer and volume strain during regional metamorphism of pelites: Geology, v. 19, no. 8, p. 855-858.

-, 1994, Mass transfer during Barrovian metamorphism of pelites, south-central Connecticut; I, Evidence for changes in composition and volume: American Journal of Science, v. 294, no. 8, p. 989-1057.

-, 1997, Crustal mass transfer and index mineral growth in Barrow's garnet zone, northeast Scotland: Geology, v. 25, no. 1, p. 73-76.

Alessio, K. L., Hand, M., Kelsey, D. E., Williams, M. A., Morrissey, L. J., and Barovich, K., 2018, Conservation of deep crustal heat production: Geology, v. 46, no. 4, p. 335-338.

Ashwal, L. D., Tucker, R. D., and Zinner, E. K., 1999, Slow cooling of deep crustal granulites and Pb-loss in zircon: Geochimica et Cosmochimica Acta, v. 63, no. 18, p. 2839-2851.

Ayers, J. C., and Peters, T. J., 2018, Zircon/fluid trace element partition coefficients measured by recrystallization of Mud Tank zircon at 1.5 GPa and 800–1000° C: Geochimica et Cosmochimica Acta, v. 223, p. 60-74.

Baldwin, J., Powell, R., White, R., and Štípská, P., 2015, Using calculated chemical potential relationships to account for replacement of kyanite by symplectite in high pressure granulites: Journal of Metamorphic Geology, v. 33, no. 3, p. 311-330.

Beaumont, C., Jamieson, R. A., Nguyen, M. H., and Medvedev, S., 2004, Crustal channel flows: 1. Numerical models with applications to the tectonics of the Himalayan-Tibetan orogen: Journal of Geophysical Research B: Solid Earth, v. 109, no. 6, p. B06406 06401-06429.

Beaumont, C., Nguyen, M. H., Jamieson, R. A., and Ellis, S., 2006, Crustal flow modes in large hot orogens, in Law, R. D., Searle, M. P., and Godin, L., eds., Geological Society Special Publication, Volume 268, p. 91-145.

Bell, E. A., Boehnke, P., Barboni, M., and Harrison, T. M., 2019, Tracking chemical alteration in magmatic zircon using rare earth element abundances: Chemical Geology.

Belousova, E., Griffin, W. L., O'Reilly, S. Y., and Fisher, N., 2002,

Igneous zircon: trace element composition as an indicator of source rock type: Contributions to mineralogy and petrology, v. 143, no. 5, p. 602-622.

Bhattacharya, A., Das, H. H., Bell, E., Bhattacharya, A., Chatterjee, N., Saha, L., and Dutt, A., 2016, Restoration of Late Neoarchean–Early Cambrian tectonics in the Rengali orogen and its environs (eastern India): The Antarctic connection: Lithos, v. 263, p. 190-212.

Biswal, T. K., De Waele, B., and Ahuja, H., 2007, Timing and dynamics of the juxtaposition of the Eastern Ghats mobile belt against the Bhandara Craton, India: A structural and zircon U-Pb SHRIMP study of the fold-thrust belt and associated nepheline syenite plutons: Tectonics, v. 26, no. 4.

Black, L. P., Sheraton, J. W., and James, P. R., 1986, Late Archaean granites of the Napier Complex, Enderby Land, Antarctica: A comparison of Rb-Sr, Sm-Nd and U-Pb isotopic systematics in a complex terrain: Precambrian Research, v. 32, no. 4, p. 343-368.

Blereau, E., Johnson, T. E., Clark, C., Taylor, R. J. M., Kinny, P. D., and Hand, M., 2017, Reappraising the P–T evolution of the Rogaland–Vest Agder Sector, southwestern Norway: Geoscience Frontiers, v. 8, no. 1, p. 1-14.

Boehnke, P., Watson, E. B., Trail, D., Harrison, T. M., and Schmitt, A. K., 2013, Zircon saturation re-revisited: Chemical Geology, v. 351, p. 324-334.

Boger, S. D., Hirdes, W., Ferreira, C. A. M., Jenett, T., Dallwig, R., and Fanning, C. M., 2015, The 580-520Ma Gondwana suture of Madagascar and its continuation into Antarctica and Africa: Gondwana Research, v. 28, no. 3, p. 1048-1060.

Boger, S. D., Wilson, C. J. L., and Fanning, C. M., 2001, Early Paleozoic tectonism within the East Antarctic craton: The final suture between east and west Gondwana?: Geology, v. 29, no. 5, p. 463-466.

Bohlen, S. R., 1991, On the formation of granulites: Journal of Metamorphic Geology, v. 9, no. 3, p. 223-229.

Bose, S., Das, K., Torimoto, J., Arima, M., and Dunkley, D. J., 2016, Evolution of the Chilka Lake granulite complex, northern Eastern Ghats Belt, India: First evidence of ~ 780 Ma decompression of the deep crust and its implication on the India–Antarctica correlation: Lithos, v. 263, p. 161-189.

Brady, J. B., 1995, Diffusion data for silicate minerals, glasses, and liquids: Mineral Physics and Crystallography: A Handbook of Physical

Constants, v. 2, p. 269-290.

Brown, M., 2007, Metamorphism, Plate Tectonics, and the Supercontinent Cycle: Earth Science Frontiers, v. 14, no. 1, p. 1-18.

Brown, M., Averkin, Y. A., McLellan, E. L., and Sawyer, E. W., 1995, Melt segregation in migmatites: Journal of Geophysical Research: Solid Earth, v. 100, no. B8, p. 15655-15679.

Brown, M., and Dallmeyer, R. D., 1996, Rapid Variscan exhumation and the role of magma in core complex formation: southern Brittany metamorphic belt, France: Journal of metamorphic Geology, v. 14, no. 3, p. 361-379.

Brown, M., and Johnson, T. E., 2018, Secular change in metamorphism and the onset of global plate tectonics: American Mineralogist.

Carlson, W. D., 2006, Rates of Fe, Mg, Mn, and Ca diffusion in garnet: American Mineralogist, v. 91, no. 1, p. 1-11.

Carlson, W. D., Pattison, D. R., and Caddick, M. J., 2015, Beyond the equilibrium paradigm: How consideration of kinetics enhances metamorphic interpretation: American Mineralogist, v. 100, no. 8-9, p. 1659-1667.

Carson, C. J., Ague, J. J., and Coath, C. D., 2002, U-Pb geochronology from Tonagh Island, East Antarctica: Implications for the timing of ultra-high temperature metamorphism of the Napier Complex: Precambrian Research, v. 116, no. 3-4, p. 237-263.

Cavalcante, G. C. G., Viegas, G., Archanjo, C. J., and da Silva, M. E., 2016, The influence of partial melting and melt migration on the rheology of the continental crust: Journal of Geodynamics, v. 101, p. 186-199.

Cawood, P. A., Hawkesworth, C. J., and Dhuime, B., 2012, Detrital zircon record and tectonic setting: Geology, v. 40, no. 10, p. 875-878.

Cawood, P. A., Kröner, A., Collins, W. J., Kusky, T. M., Mooney, W. D., and Windley, B. F., 2009, Accretionary orogens through Earth history: Geological Society, London, Special Publications, v. 318, no. 1, p. 1-36.

Cawood, P. A., and Nemchin, A. A., 2001, Paleogeographic development of the east Laurentian margin: Constraints from U-Pb dating of detrital zircons in the Newfoundland Appalachians: Geological Society of America Bulletin, v. 113, no. 9, p. 1234-1246.

Cawood, P. A., Nemchin, A. A., and Strachan, R., 2007, Provenance record of Laurentian passive-margin strata in the northern Caledonides: Implications for paleodrainage and paleogeography: Bulletin of the Geological Society of America, v. 119, no. 7-8, p. 993-1003.

Chakraborty, S., 2008, Diffusion in solid silicates: a tool to track timescales of processes comes of age: Annu. Rev. Earth Planet. Sci., v. 36, p. 153-190.

Chakraborty, S., and Ganguly, J., 1992, Cation diffusion in aluminosilicate garnets: experimental determination in spessartine-almandine diffusion couples, evaluation of effective binary diffusion coefficients, and applications: Contributions to Mineralogy and petrology, v. 111, no. 1, p. 74-86.

Cherniak, D., 2010, Diffusion in accessory minerals: zircon, titanite, apatite, monazite and xenotime: Reviews in Mineralogy and Geochemistry, v. 72, no. 1, p. 827-869.

Cherniak, D., and Watson, E., 2001, Pb diffusion in zircon: Chemical Geology, v. 172, no. 1-2, p. 5-24.

Cherniak, D. J., 2000, Pb diffusion in rutile: Contributions to Mineralogy and Petrology, v. 139, no. 2, p. 198-207.

Clark, C., Fitzsimons, I. C. W., Healy, D., and Harley, S. L., 2011, How does the continental crust get really hot?: Elements, v. 7, no. 4, p. 235-240.

Clark, C., Healy, D., Johnson, T., Collins, A. S., Taylor, R. J., Santosh, M., and Timms, N. E., 2015, Hot orogens and supercontinent amalgamation: A Gondwanan example from southern India: Gondwana Research, v. 28, no. 4, p. 1310-1328.

Clark, C., Kinny, P. D., and Harley, S. L., 2012, Sedimentary provenance and age of metamorphism of the Vestfold Hills, East Antarctica: Evidence for a piece of Chinese Antarctica?: Precambrian Research, v. 196-197, p. 23-45.

Clark, C., Kirkland, C. L., Spaggiari, C. V., Oorschot, C., Wingate, M. T. D., and Taylor, R. J., 2014, Proterozoic granulite formation driven by mafic magmatism: An example from the Fraser Range Metamorphics, Western Australia: Precambrian Research, v. 240, p. 1-21.

Clark, C., Taylor, R. J. M., Kylander-Clark, A. R. C., and Hacker, Bradley R., 2018, Prolonged (>100 Ma) ultrahigh temperature metamorphism in

the Napier Complex, East Antarctica: A petrochronological investigation of Earth's hottest crust: Journal of Metamorphic Geology, v. 36, no. 9, p. 1117-1139.

Clarke, G. L., Daczko, N., Klepeis, K., and Rushmer, T., 2005, Roles for fluid and/or melt advection in forming high-P mafic migmatites, Fiordland, New Zealand: Journal of Metamorphic Geology, v. 23, no. 7, p. 557-567.

Cochrane, R., Spikings, R. A., Chew, D., Wotzlaw, J.-F., Chiaradia, M., Tyrrell, S., Schaltegger, U., and Van der Lelij, R., 2014, High temperature (> 350 C) thermochronology and mechanisms of Pb loss in apatite: Geochimica et Cosmochimica Acta, v. 127, p. 39-56.

Collins, A. S., Fitzsimons, I. C. W., Hulscher, B., and Razakamanana, T., 2003a, Structure of the eastern margin of the East African Orogen in central Madagascar: Precambrian Research, v. 123, no. 2-4, p. 111-133.

Collins, A. S., Kinny, P. D., and Razakamanana, T., 2012, Depositional age, provenance and metamorphic age of metasedimentary rocks from southern Madagascar: Gondwana Research, v. 21, no. 2-3, p. 353-361.

Collins, A. S., Kröner, A., Fitzsimons, I. C. W., and Razakamanana, T., 2003b, Detrital footprint of the Mozambique ocean: U-Pb SHRIMP and Pb evaporation zircon geochronology of metasedimentary gneisses in eastern Madagascar: Tectonophysics, v. 375, no. 1-4, p. 77-99.

Collins, A. S., Santosh, M., Braun, I., and Clark, C., 2007, Age and sedimentary provenance of the Southern Granulites, South India: U-Th-Pb SHRIMP secondary ion mass spectrometry: Precambrian Research, v. 155, no. 1-2, p. 125-138.

Compston, W., Williams, I., and Meyer, C., 1984, U-Pb geochronology of zircons from lunar breccia 73217 using a sensitive high mass-resolution ion microprobe: Journal of Geophysical Research: Solid Earth, v. 89, no. S02.

Connolly, J. A. D., and Thompson, A. B., 1989, Fluid and enthalpy production during regional metamorphism: Contributions to Mineralogy and Petrology, v. 102, no. 3, p. 347-366.

Corfu, F., Hanchar, J. M., Hoskin, P. W., and Kinny, P., 2003, Atlas of zircon textures: Reviews in mineralogy and geochemistry, v. 53, no. 1, p. 469-500.

Corfu, F., Heaman, L. M., and Rogers, G., 1994, Polymetamorphic

evolution of the Lewisian complex, NW Scotland, as recorded by U-Pb isotopic compositions of zircon, titanite and rutile: Contributions to Mineralogy and Petrology, v. 117, no. 3, p. 215-228.

Currie, C. A., and Hyndman, R. D., 2006, The thermal structure of subduction zone back arcs: Journal of Geophysical Research: Solid Earth, v. 111, no. B8, p. n/a-n/a.

Das, K., Bose, S., Karmakar, S., Dunkley, D. J., and Dasgupta, S., 2011, Multiple tectonometamorphic imprints in the lower crust: First evidence of ca. 950Ma (zircon U-Pb SHRIMP) compressional reworking of UHT aluminous granulites from the Eastern Ghats Belt, India: Geological Journal, v. 46, no. 2-3, p. 217-239.

Dasgupta, S., 1995, Pressure-temperature evolutionary history of the Eastern Ghats granulite province: recent advances and some thoughts: Memoirs - Geological Society of India, v. 34, p. 101-110.

Dasgupta, S., Bose, S., and Das, K., 2013, Tectonic evolution of the Eastern Ghats Belt, India: Precambrian Research, v. 227, p. 247-258.

Dégi, J., Abart, R., Török, K., Bali, E., Wirth, R., and Rhede, D., 2010, Symplectite formation during decompression induced garnet breakdown in lower crustal mafic granulite xenoliths: mechanisms and rates: Contributions to Mineralogy and Petrology, v. 159, no. 3, p. 293-314.

Dharma Rao, C. V., Santosh, M., and Chmielowski, R. M., 2012a, Sapphirine granulites from Panasapattu, Eastern Ghats belt, India: Ultrahigh-temperature metamorphism in a Proterozoic convergent plate margin: Geoscience Frontiers, v. 3, no. 1, p. 9-31.

Dharma Rao, C. V., Santosh, M., and Dong, Y., 2012b, U-Pb zircon chronology of the Pangidi-Kondapalle layered intrusion, Eastern Ghats belt, India: Constraints on Mesoproterozoic arc magmatism in a convergent margin setting: Journal of Asian Earth Sciences, v. 49, p. 362-375.

Diener, J., and Powell, R., 2012, Revised activity–composition models for clinopyroxene and amphibole: Journal of Metamorphic Geology, v. 30, no. 2, p. 131-142.

Diener, J. F., and Fagereng, Å., 2014, The influence of melting and melt drainage on crustal rheology during orogenesis: Journal of Geophysical Research: Solid Earth, v. 119, no. 8, p. 6193-6210.

Diener, J. F. A., White, R. W., and Powell, R., 2008, Granulite facies metamorphism and subsolidus fluid-absent reworking, Strangways Range, Arunta Block, central Australia: Journal of Metamorphic Geology, v. 26, no. 6, p. 603-622.

Dobmeier, C. J., and Raith, M. M., 2003, Crustal architecture and evolution of the Eastern Ghats Belt and adjacent regions of India, Geological Society Special Publication, Volume 206, p. 145-168.

Dohmen, R., and Chakraborty, S., 2003, Mechanism and kinetics of element and isotopic exchange mediated by a fluid phase: American Mineralogist, v. 88, no. 8-9, p. 1251-1270.

Dorfler, K. M., Caddick, M. J., and Tracy, R. J., 2015, Thermodynamic modeling of crustal melting using xenolith analogs from the Cortlandt Complex, New York, USA: Journal of Petrology, v. 56, no. 2, p. 389-408.

Doukkari, S. A., Diener, J. F., Ouzegane, K., and Kienast, J. R., 2018, Mineral equilibrium modelling and calculated chemical potential relations of reaction textures in the ultrahigh-temperature In Ouzzal terrane (In Hihaou area, Western Hoggar, Algeria): Journal of Metamorphic Geology, v. 36, no. 9, p. 1175-1198.

Dragovic, B., Guevara, V. E., Caddick, M. J., Baxter, E. F., and Kylander-Clark, A. R. C., 2016, A pulse of cryptic granulite-facies metamorphism in the Archean Wyoming Craton revealed by Sm–Nd garnet and U–Pb monazite geochronology: Precambrian Research, v. 283, p. 24-49.

Droop, G. R., and Bucher-Nurminen, K., 1984, Reaction textures and metamorphic evolution of sapphirine-bearing granulites from the Gruf Complex, Italian Central Alps: Journal of Petrology, v. 25, no. 3, p. 766-803.

Ferry, J. M., and Watson, E. B., 2007, New thermodynamic models and revised calibrations for the Ti-in-zircon and Zr-in-rutile thermometers: Contributions to Mineralogy and Petrology, v. 154, no. 4, p. 429-437.

Fitzsimons, I. C. W., 2000, A review of tectonic events in the east antarctic shield and their implications for gondwana and earlier supercontinents: Journal of African Earth Sciences, v. 31, no. 1, p. 3-23.

Foster, G., Kinny, P., Vance, D., Prince, C., and Harris, N., 2000, The significance of monazite U–Th–Pb age data in metamorphic assemblages; a combined study of monazite and garnet chronometry: Earth and Planetary Science Letters, v. 181, no. 3, p. 327-340.

Fraser, G., Ellis, D., and Eggins, S., 1997, Zirconium abundance in granulite-facies minerals, with implications for zircon geochronology in high-grade rocks: Geology, v. 25, no. 7, p. 607-610.

Fritz, H., Abdelsalam, M., Ali, K. A., Bingen, B., Collins, A. S., Fowler, A. R., Ghebreab, W., Hauzenberger, C. A., Johnson, P. R., Kusky, T. M., Macey, P., Muhongo, S., Stern, R. J., and Viola, G., 2013, Orogen styles in the East African Orogen: A review of the Neoproterozoic to Cambrian tectonic evolution: Journal of African Earth Sciences, v. 86, p. 65-106.

Fu, B., Page, F. Z., Cavosie, A. J., Fournelle, J., Kita, N. T., Lackey, J. S., Wilde, S. A., and Valley, J. W., 2008, Ti-in-zircon thermometry: applications and limitations: Contributions to Mineralogy and Petrology, v. 156, no. 2, p. 197-215.

Fyfe, W. S., and Turner, F. J., 1966, Reappraisal of the metamorphic facies concept: Contributions to Mineralogy and Petrology, v. 12, no. 4, p. 354-364.

Gaidies, F., Pattison, D., and De Capitani, C., 2011, Toward a quantitative model of metamorphic nucleation and growth: Contributions to Mineralogy and Petrology, v. 162, no. 5, p. 975.

Galli, A., Le Bayon, B., Schmidt, M. W., Burg, J. P., Caddick, M. J., and Reusser, E., 2011, Granulites and charnockites of the Gruf Complex: Evidence for Permian ultra-high temperature metamorphism in the Central Alps: Lithos, v. 124, no. 1-2, p. 17-45.

Gehrels, G., 2011, Detrital zircon U-Pb geochronology: Current methods and new opportunities: Tectonics of sedimentary basins: Recent advances, p. 45-62.

Gehrels, G., 2014, Detrital zircon U-Pb geochronology applied to tectonics, Annual Review of Earth and Planetary Sciences, Volume 42, Annual Reviews Inc., p. 127-149.

Geisler, T., Pidgeon, R. T., Kurtz, R., Van Bronswijk, W., and Schleicher, H., 2003, Experimental hydrothermal alteration of partially metamict zircon: American Mineralogist, v. 88, no. 10, p. 1496-1513.

Geisler, T., Schaltegger, U., and Tomaschek, F., 2007, Re-equilibration of zircon in aqueous fluids and melts: Elements, v. 3, no. 1, p. 43-50.

Green, E., White, R., Diener, J., Powell, R., Holland, T., and Palin, R.,

2016, Activity–composition relations for the calculation of partial melting equilibria in metabasic rocks: Journal of Metamorphic Geology, v. 34, no. 9, p. 845-869.

Grew, E. S., Carson, C. J., Christy, A. G., Maas, R., Yaxley, G. M., Boger, S. D., and Fanning, C. M., 2012, New constraints from U–Pb, Lu–Hf and Sm–Nd isotopic data on the timing of sedimentation and felsic magmatism in the Larsemann Hills, Prydz Bay, East Antarctica: Precambrian Research, v. 206, p. 87-108.

Grimes, C., Wooden, J., Cheadle, M., and John, B., 2015, "Fingerprinting" tectono-magmatic provenance using trace elements in igneous zircon: Contributions to Mineralogy and Petrology, v. 170, no. 5-6, p. 46.

Grimes, C. B., John, B. E., Kelemen, P., Mazdab, F., Wooden, J., Cheadle, M. J., Hanghøj, K., and Schwartz, J., 2007, Trace element chemistry of zircons from oceanic crust: A method for distinguishing detrital zircon provenance: Geology, v. 35, no. 7, p. 643-646.

Guevara, V.E., Caddick, M.J. (2016). Shooting at a moving target. Phase equilibrium modelling of high temperature metamorphism. Journal of Metamorphic Petrology, 34(3), 209-235.

Gupta, S., 2012, Strain localization, granulite formation and geodynamic setting of 'hot orogens': A case study from the Eastern Ghats Province, India: Geological Journal, v. 47, no. 2-3, p. 334-351.

Hacker, B. R., Gnos, E., Ratschbacher, L., Grove, M., McWilliams, M., Sobolev, S. V., Wan, J., and Wu, Z., 2000, Hot and dry deep crustal xenoliths from Tibet: Science, v. 287, no. 5462, p. 2463-2466.

Hacker, B. R., Ritzwoller, M. H., and Xie, J., 2014, Partially melted, mica-bearing crust in central tibet: Tectonics, v. 33, no. 7, p. 1408-1424.

Halpin, J. A., Clarke, G. L., White, R. W., and Kelsey, D. E., 2007a, Contrasting P-T-t paths for Neoproterozoic metamorphism in MacRobertson and Kemp Lands, east Antarctica: Journal of Metamorphic Geology, v. 25, no. 6, p. 683-701.

Halpin, J. A., Gerakiteys, C., Clarke, G., Belousova, E., and Griffin, W., 2005, In-situ U–Pb geochronology and Hf isotope analyses of the Rayner Complex, east Antarctica: Contributions to Mineralogy and Petrology, v. 148, no. 6, p. 689-706.

Halpin, J. A., White, R. W., Clarke, G. L., and Kelsey, D. E., 2007b, The Proterozoic P-T-t evolution of the Kemp Land Coast, East Antarctica; constraints from Si-saturated and Si-undersaturated metapelites: Journal of Petrology, v. 48, no. 7, p. 1321-1349.

Harley, S. L., 1989, The origins of granulites: A metamorphic perspective: Geological Magazine, v. 126, no. 3, p. 215-247.

-, 1994, Cordierite as a sensor of fluid and melt distribution in crustal metamorphism: Mineralogical Magazine, v. 58, no. 1, p. 374-375.

-, 1998a, On the occurrence and characterization of ultrahigh-temperature crustal metamorphism, Geological Society Special Publication, Volume 138, p. 81-107.

-, 1998b, Ultrahigh temperature granulite metamorphism (1050°C, 12 kbar) and decompression in garnet (Mg70) - orthopyroxene-sillimanite gneisses from the Rauer Group, East Antarctica: Journal of Metamorphic Geology, v. 16, no. 4, p. 541-562.

-, 2003, Archaean-Cambrian crustal development of East Antarctica: Metamorphic characteristics and tectonic implications, Geological Society Special Publication, Volume 206, p. 203-230.

-, 2008, Refining the P-T records of UHT crustal metamorphism: Journal of Metamorphic Geology, v. 26, no. 2, p. 125-154.

-, 2016, A matter of time: The importance of the duration of UHT metamorphism: Journal of Mineralogical and Petrological Sciences, v. 111, no. 2, p. 50-72.

Harley, S. L., Hensen, B. J., and Sheraton, J. W., 1990, Two-stage decompression in orthopyroxene–sillimanite granulites from Forefinger Point, Enderby Land, Antarctica: implications for the evolution of the Archaean Napier Complex: Journal of Metamorphic Geology, v. 8, no. 6, p. 591-613.

Harley, S. L., and Kelly, N. M., 2007, Zircon: Tiny but timely: Elements, v. 3, no. 1, p. 13-18.

Harley, S. L., Kelly, N. M., and Möller, A., 2007, Zircon behaviour and the thermal histories of moutain chains: Elements, v. 3, no. 1, p. 25-30.

Harley, S. L., and Nandakumar, V., 2016, New evidence for Palaeoproterozoic high grade metamorphism in the Trivandrum Block,

Southern India: Precambrian Research, v. 280, p. 120-138.

Harris, N., Caddick, M., Kosler, J., Goswami, S., Vance, D., and Tindle, A., 2004, The pressure–temperature–time path of migmatites from the Sikkim Himalaya: Journal of Metamorphic Geology, v. 22, no. 3, p. 249-264.

Henderson, B., Collins, A. S., Payne, J., Forbes, C., and Saha, D., 2014, Geologically constraining India in Columbia: The age, isotopic provenance and geochemistry of the protoliths of the Ongole Domain, Southern Eastern Ghats, India: Gondwana Research, v. 26, no. 3-4, p. 888-906.

Hermann, J., Rubatto, D., Korsakov, A., and Shatsky, V. S., 2001, Multiple zircon growth during fast exhumation of diamondiferous, deeply subducted continental crust (Kokchetav Massif, Kazakhstan): Contributions to Mineralogy and Petrology, v. 141, no. 1, p. 66-82.

Hess, K., and Dingwell, D. B., 1996, Viscosities of hydrous leucogranitic melts: A non-Arrhenian model: American Mineralogist: Journal of Earth and Planetary Materials, v. 81, no. 9-10, p. 1297-1300.

Hier-Majumder, S., Leo, P. H., and Kohlstedt, D. L., 2004, On grain boundary wetting during deformation: Acta materialia, v. 52, no. 12, p. 3425-3433.

Hier-Majumder, S., Ricard, Y., and Bercovici, D., 2006, Role of grain boundaries in magma migration and storage: Earth and Planetary Science Letters, v. 248, no. 3-4, p. 735-749.

Hinthorne, J., Andersen, C., Conrad, R., and Lovering, J., 1979, Single-grain 207Pb206Pb and U/Pb age determinations with a 10-μm spatial resolution using the ion microprobe mass analyzer (IMMA): Chemical Geology, v. 25, no. 4, p. 271-303.

Hippe, K., Möller, A., von Quadt, A., Peytcheva, I., and Hammerschmidt, K., 2016, Zircon geochronology of the Koraput alkaline complex: Insights from combined geochemical and U-Pb-Hf isotope analyses, and implications for the timing of alkaline magmatism in the Eastern Ghats Belt, India: Gondwana Research, v. 34, p. 205-220.

Hobbs, B. E., Ord, A., and Regenauer-Lieb, K., 2011, The thermodynamics of deformed metamorphic rocks: a review: Journal of Structural Geology, v. 33, no. 5, p. 758-818.

Hokada, T., and Harley, S. L., 2004, Zircon growth in UHT leucosome:

Constraints from zircon-garnet rare earth elements (REE) relations in Napier Complex, East Antarctica: Journal of Mineralogical and Petrological Sciences, v. 99, no. 4, p. 180-190.

Hokada, T., Harley, S. L., Dunkley, D. J., Kelly, N. M., and Yokoyama, K., 2016, Peak and post-peak development of UHT metamorphism at Mather Peninsula, Rauer Islands: Zircon and monazite U-Th-Pb and REE chemistry constraints: Journal of Mineralogical and Petrological Sciences, v. 111, no. 2, p. 89-103.

Hokada, T., Misawa, K., Yokoyama, K., Shiraishi, K., and Yamaguchi, A., 2004, SHRIMP and electron micropobe chronology of UHT metamorphism in the Napier Complex, East Antarctica: Implications for zircon growth at >1,000 °C: Contributions to Mineralogy and Petrology, v. 147, no. 1, p. 1-20.

Holder, R. M., Hacker, B. R., Horton, F., and Rakotondrazafy, A. M., 2018, Ultrahigh-temperature osumilite gneisses in southern Madagascar record combined heat advection and high rates of radiogenic heat production in a long-lived high-T orogen: Journal of Metamorphic Geology, v. 36, no. 7, p. 855-880.

Holland, T., and Powell, R., 2003, Activity–composition relations for phases in petrological calculations: an asymmetric multicomponent formulation: Contributions to Mineralogy and Petrology, v. 145, no. 4, p. 492-501.

Holland, T. I. M., and Powell, R., 2001, Calculation of phase relations involving haplogranitic melts using an internally consistent thermodynamic dataset: Journal of Petrology, v. 42, no. 4, p. 673-683.

Holland, T. J. B., and Powell, R., 1990, An enlarged and updated internally consistent thermodynamic dataset with uncertainties and correlations: the system K2O–Na2O–CaO–MgO–MnO–FeO–Fe2O3–Al2O3–TiO2–SiO2–C–H2–O2: Journal of Metamorphic Geology, v. 8, no. 1, p. 89-124.

-, 2011, An improved and extended internally consistent thermodynamic dataset for phases of petrological interest, involving a new equation of state for solids: Journal of Metamorphic Geology, v. 29, no. 3, p. 333-383.

Holtz, F., Roux, J., Ohlhorst, S., Behrens, H., and Schulze, F., 1999, The effects of silica and water on the viscosity of hydrous quartzofeldspathic melts: American Mineralogist, v. 84, no. 1-2, p. 27-36.

Horie, K., Hokada, T., Hiroi, Y., Motoyoshi, Y., and Shiraishi, K., 2012, Contrasting Archaean crustal records in western part of the Napier Complex, East Antarctica: New constraints from SHRIMP geochronology: Gondwana Research, v. 21, no. 4, p. 829-837.

Horton, F., Hacker, B., Kylander-Clark, A., Holder, R., and Jöns, N., 2016, Focused radiogenic heating of middle crust caused ultrahigh temperatures in southern Madagascar: Tectonics, v. 35, no. 2, p. 293-314.

Hoskin, P. W., 2005, Trace-element composition of hydrothermal zircon and the alteration of Hadean zircon from the Jack Hills, Australia: Geochimica et Cosmochimica Acta, v. 69, no. 3, p. 637-648.

Hyndman, R. D., 2015, Tectonic consequences of a uniformly hot backarc and why is the cordilleran mountain belt high?: Geoscience Canada, v. 42, no. 4, p. 383-402.

Hyndman, R. D., and Currie, C. A., 2011, Why is the North America Cordillera high? Hot backarcs, thermal isostasy, and mountain belts: Geology, v. 39, no. 8, p. 783-786.

Jackson, S. E., Pearson, N. J., Griffin, W. L., and Belousova, E. A., 2004, The application of laser ablation-inductively coupled plasma-mass spectrometry to in situ U–Pb zircon geochronology: Chemical Geology, v. 211, no. 1-2, p. 47-69.

Jamieson, R. A., and Beaumont, C., 2011, Coeval thrusting and extension during lower crustal ductile flow - implications for exhumation of high-grade metamorphic rocks: Journal of Metamorphic Geology, v. 29, no. 1, p. 33-51.

Jamieson, R. A., Beaumont, C., Medvedev, S., and Nguyen, M. H., 2004, Crustal channel flows: 2. Numerical models with implications for metamorphism in the Himalayan-Tibetan orogen: Journal of Geophysical Research B: Solid Earth, v. 109, no. 6, p. B06407 06401-06424.

Jamieson, R. A., Beaumont, C., Warren, C. J., and Nguyen, M. H., 2010, The Grenville Orogen explained? Applications and limitations of integrating numerical models with geological and geophysical data: Canadian Journal of Earth Sciences, v. 47, no. 4, p. 517-539.

Johnson, T., Brown, M., and White, R., 2010, Petrogenetic modelling of strongly residual metapelitic xenoliths within the southern Platreef, Bushveld Complex, South Africa: Journal of Metamorphic Geology, v. 28, no. 3, p. 269-

291.

Johnson, T. E., Gibson, R. L., Brown, M., Buick, I. S., and Cartwright, I., 2003, Partial melting of metapelitic rocks beneath the Bushveld Complex, South Africa: Journal of Petrology, v. 44, no. 5, p. 789-813.

Kamineni, D. C., and Rao, A. T., 1988, Sapphirine-Bearing Quartzite from the Eastern Ghats Granulite Terrain, Vizianagaram, India: The Journal of Geology, v. 96, no. 2, p. 209-220.

Kelly, N. M., Clarke, G. L., and Fanning, C. M., 2002, A two-stage evolution of the Neoproterozoic Rayner Structural Episode: New U-Pb sensitive high resolution ion microprobe constraints from the Oygarden Group, Kemp Land, East Antarctica: Precambrian Research, v. 116, no. 3-4, p. 307-330.

Kelly, N. M., and Harley, S. L., 2004, Orthopyroxene-corundum in Mg-Al-rich granulites from the Oygarden islands, East Antarctica: Journal of Petrology, v. 45, no. 7, p. 1481-1512.

-, 2005, An integrated microtextural and chemical approach to zircon geochronology: Refining the Archaean history of the Napier Complex, east Antarctica: Contributions to Mineralogy and Petrology, v. 149, no. 1, p. 57-84.

Kelsey, D. E., 2008, On ultrahigh-temperature crustal metamorphism: Gondwana Research, v. 13, no. 1, p. 1-29.

Kelsey, D. E., Clark, C., and Hand, M., 2008, Thermobarometric modelling of zircon and monazite growth in melt-bearing systems: Examples using model metapelitic and metapsammitic granulites: Journal of Metamorphic Geology, v. 26, no. 2, p. 199-212.

Kelsey, D. E., and Hand, M., 2015, On ultrahigh temperature crustal metamorphism: Phase equilibria, trace element thermometry, bulk composition, heat sources, timescales and tectonic settings: Geoscience Frontiers, v. 6, no. 3, p. 311-356.

Kelsey, D. E., Morrissey, L. J., Hand, M., Clark, C., Tamblyn, R., Gaehl, A. A., and Marshall, S., 2017, Significance of post-peak metamorphic reaction microstructures in the ultrahigh temperature Eastern Ghats Province, India: Journal of Metamorphic Geology, v. 35, no. 9, p. 1081-1109.

Kelsey, D. E., and Powell, R., 2011, Progress in linking accessory mineral growth and breakdown to major mineral evolution in metamorphic rocks:

A thermodynamic approach in the Na 2O-CaO-K 2O-FeO-MgO-Al 2O 3-SiO 2-H 2O-TiO 2-ZrO 2 system: Journal of Metamorphic Geology, v. 29, no. 1, p. 151-166.

Kinny, P., Black, L., and Sheraton, J., 1997, Zircon U-Pb ages and geochemistry of igneous and metamorphic rocks in the northern Prince Charles Mountains, Antarctica: AGSO Journal of Australian Geology and Geophysics, v. 16, no. 5, p. 637-654.

Kinny, P. D., Black, L. P., and Sheraton, J. W., 1993, Zircon ages and the distribution of Archaean and Proterozoic rocks in the Rauer Islands: Antarctic Science, v. 5, no. 2, p. 193-206.

Korhonen, F. J., Brown, M., Clark, C., and Bhattacharya, S., 2013a, Osumilite-melt interactions in ultrahigh temperature granulites: Phase equilibria modelling and implications for the P-T-t evolution of the eastern ghats province, india: Journal of Metamorphic Geology, v. 31, no. 8, p. 881-907.

Korhonen, F. J., Brown, M., Clark, C., Foden, J. D., and Taylor, R., 2015, Are granites and granulites consanguineous?: Geology, v. 43, no. 11, p. 991-994.

Korhonen, F. J., Clark, C., Brown, M., Bhattacharya, S., and Taylor, R., 2013b, How long-lived is ultrahigh temperature (UHT) metamorphism? Constraints from zircon and monazite geochronology in the Eastern Ghats orogenic belt, India: Precambrian Research, v. 234, p. 322-350.

Korhonen, F. J., Clark, C., Brown, M., and Taylor, R. J. M., 2014, Taking the temperature of Earth's hottest crust: Earth and Planetary Science Letters, v. 408, p. 341-354.

Korhonen, F. J., Saw, A. K., Clark, C., Brown, M., and Bhattacharya, S., 2011, New constraints on UHT metamorphism in the Eastern Ghats Province through the application of phase equilibria modelling and in situ geochronology: Gondwana Research, v. 20, no. 4, p. 764-781.

Korzhinskiĭ, D. S., 1959, Physicochemical basis of the analysis of the paragenesis of minerals, Consultants Bureau.

Kovach, V. P., Simmat, R., Rickers, K., Berezhnaya, N. G., Salnikova, E. B., Dobmeier, C., Raith, M. M., Yakovleva, S. Z., and Kotov, A. B., 2001, The Western Charnockite Zone of the Eastern Ghats Belt, India - An Independent Crustal Province of Late Archaean (2.8 Ga) and Palaeoproterozoic (1.7-1.6

Ga) Terrains: Gondwana Research, v. 4, no. 4, p. 666-667.

Kumar, P. S., Menon, R., and Reddy, G. K., 2007, The role of radiogenic heat production in the thermal evolution of a Proterozoic granulite-facies orogenic belt: Eastern Ghats, Indian Shield: Earth and Planetary Science Letters, v. 254, no. 1-2, p. 39-54.

Kunz, B. E., Regis, D., and Engi, M., 2018, Zircon ages in granulite facies rocks: decoupling from geochemistry above 850° C?: Contributions to Mineralogy and Petrology, v. 173, no. 3, p. 26.

Kusiak, M. A., Whitehouse, M. J., Wilde, S. A., Dunkley, D. J., Menneken, M., Nemchin, A. A., and Clark, C., 2013, Changes in zircon chemistry during archean UHT metamorphism in the Napier Complex, Antarctica: American Journal of Science, v. 313, no. 9, p. 933-967.

Li, X., Long, W., Li, Q., Liu, Y., Zheng, Y., Yang, Y., Chamberlain, K., Wan, D., Guo, C., and Wang, X., 2010, Penglai zircon megacryst: A potential new working reference for microbeam analysis of Hf-O isotopes and U-Pb age: Geostandard and Geoanalytical Research, v. 34: doi, v. 10, p. 117-134.

Li, Z.-X., Bogdanova, S., Collins, A., Davidson, A., De Waele, B., Ernst, R., Fitzsimons, I., Fuck, R., Gladkochub, D., and Jacobs, J., 2008, Assembly, configuration, and break-up history of Rodinia: a synthesis: Precambrian research, v. 160, no. 1-2, p. 179-210.

Liu, Y., Hu, Z., Zong, K., Gao, C., Gao, S., Xu, J., and Chen, H., 2010, Reappraisement and refinement of zircon U-Pb isotope and trace element analyses by LA-ICP-MS: Chinese Science Bulletin, v. 55, no. 15, p. 1535-1546.

MacQueen, J., Some methods for classification and analysis of multivariate observations, in Proceedings Proceedings of the fifth Berkeley symposium on mathematical statistics and probability1967, Volume 1, Oakland, CA, USA, p. 281-297.

McKenzie, D., and Priestley, K., 2008, The influence of lithospheric thickness variations on continental evolution: Lithos, v. 102, no. 1-2, p. 1-11.

Merdith, A. S., Collins, A. S., Williams, S. E., Pisarevsky, S., Foden, J. D., Archibald, D. B., Blades, M. L., Alessio, B. L., Armistead, S., and Plavsa, D., 2017, A full-plate global reconstruction of the Neoproterozoic: Gondwana Research, v. 50, p. 84-134.

Mezger, K., and Cosca, M. A., 1999, The thermal history of the

Eastern Ghats Belt (India) as revealed by U-Pb and 40Ar/39Ar dating of metamorphic and magmatic minerals: Implications for the SWEAT correlation: Precambrian Research, v. 94, no. 3-4, p. 251-271.

Mezger, K., and Krogstad, E., 1997, Interpretation of discordant U-Pb zircon ages: An evaluation: Journal of metamorphic Geology, v. 15, no. 1, p. 127-140.

Mezger, K., Rawnsley, C., Bohlen, S., and Hanson, G., 1991, U-Pb garnet, sphene, monazite, and rutile ages: implications for the duration of high-grade metamorphism and cooling histories, Adirondack Mts., New York: The Journal of Geology, v. 99, no. 3, p. 415-428.

Mikhalsky, E. V., Beliatsky, B. V., Sheraton, J. W., and Roland, N. W., 2006, Two distinct Precambrian terranes in the Southern Prince Charles Mountains, East Antarctica: SHRIMP dating and geochemical constraints: Gondwana Research, v. 9, no. 3, p. 291-309.

Mikhalsky, E. V., Sheraton, J. W., Laiba, A. A., and Beliatsky, B. V., 1996, Geochemistry and origin of Mesoproterozoic metavolcanic rocks from Fisher Massif, Prince Charles Mountains, East Antarctica: Antarctic Science, v. 8, no. 1, p. 85-104.

Mitchell, R. J., Johnson, T. E., Clark, C., Gupta, S., Brown, M., Harley, S. L., and Taylor, R., 2019, Neoproterozoic evolution and Cambrian reworking of ultrahigh temperature granulites in the Eastern Ghats Province, India: Journal of Metamorphic Geology, v. 37, no. 7, p. 977-1006.

Mohan, A., Tripathi, P., and Motoyoshi, Y., 1997, Reaction history of sapphirine granulites and a decompressional P-T path in a granulite complex from the Eastern Ghats: Proceedings of the Indian Academy of Sciences, Earth and Planetary Sciences, v. 106, no. 3, p. 115-129.

Möller, A., Mezger, K., and Schenk, V., 2000, U-Pb dating of metamorphic minerals: Pan-African metamorphism and prolonged slow cooling of high pressure granulites in Tanzania, East Africa: Precambrian Research, v. 104, no. 3-4, p. 123-146.

Morrissey, L. J., Hand, M., Kelsey, D. E., and Wade, B. P., 2016, Cambrian high-temperature reworking of the Rayner-Eastern ghats terrane: Constraints from the Northern Prince Charles Mountains region, East Antarctica: Journal of Petrology, v. 57, no. 1, p. 53-91.

Mungall, J. E., 2002, Empirical models relating viscosity and tracer

diffusion in magmatic silicate melts: Geochimica et Cosmochimica Acta, v. 66, no. 1, p. 125-143.

Nanda, J., Gupta, S., and Hacker, B., 2018, U-Pb zircon and titanite ages from granulites of the Koraput area–evidence for Columbia, Rodinia and Gondwana from the Eastern Ghats Province, India: Precambrian Research, v. 314, p. 394-413.

Nasdala, L., Zhang, M., Kempe, U., Panczer, G., Gaft, M., Andrut, M., and Plötze, M., 2003, Spectroscopic methods applied to zircon: Reviews in Mineralogy and Geochemistry, v. 53, no. 1, p. 427-467.

Nemchin, A. A., and Cawood, P. A., 2005, Discordance of the U–Pb system in detrital zircons: implication for provenance studies of sedimentary rocks: Sedimentary Geology, v. 182, no. 1-4, p. 143-162.

Ogilvie, P., and Gibson, R. L., 2017, Arrested development-a comparative analysis of multilayer corona textures in high-grade metamorphic rocks: Solid Earth, v. 8, no. 1, p. 93.

Palin, R. M., Weller, O. M., Waters, D. J., and Dyck, B., 2016, Quantifying geological uncertainty in metamorphic phase equilibria modelling; a Monte Carlo assessment and implications for tectonic interpretations: Geoscience Frontiers, v. 7, no. 4, p. 591-607.

Paton, C., Hellstrom, J., Paul, B., Woodhead, J., and Hergt, J., 2011, Iolite: Freeware for the visualisation and processing of mass spectrometric data: Journal of Analytical Atomic Spectrometry, v. 26, no. 12, p. 2508-2518.

Pattison, D. R., and Spear, F. S., 2018, Kinetic control of staurolite–Al2SiO5 mineral assemblages: Implications for Barrovian and Buchan metamorphism: Journal of Metamorphic Geology, v. 36, no. 6, p. 667-690.

Pattison, D. R. M., de Capitani, C., and Gaidies, F., 2011, Petrological consequences of variations in metamorphic reaction affinity: Journal of Metamorphic Geology, v. 29, no. 9, p. 953-977.

Perchuk, A., Safonov, O., Smit, C., Van Reenen, D., Zakharov, V., and Gerya, T., 2016, Precambrian ultra-hot orogenic factory: Making and reworking of continental crust: Tectonophysics.

Phillips, G., Wilson, C. J., Campbell, I., and Allen, C. M., 2006, U–Th–Pb detrital zircon geochronology from the southern Prince Charles mountains, east Antarctica—defining the Archaean to Neoproterozoic Ruker

province: Precambrian Research, v. 148, no. 3-4, p. 292-306.

Plavsa, D., Collins, A. S., Foden, J. D., and Clark, C., 2015, The evolution of a Gondwanan collisional orogen: A structural and geochronological appraisal from the Southern Granulite Terrane, South India: Tectonics, v. 34, no. 5, p. 820-857.

Plavsa, D., Collins, A. S., Foden, J. F., Kropinski, L., Santosh, M., Chetty, T. R. K., and Clark, C., 2012, Delineating crustal domains in Peninsular India: Age and chemistry of orthopyroxene-bearing felsic gneisses in the Madurai Block: Precambrian Research, v. 198-199, p. 77-93.

Plavsa, D., Collins, A. S., Payne, J. L., Foden, J. D., Clark, C., and Santosh, M., 2014, Detrital zircons in basement metasedimentary protoliths unveil the origins of southern India: Bulletin of the Geological Society of America, v. 126, no. 5-6, p. 791-812.

Powell, R., Evans, K., Green, E., and White, R., 2018, On equilibrium in non-hydrostatic metamorphic systems: Journal of Metamorphic Geology, v. 36, no. 4, p. 419-438.

Pownall, J. M., 2015, UHT metamorphism on Seram, eastern Indonesia: Reaction microstructures and P-T evolution of spinel-bearing garnet-sillimanite granulites from the Kobipoto Complex: Journal of Metamorphic Geology, v. 33, no. 9, p. 909-935.

Prakash, D., Singh, P. C., Singh, C. K., Tewari, S., Arima, M., and Frimmel, H. E., 2015, Reaction textures and metamorphic evolution of sapphirine-spinel-bearing and associated granulites from Diguva Sonaba, Eastern Ghats Mobile Belt, India: Geological Magazine, v. 152, no. 2, p. 316-340.

Rickers, K., Mezger, K., and Raith, M. M., 2001a, Evolution of the continental crust in the Proterozoic Eastern Ghats Belt, India and new constraints for Rodinia reconstruction: Implications from Sm-Nd, Rb-Sr and Pb-Pb isotopes: Precambrian Research, v. 112, no. 3-4, p. 183-210.

Rickers, K., Raith, M., and Dasgupta, S., 2001b, Multistage reaction textures in xenolithic high-MgAl granulites at Anakapalle, Eastern Ghats Belt, India: Examples of contact polymetamorphism and infiltration-driven metasomatism: Journal of Metamorphic Geology, v. 19, no. 5, p. 561-580.

Roberts, N. M., and Spencer, C. J., 2015, The zircon archive of continent formation through time: Geological Society, London, Special Publications, v.

389, no. 1, p. 197-225.

Rosenberg, C., and Handy, M., 2001, Mechanisms and orientation of melt segregation paths during pure shearing of a partially molten rock analog (norcamphor–benzamide): Journal of Structural Geology, v. 23, no. 12, p. 1917-1932.

-, 2005, Experimental deformation of partially melted granite revisited: implications for the continental crust: Journal of metamorphic Geology, v. 23, no. 1, p. 19-28.

Rubatto, D., 2002, Zircon trace element geochemistry: Partitioning with garnet and the link between U-Pb ages and metamorphism: Chemical Geology, v. 184, no. 1-2, p. 123-138.

Rubatto, D., and Gebauer, D., 2000, Use of cathodoluminescence for U-Pb zircon dating by ion microprobe: some examples from the Western Alps, Cathodoluminescence in geosciences, Springer, p. 373-400.

Rubatto, D., and Hermann, J., 2007, Experimental zircon/melt and zircon/garnet trace element partitioning and implications for the geochronology of crustal rocks: Chemical Geology, v. 241, no. 1-2, p. 38-61.

Rubatto, D., and Hermann, J. r., 2001, Exhumation as fast as subduction?: Geology, v. 29, no. 1, p. 3-6.

Rubatto, D., Williams, I. S., and Buick, I. S., 2001, Zircon and monazite response to prograde metamorphism in the Reynolds Range, central Australia: Contributions to Mineralogy and Petrology, v. 140, no. 4, p. 458-468.

Rudnick, R. L., and Fountain, D. M., 1995, Nature and composition of the continental crust: A lower crustal perspective: Reviews of Geophysics, v. 33, no. 3, p. 267-309.

Sajeev, K., Osanai, Y., and Santosh, M., 2004, Ultrahigh-temperature metamorphism followed by two-stage decompression of garnet-orthopyroxene-sillimanite granulites from Ganguvarpatti, Madurai block, southern India: Contributions to Mineralogy and Petrology, v. 148, no. 1, p. 29-46.

Sandiford, M., and Powell, R., 1986, Deep crustal metamorphism during continental extension: modern and ancient examples: Earth and Planetary Science Letters, v. 79, no. 1-2, p. 151-158.

Sarkar, G., Corfu, F., Paul, D., McNaughton, N., Gupta, S., and Bishui, P., 1993, Early Archean crust in Bastar Craton, Central India—a geochemical and isotopic study: Precambrian Research, v. 62, no. 1-2, p. 127-137.

Sarkar, S., Dasgupta, S., and Fukuoka, M., 2003, Petrological evolution of a suite of spinel granulites from Vizianagram, Eastern Ghats Belt, India, and genesis of sapphirine-bearing assemblages: Journal of Metamorphic Geology, v. 21, no. 9, p. 899-913.

Sarkar, T., and Schenk, V., 2014, Two-stage granulite formation in a Proterozoic magmatic arc (Ongole domain of the Eastern Ghats Belt, India): Part 1. Petrology and pressure-temperature evolution: Precambrian Research, v. 255, no. P1, p. 485-509.

-, 2016, Early Mesoproterozoic (1.6–1.5 Ga) granulite facies events in the Ongole domain: geodynamic significance and global correlation: Journal of Metamorphic Geology, v. 34, no. 8, p. 765-784.

Sarkar, T., Schenk, V., and Berndt, J., 2015, Formation and evolution of a Proterozoic magmatic arc: geochemical and geochronological constraints from meta-igneous rocks of the Ongole domain, Eastern Ghats Belt, India: Contributions to Mineralogy and Petrology, v. 169, no. 1, p. 1-27.

Sawant, A. D., Gupta, S., Clark, C., and Misra, S., 2017, The Rauer-Rengali connection in the Indo-Antarctica amalgam: Evidence from structure, metamorphism and geochronology, Geological Society Special Publication, Volume 457, Geological Society of London, p. 171-196.

Sawyer, E., 1996, Melt segregation and magma flow in migmatites: implications for the generation of granite magmas: Earth and Environmental Science Transactions of the Royal Society of Edinburgh, v. 87, no. 1-2, p. 85-94.

-, 2010, Migmatites formed by water-fluxed partial melting of a leucogranodiorite protolith: Microstructures in the residual rocks and source of the fluid: Lithos, v. 116, no. 3-4, p. 273-286.

Schorn, S., and Diener, J., 2017, Details of the gabbro-to-eclogite transition determined from microtextures and calculated chemical potential relationships: Journal of Metamorphic Geology, v. 35, no. 1, p. 55-75.

Schorn, S., Diener, J. F., Powell, R., and Stüwe, K., 2018, Thermal buffering in the orogenic crust: Geology, v. 46, no. 7, p. 643-646.

Schulze, F., Behrens, H., Holtz, F., Roux, J., and Johannes, W., 1996, The influence of H2O on the viscosity of a haplogranitic melt: American Mineralogist, v. 81, no. 9-10, p. 1155-1165.

Scibiorski, E., Tohver, E., and Jourdan, F., 2015, Rapid cooling and exhumation in the western part of the Mesoproterozoic Albany-Fraser Orogen, Western Australia: Precambrian Research, v. 265, p. 232-248.

Simmat, R., and Raith, M. M., 2008, U-Th-Pb monazite geochronometry of the Eastern Ghats Belt, India: Timing and spatial disposition of poly-metamorphism: Precambrian Research, v. 162, no. 1-2, p. 16-39.

Sizova, E., Gerya, T., and Brown, M., 2014, Contrasting styles of Phanerozoic and Precambrian continental collision: Gondwana Research, v. 25, no. 2, p. 522-545.

Sláma, J., Košler, J., Condon, D. J., Crowley, J. L., Gerdes, A., Hanchar, J. M., Horstwood, M. S. A., Morris, G. A., Nasdala, L., Norberg, N., Schaltegger, U., Schoene, B., Tubrett, M. N., and Whitehouse, M. J., 2008, Plešovice zircon - A new natural reference material for U-Pb and Hf isotopic microanalysis: Chemical Geology, v. 249, no. 1-2, p. 1-35.

Spear, F., 2014, The duration of near-peak metamorphism from diffusion modelling of garnet zoning: Journal of Metamorphic Geology, v. 32, no. 8, p. 903-914.

Spear, F. S., and Parrish, R. R., 1996, Petrology and cooling rates of the Valhalla complex, British Columbia, Canada: Journal of Petrology, v. 37, no. 4, p. 733-765.

Spear, F. S., and Pattison, D. R., 2017, The implications of overstepping for metamorphic assemblage diagrams (MADs): Chemical Geology, v. 457, p. 38-46.

Stacey, J. S., and Kramers, J. D., 1975, Approximation of terrestrial lead isotope evolution by a two-stage model: Earth and planetary science letters, v. 26, no. 2, p. 207-221.

Stern, R. A., 2001, A new isotopic and trace-element standard for the ion microprobe: preliminary thermal ionization mass spectrometry (TIMS) U-Pb and electron-microprobe data, Ressources naturelles Canada.

Stevens, G., and Clemens, J., 1993, Fluid-absent melting and the roles of

fluids in the lithosphere: a slanted summary?: Chemical Geology, v. 108, no. 1-4, p. 1-17.

Štípská, P., Powell, R., White, R., and Baldwin, J., 2010, Using calculated chemical potential relationships to account for coronas around kyanite: an example from the Bohemian Massif: Journal of Metamorphic Geology, v. 28, no. 1, p. 97-116.

Stüwe, K., 1995, Thermal buffering effects at the solidus. Implications for the equilibration of partially melted metamorphic rocks: Tectonophysics, v. 248, no. 1-2, p. 39-51.

Takei, Y., 2005, Deformation-induced grain boundary wetting and its effects on the acoustic and rheological properties of partially molten rock analogue: Journal of Geophysical Research: Solid Earth, v. 110, no. B12.

Taylor, R., Clark, C., and Reddy, S. M., 2012, The effect of grain orientation on secondary ion mass spectrometry (SIMS) analysis of rutile: Chemical Geology, v. 300-301, p. 81-87.

Taylor, R. J. M., Clark, C., Harley, S. L., Kylander-Clark, A. R. C., Hacker, B. R., and Kinny, P. D., 2017, Interpreting granulite facies events through rare earth element partitioning arrays: Journal of Metamorphic Geology, v. 35, no. 7, p. 759-775.

Taylor, R. J. M., Harley, S. L., Hinton, R. W., Elphick, S., Clark, C., and Kelly, N. M., 2015, Experimental determination of REE partition coefficients between zircon, garnet and melt: A key to understanding high-T crustal processes: Journal of Metamorphic Geology, v. 33, no. 3, p. 231-248.

Taylor, R. J. M., Kirkland, C. L., and Clark, C., 2016, Accessories after the facts: Constraining the timing, duration and conditions of high-temperature metamorphic processes: Lithos, v. 264, p. 239-257.

Thompson, A. B., and Connolly, J. A., 1995, Melting of the continental crust: some thermal and petrological constraints on anatexis in continental collision zones and other tectonic settings: Journal of Geophysical Research: Solid Earth, v. 100, no. B8, p. 15565-15579.

Thompson Jr, J. B., 1957a, The graphical analysis of mineral assemblages in pelitic schists: American Mineralogist: Journal of Earth and Planetary Materials, v. 42, no. 11-12, p. 842-858.

-, 1957b, The graphical analysis of mineral assemblages in pelitic

schists: Am. Mineral., v. 42, p. 842–858.

Thompson, P., Harley, S. L., and Carrington, D. P., 2001, The distribution of H 2 O–CO 2 between cordierite and granitic melt under fluid-saturated conditions at 5ákbar and 900á□ C: Contributions to Mineralogy and Petrology, v. 142, no. 1, p. 107-118.

Trail, D., Watson, E. B., and Tailby, N. D., 2012, Ce and Eu anomalies in zircon as proxies for the oxidation state of magmas: Geochimica et Cosmochimica Acta, v. 97, p. 70-87.

Upadhyay, D., Gerdes, A., and Raith, M. M., 2009, Unraveling sedimentary provenance and tectonothermal history of high-temperature metapelites, using zircon and monazite chemistry: A case study from the eastern ghats belt, India: Journal of Geology, v. 117, no. 6, p. 665-683.

Vanderhaeghe, O., and Teyssier, C., 2001, Partial melting and flow of orogens: Tectonophysics, v. 342, no. 3-4, p. 451-472.

Vavra, G., Gebauer, D., Schmid, R., and Compston, W., 1996, Multiple zircon growth and recrystallization during polyphase late carboniferous to triassic metamorphism in granulites of the Ivrea Zone (Southern Alps): An ion microprobe (SHRIMP) study: Contributions to Mineralogy and Petrology, v. 122, no. 4, p. 337-358.

Vavra, G., Schmid, R., and Gebauer, D., 1999, Internal morphology, habit and U-Th-Pb microanalysis of amphibolite-to-granulite facies zircons: Geochronology of the Ivrea Zone (Southern Alps): Contributions to Mineralogy and Petrology, v. 134, no. 4, p. 380-404.

Vermeesch, P., 2012, On the visualisation of detrital age distributions: Chemical Geology, v. 312, p. 190-194.

Viete, D. R., and Lister, G. S., 2017, On the significance of short-duration regional metamorphism: Journal of the Geological Society, v. 174, no. 3, p. 377-392.

Vry, J. K., and Baker, J. A., 2006, LA-MC-ICPMS Pb-Pb dating of rutile from slowly cooled granulites: Confirmation of the high closure temperature for Pb diffusion in rutile: Geochimica et Cosmochimica Acta, v. 70, no. 7, p. 1807-1820.

Walte, N. P., Bons, P. D., and Passchier, C. W., 2005, Deformation of melt-bearing systems—insight from in situ grain-scale analogue experiments:

Journal of Structural Geology, v. 27, no. 9, p. 1666-1679.

Wang, W., Liu, X., Zhao, Y., Zheng, G., and Chen, L., 2016, U-Pb zircon ages and Hf isotopic compositions of metasedimentary rocks from the Grove Subglacial Highlands, East Antarctica: Constraints on the provenance of protoliths and timing of sedimentation and metamorphism: Precambrian Research, v. 275, p. 135-150.

Waters, D. J., 2001, The significance of prograde and retrograde quartz-bearing intergrowth microstructures in partially melted granulite-facies rocks: Lithos, v. 56, no. 1, p. 108-110.

Watson, E. B., 1982, Melt infiltration and magma evolution: Geology, v. 10, no. 5, p. 236-240.

Watson, E. B., Harrison, T. M., and Ryerson, F. J., 1985, Diffusion of Sm, Sr, and Pb in fluorapatite: Geochimica et Cosmochimica Acta, v. 49, no. 8, p. 1813-1823.

Wetherill, G. W., 1956, Discordant uranium-lead ages, I: Eos, Transactions American Geophysical Union, v. 37, no. 3, p. 320-326.

Wheller, C. J., and Powell, R., 2014, A new thermodynamic model for sapphirine: Calculated phase equilibria in K2O-FeO-MgO-Al2O3-SiO2-H2O-TiO2-Fe2O3: Journal of Metamorphic Geology, v. 32, no. 3, p. 287-299.

White, R. W., and Powell, R., 2002, Melt loss and the preservation of granulite facies mineral assemblages: Journal of Metamorphic Geology, v. 20, no. 7, p. 621-632.

-, 2010, Retrograde melt-residue interaction and the formation of near-anhydrous leucosomes in migmatites: Journal of Metamorphic Geology, v. 28, no. 6, p. 579-597.

-, 2011, On the interpretation of retrograde reaction textures in granulite facies rocks: Journal of Metamorphic Geology, v. 29, no. 1, p. 131-149.

White, R. W., Powell, R., and Baldwin, J. A., 2008, Calculated phase equilibria involving chemical potentials to investigate the textural evolution of metamorphic rocks: Journal of Metamorphic Geology, v. 26, no. 2, p. 181-198.

White, R. W., Powell, R., and Clarke, G. L., 2002, The interpretation of reaction textures in Fe-rich metapelitic granulites of the Musgrave Block, Central Australia: Constraints from mineral equilibria calculations in the

system: Journal of Metamorphic Geology, v. 20, no. 1, p. 41-55.

White, R. W., Powell, R., and Holland, T. J. B., 2007, Progress relating to calculation of partial melting equilibria for metapelites: Journal of Metamorphic Geology, v. 25, no. 5, p. 511-527.

White, R. W., Powell, R., Holland, T. J. B., Johnson, T. E., and Green, E. C. R., 2014, New mineral activity-composition relations for thermodynamic calculations in metapelitic systems: Journal of Metamorphic Geology, v. 32, no. 3, p. 261-286.

Whitney, D. L., and Evans, B. W., 2010, Abbreviations for names of rock-forming minerals: American Mineralogist, v. 95, no. 1, p. 185-187.

Wiedenbeck, M., Alle, P., Corfu, F., Griffin, W., Meier, M., Oberli, F. v., Quadt, A. v., Roddick, J., and Spiegel, W., 1995, Three natural zircon standards for U-Th-Pb, Lu-Hf, trace element and REE analyses: Geostandards and Geoanalytical Research, v. 19, no. 1, p. 1-23.

Williams, S. E., Dietmar Müller, R., Landgrebe, T. C. W., and Whittaker, J. M., 2012, An open-source software environment for visualizing and refining plate tectonic reconstructions using high-resolution geological and geophysical data sets: GSA Today, v. 22, no. 4-5, p. 4-9.

Yakymchuk, C., and Brown, M., 2014, Behaviour of zircon and monazite during crustal melting: Journal of the Geological Society, v. 171, no. 4, p. 465-479.

Yakymchuk, C., and Brown, M., 2019, Divergent behaviour of Th and U during anatexis: Implications for the thermal evolution of orogenic crust: Journal of Metamorphic Geology, v. 37, no. 7, p. 899-916.

Yakymchuk, C., Clark, C., and White, R. W., 2017, Phase relations, reaction sequences and petrochronology: Reviews in Mineralogy and Geochemistry, v. 83, no. 1, p. 13-53.

Yakymchuk, C., and Godin, L., 2012, Coupled role of deformation and metamorphism in the construction of inverted metamorphic sequences: an example from far-northwest Nepal: Journal of Metamorphic Geology, v. 30, no. 5, p. 513-535.

Young, D., and Ellis, D., The intrusive Mawson charnockites: Evidence for a compressional plate margins of the Proterozoic mobile belt of East Antarctica, in Proceedings International symposium on Antarctic earth

sciences. 51991, p. 25-31.

Zhao, J. X., Ellis, D. J., Kilpatrick, J. A., and McCulloch, M. T., 1997, Geochemical and Sr-Nd isotopic study of charnockites and related rocks in the northern Prince Charles Mountains, East Antarctica: Implications for charnockite petrogenesis and proterozoic crustal evolution: Precambrian Research, v. 81, no. 1-2, p. 37-66.

Every reasonable effort has been made to acknowledge the owners of copyright material. I would be pelased to hear from any copyright owner who has been omitted or incorrectly acknowledged.

Appendix A | First author journal publications

Chapter 2 | Protolith heterogeneity, melt loss and the development of microstructures in granulites

Statement of authorship

Title: Mitchell, R. J., Johnson, T. E., Clark, C., Gupta, S., Brown, M., Harley, S. L., and Taylor, R., 2019, Protolith heterogeneity, melt loss and the development of microstructures in granulites: Journal of Metamorphic Geology, in review.

Status: Submitted (Journal of Metamorphic Geology, Wiley)

Author Contributions

By signing the Statement of Authorship, each author certifies that their stated contribution to the publication is accurate and that permission is granted for the publication to be included in the candidate's thesis.

Name of principal author (candidate): Ruairidh J. Mitchell
Contribution: Project design, phase equilibrium modelling, interpretation and drafting the manuscript
Overall percentage: 70%

Signature:  Date: 04/12/2019

Name of co-author: Tim E. Johnson
Contribution: Assisted with project design, phase equilibrium modelling, interpretation, and drafting the manuscript
Overall percentage: 10%

Signature:  Date: 04-12-2019

Name of co-author: Katy Evans
Contribution to the paper: Assisted with phase equilibrium modelling, interpretation and drafting the manuscript

Overall percentage: 10%

Signature: 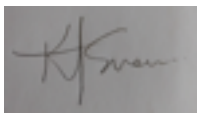 Date: 5-12-2019

Name of co-author: Saibal Gupta
Contribution to the paper: Assisted with the overall interpretation and drafting the manuscript
Overall percentage: 8%

Signature:  Date: 10-12-2019

Name of co-author: Chris Clark
Contribution to the paper: Supervised the project design
Overall percentage: 2%

Signature: 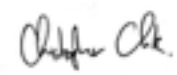 Date: 04-12-2019

Chapter 3 | Neoproterozoic evolution and Cambrian reworking of granulites from Vizianagaram, Eastern Ghats Province

Statement of authorship

Status: Published (Journal of Metamorphic Petrology, Wiley)

Mitchell, R. J., Johnson, T. E., Clark, C., Gupta, S., Brown, M., Harley, S. L., and Taylor, R., 2019, Neoproterozoic evolution and Cambrian reworking of ultrahigh temperature granulites in the Eastern Ghats Province, India: Journal of Metamorphic Geology, v. 37, no. 7, p. 977-1006.

Author Contributions

By signing the Statement of Authorship, each author certifies that their stated contribution to the publication is accurate and that permission is granted for the publication to be included in the candidate's thesis.

Name of principal author (candidate): Ruairidh J. Mitchell
Contribution: Sample descriptions, petrography, phase equilibrium modelling, LA-ICPMS analyses, overall interpretation, drafting the manuscript
Overall percentage: 60%

Signature: Date: 04/12/2019

Name of co-author: Tim E. Johnson
Contribution: Assisted with petrography, phase equilibrium modelling and the overall interpretation, and drafting the manuscript
Overall percentage: 10%

Signature: Date: 4-12-2019

Name of co-author: Chris Clark
Contribution: Fieldwork, assisted with geochronology, overall interpretation and drafting the manuscript
Overall percentage: 8%

Signature: Date: 4-12-2019

Name of co-author: Saibal Gupta
Contribution: Assisted with the overall interpretation and drafting the manuscript
Overall percentage: 5%

Signature: Date: 10-12-2019

Name of co-author: Michael Brown
Contribution: Fieldwork, assistance with the overall interpretation and drafting the manuscript
Overall percentage: 10%

Signature: Date: 4-12-2019

Name of co-author: Simon L. Harley
Contribution: Cordierite volatile SIMS analyses, assisted with the overall interpretation and drafting the manuscript
Overall percentage: 5%

Signature: Date: 4-12-2019

Name of co-author: Richard Taylor
Contribution: Zircon and monazite SHRIMP analyses and sample preparation
Overall percentage: 2%

Signature: Date: 4-12-2019

The John Wiley and Sons licence is attached.

JOHN WILEY AND SONS LICENSE
TERMS AND CONDITIONS

Dec 01, 2019

This Agreement between Ruairidh Mitchell ("You") and John Wiley and Sons ("John Wiley and Sons") consists of your license details and the terms and conditions provided by John Wiley and Sons and Copyright Clearance Center.

License Number	4711190197244
License date	Nov 17, 2019
Licensed Content Publisher	John Wiley and Sons
Licensed Content Publication	Journal of Metamorphic Geology
Licensed Content Title	Neoproterozoic evolution and Cambrian reworking of ultrahigh temperature granulites in the Eastern Ghats Province, India
Licensed Content Author	Richard Taylor, Simon L. Harley, Michael Brown, et al
Licensed Content Date	Oct 28, 2018
Licensed Content Volume	37

Licensed Content Issue	7
Licensed Content Pages	30
Type of use	Dissertation/Thesis
Requestor type	Author of this Wiley article
Format	Print and electronic
Portion	Full article
Will you be translating?	No
Title of your thesis / dissertation	UHT METAMORPHISM. CAN INTEGRATED THERMOBAROMETRY AND GEOCHRONOLOGY QUANTIFY LOWER CRUSTAL PROCESSES IN ULTRA-HOT OROGENS?
Expected completion date	Dec 2019
Expected size (number of pages)	200
Requestor Location	Ruairidh Mitchell Unit 312, 69 King George Street Victoria Park Perth, Western Australia 6100

Australia
Attn: Ruairidh Mitchell

Publisher Tax ID	EU826007151
Total	0.00 AUD

Terms and Conditions

TERMS AND CONDITIONS

This copyrighted material is owned by or exclusively licensed to John Wiley & Sons, Inc. or one of its group companies (each a"Wiley Company") or handled on behalf of a society with which a Wiley Company has exclusive publishing rights in relation to a particular work (collectively "WILEY"). By clicking "accept" in connection with completing this licensing transaction, you agree that the following terms and conditions apply to this transaction (along with the billing and payment terms and conditions established by the Copyright Clearance Center Inc., ("CCC's Billing and Payment terms and conditions"), at the time that you opened your RightsLink account (these are available at any time at http://myaccount.copyright.com).

Terms and Conditions

- The materials you have requested permission to reproduce or reuse (the "Wiley Materials") are protected by copyright.
- You are hereby granted a personal, non-exclusive, non-sub licensable (on a stand-alone basis), non-transferable, worldwide, limited license to reproduce the Wiley Materials for the purpose specified in the licensing process. This license, **and any CONTENT (PDF or image file) purchased as part of your order,** is for a one-time use only and limited to any maximum distribution number specified in the license. The first instance of republication or reuse granted by this license must be completed within two years of the date of the grant of this license (although copies prepared before the end date may be distributed thereafter). The Wiley Materials shall not be used in any other manner or for any other purpose, beyond what is granted in the license. Permission is granted subject to an appropriate acknowledgement given to the author, title of the material/book/journal and the publisher. You shall also duplicate the copyright notice that appears in the Wiley publication in your use of the Wiley Material. Permission is also granted on the understanding that nowhere in the text is a previously published source acknowledged for all or part of this Wiley Material. Any third party content is expressly excluded from this permission.

- With respect to the Wiley Materials, all rights are reserved. Except as expressly granted by the terms of the license, no part of the Wiley Materials may be copied, modified, adapted (except for minor reformatting required by the new Publication), translated, reproduced, transferred or distributed, in any form or by any means, and no derivative works may be made based on the Wiley Materials without the prior permission of the respective copyright owner.**For STM Signatory Publishers clearing permission under the terms of the STM Permissions Guidelines only, the terms of the license are extended to include subsequent editions and for editions in other languages, provided such editions are for the work as a whole in situ and does not involve the separate exploitation of the permitted figures or extracts,** You may not alter, remove or suppress in any manner any copyright, trademark or other notices displayed by the Wiley Materials. You may not license, rent, sell, loan, lease, pledge, offer as security, transfer or assign the Wiley Materials on a stand-alone basis, or any of the rights granted to you hereunder to any other person.

- The Wiley Materials and all of the intellectual property rights therein shall at all times remain the exclusive property of John Wiley & Sons Inc, the Wiley Companies, or their respective licensors, and your interest therein is only that of having possession of and the right to reproduce the Wiley Materials pursuant to Section 2 herein during the continuance of this Agreement. You agree that you own no right, title or interest in or to the Wiley Materials or any of the intellectual property rights therein. You shall have no rights hereunder other than the license as provided for above in Section 2. No right, license or interest to any trademark, trade name, service mark or other branding ("Marks") of WILEY or its licensors is granted hereunder, and you agree that you shall not assert any such right, license or interest with respect thereto

- NEITHER WILEY NOR ITS LICENSORS MAKES ANY WARRANTY OR REPRESENTATION OF ANY KIND TO YOU OR ANY THIRD PARTY, EXPRESS, IMPLIED OR STATUTORY, WITH RESPECT TO THE MATERIALS OR THE ACCURACY OF ANY INFORMATION CONTAINED IN THE MATERIALS, INCLUDING, WITHOUT LIMITATION, ANY IMPLIED WARRANTY OF MERCHANTABILITY, ACCURACY, SATISFACTORY QUALITY, FITNESS FOR A PARTICULAR PURPOSE, USABILITY, INTEGRATION OR NON-INFRINGEMENT AND ALL SUCH WARRANTIES ARE HEREBY EXCLUDED BY WILEY AND ITS LICENSORS AND WAIVED BY YOU.

- WILEY shall have the right to terminate this Agreement immediately upon breach of this Agreement by you.

- You shall indemnify, defend and hold harmless WILEY, its Licensors and their respective directors, officers, agents and employees, from and against any actual or threatened claims, demands, causes of action or proceedings arising from any breach of this Agreement by you.

- IN NO EVENT SHALL WILEY OR ITS LICENSORS BE LIABLE TO YOU OR ANY OTHER PARTY OR ANY OTHER PERSON OR ENTITY FOR ANY SPECIAL, CONSEQUENTIAL, INCIDENTAL, INDIRECT, EXEMPLARY OR PUNITIVE DAMAGES, HOWEVER CAUSED, ARISING OUT OF OR IN

CONNECTION WITH THE DOWNLOADING, PROVISIONING, VIEWING OR USE OF THE MATERIALS REGARDLESS OF THE FORM OF ACTION, WHETHER FOR BREACH OF CONTRACT, BREACH OF WARRANTY, TORT, NEGLIGENCE, INFRINGEMENT OR OTHERWISE (INCLUDING, WITHOUT LIMITATION, DAMAGES BASED ON LOSS OF PROFITS, DATA, FILES, USE, BUSINESS OPPORTUNITY OR CLAIMS OF THIRD PARTIES), AND WHETHER OR NOT THE PARTY HAS BEEN ADVISED OF THE POSSIBILITY OF SUCH DAMAGES. THIS LIMITATION SHALL APPLY NOTWITHSTANDING ANY FAILURE OF ESSENTIAL PURPOSE OF ANY LIMITED REMEDY PROVIDED HEREIN.

- Should any provision of this Agreement be held by a court of competent jurisdiction to be illegal, invalid, or unenforceable, that provision shall be deemed amended to achieve as nearly as possible the same economic effect as the original provision, and the legality, validity and enforceability of the remaining provisions of this Agreement shall not be affected or impaired thereby.

- The failure of either party to enforce any term or condition of this Agreement shall not constitute a waiver of either party's right to enforce each and every term and condition of this Agreement. No breach under this agreement shall be deemed waived or excused by either party unless such waiver or consent is in writing signed by the party granting such waiver or consent. The waiver by or consent of a party to a breach of any provision of this Agreement shall not operate or be construed as a waiver of or consent to any other or subsequent breach by such other party.

- This Agreement may not be assigned (including by operation of law or otherwise) by you without WILEY's prior written consent.

- Any fee required for this permission shall be non-refundable after thirty (30) days from receipt by the CCC.

- These terms and conditions together with CCC's Billing and Payment terms and conditions (which are incorporated herein) form the entire agreement between you and WILEY concerning this licensing transaction and (in the absence of fraud) supersedes all prior agreements and representations of the parties, oral or written. This Agreement may not be amended except in writing signed by both parties. This Agreement shall be binding upon and inure to the benefit of the parties' successors, legal representatives, and authorized assigns.

- In the event of any conflict between your obligations established by these terms and conditions and those established by CCC's Billing and Payment terms and conditions, these terms and conditions shall prevail.

- WILEY expressly reserves all rights not specifically granted in the combination of (i) the license details provided by you and accepted in the course of this licensing transaction, (ii) these terms and conditions and (iii) CCC's Billing and Payment terms and conditions.

- This Agreement will be void if the Type of Use, Format, Circulation, or Requestor Type was misrepresented during the licensing process.

- This Agreement shall be governed by and construed in accordance with the laws of the State of New York, USA, without regards to such state's conflict of law rules. Any legal action, suit or proceeding arising out of or relating to these Terms and Conditions or the breach thereof shall be instituted in a court of competent jurisdiction in New York County in the State of New York in the United States of America and each party hereby consents and submits to the personal jurisdiction of such court, waives any objection to venue in such court and consents to service of process by registered or certified mail, return receipt requested, at the last known address of such party.

WILEY OPEN ACCESS TERMS AND CONDITIONS

Wiley Publishes Open Access Articles in fully Open Access Journals and in Subscription journals offering Online Open. Although most of the fully Open Access journals publish open access articles under the terms of the Creative Commons Attribution (CC BY) License only, the subscription journals and a few of the Open Access Journals offer a choice of Creative Commons Licenses. The license type is clearly identified on the article.

The Creative Commons Attribution License

The Creative Commons Attribution License (CC-BY) allows users to copy, distribute and transmit an article, adapt the article and make commercial use of the article. The CC-BY license permits commercial and non-

Creative Commons Attribution Non-Commercial License

The Creative Commons Attribution Non-Commercial (CC-BY-NC)License permits use, distribution and reproduction in any medium, provided the original work is properly cited and is not used for commercial purposes.(see below)

Creative Commons Attribution-Non-Commercial-NoDerivs License

The Creative Commons Attribution Non-Commercial-NoDerivs License (CC-BY-NC-ND) permits use, distribution and reproduction in any medium, provided the original work is properly cited, is not used for commercial purposes and no modifications or adaptations are made. (see below)

Use by commercial "for-profit" organizations

Use of Wiley Open Access articles for commercial, promotional, or marketing purposes requires further explicit permission from Wiley and will be subject to a fee.

Further details can be found on Wiley Online Library
http://olabout.wiley.com/WileyCDA/Section/id-410895.html

Other Terms and Conditions:

v1.10 Last updated September 2015

Questions? customercare@copyright.com or +1-855-239-3415 (toll free in the US) or +1-978-646-2777.

Chapter 4 | Deciphering the zircon record in a long-lived granulite terrane

Statement of authorship

Status: in preparation

Mitchell, R. J., Johnson, T. E., Clark, C., Brown, M., Kirkland, C., Gupta, S., 2019, Deciphering the zircon record in a long-lived granulite terrane: in preparation.

Author Contributions

By signing the Statement of Authorship, each author certifies that their stated contribution to the publication is accurate and that permission is granted for the publication to be included in the candidate's thesis.

Name of principal author (candidate): Ruairidh J. Mitchell
Contribution to the paper: Fieldowork, sample descriptions and interpretation, sample preparation, SEM imaging, zircon LASS analysis, data processing, interpretation and drafting the manuscript
Overall percentage: 60%

Signature: Date: 04/12/2019

Name of co-author: Tim E. Johnson
Contribution to the paper: Fieldwork, assisted with the overall interpretation, and drafting the manuscript
Overall Percentage: 10%

Signature: Date: 4-12-2019

Name of co-author: Chris Clark
Contribution to the paper: Fieldwork, assisted with geochronology, overall interpretation interpretation and drafting the manuscript
Overall Percentage: 10%

Signature: Date: 4-12-2019

Name of co-author: Michael Brown
Contribution to the paper: Fieldwork, assistance with the overall interpretation and drafting the manuscript
Overall Percentage: 10%

Signature: Date: 4-12-2019

Name of co-author: Christopher Kirkland
Contribution to the paper: Assisted with geochronology, overall interpretation and drafting the manuscript
Overall Percentage: 5%

Signature: Date: 4-12-2019

Name of co-author: Saibal Gupta
Contribution to the paper: Fieldwork, assisted with the overall interpretation and drafting the manuscript
Overall Percentage: 5%

Signature: Date: 10-12-2019

Appendix B | Supplamentary information for Chapter 2: Controls on the scales of equilibrium during granulite facies metamorphism

B.1 | A petrogenetic grid calculated in the NKFMASH chemical system.

The fixed μK2O and μNa2O values are incurred when silicate melt in equilibrium with the 47-a residuum at P–T points 1-3. Henceforth, the univariant reaction lines are coloured black (point 1; 1000 °C, 7.6 kbar), blue (point 2; 1000 °C, 7.3 kbar) and green (point 3; 1000 °C, 7.0 kbar). Solid lines are SiO2 saturated univariant reactions and dotted lines are SiO2 undersaturated univariant reactions.

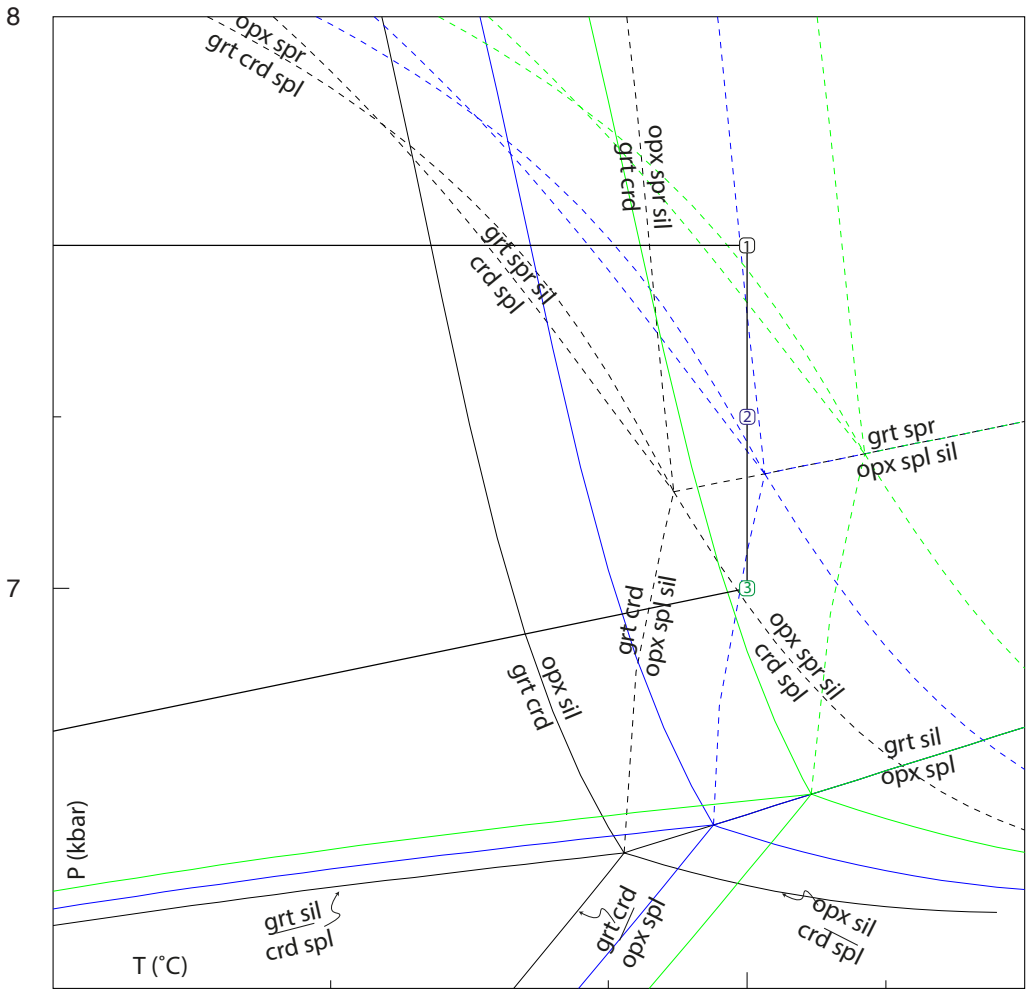

μ_{K2O} = -992.00 kJmol^{-1} μ_{Na2O} = -929.81 kJmol^{-1}

μ_{K2O} = -993.37 kJmol^{-1} μ_{Na2O} = -930.98 kJmol^{-1}

μ_{K2O} = -994.80 kJmol^{-1} μ_{Na2O} = -932.46 kJmol^{-1}

B.2 | A petrogenetic grid calculated in the NCKFMASH chemical system

The fixed μK2O and μNa2O values are incurred when silicate melt is in equilibrium with the 47-a residuum at P–T points 1-3. Henceforth, the univariant reaction lines are coloured black (point 1; 1000 °C, 7.6 kbar), blue (point 2; 1000 °C, 7.3 kbar) and green (point 3; 1000 °C, 7.0 kbar). Solid lines are SiO2 saturated univariant reactions and dotted lines are SiO2 undersaturated univariant reactions.

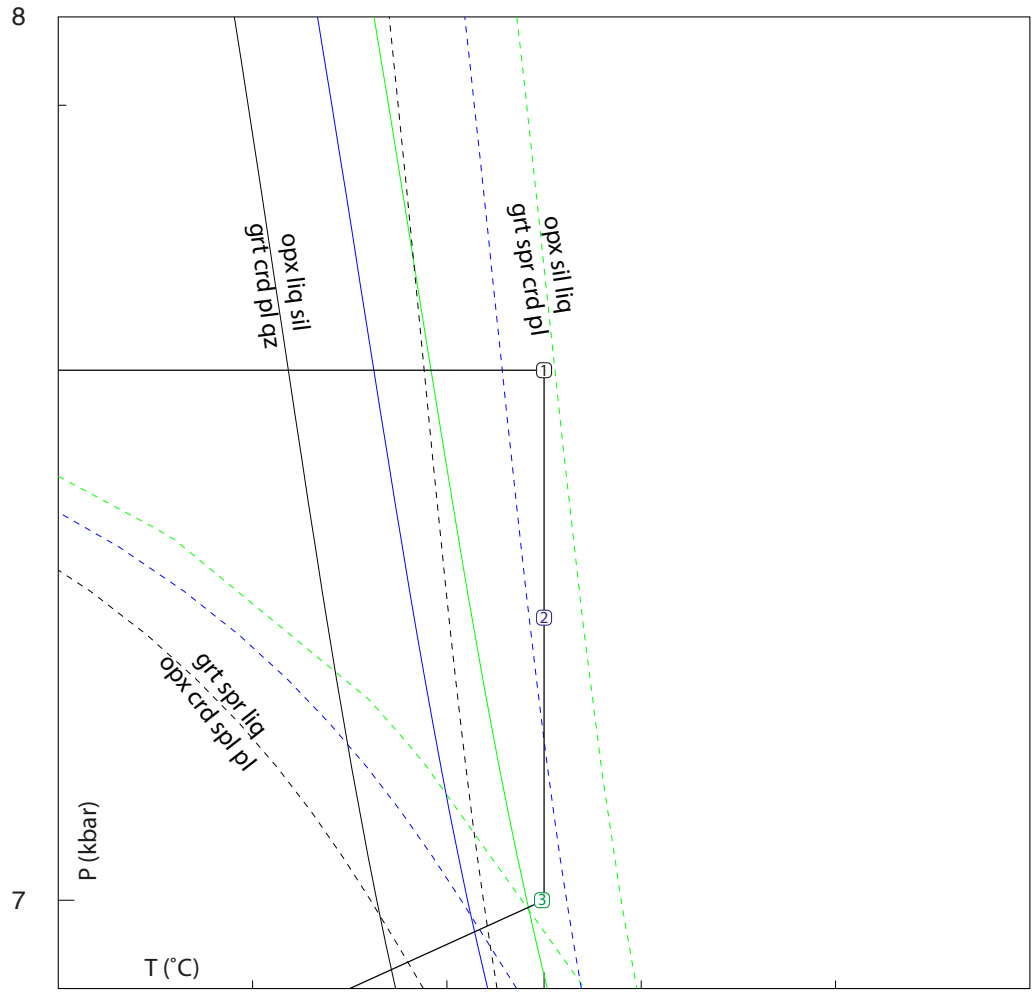

μ_{K2O} = -992.00 kJmol^{-1} μ_{Na2O} = -929.81 kJmol^{-1} 1000

μ_{K2O} = -993.37 kJmol^{-1} μ_{Na2O} = -930.98 kJmol^{-1}

μ_{K2O} = -994.80 kJmol^{-1} μ_{Na2O} = -932.46 kJmol^{-1}

Appendix C | Supplamentary information for Chapter 3: Neoproterozoic evolution and Cambrian reworking of granulites from Vizianagaram, Eastern Ghats Province

C.1 | Analytical protocol for phase mapping using the TESCAN TIMA FEG–SEM

TIMA HiRes liberation analysis protocol

Tescan TIMA3 FEG-SEM
MMF – John de Laeter Centre, Curtin University
500µm field width
50µm pixel width
1000 counts/pixel
4 PulseTor 30 EDX detectors
15µm working distance
25keV beam energy
0.05µm spot size

Polished thin sections of the samples were loaded into a TESCAN TIMA3 FEG-SEM at the John de Laeter Centre, Curtin University for automated HiRes liberation analyses. Each thin section contained 2960-3040 fields of 500µm width, each divided into pixels of 50µm were subject to 1000 counts per pixel. Four PulseTor 30 EDX detectors operated at a working distance of 15µm, with a beam energy of 25 keV and spot size of 0.05µm. BSE and elemental X-ray maps and gradient maps were calculated from the output and used with paramaterised X-ray intensity brackets from a mineral database to define phases in each pixel and phase boundaries in each field. The fields are then stitched together to form a thin section scale phase map.

C.2 | EPMA major element analysis for main phases in samples EGB-09-45, -47. Cations per formula unit (PFU).

PFU	Si	Ti	Al	Fe	Mn	Mg	Ca	Na	K	Cr	Ni	Total	O
Magnetite													
45-1	0.00	0.00	0.02	3.92	0.00	0.00	0.00	0.01	0.00	0.02	0.00	3.98	4
45-23	0.01	0.00	0.01	3.95	0.00	0.00	0.00	0.00	0.00	0.01	0.00	3.98	4
45-24	0.01	0.00	0.01	3.95	0.00	0.00	0.00	0.00	0.00	0.01	0.00	3.98	4
45-77	0.00	0.00	0.01	3.96	0.00	0.00	0.00	0.00	0.00	0.01	0.00	3.99	4
45-78	0.00	0.00	0.01	3.96	0.00	0.00	0.00	0.00	0.00	0.01	0.00	3.99	4
45-82	0.01	0.00	0.01	3.95	0.00	0.00	0.00	0.00	0.00	0.01	0.00	3.98	4
45-83	0.00	0.00	0.01	3.95	0.00	0.00	0.00	0.00	0.00	0.01	0.00	3.99	4
45-91	0.00	0.00	0.02	3.94	0.00	0.01	0.00	0.01	0.00	0.01	0.00	3.99	4
45-92	0.00	0.00	0.02	3.95	0.00	0.00	0.00	0.00	0.00	0.01	0.00	3.98	4
45-93	0.00	0.00	0.01	3.95	0.00	0.00	0.00	0.00	0.00	0.01	0.00	3.98	4
45-94	0.01	0.00	0.01	3.95	0.00	0.00	0.00	0.00	0.00	0.01	0.00	3.98	4
47A-36	0.00	0.00	0.01	3.91	0.00	0.01	0.00	0.00	0.00	0.03	0.01	3.97	4
Ilmenite													
45-5	0.00	0.36	0.01	2.23	0.00	0.01	0.00	0.00	0.00	0.01	0.00	2.62	3
45-6	0.00	0.87	0.00	1.20	0.00	0.04	0.00	0.00	0.00	0.00	0.00	2.13	3
45-8	0.00	0.24	0.01	2.48	0.00	0.00	0.00	0.00	0.00	0.01	0.00	2.74	3
45-9	0.00	0.37	0.01	2.20	0.00	0.02	0.00	0.00	0.00	0.01	0.00	2.62	3
45-10	0.00	0.96	0.00	1.05	0.01	0.01	0.00	0.00	0.00	0.00	0.00	2.03	3
45-11	0.00	0.39	0.00	2.18	0.00	0.01	0.00	0.00	0.00	0.01	0.00	2.60	3
45-12	0.00	0.39	0.01	2.17	0.00	0.02	0.00	0.01	0.00	0.01	0.00	2.60	3
45-17	0.00	0.96	0.00	1.06	0.01	0.00	0.00	0.00	0.00	0.00	0.00	2.04	3
45-19	0.00	0.33	0.01	2.30	0.00	0.01	0.00	0.01	0.00	0.01	0.00	2.67	3
45-44	0.00	0.34	0.01	2.28	0.00	0.02	0.00	0.00	0.00	0.01	0.00	2.66	3
45-45	0.00	0.46	0.00	2.02	0.00	0.02	0.00	0.01	0.00	0.01	0.00	2.53	3
45-46	0.00	0.34	0.00	2.28	0.00	0.01	0.00	0.01	0.00	0.01	0.00	2.66	3
45-79	0.00	0.96	0.00	1.00	0.01	0.06	0.00	0.00	0.00	0.00	0.00	2.03	3
45-80	0.00	0.53	0.00	1.90	0.00	0.03	0.00	0.00	0.00	0.00	0.00	2.47	3
45-81	0.00	0.34	0.01	2.29	0.00	0.01	0.00	0.00	0.00	0.00	0.00	2.65	3
45-86	0.00	0.93	0.00	1.08	0.01	0.05	0.00	0.00	0.00	0.00	0.00	2.07	3
45-87	0.00	0.94	0.00	1.05	0.01	0.05	0.00	0.00	0.00	0.00	0.00	2.06	3

45-88	0.00	0.90	0.00	1.14	0.01	0.04	0.00	0.00	0.00	0.00	0.00	2.10	3
45-100	0.00	0.64	0.00	1.70	0.00	0.01	0.00	0.00	0.00	0.00	0.00	2.36	3
47A-10	0.00	0.91	0.00	1.06	0.00	0.11	0.00	0.00	0.00	0.00	0.00	2.09	3
47A-11	0.00	0.95	0.00	0.96	0.00	0.12	0.00	0.00	0.00	0.00	0.00	2.05	3
47A-94	0.00	0.31	0.01	2.33	0.00	0.01	0.00	0.00	0.00	0.01	0.00	2.68	3
47A-125	0.00	0.93	0.00	1.05	0.00	0.07	0.00	0.00	0.00	0.00	0.00	2.06	3
47A-126	0.00	0.94	0.00	1.02	0.00	0.07	0.00	0.00	0.00	0.00	0.00	2.05	3
47A-152	0.00	0.95	0.00	0.97	0.00	0.12	0.00	0.00	0.00	0.00	0.00	2.05	3
47A-153	0.00	0.84	0.00	1.18	0.00	0.11	0.00	0.00	0.00	0.01	0.00	2.15	3
47A-209	0.00	0.92	0.00	1.01	0.00	0.13	0.00	0.00	0.00	0.00	0.00	2.07	3
47A-210	0.00	0.77	0.00	1.36	0.00	0.07	0.00	0.00	0.00	0.01	0.00	2.22	3
47A-244	0.00	0.93	0.00	0.98	0.01	0.14	0.00	0.00	0.00	0.00	0.00	2.06	3
47A-245	0.00	0.97	0.00	0.91	0.00	0.15	0.00	0.01	0.00	0.00	0.00	2.03	3
47B-10	0.03	0.96	0.01	0.91	0.01	0.09	0.00	0.00	0.00	0.00	0.00	2.01	3
47B-15	0.00	0.92	0.00	1.04	0.00	0.10	0.00	0.00	0.00	0.01	0.00	2.08	3
47B-16	0.00	0.94	0.00	1.04	0.01	0.07	0.00	0.01	0.00	0.01	0.00	2.06	3
47B-35	0.00	0.95	0.00	0.96	0.00	0.12	0.00	0.00	0.00	0.00	0.00	2.04	3
47B-134	0.00	0.94	0.00	1.00	0.00	0.10	0.00	0.00	0.00	0.00	0.00	2.06	3
47B-135	0.00	0.31	0.01	2.31	0.00	0.02	0.00	0.00	0.00	0.02	0.00	2.67	3
47B-160	0.00	0.94	0.00	0.98	0.00	0.12	0.00	0.00	0.00	0.00	0.00	2.06	3
47B-161	0.00	0.94	0.00	0.99	0.00	0.12	0.00	0.00	0.00	0.00	0.00	2.06	3
47B-172	0.00	0.88	0.00	1.14	0.00	0.07	0.00	0.00	0.00	0.00	0.00	2.11	3

Spinel													
45-3	0.00	0.00	1.95	0.65	0.00	0.40	0.00	0.00	0.00	0.01	0.00	3.01	4
45-4	0.00	0.00	1.95	0.66	0.01	0.39	0.00	0.00	0.00	0.01	0.00	3.02	4
45-84	0.00	0.00	1.96	0.56	0.01	0.48	0.00	0.00	0.00	0.01	0.00	3.01	4
45-85	0.01	0.00	1.96	0.54	0.01	0.47	0.00	0.00	0.00	0.01	0.00	3.00	4
45-89	0.00	0.00	1.96	0.59	0.00	0.46	0.00	0.00	0.00	0.01	0.00	3.02	4
45-90	0.00	0.00	1.95	0.58	0.00	0.48	0.00	0.00	0.00	0.01	0.00	3.02	4
45-96	0.00	0.00	1.95	0.61	0.00	0.45	0.00	0.00	0.00	0.00	0.00	3.02	4
45-97	0.00	0.01	1.95	0.60	0.00	0.45	0.00	0.00	0.00	0.00	0.00	3.01	4
47A-34	0.00	0.00	1.93	0.63	0.00	0.42	0.00	0.00	0.00	0.03	0.01	3.02	4
47A-35	0.00	0.00	1.93	0.64	0.00	0.41	0.00	0.00	0.00	0.03	0.01	3.02	4
47A-93	0.00	0.00	1.93	0.63	0.00	0.41	0.00	0.00	0.00	0.03	0.01	3.02	4
47A-95	0.01	0.00	1.99	0.59	0.00	0.36	0.00	0.00	0.00	0.03	0.01	2.98	4
47A-96	0.00	0.00	1.91	0.65	0.00	0.41	0.00	0.00	0.00	0.03	0.01	3.03	4
47A-97	0.01	0.00	1.84	0.77	0.00	0.39	0.00	0.00	0.00	0.03	0.01	3.05	4

47A-98	0.00	0.00	1.91	0.67	0.00	0.40	0.00	0.00	0.00	0.03	0.01	3.03	4
47A-127	0.00	0.00	1.92	0.49	0.00	0.55	0.00	0.00	0.00	0.05	0.01	3.01	4
47A-130	0.00	0.00	1.92	0.48	0.00	0.55	0.00	0.00	0.00	0.04	0.01	3.02	4
47A-131	0.00	0.00	1.91	0.54	0.00	0.51	0.00	0.00	0.00	0.04	0.01	3.02	4
47A-132	0.00	0.00	1.93	0.57	0.00	0.47	0.00	0.00	0.00	0.03	0.01	3.02	4
47A-133	0.00	0.00	1.94	0.57	0.00	0.46	0.00	0.00	0.00	0.03	0.01	3.01	4
47A-200	0.00	0.00	1.90	0.64	0.00	0.43	0.00	0.00	0.00	0.04	0.01	3.03	4
47A-214	0.00	0.00	1.88	0.51	0.00	0.56	0.00	0.00	0.00	0.06	0.01	3.03	4
47A-215	0.00	0.00	1.89	0.51	0.00	0.56	0.00	0.00	0.00	0.06	0.01	3.03	4
47B-11	0.00	0.00	1.90	0.52	0.00	0.54	0.00	0.00	0.00	0.05	0.01	3.03	4
47B-12	0.00	0.00	1.91	0.53	0.00	0.54	0.00	0.00	0.00	0.04	0.01	3.02	4
47B-52	0.00	0.00	1.87	0.55	0.00	0.55	0.00	0.00	0.00	0.05	0.01	3.04	4
47B-53	0.00	0.00	1.88	0.56	0.00	0.54	0.00	0.00	0.00	0.05	0.01	3.04	4
47B-99	0.00	0.00	1.88	0.50	0.00	0.57	0.00	0.00	0.00	0.06	0.01	3.03	4
47B-147	0.00	0.00	1.66	0.94	0.00	0.51	0.00	0.00	0.00	0.02	0.01	3.15	4
47B-164	0.00	0.00	1.87	0.42	0.00	0.63	0.00	0.00	0.00	0.09	0.01	3.02	4
47B-165	0.01	0.00	1.84	0.49	0.00	0.60	0.00	0.00	0.00	0.08	0.01	3.03	4
47B-170	0.00	0.00	1.90	0.51	0.00	0.58	0.00	0.00	0.00	0.03	0.01	3.03	4
47B-171	0.00	0.00	1.89	0.56	0.00	0.55	0.00	0.00	0.00	0.03	0.01	3.04	4

Sapphirine

47A-32	1.72	0.01	8.18	1.42	0.01	2.73	0.00	0.00	0.00	0.06	0.01	14.15	20
47A-33	1.69	0.01	8.27	1.35	0.01	2.75	0.00	0.00	0.00	0.06	0.01	14.14	20
47A-37	1.75	0.01	8.14	1.45	0.01	2.71	0.00	0.01	0.00	0.06	0.01	14.15	20
47A-90	1.70	0.01	8.19	1.43	0.01	2.74	0.00	0.00	0.00	0.06	0.01	14.17	20
47A-91	1.73	0.00	8.17	1.41	0.01	2.75	0.00	0.01	0.00	0.06	0.01	14.16	20
47A-92	1.63	0.01	8.37	1.34	0.01	2.72	0.00	0.00	0.00	0.06	0.01	14.15	20
47A-108	1.74	0.01	8.15	1.34	0.01	2.77	0.01	0.02	0.00	0.08	0.01	14.14	20
47A-109	0.61	0.00	9.19	2.32	0.01	2.42	0.00	0.01	0.00	0.13	0.03	14.73	20
47A-110	1.75	0.01	8.11	1.38	0.01	2.80	0.00	0.01	0.00	0.08	0.01	14.15	20
47A-111	1.65	0.00	8.40	1.20	0.00	2.78	0.00	0.00	0.00	0.05	0.01	14.12	20
47A-112	0.52	0.00	9.11	2.88	0.01	2.16	0.00	0.02	0.00	0.13	0.03	14.87	20
47A-128	1.73	0.01	8.14	1.41	0.01	2.78	0.00	0.01	0.00	0.07	0.01	14.16	20
47A-129	1.67	0.01	8.26	1.39	0.01	2.76	0.00	0.00	0.00	0.06	0.01	14.17	20
47A-134	1.67	0.00	8.24	1.31	0.01	2.83	0.00	0.01	0.00	0.09	0.01	14.17	20
47A-135	1.64	0.01	8.33	1.27	0.01	2.76	0.00	0.00	0.00	0.10	0.01	14.14	20
47A-136	1.64	0.01	8.34	1.27	0.01	2.75	0.00	0.00	0.00	0.10	0.01	14.13	20
47A-197	1.73	0.01	8.19	1.25	0.00	2.87	0.00	0.00	0.00	0.07	0.01	14.13	20
47A-198	1.72	0.01	8.19	1.24	0.00	2.87	0.00	0.00	0.00	0.08	0.01	14.13	20

47A-199	1.72	0.01	8.23	1.20	0.01	2.84	0.00	0.01	0.00	0.09	0.01	14.12	20
47A-239	1.71	0.01	8.16	1.36	0.01	2.73	0.01	0.08	0.01	0.10	0.01	14.20	20
47A-240	1.61	0.00	8.43	1.28	0.01	2.69	0.01	0.00	0.00	0.10	0.01	14.13	20
47A-241	1.85	0.01	7.94	1.38	0.01	2.86	0.00	0.00	0.00	0.07	0.01	14.14	20
47A-242	1.80	0.01	7.99	1.36	0.01	2.89	0.00	0.00	0.00	0.07	0.01	14.15	20
47A-243	1.76	0.01	8.08	1.34	0.01	2.85	0.00	0.01	0.00	0.09	0.01	14.15	20
47A-248	1.74	0.01	8.09	1.31	0.01	2.86	0.00	0.02	0.00	0.10	0.01	14.16	20
47A-249	1.71	0.01	8.13	1.30	0.01	2.89	0.00	0.01	0.00	0.10	0.01	14.17	20
47B-13	1.72	0.01	8.22	1.21	0.01	2.90	0.00	0.00	0.00	0.07	0.01	14.13	20
47B-100	1.81	0.01	8.01	1.29	0.01	2.89	0.00	0.03	0.00	0.08	0.01	14.15	20
47B-104	1.78	0.01	8.04	1.29	0.01	2.93	0.00	0.00	0.00	0.07	0.01	14.15	20
47B-130	1.77	0.01	8.04	1.40	0.01	2.86	0.00	0.01	0.00	0.06	0.01	14.17	20
47B-131	1.77	0.02	8.06	1.41	0.01	2.82	0.00	0.01	0.00	0.07	0.01	14.16	20
47B-132	1.72	0.01	8.15	1.38	0.01	2.83	0.00	0.00	0.00	0.06	0.01	14.17	20
47B-133	1.69	0.01	8.19	1.35	0.01	2.84	0.01	0.00	0.00	0.06	0.01	14.17	20

Orthopyroxene

45-26	1.76	0.01	0.41	0.75	0.01	1.08	0.00	0.01	0.00	0.00	0.00	4.03	6
45-27	1.77	0.01	0.38	0.76	0.01	1.09	0.00	0.02	0.00	0.00	0.00	4.04	6
45-28	1.76	0.01	0.40	0.75	0.01	1.09	0.00	0.01	0.00	0.00	0.00	4.03	6
45-29	1.77	0.01	0.39	0.75	0.01	1.10	0.00	0.00	0.00	0.00	0.00	4.03	6
45-30	1.77	0.01	0.40	0.75	0.01	1.09	0.00	0.00	0.00	0.00	0.00	4.03	6
45-31	1.81	0.00	0.32	0.76	0.01	1.12	0.00	0.01	0.00	0.00	0.00	4.04	6
45-32	1.75	0.01	0.42	0.75	0.01	1.09	0.00	0.01	0.00	0.00	0.00	4.04	6
45-34	1.77	0.00	0.39	0.74	0.01	1.10	0.00	0.00	0.00	0.00	0.00	4.03	6
45-35	1.76	0.00	0.41	0.74	0.01	1.11	0.00	0.01	0.00	0.00	0.00	4.04	6
45-36	1.77	0.01	0.40	0.73	0.01	1.11	0.00	0.01	0.00	0.00	0.00	4.03	6
45-37	1.79	0.00	0.36	0.75	0.01	1.11	0.00	0.01	0.00	0.00	0.00	4.03	6
45-101	1.76	0.01	0.41	0.73	0.01	1.11	0.00	0.00	0.00	0.00	0.00	4.03	6
45-102	1.77	0.00	0.40	0.70	0.01	1.12	0.00	0.00	0.00	0.00	0.00	4.02	6
45-103	1.75	0.00	0.43	0.73	0.01	1.09	0.00	0.00	0.00	0.00	0.00	4.03	6
45-104	1.77	0.01	0.40	0.72	0.01	1.11	0.00	0.00	0.00	0.00	0.00	4.02	6
45-105	1.75	0.01	0.43	0.74	0.01	1.09	0.00	0.00	0.00	0.00	0.00	4.03	6
45-106	1.80	0.01	0.33	0.72	0.01	1.14	0.00	0.00	0.00	0.00	0.00	4.02	6
45-107	1.75	0.00	0.44	0.72	0.01	1.10	0.00	0.00	0.00	0.00	0.00	4.03	6
45-108	1.79	0.00	0.37	0.71	0.01	1.13	0.00	0.00	0.00	0.00	0.00	4.02	6
47A-15	1.76	0.01	0.42	0.63	0.01	1.20	0.00	0.00	0.00	0.00	0.00	4.03	6
47A-16	1.78	0.01	0.39	0.62	0.00	1.21	0.00	0.00	0.00	0.00	0.00	4.02	6

47A-17	1.79	0.01	0.35	0.69	0.01	1.17	0.00	0.00	0.00	0.00	0.00	4.03	6
47A-18	1.80	0.01	0.34	0.68	0.01	1.19	0.00	0.00	0.00	0.00	0.00	4.03	6
47A-19	1.76	0.01	0.42	0.63	0.00	1.19	0.00	0.00	0.00	0.00	0.00	4.02	6
47A-20	1.80	0.01	0.36	0.62	0.00	1.21	0.00	0.00	0.00	0.00	0.00	4.01	6
47A-21	1.80	0.01	0.35	0.65	0.01	1.19	0.00	0.00	0.00	0.00	0.00	4.02	6
47A-22	1.79	0.01	0.36	0.65	0.01	1.19	0.00	0.00	0.00	0.00	0.00	4.02	6
47A-24	1.78	0.01	0.39	0.65	0.01	1.19	0.00	0.00	0.00	0.00	0.00	4.02	6
47A-25	1.78	0.01	0.37	0.66	0.01	1.21	0.00	0.00	0.00	0.00	0.00	4.03	6
47A-26	1.75	0.01	0.42	0.66	0.01	1.17	0.00	0.00	0.00	0.00	0.00	4.03	6
47A-27	1.77	0.01	0.40	0.67	0.00	1.18	0.00	0.01	0.00	0.00	0.00	4.03	6
47A-30	1.77	0.01	0.41	0.66	0.01	1.16	0.00	0.00	0.00	0.00	0.00	4.02	6
47A-31	1.79	0.01	0.37	0.65	0.01	1.19	0.00	0.00	0.00	0.00	0.00	4.02	6
47A-49	1.76	0.01	0.41	0.66	0.01	1.19	0.00	0.00	0.00	0.00	0.00	4.03	6
47A-50	1.80	0.01	0.35	0.64	0.01	1.20	0.00	0.01	0.00	0.00	0.00	4.02	6
47A-51	1.76	0.00	0.44	0.54	0.00	1.24	0.01	0.01	0.00	0.00	0.00	4.03	6
47A-75	1.79	0.01	0.35	0.65	0.01	1.22	0.00	0.00	0.00	0.00	0.00	4.03	6
47A-76	1.78	0.01	0.37	0.64	0.01	1.21	0.00	0.00	0.00	0.00	0.00	4.03	6
47A-78	1.80	0.01	0.33	0.64	0.00	1.22	0.00	0.00	0.00	0.00	0.00	4.02	6
47A-84	1.79	0.01	0.36	0.64	0.01	1.21	0.00	0.00	0.00	0.00	0.00	4.02	6
47A-171	1.77	0.01	0.39	0.67	0.01	1.17	0.00	0.00	0.00	0.00	0.00	4.02	6
47A-172	1.78	0.01	0.38	0.68	0.01	1.16	0.00	0.00	0.00	0.00	0.00	4.02	6
47A-173	1.78	0.01	0.37	0.68	0.01	1.17	0.00	0.00	0.00	0.00	0.00	4.03	6
47A-174	1.80	0.01	0.35	0.66	0.01	1.18	0.00	0.00	0.00	0.00	0.00	4.02	6
47A-175	1.81	0.01	0.32	0.66	0.01	1.21	0.00	0.00	0.00	0.00	0.00	4.02	6
47A-176	1.81	0.01	0.33	0.67	0.01	1.20	0.00	0.00	0.00	0.00	0.00	4.03	6
47A-177	1.82	0.00	0.32	0.64	0.01	1.21	0.00	0.00	0.00	0.01	0.00	4.02	6
47A-178	1.79	0.01	0.36	0.65	0.01	1.20	0.00	0.00	0.00	0.01	0.00	4.02	6
47A-179	1.81	0.00	0.33	0.66	0.01	1.20	0.00	0.01	0.00	0.00	0.00	4.03	6
47A-230	1.79	0.01	0.37	0.66	0.01	1.18	0.00	0.00	0.00	0.00	0.00	4.02	6
47A-231	1.77	0.01	0.40	0.66	0.01	1.16	0.00	0.00	0.00	0.00	0.00	4.02	6
47A-254	1.78	0.01	0.39	0.60	0.01	1.23	0.00	0.00	0.00	0.00	0.00	4.02	6
47B-91	1.82	0.00	0.31	0.61	0.01	1.26	0.00	0.00	0.00	0.00	0.00	4.02	6
47B-178	1.76	0.01	0.39	0.73	0.01	1.13	0.00	0.00	0.00	0.00	0.00	4.04	6
47B-179	1.76	0.01	0.37	0.73	0.01	1.14	0.00	0.00	0.00	0.00	0.00	4.04	6
47B-180	1.77	0.01	0.39	0.72	0.00	1.13	0.00	0.00	0.00	0.00	0.00	4.03	6
47B-181	1.77	0.01	0.39	0.70	0.01	1.14	0.00	0.00	0.00	0.00	0.00	4.03	6
47B-182	1.77	0.01	0.40	0.71	0.01	1.13	0.00	0.00	0.00	0.00	0.00	4.03	6
47B-183	1.80	0.01	0.34	0.72	0.01	1.15	0.00	0.00	0.00	0.00	0.00	4.03	6
47B-201	1.78	0.01	0.38	0.70	0.01	1.15	0.00	0.00	0.00	0.00	0.00	4.03	6
47B-202	1.76	0.03	0.37	0.72	0.01	1.14	0.00	0.00	0.00	0.00	0.00	4.03	6
47B-217	1.82	0.00	0.32	0.62	0.01	1.24	0.00	0.00	0.00	0.00	0.00	4.02	6

Cordierite

45-2	5.04	0.00	3.88	0.38	0.01	1.68	0.01	0.01	0.01	0.00	0.00	11.02	18
45-71	5.09	0.00	3.88	0.37	0.01	1.62	0.00	0.00	0.00	0.00	0.00	10.97	18
45-72	5.04	0.00	3.89	0.34	0.01	1.69	0.00	0.05	0.01	0.00	0.00	11.04	18
45-73	5.04	0.00	3.90	0.33	0.01	1.72	0.00	0.01	0.00	0.00	0.00	11.01	18
45-74	5.05	0.00	3.90	0.33	0.00	1.70	0.00	0.02	0.00	0.00	0.00	11.01	18
45-75	5.06	0.00	3.89	0.37	0.00	1.65	0.00	0.00	0.00	0.01	0.00	10.99	18
45-76	5.05	0.01	3.88	0.37	0.01	1.69	0.00	0.01	0.00	0.00	0.00	11.01	18
45-115	5.04	0.00	3.90	0.32	0.00	1.73	0.00	0.00	0.00	0.00	0.00	11.01	18
47A-41	5.00	0.00	3.94	0.33	0.01	1.73	0.00	0.01	0.00	0.01	0.00	11.03	18
47A-44	5.02	0.00	3.94	0.32	0.00	1.69	0.00	0.03	0.00	0.00	0.00	11.02	18
47A-45	5.07	0.00	3.87	0.32	0.00	1.72	0.00	0.01	0.00	0.00	0.00	11.00	18
47A-46	4.95	0.01	3.47	0.84	0.00	1.95	0.07	0.01	0.02	0.00	0.01	11.33	18
47A-54	5.03	0.00	3.94	0.29	0.00	1.73	0.00	0.01	0.00	0.00	0.00	11.01	18
47A-68	5.08	0.00	3.88	0.32	0.00	1.69	0.00	0.02	0.00	0.00	0.00	10.99	18
47A-69	5.03	0.00	3.89	0.36	0.00	1.71	0.00	0.02	0.00	0.00	0.00	11.03	18
47A-70	5.06	0.00	3.88	0.34	0.00	1.70	0.00	0.02	0.00	0.00	0.00	11.01	18
47A-71	5.06	0.00	3.88	0.30	0.00	1.75	0.00	0.01	0.00	0.00	0.00	11.01	18
47A-86	4.94	0.00	4.15	0.28	0.01	1.57	0.01	0.01	0.00	0.00	0.00	10.99	18
47A-88	5.04	0.00	3.91	0.27	0.00	1.78	0.00	0.00	0.00	0.00	0.00	11.01	18
47A-89	5.05	0.00	3.89	0.27	0.00	1.79	0.00	0.01	0.00	0.00	0.00	11.01	18
47A-156	5.03	0.00	3.90	0.31	0.00	1.75	0.00	0.02	0.00	0.00	0.00	11.03	18
47A-157	5.07	0.00	3.88	0.31	0.00	1.73	0.00	0.02	0.00	0.00	0.00	11.01	18
47A-158	5.04	0.00	3.90	0.27	0.00	1.78	0.00	0.02	0.00	0.00	0.00	11.01	18
47A-168	5.05	0.00	3.91	0.32	0.00	1.72	0.00	0.01	0.00	0.00	0.00	11.00	18
47A-169	5.05	0.00	3.90	0.32	0.01	1.70	0.00	0.02	0.00	0.00	0.00	11.01	18
47A-170	5.04	0.00	3.91	0.33	0.01	1.71	0.00	0.02	0.00	0.00	0.00	11.02	18
47A-201	5.06	0.01	3.86	0.21	0.00	1.85	0.00	0.01	0.01	0.00	0.00	11.01	18
47A-205	5.05	0.01	3.87	0.22	0.00	1.84	0.00	0.01	0.00	0.00	0.00	11.01	18
47A-206	5.05	0.01	3.88	0.20	0.00	1.85	0.00	0.02	0.00	0.00	0.00	11.02	18
47A-218	5.28	0.00	3.67	0.21	0.00	1.70	0.00	0.02	0.00	0.01	0.00	10.90	18
47A-228	5.04	0.00	3.90	0.30	0.00	1.74	0.00	0.03	0.00	0.00	0.00	11.03	18
47A-229	5.03	0.00	3.90	0.29	0.00	1.76	0.00	0.02	0.00	0.00	0.00	11.02	18
47A-246	5.03	0.00	3.90	0.24	0.00	1.83	0.00	0.02	0.00	0.00	0.00	11.04	18
47A-247	5.04	0.00	3.91	0.23	0.00	1.80	0.00	0.01	0.00	0.00	0.00	11.01	18
47B-36	5.04	0.00	3.90	0.25	0.01	1.80	0.00	0.01	0.00	0.00	0.00	11.02	18
47B-39	5.06	0.00	3.86	0.22	0.00	1.86	0.00	0.01	0.00	0.00	0.00	11.01	18

47B-60	5.04	0.00	3.89	0.32	0.00	1.73	0.00	0.01	0.00	0.00	0.00	11.02	18
47B-72	5.02	0.00	3.94	0.33	0.01	1.70	0.00	0.01	0.00	0.00	0.00	11.01	18
47B-73	5.04	0.00	3.90	0.33	0.00	1.72	0.00	0.01	0.00	0.00	0.00	11.01	18
47B-74	5.07	0.00	3.88	0.29	0.00	1.73	0.00	0.01	0.00	0.00	0.00	10.99	18
47B-77	5.06	0.00	3.89	0.36	0.00	1.67	0.00	0.01	0.00	0.01	0.00	11.00	18
47B-78	5.06	0.00	3.90	0.36	0.00	1.65	0.00	0.01	0.00	0.00	0.00	10.99	18
47B-79	5.04	0.00	3.92	0.37	0.00	1.65	0.00	0.01	0.00	0.00	0.00	11.00	18
47B-80	5.38	0.00	3.56	0.33	0.00	1.33	0.00	0.09	0.38	0.00	0.00	11.07	18
47B-148	5.07	0.00	3.87	0.34	0.01	1.70	0.00	0.01	0.00	0.00	0.00	11.00	18
47B-149	5.10	0.00	3.85	0.34	0.00	1.68	0.00	0.01	0.00	0.00	0.00	10.98	18
47B-173	5.05	0.01	3.86	0.22	0.00	1.85	0.00	0.01	0.00	0.00	0.00	11.01	18
47B-208	5.06	0.00	3.85	0.26	0.00	1.80	0.00	0.04	0.02	0.00	0.00	11.04	18
47B-216	5.01	0.00	3.89	0.28	0.01	1.84	0.01	0.02	0.01	0.00	0.00	11.06	18

Garnet

45-13	3.02	0.00	1.96	1.59	0.07	1.28	0.07	0.01	0.00	0.00	0.00	8.00	12
45-14	3.02	0.00	1.96	1.61	0.06	1.26	0.08	0.00	0.00	0.00	0.00	8.01	12
45-21	3.01	0.00	1.96	1.61	0.06	1.29	0.07	0.02	0.00	0.00	0.00	8.02	12
45-22	3.00	0.00	1.98	1.71	0.08	1.14	0.10	0.01	0.00	0.00	0.00	8.02	12
45-25	3.03	0.00	1.95	1.70	0.08	1.16	0.08	0.00	0.00	0.01	0.00	8.00	12
45-39	3.01	0.00	1.97	1.63	0.07	1.25	0.07	0.00	0.00	0.00	0.00	8.01	12
45-41	3.01	0.00	1.95	1.64	0.07	1.25	0.07	0.02	0.01	0.01	0.00	8.02	12
47A-29	3.01	0.00	1.97	1.51	0.04	1.38	0.09	0.01	0.00	0.00	0.00	8.01	12
47A-114	3.02	0.00	1.97	1.66	0.05	1.20	0.10	0.00	0.00	0.01	0.00	8.00	12
47A-115	3.02	0.00	1.98	1.65	0.05	1.16	0.11	0.00	0.00	0.01	0.00	7.99	12
47A-138	3.02	0.00	1.96	1.52	0.04	1.37	0.09	0.00	0.00	0.00	0.00	8.00	12
47A-139	3.01	0.00	1.97	1.50	0.04	1.38	0.09	0.01	0.00	0.00	0.00	8.00	12
47A-140	3.02	0.00	1.96	1.51	0.04	1.40	0.08	0.00	0.00	0.00	0.00	8.00	12
47A-141	2.98	0.00	1.98	1.52	0.04	1.41	0.09	0.00	0.00	0.00	0.00	8.02	12
47A-142	3.00	0.00	1.98	1.50	0.04	1.40	0.09	0.00	0.00	0.01	0.00	8.01	12
47A-143	3.00	0.00	1.98	1.49	0.04	1.40	0.09	0.01	0.00	0.00	0.01	8.01	12
47A-144	3.00	0.00	1.98	1.50	0.04	1.40	0.08	0.00	0.00	0.00	0.00	8.01	12
47A-145	3.00	0.00	1.97	1.50	0.04	1.42	0.09	0.00	0.00	0.00	0.00	8.02	12
47A-146	3.00	0.00	1.97	1.49	0.04	1.42	0.08	0.00	0.00	0.00	0.00	8.01	12
47A-147	3.01	0.00	1.97	1.51	0.04	1.37	0.10	0.01	0.00	0.00	0.00	8.01	12
47A-148	3.02	0.00	1.96	1.52	0.04	1.36	0.10	0.00	0.00	0.00	0.00	8.00	12
47A-149	3.02	0.00	1.97	1.53	0.04	1.31	0.11	0.00	0.00	0.00	0.00	7.99	12
47A-216	3.02	0.00	1.95	1.46	0.04	1.44	0.09	0.00	0.00	0.01	0.00	8.00	12

47A-217	3.05	0.00	1.93	1.42	0.03	1.45	0.09	0.02	0.00	0.01	0.00	7.99	12
47A-219	3.01	0.00	1.96	1.47	0.04	1.42	0.10	0.01	0.00	0.00	0.00	8.01	12
47A-220	3.02	0.00	1.97	1.44	0.04	1.42	0.08	0.00	0.00	0.00	0.00	7.99	12
47A-221	3.00	0.00	1.98	1.45	0.03	1.43	0.09	0.01	0.00	0.01	0.00	8.01	12
47A-222	3.02	0.00	1.95	1.45	0.03	1.45	0.09	0.01	0.00	0.00	0.00	8.01	12
47A-223	3.03	0.00	1.92	1.46	0.03	1.46	0.09	0.01	0.00	0.00	0.00	8.01	12
47A-224	3.02	0.00	1.96	1.44	0.04	1.46	0.08	0.00	0.00	0.00	0.00	8.00	12
47A-225	3.04	0.00	1.94	1.42	0.04	1.43	0.09	0.02	0.01	0.00	0.00	8.00	12
47A-226	3.00	0.00	1.97	1.44	0.04	1.48	0.09	0.00	0.00	0.00	0.00	8.01	12
47A-227	3.03	0.00	1.95	1.43	0.03	1.46	0.09	0.00	0.00	0.00	0.00	8.00	12
47A-232	3.01	0.00	1.96	1.54	0.04	1.35	0.09	0.00	0.00	0.00	0.00	8.00	12
47A-233	3.01	0.00	1.97	1.53	0.04	1.35	0.08	0.00	0.00	0.01	0.00	8.00	12
47A-234	3.01	0.00	1.97	1.53	0.05	1.34	0.08	0.01	0.00	0.01	0.00	8.00	12
47A-235	3.02	0.00	1.95	1.58	0.05	1.30	0.09	0.01	0.00	0.00	0.00	8.00	12
47A-236	3.02	0.00	1.96	1.56	0.05	1.29	0.09	0.00	0.00	0.01	0.00	7.99	12
47A-255	3.02	0.00	1.98	1.54	0.05	1.28	0.11	0.03	0.00	0.00	0.00	8.00	12
47A-256	3.03	0.00	1.96	1.54	0.05	1.33	0.09	0.01	0.00	0.00	0.00	8.00	12
47A-257	3.01	0.00	1.97	1.53	0.04	1.33	0.10	0.01	0.00	0.00	0.00	8.00	12
47B-19	3.00	0.00	1.96	1.49	0.04	1.43	0.09	0.01	0.00	0.00	0.00	8.02	12
47B-20	3.00	0.00	1.97	1.47	0.04	1.44	0.09	0.00	0.00	0.00	0.00	8.01	12
47B-21	2.99	0.00	1.97	1.46	0.04	1.45	0.09	0.01	0.00	0.00	0.00	8.02	12
47B-22	2.99	0.00	1.98	1.47	0.04	1.46	0.09	0.01	0.00	0.00	0.00	8.03	12
47B-23	2.99	0.00	1.97	1.47	0.04	1.44	0.09	0.01	0.00	0.01	0.00	8.02	12
47B-24	3.00	0.00	1.98	1.45	0.04	1.45	0.09	0.00	0.00	0.01	0.00	8.01	12
47B-25	2.99	0.00	1.99	1.45	0.04	1.44	0.09	0.00	0.00	0.01	0.00	8.01	12
47B-26	2.98	0.00	1.99	1.47	0.03	1.45	0.09	0.00	0.00	0.01	0.00	8.02	12
47B-27	2.99	0.00	1.98	1.46	0.04	1.45	0.09	0.00	0.00	0.01	0.00	8.02	12
47B-28	2.99	0.00	1.98	1.48	0.04	1.41	0.09	0.01	0.00	0.00	0.00	8.02	12
47B-29	3.00	0.00	1.97	1.49	0.04	1.41	0.09	0.00	0.00	0.00	0.00	8.01	12
47B-30	3.00	0.00	1.97	1.48	0.04	1.43	0.09	0.00	0.00	0.00	0.00	8.01	12
47B-31	3.00	0.00	1.99	1.49	0.04	1.39	0.09	0.01	0.00	0.01	0.00	8.01	12
47B-32	3.00	0.00	1.96	1.50	0.04	1.41	0.09	0.01	0.00	0.00	0.00	8.02	12
47B-33	3.01	0.00	1.96	1.48	0.04	1.40	0.10	0.00	0.00	0.00	0.00	8.00	12
47B-34	3.01	0.00	1.98	1.47	0.04	1.39	0.09	0.00	0.00	0.01	0.00	7.99	12
47B-40	3.41	0.00	2.32	0.79	0.00	0.83	0.06	0.02	0.03	0.00	0.00	7.46	12
47B-42	3.00	0.00	1.98	1.60	0.04	1.28	0.10	0.00	0.00	0.00	0.00	8.01	12
47B-43	2.98	0.00	1.99	1.61	0.04	1.29	0.10	0.00	0.00	0.00	0.00	8.02	12
47B-44	2.99	0.00	2.00	1.66	0.05	1.20	0.10	0.00	0.00	0.00	0.00	8.01	12
47B-56	3.01	0.00	1.96	1.65	0.05	1.25	0.09	0.00	0.00	0.00	0.00	8.01	12
47B-57	3.00	0.00	1.97	1.63	0.05	1.26	0.09	0.00	0.00	0.00	0.00	8.01	12
47B-58	3.01	0.00	1.97	1.62	0.04	1.27	0.09	0.00	0.00	0.00	0.00	8.00	12

47B-83	2.99	0.00	1.98	1.40	0.03	1.53	0.09	0.00	0.00	0.00	0.00	8.02	12
47B-84	2.99	0.00	1.99	1.41	0.03	1.50	0.09	0.00	0.00	0.00	0.00	8.01	12
47B-85	2.99	0.00	1.99	1.44	0.04	1.47	0.09	0.00	0.00	0.01	0.00	8.01	12
47B-86	3.00	0.00	1.97	1.45	0.04	1.46	0.09	0.00	0.00	0.00	0.00	8.02	12
47B-87	3.00	0.00	1.98	1.47	0.04	1.41	0.09	0.01	0.00	0.00	0.00	8.01	12
47B-88	2.99	0.00	1.99	1.52	0.04	1.37	0.09	0.00	0.00	0.00	0.00	8.01	12
47B-90	3.34	0.00	2.41	0.50	0.00	1.14	0.04	0.02	0.02	0.00	0.00	7.48	12
47B-95	3.01	0.00	1.97	1.43	0.04	1.47	0.09	0.01	0.00	0.00	0.00	8.01	12
47B-102	3.00	0.00	1.96	1.48	0.04	1.43	0.10	0.00	0.00	0.00	0.00	8.01	12
47B-103	3.39	0.00	2.27	0.92	0.00	0.78	0.08	0.02	0.03	0.00	0.00	7.50	12
47B-136	3.01	0.00	1.97	1.57	0.04	1.32	0.08	0.02	0.00	0.00	0.00	8.01	12
47B-137	3.00	0.00	1.99	1.59	0.04	1.27	0.10	0.01	0.00	0.00	0.00	8.01	12
47B-140	3.00	0.00	1.97	1.47	0.04	1.44	0.09	0.00	0.00	0.00	0.00	8.01	12
47B-141	2.98	0.00	1.97	1.49	0.04	1.46	0.08	0.00	0.00	0.00	0.00	8.03	12
47B-142	3.00	0.00	1.97	1.47	0.04	1.45	0.08	0.01	0.00	0.00	0.00	8.02	12
47B-143	2.99	0.00	1.98	1.47	0.04	1.45	0.09	0.00	0.00	0.00	0.00	8.02	12
47B-144	3.00	0.00	1.97	1.47	0.04	1.46	0.09	0.00	0.00	0.00	0.00	8.02	12
47B-145	3.00	0.00	1.97	1.47	0.04	1.44	0.09	0.01	0.00	0.00	0.00	8.01	12
47B-146	3.00	0.00	1.96	1.47	0.04	1.44	0.09	0.01	0.00	0.00	0.00	8.02	12
47B-154	3.00	0.00	1.98	1.67	0.05	1.21	0.09	0.00	0.00	0.00	0.00	8.01	12
47B-155	3.00	0.00	1.98	1.67	0.05	1.19	0.10	0.00	0.00	0.01	0.00	8.00	12
47B-167	3.00	0.00	1.97	1.45	0.04	1.45	0.09	0.00	0.00	0.01	0.00	8.01	12
47B-184	3.01	0.00	1.97	1.49	0.04	1.39	0.09	0.00	0.00	0.00	0.00	8.00	12
47B-185	3.02	0.01	1.96	1.49	0.04	1.39	0.09	0.00	0.00	0.00	0.00	8.00	12
47B-186	2.99	0.00	1.98	1.48	0.04	1.44	0.09	0.01	0.00	0.00	0.00	8.02	12
47B-189	3.01	0.00	1.98	1.38	0.03	1.51	0.08	0.00	0.00	0.01	0.00	8.00	12
47B-190	3.01	0.00	1.97	1.39	0.03	1.51	0.08	0.00	0.00	0.00	0.00	8.00	12
47B-191	3.00	0.00	1.96	1.40	0.03	1.52	0.09	0.01	0.00	0.00	0.00	8.02	12
47B-192	3.00	0.00	1.97	1.39	0.03	1.52	0.09	0.00	0.00	0.01	0.00	8.01	12
47B-193	3.00	0.00	1.97	1.37	0.03	1.54	0.09	0.00	0.00	0.01	0.00	8.01	12
47B-194	2.99	0.00	1.98	1.38	0.03	1.53	0.09	0.01	0.00	0.00	0.00	8.02	12
47B-195	3.00	0.00	1.98	1.37	0.03	1.52	0.09	0.00	0.00	0.00	0.00	8.01	12
47B-196	3.00	0.00	1.98	1.38	0.03	1.53	0.09	0.00	0.00	0.00	0.00	8.01	12
47B-197	3.01	0.00	1.96	1.38	0.03	1.52	0.09	0.01	0.00	0.00	0.00	8.01	12
47B-198	3.01	0.00	1.97	1.39	0.04	1.51	0.09	0.00	0.00	0.00	0.00	8.01	12
47B-199	3.01	0.00	1.96	1.48	0.04	1.44	0.08	0.00	0.00	0.00	0.00	8.01	12
47B-200	3.01	0.00	1.96	1.49	0.04	1.41	0.10	0.00	0.00	0.01	0.00	8.01	12
47B-203	3.02	0.00	1.95	1.56	0.04	1.33	0.09	0.01	0.00	0.00	0.00	8.01	12
47B-204	3.01	0.00	1.96	1.58	0.05	1.32	0.08	0.00	0.00	0.00	0.00	8.01	12
47B-205	3.02	0.00	1.96	1.56	0.04	1.32	0.09	0.00	0.00	0.00	0.00	8.00	12
47B-206	3.01	0.00	1.96	1.57	0.05	1.33	0.09	0.01	0.00	0.00	0.00	8.01	12

47B-209	3.03	0.00	1.95	1.42	0.03	1.47	0.09	0.00	0.00	0.00	0.00	8.00	12
47B-210	3.02	0.00	1.97	1.43	0.03	1.45	0.09	0.00	0.00	0.00	0.00	7.99	12
47B-211	2.99	0.00	1.98	1.43	0.04	1.48	0.09	0.01	0.00	0.00	0.00	8.02	12
47B-212	3.00	0.00	1.98	1.44	0.04	1.46	0.08	0.00	0.00	0.00	0.00	8.01	12
47B-213	2.98	0.00	1.98	1.44	0.03	1.49	0.09	0.00	0.00	0.01	0.00	8.03	12
47B-214	2.97	0.00	1.99	1.46	0.03	1.47	0.09	0.00	0.00	0.00	0.00	8.03	12
47B-215	2.98	0.00	2.00	1.49	0.04	1.43	0.08	0.01	0.00	0.00	0.00	8.02	12

Biotite

47A-116	2.82	0.27	1.20	0.58	0.00	1.96	0.00	0.01	0.90	0.00	0.01	7.76	11
47A-117	2.82	0.26	1.21	0.55	0.00	2.01	0.00	0.01	0.90	0.00	0.00	7.77	11
47A-118	2.80	0.31	1.21	0.62	0.00	1.89	0.00	0.02	0.89	0.00	0.00	7.74	11
47A-119	2.81	0.29	1.20	0.59	0.00	1.94	0.00	0.02	0.90	0.00	0.01	7.75	11
47A-120	2.80	0.29	1.22	0.61	0.00	1.91	0.00	0.01	0.89	0.00	0.01	7.75	11
47A-258	2.81	0.35	1.21	0.39	0.00	2.01	0.00	0.05	0.84	0.01	0.01	7.68	11
47A-259	2.80	0.35	1.21	0.39	0.00	2.03	0.00	0.06	0.85	0.01	0.00	7.70	11
47B-115	2.83	0.26	1.18	0.37	0.00	2.18	0.00	0.04	0.92	0.01	0.00	7.80	11
47B-116	2.82	0.32	1.16	0.35	0.00	2.14	0.00	0.04	0.91	0.00	0.00	7.74	11
47B-151	2.83	0.25	1.19	0.47	0.00	2.10	0.00	0.02	0.94	0.00	0.00	7.80	11
47B-152	2.88	0.22	1.36	0.43	0.00	1.91	0.00	0.01	0.82	0.00	0.00	7.64	11
47B-187	2.83	0.22	1.18	0.39	0.00	2.25	0.00	0.02	0.94	0.00	0.00	7.84	11

Alkalifeldspar

45-65	3.01	0.00	0.98	0.00	0.00	0.00	0.01	0.24	0.76	0.00	0.00	5.00	8
45-66	3.01	0.00	0.98	0.00	0.00	0.00	0.02	0.35	0.62	0.00	0.00	4.98	8
45-67	3.02	0.00	0.97	0.00	0.00	0.00	0.00	0.11	0.89	0.00	0.00	5.00	8
45-68	3.01	0.00	0.98	0.00	0.00	0.00	0.00	0.14	0.87	0.00	0.00	5.01	8
45-69	3.01	0.00	0.98	0.00	0.00	0.00	0.00	0.12	0.86	0.00	0.00	4.99	8
45-70	3.01	0.00	0.98	0.01	0.00	0.00	0.00	0.15	0.83	0.00	0.00	4.99	8
45-121	3.01	0.00	0.98	0.01	0.00	0.00	0.00	0.14	0.85	0.00	0.00	4.99	8
45-125	3.00	0.00	0.98	0.01	0.00	0.01	0.01	0.39	0.62	0.00	0.00	5.02	8
45-126	3.01	0.00	0.99	0.01	0.00	0.00	0.01	0.31	0.64	0.00	0.00	4.97	8
45-135	3.01	0.00	0.98	0.00	0.00	0.00	0.02	0.66	0.28	0.00	0.00	4.96	8
45-136	3.01	0.00	0.99	0.01	0.00	0.00	0.01	0.28	0.70	0.00	0.00	4.99	8
47A-47	3.00	0.00	1.00	0.00	0.00	0.00	0.01	0.14	0.82	0.00	0.00	4.98	8

47A-48	3.00	0.00	1.00	0.00	0.00	0.00	0.02	0.17	0.79	0.00	0.00	4.98	8
47A-58	3.01	0.00	0.99	0.00	0.00	0.00	0.01	0.14	0.82	0.00	0.00	4.98	8
47A-59	3.00	0.00	1.00	0.00	0.00	0.00	0.02	0.17	0.78	0.00	0.00	4.97	8
47A-60	3.00	0.00	1.00	0.00	0.00	0.00	0.01	0.19	0.75	0.00	0.00	4.96	8
47A-61	3.01	0.00	0.98	0.00	0.00	0.00	0.01	0.20	0.76	0.00	0.00	4.98	8
47A-62	3.01	0.00	1.00	0.00	0.00	0.00	0.02	0.19	0.75	0.00	0.00	4.96	8
47A-63	3.01	0.00	0.99	0.00	0.00	0.00	0.01	0.10	0.84	0.00	0.00	4.96	8
47A-64	3.01	0.00	0.99	0.00	0.00	0.00	0.01	0.15	0.81	0.00	0.00	4.97	8
47A-65	2.94	0.00	1.06	0.00	0.00	0.00	0.08	0.27	0.62	0.00	0.00	4.98	8
47A-66	2.98	0.00	1.02	0.00	0.00	0.00	0.03	0.19	0.75	0.00	0.00	4.98	8
47A-67	3.00	0.00	1.00	0.00	0.00	0.00	0.01	0.13	0.83	0.00	0.00	4.98	8
47A-81	3.01	0.00	0.98	0.01	0.00	0.03	0.01	0.15	0.81	0.00	0.00	4.98	8
47A-83	3.01	0.00	0.99	0.00	0.00	0.00	0.01	0.16	0.79	0.00	0.00	4.97	8
47A-154	3.00	0.00	0.99	0.01	0.00	0.00	0.01	0.20	0.76	0.00	0.00	4.98	8
47A-180	3.01	0.00	0.99	0.00	0.00	0.00	0.01	0.20	0.74	0.00	0.00	4.96	8
47A-181	3.01	0.00	0.99	0.00	0.00	0.00	0.01	0.15	0.80	0.00	0.00	4.97	8
47A-182	3.01	0.00	0.99	0.00	0.00	0.00	0.01	0.14	0.81	0.00	0.00	4.97	8
47A-183	3.01	0.00	0.99	0.00	0.00	0.00	0.01	0.14	0.80	0.00	0.00	4.96	8
47A-184	3.01	0.00	0.99	0.00	0.00	0.00	0.01	0.15	0.81	0.00	0.00	4.97	8
47A-185	3.01	0.00	0.99	0.00	0.00	0.00	0.01	0.19	0.75	0.00	0.00	4.96	8
47A-186	3.00	0.00	1.00	0.00	0.00	0.00	0.02	0.23	0.72	0.00	0.00	4.97	8
47A-187	3.00	0.00	1.01	0.00	0.00	0.00	0.01	0.16	0.79	0.00	0.00	4.97	8
47A-207	3.00	0.00	1.00	0.00	0.00	0.00	0.02	0.17	0.77	0.00	0.00	4.96	8
47A-208	3.01	0.00	1.00	0.00	0.00	0.00	0.00	0.11	0.84	0.00	0.00	4.97	8
47B-17	2.98	0.00	1.00	0.01	0.00	0.00	0.01	0.16	0.84	0.00	0.00	5.01	8
47B-41	2.99	0.00	0.99	0.01	0.00	0.00	0.00	0.29	0.73	0.00	0.00	5.02	8
47B-46	2.99	0.00	1.00	0.02	0.00	0.00	0.01	0.17	0.81	0.00	0.00	5.00	8
47B-49	2.99	0.00	1.00	0.01	0.00	0.00	0.02	0.28	0.70	0.00	0.00	5.00	8
47B-64	3.00	0.00	0.99	0.00	0.00	0.00	0.01	0.17	0.83	0.00	0.00	5.00	8
47B-65	2.99	0.00	1.00	0.00	0.00	0.00	0.03	0.20	0.76	0.00	0.00	4.99	8
47B-68	3.00	0.00	0.98	0.00	0.00	0.00	0.01	0.13	0.87	0.00	0.00	5.00	8
47B-69	3.00	0.00	0.99	0.00	0.00	0.00	0.00	0.14	0.86	0.00	0.00	5.00	8
47B-70	2.98	0.00	1.01	0.00	0.00	0.01	0.02	0.17	0.79	0.00	0.00	4.99	8
47B-71	3.01	0.00	0.99	0.00	0.00	0.00	0.01	0.09	0.89	0.00	0.00	4.99	8
47B-97	3.00	0.00	0.99	0.00	0.00	0.00	0.01	0.12	0.86	0.00	0.00	4.99	8
47B-123	3.01	0.00	0.98	0.00	0.00	0.00	0.01	0.22	0.78	0.00	0.00	5.00	8
47B-124	3.00	0.00	0.99	0.00	0.00	0.00	0.02	0.23	0.76	0.00	0.00	5.00	8
47B-125	3.00	0.00	1.00	0.00	0.00	0.00	0.01	0.22	0.75	0.00	0.00	4.99	8
47B-126	3.00	0.00	0.99	0.00	0.00	0.00	0.02	0.20	0.78	0.00	0.00	5.00	8
47B-127	3.00	0.00	0.99	0.00	0.00	0.00	0.02	0.27	0.71	0.00	0.00	4.99	8
47B-138	3.00	0.00	0.98	0.01	0.00	0.02	0.01	0.25	0.71	0.00	0.00	4.98	8

47B-156	3.01	0.00	0.98	0.00	0.00	0.00	0.01	0.18	0.82	0.00	0.00	5.00	8
47B-157	3.01	0.00	0.97	0.00	0.00	0.00	0.01	0.13	0.88	0.00	0.00	5.00	8
47B-174	3.01	0.00	0.98	0.01	0.00	0.00	0.02	0.24	0.75	0.00	0.00	5.00	8

Plagioclase

47A-73	2.66	0.00	1.30	0.02	0.00	0.04	0.38	0.58	0.00	0.00	0.00	4.99	8
47A-74	2.63	0.00	1.32	0.04	0.00	0.05	0.36	0.60	0.01	0.00	0.00	5.01	8
47B-63	2.67	0.00	1.32	0.00	0.00	0.00	0.36	0.58	0.06	0.00	0.00	4.99	8

Sillimanite

45-20	1.02	0.00	1.95	0.04	0.00	0.00	0.00	0.01	0.00	0.00	0.00	3.01	5
45-40	1.01	0.00	1.96	0.03	0.00	0.00	0.00	0.00	0.00	0.00	0.00	3.01	5
45-42	1.01	0.00	1.96	0.03	0.00	0.00	0.00	0.00	0.00	0.00	0.00	3.01	5
45-47	1.02	0.00	1.96	0.03	0.00	0.00	0.00	0.00	0.00	0.00	0.00	3.01	5
45-48	1.02	0.00	1.95	0.04	0.00	0.00	0.00	0.00	0.00	0.00	0.00	3.01	5
45-49	1.01	0.00	1.96	0.03	0.00	0.00	0.00	0.00	0.00	0.00	0.00	3.01	5
45-50	1.02	0.00	1.95	0.03	0.00	0.00	0.00	0.00	0.00	0.00	0.00	3.01	5
45-51	1.01	0.00	1.95	0.04	0.00	0.00	0.00	0.00	0.00	0.00	0.00	3.01	5
45-52	1.01	0.00	1.96	0.03	0.00	0.00	0.00	0.00	0.00	0.00	0.00	3.01	5
45-53	1.02	0.00	1.95	0.03	0.00	0.00	0.00	0.00	0.00	0.00	0.00	3.00	5
45-54	1.02	0.00	1.95	0.03	0.00	0.00	0.00	0.00	0.00	0.00	0.00	3.00	5
45-55	1.02	0.00	1.95	0.03	0.00	0.00	0.00	0.00	0.00	0.00	0.00	3.01	5
45-56	1.02	0.00	1.95	0.03	0.00	0.00	0.00	0.00	0.00	0.00	0.00	3.01	5
45-59	1.02	0.00	1.95	0.03	0.00	0.00	0.00	0.00	0.00	0.00	0.00	3.01	5
45-60	1.01	0.00	1.96	0.03	0.00	0.00	0.00	0.00	0.00	0.00	0.00	3.01	5
45-109	1.02	0.00	1.96	0.03	0.00	0.00	0.00	0.00	0.00	0.00	0.00	3.01	5
45-110	1.02	0.00	1.96	0.03	0.00	0.00	0.00	0.00	0.00	0.00	0.00	3.00	5
45-111	1.01	0.00	1.96	0.03	0.00	0.00	0.00	0.00	0.00	0.00	0.00	3.01	5
45-112	1.01	0.00	1.96	0.03	0.00	0.00	0.00	0.00	0.00	0.00	0.00	3.01	5
45-113	1.02	0.00	1.96	0.03	0.00	0.00	0.00	0.00	0.00	0.00	0.00	3.00	5
45-114	1.01	0.00	1.97	0.03	0.00	0.00	0.00	0.00	0.00	0.00	0.00	3.01	5
45-119	1.02	0.00	1.95	0.03	0.00	0.00	0.00	0.00	0.00	0.00	0.00	3.00	5
45-120	1.02	0.00	1.96	0.03	0.00	0.00	0.00	0.00	0.00	0.00	0.00	3.01	5
45-123	1.02	0.00	1.95	0.03	0.00	0.00	0.00	0.00	0.00	0.00	0.00	3.00	5

45-124	1.01	0.00	1.96	0.03	0.00	0.00	0.00	0.00	0.00	0.00	0.00	3.01	5
45-127	1.02	0.00	1.95	0.03	0.00	0.00	0.00	0.00	0.00	0.00	0.00	3.00	5
45-128	1.01	0.00	1.96	0.03	0.00	0.00	0.00	0.00	0.00	0.00	0.00	3.00	5
47A-38	1.01	0.00	1.96	0.03	0.00	0.00	0.00	0.00	0.00	0.00	0.00	3.01	5
47A-39	1.00	0.00	1.97	0.03	0.00	0.00	0.00	0.00	0.00	0.00	0.00	3.01	5
47A-40	1.01	0.00	1.97	0.03	0.00	0.00	0.00	0.00	0.00	0.00	0.00	3.01	5
47A-52	1.01	0.00	1.96	0.03	0.00	0.00	0.00	0.00	0.00	0.00	0.00	3.00	5
47A-53	1.01	0.00	1.96	0.02	0.00	0.00	0.00	0.00	0.00	0.00	0.00	3.01	5
47A-57	1.00	0.00	1.98	0.02	0.00	0.00	0.00	0.00	0.00	0.00	0.00	3.01	5
47A-77	1.01	0.00	1.96	0.02	0.00	0.00	0.00	0.00	0.00	0.00	0.00	3.01	5
47A-86	1.01	0.00	1.96	0.03	0.00	0.00	0.00	0.00	0.00	0.00	0.00	3.01	5
47A-237	1.01	0.00	1.96	0.02	0.00	0.00	0.00	0.00	0.00	0.01	0.00	3.00	5
47A-238	1.00	0.00	1.97	0.02	0.00	0.00	0.00	0.01	0.00	0.01	0.00	3.01	5
47A-250	1.01	0.00	1.97	0.03	0.00	0.00	0.00	0.00	0.00	0.00	0.00	3.01	5
47A-251	1.01	0.00	1.96	0.03	0.00	0.00	0.00	0.00	0.00	0.00	0.00	3.01	5
47A-253	1.02	0.00	1.95	0.02	0.00	0.00	0.00	0.00	0.00	0.01	0.00	3.00	5
47B-14	1.01	0.00	1.97	0.02	0.00	0.00	0.00	0.00	0.00	0.00	0.00	3.01	5
47B-45	1.01	0.00	1.97	0.04	0.00	0.00	0.00	0.00	0.00	0.00	0.00	3.01	5
47B-48	1.01	0.00	1.96	0.03	0.00	0.00	0.00	0.00	0.00	0.00	0.00	3.01	5
47B-51	1.01	0.00	1.96	0.03	0.00	0.00	0.00	0.00	0.00	0.00	0.00	3.01	5
47B-59	1.01	0.00	1.96	0.03	0.00	0.00	0.00	0.00	0.00	0.00	0.00	3.01	5
47B-61	1.00	0.00	1.98	0.02	0.00	0.00	0.00	0.00	0.00	0.00	0.00	3.01	5
47B-75	1.01	0.00	1.97	0.02	0.00	0.00	0.00	0.00	0.00	0.00	0.00	3.01	5
47B-76	1.00	0.00	1.98	0.03	0.00	0.00	0.00	0.00	0.00	0.00	0.00	3.01	5
47B-101	1.01	0.00	1.97	0.03	0.00	0.00	0.00	0.00	0.00	0.00	0.00	3.01	5
47B-158	1.01	0.00	1.96	0.03	0.00	0.00	0.00	0.00	0.00	0.00	0.00	3.01	5
47B-159	1.01	0.00	1.96	0.03	0.00	0.00	0.00	0.00	0.00	0.00	0.00	3.01	5
47B-162	1.01	0.00	1.97	0.03	0.00	0.00	0.00	0.00	0.00	0.00	0.00	3.01	5
47B-163	1.00	0.00	1.97	0.02	0.00	0.00	0.00	0.00	0.00	0.00	0.00	3.01	5
47B-166	1.00	0.00	1.97	0.03	0.00	0.00	0.00	0.00	0.00	0.00	0.00	3.01	5
47B-168	1.01	0.00	1.96	0.03	0.00	0.00	0.00	0.00	0.00	0.00	0.00	3.01	5
47B-169	1.01	0.00	1.97	0.02	0.00	0.00	0.00	0.00	0.00	0.00	0.00	3.01	5

Quartz

45-15	1.00	0.00	0.00	0.00	0.00	0.00	0.00	0.00	0.00	0.00	0.00	1.00	2
45-16	1.00	0.00	0.00	0.00	0.00	0.00	0.00	0.00	0.00	0.00	0.00	1.00	2
45-18	1.00	0.00	0.00	0.00	0.00	0.00	0.00	0.00	0.00	0.00	0.00	1.00	2
45-43	1.00	0.00	0.00	0.00	0.00	0.00	0.00	0.00	0.00	0.00	0.00	1.00	2

45-57	1.00	0.00	0.00	0.00	0.00	0.00	0.00	0.00	0.00	0.00	0.00	1.00	2
45-58	1.00	0.00	0.00	0.00	0.00	0.00	0.00	0.00	0.00	0.00	0.00	1.00	2
45-61	1.00	0.00	0.00	0.00	0.00	0.00	0.00	0.00	0.00	0.00	0.00	1.00	2
45-62	1.00	0.00	0.00	0.00	0.00	0.00	0.00	0.00	0.00	0.00	0.00	1.00	2
45-63	1.00	0.00	0.00	0.00	0.00	0.00	0.00	0.00	0.00	0.00	0.00	1.00	2
45-64	1.00	0.00	0.00	0.00	0.00	0.00	0.00	0.00	0.00	0.00	0.00	1.00	2
45-116	1.00	0.00	0.00	0.00	0.00	0.00	0.00	0.00	0.00	0.00	0.00	1.00	2
45-117	1.00	0.00	0.00	0.00	0.00	0.00	0.00	0.00	0.00	0.00	0.00	1.00	2
45-118	1.00	0.00	0.00	0.00	0.00	0.00	0.00	0.00	0.00	0.00	0.00	1.00	2
45-129	1.00	0.00	0.00	0.00	0.00	0.00	0.00	0.00	0.00	0.00	0.00	1.00	2
45-130	1.00	0.00	0.00	0.00	0.00	0.00	0.00	0.00	0.00	0.00	0.00	1.00	2
45-131	1.00	0.00	0.00	0.00	0.00	0.00	0.00	0.00	0.00	0.00	0.00	1.00	2
45-132	1.00	0.00	0.00	0.00	0.00	0.00	0.00	0.00	0.00	0.00	0.00	1.00	2
45-133	1.00	0.00	0.00	0.00	0.00	0.00	0.00	0.00	0.00	0.00	0.00	1.00	2
45-134	1.00	0.00	0.00	0.00	0.00	0.00	0.00	0.00	0.00	0.00	0.00	1.00	2
47A-42	1.00	0.00	0.00	0.00	0.00	0.00	0.00	0.00	0.00	0.00	0.00	1.00	2
47A-43	1.00	0.00	0.00	0.00	0.00	0.00	0.00	0.00	0.00	0.00	0.00	1.00	2
47A-72	1.00	0.00	0.00	0.00	0.00	0.00	0.00	0.00	0.00	0.00	0.00	1.00	2
47A-82	1.00	0.00	0.00	0.00	0.00	0.00	0.00	0.00	0.00	0.00	0.00	1.00	2
47A-113	0.99	0.00	0.01	0.01	0.00	0.01	0.00	0.00	0.00	0.00	0.00	1.01	2
47A-137	1.00	0.00	0.00	0.00	0.00	0.00	0.00	0.00	0.00	0.00	0.00	1.00	2
47A-150	1.00	0.00	0.00	0.01	0.00	0.00	0.00	0.00	0.00	0.00	0.00	1.00	2
47A-151	1.00	0.00	0.00	0.00	0.00	0.00	0.00	0.00	0.00	0.00	0.00	1.00	2
47A-155	1.00	0.00	0.00	0.00	0.00	0.00	0.00	0.00	0.00	0.00	0.00	1.00	2
47A-159	1.00	0.00	0.00	0.00	0.00	0.00	0.00	0.00	0.00	0.00	0.00	1.00	2
47A-160	1.00	0.00	0.00	0.00	0.00	0.00	0.00	0.00	0.00	0.00	0.00	1.00	2
47A-161	1.00	0.00	0.00	0.00	0.00	0.00	0.00	0.00	0.00	0.00	0.00	1.00	2
47A-162	1.00	0.00	0.00	0.00	0.00	0.00	0.00	0.00	0.00	0.00	0.00	1.00	2
47A-163	1.00	0.00	0.00	0.00	0.00	0.00	0.00	0.00	0.00	0.00	0.00	1.00	2
47A-164	1.00	0.00	0.00	0.00	0.00	0.00	0.00	0.00	0.00	0.00	0.00	1.00	2
47A-165	1.00	0.00	0.00	0.00	0.00	0.00	0.00	0.00	0.00	0.00	0.00	1.00	2
47A-166	1.00	0.00	0.00	0.00	0.00	0.00	0.00	0.00	0.00	0.00	0.00	1.00	2
47A-167	1.00	0.00	0.00	0.00	0.00	0.00	0.00	0.00	0.00	0.00	0.00	1.00	2
47A-252	1.00	0.00	0.00	0.00	0.00	0.00	0.00	0.00	0.00	0.00	0.00	1.00	2
47B-18	1.00	0.00	0.00	0.00	0.00	0.00	0.00	0.00	0.00	0.00	0.00	1.00	2
47B-38	1.00	0.00	0.00	0.00	0.00	0.00	0.00	0.00	0.00	0.00	0.00	1.00	2
47B-50	1.00	0.00	0.00	0.00	0.00	0.00	0.00	0.00	0.00	0.00	0.00	1.00	2
47B-54	1.00	0.00	0.00	0.00	0.00	0.00	0.00	0.00	0.00	0.00	0.00	1.00	2
47B-55	1.00	0.00	0.00	0.00	0.00	0.00	0.00	0.00	0.00	0.00	0.00	1.00	2
47B-66	1.00	0.00	0.00	0.00	0.00	0.00	0.00	0.00	0.00	0.00	0.00	1.00	2
47B-67	1.00	0.00	0.00	0.00	0.00	0.00	0.00	0.00	0.00	0.00	0.00	1.00	2

47B-81	1.00	0.00	0.00	0.00	0.00	0.00	0.00	0.00	0.00	0.00	0.00	1.00	2
47B-82	1.00	0.00	0.00	0.00	0.00	0.00	0.00	0.00	0.00	0.00	0.00	1.00	2
47B-93	1.00	0.00	0.00	0.00	0.00	0.00	0.00	0.00	0.00	0.00	0.00	1.00	2
47B-94	1.00	0.00	0.00	0.00	0.00	0.00	0.00	0.00	0.00	0.00	0.00	1.00	2
47B-96	1.00	0.00	0.00	0.00	0.00	0.00	0.00	0.00	0.00	0.00	0.00	1.00	2
47B-98	1.00	0.00	0.00	0.00	0.00	0.00	0.00	0.00	0.00	0.00	0.00	1.00	2
47B-121	1.00	0.00	0.00	0.00	0.00	0.00	0.00	0.00	0.00	0.00	0.00	1.00	2
47B-122	1.00	0.00	0.00	0.00	0.00	0.00	0.00	0.00	0.00	0.00	0.00	1.00	2
47B-128	1.00	0.00	0.00	0.00	0.00	0.00	0.00	0.00	0.00	0.00	0.00	1.00	2
47B-129	1.00	0.00	0.00	0.00	0.00	0.00	0.00	0.00	0.00	0.00	0.00	1.00	2
47B-139	1.00	0.00	0.00	0.00	0.00	0.00	0.00	0.00	0.00	0.00	0.00	1.00	2
47B-150	1.00	0.00	0.00	0.00	0.00	0.00	0.00	0.00	0.00	0.00	0.00	1.00	2
47B-153	0.99	0.00	0.00	0.00	0.00	0.01	0.00	0.00	0.00	0.00	0.00	1.01	2
47B-175	1.00	0.00	0.00	0.00	0.00	0.00	0.00	0.00	0.00	0.00	0.00	1.00	2
47B-188	1.00	0.00	0.00	0.00	0.00	0.00	0.00	0.00	0.00	0.00	0.00	1.00	2
47B-207	1.00	0.00	0.00	0.00	0.00	0.00	0.00	0.00	0.00	0.00	0.00	1.00	2

C.3 | SIMS Cordierite volatile analyses for samples EGB-09-45 and -47.

samples	H2O	CO2	MW	n(H2O)	m(CO2)
EGB-09-47					
1	0.385	0.429	595.0	0.129	0.059
2	0.349	0.557	595.0	0.117	0.076
3	0.366	0.357	595.0	0.122	0.049
4	0.383	0.284	595.0	0.128	0.039
5	0.378	0.275	595.0	0.126	0.038
6	0.389	0.532	595.0	0.130	0.073
7	0.359	0.353	595.0	0.120	0.048
8	0.356	0.350	595.0	0.119	0.048
9	0.350	0.383	595.0	0.117	0.052
10	0.338	0.392	595.0	0.113	0.054
11	0.297	0.587	595.0	0.099	0.080
12	0.356	0.419	595.0	0.119	0.057
13	0.332	0.480	595.0	0.111	0.066
14	0.367	1.276	595.0	0.123	0.175
15	0.370	0.555	595.0	0.124	0.076
	0.358	0.482	595	0.120	0.066
	0.024	0.241		0.008	0.033
mean	0.358	0.425	595	0.112	0.058
1sd	0.089	0.102		0.030	0.014
EGB-09-45					
1	0.296	0.492	595.0	0.099	0.067
2	0.321	0.628	595.0	0.107	0.086
3	0.307	0.570	595.0	0.103	0.078
4	0.280	0.516	595.0	0.093	0.071
5	0.290	0.528	595.0	0.097	0.072
6	0.306	0.462	595.0	0.102	0.063
7	0.317	0.378	595.0	0.106	0.052
8	0.309	0.405	595.0	0.103	0.055
9	0.287	0.513	595.0	0.096	0.070
10	0.292	0.498	595.0	0.098	0.068
11	0.306	0.554	595.0	0.102	0.076
12	0.262	0.495	595.0	0.087	0.068
13	0.307	0.643	595.0	0.103	0.088
14	0.288	0.537	595.0	0.096	0.073
15	0.335	0.485	595.0	0.112	0.066
mean	0.300	0.513	595	0.100	0.070
1sd	0.018	0.071		0.006	0.010

C.4 | CL images of zircon grains in samples EGB-09-45, 47 and -55 with SHRIMP analysis spots. Data points given in A.5

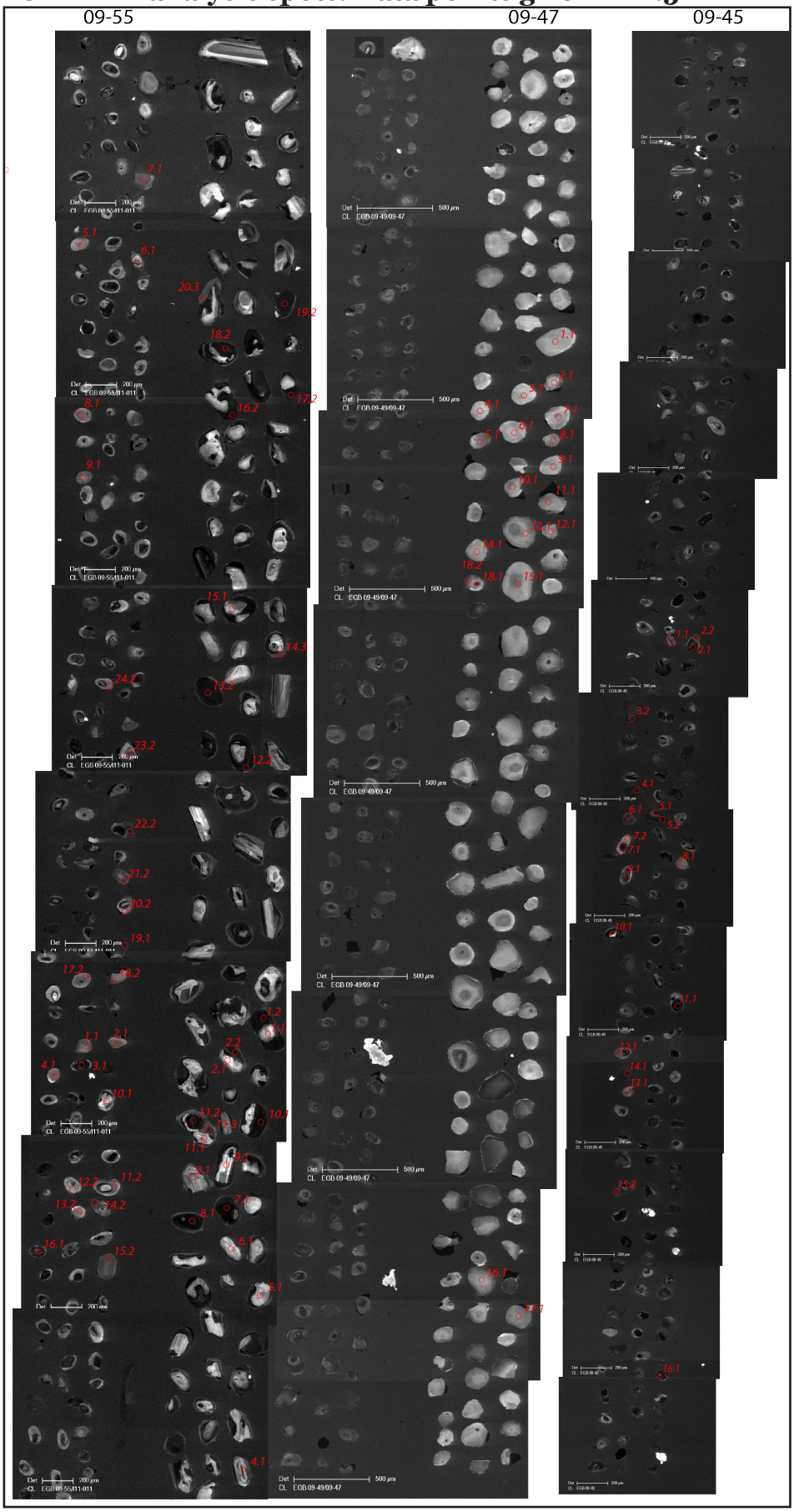

C.5 | Raw data tables for SHRIMP zircon and monazite U–Pb analyses

Zircon SHRIMP U-Pb data table

Spot	204Pb /206Pb	±%	% 206Pbc	ppm U	ppm Th	4-corr ppm 206Pb*	232Th /238U	±%	(1) 206Pb /238U Age		(1) 207Pb /235U Age		(1) 207Pb /206Pb Age		7/35 % Dis-cor-dant	7/6 % Dis-cor-dant	(1) 238U /206Pb*		±%	(1) 207Pb* /206Pb*		±%	(1) 207Pb* /235U		±%	(1) 206Pb* /238U	
0947-1.1	1.5E-4	58	0.25	53	128	10	2.49	0.44	1279	±35	1162	±45	948	±50	-9	-39	4.6	3.0	0.071	2.4	2.14	3.9	0.219	3.0	0.8		
0947-2.1	3.5E-4	58	0.62	48	112	4	2.40	0.47	649	±19	671	±42	744	±114	3	+13	9.4	3.1	0.064	5.4	0.94	6.2	0.106	3.1	0.5		
0947-3.1	3.1E-4	50	0.53	54	123	7	2.37	0.47	915	±16	892	±51	835	±111	-3	-10	6.6	1.9	0.067	5.3	1.41	5.7	0.152	1.9	0.3		
0947-4.1	2.8E-4	58	0.48	47	107	6	2.34	0.57	894	±17	852	±41	744	±93	-5	-22	6.7	2.1	0.064	4.4	1.31	4.8	0.149	2.1	0.4		
0947-5.1	2.5E-4	41	0.41	89	146	15	1.70	0.40	1186	±69	1051	±73	781	±58	-11	-57	4.9	6.4	0.065	2.8	1.82	7.0	0.202	6.4	0.9		
0947-6.1	1.8E-4	71	0.30	44	103	7	2.42	0.92	1047	±21	1040	±41	1026	±66	-1	-2	5.7	2.2	0.073	3.3	1.79	3.9	0.176	2.2	0.6		
0947-7.1	1.3E-4	100	0.22	51	115	6	2.33	0.57	871	±18	911	±39	1010	±73	5	+15	6.9	2.2	0.073	3.6	1.45	4.2	0.145	2.2	0.5		
0947-8.1	-9.3E-5	100	--	64	150	8	2.43	0.49	838	±28	878	±40	980	±59	5	+16	7.2	3.6	0.072	2.9	1.37	4.6	0.139	3.6	0.8		
0947-9.1	2.7E-4	71	0.46	49	110	6	2.33	0.57	798	±17	796	±60	792	±150	-0	-1	7.6	2.3	0.066	7.2	1.19	7.5	0.132	2.3	0.3		
0947-10.1	-1.4E-4	100	--	51	122	5	2.48	0.56	751	±16	797	±35	929	±79	6	+20	8.1	2.2	0.070	3.9	1.19	4.4	0.124	2.2	0.5		
0947-11.1	4.8E-4	50	0.84	52	130	7	2.57	0.57	883	±19	879	±55	869	±121	-0	-2	6.8	2.3	0.068	5.9	1.38	6.3	0.147	2.3	0.4		
0947-12.1	2.8E-4	71	0.48	54	127	6	2.42	0.57	802	±26	797	±61	783	±143	-1	-3	7.6	3.4	0.065	6.8	1.19	7.6	0.132	3.4	0.4		
0947-13.1	4.5E-4	50	0.77	49	118	7	2.48	0.61	1031	±23	971	±75	835	±152	-6	-25	5.8	2.4	0.067	7.3	1.60	7.7	0.174	2.4	0.3		
0947-14.1	6.1E-4	45	1.04	51	127	7	2.59	0.60	949	±21	928	±64	878	±133	-2	-9	6.3	2.4	0.068	6.4	1.49	6.8	0.159	2.4	0.4		
0947-15.1	3.4E-4	50	0.59	93	139	10	1.54	0.47	738	±28	787	±46	929	±85	7	+22	8.2	4.1	0.070	4.1	1.17	5.8	0.121	4.1	0.7		
0947-16.1	---	100	0.00	56	136	5	2.49	0.43	645	±18	655	±24	686	±51	1	+6	9.5	2.9	0.062	2.4	0.91	3.7	0.105	2.9	0.8		
0947-17.1	1.5E-4	71	0.26	64	154	6	2.47	0.40	718	±21	750	±33	846	±63	4	+16	8.5	3.1	0.067	3.0	1.09	4.4	0.118	3.1	0.7		
0947-18.1	2.6E-5	100	0.05	101	133	14	1.36	0.52	936	±31	1243	±70	1822	±79	33	+52	6.4	3.6	0.111	4.4	2.40	5.6	0.156	3.6	0.6		

0947-18.2	6.0E-5	58	0.10	115	110	17	0.99	0.28	997	±12	974	±29	922	±54	-2	-9	6.0	1.3	0.070	2.6	1.61	2.9	0.167	1.3	0.5
0945-1.1	1.9E-5	35	0.03	307	148	124	0.50	0.45	2484	±144	2473	±178	2464	±30	-0	-1	2.1	7.0	0.161	1.8	10.42	7.2	0.470	7.0	1.0
0945-2.1	-7.5E-6	58	--	929	23	120	0.03	0.38	905	±10	903	±13	898	±15	-0	-1	6.6	1.2	0.069	0.7	1.43	1.4	0.151	1.2	0.9
0945-2.2	---	---	0.00	347	159	43	0.47	0.43	863	±12	874	±16	904	±23	1	+5	7.0	1.5	0.069	1.1	1.37	1.9	0.143	1.5	0.8
0945-3.2	7.8E-6	71	0.01	560	187	75	0.34	0.16	937	±10	945	±12	961	±15	1	+3	6.4	1.1	0.071	0.7	1.54	1.3	0.157	1.1	0.8
0945-4.1	20.0E-5	45	0.03	538	238	74	0.46	0.15	962	±14	968	±18	983	±23	1	+2	6.2	1.5	0.072	1.1	1.60	1.9	0.161	1.5	0.8
0945-5.1	-2.9E-5	41	--	477	115	62	0.25	0.32	901	±13	911	±21	935	±34	1	+4	6.7	1.6	0.070	1.7	1.45	2.3	0.150	1.6	0.7
0945-5.2	5.9E-5	35	0.10	594	94	42	0.16	0.21	505	±5	503	±7	492	±19	-0	-3	12.3	1.1	0.057	0.9	0.64	1.4	0.081	1.1	0.8
0945-6.1	9.9E-6	71	0.02	356	135	58	0.39	0.20	1117	±37	1097	±40	1057	±12	-2	-6	5.3	3.6	0.075	0.6	1.94	3.6	0.189	3.6	1.0
0945-7.1	5.6E-6	38	0.01	1013	201	394	0.21	0.15	2409	±38	2430	±51	2448	±15	1	+2	2.2	1.9	0.159	0.9	9.95	2.1	0.453	1.9	0.9
0945-7.2	1.1E-4	45	0.20	142	110	14	0.80	0.26	685	±13	712	±18	796	±33	4	+15	8.9	2.0	0.066	1.6	1.02	2.5	0.112	2.0	0.8
0945-8.1	-6.8E-5	45	--	151	144	22	0.98	0.24	1016	±12	1002	±17	971	±23	-1	-5	5.9	1.3	0.071	1.1	1.68	1.7	0.171	1.3	0.8
0945-9.1	7.8E-6	58	0.01	468	218	111	0.48	0.64	1575	±51	1821	±119	2115	±94	16	+29	3.6	3.7	0.131	5.4	5.01	6.5	0.277	3.7	0.6
0945-10.1	4.9E-6	100	0.01	301	56	52	0.19	0.27	1179	±31	1580	±85	2165	±79	34	+50	5.0	2.9	0.135	4.5	3.74	5.4	0.201	2.9	0.5
0945-11.1	1.2E-6	100	0.00	1061	609	215	0.59	0.10	1364	±32	1631	±52	1996	±32	20	+35	4.2	2.6	0.123	1.8	3.99	3.2	0.236	2.6	0.8
0945-12.1	-3.2E-5	58	--	179	152	28	0.87	0.22	1084	±28	1089	±44	1097	±59	0	+1	5.5	2.8	0.076	2.9	1.92	4.1	0.183	2.8	0.7
0945-13.1	2.0E-5	45	0.03	283	163	75	0.59	2.15	1746	±35	1824	±94	1915	±82	5	+10	3.2	2.3	0.117	4.6	5.03	5.1	0.311	2.3	0.5
0945-14.2	2.1E-5	50	0.04	508	182	58	0.37	0.33	806	±8	820	±15	859	±31	2	+7	7.5	1.1	0.068	1.5	1.24	1.9	0.133	1.1	0.6
0945-15.2	3.9E-5	45	0.07	375	196	36	0.54	0.17	690	±12	700	±14	730	±17	1	+6	8.8	1.8	0.064	0.8	0.99	2.0	0.113	1.8	0.9
0945-16.1	8.4E-6	45	0.01	1468	158	170	0.11	3.52	816	±11	921	±21	1183	±35	13	+33	7.4	1.4	0.079	1.8	1.48	2.2	0.135	1.4	0.6
0945-17.1	5.7E-6	71	0.01	487	150	97	0.32	0.48	1343	±31	1950	±113	2675	±87	45	+55	4.3	2.5	0.182	5.2	5.82	5.8	0.232	2.5	0.4
0945-17.2	8.9E-6	100	0.02	513	95	37	0.19	0.22	519	±6	523	±7	536	±17	1	+3	11.9	1.1	0.058	0.8	0.67	1.4	0.084	1.1	0.8
0955-1.1	---	100	0.00	129	221	15	1.77	0.26	806	±24	814	±35	834	±60	1	+4	7.5	3.1	0.067	2.9	1.23	4.2	0.133	3.1	0.7
0955-2.1	-1.7E-5	100	--	168	200	22	1.23	0.24	901	±11	957	±16	1087	±20	6	+18	6.7	1.3	0.076	1.0	1.57	1.6	0.150	1.3	0.8

0955-3.1	3.6E-6	100	0.01	1174	141	103	0.12	0.65	630	±11	685	±17	873	±34	9	+29	9.7	1.8	0.068	1.7	0.96	2.4	0.103	1.8	0.7
0955-4.1	-1.1E-4	45	--	137	205	19	1.55	0.26	950	±20	951	±30	952	±44	0	+0	6.3	2.3	0.071	2.1	1.55	3.1	0.159	2.3	0.7
0955-5.1	---	100	0.00	148	165	19	1.15	0.26	920	±26	934	±33	967	±39	2	+5	6.5	3.0	0.071	1.9	1.51	3.5	0.153	3.0	0.8
0955-6.1	5.8E-6	100	0.01	210	120	66	0.59	0.25	2009	±52	1997	±97	1986	±67	-1	-1	2.7	3.0	0.122	3.8	6.15	4.8	0.366	3.0	0.6
0955-7.1	---	---	0.00	226	185	25	0.85	0.22	779	±22	807	±28	882	±37	3	+12	7.8	3.0	0.068	1.8	1.21	3.5	0.129	3.0	0.9
0955-8.1	1.7E-5	100	0.03	157	222	19	1.46	0.22	859	±14	849	±27	822	±55	-1	-5	7.0	1.7	0.067	2.6	1.31	3.1	0.143	1.7	0.5
0955-9.1	4.5E-5	71	0.08	129	139	16	1.11	0.59	862	±16	880	±26	925	±45	2	+7	7.0	2.0	0.070	2.2	1.38	3.0	0.143	2.0	0.7
0955-10.1	6.4E-5	45	0.09	81	136	34	1.73	0.35	2568	±107	2500	±127	2446	±11	-3	-6	2.0	5.0	0.159	0.7	10.73	5.1	0.489	5.0	1.0
0955-11.2	1.5E-4	38	0.26	151	199	20	1.36	0.27	944	±15	920	±28	865	±51	-2	-10	6.3	1.7	0.068	2.5	1.48	3.0	0.158	1.7	0.6

Monazite
SHRIMP U-Pb
data table

Spot	% 206Pbc	232Th /238U	±%	206Pb /238U Age		207Pb /235U Age		207Pb /206Pb Age		% Dis-cor-dant	Total 238U /206Pb	±%	Total 207Pb /206Pb	±%	207Pb* /235U	±%	206Pb* /238U	±%	err corr
0947-1.1	630	131	3.0	853	±11	833	±26	848	±39	-1	7.1	1.3	0.067	1.3	1.30	4.7	0.142	1.4	0.3
0947-1.2	1599	42	2.8	943	±10	930	±16	939	±16	-0	6.3	1.2	0.070	0.8	1.52	1.7	0.158	1.2	0.7
0947-2.1	165	321	3.3	807	±17	909	±50	835	±73	+3	7.5	1.9	0.069	2.4	1.27	8.7	0.133	2.2	0.3
0947-3.1	357	154	3.1	894	±14	982	±33	920	±33	+3	6.7	1.6	0.072	1.6	1.47	3.6	0.149	1.6	0.5
0947-4.1	440	123	3.0	943	±14	963	±30	949	±33	+1	6.4	1.5	0.071	1.5	1.55	3.5	0.157	1.6	0.4
0947-5.1	177	382	3.4	870	±19	879	±49	872	±69	+0	6.9	2.0	0.068	2.4	1.36	7.9	0.144	2.2	0.3
0947-6.1	6063	8	2.8	914	±9	911	±14	913	±12	-0	6.6	1.1	0.069	0.7	1.46	1.3	0.152	1.1	0.9
0947-7.1	119	267	3.4	537	±11	601	±66	550	±43	+2	11.5	1.9	0.060	3.0	0.72	7.9	0.087	2.0	0.3
0947-8.1	80	400	3.7	522	±14	911	±80	601	±59	+15	11.9	2.2	0.069	3.9	0.81	9.9	0.084	2.6	0.3
0947-9.1	293	170	3.1	796	±13	914	±38	828	±41	+4	7.6	1.6	0.070	1.8	1.26	5.0	0.131	1.7	0.3
0947-10.1	215	236	3.3	881	±16	937	±44	898	±50	+2	6.8	1.9	0.070	2.1	1.42	5.5	0.147	1.9	0.4
0947-11.1	206	309	3.3	914	±18	1010	±44	942	±67	+3	6.6	1.9	0.073	2.2	1.53	7.1	0.152	2.1	0.3
0947-12.1	236	255	3.9	863	±25	889	±43	870	±67	+1	7.0	2.8	0.069	2.1	1.36	7.7	0.143	2.9	0.4
0947-13.1	589	91	2.9	930	±12	927	±26	929	±23	-0	6.4	1.4	0.070	1.3	1.50	2.5	0.155	1.4	0.6
0947-14.1	182	421	3.4	936	±20	1031	±46	965	±69	+3	6.4	2.0	0.074	2.3	1.59	7.2	0.156	2.2	0.3
0947-15.1	164	328	3.4	827	±21	933	±81	856	±104	+4	7.3	2.0	0.070	3.9	1.32	12.1	0.137	2.5	0.2
0947-16.1	184	327	3.3	863	±19	1018	±46	908	±86	+5	7.0	1.9	0.073	2.3	1.44	9.5	0.143	2.3	0.2
0947-17.1	410	114	3.0	872	±12	958	±31	897	±27	+3	6.9	1.5	0.071	1.5	1.42	3.0	0.145	1.5	0.5
0947-18.1	491	118	3.4	852	±17	935	±29	875	±31	+3	7.1	2.1	0.070	1.4	1.37	3.5	0.141	2.1	0.6
0947-19.1	3162	14	2.8	871	±9	894	±12	878	±11	+1	6.9	1.1	0.069	0.6	1.37	1.3	0.145	1.1	0.9
0955-1.1	332	187	3.6	788	±19	831	±91	800	±42	+1	7.7	2.4	0.067	3.4	1.20	5.3	0.130	2.5	0.5
0955-2.1A	412	199	3.0	910	±13	811	±81	882	±39	-3	6.6	1.5	0.066	1.6	1.38	4.4	0.152	1.5	0.3
0955-1.2A	365	73	3.0	495	±7	490	±80	495	±20	-0	12.5	1.3	0.057	2.0	0.63	4.1	0.080	1.4	0.3
0955-3.1	293	266	3.1	862	±14	883	±84	868	±41	+1	7.0	1.6	0.068	1.8	1.35	4.7	0.143	1.7	0.4
0955-4.1	535	74	2.9	509	±7	533	±108	513	±28	+1	12.2	1.2	0.058	1.4	0.66	5.5	0.082	1.3	0.2
0955-5.1	1577	32	2.8	823	±9	786	±24	813	±13	-1	7.3	1.1	0.065	0.8	1.23	1.6	0.136	1.1	0.7
0955-6.1	312	212	3.3	890	±14	921	±79	899	±40	+1	6.8	1.6	0.070	1.8	1.42	4.4	0.148	1.7	0.4

0955-7.1	450	113	2.9	736	±10	803	±44	753	±19	+2	8.3	1.4	0.066	1.5	1.10	2.6	0.121	1.4	0.5
0955-8.1	452	101	3.0	535	±7	535	±84	535	±23	+0	11.6	1.3	0.058	1.6	0.69	4.4	0.086	1.3	0.3
0955-9.1	626	88	3.1	750	±9	821	±63	768	±26	+2	8.1	1.3	0.066	1.3	1.13	3.4	0.123	1.3	0.4
0955-10.1	284	273	3.7	939	±23	982	±98	952	±56	+1	6.4	2.5	0.072	1.8	1.55	5.8	0.157	2.6	0.4
0955-11.1	365	186	3.1	941	±15	889	±80	926	±41	-2	6.4	1.6	0.069	3.0	1.49	4.4	0.157	1.6	0.4
0955-12.1	375	122	3.0	922	±14	882	±79	910	±39	-1	6.5	1.5	0.068	1.6	1.45	4.3	0.154	1.6	0.4
0955-12.2	314	169	3.1	904	±15	922	±91	910	±45	+1	6.6	1.6	0.070	2.9	1.45	5.0	0.151	1.7	0.3
0955-13.1	288	220	3.3	840	±14	837	±111	839	±51	-0	7.2	1.7	0.067	1.9	1.28	6.1	0.139	1.8	0.3
0955-14.1	341	196	3.0	861	±13	933	±72	882	±36	+2	7.0	1.6	0.070	1.7	1.38	4.1	0.143	1.6	0.4
0955-15.1	551	76	2.9	583	±7	553	±72	577	±22	-1	10.6	1.3	0.059	1.4	0.76	3.8	0.095	1.3	0.3
0955-16.1	346	214	3.1	903	±14	870	±87	894	±43	-1	6.6	1.6	0.068	1.7	1.41	4.8	0.150	1.6	0.3

C.6 | Raw data table for LA-ICPMS zircon U–Pb analyses

Grain ID	Group ID	238/206	238/206 prop2sd	207/206	207/206 prop2sd	U/Pb age	U/Pb age u/c	Pb/Pb age	Pb/Pb age u/c	7-6 discord %	35-7 discord %	U (ppm)	Th (ppm)	Pb (ppm)
45Z - 1		10.65	0.74	0.06	0	578	39	723	130	25.09	-24.15	1850	86000	18500
45Z - 2	Mm	9.81	0.39	0.07	0	625	23	794	140	27.04	-8.49	702	379	109
45Z - 3	Mm	9.12	0.37	0.07	0	670	26	791	130	18.06	-6.69	1104	160	52
45Z - 4												0.01	0.03	0.09
45Z - 5	Mm	5.92	0.49	0.08	0	1005	77	1105	110	9.95	-4.38	1424	1011	416
45Z - 6	Mo	11.06	0.39	0.06	0	558	19	620	160	11.09	-5.73	525	165.4	45.3
45Z - 7	Mo	10.05	0.36	0.06	0	611	21	740	150	21.11	-7.28	890	1900	640
45Z - 8	Mo	12.17	0.53	0.06	0	509	21	560	210	10.02	-5.57	378	110	27
47AZ - 1	Ms	8.9	0.46	0.06	0.01	686	33	320	400	-53.35	7.19	50.8	132.7	41.6
47AZ - 10	Ms	6.15	0.23	0.07	0	971	35	910	150	-6.28	1.36	54.6	134.8	64.9
47AZ - 11	Ms	6.47	0.25	0.07	0.01	926	34	810	190	-12.53	2.66	56.1	141	64.1
47AZ - 12	Ms	6.37	0.26	0.07	0	940	35	820	200	-12.77	2.51	56.2	139.9	65.7
47AZ - 13	Ms	7.66	0.31	0.07	0.01	791	30	810	200	2.4	-2.59	46.7	114.4	43.5
47AZ - 2	Ms	8.42	0.32	0.06	0.01	723	26	660	240	-8.71	0.98	41.5	91.3	29.2
47AZ - 3	Ms	6.39	0.25	0.07	0	937	35	880	180	-6.08	1.3	55.5	139	60
47AZ - 4	Ms	6.22	0.26	0.07	0.01	961	37	930	200	-3.23	0.31	49.4	124	55.6
47AZ - 5	Ms	6.05	0.25	0.07	0.01	986	37	950	190	-3.65	0.41	56.1	143.6	66.1
47AZ - 6	Ms	6.77	0.27	0.07	0.01	888	33	790	220	-11.04	1.6	49	119.2	49.7
47AZ - 7	Ms	8.03	0.34	0.07	0.01	756	30	710	240	-6.08	0.27	46	105.1	37.4
47AZ - 8	Ms	6.32	0.25	0.07	0.01	946	35	800	200	-15.43	3.61	54.9	142.9	65.4
47AZ - 9	Ms	6.4	0.24	0.07	0.01	935	33	960	180	2.67	-1.58	67.8	130.4	63.7
47B Z - 1	Ms	9.37	0.38	0.08	0.01	654	25	980	240	49.85	-13.03	55.8	119	39.1
47B Z - 10	Mo	12.77	0.67	0.07	0.01	486	24	650	270	33.74	-10.33	107.3	18.1	3.95
47B Z - 11	Mo	16.37	0.72	0.06	0.01	382	17	390	260	2.09	-23.6	81.1	3.77	1.15
47B Z - 2	Ms	9.75	0.4	0.06	0.01	630	25	560	260	-11.11	-0.63	49.3	124.6	37.5
47B Z - 3	O	5.67	0.21	0.09	0.01	1047	36	1340	160	27.98	-8	478	173	81.4
47B Z - 4	O	6.66	0.28	0.07	0	901	34	953	120	5.77	-0.66	506	47.3	21.6
47B Z - 5	Mm	6	0.22	0.07	0	993	34	983	120	-1.01	0.4	390	96.9	46.1
47B Z - 6	Mm	8.05	0.54	0.09	0	754	48	1290	150	71.09	-29.86	246.5	166.7	93.1
47B Z - 7												-0.01	0	-0.01
47B Z - 8	Ms	9.43	1.6	0.05	0.07	640	110	-1300	1400	-303.13	113.33	5.45	3.95	1.45
47B Z - 9	Ms	4.55	1.76	0.19	0.14	1270	440	2000	1500	57.48	-21.12	0.5	0.09	-0.07
55BZr - 1	Mo	12.63	0.43	0.06	0	491	16	546	140	11.2	-5.03	791	149.4	33.2
55BZr - 2	Mm	9.58	0.36	0.07	0	640	23	948	130	48.13	-12.57	1131	264	84.9
55BZr - 3	Mo	11.53	0.45	0.06	0	536	20	480	190	-10.45	-1.83	281	110.1	24.8
55BZr - 4	Ms	6.81	0.25	0.07	0	884	31	900	140	1.81	-3.39	282	236	102.6
55BZr - 5	Ms	7.13	0.27	0.07	0	846	31	800	190	-5.44	1.32	106.6	240.9	86.2

Mm = metamict

Ms = sector zoned

Mo = metamorphic overgrowth

O = oscillatory zoned

C.7 | Raw data table for LA-ICPMS zircon REE and Ti analyses

Grain ID	La (ppm)	Ce (ppm)	Pr (ppm)	Nd (ppm)	Sm (ppm)	Eu (ppm)	Gd (ppm)	Tb (ppm)	Dy (ppm)	Ho (ppm)	Er (ppm)	Tm (ppm)	Yb (ppm)	Lu (ppm)
45Z - 1.d	2.30E+8	2.80E+7	4.50E+7	3.30E+6	1.40E+7	9.10E+5	5.50E+4	3.40E+4	3.20E+6	1.40E+8	1.10E+7	5.40E+8	1.20E+10	2.40E+8
45Z - 2.d	9.10	2.90	13.00	2.70	24.00	4.70	160.00	0.30	4.60	25.00	2.10	2.80	41.00	28.00
45Z - 3.d	3.70	1.60	9.80	2.60	30.00	6.70	170.00	0.39	4.70	42.00	3.40	1.00	14.00	55.00
45Z - 4.d	0.00	0.00	0.00	0.00	0.00	0.00	0.00	0.00	0.00	0.00	0.00	0.00	0.00	0.00
45Z - 5.d	5.70	1.70	7.40	1.80	18.00	3.40	120.00	0.31	4.00	25.00	3.30	3.50	31.00	140.00
45Z - 6.d	6.60	1.60	6.50	1.50	7.90	1.20	160.00	0.36	5.20	9.60	1.20	0.76	4.60	12.00
45Z - 7.d	200.00	25.00	38.00	3.60	18.00	2.80	130.00	0.38	4.10	36.00	2.90	190.00	2800.00	120.00
45Z - 8.d	7.40	2.80	9.50	1.60	13.00	2.20	770.00	0.33	8.10	8.10	1.30	0.60	6.00	21.00
47AZ - 1.d	3.40	0.71	2.20	0.45	2.30	0.40	160.00	0.12	3.20	1.50	0.37	0.60	3.60	1.60
47AZ - 10.d	2.30	0.58	1.70	0.28	2.10	0.30	120.00	0.07	1.50	0.96	0.23	0.28	3.10	1.10
47AZ - 11.d	2.00	0.58	1.90	0.33	1.90	0.32	97.00	0.10	1.90	1.20	0.26	0.41	2.10	1.20
47AZ - 12.d	2.00	0.45	2.10	0.33	1.90	0.37	120.00	0.07	2.20	1.20	0.26	0.46	2.70	1.20
47AZ - 13.d	2.20	0.44	1.50	0.32	1.60	0.28	120.00	0.11	1.80	0.77	0.21	0.32	1.60	0.93
47AZ - 2.d	1.40	0.44	1.10	0.27	1.40	0.19	89.00	0.09	1.90	0.69	0.17	0.25	1.90	0.80
47AZ - 3.d	2.00	0.71	1.70	0.39	1.90	0.34	94.00	0.10	1.70	1.20	0.25	0.39	2.20	0.89
47AZ - 4.d	2.40	0.47	1.80	0.37	2.10	0.32	120.00	0.09	2.00	1.20	0.24	0.40	2.40	0.97
47AZ - 5.d	2.20	0.50	1.80	0.42	1.70	0.33	120.00	0.08	1.60	0.95	0.26	0.44	2.70	1.60
47AZ - 6.d	1.80	0.56	1.80	0.45	1.70	0.26	88.00	0.10	1.70	0.87	0.25	0.30	1.80	0.90
47AZ - 7.d	1.50	0.44	1.20	0.29	1.40	0.22	100.00	0.10	1.60	0.97	0.20	0.25	2.10	0.99
47AZ - 8.d	2.00	0.58	1.90	0.26	1.70	0.29	100.00	0.10	1.70	0.99	0.22	0.46	2.40	1.30
47AZ - 9.d	2.00	0.53	1.50	0.36	1.70	0.31	110.00	0.11	2.00	1.20	0.31	0.30	3.50	2.70
47B Z - 1.d	2.60	0.69	2.00	0.29	1.90	0.26	110.00	0.12	1.40	2.90	0.26	0.33	4.70	4.90
47B Z - 10.d	3.60	1.00	3.40	0.73	3.00	0.63	160.00	0.13	3.80	2.50	0.34	0.15	0.93	2.60
47B Z - 11.d	6.50	1.60	3.60	0.84	4.70	1.10	180.00	0.18	4.30	2.70	0.36	0.10	0.63	5.40
47B Z - 2.d	1.70	0.53	1.10	0.32	1.70	0.29	110.00	0.10	1.90	0.71	0.20	0.25	2.40	1.10
47B Z - 3.d	5.20	1.70	6.70	1.70	14.00	2.60	150.00	0.59	3.50	8.30	3.50	1.30	8.00	12.00
47B Z - 4.d	7.40	1.90	6.00	1.20	6.40	1.10	130.00	0.52	3.80	18.00	1.90	0.36	2.30	12.00
47B Z - 5.d	5.20	1.70	4.80	1.30	8.30	1.40	130.00	0.50	3.40	18.00	2.00	0.58	3.40	13.00
47B Z - 6.d	18.00	6.50	28.00	5.50	48.00	9.50	150.00	0.21	5.00	55.00	5.10	3.70	19.00	66.00
47B Z - 7.d	0.00	0.00	0.00	0.00	0.00	0.00	0.00	0.00	0.00	0.00	0.00	0.00	0.00	0.00
47B Z - 8.d	9.60	2.80	9.70	1.60	10.00	1.80	410.00	0.36	40.00	4.30	1.40	1.40	3.00	4.70
47B Z - 9.d	110.00	9.20	110.00	2.40	67.00	3.40	1700.00	28.00	14000.00	320.00	330.00	170.00	48.00	68.00
55BZr - 1.d	1.90	0.40	1.00	0.19	0.97	0.15	140.00	0.14	3.00	8.90	0.98	0.51	6.50	18.00
55BZr - 2.d	4.50	1.60	7.90	2.10	18.00	4.50	200.00	0.48	3.70	50.00	4.70	2.40	29.00	69.00
55BZr - 3.d	5.50	2.20	16.00	3.90	27.00	5.00	180.00	0.19	3.80	4.70	0.66	0.38	2.80	6.70

55BZr - 4.d	4.70	1.80	5.60	1.20	5.40	0.86	120.00	0.14	3.90	5.10	0.84	0.67	4.40	5.30
55BZr - 5.d	3.30	1.20	4.40	0.63	3.60	0.54	130.00	0.11	1.40	1.70	0.37	0.67	4.20	2.50

Grain ID	Ti_ ppm_49	Ti in zr (K)	Ti in zr (°C)											
45Z - 1.d	3.10E+6	-10491.07	-10764.07											
45Z - 2.d	17.2	1057.71	784.71											
45Z - 3.d	19.6	1070.43	797.43											
45Z - 4.d														
45Z - 5.d	24.8	1094.13	821.13											
45Z - 6.d	20.4	1074.38	801.38											
45Z - 7.d	22.2	1082.84	809.84											
45Z - 8.d	25.5	1097.00	824.00											
47AZ - 1.d	59	1191.28	918.28											
47AZ - 10.d	52.3	1176.75	903.75											
47AZ - 11.d	54.7	1182.11	909.11											
47AZ - 12.d	56.6	1186.23	913.23											
47AZ - 13.d	47.1	1164.40	891.40											
47AZ - 2.d	56.7	1186.44	913.44											
47AZ - 3.d	58.2	1189.61	916.61											
47AZ - 4.d	51.3	1174.45	901.45											
47AZ - 5.d	55.6	1184.08	911.08											
47AZ - 6.d	54.3	1181.23	908.23											
47AZ - 7.d	48.1	1166.86	893.86											
47AZ - 8.d	56.8	1186.66	913.66											
47AZ - 9.d	45.2	1159.62	886.62											
47B Z - 1.d	37.4	1138.12	865.12											
47B Z - 10.d	24.9	1094.54	821.54											
47B Z - 11.d	23.2	1087.30	814.30											
47B Z - 2.d	47.6	1165.64	892.64											
47B Z - 3.d	57	1187.08	914.08											
47B Z - 4.d	48.4	1167.59	894.59											
47B Z - 5.d	68	1208.86	935.86											
47B Z - 6.d	31.9	1120.68	847.68											
47B Z - 7.d														
47B Z - 8.d	390	1477.07	1204.07											
47B Z - 9.d	176000	6605.73	6332.73											
55BZr - 1.d	24.1	1091.19	818.19											
55BZr - 2.d	153	1320.15	1047.15											
55BZr - 3.d	18.7	1065.81	792.81											
55BZr - 4.d	42	1151.19	878.19											

C.8 | CL images of zircon grains in samples EGB-09-45, 47 and -55 with SHRIMP analysis spots. Data points given in A.5

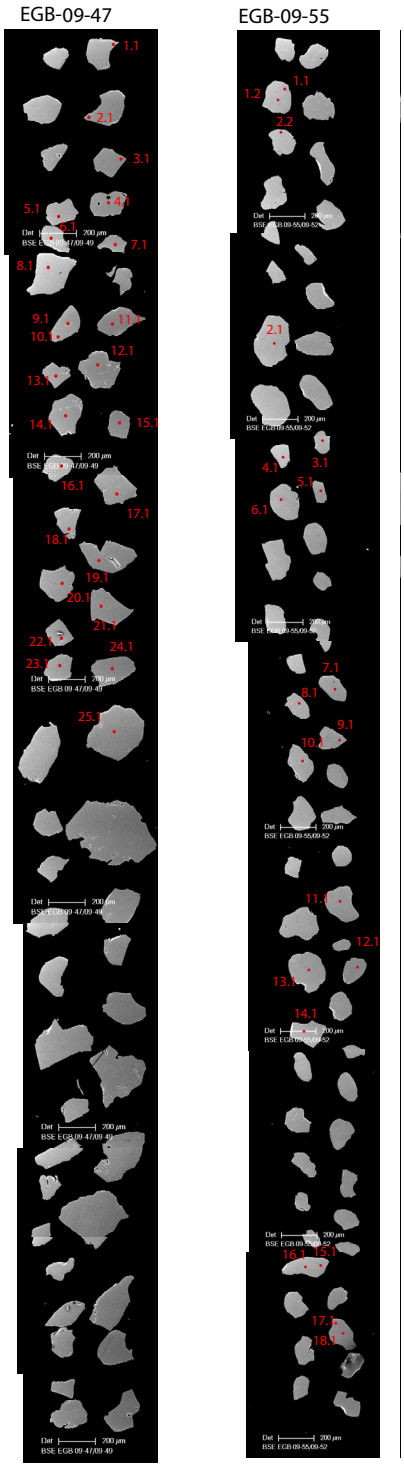

C.9 | Field photos for samples EGB-09-45 and -47.

Above – Outcrop photo of EGB-09-45, showing the sampled lithological layering; dark layers are orthopyroxene–sillimanite–cordierite bearing.
Below – Sample location for EGB-09-47.

C.10 | Fully annotated *P–T* pseudosections calculated using THERMOCALC 3.40 for samples EGB-09-45 and -47 using XRF whole-rock compositions.

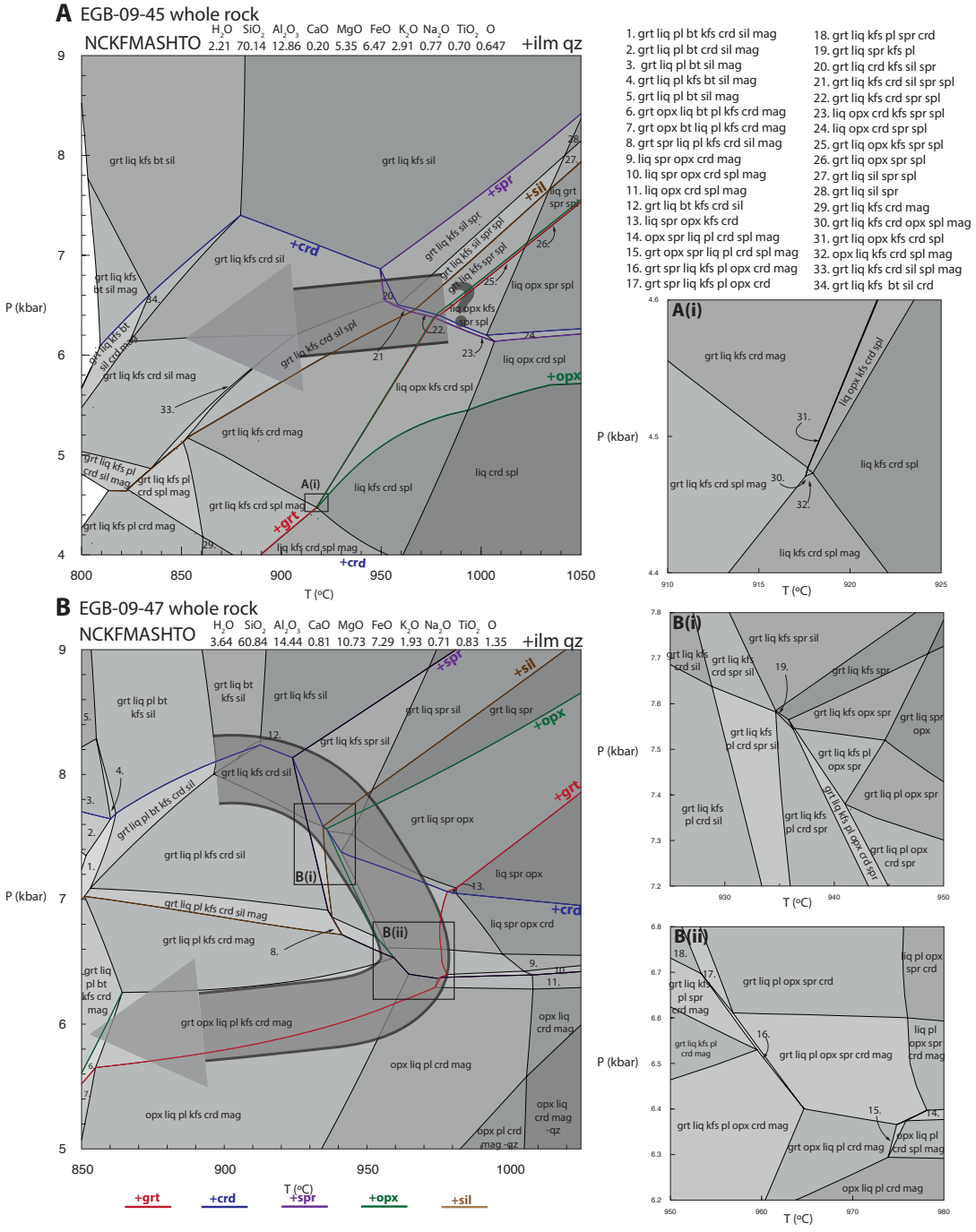

C.11 | Fully annotated *P–T* pseudosections calculated using THERMOCALC 3.40 for domains 1 and 2 in sample EGB-09-45 and using domainal compositions shown in Table 3.1

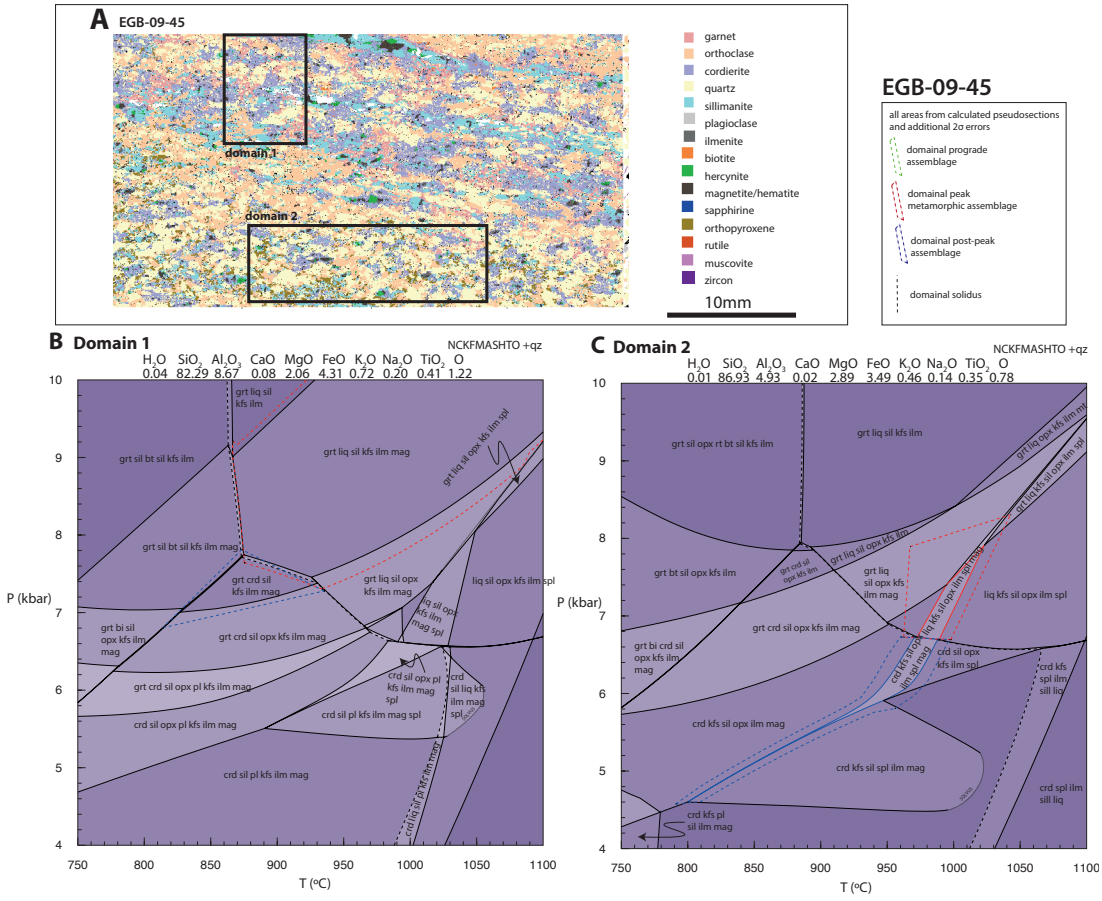

C.12 | Fully annotated *P–T* pseudosections calculated using THERMOCALC 3.40 for domains 1, 2, 3 and 4 in sample EGB-09-45 and using domainal compositions shown in Table 3.1

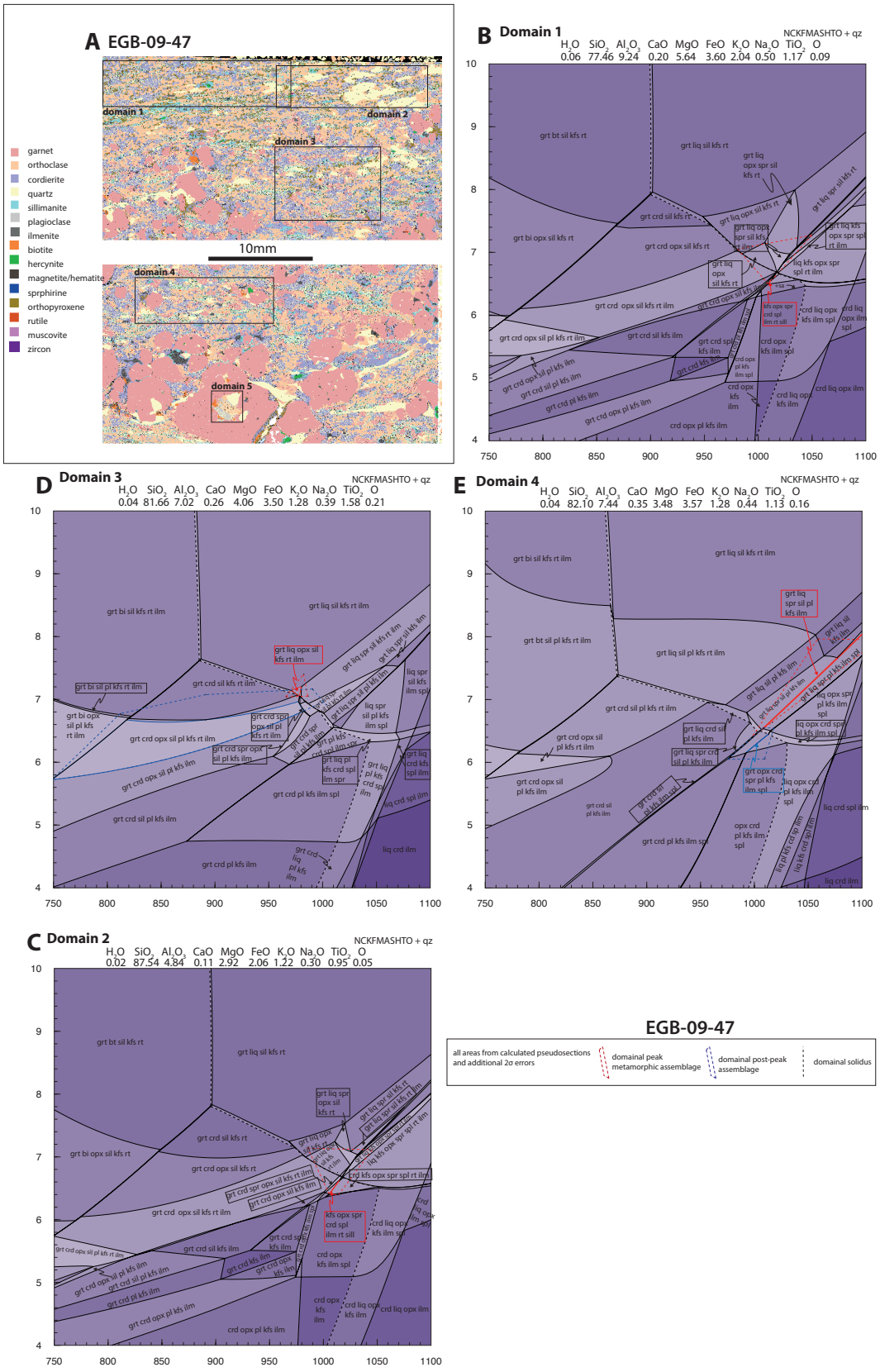

Appendix D | Supplamentary information for Chapter 4: Deciphering the zircon record in a hot orogen

D.1 | Calculated pseudosection and aTiO2-cooling prole for a representative khondalite composition and fit for Ti-in-zircon correction

Pressure–temperature pseudosections were calculated using THERMOCALC 3.45 and the ds6 internally consistent thermodynamic dataset (Holland and Powell (2011); tc–ds62.txt, updated 6 February 2012). Pseudosections were calculated in the Na2O–CaO–K2O–FeO–MgO–Al2O3–SiO2–H2O–TiO2–Fe2O3 (NCKFMASHTO) chemical system using the following solution models: biotite, garnet, cordierite, orthopyroxene, silicate melt, ilmenite from White et al. (2014); sapphirine from Wheller & Powell (2014), ternary feldspar from Holland & Powell (2003) and spinel–magnetite from White, Powell & Clarke (2002). Whole rock compositions for initial P–T pseudosections are based on whole rock XRF analyses for which loss-on-ignition (LOI) and Fe titration were used to constrain maximum H2O and Fe2O3 concentrations, respectively.

Holland, T. J. B., & Powell, R. (2003). Activity-composition relations for phass in petrological calculations: an asymmetric multicomponent formation. Contributions to Mineralogy and Petrology, 145(4), 492-501

Holland, T. J. B., & Powell, R. (2011). An improved and extended internally consistent thermodynamic dataset for phases of petrological interest, involving a new equation of state for solids. Journal of Metamorphic Geology, 29(3), 333-383. doi:10.1111/j.1525-1314.2010.00923.x

Wheller, D. J., & Powell, R. (2014). A new thermodynamic model for sapphirine: Calculated phase equilibria in K2O-FeO-MgO-Al2O3-SiO2-H2O-TiO2-Fe2O3. Journal of Metamorphic Geology, 32(3), 287-299. doi:10.1111/-jmg.12067

White, R. W., Powell, R., Holland, T. J. B., Johnson, T. E., & Green, E. D. R. (2014). New mineral activity-composition relations for thermodynamic calculations in metapelitic systems. Journal of Metamorphic Geology, 32(3), 261-286. doi:10.1111/jmg.12071

White, R. W., Powell, R., & Clarke, G. L. (2002). The interpretation of reaction textures in Fe-rich metapelitic granulites of the Musgrave Block, central Australia: constraints from mineral equilibria calculations in the system K2O-FeO-MgO-Al2O3-SiO2-H2O-TiO2-Fe2O3. Journal of Metamorphic Geology, 20(1), 41-55.

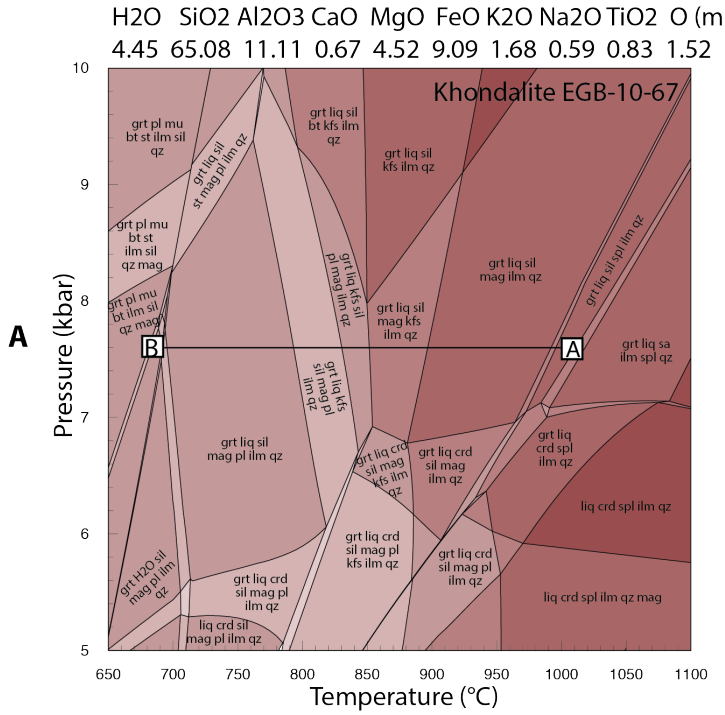

A) P–T pseudosection for a representative knondalite EGB-10-67 with the given composition.

Isobaric cooling path at 7.6 kbar from 1000 °C to the

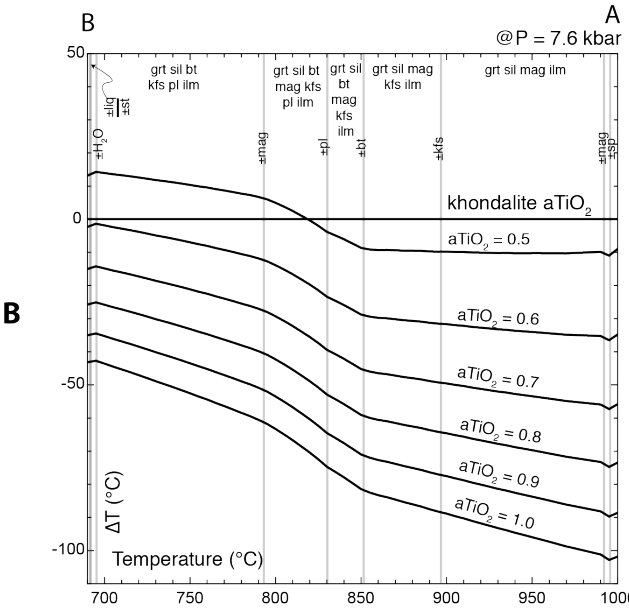

B) ΔT vs temperature for hupothetical Ti-in-zircon thermometry results along the isobaric cooling path A-B normalised to khondalite $aTiO_2$ values.

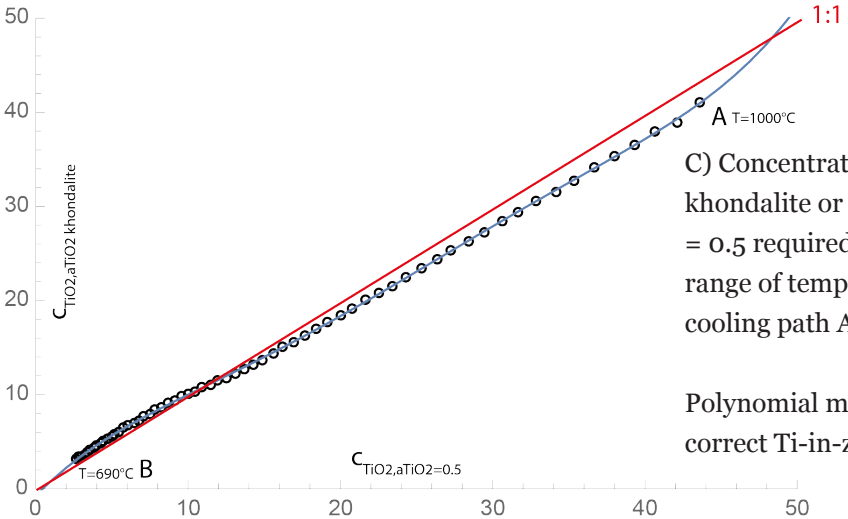

C) Concentration of TiO2 in a khondalite or with fixed $aTiO_2$ = 0.5 required to calculate a range of temperatured on the cooling path A-B

Polynomial model fit used to correct Ti-in-zircon

D.2 | Mathematica 11.0 script for k-means clustering of zircon analyses from samples 17-37, -59, -66 and -91

```
(*input from raw data .txt file*)
input=Import[“insert file path here”,”Table”];
(*corresponding data columns from .txt file*)
La=input[[All,96]];
Ce=input[[All,97]];
Nd=input[[All,98]];
Sm=input[[All,99]];
Eu=input[[All,100]];
Gd=input[[All,101]];
Dy=input[[All,102]];
Ho=input[[All,103]];
Er=input[[All,104]];
Tm=input[[All,105]];
Yb=input[[All,106]];
Lu=input[[All,107]];
Nb=input[[All,62]];
Ybc=input[[All,84]];
U=input[[All,46]];
Th=input[[All,48]];
Pb=input[[All,50]];
Uerr=input[[All,47]];
Therr=input[[All,49]];
Pberr=input[[All,51]];
Hf=input[[All,88]];
Ti=input[[All,58]];
UTh=input[[All,52]];
Y=input[[All,60]];
Tierr=input[[All,59]];
UPb3806=input[[All,14]];
PbTh0832=input[[All,22]];
PbPb0608=input[[All,25]];
```

```
PbPb0706=input[[All,17]];
UPb3806err=input[[All,15]];
PbPb0706err=input[[All,18]];
name =input[[All,3]];
age3806=input[[All,31]];
age0706=input[[All,37]];
age3806err=input[[All,33]];
age0706err=input[[All,39]];

(* Eu, Ce anomalies and other ratios *)
EuA=Eu/Sqrt[(Sm^2+Gd^2)];
CeA=Ce/Sqrt[(La^2+Nd^2)];
LuGd=Lu/Gd;
UYb=U/Yb;
NbYb=Nb/Yb;
YbGd=Yb/Gd;
LREE1=Dy*0.254/(Nd*0.467)+Dy*0.254/(Sm*0.153);

(*Log of anomalies and other  ratios *)
LEuA=Log[10, EuA];
LCeA=Log[10,CeA];
LY=Log[10, Y];
LUTh=Log[10,UTh]
LLuGd=Log[10,LuGd]
LYbGd=Log[10,YbGd]
lLREE1=Log[10,LREE1];


data=Transpose[{name,LEuA,LCeA,LY,LLuGd,LUTh,lLREE1}];

(*Select data for clustering based on Log[EuA], Log[CeA], Log[Y],
Log[*LREE1]*)
ldata=data[[All,{2,3,4,7}]]->data;
cluster=FindClusters[ldata,3,Method->"KMeans"];

(*Select data belonging to each cluster - c1, c2 and c3 *)
c1=cluster[[1,All]]
c2=cluster[[2,All]]
c3=cluster[[3,All]]
```

```
(*Sort each cluster by analysis name *)
points1=Sort[c1[[All,1]]]
points2=Sort[c2[[All,1]]]
points3=Sort[c3[[All,1]]]

(*Sort input data by analysis name *)
```

D.3 | Cathodoluminescence (CL) images and LASS analysis spots of zircon from samples 17-37, -59, -66, -72, -78 and -91.

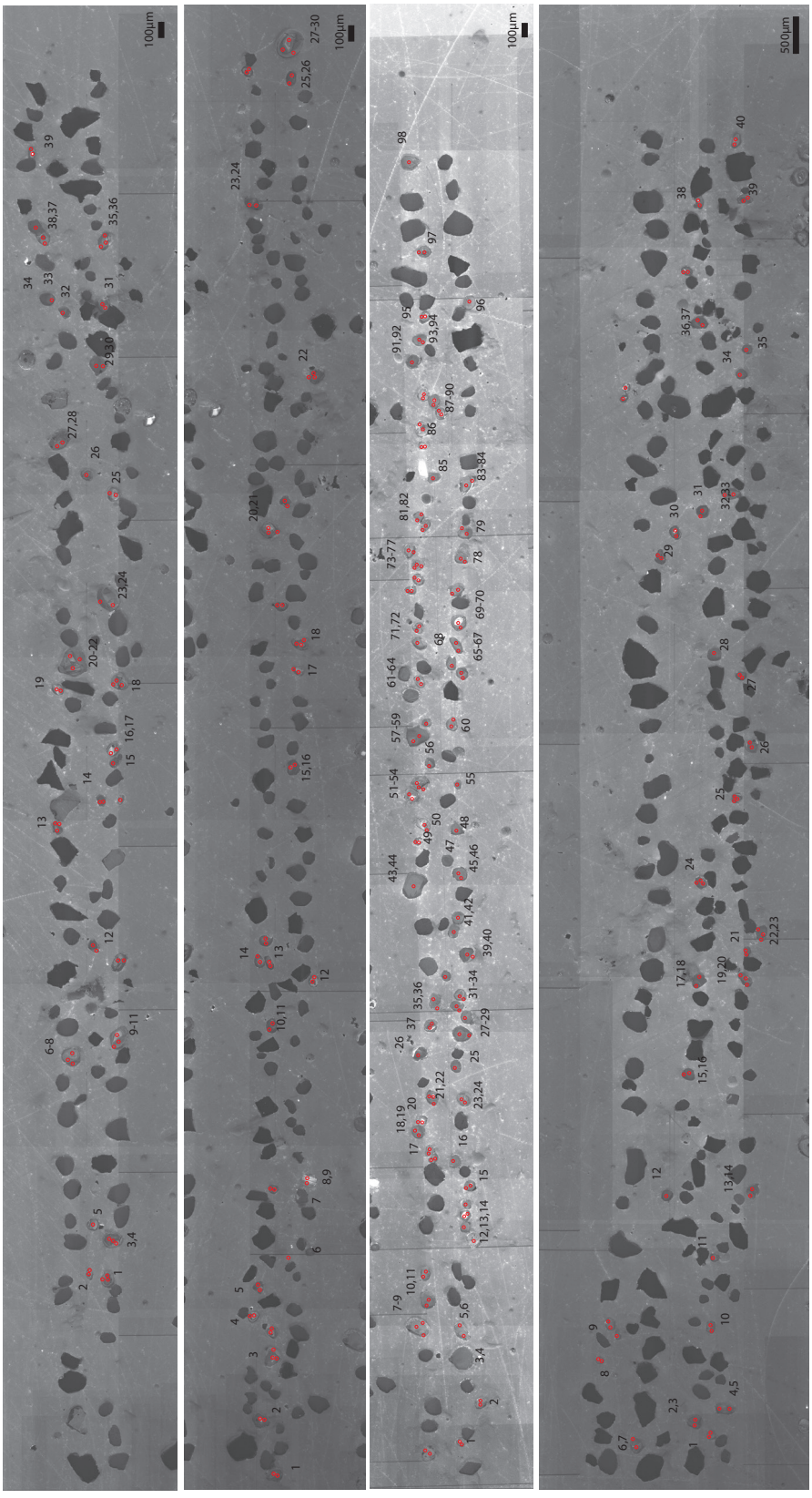
EGB-17-66
EGB-17-72
EGB-17-59
EGB-17-37
100µm
100µm
100µm
500µm

Prefix -1

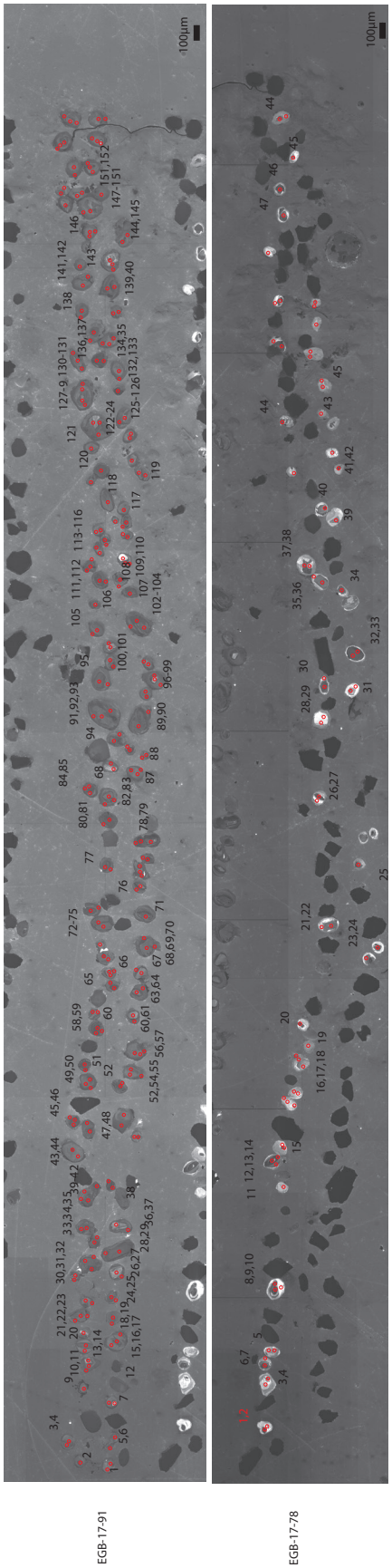

Prefix -2

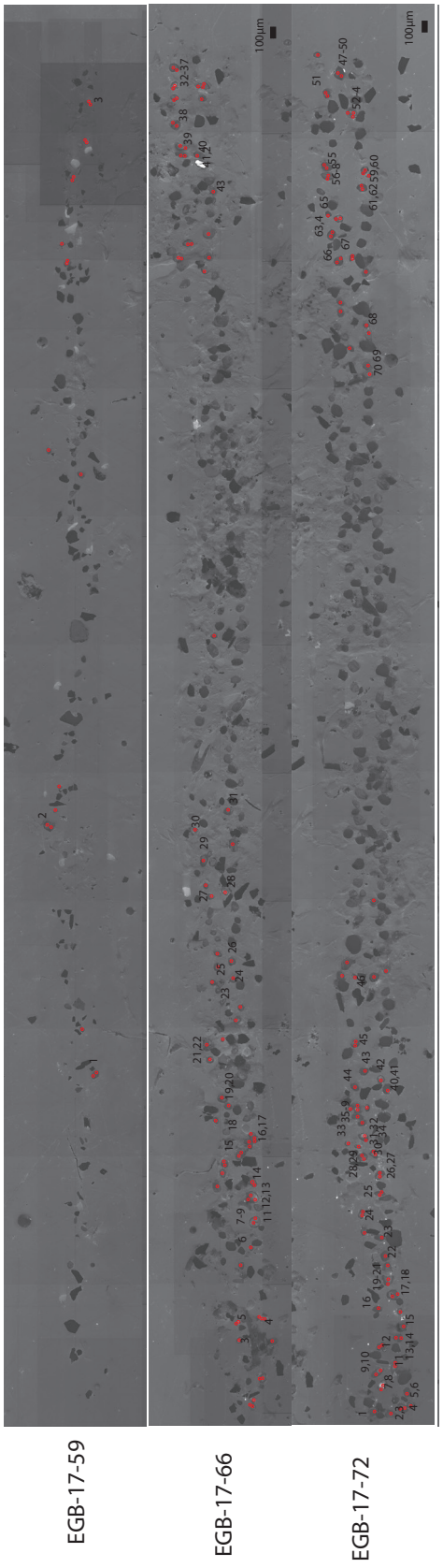

Prefix -2

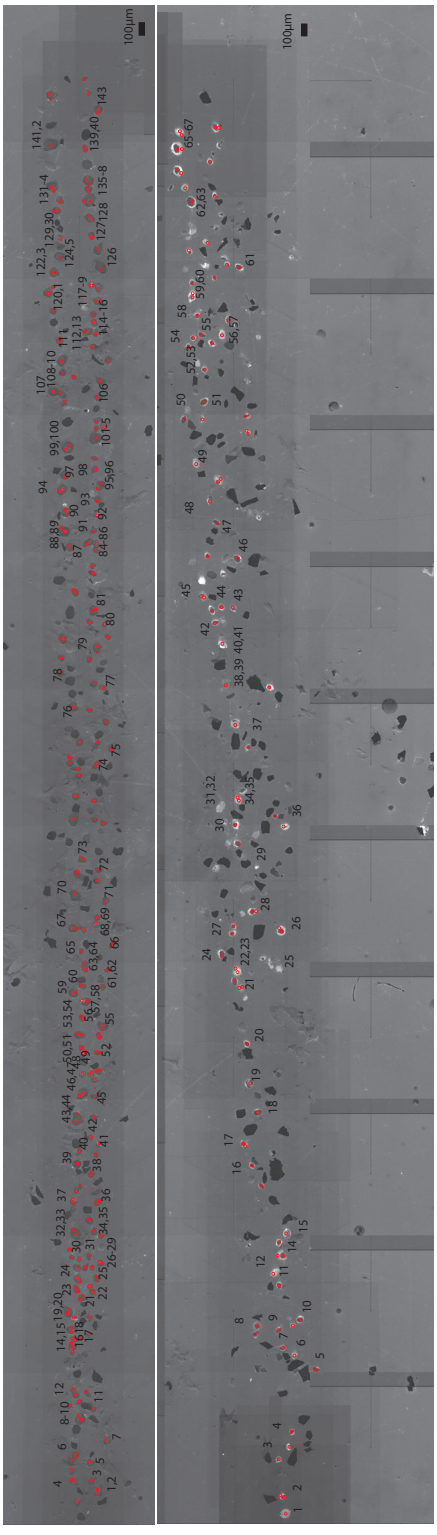

EGB-17-37

EGB-17-78

D.4 | Laser Ablation Split-Stream (LASS) U–Pb and trace element data tables for samples 17-37, -59, -66, -72, -78 and -91.

Zircon U–Pb data tables

Zircon analysis spot	206/238	206/238 Int2SE	206/238 Prop2SE	238/206	238/206 Prop2SE	207/206	207/206 Int2SE	207/206 Prop2SE	Age 206/238	Age 206/238 Int2SE	Age 206/238 Prop2SE	Age 207/206	Age 207/206 Int2SE	Age 207/206 Prop2SE	206/204	206/204 Int2SE	207/204	207/204 Int2SE	208/204	208/204 Int2SE	U/Th	U/Th Int2SE
17-37-1 - 1	0.122	0.004	0.004	8.210	0.276	0.068	0.001	0.001	741	22	23	853	33	33	1.1E+05	8.1E+04	7.5E+03	5.4E+03	1.0E+04	7.1E+03	3.51	0.44
17-37-1 - 2	0.148	0.003	0.004	6.739	0.163	0.069	0.000	0.000	892	17	20	895	11	11	-5.0E+05	1.6E+05	-3.0E+04	1.1E+04	7.0E+02	7.9E+03	3.77	0.07
17-37-1 - 3	0.123	0.007	0.008	8.104	0.493	0.065	0.001	0.001	749	42	43	778	39	39	6.0E+04	6.9E+04	3.6E+03	4.4E+03	5.3E+03	5.9E+03	3.26	0.04
17-37-1 - 4	0.091	0.004	0.004	11.013	0.461	0.058	0.001	0.001	560	21	22	523	20	20	5.7E+04	5.5E+04	3.3E+03	3.2E+03	6.2E+03	5.2E+03	1.85	0.29
17-37-1 - 5	0.083	0.001	0.002	12.107	0.220	0.057	0.000	0.000	511.7	6.2	8.8	504	14	14	-7.0E+05	1.4E+05	-4.3E+03	7.9E+03	-5.8E+03	9.6E+03	4.68	0.55
17-37-1 - 6	0.105	0.006	0.006	9.524	0.517	0.063	0.001	0.001	643	32	33	690	37	37	1.1E+05	6.9E+04	6.7E+03	4.2E+03	6.3E+03	4.1E+03	4.84	0.24
17-37-1 - 7	0.083	0.000	0.001	12.008	0.159	0.058	0.000	0.000	515.7	2.2	6.6	510	16	16	4.8E+04	6.3E+04	2.7E+03	3.6E+03	1.3E+03	1.8E+03	11.01	0.32
17-37-1 - 8	0.170	0.014	0.015	5.882	0.519	0.077	0.003	0.003	1010	80	81	1105	80	80	-9.0E+03	1.5E+05	-1.0E+03	1.2E+04	7.0E+04	1.0E+04	3.15	0.49
17-37-1 - 9	0.163	0.015	0.015	6.135	0.565	0.078	0.003	0.003	968	81	82	1131	91	91	-4.0E+05	1.9E+05	-2.0E+04	1.4E+04	1.0E+04	3.1E+04	2.63	0.54
17-37-1 - 10	0.094	0.002	0.002	10.593	0.224	0.061	0.001	0.001	581.3	9.4	12	641	23	23	-4.0E+03	1.0E+05	-2.0E+02	6.2E+03	2.2E+03	7.2E+03	3.73	0.21
17-37-1 - 11	0.084	0.001	0.001	11.973	0.186	0.057	0.000	0.000	517.1	4.4	7.6	505	14	14	-2.6E+04	3.4E+04	-1.5E+03	1.9E+03	-2.0E+03	2.7E+03	3.57	0.18
17-37-1 - 12	0.174	0.009	0.010	5.757	0.318	0.076	0.003	0.003	1031	51	53	1080	67	67	1.8E+05	1.2E+05	1.4E+04	8.9E+03	1.9E+04	1.2E+04	2.86	0.18
17-37-1 - 13	0.100	0.004	0.004	10.050	0.404	0.062	0.001	0.001	611	22	23	653	37	37	-1.6E+05	2.7E+05	-1.0E+04	1.7E+04	-3.9E+03	6.1E+03	11.55	0.59
17-37-1 - 14	0.085	0.000	0.001	11.743	0.165	0.058	0.000	0.000	526.9	2.7	6.9	528	12	12	5.7E+04	5.1E+04	3.3E+03	2.9E+03	1.6E+03	1.4E+03	10.67	0.18
17-37-1 - 15	0.121	0.005	0.005	8.278	0.349	0.071	0.001	0.001	735	28	29	940	38	38	5.3E+04	4.5E+04	3.7E+03	3.1E+03	5.4E+03	4.5E+03	2.71	0.07
17-37-1 - 16	0.150	0.002	0.003	6.658	0.115	0.069	0.000	0.000	901.9	9.8	14	908	11	11	9.0E+04	8.1E+04	6.0E+02	5.6E+03	9.0E+02	7.9E+03	2.83	0.04
17-37-1 - 17	0.085	0.001	0.002	11.765	0.249	0.058	0.001	0.001	525.6	8.6	11	523	19	19	7.0E+05	3.0E+05	4.0E+04	1.7E+04	2.7E+03	8.8E+03	7.30	1.00
17-37-1 - 18	0.083	0.001	0.001	11.979	0.172	0.058	0.000	0.000	516.8	3.4	7.1	517	12	12	3.1E+04	8.0E+04	1.8E+03	4.6E+03	1.4E+03	3.6E+03	6.33	0.18
17-37-1 - 19	0.096	0.007	0.007	10.438	0.752	0.062	0.002	0.002	589	40	40	666	69	69	-7.0E+05	2.3E+05	-5.0E+04	1.6E+04	-1.3E+04	2.1E+04	9.90	1.80
17-37-1 - 20	0.094	0.003	0.003	10.593	0.337	0.060	0.001	0.001	581	16	18	602	21	21	4.7E+04	4.3E+04	2.8E+03	2.5E+03	1.6E+03	1.5E+03	7.71	0.64
17-37-1 - 21	0.146	0.009	0.009	6.835	0.420	0.075	0.003	0.003	879	50	51	1052	90	90	-2.0E+04	9.9E+04	-9.0E+02	7.3E+03	-2.8E+03	7.6E+03	4.89	0.81
17-37-1 - 22	0.111	0.009	0.009	9.025	0.741	0.076	0.006	0.006	676	52	53	1050	150	150	8.0E+05	1.1E+05	7.0E+04	1.0E+04	1.3E+04	1.3E+04	4.51	0.75
17-37-1 - 23	0.086	0.001	0.002	11.614	0.216	0.058	0.000	0.000	534.7	8.4	11	524	15	15	2.3E+04	3.0E+04	1.3E+03	1.7E+03	1.1E+03	2.2E+03	4.09	0.25
17-37-1 - 24	0.216	0.011	0.012	4.630	0.257	0.086	0.002	0.002	1257	61	63	1324	55	55	-5.0E+04	7.5E+04	-5.0E+02	6.4E+03	-2.0E+04	1.5E+04	1.65	0.21
17-37-1 - 25	0.129	0.008	0.008	7.764	0.464	0.069	0.002	0.002	780	43	44	891	52	52	-3.9E+04	9.1E+04	-2.8E+03	6.6E+03	-2.0E+02	4.7E+03	5.10	0.38
17-37-1 - 26	0.143	0.003	0.003	6.998	0.157	0.069	0.000	0.000	861	15	18	883	13	13	5.8E+04	9.1E+04	3.9E+03	6.2E+03	3.6E+03	7.6E+03	4.90	1.70
17-37-1 - 27	0.088	0.001	0.001	11.310	0.166	0.058	0.001	0.001	546.2	4.4	7.9	538	20	20	4.0E+04	3.0E+04	2.4E+03	1.7E+03	3.0E+03	2.3E+03	3.56	0.16
17-37-1 - 28	0.085	0.001	0.001	11.733	0.193	0.058	0.000	0.000	527.2	5.4	8.4	520	13	13	6.7E+04	5.6E+04	3.8E+03	3.3E+03	1.7E+03	1.5E+03	11.05	0.15
17-37-1 - 29	0.109	0.004	0.004	9.174	0.320	0.080	0.003	0.003	666	20	22	1181	85	85	8.0E+05	1.0E+05	6.6E+03	9.2E+03	1.0E+04	1.5E+04	2.27	0.20

17-37-1 - 30	0.117	0.005	0.005	8.525	0.342	0.067	0.001	0.001	715	26	27	830	38	38	-1.5E+04	7.5E+04	-9.0E+02	4.9E+03	-1.3E+03	8.9E+03	2.26	0.22
17-37-1 - 31	0.131	0.005	0.006	7.651	0.322	0.067	0.001	0.001	791	30	31	833	26	26	3.1E+04	7.1E+04	2.0E+03	4.8E+03	1.1E+03	4.6E+03	4.79	0.73
17-37-1 - 32	0.091	0.002	0.002	10.965	0.289	0.060	0.000	0.000	563	13	14	586	17	17	-7.0E+05	1.9E+05	-4.0E+04	1.1E+04	-6.0E+04	1.7E+04	3.48	0.08
17-37-1 - 33	0.113	0.004	0.004	8.889	0.324	0.077	0.004	0.004	687	22	24	1106	96	96	-7.0E+05	1.4E+05	-5.0E+04	1.1E+04	-3.0E+04	1.2E+04	7.00	3.50
17-37-1 - 34	0.134	0.002	0.002	7.446	0.128	0.068	0.000	0.000	812.5	8.8	13	857	11	11	1.5E+05	1.3E+05	9.9E+03	8.9E+03	1.4E+04	1.2E+04	2.86	0.09
17-37-1 - 35	0.114	0.003	0.003	8.757	0.238	0.064	0.001	0.001	697	16	18	752	18	18	-2.4E+04	6.6E+04	-1.5E+03	4.2E+03	-2.3E+03	6.3E+03	2.86	0.04
17-37-1 - 36	0.137	0.004	0.004	7.278	0.217	0.073	0.001	0.001	830	21	23	1014	23	23	4.1E+04	3.8E+04	3.0E+03	2.7E+03	5.9E+03	3.6E+03	2.49	0.32
17-37-1 - 37	0.094	0.004	0.004	10.638	0.419	0.060	0.001	0.001	579	20	22	611	22	22	2.5E+05	5.8E+05	1.5E+04	3.5E+04	1.4E+04	3.5E+04	5.90	0.83
17-37-1 - 38	0.100	0.003	0.003	10.030	0.332	0.062	0.001	0.001	612	18	19	681	22	22	6.5E+04	8.3E+04	4.1E+03	5.1E+03	2.8E+03	4.9E+03	3.97	0.12
17-37-1 - 39	0.088	0.001	0.002	11.377	0.207	0.060	0.001	0.001	543	6.7	9.4	594	21	21	1.8E+04	6.8E+04	1.1E+03	4.0E+03	1.3E+03	4.1E+03	5.80	0.41
17-37-1 - 40	0.107	0.005	0.005	9.381	0.431	0.068	0.002	0.002	653	27	28	873	54	54	3.9E+04	4.8E+04	2.7E+03	3.1E+03	5.9E+03	5.9E+03	1.97	0.31
17-37-2 - 1	0.103	0.003	0.004	9.699	0.367	0.064	0.001	0.001	632	20	23	739	30	35	-1.2E+04	9.7E+04	-7.0E+02	6.0E+03	6.0E+02	4.5E+03	6.28	0.60
17-37-2 - 2	0.105	0.003	0.004	9.551	0.347	0.064	0.001	0.001	642	19	22	743	42	46	2.1E+04	4.6E+04	1.5E+03	2.9E+03	1.6E+03	3.4E+03	4.06	0.23
17-37-2 - 3	0.138	0.005	0.006	7.236	0.309	0.068	0.001	0.001	834	30	34	870	23	29	2.0E+05	1.2E+05	1.3E+03	8.1E+03	1.0E+04	1.0E+04	3.54	0.35
17-37-2 - 4	0.114	0.005	0.005	8.764	0.399	0.068	0.002	0.002	696	27	30	856	70	72	1.7E+04	4.9E+04	1.2E+03	3.3E+03	5.0E+02	4.0E+03	5.62	0.72
17-37-2 - 5	0.105	0.005	0.005	9.488	0.459	0.069	0.001	0.002	645	28	30	887	39	43	4.5E+04	4.3E+04	3.0E+03	2.9E+03	2.8E+03	2.7E+03	5.95	0.75
17-37-2 - 6	0.109	0.005	0.005	9.191	0.422	0.065	0.001	0.001	665	26	29	774	33	38	6.0E+04	6.1E+04	6.0E+02	4.0E+03	9.0E+02	3.8E+03	3.99	0.35
17-37-2 - 7	0.165	0.007	0.008	6.079	0.285	0.080	0.002	0.002	981	39	43	1181	40	44	1.1E+04	7.0E+04	1.0E+03	5.6E+03	2.0E+04	1.1E+04	1.86	0.06
17-37-2 - 8	0.145	0.008	0.008	6.878	0.397	0.074	0.002	0.002	874	44	47	1033	59	62	9.9E+04	4.8E+04	7.1E+03	3.3E+03	1.3E+04	7.7E+03	4.20	1.50
17-37-2 - 9	0.106	0.004	0.004	9.443	0.392	0.064	0.001	0.001	649	22	25	725	25	31	5.6E+04	3.3E+04	3.5E+03	2.1E+03	3.2E+03	2.1E+03	7.70	1.60
17-37-2 - 10	0.133	0.004	0.005	7.513	0.265	0.067	0.000	0.001	805	22	27	836	12	21	-4.0E+05	1.2E+05	-2.9E+03	7.7E+03	-4.0E+02	8.7E+03	4.25	0.70
17-37-2 - 11	0.088	0.003	0.003	11.390	0.402	0.062	0.001	0.001	543	15	18	679	28	33	1.2E+04	2.4E+04	7.0E+02	1.4E+03	6.0E+02	1.2E+03	6.07	0.62
17-37-2 - 12	0.160	0.007	0.007	6.254	0.286	0.069	0.000	0.001	956	36	40	911	10	20	9.4E+04	8.1E+04	6.5E+03	5.7E+03	8.1E+03	7.1E+03	3.38	0.05
17-37-2 - 13	0.102	0.007	0.007	9.852	0.689	0.067	0.002	0.002	622	40	41	860	77	80	-2.3E+04	8.5E+04	0.0E+00	4.7E+03	3.0E+02	7.3E+03	2.53	0.88
17-37-2 - 14	0.095	0.005	0.006	10.482	0.615	0.062	0.002	0.002	587	31	33	649	53	56	-8.0E+04	8.1E+04	-3.0E+02	4.7E+03	-1.0E+02	5.3E+03	3.88	0.25
17-37-2 - 15	0.123	0.010	0.010	8.163	0.666	0.086	0.007	0.007	743	56	58	1270	160	160	2.2E+04	3.5E+04	2.6E+03	3.6E+03	2.0E+03	2.5E+03	4.26	0.81
17-37-2 - 16	0.169	0.016	0.016	5.917	0.560	0.080	0.004	0.004	1000	89	91	1180	110	110	1.7E+05	2.2E+05	1.2E+04	1.5E+04	1.2E+04	1.3E+04	4.03	0.67
17-37-2 - 17	0.193	0.015	0.016	5.181	0.430	0.083	0.002	0.002	1133	82	84	1255	40	43	7.4E+04	8.1E+04	6.3E+03	6.8E+03	1.9E+04	2.3E+04	1.22	0.15
17-37-2 - 18	0.113	0.006	0.006	8.865	0.479	0.066	0.001	0.001	688	33	35	806	38	41	2.1E+04	4.4E+04	1.4E+03	2.9E+03	2.0E+03	3.3E+03	7.90	2.50
17-37-2 - 19	0.237	0.032	0.033	4.219	0.588	0.095	0.003	0.003	1360	170	170	1521	66	68	1.2E+04	4.9E+04	7.0E+02	4.6E+03	1.0E+02	5.0E+03	3.14	0.40
17-37-2 - 20	0.108	0.003	0.004	9.276	0.318	0.064	0.000	0.001	660	18	22	728	16	24	0.0E+00	5.4E+04	-1.0E+02	3.4E+03	-1.0E+02	5.2E+03	3.16	0.10
17-37-2 - 21	0.087	0.005	0.005	11.534	0.678	0.060	0.001	0.001	535	28	30	602	37	42	4.0E+05	1.0E+05	2.4E+03	6.2E+03	2.4E+03	5.9E+03	5.98	0.65
17-37-2 - 22	0.124	0.011	0.011	8.065	0.715	0.073	0.003	0.003	752	64	66	983	94	96	-1.0E+05	9.8E+04	-1.4E+03	7.5E+03	-4.0E+04	1.1E+04	4.25	0.79

17-37-2 - 23	0.109	0.004	0.004	9.149	0.368	0.063	0.001	0.001	669	23	26	705	34	39	1.5E+04	6.4E+04	1.0E+03	4.1E+03	8.0E+02	4.3E+03	4.68	0.36
17-37-2 - 24	0.159	0.011	0.012	6.289	0.475	0.084	0.003	0.003	950	63	66	1283	73	75	1.2E+05	8.6E+04	1.1E+04	7.8E+03	2.0E+04	1.4E+04	1.76	0.20
17-37-2 - 25	0.137	0.007	0.008	7.283	0.398	0.069	0.001	0.001	829	40	43	892	25	31	6.0E+05	1.9E+05	4.0E+04	1.3E+04	2.0E+04	1.5E+04	4.16	0.75
17-37-2 - 26	0.117	0.005	0.006	8.569	0.433	0.068	0.001	0.001	711	31	34	868	36	40	3.9E+04	6.4E+04	2.5E+03	4.2E+03	2.8E+03	5.1E+03	3.79	0.34
17-37-2 - 27	0.077	0.003	0.003	12.937	0.569	0.060	0.001	0.001	480	18	20	596	44	48	-3.0E+04	5.5E+04	-1.0E+02	3.1E+03	-1.0E+02	2.0E+03	10.90	1.90
17-37-2 - 28	0.139	0.005	0.006	7.220	0.302	0.072	0.001	0.001	836	29	33	976	33	37	6.2E+04	4.5E+04	4.5E+03	3.3E+03	4.8E+03	5.3E+03	3.16	0.41
17-37-2 - 29	0.173	0.012	0.012	5.780	0.401	0.082	0.002	0.002	1024	65	67	1237	42	45	2.6E+04	1.9E+04	2.0E+03	1.5E+03	3.6E+03	2.6E+03	1.97	0.20
17-37-2 - 30	0.086	0.005	0.005	11.641	0.691	0.065	0.001	0.001	531	29	30	759	33	37	2.7E+04	1.9E+04	1.7E+03	1.2E+03	1.5E+03	1.1E+03	6.56	0.95
17-37-2 - 31	0.091	0.004	0.005	10.953	0.564	0.060	0.000	0.001	563	25	27	584	18	25	-5.0E+05	1.4E+05	-2.7E+03	8.0E+03	-4.0E+04	1.3E+04	3.62	0.58
17-37-2 - 32	0.095	0.004	0.005	10.537	0.522	0.063	0.002	0.002	584	25	28	695	59	62	2.3E+04	2.3E+04	1.4E+03	1.5E+03	1.6E+03	1.1E+03	6.75	0.52
17-37-2 - 33	0.083	0.001	0.002	11.990	0.288	0.058	0.000	0.001	516.4	6.6	12	513	13	23	2.3E+04	4.2E+04	1.3E+03	2.4E+03	8.0E+02	1.5E+03	8.55	0.14
17-37-2 - 34	0.105	0.005	0.005	9.533	0.473	0.064	0.001	0.001	642	28	30	738	30	35	1.5E+04	4.8E+04	1.0E+03	3.0E+03	1.3E+03	2.9E+03	4.37	0.37
17-37-2 - 35	0.096	0.004	0.005	10.428	0.500	0.066	0.000	0.001	590	25	27	793	15	23	8.2E+04	4.5E+04	5.4E+03	3.0E+03	6.3E+03	3.5E+03	4.25	0.28
17-37-2 - 36	0.110	0.007	0.007	9.124	0.608	0.077	0.001	0.001	670	41	42	1124	19	25	6.5E+04	4.3E+04	5.0E+03	3.3E+03	1.0E+04	6.9E+03	2.32	0.16
17-37-2 - 37	0.130	0.003	0.004	7.698	0.219	0.067	0.001	0.001	787	15	21	850	19	26	6.0E+05	1.0E+05	4.2E+03	6.7E+03	6.0E+04	1.1E+04	3.13	0.18
17-37-2 - 38	0.093	0.007	0.007	10.753	0.798	0.067	0.003	0.003	572	39	41	819	79	81	-7.9E+04	9.6E+04	-5.1E+03	6.1E+03	-4.4E+03	9.1E+03	5.90	1.90
17-37-2 - 39	0.084	0.001	0.002	11.878	0.268	0.058	0.000	0.001	521.1	5	11	541	16	24	7.6E+04	4.4E+04	4.4E+03	2.6E+03	2.6E+03	1.5E+03	9.62	0.53
17-37-2 - 40	0.314	0.040	0.040	3.185	0.406	0.143	0.013	0.013	1740	200	200	2170	210	210	1.1E+05	1.3E+05	1.5E+04	2.0E+04	8.0E+04	1.2E+04	4.30	1.10
17-37-2 - 41	0.158	0.011	0.011	6.329	0.441	0.075	0.002	0.002	946	59	62	1066	58	60	3.4E+04	1.7E+04	2.7E+03	1.3E+03	1.1E+04	5.9E+03	1.01	0.08
17-37-2 - 42	0.144	0.012	0.013	6.944	0.627	0.075	0.003	0.003	864	71	73	1042	76	78	3.6E+04	4.0E+04	2.7E+03	3.1E+03	4.6E+03	5.6E+03	2.82	0.54
17-37-2 - 43	0.090	0.005	0.005	11.111	0.617	0.062	0.001	0.001	555	28	30	670	46	51	-2.0E+05	1.1E+05	-1.1E+03	6.8E+03	-1.2E+03	4.4E+03	8.57	0.91
17-37-2 - 44	0.082	0.004	0.004	12.255	0.601	0.060	0.001	0.001	505	22	24	603	38	42	2.6E+04	3.1E+04	1.5E+03	1.8E+03	9.0E+02	1.3E+03	7.60	0.41
17-37-2 - 45	0.116	0.026	0.026	8.621	1.932	0.068	0.003	0.003	700	140	140	866	77	79	3.1E+04	7.0E+04	2.1E+03	4.4E+03	3.0E+03	7.7E+03	2.40	1.20
17-37-2 - 46	0.161	0.004	0.006	6.203	0.212	0.076	0.001	0.001	963	25	30	1103	27	32	2.0E+05	1.1E+05	1.7E+03	8.4E+03	8.0E+04	4.7E+04	0.90	0.07
17-37-2 - 47	0.094	0.004	0.004	10.638	0.441	0.060	0.001	0.001	579	20	23	616	32	37	4.0E+04	3.2E+04	3.0E+02	1.9E+03	2.0E+02	2.3E+03	4.20	0.14
17-37-2 - 48	0.226	0.016	0.017	4.425	0.333	0.088	0.003	0.003	1310	85	88	1370	73	75	6.9E+04	5.6E+04	6.4E+03	5.0E+03	9.5E+03	7.3E+03	2.52	0.33
17-37-2 - 49	0.107	0.002	0.003	9.355	0.254	0.063	0.001	0.001	655	11	17	704	22	29	-1.3E+05	1.4E+05	-8.3E+03	8.8E+03	-1.1E+04	1.2E+04	7.70	2.40
17-37-2 - 50	0.202	0.013	0.014	4.950	0.343	0.082	0.002	0.002	1184	72	75	1232	46	49	-2.7E+04	4.8E+04	-2.3E+03	3.8E+03	-3.4E+03	4.6E+03	3.74	0.68
17-37-2 - 51	0.108	0.010	0.010	9.242	0.837	0.066	0.002	0.002	660	55	57	784	65	68	-3.4E+04	7.3E+04	-2.4E+03	4.9E+03	-2.9E+03	4.0E+03	6.26	0.98
17-37-2 - 52	0.104	0.005	0.006	9.643	0.511	0.065	0.001	0.001	636	30	32	783	44	48	4.1E+04	9.2E+04	8.0E+02	7.2E+03	2.1E+03	7.7E+03	4.70	0.51
17-37-2 - 53	0.087	0.002	0.003	11.534	0.372	0.061	0.001	0.001	536	13	16	641	23	29	5.7E+04	8.6E+04	3.5E+03	5.3E+03	1.0E+04	1.4E+04	2.27	0.32
17-37-2 - 54	0.092	0.002	0.003	10.881	0.296	0.062	0.001	0.001	567	10	15	659	32	37	5.0E+04	5.5E+04	3.0E+03	3.3E+03	2.0E+03	2.1E+03	5.79	0.65
17-37-2 - 55	0.086	0.001	0.002	11.601	0.283	0.057	0.000	0.001	532.8	6.7	12	508	14	23	5.6E+04	3.1E+04	3.2E+03	1.8E+03	2.2E+03	1.3E+03	6.89	0.27

17-37-2 - 56	0.101	0.005	0.005	9.891	0.519	0.065	0.001	0.001	620	29	31	766	32	36	2.3E+04	5.7E+04	1.6E+03	3.7E+03	2.8E+03	7.7E+03	2.12	0.09
17-37-2 - 57	0.245	0.017	0.018	4.082	0.300	0.090	0.003	0.003	1410	91	94	1403	72	74	2.1E+04	1.5E+04	1.9E+03	1.5E+03	5.3E+03	4.4E+03	1.33	0.25
17-37-2 - 58	0.097	0.006	0.006	10.288	0.646	0.061	0.001	0.001	597	34	36	638	39	43	-2.9E+04	9.5E+04	-1.7E+03	5.5E+03	-1.1E+03	3.5E+03	8.07	0.54
17-37-2 - 59	0.099	0.005	0.006	10.142	0.566	0.067	0.002	0.002	606	30	32	844	69	72	3.0E+04	5.3E+04	1.8E+03	3.3E+03	7.0E+02	2.1E+03	5.30	1.00
17-37-2 - 60	0.127	0.004	0.005	7.886	0.286	0.069	0.001	0.001	770	22	26	905	28	33	6.0E+04	4.3E+04	4.1E+03	3.0E+03	4.1E+03	3.1E+03	4.36	0.52
17-37-2 - 61	0.084	0.002	0.002	11.862	0.310	0.059	0.001	0.001	521.6	8.7	13	576	20	27	8.7E+04	6.6E+04	5.1E+03	3.8E+03	8.1E+03	6.3E+03	3.45	0.28
17-37-2 - 62	0.117	0.006	0.006	8.569	0.448	0.067	0.001	0.001	711	33	35	834	31	36	5.2E+04	5.2E+04	3.5E+03	3.5E+03	4.8E+03	5.0E+03	3.46	0.40
17-37-2 - 63	0.099	0.001	0.002	10.152	0.237	0.061	0.000	0.001	605.5	7.2	14	651	14	23	1.3E+05	1.5E+05	8.2E+03	9.1E+03	1.2E+04	1.3E+04	3.30	0.05
17-37-2 - 64	0.098	0.002	0.003	10.235	0.262	0.061	0.001	0.001	600.7	8.8	14	638	23	30	4.0E+05	1.2E+05	2.3E+03	7.2E+03	4.0E+04	1.2E+04	3.15	0.07
17-37-2 - 65	0.097	0.010	0.010	10.320	1.054	0.065	0.002	0.002	595	57	58	780	55	58	4.0E+05	1.3E+05	2.8E+03	8.3E+03	4.0E+04	1.0E+04	6.00	1.10
17-37-2 - 66	0.104	0.007	0.008	9.662	0.709	0.066	0.001	0.001	634	42	44	786	32	37	1.4E+04	5.3E+04	8.0E+02	3.4E+03	7.0E+02	2.2E+03	7.90	1.40
17-37-2 - 67	0.089	0.001	0.002	11.213	0.251	0.059	0.001	0.001	550.7	5.9	12	579	37	42	5.2E+04	6.6E+04	3.0E+03	3.8E+03	3.2E+03	4.0E+03	5.17	0.48
17-37-2 - 68	0.186	0.018	0.019	5.376	0.549	0.090	0.007	0.007	1100	100	100	1370	150	160	5.2E+04	2.6E+04	4.7E+03	2.8E+03	2.7E+03	2.3E+03	6.80	1.70
17-37-2 - 69	0.133	0.005	0.006	7.519	0.328	0.069	0.001	0.001	805	30	33	895	36	40	1.7E+05	6.7E+05	1.1E+04	4.7E+04	4.0E+04	2.5E+04	8.60	1.10
17-37-2 - 70	0.085	0.001	0.002	11.779	0.291	0.058	0.000	0.001	525.4	7.4	12	516	14	23	-2.0E+04	8.8E+04	-2.0E+02	5.2E+03	4.1E+03	2.5E+03	2.92	0.05
17-37-2 - 71	0.090	0.008	0.009	11.099	1.047	0.068	0.003	0.003	555	49	50	867	71	73	-3.0E+04	9.7E+04	-1.8E+03	6.3E+03	-5.0E+02	3.8E+03	10.80	1.70
17-37-2 - 72	0.150	0.008	0.009	6.689	0.398	0.120	0.011	0.011	897	47	50	1880	190	190	-1.0E+05	1.3E+05	0.0E+00	1.7E+04	-1.0E+03	1.4E+04	3.67	0.24
17-37-2 - 73	0.095	0.003	0.003	10.537	0.378	0.062	0.001	0.001	584	16	20	671	20	27	2.0E+05	1.5E+05	1.1E+03	9.3E+03	7.0E+02	6.0E+03	10.56	0.69
17-37-2 - 74	0.138	0.009	0.009	7.252	0.489	0.068	0.001	0.001	832	51	53	861	42	46	1.3E+05	1.7E+05	9.0E+04	1.2E+04	1.3E+04	1.6E+04	3.98	0.68
17-37-2 - 75	0.117	0.004	0.005	8.576	0.353	0.065	0.001	0.001	711	24	28	778	29	34	3.5E+04	5.5E+04	2.4E+03	3.6E+03	3.1E+03	4.3E+03	3.97	0.25
17-37-2 - 76	0.142	0.004	0.005	7.027	0.247	0.073	0.002	0.002	857	23	28	995	57	60	3.0E+05	3.5E+05	2.1E+04	2.4E+04	2.9E+04	3.4E+04	4.08	0.73
17-37-2 - 77	0.095	0.003	0.003	10.526	0.355	0.061	0.001	0.001	585	15	19	642	37	41	7.0E+05	1.2E+05	3.8E+03	7.5E+03	5.0E+04	1.0E+04	4.30	0.62
17-37-2 - 78	0.108	0.005	0.005	9.276	0.465	0.063	0.001	0.001	659	29	31	707	23	29	4.6E+04	6.6E+04	2.7E+03	4.1E+03	4.6E+03	5.9E+03	3.55	0.36
17-37-2 - 79	0.118	0.008	0.008	8.511	0.594	0.065	0.001	0.001	715	45	47	757	36	40	-7.0E+05	1.4E+05	-4.8E+03	9.2E+03	-1.3E+03	4.5E+03	8.01	0.92
17-37-2 - 80	0.117	0.012	0.012	8.547	0.877	0.066	0.002	0.002	709	69	70	802	47	51	7.0E+05	1.1E+05	4.7E+03	7.6E+03	4.4E+03	7.3E+03	4.94	0.51
17-37-2 - 81	0.136	0.004	0.004	7.331	0.236	0.076	0.002	0.002	824	20	25	1091	39	43	-7.0E+05	2.9E+05	-6.0E+04	2.1E+04	-4.0E+04	1.3E+04	7.99	0.79
17-37-2 - 82	0.116	0.009	0.009	8.621	0.684	0.076	0.003	0.003	706	52	53	1081	69	71	-3.0E+05	1.8E+05	-2.0E+04	1.4E+04	-4.0E+04	1.7E+04	7.40	1.40
17-37-2 - 83	0.097	0.005	0.005	10.341	0.577	0.068	0.003	0.003	594	30	32	846	81	82	7.7E+04	8.6E+04	5.0E+03	5.6E+03	2.2E+03	2.7E+03	8.40	0.75
17-37-2 - 84	0.183	0.013	0.013	5.464	0.388	0.085	0.002	0.002	1080	70	73	1309	41	44	8.5E+04	4.4E+04	7.3E+03	3.8E+03	1.0E+04	5.5E+03	2.40	0.11
17-37-2 - 85	0.115	0.010	0.010	8.734	0.763	0.077	0.003	0.003	697	57	58	1110	65	67	6.1E+04	5.5E+04	4.4E+03	4.0E+03	4.2E+03	3.9E+03	6.90	0.50
17-37-2 - 86	0.124	0.004	0.004	8.052	0.285	0.074	0.001	0.002	755	21	25	1039	34	38	5.5E+04	4.1E+04	4.0E+03	3.0E+03	2.5E+04	2.2E+04	1.15	0.23
17-37-2 - 87	0.114	0.006	0.007	8.803	0.504	0.065	0.002	0.002	693	35	38	776	56	59	6.6E+04	6.4E+04	4.4E+03	4.1E+03	5.2E+03	4.0E+03	4.81	0.55
17-37-2 - 88	0.219	0.012	0.013	4.566	0.271	0.080	0.002	0.002	1273	64	68	1187	46	49	1.0E+05	9.2E+04	7.9E+03	7.3E+03	8.4E+03	8.7E+03	6.30	2.20

17-37-2 - 89	0.132	0.006	0.007	7.564	0.372	0.069	0.001	0.001	800	33	37	889	25	30	7.4E+04	8.8E+04	5.0E+03	5.9E+03	8.0E+02	1.4E+03	29.40	3.60
17-37-2 - 90	0.173	0.012	0.012	5.780	0.401	0.075	0.002	0.002	1025	66	69	1049	63	65	-8.0E+05	2.0E+05	-6.0E+04	1.5E+04	-9.0E+04	2.0E+04	3.46	0.90
17-37-2 - 91	0.092	0.004	0.005	10.893	0.558	0.068	0.001	0.001	566	25	28	877	32	36	1.0E+05	8.8E+04	6.0E+02	5.9E+03	-4.0E+02	4.8E+03	8.20	1.60
17-37-2 - 92	0.122	0.007	0.007	8.224	0.480	0.076	0.002	0.003	739	39	41	1075	65	67	1.0E+03	2.0E+04	-1.0E+02	1.7E+03	-3.0E+02	2.7E+03	2.58	0.33
17-37-2 - 93	0.110	0.007	0.007	9.116	0.573	0.068	0.001	0.001	670	38	41	875	37	41	7.7E+04	7.0E+04	5.5E+03	4.9E+03	7.7E+03	6.5E+03	3.94	0.52
17-37-2 - 94	0.132	0.006	0.007	7.576	0.385	0.072	0.002	0.002	799	35	38	985	54	56	-3.3E+04	6.8E+04	-2.1E+03	4.8E+03	-1.4E+03	4.2E+03	7.30	1.10
17-37-2 - 95	0.124	0.010	0.011	8.065	0.715	0.066	0.001	0.001	752	59	60	800	36	40	5.0E+05	2.2E+05	4.0E+04	1.4E+04	2.7E+03	5.6E+03	11.70	1.80
17-37-2 - 96	0.117	0.004	0.005	8.540	0.343	0.065	0.001	0.001	713	24	27	781	21	27	9.0E+05	1.2E+05	5.9E+03	8.0E+03	1.5E+03	3.0E+03	15.80	3.20
17-37-2 - 97	0.141	0.007	0.008	7.107	0.399	0.071	0.002	0.002	847	42	44	952	65	67	1.3E+05	3.8E+05	1.1E+04	2.8E+04	1.5E+04	3.9E+04	2.86	0.14
17-37-2 - 98	0.134	0.003	0.004	7.463	0.239	0.068	0.001	0.001	811	19	24	854	21	28	2.0E+05	2.4E+05	1.0E+04	1.7E+04	1.0E+04	1.7E+04	3.86	0.08
17-37-2 - 99	0.150	0.006	0.007	6.658	0.310	0.080	0.005	0.005	901	35	39	1170	120	120	1.1E+05	1.3E+05	3.7E+03	4.0E+03	1.9E+04	2.3E+04	2.17	0.30
17-37-2 - 100	0.134	0.004	0.004	7.479	0.246	0.067	0.001	0.001	809	20	25	839	20	26	2.7E+04	4.2E+04	1.8E+03	2.8E+03	2.7E+03	4.1E+03	2.96	0.03
17-37-2 - 101	0.151	0.002	0.004	6.640	0.168	0.069	0.000	0.001	904	13	21	903	13	22	-6.0E+05	1.1E+05	-4.2E+03	7.4E+03	-3.9E+03	6.9E+03	4.60	0.03
17-37-2 - 102	0.150	0.003	0.005	6.671	0.200	0.069	0.001	0.001	900	19	25	909	17	24	2.2E+05	2.6E+05	1.6E+04	1.8E+04	1.4E+04	1.6E+04	4.81	0.07
17-37-2 - 103	0.145	0.005	0.006	6.901	0.276	0.071	0.001	0.001	872	29	33	947	22	28	5.0E+05	1.2E+05	3.6E+03	8.7E+03	3.1E+03	8.5E+03	6.70	0.66
17-37-2 - 104	0.074	0.003	0.004	13.532	0.641	0.071	0.002	0.002	459	19	21	960	44	47	6.0E+04	4.1E+04	4.2E+03	2.9E+03	4.7E+03	3.3E+03	5.23	0.34
17-37-2 - 105	0.132	0.013	0.013	7.576	0.746	0.080	0.002	0.002	796	72	74	1207	46	50	7.2E+04	9.6E+04	5.5E+03	7.4E+03	3.4E+03	4.6E+03	7.67	0.82
17-37-2 - 106	0.129	0.012	0.012	7.752	0.721	0.093	0.004	0.004	778	67	68	1468	85	86	2.2E+04	6.6E+04	2.2E+03	6.6E+03	7.0E+04	1.9E+04	2.49	0.72
17-37-2 - 107	0.125	0.004	0.004	8.026	0.277	0.068	0.001	0.001	757	20	24	867	36	40	4.9E+04	3.3E+04	4.1E+03	1.7E+03	6.7E+03	2.9E+03	3.99	0.36
17-37-2 - 108	0.124	0.005	0.005	8.065	0.351	0.066	0.001	0.001	753	28	31	801	29	34	1.4E+05	6.2E+04	8.8E+03	4.1E+03	5.1E+03	3.2E+03	17.00	2.80
17-37-2 - 109	0.159	0.002	0.004	6.293	0.143	0.070	0.001	0.001	950.7	9.3	20	912	16	23	6.0E+05	1.3E+05	3.8E+03	9.3E+03	5.0E+04	1.3E+04	3.00	0.06
17-37-2 - 110	0.155	0.003	0.005	6.447	0.187	0.069	0.000	0.001	929	18	25	905	11	20	1.0E+05	8.1E+04	6.9E+03	5.6E+03	9.4E+03	7.7E+03	3.14	0.05
17-37-2 - 111	0.086	0.002	0.002	11.587	0.309	0.058	0.001	0.001	533.8	9	14	527	23	30	-1.7E+04	7.1E+04	-1.1E+03	4.2E+03	-1.0E+03	4.0E+03	5.95	0.50
17-37-2 - 112	0.144	0.009	0.009	6.935	0.428	0.074	0.001	0.002	867	47	50	1048	38	41	3.9E+04	6.0E+04	2.8E+03	4.4E+03	1.0E+03	4.3E+03	3.70	1.00
17-37-2 - 113	0.144	0.007	0.008	6.930	0.379	0.071	0.001	0.001	868	41	44	954	29	34	8.0E+05	3.5E+05	5.0E+04	2.4E+04	2.0E+04	1.2E+04	12.60	2.70
17-37-2 - 114	0.124	0.002	0.003	8.058	0.221	0.066	0.001	0.001	754	13	19	796	17	25	6.8E+04	3.5E+04	4.5E+03	2.3E+03	5.1E+03	2.7E+03	4.09	0.17
17-37-2 - 115	0.097	0.006	0.006	10.363	0.644	0.064	0.002	0.002	593	33	35	734	49	52	1.2E+04	4.4E+04	8.0E+02	2.7E+03	1.0E+03	2.9E+03	5.04	0.37
17-37-2 - 116	0.111	0.005	0.005	9.050	0.409	0.068	0.001	0.001	675	26	29	852	23	29	-1.1E+05	1.1E+05	-7.0E+03	6.9E+03	-7.5E+03	7.5E+03	4.29	0.16
17-37-2 - 117	0.133	0.006	0.006	7.530	0.357	0.071	0.002	0.002	803	33	36	949	51	54	3.1E+04	9.4E+04	2.0E+03	6.6E+03	1.9E+03	5.7E+03	5.15	0.45
17-37-2 - 118	0.087	0.001	0.002	11.521	0.279	0.059	0.001	0.001	536.4	7.4	13	573	23	29	4.6E+04	4.4E+04	2.7E+03	2.6E+03	2.4E+03	2.2E+03	6.05	0.09
17-37-2 - 119	0.367	0.005	0.009	2.723	0.067	0.153	0.001	0.002	2016	25	43	2380	11	18	-5.0E+05	1.9E+05	-7.0E+04	2.9E+04	-1.8E+04	7.9E+04	0.66	0.01
17-37-2 - 120	0.137	0.005	0.005	7.305	0.277	0.070	0.001	0.001	827	25	30	916	33	37	4.0E+03	1.0E+05	6.0E+02	7.1E+03	1.1E+03	2.7E+03	14.30	1.30
17-37-2 - 121	0.128	0.008	0.008	7.806	0.494	0.070	0.002	0.002	776	45	47	920	57	60	9.1E+04	6.0E+04	7.9E+03	4.9E+03	9.7E+03	6.1E+03	4.37	0.52

17-37-2 - 122	0.084	0.002	0.003	11.962	0.358	0.060	0.001	0.001	517	11	15	597	43	46	4.4E+04	4.9E+04	2.6E+03	2.9E+03	2.1E+03	2.1E+03	7.02	0.63
17-37-2 - 123	0.107	0.029	0.029	9.346	2.533	0.060	0.001	0.001	640	150	150	598	35	39	8.7E+04	7.2E+04	5.0E+03	4.2E+03	6.3E+03	5.2E+03	4.19	0.74
17-37-2 - 124	0.098	0.004	0.004	10.256	0.431	0.062	0.001	0.001	599	21	24	680	23	30	9.0E+04	5.4E+04	7.0E+02	3.3E+03	7.0E+02	3.6E+03	4.43	0.20
17-37-2 - 125	0.155	0.010	0.011	6.452	0.458	0.069	0.001	0.001	929	58	61	901	40	43	5.2E+04	6.3E+04	3.4E+03	4.2E+03	3.7E+03	4.7E+03	3.88	0.19
17-37-2 - 126	0.086	0.001	0.002	11.623	0.257	0.058	0.000	0.001	532	5.4	11	524	18	26	-8.0E+05	1.0E+05	-4.6E+03	5.8E+03	-8.0E+04	1.1E+04	3.19	0.12
17-37-2 - 127	0.092	0.001	0.002	10.929	0.275	0.060	0.001	0.001	564.1	8.3	14	583	32	37	3.1E+04	2.7E+04	1.9E+03	1.6E+03	1.5E+03	1.7E+03	5.27	0.42
17-37-2 - 128	0.141	0.005	0.006	7.102	0.288	0.076	0.001	0.001	849	28	32	1086	24	29	1.0E+05	1.1E+05	7.9E+03	8.2E+03	6.3E+03	7.8E+03	3.64	0.48
17-37-2 - 129	0.120	0.002	0.003	8.333	0.229	0.066	0.001	0.001	730	13	19	804	20	27	1.1E+05	1.1E+05	7.3E+03	7.2E+03	8.4E+03	8.5E+03	4.02	0.20
17-37-2 - 130	0.164	0.011	0.011	6.098	0.409	0.092	0.004	0.005	979	61	64	1445	90	91	9.4E+04	6.7E+04	8.9E+03	7.0E+03	1.2E+04	9.1E+03	2.40	0.17
17-37-2 - 131	0.111	0.005	0.006	8.993	0.445	0.065	0.001	0.002	679	30	32	761	46	50	2.0E+04	6.3E+04	1.3E+03	4.2E+03	2.8E+03	6.2E+03	5.90	1.70
17-37-2 - 132	0.107	0.015	0.015	9.346	1.310	0.068	0.001	0.001	652	90	90	879	64	71	6.7E+04	2.3E+04	4.5E+03	1.6E+03	2.5E+03	7.6E+02	8.68	0.96
17-37-2 - 133	0.125	0.002	0.003	7.994	0.204	0.066	0.000	0.001	760	12	18	819	13	22	4.2E+05	4.5E+05	2.8E+04	2.9E+04	3.2E+04	3.6E+04	4.47	0.50
17-37-2 - 134	0.115	0.004	0.004	8.673	0.316	0.065	0.001	0.001	703	20	24	762	24	30	8.6E+04	5.9E+04	5.5E+03	3.7E+03	4.0E+03	3.1E+03	6.82	0.66
17-37-2 - 135	0.177	0.019	0.019	5.650	0.606	0.083	0.004	0.004	1040	100	100	1255	88	89	7.2E+04	8.4E+04	6.2E+03	7.2E+03	1.8E+04	2.2E+04	1.94	0.40
17-37-2 - 136	0.120	0.003	0.004	8.326	0.263	0.065	0.001	0.001	731	17	22	763	23	29	4.5E+04	2.4E+04	3.0E+03	1.6E+03	3.8E+03	2.0E+03	3.51	0.08
17-37-2 - 137	0.101	0.003	0.004	9.930	0.365	0.062	0.001	0.001	618	19	22	680	25	31	4.3E+04	5.5E+04	2.7E+03	3.4E+03	1.2E+03	2.2E+03	9.10	1.70
17-37-2 - 138	0.128	0.009	0.009	7.825	0.551	0.070	0.002	0.002	774	49	51	909	56	59	2.5E+04	8.9E+04	2.1E+03	6.4E+03	4.0E+04	1.1E+04	2.70	0.18
17-37-2 - 139	0.092	0.005	0.005	10.917	0.632	0.060	0.001	0.001	564	29	31	608	39	42	4.7E+04	5.9E+04	2.9E+03	3.5E+03	1.8E+03	1.9E+03	9.80	0.16
17-37-2 - 140	0.125	0.003	0.004	7.994	0.236	0.067	0.001	0.001	760	16	21	846	27	32	6.4E+04	5.8E+04	4.4E+03	3.9E+03	9.3E+03	6.5E+03	4.32	0.80
17-37-2 - 141	0.134	0.004	0.005	7.452	0.272	0.067	0.001	0.001	812	24	28	849	24	30	9.0E+05	2.4E+05	6.0E+04	1.6E+04	5.0E+04	1.7E+04	4.27	0.39
17-37-2 - 142	0.153	0.001	0.003	6.549	0.137	0.069	0.000	0.001	915.8	5.7	18	898	12	21	1.2E+05	2.7E+05	8.0E+04	1.8E+04	8.0E+04	1.8E+04	4.34	0.05
17-37-2 - 143	0.101	0.006	0.006	9.921	0.600	0.063	0.003	0.003	618	34	35	682	83	84	3.0E+04	3.4E+04	2.0E+02	2.1E+03	1.0E+03	4.9E+03	1.71	0.31
17-59-1 - 1	0.139	0.001	0.002	7.179	0.119	0.067	0.000	0.000	840.9	8.2	13	840	10	10	8.8E+04	6.5E+04	5.9E+03	4.3E+03	3.5E+03	2.4E+03	8.54	0.78
17-59-1 - 2	0.148	0.002	0.003	6.780	0.138	0.069	0.000	0.000	887	14	17	897	14	14	3.4E+04	6.4E+04	2.3E+03	4.4E+03	3.1E+03	5.1E+03	3.58	0.31
17-59-1 - 3	0.157	0.001	0.002	6.357	0.097	0.070	0.000	0.000	941.9	7.6	13	935.4	7.1	7.1	1.4E+05	1.1E+05	9.9E+03	7.4E+03	8.1E+03	6.1E+03	4.83	0.07
17-59-1 - 4	0.163	0.002	0.003	6.143	0.106	0.071	0.000	0.000	972	11	16	947	10	10	4.0E+05	1.4E+05	3.0E+04	1.0E+04	2.5E+03	7.9E+03	5.00	0.13
17-59-1 - 5	0.127	0.001	0.002	7.868	0.111	0.067	0.000	0.000	771.2	5.3	11	825	15	15	9.0E+03	1.1E+05	5.0E+02	7.1E+03	7.0E+02	7.7E+03	4.32	0.25
17-59-1 - 6	0.102	0.004	0.004	9.785	0.364	0.063	0.001	0.001	627	21	22	705	33	33	2.6E+04	2.3E+04	1.6E+03	1.4E+03	9.0E+02	7.5E+02	13.30	2.60
17-59-1 - 7	0.135	0.002	0.003	7.429	0.144	0.067	0.000	0.000	814	11	15	842	13	13	1.7E+04	6.5E+04	1.1E+03	4.3E+03	1.4E+03	5.5E+03	3.00	0.11
17-59-1 - 8	0.150	0.001	0.002	6.688	0.094	0.069	0.000	0.000	898.3	4.9	12	892	13	13	6.8E+04	2.6E+04	4.7E+03	1.8E+03	7.3E+03	2.8E+03	2.60	0.02
17-59-1 - 9	0.153	0.001	0.002	6.540	0.090	0.070	0.000	0.000	917.2	4.4	12	920	12	12	5.0E+04	6.7E+04	4.0E+02	4.7E+03	5.0E+02	7.1E+03	2.63	0.03
17-59-1 - 10	0.140	0.002	0.002	7.138	0.122	0.068	0.001	0.001	845.4	9.2	14	852	16	16	8.0E+05	1.5E+05	5.0E+04	1.0E+04	5.0E+04	1.0E+04	4.03	0.05
17-59-1 - 11	0.147	0.002	0.003	6.807	0.130	0.069	0.000	0.000	884	12	16	885.4	8.5	8.5	8.0E+03	1.5E+05	0.0E+00	1.1E+04	0.0E+00	1.1E+04	4.09	0.06

17-59-1 - 12	0.151	0.005	0.005	6.623	0.215	0.075	0.002	0.002	906	25	28	1067	46	46	-4.0E+05	1.3E+05	-3.0E+03	9.7E+03	-2.0E+04	1.0E+04	4.52	0.56
17-59-1 - 13	0.318	0.008	0.009	3.144	0.089	0.143	0.002	0.002	1779	39	44	2256	24	24	4.5E+04	3.6E+04	6.3E+03	4.9E+03	1.1E+04	9.3E+03	1.00	0.10
17-59-1 - 14	0.108	0.003	0.003	9.242	0.256	0.063	0.001	0.001	662	16	18	719	17	17	1.1E+05	6.8E+04	6.8E+03	4.3E+03	4.9E+03	3.1E+03	6.13	0.09
17-59-1 - 15	0.220	0.009	0.009	4.556	0.187	0.083	0.002	0.002	1278	45	47	1260	36	36	9.6E+04	7.5E+04	7.6E+03	5.9E+03	1.4E+04	1.2E+04	1.23	0.22
17-59-1 - 16	0.132	0.002	0.003	7.582	0.161	0.067	0.000	0.000	799	13	16	829	12	12	3.3E+04	5.3E+04	2.1E+03	3.5E+03	1.5E+03	3.4E+03	5.50	0.60
17-59-1 - 17	0.121	0.003	0.003	8.258	0.225	0.067	0.001	0.001	737	17	19	848	27	27	5.9E+04	3.1E+04	4.0E+03	2.0E+03	5.6E+03	2.9E+03	3.89	0.68
17-59-1 - 18	0.139	0.004	0.004	7.210	0.229	0.067	0.000	0.000	837	23	25	846	14	14	1.0E+05	1.2E+05	6.9E+03	7.9E+03	6.4E+03	7.2E+03	4.46	0.06
17-59-1 - 19	0.139	0.002	0.002	7.184	0.124	0.068	0.000	0.000	840	9.1	13	873	11	11	8.8E+04	2.6E+04	6.0E+03	1.8E+03	4.6E+03	2.3E+03	4.60	0.13
17-59-1 - 20	0.143	0.002	0.002	6.988	0.117	0.069	0.001	0.001	862.1	8.9	14	901	17	17	8.0E+05	2.6E+05	6.0E+04	1.8E+04	4.8E+03	7.2E+03	13.90	3.40
17-59-1 - 21	0.239	0.013	0.013	4.184	0.228	0.114	0.004	0.004	1380	66	68	1851	60	60	7.6E+04	6.0E+04	6.4E+03	5.1E+03	5.9E+03	3.7E+03	2.87	0.62
17-59-1 - 22	0.207	0.006	0.007	4.843	0.155	0.098	0.003	0.003	1209	32	35	1575	61	61	1.1E+05	2.2E+05	3.0E+04	1.7E+04	2.5E+03	7.7E+03	7.90	1.20
17-59-1 - 23	0.099	0.002	0.002	10.142	0.195	0.062	0.001	0.001	606.1	8.7	11	675	27	27	-2.3E+04	2.9E+04	-1.5E+03	1.8E+03	-1.3E+03	1.5E+03	4.11	0.58
17-59-1 - 24	0.105	0.007	0.007	9.497	0.604	0.062	0.001	0.001	644	38	39	677	37	37	-3.6E+04	8.8E+04	-2.1E+03	5.6E+03	-3.0E+02	2.8E+03	13.10	2.70
17-59-1 - 25	0.157	0.006	0.007	6.353	0.270	0.074	0.002	0.002	942	36	38	1046	53	53	5.0E+05	1.3E+05	2.7E+03	9.9E+03	4.0E+03	5.6E+03	5.85	0.51
17-59-1 - 26	0.171	0.013	0.014	5.848	0.479	0.094	0.009	0.009	1013	74	74	1430	180	180	1.3E+05	1.4E+05	9.0E+04	1.2E+04	6.0E+04	1.0E+04	7.10	2.40
17-59-1 - 27	0.098	0.009	0.009	10.173	0.973	0.076	0.002	0.002	603	55	55	1091	46	46	-1.0E+05	1.2E+05	-9.0E+02	8.4E+03	3.0E+02	3.5E+03	8.53	0.62
17-59-1 - 28	0.157	0.003	0.004	6.386	0.147	0.070	0.000	0.000	938	17	20	925	12	12	1.7E+05	1.4E+05	1.2E+04	9.4E+03	7.3E+03	8.4E+03	4.79	0.31
17-59-1 - 29	0.159	0.003	0.003	6.289	0.131	0.070	0.000	0.000	951	14	18	920.9	9.9	9.9	9.0E+04	7.8E+04	6.2E+03	5.4E+03	3.7E+03	3.9E+03	7.57	0.96
17-59-1 - 30	0.134	0.002	0.002	7.479	0.123	0.067	0.000	0.000	809.1	8.3	13	839	11	11	6.8E+04	5.9E+04	3.0E+03	4.9E+03	3.1E+03	4.8E+03	5.04	0.98
17-59-1 - 31	0.138	0.002	0.002	7.252	0.126	0.067	0.001	0.001	832.9	9.8	14	850	18	18	4.3E+04	8.5E+04	2.9E+03	5.7E+03	2.8E+03	5.5E+03	4.31	0.19
17-59-1 - 32	0.142	0.003	0.003	7.032	0.168	0.075	0.003	0.003	857	16	19	1058	80	80	1.6E+05	9.0E+04	1.2E+04	6.7E+03	1.1E+04	5.3E+03	3.66	0.31
17-59-1 - 33	0.119	0.004	0.004	8.432	0.277	0.065	0.000	0.000	722	20	22	788	14	14	1.4E+05	4.7E+04	8.9E+03	3.0E+03	2.7E+03	9.6E+02	16.90	2.20
17-59-1 - 34	0.139	0.002	0.002	7.184	0.124	0.068	0.000	0.000	840.2	8.9	13	856	13	13	6.0E+04	6.1E+04	1.8E+03	3.3E+03	8.0E+02	4.7E+03	3.35	0.04
17-59-1 - 35	0.132	0.001	0.002	7.587	0.127	0.067	0.000	0.000	798.2	8	12	844	12	12	3.5E+04	7.0E+04	2.4E+03	4.7E+03	2.5E+03	5.3E+03	3.70	0.07
17-59-1 - 36	0.105	0.003	0.003	9.542	0.310	0.064	0.000	0.000	642	18	20	725	16	16	5.0E+05	3.0E+05	3.0E+04	1.9E+04	3.0E+04	1.7E+04	4.75	0.10
17-59-1 - 37	0.243	0.011	0.011	4.115	0.186	0.118	0.005	0.005	1402	55	57	1909	82	82	4.0E+04	8.0E+04	1.0E+03	1.1E+04	4.0E+04	2.9E+04	0.99	0.16
17-59-1 - 38	0.155	0.002	0.003	6.456	0.113	0.069	0.000	0.000	928	10	15	899	12	12	8.0E+04	9.7E+04	6.0E+02	6.7E+03	7.0E+02	5.4E+03	5.80	0.52
17-59-1 - 39	0.140	0.002	0.003	7.158	0.149	0.068	0.000	0.000	843	13	16	875	11	11	6.0E+03	1.4E+05	5.0E+02	9.2E+03	1.0E+03	1.3E+04	3.17	0.24
17-59-1 - 40	0.154	0.001	0.002	6.502	0.097	0.069	0.000	0.000	922.2	6.6	13	903.7	8.4	8.4	1.4E+05	1.1E+05	9.3E+03	7.8E+03	4.7E+03	5.7E+03	6.11	0.18
17-59-1 - 41	0.118	0.003	0.003	8.489	0.216	0.064	0.000	0.000	718	15	17	743	16	16	2.0E+05	1.7E+05	1.0E+03	1.1E+04	1.0E+03	9.5E+03	4.74	0.10
17-59-1 - 42	0.139	0.003	0.003	7.199	0.171	0.068	0.001	0.001	838	16	19	875	22	22	6.0E+05	2.9E+05	4.0E+04	1.9E+04	7.0E+04	1.9E+04	5.90	1.10
17-59-1 - 43	0.164	0.003	0.004	6.094	0.134	0.071	0.000	0.000	979	16	20	944	13	13	-1.3E+05	4.0E+05	-9.0E+04	2.8E+04	-8.0E+04	2.7E+04	3.96	0.17
17-59-1 - 44	0.159	0.002	0.003	6.305	0.103	0.071	0.000	0.000	948.8	8.9	14	942.5	7.9	7.9	1.0E+05	1.9E+05	7.0E+04	1.3E+04	8.0E+04	1.4E+04	3.62	0.06

17-59-1 - 45	0.166	0.012	0.013	6.024	0.472	0.077	0.003	0.003	986	69	70	1094	87	87	7.1E+04	1.0E+04	5.3E+03	7.9E+02	4.8E+03	9.7E+02	5.59	0.55
17-59-1 - 46	0.153	0.003	0.004	6.536	0.162	0.069	0.000	0.000	918	18	21	909	11	11	4.4E+04	6.8E+04	3.0E+03	4.7E+03	3.1E+03	4.8E+03	3.87	0.04
17-59-1 - 47	0.146	0.002	0.003	6.835	0.140	0.068	0.000	0.000	880	13	17	875	10	10	-3.0E+05	3.0E+05	-2.0E+04	2.1E+04	-2.0E+04	1.9E+04	4.13	0.09
17-59-1 - 48	0.097	0.001	0.002	10.331	0.171	0.061	0.000	0.000	595.8	6.4	9.6	621	15	15	3.9E+04	4.7E+04	2.3E+03	2.8E+03	3.3E+03	4.1E+03	3.18	0.03
17-59-1 - 49	0.124	0.009	0.010	8.045	0.621	0.065	0.001	0.001	754	53	54	777	23	23	-2.0E+04	4.2E+04	-2.0E+02	2.6E+03	-2.0E+02	2.4E+03	4.81	0.73
17-59-1 - 50	0.212	0.006	0.006	4.726	0.136	0.084	0.002	0.002	1237	29	33	1284	35	35	-5.0E+06	1.2E+06	-5.0E+05	1.1E+05	-1.5E+05	3.3E+05	1.22	0.09
17-59-1 - 51	0.109	0.001	0.002	9.200	0.161	0.064	0.000	0.000	665.1	7.7	11	725	11	11	2.2E+04	3.5E+04	1.4E+03	2.2E+03	2.1E+03	2.7E+03	5.03	0.34
17-59-1 - 52	0.098	0.003	0.003	10.246	0.304	0.061	0.001	0.001	600	15	17	642	20	20	1.4E+04	8.3E+04	9.0E+02	4.9E+03	9.0E+02	3.3E+03	9.60	1.30
17-59-1 - 53	0.307	0.015	0.015	3.257	0.159	0.138	0.004	0.004	1721	74	77	2188	54	54	1.1E+05	1.0E+05	1.4E+04	1.4E+04	1.9E+04	2.0E+04	1.65	0.20
17-59-1 - 54	0.160	0.005	0.005	6.242	0.203	0.082	0.002	0.002	958	27	29	1231	42	42	2.4E+05	1.8E+05	1.6E+04	1.3E+04	8.6E+03	6.7E+03	9.47	0.74
17-59-1 - 55	0.144	0.005	0.005	6.954	0.237	0.067	0.001	0.001	865	25	27	849	17	17	-3.0E+05	1.7E+05	-2.0E+04	1.2E+04	-6.0E+02	9.3E+03	11.00	1.90
17-59-1 - 56	0.130	0.003	0.003	7.698	0.201	0.067	0.001	0.001	787	17	19	837	17	17	4.3E+05	5.3E+05	2.9E+04	3.6E+04	3.8E+04	4.7E+04	3.13	0.05
17-59-1 - 57	0.088	0.006	0.006	11.325	0.731	0.069	0.001	0.001	545	33	34	883	41	41	1.4E+05	9.4E+04	1.0E+04	6.8E+03	1.4E+04	9.7E+03	3.34	0.43
17-59-1 - 58	0.146	0.003	0.004	6.849	0.178	0.068	0.000	0.000	878	19	22	862	12	12	-5.5E+04	4.1E+04	-3.7E+03	2.8E+03	-3.6E+03	2.6E+03	4.13	0.11
17-59-1 - 59	0.117	0.003	0.003	8.584	0.251	0.067	0.001	0.001	710	18	20	824	19	19	7.9E+04	6.3E+04	5.1E+03	4.2E+03	5.2E+03	2.8E+03	8.40	1.40
17-59-1 - 60	0.138	0.005	0.005	7.225	0.256	0.069	0.001	0.001	835	26	28	906	17	17	7.0E+04	8.5E+04	4.7E+03	5.8E+03	2.0E+03	5.2E+03	11.40	3.10
17-59-1 - 61	0.138	0.007	0.007	7.236	0.361	0.070	0.002	0.002	834	37	39	904	61	61	4.1E+04	6.9E+04	2.9E+03	5.2E+03	1.8E+03	4.0E+03	22.60	6.30
17-59-1 - 62	0.146	0.001	0.002	6.869	0.099	0.068	0.000	0.000	876.2	5.3	12	865	13	13	1.4E+05	8.9E+04	9.3E+03	5.9E+03	1.1E+04	6.9E+03	3.32	0.07
17-59-1 - 63	0.150	0.002	0.003	6.649	0.111	0.069	0.000	0.000	903	9.5	14	897	11	11	5.0E+05	1.4E+05	3.4E+03	9.6E+03	3.0E+03	8.4E+03	4.48	0.07
17-59-1 - 64	0.154	0.002	0.003	6.498	0.110	0.070	0.000	0.000	922.7	9.8	15	920.9	8.7	8.7	2.0E+05	2.2E+05	1.0E+04	1.6E+04	1.0E+04	1.7E+04	3.69	0.06
17-59-1 - 65	0.133	0.003	0.004	7.547	0.199	0.071	0.002	0.002	802	17	20	964	44	44	3.7E+04	4.3E+04	2.5E+03	3.0E+03	7.0E+03	6.8E+03	2.11	0.26
17-59-1 - 66	0.136	0.001	0.002	7.361	0.108	0.067	0.000	0.000	821.2	5.4	11	851	15	15	3.9E+04	7.9E+04	2.6E+03	5.3E+03	3.0E+03	6.1E+03	3.59	0.05
17-59-1 - 67	0.155	0.004	0.004	6.435	0.170	0.070	0.001	0.001	931	20	23	922	15	15	1.0E+05	1.3E+05	4.0E+04	1.0E+04	0.0E+00	7.7E+03	4.75	0.15
17-59-1 - 68	0.142	0.001	0.002	7.047	0.104	0.068	0.000	0.000	855.4	6.5	12	868.2	8.2	8.2	1.5E+05	1.1E+05	1.0E+04	7.7E+03	8.1E+03	6.4E+03	5.27	0.22
17-59-1 - 69	0.121	0.004	0.004	8.244	0.258	0.074	0.003	0.003	738	20	22	1012	75	75	2.0E+04	2.3E+04	1.4E+03	1.8E+03	4.3E+03	4.8E+03	1.32	0.02
17-59-1 - 70	0.112	0.002	0.002	8.953	0.168	0.071	0.002	0.002	682.7	9.3	12	939	48	48	2.2E+04	3.0E+04	1.5E+03	2.1E+03	4.5E+03	6.4E+03	1.35	0.05
17-59-1 - 71	0.144	0.004	0.005	6.959	0.223	0.074	0.002	0.002	865	24	26	1034	47	47	1.0E+05	8.0E+04	7.4E+03	6.2E+03	5.1E+03	4.3E+03	7.30	1.10
17-59-1 - 72	0.141	0.008	0.009	7.072	0.430	0.085	0.010	0.010	851	47	48	1210	190	190	3.0E+05	1.1E+05	3.2E+03	9.4E+03	-1.0E+02	8.5E+03	9.70	3.40
17-59-1 - 73	0.162	0.010	0.010	6.173	0.381	0.074	0.001	0.001	965	56	57	1037	39	39	3.2E+05	3.7E+05	2.4E+04	2.8E+04	1.9E+04	2.1E+04	5.16	0.44
17-59-1 - 74	0.124	0.005	0.005	8.058	0.331	0.067	0.001	0.001	754	28	29	827	36	36	2.0E+04	2.5E+04	1.0E+02	1.7E+03	1.0E+02	1.4E+03	5.33	0.32
17-59-1 - 75	0.095	0.001	0.002	10.515	0.188	0.060	0.000	0.000	585.8	7	10	608	15	15	-5.0E+05	1.8E+05	-3.0E+04	1.1E+04	-5.0E+02	4.9E+03	11.20	1.30
17-59-1 - 76	0.127	0.002	0.002	7.880	0.149	0.068	0.000	0.000	770	10	14	860.2	8.4	8.4	1.9E+05	1.1E+05	1.3E+04	7.1E+03	1.2E+04	6.4E+03	4.03	0.13
17-59-1 - 77	0.128	0.003	0.003	7.806	0.201	0.066	0.000	0.000	777	17	19	819.3	9.6	9.6	1.3E+05	1.1E+05	8.5E+03	7.2E+03	1.1E+04	9.1E+03	3.05	0.06

17-59-1 - 78	0.131	0.002	0.002	7.616	0.133	0.069	0.001	0.001	795	9	13	882	22	22	-1.1E+05	2.9E+05	-7.0E+04	1.9E+04	1.0E+03	4.3E+03	34.40	6.20
17-59-1 - 79	0.103	0.002	0.002	9.747	0.199	0.062	0.000	0.000	629.7	9.8	12	688	16	16	1.0E+05	1.1E+05	6.0E+02	6.8E+03	8.0E+02	6.0E+03	4.90	0.11
17-59-1 - 80	0.154	0.001	0.002	6.515	0.098	0.069	0.000	0.000	920.4	6.8	13	905.5	9.5	9.5	6.0E+05	1.1E+05	4.4E+03	7.4E+03	-2.0E+04	1.3E+04	4.57	0.09
17-59-1 - 81	0.131	0.002	0.003	7.639	0.146	0.078	0.001	0.001	793	11	14	1140	35	35	4.8E+04	8.6E+04	3.9E+03	6.6E+03	4.5E+03	6.7E+03	4.65	0.57
17-59-1 - 82	0.130	0.005	0.005	7.704	0.285	0.075	0.003	0.003	786	26	27	1055	86	86	6.0E+05	2.1E+05	3.0E+04	1.6E+04	1.7E+03	7.0E+03	12.98	0.79
17-59-1 - 83	0.163	0.001	0.002	6.124	0.090	0.071	0.000	0.000	975	6.7	13	952.4	8.7	8.7	6.0E+05	1.1E+05	4.2E+03	7.7E+03	6.0E+04	1.1E+04	2.62	0.03
17-59-1 - 84	0.157	0.002	0.003	6.357	0.101	0.070	0.000	0.000	941.7	8.6	14	926	12	12	1.1E+05	7.5E+04	7.6E+03	5.2E+03	9.9E+03	6.9E+03	2.96	0.05
17-59-1 - 85	0.119	0.002	0.003	8.425	0.185	0.064	0.001	0.001	726	11	13	740	19	19	3.2E+04	7.6E+04	2.1E+03	4.7E+03	2.5E+03	8.0E+03	2.70	1.00
17-59-1 - 86	0.159	0.006	0.007	6.289	0.261	0.080	0.002	0.002	950	35	36	1184	51	51	-1.0E+05	1.7E+05	-1.0E+04	1.3E+04	-1.0E+04	2.1E+04	3.00	1.80
17-59-1 - 87	0.114	0.009	0.010	8.795	0.735	0.062	0.001	0.001	692	53	54	681	26	26	-7.0E+04	3.1E+04	-5.0E+02	1.9E+03	6.0E+02	2.2E+03	7.50	3.40
17-59-1 - 88	0.159	0.008	0.008	6.274	0.319	0.074	0.001	0.001	952	43	45	1034	36	36	-1.0E+05	2.1E+05	-1.0E+03	1.6E+04	0.0E+00	1.7E+04	3.07	0.26
17-59-1 - 89	0.101	0.004	0.004	9.911	0.403	0.064	0.001	0.001	619	23	24	736	22	22	1.4E+05	1.3E+05	8.9E+03	8.3E+03	3.0E+03	2.9E+03	8.30	1.30
17-59-1 - 90	0.130	0.002	0.003	7.716	0.167	0.067	0.001	0.001	785	13	16	838	16	16	-2.0E+05	1.6E+05	-1.0E+04	1.1E+04	-2.0E+04	1.4E+04	3.28	0.04
17-59-1 - 91	0.148	0.003	0.003	6.743	0.141	0.069	0.000	0.000	891	14	17	890	11	11	1.6E+05	1.7E+05	1.1E+04	1.2E+04	6.4E+03	9.5E+03	7.20	1.20
17-59-1 - 92	0.157	0.001	0.002	6.355	0.089	0.070	0.000	0.000	942	5.5	12	932	11	11	0.0E+00	1.1E+05	0.0E+00	7.7E+03	-1.0E+02	6.1E+03	4.85	0.08
17-59-1 - 93	0.162	0.001	0.002	6.180	0.092	0.070	0.000	0.000	966.5	6.7	13	939.1	8.5	8.5	-9.0E+05	1.2E+05	-6.2E+03	8.4E+03	-6.2E+03	8.0E+03	3.95	0.12
17-59-1 - 94	0.160	0.003	0.003	6.266	0.126	0.070	0.000	0.000	954	14	18	941	11	11	6.0E+05	1.7E+05	4.0E+04	1.2E+04	5.0E+04	1.1E+04	3.77	0.11
17-59-1 - 95	0.217	0.011	0.011	4.608	0.234	0.113	0.005	0.005	1264	57	59	1820	100	100	3.0E+05	1.2E+05	3.0E+04	1.4E+04	-7.0E+04	1.8E+04	1.84	0.10
17-59-1 - 96	0.148	0.001	0.002	6.753	0.096	0.069	0.000	0.000	890.2	5.3	12	904	14	14	9.0E+04	9.4E+04	6.0E+02	6.5E+03	9.0E+02	8.4E+03	3.02	0.03
17-59-1 - 97	0.196	0.003	0.004	5.102	0.094	0.084	0.001	0.001	1154	14	19	1287	12	12	9.0E+05	1.3E+05	8.0E+04	1.1E+04	1.2E+04	1.9E+04	1.91	0.05
17-59-1 - 98	0.153	0.002	0.003	6.536	0.115	0.069	0.000	0.000	917	11	15	898	12	12	-3.6E+05	5.1E+05	-2.5E+04	3.5E+04	-2.1E+04	2.9E+04	4.94	0.11
17-59-2 - 1	0.139	0.003	0.004	7.210	0.208	0.069	0.000	0.001	837	17	23	892	14	22	6.5E+04	5.6E+04	4.5E+03	3.9E+03	4.0E+03	3.7E+03	4.88	0.50
17-59-2 - 2	0.167	0.004	0.006	5.974	0.196	0.079	0.001	0.001	998	24	31	1161	32	36	-8.0E+05	1.6E+05	-6.0E+04	1.2E+04	-1.3E+03	2.8E+03	15.03	0.97
17-59-2 - 3	0.108	0.011	0.012	9.259	1.029	0.069	0.002	0.002	659	66	67	895	44	47	1.1E+05	7.3E+04	7.3E+03	5.0E+03	6.4E+03	4.6E+03	6.70	1.40
17-59-2 - 4	0.192	0.013	0.014	5.208	0.380	0.082	0.004	0.004	1129	71	74	1230	95	96	4.6E+04	8.5E+04	4.6E+03	7.2E+03	2.6E+04	2.7E+04	1.86	0.36
17-66-1 - 1	0.118	0.005	0.005	8.453	0.357	0.084	0.001	0.001	721	28	29	1287	21	21	7.9E+04	3.2E+04	6.6E+03	2.6E+03	1.8E+04	7.5E+03	1.49	0.05
17-66-1 - 2	0.147	0.004	0.004	6.798	0.180	0.073	0.001	0.001	884	19	22	1022	16	16	0.0E+00	1.1E+05	-1.0E+02	8.2E+03	1.1E+04	2.2E+04	1.89	0.15
17-66-1 - 3	0.203	0.014	0.014	4.926	0.340	0.090	0.002	0.002	1191	75	76	1417	41	41	1.3E+05	1.4E+05	1.1E+04	1.3E+04	4.5E+04	5.7E+04	0.83	0.14
17-66-1 - 4	0.246	0.005	0.006	4.068	0.091	0.093	0.001	0.001	1416	24	29	1483	15	15	-6.0E+05	3.7E+05	-6.0E+04	3.4E+04	-3.0E+05	1.7E+05	0.64	0.03
17-66-1 - 5	0.330	0.007	0.008	3.027	0.075	0.141	0.001	0.001	1840	34	40	2232	15	15	6.0E+05	2.1E+05	8.0E+04	2.9E+04	6.0E+04	2.2E+04	2.54	0.09
17-66-1 - 6	0.384	0.011	0.012	2.604	0.081	0.152	0.002	0.002	2093	50	55	2370	16	16	1.3E+05	1.6E+05	1.9E+04	2.3E+04	2.5E+04	3.2E+04	1.21	0.01
17-66-1 - 7	0.218	0.017	0.017	4.587	0.358	0.107	0.008	0.008	1268	88	89	1690	150	150	1.0E+06	1.2E+05	1.0E+05	1.4E+04	9.0E+04	1.5E+04	4.80	1.00
17-66-1 - 8	0.169	0.006	0.007	5.914	0.231	0.076	0.002	0.002	1007	34	36	1077	55	55	5.0E+05	1.5E+05	3.0E+04	1.1E+04	2.0E+03	6.7E+03	8.01	0.21

17-66-1 - 9	0.193	0.008	0.008	5.195	0.213	0.078	0.001	0.001	1134	41	43	1151	38	38	1.9E+05	1.3E+05	1.5E+04	1.0E+04	5.5E+04	4.2E+04	1.20	0.30
17-66-1 - 10	0.166	0.009	0.009	6.013	0.336	0.073	0.001	0.001	990	49	51	1000	37	37	3.4E+04	7.7E+04	2.5E+03	5.4E+03	-1.9E+03	7.1E+03	11.30	3.40
17-66-1 - 11	0.199	0.002	0.003	5.025	0.083	0.080	0.001	0.001	1170	12	18	1185	17	17	-2.8E+04	8.5E+04	-2.1E+03	6.5E+03	-7.0E+04	2.0E+04	1.16	0.12
17-66-1 - 12	0.226	0.005	0.006	4.423	0.110	0.120	0.002	0.002	1314	25	29	1951	23	23	-1.7E+05	7.2E+05	-2.3E+04	8.7E+04	-5.0E+05	2.2E+05	0.77	0.03
17-66-1 - 13	0.168	0.014	0.014	5.952	0.496	0.094	0.002	0.002	997	77	77	1507	39	39	2.0E+05	1.5E+05	2.0E+04	1.4E+04	8.0E+04	4.5E+04	0.74	0.04
17-66-1 - 14	0.152	0.001	0.002	6.580	0.091	0.069	0.000	0.000	912	4.4	12	907	7.6	7.6	1.6E+05	1.9E+05	1.1E+04	1.3E+04	4.3E+03	5.2E+03	9.84	0.44
17-66-1 - 15	0.105	0.003	0.003	9.533	0.254	0.069	0.001	0.001	643	15	17	891	16	16	1.5E+05	2.5E+04	9.9E+03	1.7E+03	2.4E+04	4.1E+03	1.75	0.03
17-66-1 - 16	0.182	0.010	0.010	5.482	0.295	0.107	0.004	0.004	1078	51	53	1739	65	65	-3.0E+05	1.1E+05	-3.0E+04	1.2E+04	-3.0E+04	1.3E+04	2.20	0.25
17-66-1 - 17	0.207	0.014	0.014	4.831	0.327	0.113	0.005	0.005	1211	72	74	1824	78	78	5.0E+05	2.1E+05	8.0E+04	2.3E+04	6.0E+04	2.2E+04	2.43	0.05
17-66-1 - 18	0.148	0.006	0.006	6.780	0.267	0.071	0.001	0.001	886	31	33	951	26	26	2.5E+05	4.0E+05	1.9E+04	2.8E+04	-4.0E+04	6.5E+04	1.61	0.15
17-66-1 - 19	0.182	0.006	0.006	5.504	0.188	0.078	0.002	0.002	1076	31	34	1148	43	43	8.0E+03	1.5E+05	0.0E+00	1.2E+04	-2.0E+04	1.1E+04	9.50	1.40
17-66-1 - 20	0.246	0.013	0.014	4.065	0.231	0.094	0.001	0.001	1416	68	70	1495	28	28	2.0E+05	3.3E+05	1.8E+04	3.1E+04	8.0E+05	1.3E+05	0.67	0.03
17-66-1 - 21	0.243	0.009	0.009	4.124	0.155	0.092	0.001	0.001	1399	44	47	1462	25	25	-1.1E+05	1.7E+05	-1.0E+05	1.6E+04	-2.7E+04	4.6E+04	1.15	0.20
17-66-1 - 22	0.186	0.021	0.022	5.376	0.636	0.080	0.004	0.004	1090	110	120	1170	110	110	2.0E+05	1.4E+05	1.0E+03	1.0E+04	-8.0E+04	1.4E+04	8.10	3.10
17-66-1 - 23	0.243	0.012	0.012	4.115	0.203	0.091	0.002	0.002	1398	61	63	1444	44	44	1.4E+05	3.4E+05	1.2E+04	2.9E+04	1.3E+04	3.1E+04	2.30	0.45
17-66-1 - 24	0.199	0.016	0.017	5.025	0.429	0.085	0.004	0.004	1166	88	89	1283	89	89	2.9E+04	7.3E+04	2.5E+03	6.0E+03	0.0E+00	6.8E+03	2.90	1.20
17-66-1 - 25	0.173	0.002	0.003	5.787	0.104	0.073	0.001	0.001	1027	12	17	1024	16	16	1.1E+05	1.6E+05	8.0E+04	1.2E+04	4.7E+03	6.7E+03	6.30	0.16
17-66-1 - 26	0.118	0.005	0.006	8.467	0.394	0.072	0.001	0.001	719	31	32	970	33	33	2.0E+04	9.1E+04	1.6E+03	6.4E+03	2.0E+03	7.8E+03	3.30	0.10
17-66-1 - 27	0.215	0.019	0.019	4.651	0.411	0.112	0.006	0.006	1251	98	99	1800	100	100	3.4E+05	2.5E+05	3.6E+04	2.5E+04	5.0E+04	3.7E+04	1.86	0.08
17-66-1 - 28	0.176	0.004	0.005	5.688	0.159	0.101	0.003	0.003	1044	24	27	1628	46	46	1.6E+05	7.2E+04	1.7E+04	7.5E+03	2.0E+04	6.7E+03	1.89	0.14
17-66-1 - 29	0.155	0.001	0.002	6.457	0.088	0.069	0.000	0.000	928.2	4.9	12	899.9	6.7	6.7	1.3E+05	3.2E+05	9.0E+04	2.2E+04	1.8E+03	6.0E+03	16.00	1.20
17-66-1 - 30	0.156	0.003	0.004	6.410	0.152	0.069	0.000	0.000	934	17	20	900.4	9	9	7.0E+06	1.1E+06	5.0E+04	7.4E+04	2.1E+04	3.0E+04	7.49	0.68
17-66-1 - 31	0.180	0.008	0.009	5.552	0.268	0.082	0.003	0.003	1066	46	48	1221	68	68	4.0E+05	2.2E+05	1.2E+04	2.4E+04	6.0E+03	9.8E+03	10.50	1.50
17-66-1 - 32	0.151	0.004	0.004	6.627	0.176	0.079	0.001	0.001	906	19	22	1160	27	27	-1.1E+05	2.8E+05	-8.0E+04	2.1E+04	-1.6E+04	4.3E+04	1.66	0.08
17-66-1 - 33	0.141	0.003	0.003	7.087	0.171	0.069	0.001	0.001	851	16	19	900	19	19	1.3E+05	1.2E+05	8.9E+03	8.4E+03	5.4E+03	5.8E+03	6.94	0.55
17-66-1 - 34	0.151	0.002	0.003	6.618	0.118	0.068	0.000	0.000	907	11	15	874.8	7.2	7.2	1.0E+06	1.8E+05	6.0E+04	1.2E+04	4.9E+03	3.5E+03	8.64	0.14
17-66-1 - 35	0.283	0.019	0.020	3.534	0.250	0.137	0.004	0.004	1600	98	99	2184	56	56	3.0E+03	2.5E+05	1.0E+03	3.3E+04	2.0E+04	4.0E+04	1.60	0.05
17-66-1 - 36	0.270	0.023	0.023	3.704	0.316	0.129	0.006	0.006	1530	120	120	2073	79	79	2.1E+05	3.5E+05	2.9E+04	4.5E+04	1.3E+05	1.8E+05	1.51	0.42
17-66-1 - 37	0.145	0.002	0.003	6.887	0.138	0.069	0.001	0.001	874	13	17	902	15	15	4.0E+05	1.9E+05	3.0E+04	1.3E+04	1.0E+03	4.6E+03	10.63	0.15
17-66-1 - 38	0.141	0.005	0.005	7.107	0.268	0.076	0.001	0.001	848	28	30	1096	14	14	9.0E+05	2.8E+05	7.0E+04	2.1E+04	2.7E+03	8.1E+03	9.45	0.34
17-66-1 - 39	0.138	0.003	0.003	7.241	0.163	0.078	0.002	0.002	834	15	18	1142	64	64	1.3E+05	1.9E+05	9.0E+04	1.4E+04	7.0E+04	1.6E+04	4.27	0.86
17-66-2 - 1	0.200	0.020	0.020	5.000	0.500	0.079	0.002	0.003	1170	100	110	1172	60	63	-8.0E+05	2.7E+05	-6.0E+04	1.9E+04	-1.0E+03	1.2E+04	4.80	1.50
17-66-2 - 2	0.131	0.006	0.007	7.622	0.389	0.070	0.001	0.001	794	35	38	925	36	40	1.1E+05	9.3E+04	7.6E+03	6.8E+03	-4.3E+04	9.3E+04	10.40	2.00

17-66-2 - 3	0.380	0.029	0.030	2.632	0.208	0.165	0.004	0.004	2070	140	140	2501	38	41	4.0E+05	1.5E+05	7.0E+04	2.4E+04	7.0E+04	1.6E+04	3.37	0.80
17-66-2 - 4	0.194	0.006	0.007	5.165	0.181	0.078	0.001	0.001	1140	30	37	1147	20	26	6.0E+04	7.6E+04	4.6E+03	5.8E+03	4.5E+03	5.4E+03	4.17	0.27
17-66-2 - 5	0.168	0.014	0.015	5.952	0.531	0.080	0.002	0.002	996	80	82	1193	40	43	2.0E+05	1.6E+05	2.0E+04	1.2E+04	9.0E+04	2.2E+04	4.57	0.90
17-66-2 - 6	0.149	0.003	0.004	6.711	0.194	0.069	0.000	0.001	895	18	24	911	15	23	-1.5E+05	1.3E+05	-1.0E+04	9.3E+03	-5.5E+03	5.0E+03	7.91	0.23
17-66-2 - 7	0.256	0.014	0.015	3.906	0.229	0.097	0.001	0.001	1468	73	78	1558	13	20	3.0E+05	1.1E+05	3.0E+04	1.1E+04	5.0E+04	1.6E+04	1.91	0.11
17-66-2 - 8	0.150	0.008	0.008	6.671	0.365	0.073	0.001	0.002	899	43	47	1003	39	42	3.0E+04	4.7E+04	3.0E+02	3.4E+03	-1.0E+02	1.7E+03	11.50	1.50
17-66-2 - 9	0.162	0.016	0.016	6.173	0.610	0.096	0.013	0.013	967	84	86	1430	210	210	2.5E+04	1.4E+04	2.0E+03	9.7E+02	1.3E+04	7.5E+03	12.20	3.90
17-66-2 - 10	0.860	0.510	0.510	1.163	0.690	0.085	0.003	0.003	3.50E+03	1.30E+03	1.30E+03	1307	58	60	5.6E+03	3.2E+03	4.7E+02	2.6E+02	4.9E+04	2.2E+04	0.09	0.07
17-66-2 - 11	0.131	0.008	0.008	7.651	0.486	0.071	0.003	0.003	791	45	47	940	74	76	2.7E+04	5.8E+04	1.8E+03	4.4E+03	3.9E+03	8.1E+03	4.90	0.99
17-66-2 - 12	0.284	0.017	0.018	3.521	0.223	0.136	0.003	0.004	1608	83	88	2165	43	45	9.6E+04	8.2E+04	1.4E+04	1.2E+04	1.3E+04	1.1E+04	2.05	0.04
17-66-2 - 13	0.324	0.025	0.026	3.086	0.248	0.140	0.004	0.005	1800	120	120	2212	53	55	1.2E+05	1.2E+05	1.1E+04	1.4E+04	2.0E+04	2.0E+04	1.73	0.07
17-66-2 - 14	0.143	0.004	0.005	6.974	0.219	0.069	0.000	0.001	864	20	25	887	14	23	5.0E+06	1.0E+06	3.5E+04	7.1E+04	4.7E+03	9.5E+03	29.30	3.10
17-66-2 - 15	0.151	0.003	0.004	6.640	0.176	0.070	0.000	0.001	904	15	22	919	14	22	4.0E+05	1.4E+05	3.0E+04	1.0E+04	1.0E+03	1.2E+03	30.20	3.50
17-66-2 - 16	0.196	0.010	0.011	5.102	0.286	0.089	0.003	0.003	1153	56	60	1384	78	80	3.0E+03	1.8E+05	0.0E+00	1.7E+04	-2.0E+04	2.2E+04	3.32	0.72
17-66-2 - 17	0.216	0.009	0.010	4.627	0.214	0.083	0.003	0.003	1260	48	53	1266	68	70	4.3E+04	7.7E+04	3.7E+03	6.8E+03	3.0E+04	2.6E+04	2.30	1.10
17-66-2 - 18	0.161	0.004	0.005	6.200	0.204	0.075	0.002	0.002	964	23	29	1051	50	53	5.7E+04	8.1E+04	4.1E+03	6.4E+03	1.6E+03	2.1E+03	14.00	1.90
17-66-2 - 19	-0.001	0.001	0.001	-1282.051	1101.249	0.597	0.002	0.005	-5	4.3	4.3	4499.6	4.7	13	-2.3E+01	3.9E+00	-1.4E+01	2.4E+00	-2.9E+01	5.0E+00	0.03	0.00
17-66-2 - 20	0.134	0.004	0.005	7.468	0.251	0.070	0.001	0.001	810	21	26	916	25	30	-4.0E+05	2.7E+05	-3.0E+04	1.9E+04	-2.0E+04	1.1E+04	6.84	0.55
17-66-2 - 21	0.186	0.005	0.006	5.371	0.182	0.077	0.001	0.001	1101	28	34	1119	13	21	-1.7E+04	8.8E+04	-1.3E+03	6.8E+03	-2.0E+04	1.3E+04	1.76	0.19
17-66-2 - 22	0.353	0.013	0.015	2.833	0.120	0.146	0.002	0.002	1947	64	72	2295	24	28	8.0E+04	9.6E+04	1.2E+04	1.4E+04	3.2E+04	3.8E+04	0.76	0.05
17-66-2 - 23	0.178	0.009	0.010	5.618	0.303	0.106	0.005	0.005	1054	49	53	1703	84	85	1.3E+05	1.3E+05	1.6E+04	1.3E+04	5.8E+03	4.9E+03	10.30	1.10
17-66-2 - 24	0.171	0.013	0.013	5.848	0.445	0.075	0.002	0.002	1014	70	72	1053	50	53	5.6E+04	5.2E+04	4.3E+03	4.1E+03	4.6E+03	5.3E+03	7.90	2.90
17-66-2 - 25	0.207	0.017	0.018	4.831	0.420	0.181	0.021	0.021	1208	94	97	2510	260	260	2.5E+04	8.1E+04	1.0E+03	1.8E+04	1.0E+04	1.8E+04	2.57	0.76
17-66-2 - 26	0.144	0.005	0.006	6.925	0.293	0.071	0.001	0.001	869	30	34	962	31	35	3.7E+04	8.7E+04	2.8E+03	6.2E+03	6.0E+02	2.0E+03	14.20	1.10
17-66-2 - 27	0.167	0.005	0.006	5.992	0.215	0.079	0.001	0.001	994	28	33	1182	23	29	1.7E+05	1.9E+05	1.3E+04	1.5E+04	1.5E+04	1.7E+04	3.82	0.53
17-66-2 - 28	0.214	0.009	0.010	4.679	0.208	0.118	0.003	0.003	1248	45	50	1925	43	45	2.7E+04	5.5E+04	3.2E+03	6.7E+03	5.0E+04	1.0E+04	1.58	0.04
17-66-2 - 29	0.145	0.003	0.004	6.911	0.205	0.086	0.004	0.004	871	18	24	1309	93	95	5.6E+04	4.9E+04	4.6E+03	4.5E+03	7.0E+03	8.3E+03	2.60	0.59
17-66-2 - 30	0.308	0.033	0.033	3.247	0.348	0.135	0.009	0.009	1720	160	170	2130	130	130	1.3E+05	5.1E+05	1.4E+04	7.0E+04	3.0E+04	3.0E+04	5.79	0.85
17-66-2 - 31	0.099	0.002	0.003	10.081	0.274	0.061	0.000	0.001	609	11	16	628	16	24	5.3E+04	3.7E+04	3.2E+03	2.3E+03	1.2E+03	8.8E+02	16.00	3.50
17-66-2 - 32	0.190	0.010	0.010	5.260	0.277	0.079	0.002	0.002	1120	53	57	1173	60	62	1.1E+05	6.4E+04	8.9E+03	5.2E+03	1.0E+04	6.6E+03	3.54	0.88
17-66-2 - 33	0.216	0.013	0.013	4.630	0.279	0.086	0.002	0.002	1258	66	70	1339	40	43	1.6E+04	9.3E+04	1.2E+03	7.9E+03	1.0E+05	1.3E+04	1.67	0.39
17-66-2 - 34	0.217	0.013	0.014	4.608	0.297	0.085	0.002	0.003	1265	70	74	1302	60	62	4.9E+04	6.6E+04	3.8E+03	5.9E+03	4.0E+04	1.7E+04	7.10	5.20
17-66-2 - 35	0.163	0.006	0.007	6.131	0.252	0.076	0.001	0.002	973	32	37	1083	36	40	1.4E+05	2.4E+05	1.0E+04	1.8E+04	2.8E+04	5.2E+04	1.27	0.08

17-66-2 - 36	0.182	0.014	0.014	5.495	0.423	0.076	0.002	0.002	1073	76	79	1086	46	49	-1.2E+06	2.5E+06	-9.0E+05	1.9E+05	-2.2E+05	4.4E+05	4.30	1.50
17-66-2 - 37	0.229	0.012	0.013	4.367	0.248	0.088	0.002	0.002	1328	63	67	1383	39	42	-2.0E+05	3.4E+05	-3.0E+04	3.0E+04	-1.1E+04	6.8E+04	1.58	0.19
17-66-2 - 38	0.193	0.007	0.008	5.195	0.205	0.081	0.001	0.001	1134	35	41	1224	25	30	1.0E+05	1.3E+05	8.0E+04	1.1E+04	1.3E+04	1.8E+04	2.16	0.05
17-66-2 - 39	0.154	0.006	0.007	6.510	0.288	0.081	0.002	0.002	921	34	38	1221	54	57	2.3E+04	5.8E+04	3.3E+03	5.4E+03	2.9E+03	7.2E+03	2.33	0.04
17-66-2 - 40	0.155	0.005	0.006	6.435	0.236	0.073	0.001	0.001	931	27	32	1005	16	23	-2.5E+05	3.4E+05	-1.8E+04	2.5E+04	-2.6E+04	3.8E+04	2.83	0.20
17-66-2 - 41	0.199	0.004	0.005	5.030	0.137	0.083	0.001	0.001	1168	20	29	1256	23	28	8.0E+04	3.2E+04	6.0E+02	2.7E+03	6.0E+04	1.6E+04	0.70	0.11
17-66-2 - 42	0.216	0.007	0.009	4.623	0.182	0.083	0.002	0.002	1262	39	45	1258	38	41	-3.1E+03	7.3E+03	-2.6E+02	6.0E+02	-8.0E+02	1.8E+03	1.08	0.05
17-66-2 - 43	0.169	0.008	0.008	5.917	0.287	0.079	0.001	0.001	1006	41	45	1168	21	27	2.1E+05	1.6E+05	1.7E+04	1.3E+04	1.0E+04	6.9E+03	7.05	0.56
17-72-1 - 1	0.158	0.007	0.007	6.337	0.297	0.087	0.003	0.003	944	40	41	1355	75	75	1.7E+05	1.8E+05	1.4E+04	1.5E+04	9.6E+03	9.2E+03	6.50	1.90
17-72-1 - 2	0.152	0.004	0.004	6.562	0.185	0.071	0.001	0.001	914	22	24	950	18	18	1.5E+05	1.7E+05	1.0E+04	1.2E+04	1.9E+03	4.2E+03	25.30	6.60
17-72-1 - 3	0.125	0.002	0.003	8.026	0.174	0.066	0.000	0.000	757	13	16	811	12	12	1.7E+05	9.2E+04	1.1E+04	6.1E+03	2.2E+03	1.1E+03	20.08	0.93
17-72-1 - 4	0.263	0.012	0.012	3.802	0.173	0.094	0.001	0.001	1502	59	61	1501	14	14	6.0E+05	1.9E+05	6.0E+04	1.8E+04	1.4E+04	4.4E+04	1.18	0.03
17-72-1 - 5	0.089	0.001	0.001	11.266	0.165	0.059	0.000	0.000	548.2	3.8	7.7	577	13	13	1.1E+05	9.0E+04	6.1E+03	5.3E+03	2.0E+03	1.7E+03	13.95	0.38
17-72-1 - 6	0.127	0.004	0.004	7.893	0.249	0.066	0.001	0.001	769	21	23	806	19	19	-2.2E+04	9.8E+04	-1.5E+03	6.5E+03	-4.0E+02	1.2E+03	22.80	2.30
17-72-1 - 7	0.091	0.002	0.002	10.989	0.290	0.060	0.001	0.001	562	13	14	584	19	19	-1.2E+05	1.9E+05	-7.0E+04	1.1E+04	-1.6E+03	2.7E+03	21.28	0.80
17-72-1 - 8	0.175	0.016	0.016	5.714	0.522	0.075	0.002	0.002	1036	87	88	1061	64	64	8.0E+04	9.5E+04	6.3E+03	7.1E+03	1.2E+04	1.5E+04	7.40	2.80
17-72-1 - 9	0.171	0.014	0.014	5.848	0.479	0.075	0.002	0.002	1012	76	77	1067	63	63	-7.0E+05	1.0E+05	-4.6E+03	7.6E+03	1.0E+02	9.8E+03	10.00	3.90
17-72-1 - 10	0.160	0.003	0.003	6.250	0.125	0.080	0.001	0.001	957	14	18	1207	16	16	2.0E+05	1.4E+05	2.0E+04	1.1E+04	-1.0E+04	2.3E+04	4.89	0.99
17-72-1 - 11	0.142	0.003	0.003	7.067	0.150	0.069	0.000	0.000	853	14	17	884.8	9.4	9.4	1.1E+05	1.4E+05	7.6E+03	9.8E+03	1.3E+03	1.6E+03	29.40	3.10
17-72-1 - 12	0.155	0.007	0.007	6.439	0.290	0.074	0.001	0.001	930	38	39	1040	28	28	-1.1E+05	5.2E+05	-8.0E+04	3.9E+04	-5.0E+04	1.6E+04	11.20	1.10
17-72-1 - 13	0.168	0.012	0.012	5.952	0.425	0.078	0.005	0.005	999	67	68	1110	110	110	-4.0E+05	2.2E+05	-5.0E+04	2.0E+04	-1.5E+03	4.9E+03	16.50	1.60
17-72-1 - 14	0.097	0.001	0.001	10.338	0.139	0.060	0.000	0.000	595.2	3.3	7.9	615	15	15	1.6E+04	6.2E+04	1.0E+03	3.7E+03	3.0E+02	1.3E+03	13.70	0.31
17-72-1 - 15	0.110	0.002	0.003	9.099	0.224	0.066	0.001	0.001	672	14	16	791	23	23	2.0E+05	1.2E+05	1.3E+03	7.6E+03	6.0E+02	2.9E+03	11.64	0.40
17-72-1 - 16	0.095	0.001	0.002	10.560	0.190	0.061	0.000	0.000	585.5	8.5	12	633	16	16	2.0E+05	1.2E+05	1.2E+04	7.4E+03	2.4E+03	1.4E+03	22.66	0.85
17-72-1 - 17	0.157	0.008	0.008	6.357	0.315	0.076	0.001	0.001	941	42	44	1102	32	32	5.4E+04	4.3E+04	4.2E+03	3.2E+03	5.8E+03	4.2E+03	3.49	0.81
17-72-1 - 18	0.208	0.010	0.010	4.812	0.229	0.084	0.001	0.001	1216	51	53	1293	34	34	5.0E+05	1.9E+05	4.0E+04	1.6E+04	1.3E+04	1.1E+04	2.79	0.45
17-72-1 - 19	0.195	0.009	0.009	5.133	0.235	0.082	0.001	0.001	1146	46	48	1252	21	21	2.0E+05	1.7E+05	2.0E+04	1.4E+04	-1.0E+04	4.0E+04	2.07	0.31
17-72-1 - 20	0.252	0.020	0.020	3.968	0.315	0.128	0.004	0.004	1440	100	100	2054	60	60	1.3E+05	1.4E+05	1.7E+04	1.8E+04	2.9E+04	3.2E+04	1.27	0.04
17-72-1 - 21	0.181	0.012	0.013	5.525	0.397	0.085	0.002	0.002	1067	68	69	1300	50	50	-1.2E+05	4.6E+05	-1.2E+04	4.2E+04	-2.5E+04	9.9E+04	1.14	0.04
17-72-1 - 22	0.127	0.004	0.004	7.874	0.242	0.066	0.001	0.001	771	20	22	813	17	17	8.9E+04	7.5E+04	6.0E+03	5.1E+03	1.2E+03	1.1E+03	29.10	5.80
17-72-1 - 23	0.096	0.003	0.003	10.471	0.318	0.061	0.001	0.001	588	16	17	632	47	47	-1.3E+05	2.1E+05	-8.0E+04	1.3E+04	-9.0E+02	3.0E+03	16.10	1.50
17-72-1 - 24	0.092	0.001	0.001	10.872	0.154	0.059	0.000	0.000	567.2	3.9	7.9	567	15	15	7.7E+04	6.9E+04	4.6E+03	4.1E+03	9.0E+02	7.7E+02	24.79	0.60
17-72-1 - 25	0.150	0.002	0.003	6.653	0.133	0.070	0.001	0.001	903	13	17	935	28	28	-3.0E+05	4.3E+05	-2.0E+04	3.0E+04	-4.0E+04	1.0E+04	14.70	0.85

17-72-1 - 26	0.205	0.013	0.013	4.878	0.309	0.081	0.002	0.002	1200	68	69	1213	41	41	2.2E+05	1.8E+05	1.7E+04	1.4E+04	5.3E+03	5.9E+03	9.70	2.90
17-72-1 - 27	0.252	0.004	0.005	3.964	0.083	0.096	0.001	0.001	1450	22	27	1543	13	13	1.0E+05	7.2E+04	9.9E+03	6.9E+03	2.6E+04	1.9E+04	1.05	0.02
17-72-1 - 28	0.267	0.005	0.006	3.748	0.086	0.098	0.001	0.001	1524	26	31	1589	15	15	8.0E+05	1.1E+05	8.0E+04	1.0E+04	8.0E+04	2.4E+04	1.23	0.12
17-72-1 - 29	0.175	0.015	0.015	5.714	0.490	0.079	0.003	0.003	1038	79	80	1156	80	80	2.3E+05	1.8E+05	1.8E+04	1.4E+04	2.8E+04	2.9E+04	10.20	4.20
17-72-1 - 30	0.222	0.013	0.013	4.505	0.264	0.089	0.002	0.002	1291	67	69	1394	52	52	-1.0E+03	4.7E+05	0.0E+00	4.4E+04	-2.0E+05	4.1E+05	1.51	0.32
17-72-2 - 1	0.143	0.004	0.005	7.008	0.241	0.068	0.001	0.001	860	22	28	877	20	27	7.0E+05	1.0E+05	4.6E+03	6.8E+03	1.3E+03	1.9E+03	16.40	1.20
17-72-2 - 2	0.131	0.007	0.007	7.610	0.411	0.068	0.001	0.001	795	38	40	881	26	31	4.4E+04	4.8E+04	3.0E+03	3.2E+03	1.0E+03	1.9E+03	16.80	5.30
17-72-2 - 3	0.104	0.004	0.004	9.579	0.395	0.063	0.001	0.001	640	22	25	693	26	31	7.0E+06	1.3E+06	7.7E+03	7.4E+03	2.9E+03	2.7E+03	12.60	0.46
17-72-2 - 4	0.178	0.009	0.010	5.609	0.308	0.077	0.002	0.002	1056	50	53	1103	39	42	-2.0E+05	1.3E+05	-2.0E+04	1.0E+04	3.0E+02	8.3E+03	6.56	0.94
17-72-2 - 5	0.138	0.010	0.010	7.225	0.517	0.073	0.003	0.003	834	54	56	984	92	94	-1.0E+03	9.5E+04	0.0E+00	6.9E+03	3.0E+02	2.3E+03	16.00	2.20
17-72-2 - 6	0.146	0.002	0.003	6.873	0.161	0.069	0.000	0.001	876	10	19	903	7.1	19	1.2E+05	9.4E+04	8.4E+03	6.5E+03	1.4E+03	1.1E+03	23.90	0.96
17-72-2 - 7	0.159	0.017	0.017	6.289	0.672	0.074	0.003	0.003	948	91	93	1028	71	73	-4.0E+05	1.5E+05	-3.0E+04	1.1E+04	7.0E+03	8.6E+03	8.90	2.90
17-72-2 - 8	0.161	0.002	0.004	6.215	0.147	0.070	0.000	0.001	962	11	21	934.2	9.2	20	6.0E+05	3.5E+05	4.0E+04	2.4E+04	7.0E+02	4.6E+03	26.70	3.20
17-72-2 - 9	0.186	0.010	0.010	5.379	0.289	0.086	0.001	0.001	1098	52	56	1326	24	29	1.2E+05	7.0E+04	1.0E+04	6.1E+03	3.4E+04	2.1E+04	1.15	0.08
17-72-2 - 10	0.161	0.002	0.004	6.211	0.150	0.070	0.000	0.001	962	13	22	940	10	20	1.5E+05	1.5E+05	1.0E+04	1.1E+04	3.5E+03	3.7E+03	11.92	0.51
17-72-2 - 11	0.157	0.004	0.005	6.373	0.207	0.070	0.000	0.001	939	23	29	924	12	21	-1.0E+05	2.5E+05	-7.0E+04	1.8E+04	2.0E+02	1.8E+03	15.31	0.62
17-72-2 - 12	0.143	0.012	0.013	6.993	0.636	0.073	0.002	0.002	859	70	72	999	64	67	8.0E+03	3.4E+05	1.0E+04	2.6E+04	8.0E+04	2.9E+04	4.50	1.20
17-72-2 - 13	0.101	0.002	0.003	9.940	0.296	0.063	0.001	0.001	618	13	18	700	32	37	1.9E+05	1.5E+05	1.2E+04	9.4E+03	5.3E+03	5.0E+03	17.00	1.80
17-72-2 - 14	0.115	0.049	0.049	8.696	3.705	0.060	0.000	0.001	670	230	230	584	17	24	8.0E+05	1.2E+05	4.7E+03	6.9E+03	1.0E+03	1.5E+03	17.90	4.20
17-72-2 - 15	0.105	0.003	0.004	9.488	0.342	0.067	0.001	0.001	646	18	22	823	23	29	8.7E+04	7.6E+04	5.7E+03	5.0E+03	3.3E+03	2.8E+03	9.37	0.76
17-72-2 - 16	0.121	0.001	0.003	8.299	0.193	0.066	0.000	0.001	733.5	8	16	800	14	23	-3.0E+05	6.0E+05	-2.0E+04	3.9E+04	1.0E+02	9.4E+03	21.12	0.58
17-72-2 - 17	0.186	0.003	0.005	5.385	0.136	0.083	0.001	0.001	1098	16	26	1272	16	23	-5.0E+03	1.4E+05	-1.0E+03	1.1E+04	-1.0E+04	1.5E+04	3.00	0.15
17-72-2 - 18	0.130	0.006	0.007	7.722	0.394	0.073	0.002	0.002	784	35	38	1002	48	51	3.7E+04	4.6E+04	2.9E+03	3.4E+03	4.0E+03	3.3E+03	7.10	1.80
17-72-2 - 19	0.131	0.006	0.007	7.651	0.386	0.073	0.003	0.003	791	35	38	993	85	86	9.4E+04	8.5E+04	7.0E+03	6.3E+03	2.6E+03	6.2E+03	12.30	2.80
17-72-2 - 20	0.098	0.003	0.004	10.183	0.363	0.062	0.001	0.001	604	17	21	655	17	25	4.3E+04	3.8E+04	2.6E+03	2.3E+03	5.3E+02	6.3E+02	26.70	3.00
17-72-2 - 21	0.093	0.001	0.002	10.776	0.267	0.062	0.001	0.001	572.1	7.9	13	664	31	36	3.1E+04	3.5E+04	1.9E+03	2.1E+03	6.5E+02	7.6E+02	16.40	1.60
17-72-2 - 22	0.092	0.002	0.003	10.893	0.320	0.060	0.000	0.001	566	12	16	603	16	24	3.5E+05	3.7E+05	2.1E+04	2.3E+04	7.5E+03	7.8E+03	13.18	0.71
17-72-2 - 23	0.114	0.005	0.005	8.772	0.392	0.064	0.001	0.001	695	26	29	732	20	27	1.5E+05	1.1E+05	9.4E+03	7.2E+03	2.4E+03	1.7E+03	18.59	0.77
17-72-2 - 24	0.093	0.001	0.002	10.764	0.243	0.060	0.001	0.001	572.8	6.3	13	608	21	28	1.9E+04	6.8E+04	1.1E+03	4.2E+03	1.0E+02	2.8E+03	22.00	5.60
17-72-2 - 25	0.119	0.002	0.003	8.382	0.211	0.066	0.001	0.001	726	10	17	795	17	25	-5.1E+04	9.2E+04	-3.3E+03	5.9E+03	-5.1E+02	8.6E+02	39.40	5.30
17-72-2 - 26	0.123	0.005	0.005	8.150	0.339	0.068	0.002	0.002	746	26	30	873	54	56	4.5E+04	2.4E+04	3.1E+03	1.7E+03	3.2E+03	2.4E+03	11.30	2.50
17-72-2 - 27	0.141	0.002	0.004	7.072	0.185	0.069	0.000	0.001	852	14	21	894	13	22	1.1E+05	6.7E+04	7.4E+03	4.6E+03	1.9E+03	1.2E+03	20.90	2.20
17-72-2 - 28	0.161	0.004	0.005	6.207	0.185	0.075	0.002	0.002	963	20	27	1072	44	47	9.5E+04	6.6E+04	7.3E+03	4.9E+03	3.5E+03	1.5E+03	14.20	2.70

17-72-2 - 29	0.134	0.003	0.004	7.457	0.228	0.067	0.000	0.001	811	18	23	847	11	21	4.6E+04	8.6E+04	3.2E+03	5.8E+03	8.0E+02	1.4E+03	17.00	1.40
17-72-2 - 30	0.218	0.024	0.024	4.587	0.505	0.108	0.010	0.010	1260	130	130	1690	200	200	-7.0E+05	2.5E+05	-1.1E+04	3.2E+04	-4.0E+05	1.3E+05	3.50	2.00
17-72-2 - 31	0.195	0.011	0.012	5.128	0.316	0.082	0.001	0.001	1143	60	63	1250	28	33	-1.3E+04	7.2E+04	-9.0E+02	6.0E+03	4.0E+04	3.2E+04	0.89	0.21
17-72-2 - 32	0.087	0.002	0.003	11.494	0.330	0.060	0.000	0.001	538	10	15	605	14	23	6.0E+05	2.3E+05	4.0E+04	1.4E+04	8.0E+02	3.2E+03	20.80	1.60
17-72-2 - 33	0.100	0.006	0.007	10.040	0.675	0.065	0.001	0.001	611	37	39	774	32	36	-2.3E+05	3.9E+05	-1.6E+04	2.6E+04	-8.0E+04	1.4E+04	12.00	1.90
17-72-2 - 34	0.116	0.006	0.007	8.606	0.481	0.066	0.001	0.001	708	35	37	802	42	46	8.7E+04	8.2E+04	4.2E+03	4.2E+03	3.8E+03	3.4E+03	9.20	2.50
17-72-2 - 35	0.155	0.002	0.004	6.464	0.159	0.074	0.001	0.001	927	13	21	1026	36	40	1.7E+05	2.1E+05	1.3E+04	1.5E+04	9.0E+04	1.0E+04	10.00	2.00
17-72-2 - 36	0.089	0.001	0.002	11.199	0.238	0.059	0.000	0.001	551.3	4.2	11	575	13	23	1.1E+05	1.6E+05	6.7E+03	9.5E+03	2.1E+03	2.9E+03	16.68	0.61
17-72-2 - 37	0.157	0.015	0.015	6.369	0.609	0.075	0.003	0.003	939	84	86	1061	74	76	1.4E+05	1.5E+05	1.0E+05	1.2E+04	1.1E+04	1.2E+04	8.80	2.80
17-72-2 - 38	0.123	0.010	0.011	8.130	0.727	0.068	0.002	0.002	745	60	61	865	64	66	-6.0E+05	1.2E+05	-4.5E+03	8.3E+03	-5.0E+04	1.1E+04	9.10	2.60
17-72-2 - 39	0.089	0.002	0.003	11.299	0.383	0.059	0.000	0.001	547	15	18	582	13	22	3.0E+05	1.5E+05	1.7E+03	8.9E+03	6.0E+02	3.3E+03	13.40	0.51
17-72-2 - 40	0.237	0.011	0.012	4.219	0.214	0.095	0.001	0.002	1367	57	62	1526	25	29	5.2E+04	7.6E+04	5.1E+03	7.3E+03	2.9E+04	2.7E+04	1.65	0.29
17-72-2 - 41	0.151	0.002	0.004	6.618	0.162	0.069	0.000	0.001	907	12	21	909	10	20	3.0E+05	1.9E+05	2.0E+04	1.3E+04	5.0E+02	2.4E+03	23.07	0.79
17-72-2 - 42	0.201	0.039	0.040	4.975	0.990	0.097	0.014	0.014	1150	210	210	1380	260	260	9.0E+04	7.7E+04	9.9E+03	6.6E+03	1.1E+04	8.3E+03	13.40	4.90
17-72-2 - 43	0.110	0.005	0.006	9.107	0.456	0.065	0.001	0.001	671	29	32	756	39	43	3.0E+05	2.0E+05	2.0E+04	1.3E+04	5.0E+02	3.5E+03	16.20	1.10
17-72-2 - 44	0.130	0.008	0.008	7.686	0.496	0.069	0.001	0.002	787	46	48	879	41	45	5.5E+04	7.3E+04	3.9E+03	5.2E+03	6.1E+03	4.2E+03	4.60	1.20
17-72-2 - 45	0.112	0.007	0.007	8.913	0.564	0.067	0.001	0.001	684	39	41	817	40	44	5.9E+04	5.8E+04	4.0E+03	3.9E+03	1.1E+03	1.0E+03	34.50	5.30
17-72-2 - 46	0.167	0.017	0.017	5.988	0.610	0.085	0.003	0.003	993	93	95	1315	62	64	9.8E+04	9.1E+04	8.6E+03	7.6E+03	1.9E+04	1.6E+04	1.98	0.21
17-72-2 - 47	0.102	0.004	0.004	9.804	0.404	0.062	0.001	0.001	626	21	24	665	36	40	3.6E+04	2.9E+04	2.3E+03	1.9E+03	5.5E+02	6.2E+02	17.00	1.80
17-72-2 - 48	0.133	0.006	0.007	7.496	0.388	0.082	0.004	0.004	806	37	40	1217	97	99	8.7E+04	8.7E+04	7.8E+03	7.7E+03	4.6E+03	4.8E+03	9.10	1.40
17-72-2 - 49	0.141	0.005	0.005	7.077	0.270	0.068	0.000	0.001	852	26	30	868	14	22	-3.0E+05	1.3E+05	-2.0E+03	8.5E+03	2.8E+04	5.7E+04	17.30	1.30
17-72-2 - 50	0.094	0.002	0.003	10.627	0.294	0.060	0.000	0.001	580	11	15	603	15	24	-4.0E+05	1.2E+05	-2.5E+03	7.3E+03	-7.0E+02	2.0E+03	17.40	1.20
17-72-2 - 51	0.217	0.008	0.009	4.610	0.193	0.087	0.001	0.001	1264	43	49	1355	17	24	-3.1E+05	9.6E+05	-2.7E+04	8.4E+04	-6.0E+05	1.8E+05	1.67	0.10
17-72-2 - 52	0.174	0.006	0.007	5.750	0.235	0.078	0.001	0.001	1033	34	39	1147	19	25	8.1E+04	7.8E+04	6.2E+03	6.3E+03	1.1E+04	1.0E+04	2.17	0.23
17-72-2 - 53	0.189	0.011	0.012	5.291	0.336	0.084	0.002	0.002	1111	60	63	1287	37	41	-3.3E+04	9.1E+04	-2.4E+03	7.1E+03	1.4E+03	5.7E+03	2.25	0.50
17-72-2 - 54	0.154	0.007	0.008	6.477	0.336	0.139	0.030	0.030	925	41	44	1840	360	360	1.1E+04	2.1E+04	1.0E+03	1.5E+03	1.2E+03	9.6E+02	5.97	0.83
17-72-2 - 55	0.119	0.005	0.006	8.425	0.390	0.070	0.002	0.002	722	29	32	920	49	52	6.0E+04	7.1E+04	5.0E+02	5.1E+03	1.0E+03	5.1E+03	4.99	0.83
17-72-2 - 56	0.186	0.008	0.009	5.379	0.252	0.078	0.001	0.001	1098	43	48	1134	28	33	1.0E+05	5.5E+04	7.9E+03	4.4E+03	1.6E+04	9.4E+03	3.00	1.10
17-72-2 - 57	0.187	0.008	0.009	5.359	0.261	0.077	0.001	0.001	1102	46	50	1119	30	34	-3.0E+06	1.2E+06	-2.5E+04	9.3E+04	-5.0E+05	2.0E+05	3.08	0.99
17-72-2 - 58	0.196	0.003	0.005	5.097	0.135	0.080	0.000	0.001	1155	18	28	1189	10	20	7.6E+04	9.2E+04	6.1E+03	7.4E+03	1.3E+04	1.6E+04	1.70	0.08
17-72-2 - 59	0.152	0.009	0.009	6.570	0.393	0.081	0.004	0.004	912	48	51	1190	110	110	-3.0E+05	2.4E+05	-1.0E+04	1.9E+04	1.0E+04	1.2E+04	8.20	1.90
17-72-2 - 60	0.123	0.010	0.010	8.117	0.659	0.074	0.002	0.002	747	56	58	1032	42	45	1.2E+05	1.5E+05	9.0E+04	1.2E+04	5.3E+03	6.9E+03	9.01	0.45
17-72-2 - 61	0.156	0.002	0.004	6.418	0.144	0.070	0.000	0.001	933.2	8.9	19	937.8	8.9	19	1.3E+05	1.3E+05	9.4E+03	8.9E+03	1.6E+03	1.6E+03	22.96	0.59

17-72-2 - 62	0.162	0.004	0.005	6.180	0.183	0.071	0.000	0.001	967	19	26	942	10	20	-3.6E+05	3.4E+05	-2.6E+04	2.4E+04	-4.4E+03	4.1E+03	24.03	0.62
17-72-2 - 63	0.164	0.005	0.006	6.094	0.212	0.076	0.002	0.002	979	26	32	1091	40	44	1.0E+06	1.2E+05	7.8E+03	9.3E+03	4.4E+03	4.7E+03	9.60	1.10
17-72-2 - 64	0.129	0.008	0.008	7.758	0.506	0.066	0.001	0.001	780	46	48	813	28	33	6.2E+04	9.6E+04	4.1E+03	6.3E+03	1.0E+03	1.5E+03	18.94	0.81
17-72-2 - 65	0.171	0.009	0.009	5.841	0.317	0.086	0.004	0.004	1017	47	51	1305	97	98	8.0E+05	1.2E+05	3.5E+03	7.7E+03	7.0E+02	5.0E+03	6.62	0.73
17-72-2 - 66	0.139	0.005	0.006	7.210	0.296	0.074	0.001	0.002	837	28	32	1027	36	40	7.0E+05	1.1E+05	8.2E+03	4.6E+03	3.1E+03	1.9E+03	20.50	5.00
17-72-2 - 67	0.098	0.003	0.003	10.163	0.351	0.062	0.001	0.001	605	16	20	653	41	45	8.3E+04	3.3E+04	5.2E+03	2.1E+03	2.1E+03	7.8E+02	16.80	1.20
17-72-2 - 68	0.154	0.006	0.007	6.506	0.292	0.072	0.001	0.001	921	35	39	990	29	34	1.4E+05	1.6E+05	1.0E+05	1.1E+04	2.7E+03	3.8E+03	15.30	2.60
17-72-2 - 69	0.146	0.005	0.005	6.840	0.253	0.069	0.001	0.001	879	26	31	883	16	24	-2.8E+04	7.6E+04	-1.9E+03	5.2E+03	-5.0E+02	1.2E+03	19.90	2.40
17-72-2 - 70	0.241	0.005	0.007	4.155	0.123	0.093	0.001	0.001	1390	27	37	1483	13	20	-2.0E+05	1.7E+05	-2.0E+04	1.6E+04	-5.0E+04	5.5E+04	0.78	0.04
17-78-1 - 1	0.203	0.011	0.011	4.926	0.267	0.083	0.002	0.002	1191	57	59	1268	55	55	7.8E+03	7.7E+03	6.2E+02	6.1E+02	2.6E+03	3.1E+03	0.91	0.40
17-78-1 - 2	0.146	0.001	0.002	6.859	0.099	0.069	0.000	0.000	877.5	5.9	12	884	14	14	9.9E+03	9.6E+03	8.9E+02	7.7E+02	1.5E+03	2.1E+03	9.00	3.90
17-78-1 - 3	0.172	0.009	0.009	5.821	0.298	0.076	0.002	0.002	1021	47	48	1082	54	54	2.1E+04	9.0E+03	1.6E+03	7.4E+02	1.5E+03	1.3E+03	9.70	2.30
17-78-1 - 4	0.228	0.006	0.007	4.380	0.134	0.090	0.001	0.001	1325	33	36	1437	27	27	2.1E+04	8.5E+03	1.9E+03	7.5E+02	2.7E+03	1.1E+03	2.06	0.04
17-78-1 - 5	0.214	0.013	0.014	4.673	0.306	0.083	0.003	0.003	1245	71	72	1250	58	58	5.9E+04	4.6E+04	5.0E+03	3.7E+03	6.3E+03	5.4E+03	2.80	1.10
17-78-1 - 6	0.175	0.004	0.005	5.705	0.159	0.073	0.001	0.001	1041	24	27	1004	37	37	1.1E+04	5.5E+03	8.1E+02	4.1E+02	5.5E+03	2.5E+03	0.47	0.05
17-78-1 - 7	0.246	0.026	0.026	4.065	0.430	0.099	0.005	0.005	1410	140	140	1574	90	90	5.1E+04	9.1E+04	9.0E+04	1.1E+04	3.7E+04	2.3E+04	1.16	0.34
17-78-1 - 8	0.239	0.007	0.008	4.189	0.133	0.088	0.001	0.001	1379	37	40	1387	24	24	2.4E+04	1.9E+04	2.1E+03	1.7E+03	8.4E+02	6.4E+02	6.82	0.89
17-78-1 - 9	0.272	0.024	0.024	3.676	0.324	0.095	0.003	0.003	1550	120	120	1525	56	56	2.0E+04	3.2E+04	3.0E+02	2.9E+03	6.1E+03	8.6E+03	0.81	0.28
17-78-1 - 10	0.159	0.004	0.005	6.274	0.185	0.073	0.001	0.001	953	24	26	1018	33	33	1.1E+04	2.5E+04	7.0E+02	1.9E+03	3.2E+03	5.3E+03	1.15	0.18
17-78-1 - 11	0.249	0.027	0.028	4.016	0.452	0.125	0.009	0.009	1420	140	140	1990	130	130	2.1E+05	1.3E+05	3.0E+04	1.9E+04	5.4E+03	3.1E+03	13.90	1.90
17-78-1 - 12	0.150	0.010	0.010	6.662	0.439	0.072	0.002	0.002	900	55	56	991	49	49	1.2E+05	1.6E+05	9.0E+04	1.2E+04	2.2E+03	1.9E+03	14.30	3.80
17-78-1 - 13	0.156	0.007	0.007	6.414	0.284	0.075	0.001	0.001	933	37	38	1067	24	24	3.2E+04	1.7E+04	2.4E+03	1.2E+03	1.6E+03	1.2E+03	9.80	2.00
17-78-1 - 14	0.173	0.004	0.005	5.797	0.151	0.076	0.001	0.001	1026	21	24	1100	27	27	9.0E+04	3.4E+04	6.0E+02	2.5E+03	5.0E+02	6.2E+03	2.92	0.95
17-78-1 - 15	0.169	0.002	0.003	5.924	0.112	0.076	0.001	0.001	1005	13	17	1091	18	18	1.3E+04	2.6E+04	1.0E+03	1.9E+03	3.8E+02	6.9E+02	13.50	1.30
17-78-1 - 16	0.169	0.003	0.004	5.917	0.140	0.077	0.001	0.001	1007	19	22	1111	30	30	-1.2E+04	4.5E+04	-9.0E+02	3.5E+03	2.2E+02	9.5E+02	6.34	0.81
17-78-1 - 17	0.148	0.005	0.005	6.752	0.223	0.070	0.001	0.001	890	25	27	924	23	23	5.0E+02	8.9E+03	4.0E+01	6.4E+02	1.0E+02	8.0E+03	0.29	0.00
17-78-1 - 18	0.150	0.003	0.003	6.653	0.137	0.070	0.001	0.001	902	14	17	927	26	26	1.1E+03	5.0E+03	8.0E+01	3.5E+02	1.1E+03	4.1E+03	0.36	0.04
17-78-1 - 19	0.149	0.003	0.003	6.716	0.149	0.073	0.001	0.001	894	16	19	1018	22	22	2.5E+04	2.0E+04	1.8E+03	1.4E+03	1.2E+03	1.0E+03	6.85	0.40
17-78-1 - 20	0.210	0.004	0.005	4.762	0.116	0.086	0.001	0.001	1228	23	27	1342	24	24	2.7E+04	3.2E+04	2.3E+03	2.8E+03	1.2E+03	1.3E+03	7.54	0.55
17-78-1 - 21	0.131	0.006	0.006	7.610	0.330	0.078	0.001	0.001	795	31	32	1141	31	31	9.1E+04	4.3E+04	7.2E+03	3.3E+03	2.1E+03	6.9E+02	9.20	1.80
17-78-1 - 22	0.166	0.003	0.004	6.042	0.142	0.075	0.001	0.001	987	18	22	1074	24	24	1.8E+04	5.4E+03	1.4E+03	4.3E+02	9.4E+02	1.9E+02	4.78	0.69
17-78-1 - 23	0.170	0.004	0.005	5.875	0.155	0.077	0.001	0.001	1013	22	25	1107	24	24	4.6E+04	5.2E+04	3.5E+03	3.9E+03	1.7E+03	1.9E+03	8.32	0.38
17-78-1 - 24	0.226	0.008	0.009	4.429	0.175	0.088	0.001	0.001	1312	44	47	1371	32	32	3.3E+05	7.0E+05	2.8E+04	5.9E+04	1.8E+05	3.9E+05	0.39	0.04

17-78-1 - 25	0.182	0.005	0.006	5.507	0.170	0.080	0.002	0.002	1075	28	30	1190	36	36	2.8E+04	7.2E+04	1.4E+04	2.5E+04	2.6E+03	4.3E+03	20.30	1.20
17-78-1 - 26	0.226	0.022	0.022	4.425	0.431	0.084	0.003	0.003	1300	110	110	1274	61	61	3.2E+04	1.9E+04	2.7E+03	1.6E+03	3.4E+03	2.5E+03	5.90	2.10
17-78-1 - 27	0.234	0.010	0.010	4.275	0.183	0.089	0.002	0.002	1353	51	53	1400	40	40	2.7E+04	2.2E+04	2.4E+03	1.9E+03	2.0E+03	2.0E+03	7.00	2.20
17-78-1 - 28	0.195	0.005	0.005	5.118	0.141	0.084	0.001	0.001	1150	26	29	1281	31	31	5.0E+05	1.0E+05	4.4E+03	8.8E+03	9.0E+02	1.6E+03	17.10	1.20
17-78-1 - 29	0.216	0.003	0.004	4.627	0.086	0.087	0.001	0.001	1261	16	21	1365	24	24	5.1E+04	4.8E+04	4.4E+03	4.2E+03	2.6E+03	2.5E+03	5.64	0.25
17-78-1 - 30	0.192	0.004	0.005	5.214	0.122	0.081	0.001	0.001	1131	21	25	1216	27	27	3.6E+04	9.1E+04	2.9E+03	7.5E+03	7.0E+02	1.7E+03	14.80	0.45
17-78-1 - 31	0.184	0.007	0.007	5.426	0.218	0.079	0.001	0.001	1090	38	40	1169	28	28	1.4E+04	5.5E+04	1.1E+03	4.3E+03	3.0E+02	1.1E+03	14.11	0.40
17-78-1 - 32	0.212	0.007	0.008	4.710	0.166	0.087	0.002	0.002	1240	37	40	1356	39	39	6.3E+04	5.4E+04	5.4E+03	4.7E+03	3.5E+03	3.0E+03	5.72	0.72
17-78-1 - 33	0.186	0.003	0.004	5.373	0.110	0.080	0.001	0.001	1100	16	21	1203	21	21	1.5E+04	9.8E+04	1.3E+03	7.9E+03	1.0E+02	2.0E+03	13.00	1.20
17-78-1 - 34	0.242	0.008	0.009	4.134	0.150	0.092	0.001	0.001	1395	43	46	1463	22	22	-4.1E+04	8.6E+04	-1.2E+03	6.4E+03	-1.2E+03	3.0E+03	7.70	0.49
17-78-1 - 35	0.272	0.004	0.006	3.671	0.074	0.091	0.001	0.001	1552	22	28	1450	21	21	-6.0E+05	1.3E+05	-5.0E+04	1.2E+04	-4.1E+03	8.2E+03	4.50	0.53
17-78-1 - 36	0.217	0.005	0.006	4.615	0.121	0.084	0.001	0.001	1264	27	30	1300	17	17	1.3E+05	1.2E+05	1.2E+04	1.0E+04	3.3E+03	2.9E+03	11.22	0.62
17-78-1 - 37	0.243	0.011	0.011	4.115	0.186	0.092	0.002	0.002	1402	55	57	1465	36	36	2.6E+04	2.2E+04	2.4E+03	2.1E+03	3.1E+03	2.3E+03	3.49	0.69
17-78-1 - 38	0.226	0.009	0.009	4.419	0.184	0.092	0.001	0.001	1314	47	49	1469	19	19	8.0E+04	5.8E+04	7.4E+03	5.4E+03	1.1E+03	6.2E+02	32.40	6.00
17-78-1 - 39	0.158	0.004	0.005	6.337	0.185	0.074	0.001	0.001	944	23	26	1051	22	22	2.0E+04	3.3E+04	1.0E+02	2.4E+03	5.0E+02	1.6E+03	6.20	1.20
17-78-1 - 40	0.148	0.003	0.003	6.780	0.147	0.069	0.001	0.001	887	15	18	887	15	15	7.0E+04	1.3E+04	5.2E+02	8.5E+02	1.2E+03	2.0E+03	7.10	2.20
17-78-1 - 41	0.158	0.003	0.004	6.313	0.151	0.073	0.001	0.001	948	18	21	1014	26	26	2.8E+04	7.5E+04	2.1E+03	5.5E+03	7.0E+02	1.6E+03	12.02	0.47
17-78-1 - 42	0.155	0.003	0.004	6.456	0.163	0.069	0.001	0.001	928	19	22	896	24	24	1.9E+04	1.4E+04	1.3E+03	9.7E+02	5.8E+03	3.1E+03	1.33	0.53
17-78-1 - 43	0.152	0.001	0.002	6.570	0.104	0.071	0.001	0.001	913.3	8.1	13	967	16	16	1.4E+04	3.2E+03	1.0E+03	2.3E+02	4.7E+02	9.1E+01	8.90	1.60
17-78-1 - 44	0.196	0.005	0.006	5.102	0.148	0.082	0.002	0.002	1153	27	30	1233	40	40	3.3E+04	5.2E+04	2.7E+03	4.6E+03	1.1E+03	1.7E+03	8.34	0.13
17-78-1 - 45	0.173	0.005	0.005	5.787	0.171	0.076	0.001	0.001	1027	25	28	1095	25	25	-4.0E+04	2.9E+04	-4.0E+02	2.2E+03	-1.0E+02	1.2E+03	6.79	0.33
17-78-2 - 1	0.142	0.010	0.010	7.042	0.496	0.074	0.003	0.003	857	57	59	1019	71	73	2.9E+03	9.4E+03	2.3E+02	6.6E+02	1.0E+04	1.2E+04	0.63	0.44
17-78-2 - 2	0.206	0.008	0.009	4.845	0.207	0.079	0.001	0.001	1209	41	46	1166	29	34	1.8E+04	8.2E+03	1.4E+03	6.3E+02	8.1E+02	2.1E+02	4.55	0.22
17-78-2 - 3	0.183	0.011	0.011	5.464	0.328	0.078	0.001	0.002	1080	57	60	1138	37	40	3.4E+04	5.4E+04	2.7E+03	4.2E+03	1.3E+03	2.0E+03	6.50	0.64
17-78-2 - 4	0.181	0.014	0.015	5.525	0.458	0.088	0.003	0.003	1068	77	79	1380	71	73	3.0E+05	1.3E+05	4.0E+04	1.2E+04	1.4E+03	6.8E+03	7.00	2.20
17-78-2 - 5	0.214	0.010	0.011	4.673	0.240	0.086	0.001	0.001	1247	55	60	1338	25	30	9.4E+04	7.4E+04	8.2E+03	6.3E+03	3.4E+02	6.4E+02	60.30	8.50
17-78-2 - 6	0.159	0.005	0.006	6.293	0.218	0.076	0.002	0.002	950	25	31	1085	43	46	-2.5E+04	5.2E+04	-1.8E+03	3.8E+03	-3.0E+02	5.1E+03	2.17	0.38
17-78-2 - 7	0.173	0.007	0.008	5.767	0.263	0.079	0.001	0.001	1030	40	44	1170	17	24	-4.0E+05	2.5E+05	-3.0E+04	1.9E+04	-1.6E+03	8.1E+03	9.40	1.70
17-78-2 - 8	0.149	0.008	0.009	6.698	0.390	0.072	0.001	0.002	896	46	49	973	40	44	2.6E+04	5.7E+04	2.0E+03	4.2E+03	1.2E+03	2.4E+03	9.50	1.70
17-78-2 - 9	0.191	0.012	0.013	5.236	0.356	0.083	0.003	0.003	1123	67	70	1252	62	65	5.0E+04	8.1E+04	3.0E+02	6.5E+03	-2.0E+02	6.8E+03	4.63	0.60
17-78-2 - 10	0.163	0.010	0.011	6.135	0.414	0.083	0.001	0.001	974	55	58	1269	27	32	6.0E+05	1.2E+05	5.0E+04	1.0E+04	1.1E+03	2.3E+03	15.40	1.00
17-78-2 - 11	0.291	0.021	0.022	3.436	0.260	0.104	0.003	0.003	1640	110	110	1700	47	50	9.0E+05	1.4E+05	9.0E+04	1.5E+04	3.4E+03	4.9E+03	7.50	0.64
17-78-2 - 12	0.152	0.004	0.005	6.566	0.220	0.070	0.002	0.002	913	23	28	930	43	46	1.0E+05	1.3E+04	7.1E+02	9.3E+02	6.7E+03	8.2E+03	0.44	0.01

17-78-2 - 13	0.165	0.004	0.005	6.075	0.185	0.070	0.001	0.001	982	21	28	918	25	30	2.0E+03	6.2E+03	1.4E+02	4.2E+02	1.0E+03	2.4E+03	0.73	0.05
17-78-2 - 14	0.242	0.008	0.009	4.132	0.157	0.088	0.001	0.002	1396	41	48	1386	32	36	3.7E+04	3.0E+04	3.1E+03	2.5E+03	4.0E+03	3.3E+03	2.10	0.09
17-78-2 - 15	0.217	0.009	0.010	4.606	0.202	0.087	0.002	0.002	1265	45	51	1349	35	38	8.0E+04	3.6E+04	8.0E+02	3.0E+03	1.4E+03	4.1E+03	2.07	0.37
17-78-2 - 16	0.152	0.015	0.015	6.579	0.649	0.098	0.006	0.006	910	81	83	1550	110	110	2.2E+04	1.1E+04	2.5E+03	1.2E+03	1.5E+03	7.6E+02	4.00	0.66
17-78-2 - 17	0.160	0.003	0.005	6.246	0.179	0.075	0.001	0.001	957	19	26	1054	25	31	3.3E+04	2.9E+04	2.5E+03	2.2E+03	2.0E+03	1.3E+03	5.60	1.00
17-78-2 - 18	0.200	0.007	0.008	4.998	0.195	0.088	0.001	0.001	1175	36	42	1389	18	24	1.2E+05	1.0E+05	1.1E+04	9.0E+03	2.0E+03	2.0E+03	20.10	3.10
17-78-2 - 19	0.199	0.016	0.016	5.025	0.404	0.088	0.002	0.002	1169	84	87	1382	35	39	5.0E+04	2.8E+04	4.4E+03	2.4E+03	1.3E+03	8.4E+02	10.50	1.60
17-78-2 - 20	0.177	0.006	0.007	5.637	0.213	0.086	0.001	0.001	1052	31	37	1332	19	25	5.2E+04	1.0E+04	4.4E+03	8.7E+02	2.1E+03	4.5E+02	8.10	1.00
17-78-2 - 21	0.157	0.005	0.006	6.390	0.253	0.116	0.032	0.032	937	30	35	1490	360	360	8.7E+03	4.0E+03	6.4E+02	2.8E+02	1.1E+04	6.6E+03	0.26	0.07
17-78-2 - 22	0.159	0.004	0.005	6.309	0.211	0.074	0.003	0.003	948	23	29	1041	63	65	9.0E+02	9.0E+03	4.0E+01	6.7E+02	3.0E+03	9.7E+03	0.36	0.06
17-78-2 - 23	0.155	0.005	0.006	6.443	0.232	0.071	0.001	0.001	930	26	31	946	30	35	4.8E+03	2.1E+03	3.4E+02	1.5E+02	6.1E+03	2.2E+03	0.19	0.02
17-78-2 - 24	0.202	0.005	0.006	4.948	0.152	0.084	0.001	0.001	1186	26	33	1294	19	25	3.7E+04	6.7E+04	3.2E+03	5.7E+03	6.0E+02	1.3E+03	12.40	1.00
17-78-2 - 25	0.144	0.004	0.005	6.969	0.248	0.083	0.011	0.011	864	24	29	1170	210	210	2.6E+03	8.2E+02	2.0E+02	5.4E+01	6.1E+03	2.1E+03	0.13	0.00
17-78-2 - 26	0.159	0.007	0.008	6.277	0.311	0.074	0.001	0.001	952	41	44	1028	34	38	8.2E+04	8.9E+04	5.9E+03	6.5E+03	2.6E+03	2.5E+03	8.52	0.62
17-78-2 - 27	0.145	0.004	0.005	6.897	0.219	0.075	0.001	0.001	872	21	26	1060	31	35	-6.1E+04	9.2E+04	-4.4E+03	6.8E+03	-1.1E+03	2.9E+03	10.10	2.10
17-78-2 - 28	0.132	0.006	0.007	7.564	0.372	0.069	0.000	0.001	800	34	38	907	11	20	2.7E+05	1.9E+05	1.9E+04	1.3E+04	4.1E+03	2.7E+03	20.61	0.74
17-78-2 - 29	0.134	0.004	0.005	7.440	0.288	0.069	0.001	0.001	812	25	30	885	26	31	1.3E+04	1.1E+04	9.1E+02	7.6E+02	1.2E+03	1.2E+03	6.00	1.30
17-78-2 - 30	0.147	0.007	0.008	6.826	0.359	0.070	0.001	0.001	880	40	43	921	26	31	1.0E+04	6.4E+03	7.1E+02	4.4E+02	1.3E+03	1.5E+03	1.84	0.54
17-78-2 - 31	0.178	0.004	0.005	5.615	0.161	0.077	0.001	0.001	1057	20	28	1112	31	36	-7.0E+04	2.3E+04	1.0E+02	2.0E+03	-1.1E+03	3.6E+03	1.69	0.10
17-78-2 - 32	0.148	0.003	0.004	6.739	0.191	0.069	0.001	0.001	892	17	24	901	29	33	6.0E+04	1.8E+04	4.0E+02	1.2E+03	2.3E+03	3.3E+03	1.85	0.29
17-78-2 - 33	0.149	0.002	0.004	6.729	0.159	0.070	0.001	0.001	893	10	19	915	28	33	5.6E+03	5.8E+03	3.8E+02	3.9E+02	6.8E+02	6.3E+02	2.67	0.11
17-78-2 - 34	0.134	0.004	0.005	7.474	0.263	0.070	0.001	0.002	809	22	27	926	38	41	1.4E+04	2.1E+04	1.0E+03	1.5E+03	3.5E+03	4.1E+03	1.48	0.20
17-78-2 - 35	0.216	0.004	0.006	4.634	0.129	0.088	0.001	0.001	1259	23	32	1372	21	26	1.2E+04	4.1E+04	1.0E+03	3.5E+03	5.0E+02	1.4E+03	8.95	0.65
17-78-2 - 36	0.147	0.003	0.004	6.789	0.198	0.074	0.006	0.006	886	18	24	990	120	120	-4.7E+03	7.4E+03	-2.8E+02	5.2E+02	-3.2E+03	5.1E+03	0.37	0.02
17-78-2 - 37	0.179	0.016	0.017	5.587	0.531	0.077	0.002	0.002	1058	88	91	1110	58	61	1.0E+04	9.5E+03	8.0E+02	7.1E+02	8.8E+03	6.5E+03	0.17	0.01
17-78-2 - 38	0.149	0.002	0.004	6.702	0.162	0.071	0.001	0.001	896	12	20	951	28	33	3.0E+04	2.7E+04	2.0E+02	1.8E+03	2.0E+04	2.8E+04	0.30	0.02
17-78-2 - 39	0.156	0.002	0.004	6.406	0.144	0.070	0.001	0.001	934.8	8.8	19	938	28	33	7.6E+03	7.9E+03	5.4E+02	5.5E+02	1.1E+04	1.2E+04	0.20	0.00
17-78-2 - 40	0.201	0.019	0.020	4.975	0.495	0.086	0.004	0.004	1170	100	100	1309	85	86	5.0E+04	2.0E+04	5.0E+02	1.7E+03	-4.0E+02	5.3E+03	1.74	0.57
17-78-2 - 41	0.187	0.019	0.020	5.348	0.572	0.076	0.003	0.003	1100	100	100	1088	78	79	-2.7E+03	6.3E+03	-6.0E+02	1.0E+03	-2.9E+04	4.0E+04	0.10	0.02
17-78-2 - 42	0.155	0.007	0.007	6.435	0.298	0.072	0.001	0.001	930	37	41	970	36	40	7.0E+04	1.2E+04	5.2E+02	8.1E+02	2.3E+03	3.4E+03	1.43	0.19
17-78-2 - 43	NAN	NAN	NAN			NAN	NAN	NAN	NAN	NAN	NAN	NAN	NAN	NAN	NAN	NAN	NAN	NAN	NAN	NAN	NAN	NAN
17-78-2 - 44	0.160	0.005	0.006	6.242	0.222	0.075	0.002	0.002	958	26	32	1069	40	44	1.2E+04	5.7E+04	1.0E+03	4.3E+03	1.0E+04	2.0E+04	0.69	0.21
17-78-2 - 45	0.172	0.006	0.007	5.824	0.227	0.083	0.002	0.002	1021	32	37	1260	52	54	1.6E+04	2.7E+04	1.3E+03	2.2E+03	2.6E+03	5.7E+03	1.22	0.27

17-78-2 - 46	0.168	0.008	0.009	5.949	0.301	0.077	0.002	0.002	1001	43	47	1126	38	41	6.5E+04	6.8E+04	6.6E+03	5.9E+03	2.0E+03	2.2E+03	9.50	1.00
17-78-2 - 47	0.157	0.002	0.004	6.357	0.154	0.073	0.001	0.001	942	12	21	1014	14	22	8.2E+04	3.6E+04	5.9E+03	2.6E+03	1.7E+03	6.9E+02	15.15	0.92
17-78-2 - 48	0.192	0.008	0.009	5.214	0.242	0.083	0.001	0.002	1130	43	48	1256	34	37	-9.0E+05	1.1E+05	-7.3E+03	9.0E+03	-2.5E+03	2.9E+03	10.30	1.50
17-78-2 - 49	0.205	0.019	0.019	4.878	0.452	0.084	0.004	0.004	1198	99	100	1275	87	89	2.4E+04	8.8E+03	2.1E+03	7.8E+02	3.6E+03	2.9E+03	12.00	4.20
17-78-2 - 50	0.158	0.005	0.006	6.329	0.232	0.073	0.002	0.002	945	27	32	1021	43	46	3.0E+04	2.1E+04	2.0E+02	1.5E+03	2.0E+03	9.0E+03	1.71	0.28
17-78-2 - 51	0.222	0.003	0.006	4.515	0.112	0.091	0.001	0.001	1290	18	29	1439	15	22	-1.0E+05	2.5E+05	-1.0E+04	2.3E+04	0.0E+00	3.7E+03	19.34	0.72
17-78-2 - 52	0.211	0.008	0.009	4.744	0.205	0.103	0.008	0.008	1232	43	48	1620	140	140	9.2E+04	5.4E+04	8.8E+03	4.9E+03	6.1E+03	4.1E+03	5.10	1.00
17-78-2 - 53	0.156	0.009	0.009	6.427	0.388	0.072	0.001	0.001	931	49	52	996	26	31	1.2E+04	6.0E+04	8.0E+02	4.2E+03	6.0E+02	2.7E+03	7.70	2.60
17-78-2 - 54	0.155	0.003	0.005	6.464	0.192	0.088	0.013	0.013	927	19	26	1300	210	210	7.4E+04	7.2E+04	5.7E+03	5.4E+03	4.5E+03	5.0E+03	5.90	2.00
17-78-2 - 55	0.202	0.003	0.005	4.950	0.127	0.083	0.001	0.001	1186	18	28	1263	18	24	7.3E+04	8.5E+04	5.9E+03	7.0E+03	1.0E+03	1.2E+03	19.82	0.80
17-78-2 - 56	0.154	0.002	0.004	6.515	0.153	0.070	0.001	0.001	920	11	20	913	24	30	1.2E+04	4.0E+03	8.4E+02	2.8E+02	1.6E+03	5.4E+02	2.42	0.17
17-78-2 - 57	0.152	0.002	0.004	6.579	0.156	0.071	0.001	0.001	912	11	20	939	31	36	-8.0E+04	1.7E+04	-5.0E+02	1.2E+03	-6.0E+02	2.0E+03	2.38	0.15
17-78-2 - 58	0.174	0.004	0.005	5.747	0.178	0.077	0.001	0.001	1034	22	29	1114	21	27	1.6E+05	9.4E+04	1.2E+04	7.1E+03	2.3E+03	1.4E+03	18.95	0.60
17-78-2 - 59	0.233	0.010	0.011	4.292	0.203	0.091	0.002	0.002	1350	54	59	1447	31	35	1.7E+05	3.8E+05	0.0E+00	1.1E+04	0.0E+00	1.4E+04	2.75	0.16
17-78-2 - 60	0.234	0.007	0.008	4.277	0.146	0.091	0.001	0.001	1354	34	41	1438	25	30	1.0E+04	1.4E+04	9.0E+02	1.2E+03	1.7E+03	2.2E+03	1.80	0.18
17-78-2 - 61	0.171	0.009	0.010	5.851	0.339	0.080	0.002	0.002	1016	51	54	1202	42	45	4.7E+04	7.9E+04	4.0E+03	6.4E+03	5.0E+04	2.0E+04	1.15	0.14
17-78-2 - 62	0.197	0.003	0.005	5.086	0.135	0.083	0.001	0.001	1157	18	28	1258	15	22	3.0E+05	1.8E+05	2.0E+04	1.5E+04	5.0E+02	3.1E+03	15.98	0.65
17-78-2 - 63	0.177	0.004	0.006	5.663	0.176	0.079	0.001	0.001	1048	23	30	1173	24	29	-4.0E+05	1.5E+05	-3.0E+04	1.2E+04	-1.0E+03	3.3E+03	24.50	6.00
17-78-2 - 64	0.172	0.003	0.005	5.831	0.156	0.074	0.001	0.001	1020	17	25	1038	28	33	6.0E+04	3.6E+04	5.0E+02	2.6E+03	1.0E+03	5.0E+03	2.33	0.25
17-78-2 - 65	0.181	0.012	0.012	5.525	0.366	0.076	0.004	0.004	1071	62	65	1083	90	92	2.0E+04	2.1E+04	1.8E+03	2.0E+03	8.5E+03	5.7E+03	0.37	0.12
17-78-2 - 66	0.226	0.007	0.008	4.431	0.163	0.094	0.001	0.002	1311	37	44	1509	25	30	7.0E+05	3.4E+05	7.0E+04	3.2E+04	5.0E+04	1.2E+04	11.20	1.80
17-78-2 - 67	0.179	0.007	0.008	5.602	0.254	0.074	0.001	0.001	1058	40	44	1027	27	32	-9.0E+04	1.4E+04	-7.0E+02	1.0E+03	-1.2E+03	1.4E+03	3.18	0.68
17-78-2 - 68	0.230	0.005	0.007	4.357	0.129	0.091	0.001	0.001	1331	26	36	1452	18	24	5.5E+04	8.6E+04	4.9E+03	7.6E+03	1.7E+03	3.2E+03	5.18	0.47
17-91-1 - 1	0.178	0.022	0.022	5.618	0.694	0.086	0.005	0.005	1050	120	120	1320	110	110	3.8E+04	2.5E+04	1.8E+03	2.3E+03	1.9E+03	3.5E+03	3.40	1.20
17-91-1 - 2	0.139	0.010	0.010	7.194	0.518	0.074	0.003	0.003	838	55	56	1012	83	83	5.0E+04	2.3E+04	3.6E+03	1.7E+03	1.7E+03	1.4E+03	9.80	1.50
17-91-1 - 3	0.190	0.009	0.009	5.258	0.257	0.084	0.002	0.002	1121	48	50	1292	49	49	3.7E+04	3.5E+04	5.0E+02	5.9E+03	1.9E+03	6.4E+03	2.56	0.24
17-91-1 - 4	0.144	0.003	0.003	6.930	0.163	0.074	0.002	0.002	869	16	19	1035	49	49	6.1E+04	6.8E+04	4.4E+03	4.7E+03	4.1E+03	3.6E+03	6.10	1.00
17-91-1 - 5	0.174	0.006	0.006	5.737	0.204	0.076	0.001	0.001	1035	32	34	1103	19	19	1.5E+04	7.8E+04	1.3E+03	5.8E+03	3.0E+04	1.5E+04	1.52	0.12
17-91-1 - 6	0.177	0.002	0.003	5.653	0.093	0.075	0.001	0.001	1050.2	9.7	16	1077	16	16	7.2E+04	9.8E+04	5.5E+03	7.5E+03	1.3E+04	1.7E+04	1.67	0.05
17-91-1 - 7	0.266	0.022	0.023	3.759	0.325	0.115	0.007	0.007	1510	110	120	1850	120	120	-1.0E+04	4.6E+04	0.0E+00	4.7E+03	-1.0E+02	1.7E+03	8.80	1.50
17-91-1 - 8	0.144	0.005	0.006	6.954	0.271	0.079	0.003	0.003	865	30	32	1156	81	81	4.0E+05	1.2E+05	2.6E+03	8.5E+03	1.1E+03	3.0E+03	15.70	1.20
17-91-1 - 9	0.118	0.004	0.004	8.511	0.297	0.068	0.001	0.001	716	22	24	855	27	27	8.2E+04	5.3E+04	5.5E+03	3.4E+03	5.2E+03	2.3E+03	5.15	0.94
17-91-1 - 10	0.146	0.007	0.007	6.831	0.345	0.071	0.001	0.001	880	40	42	966	18	18	-5.0E+04	4.2E+04	-4.0E+02	3.1E+03	-1.0E+04	1.2E+04	3.30	1.20

17-91-1 - 11	0.131	0.009	0.010	7.610	0.550	0.070	0.001	0.001	794	53	54	931	16	16	2.6E+04	3.0E+04	1.8E+03	2.1E+03	2.0E+03	2.8E+03	3.06	0.43
17-91-1 - 12	0.138	0.002	0.003	7.257	0.132	0.068	0.000	0.000	832	10	14	861	12	12	4.4E+04	6.3E+04	3.0E+03	4.3E+03	3.3E+03	6.3E+03	2.43	0.37
17-91-1 - 13	0.196	0.004	0.005	5.107	0.130	0.085	0.001	0.001	1153	24	27	1323	17	17	-2.2E+04	7.7E+04	-1.8E+03	6.6E+03	-2.0E+03	7.7E+03	2.76	0.08
17-91-1 - 14	0.169	0.006	0.007	5.903	0.230	0.082	0.002	0.002	1008	35	36	1228	47	47	1.0E+05	1.3E+05	1.0E+04	1.0E+04	3.0E+02	9.6E+03	3.58	0.09
17-91-1 - 15	0.139	0.002	0.003	7.215	0.135	0.071	0.001	0.001	837	11	15	976	38	38	5.2E+04	5.4E+04	3.7E+03	3.8E+03	5.0E+03	5.4E+03	4.50	1.10
17-91-1 - 16	0.185	0.005	0.006	5.417	0.161	0.079	0.001	0.001	1092	27	30	1176	26	26	4.5E+04	6.4E+04	3.6E+03	5.0E+03	1.2E+04	1.7E+04	1.14	0.06
17-91-1 - 17	0.112	0.010	0.010	8.929	0.797	0.080	0.003	0.003	682	58	59	1170	84	84	-2.3E+04	4.7E+04	-1.4E+03	3.2E+03	-8.0E+02	2.5E+03	9.70	1.50
17-91-1 - 18	0.155	0.001	0.002	6.456	0.100	0.070	0.000	0.000	928.5	7.3	13	913.6	8.3	8.3	6.3E+04	6.1E+04	4.4E+03	4.3E+03	5.2E+03	4.7E+03	4.31	0.20
17-91-1 - 19	0.151	0.001	0.002	6.636	0.101	0.070	0.000	0.000	904.9	7.4	13	922	15	15	5.6E+04	4.0E+04	3.9E+03	2.8E+03	4.6E+03	3.3E+03	3.45	0.12
17-91-1 - 20	0.195	0.003	0.004	5.120	0.092	0.079	0.001	0.001	1150	13	19	1169	17	17	2.1E+04	4.8E+04	1.6E+03	3.8E+03	6.0E+04	1.5E+04	0.99	0.02
17-91-1 - 21	0.180	0.010	0.010	5.543	0.307	0.083	0.002	0.002	1067	53	54	1266	50	50	6.9E+04	6.2E+04	5.8E+03	5.2E+03	1.4E+04	1.2E+04	1.43	0.07
17-91-1 - 22	0.128	0.008	0.008	7.819	0.495	0.074	0.002	0.002	775	45	46	1045	56	56	2.0E+04	3.8E+04	1.0E+02	3.1E+03	0.0E+00	5.8E+03	2.83	0.62
17-91-1 - 23	0.163	0.006	0.006	6.154	0.231	0.079	0.002	0.002	970	32	34	1169	36	36	3.3E+04	3.0E+04	2.5E+03	2.3E+03	5.0E+03	4.5E+03	1.89	0.03
17-91-1 - 24	0.182	0.002	0.003	5.507	0.085	0.077	0.000	0.000	1075.7	8.6	15	1114	11	11	-9.0E+05	2.1E+05	-7.0E+04	1.6E+04	-1.8E+04	3.8E+04	1.62	0.03
17-91-1 - 25	0.180	0.004	0.004	5.562	0.130	0.078	0.001	0.001	1066	19	23	1136	20	20	5.0E+05	1.4E+05	4.0E+04	1.0E+04	1.5E+04	3.4E+04	1.40	0.19
17-91-1 - 26	0.228	0.013	0.014	4.386	0.269	0.119	0.005	0.005	1320	70	72	1927	75	75	-5.1E+04	5.7E+04	-3.0E+04	1.0E+04	-9.0E+05	1.6E+05	0.64	0.15
17-91-1 - 27	0.303	0.013	0.013	3.300	0.142	0.141	0.002	0.002	1704	63	66	2234	28	28	2.2E+04	2.9E+04	4.8E+03	5.1E+03	2.8E+03	9.8E+03	1.05	0.06
17-91-1 - 28	0.178	0.006	0.006	5.631	0.190	0.081	0.001	0.001	1054	31	33	1221	29	29	-8.0E+04	6.3E+04	-5.0E+02	5.0E+03	-1.5E+03	9.8E+03	1.84	0.04
17-91-1 - 29	0.141	0.007	0.007	7.087	0.337	0.075	0.002	0.002	850	37	38	1053	55	55	1.0E+03	5.0E+04	-1.0E+02	3.5E+03	-1.3E+03	2.9E+03	5.50	1.10
17-91-1 - 30	0.113	0.002	0.002	8.873	0.181	0.067	0.001	0.001	688	11	14	848	18	18	7.7E+04	8.3E+04	5.1E+03	5.5E+03	1.5E+04	1.7E+04	1.56	0.03
17-91-1 - 31	0.158	0.006	0.006	6.345	0.238	0.073	0.001	0.001	943	31	33	1023	27	27	2.6E+04	5.8E+04	1.9E+03	4.3E+03	7.0E+04	1.4E+04	1.27	0.09
17-91-1 - 32	0.185	0.004	0.005	5.420	0.132	0.081	0.001	0.001	1091	21	24	1225	22	22	3.2E+04	3.8E+04	2.7E+03	3.1E+03	9.0E+04	1.2E+04	2.04	0.27
17-91-1 - 33	0.203	0.010	0.010	4.926	0.243	0.104	0.005	0.005	1189	54	56	1679	85	85	6.5E+04	7.1E+04	6.8E+03	8.0E+03	1.2E+04	1.3E+04	1.52	0.03
17-91-1 - 34	0.102	0.006	0.006	9.804	0.606	0.069	0.001	0.001	625	36	37	898	40	40	3.3E+04	1.4E+04	2.3E+03	9.2E+02	2.4E+03	1.1E+03	5.30	1.40
17-91-1 - 35	0.139	0.004	0.005	7.194	0.238	0.075	0.001	0.001	839	24	26	1055	36	36	4.3E+04	7.7E+04	3.0E+03	5.6E+03	5.0E+04	1.1E+04	1.95	0.10
17-91-1 - 36	0.105	0.006	0.006	9.560	0.576	0.082	0.001	0.001	641	36	37	1246	23	23	6.0E+04	3.1E+04	4.0E+02	2.6E+03	6.0E+02	7.7E+03	2.24	0.10
17-91-1 - 37	0.146	0.008	0.009	6.873	0.402	0.071	0.002	0.002	874	47	48	959	49	49	2.8E+04	4.0E+04	1.9E+03	2.9E+03	4.2E+03	7.0E+03	2.37	0.58
17-91-1 - 38	0.150	0.005	0.006	6.653	0.248	0.080	0.001	0.001	902	30	32	1199	29	29	2.5E+04	7.2E+04	1.8E+03	5.8E+03	1.9E+03	9.1E+03	3.65	0.63
17-91-1 - 39	0.211	0.014	0.014	4.739	0.314	0.086	0.003	0.003	1232	75	76	1319	74	74	3.8E+04	7.0E+04	2.8E+03	5.5E+03	1.0E+03	1.1E+04	3.10	1.30
17-91-1 - 40	0.169	0.006	0.006	5.917	0.224	0.081	0.002	0.002	1006	33	35	1224	38	38	4.0E+05	7.1E+05	3.4E+04	6.1E+04	1.1E+04	1.4E+04	1.65	0.19
17-91-1 - 41	0.247	0.007	0.007	4.054	0.122	0.093	0.001	0.001	1421	35	38	1477	14	14	-3.0E+05	1.9E+05	-3.0E+04	1.8E+04	-1.0E+03	1.6E+04	3.61	0.26
17-91-1 - 42	0.193	0.012	0.012	5.181	0.322	0.084	0.002	0.002	1134	63	65	1283	56	56	3.3E+04	8.5E+04	2.3E+03	6.5E+03	0.0E+00	1.1E+04	1.40	0.04
17-91-1 - 43	0.114	0.001	0.002	8.783	0.131	0.064	0.000	0.000	695	5.4	9.9	749	13	13	-2.9E+04	7.4E+04	-1.9E+03	4.8E+03	-4.0E+04	1.0E+04	2.12	0.03

17-91-1 - 44	0.123	0.005	0.005	8.157	0.339	0.066	0.001	0.001	745	28	29	793	25	25	6.6E+04	4.9E+04	4.3E+03	3.1E+03	7.1E+03	6.1E+03	3.75	0.60
17-91-1 - 45	0.161	0.006	0.007	6.227	0.256	0.076	0.001	0.001	959	35	37	1094	17	17	7.1E+04	7.5E+04	5.5E+03	5.7E+03	1.0E+04	1.0E+04	2.02	0.06
17-91-1 - 46	0.136	0.003	0.003	7.348	0.173	0.067	0.000	0.000	823	15	18	821	13	13	-2.4E+04	3.7E+04	-1.6E+03	2.5E+03	-1.8E+03	3.0E+03	5.40	1.20
17-91-1 - 47	0.128	0.002	0.003	7.800	0.152	0.067	0.000	0.000	777	11	14	826	14	14	2.8E+04	6.3E+03	1.9E+03	4.2E+02	3.6E+03	8.3E+02	2.20	0.04
17-91-1 - 48	0.143	0.002	0.002	6.983	0.112	0.068	0.000	0.000	862.6	8.4	13	873	15	15	-5.7E+04	9.1E+04	-3.9E+03	6.2E+03	-4.9E+03	7.6E+03	3.47	0.08
17-91-1 - 49	0.266	0.010	0.010	3.759	0.141	0.127	0.002	0.002	1519	50	53	2051	33	33	2.7E+04	2.6E+04	3.6E+03	3.3E+03	3.8E+03	3.6E+03	1.95	0.05
17-91-1 - 50	0.114	0.008	0.008	8.772	0.600	0.074	0.003	0.003	695	45	45	1008	87	87	4.2E+04	3.7E+04	2.9E+03	2.4E+03	2.4E+03	1.8E+03	11.80	2.80
17-91-1 - 51	0.197	0.004	0.005	5.074	0.121	0.083	0.001	0.001	1159	22	25	1265	17	17	1.4E+05	9.8E+04	1.2E+04	8.1E+03	4.2E+04	2.9E+04	0.98	0.02
17-91-1 - 52	0.132	0.003	0.004	7.564	0.200	0.069	0.001	0.001	800	18	20	909	18	18	5.9E+04	8.4E+04	4.2E+03	6.0E+03	1.4E+04	1.9E+04	1.39	0.06
17-91-1 - 53	0.155	0.005	0.005	6.439	0.224	0.072	0.001	0.001	930	28	30	994	32	32	9.1E+04	5.4E+04	6.6E+03	3.9E+03	7.1E+03	3.9E+03	5.80	1.80
17-91-1 - 54	0.179	0.007	0.008	5.602	0.242	0.076	0.002	0.002	1058	41	42	1080	47	47	1.2E+05	1.2E+05	8.5E+03	8.6E+03	1.2E+04	1.3E+04	3.50	1.40
17-91-1 - 55	0.167	0.009	0.009	5.984	0.329	0.074	0.002	0.002	994	50	51	1030	51	51	-1.0E+03	8.4E+04	-2.0E+02	5.8E+03	-1.4E+03	7.3E+03	3.41	0.86
17-91-1 - 56	0.139	0.002	0.002	7.189	0.119	0.068	0.001	0.001	839.6	8.5	13	865	16	16	-4.2E+04	9.7E+04	-2.9E+03	6.6E+03	-6.0E+04	1.3E+04	2.15	0.04
17-91-1 - 57	0.128	0.003	0.003	7.806	0.195	0.066	0.001	0.001	777	16	18	803	21	21	-8.0E+04	7.2E+04	-5.0E+02	4.8E+03	-1.1E+03	9.5E+03	2.12	0.03
17-91-1 - 58	0.153	0.010	0.010	6.549	0.416	0.149	0.038	0.038	914	54	55	1980	330	330	-4.5E+04	7.6E+04	-3.8E+03	6.7E+03	-1.1E+04	2.0E+04	1.32	0.04
17-91-1 - 59	0.149	0.008	0.008	6.698	0.363	0.077	0.001	0.001	896	44	45	1116	33	33	5.0E+05	1.1E+05	3.7E+03	7.9E+03	1.1E+04	2.5E+04	1.32	0.06
17-91-1 - 60	0.191	0.003	0.004	5.238	0.102	0.081	0.001	0.001	1126	15	20	1208	20	20	3.2E+04	3.0E+04	2.6E+03	2.4E+03	1.1E+04	1.1E+04	0.83	0.02
17-91-1 - 61	0.252	0.009	0.010	3.975	0.156	0.131	0.003	0.003	1446	49	51	2106	33	33	1.0E+04	2.3E+04	1.3E+03	3.0E+03	2.9E+03	6.0E+03	1.10	0.05
17-91-1 - 62	0.106	0.003	0.003	9.434	0.267	0.073	0.001	0.001	649	16	17	1018	23	23	2.0E+04	3.2E+03	1.5E+03	2.4E+02	7.1E+02	1.3E+02	21.10	2.60
17-91-1 - 63	0.181	0.013	0.014	5.525	0.427	0.085	0.004	0.004	1069	73	74	1311	79	79	-1.0E+04	2.7E+04	0.0E+00	2.4E+03	2.7E+03	2.0E+03	1.26	0.22
17-91-1 - 64	0.133	0.001	0.002	7.513	0.119	0.066	0.000	0.000	805.4	6.8	12	815	11	11	1.2E+04	5.8E+04	8.0E+02	3.8E+03	8.0E+02	4.0E+03	3.83	0.06
17-91-1 - 65	0.134	0.004	0.004	7.457	0.228	0.073	0.002	0.002	811	21	23	1004	47	47	-6.0E+04	4.5E+04	-3.0E+02	3.2E+03	3.0E+02	5.8E+03	3.28	0.37
17-91-1 - 66	0.143	0.005	0.006	6.983	0.273	0.082	0.001	0.001	862	30	31	1240	32	32	5.0E+04	4.1E+04	4.1E+03	3.3E+03	3.4E+03	3.0E+03	4.84	0.41
17-91-1 - 67	0.242	0.007	0.007	4.136	0.127	0.093	0.001	0.001	1395	35	38	1491	16	16	4.0E+05	1.0E+05	3.6E+03	9.0E+03	1.1E+04	2.8E+04	0.96	0.02
17-91-1 - 68	0.253	0.003	0.004	3.946	0.065	0.095	0.000	0.000	1456	14	22	1521.9	8.4	8.4	-1.0E+06	1.7E+05	-9.0E+04	1.6E+04	-1.9E+04	3.1E+04	1.51	0.03
17-91-1 - 69	0.224	0.008	0.009	4.458	0.169	0.090	0.002	0.002	1304	43	45	1426	35	35	8.9E+04	4.3E+04	8.2E+03	4.0E+03	1.5E+04	7.1E+03	1.68	0.08
17-91-1 - 70	0.165	0.007	0.008	6.079	0.285	0.085	0.001	0.001	981	41	43	1311	27	27	-9.0E+05	1.7E+05	-8.0E+04	1.5E+04	-1.3E+04	2.6E+04	1.97	0.08
17-91-1 - 71	0.207	0.003	0.004	4.826	0.091	0.086	0.000	0.000	1214	15	21	1342.2	9	9	9.8E+04	7.6E+04	8.4E+03	6.5E+03	1.6E+04	1.2E+04	1.74	0.04
17-91-1 - 72	0.221	0.011	0.012	4.525	0.246	0.085	0.003	0.003	1282	61	63	1312	72	72	2.0E+05	1.7E+05	1.0E+04	1.5E+04	-1.0E+04	2.3E+04	5.80	3.00
17-91-1 - 73	0.234	0.012	0.012	4.274	0.219	0.090	0.002	0.002	1355	60	62	1420	37	37	3.1E+04	9.6E+04	3.2E+03	8.6E+03	8.0E+04	1.8E+04	1.59	0.21
17-91-1 - 74	0.166	0.004	0.004	6.024	0.149	0.080	0.003	0.003	990	20	23	1190	67	67	1.2E+05	7.4E+04	9.8E+03	5.7E+03	1.5E+04	9.5E+03	2.27	0.11
17-91-1 - 75	0.173	0.007	0.007	5.784	0.234	0.077	0.002	0.002	1028	36	38	1110	43	43	4.3E+04	4.8E+04	3.5E+03	3.8E+03	4.5E+03	4.7E+03	3.17	0.11
17-91-1 - 76	0.205	0.010	0.010	4.890	0.239	0.086	0.001	0.001	1197	52	54	1328	30	30	1.7E+04	2.2E+04	1.4E+03	1.9E+03	3.4E+03	4.5E+03	1.34	0.17

17-91-1 - 77	0.144	0.005	0.006	6.935	0.274	0.076	0.001	0.001	868	31	32	1097	26	26	2.0E+05	1.2E+05	1.0E+03	9.2E+03	-5.0E+02	4.2E+03	7.73	0.82
17-91-1 - 78	0.224	0.006	0.007	4.460	0.131	0.090	0.001	0.001	1304	32	35	1414	24	24	1.0E+04	4.2E+04	3.0E+02	3.7E+03	1.0E+03	1.9E+04	0.61	0.01
17-91-1 - 79	0.112	0.002	0.003	8.945	0.208	0.066	0.001	0.001	683	13	15	800	23	23	-1.2E+04	4.9E+04	-8.0E+02	3.2E+03	0.0E+00	1.1E+04	1.22	0.13
17-91-1 - 80	0.130	0.007	0.007	7.710	0.398	0.071	0.001	0.001	785	37	38	968	22	22	6.4E+04	9.1E+04	4.4E+03	6.5E+03	5.5E+03	7.4E+03	3.66	0.07
17-91-1 - 81	0.094	0.004	0.004	10.604	0.450	0.071	0.001	0.001	581	23	24	948	35	35	3.5E+04	2.8E+04	2.5E+03	1.9E+03	3.4E+03	2.7E+03	3.56	0.12
17-91-1 - 82	0.191	0.002	0.003	5.244	0.088	0.080	0.001	0.001	1125	12	18	1192	13	13	3.2E+04	7.6E+04	2.6E+03	6.0E+03	1.2E+04	2.6E+04	0.88	0.02
17-91-1 - 83	0.119	0.004	0.005	8.439	0.320	0.067	0.001	0.001	722	24	26	845	29	29	6.7E+04	4.7E+04	4.4E+03	3.1E+03	8.8E+03	6.4E+03	2.53	0.17
17-91-1 - 84	0.136	0.010	0.010	7.331	0.532	0.074	0.003	0.003	822	55	56	1010	81	81	-4.1E+04	5.9E+04	-2.9E+03	4.2E+03	-3.0E+04	1.3E+04	1.61	0.42
17-91-1 - 85	0.125	0.003	0.003	7.981	0.210	0.066	0.001	0.001	761	17	19	800	18	18	9.0E+05	1.5E+05	6.0E+04	1.0E+04	-2.0E+04	2.4E+04	4.96	0.71
17-91-1 - 86	0.197	0.003	0.004	5.066	0.108	0.080	0.001	0.001	1161	18	22	1194	24	24	1.6E+04	3.1E+04	1.3E+03	2.5E+03	4.5E+03	8.4E+03	0.92	0.09
17-91-1 - 87	0.139	0.001	0.002	7.205	0.109	0.068	0.001	0.001	838	6.5	12	867	17	17	4.8E+04	3.6E+04	3.3E+03	2.5E+03	8.1E+03	5.5E+03	2.57	0.28
17-91-1 - 88	0.196	0.002	0.003	5.110	0.086	0.079	0.001	0.001	1152	12	18	1173	14	14	7.9E+04	8.8E+04	6.3E+03	6.9E+03	1.8E+04	2.0E+04	1.21	0.03
17-91-1 - 89	0.206	0.009	0.009	4.852	0.210	0.087	0.002	0.002	1207	46	48	1354	42	42	5.6E+04	8.0E+04	4.9E+03	7.2E+03	7.0E+04	1.1E+04	2.27	0.16
17-91-1 - 90	0.225	0.010	0.011	4.444	0.217	0.089	0.002	0.002	1306	54	56	1405	43	43	4.7E+04	7.0E+04	4.2E+03	6.2E+03	4.4E+03	7.2E+03	2.85	0.27
17-91-1 - 91	0.245	0.012	0.013	4.082	0.217	0.093	0.002	0.002	1409	63	65	1490	35	35	8.0E+04	6.3E+04	9.0E+02	6.1E+03	1.3E+03	9.6E+03	1.83	0.03
17-91-1 - 92	0.192	0.007	0.008	5.203	0.203	0.083	0.002	0.002	1132	38	40	1270	49	49	1.0E+05	1.8E+05	8.0E+04	1.4E+04	5.0E+04	1.1E+04	4.85	0.70
17-91-1 - 93	0.245	0.013	0.014	4.082	0.233	0.093	0.002	0.002	1412	71	73	1472	49	49	-4.0E+05	1.0E+05	-1.1E+03	6.7E+03	-5.0E+04	1.2E+04	2.06	0.39
17-91-1 - 94	0.160	0.004	0.005	6.250	0.184	0.075	0.001	0.001	956	24	26	1075	33	33	-5.5E+04	8.0E+04	-4.1E+03	6.1E+03	-7.0E+04	1.1E+04	2.29	0.19
17-91-1 - 95	0.273	0.011	0.012	3.663	0.161	0.097	0.002	0.002	1556	57	60	1564	46	46	-1.4E+04	6.9E+04	2.0E+02	5.7E+03	-1.0E+04	1.8E+04	0.93	0.23
17-91-1 - 96	0.140	0.005	0.005	7.128	0.264	0.073	0.002	0.002	846	27	29	999	53	53	5.0E+04	9.5E+04	3.0E+02	6.9E+03	7.0E+04	1.1E+04	2.93	0.56
17-91-1 - 97	0.135	0.008	0.008	7.391	0.453	0.067	0.001	0.001	831	52	53	829	36	36	-5.1E+04	9.7E+04	-2.0E+02	1.8E+03	-1.9E+03	8.6E+03	1.00	0.07
17-91-1 - 98	0.136	0.009	0.010	7.380	0.523	0.073	0.002	0.002	818	53	54	1007	51	51	1.8E+04	4.1E+04	1.3E+03	2.9E+03	3.3E+03	7.7E+03	1.71	0.28
17-91-1 - 99	0.147	0.005	0.006	6.817	0.260	0.072	0.002	0.002	882	30	31	984	41	41	2.6E+04	1.7E+04	1.9E+03	1.2E+03	4.6E+03	2.6E+03	1.65	0.14
17-91-1 - 100	0.130	0.005	0.005	7.722	0.286	0.071	0.001	0.001	785	25	27	943	36	36	1.8E+04	5.7E+03	1.2E+03	4.0E+02	3.0E+03	7.6E+02	1.83	0.06
17-91-1 - 101	0.199	0.004	0.005	5.020	0.129	0.087	0.002	0.002	1171	24	28	1345	39	39	2.7E+05	3.5E+05	2.2E+04	2.7E+04	2.0E+04	2.7E+04	3.55	0.22
17-91-1 - 102	0.142	0.003	0.004	7.037	0.183	0.073	0.001	0.001	856	18	21	996	31	31	1.8E+04	4.6E+04	1.4E+03	3.2E+03	8.0E+04	1.9E+04	0.73	0.04
17-91-1 - 103	0.165	0.009	0.010	6.072	0.350	0.082	0.002	0.002	981	51	52	1245	49	49	1.0E+05	8.6E+04	8.1E+03	6.8E+03	1.7E+04	1.7E+04	2.24	0.18
17-91-1 - 104	0.191	0.003	0.004	5.238	0.099	0.085	0.001	0.001	1126	15	20	1322	15	15	-9.0E+05	1.3E+05	-8.0E+04	1.1E+04	-4.8E+04	7.4E+04	0.49	0.00
17-91-1 - 105	0.143	0.002	0.003	6.974	0.141	0.069	0.000	0.000	864	13	16	899	14	14	-1.3E+04	5.1E+04	-8.0E+02	3.5E+03	-1.8E+03	8.1E+03	1.70	0.10
17-91-1 - 106	0.164	0.007	0.007	6.083	0.266	0.082	0.003	0.003	981	38	39	1219	68	68	4.1E+04	1.9E+04	3.3E+03	1.4E+03	7.7E+03	3.4E+03	1.51	0.06
17-91-1 - 107	0.109	0.004	0.005	9.217	0.382	0.064	0.001	0.001	664	25	26	754	31	31	1.9E+04	5.8E+04	1.3E+03	3.8E+03	4.0E+04	1.3E+04	1.56	0.19
17-91-1 - 108	0.130	0.011	0.011	7.692	0.651	0.082	0.004	0.004	787	64	65	1220	100	100	5.1E+04	2.5E+04	4.4E+03	2.4E+03	2.4E+03	1.3E+03	11.00	1.20
17-91-1 - 109	0.198	0.028	0.029	5.051	0.740	0.077	0.003	0.003	1160	150	150	1112	64	64	-2.6E+04	3.2E+04	-1.9E+03	2.4E+03	-3.2E+03	3.9E+03	2.10	0.28

17-91-1 - 110	0.140	0.015	0.015	7.143	0.765	0.071	0.003	0.003	841	84	84	942	81	81	7.0E+04	4.8E+04	5.0E+02	3.2E+03	7.0E+02	1.6E+03	7.90	3.00
17-91-1 - 111	0.156	0.003	0.003	6.431	0.136	0.076	0.001	0.001	931	15	18	1097	15	15	1.0E+05	1.3E+05	1.0E+04	1.0E+04	3.0E+04	2.2E+04	1.60	0.05
17-91-1 - 112	0.107	0.004	0.005	9.363	0.395	0.076	0.002	0.002	654	25	26	1082	45	45	5.0E+04	9.6E+04	3.7E+03	7.6E+03	7.0E+04	1.3E+04	2.47	0.16
17-91-1 - 113	0.149	0.003	0.004	6.707	0.175	0.075	0.001	0.001	896	19	22	1065	19	19	-2.0E+05	1.7E+05	-2.0E+04	1.2E+04	0.0E+00	2.8E+04	2.17	0.25
17-91-1 - 114	0.150	0.005	0.006	6.671	0.245	0.079	0.001	0.001	900	29	31	1162	26	26	-2.0E+03	1.5E+05	0.0E+00	1.2E+04	0.0E+00	2.5E+04	3.20	1.00
17-91-1 - 115	0.236	0.008	0.008	4.239	0.149	0.097	0.001	0.001	1365	40	43	1567	25	25	-3.4E+05	4.4E+05	-3.3E+04	4.2E+04	-7.5E+04	8.7E+04	1.56	0.11
17-91-1 - 116	0.137	0.002	0.003	7.315	0.150	0.067	0.000	0.000	826	12	16	838	14	14	4.3E+04	7.0E+04	2.9E+03	4.7E+03	4.9E+03	8.2E+03	2.23	0.12
17-91-1 - 117	0.171	0.013	0.013	5.848	0.445	0.075	0.004	0.004	1013	71	72	1047	89	89	1.0E+04	5.3E+04	1.1E+03	4.0E+03	3.4E+03	4.4E+03	7.60	2.20
17-91-1 - 118	0.130	0.011	0.011	7.692	0.651	0.077	0.003	0.003	788	61	62	1100	72	72	1.5E+04	3.9E+04	1.2E+03	2.8E+03	1.7E+03	7.1E+03	3.90	1.40
17-91-1 - 119	0.146	0.007	0.007	6.845	0.347	0.073	0.002	0.002	878	40	41	1012	64	64	4.0E+05	1.3E+05	2.2E+03	9.0E+03	-3.0E+04	1.7E+04	4.90	1.60
17-91-1 - 120	0.121	0.005	0.005	8.264	0.328	0.066	0.001	0.001	736	27	28	818	29	29	2.9E+04	3.0E+04	1.9E+03	2.0E+03	1.7E+03	1.8E+03	4.70	1.20
17-91-1 - 121	0.129	0.003	0.003	7.740	0.192	0.073	0.002	0.002	783	16	18	994	62	62	8.0E+03	1.0E+05	7.0E+02	7.0E+03	2.0E+03	3.4E+03	7.40	2.10
17-91-1 - 122	0.253	0.014	0.014	3.953	0.219	0.096	0.002	0.002	1452	70	72	1552	31	31	3.4E+04	8.0E+04	3.2E+03	7.4E+03	1.4E+04	3.4E+04	0.60	0.02
17-91-1 - 123	0.121	0.002	0.002	8.271	0.151	0.065	0.001	0.001	735.5	8.9	12	783	17	17	3.6E+04	1.5E+04	2.3E+03	9.8E+02	1.6E+03	1.1E+03	8.90	1.80
17-91-1 - 124	0.235	0.006	0.007	4.254	0.127	0.094	0.001	0.001	1361	33	36	1497	24	24	5.7E+04	5.6E+04	5.4E+03	5.4E+03	3.1E+04	3.0E+04	0.50	0.01
17-91-1 - 125	0.218	0.009	0.009	4.591	0.188	0.087	0.001	0.001	1269	45	47	1367	24	24	9.0E+04	7.5E+04	7.6E+03	6.5E+03	1.5E+04	1.3E+04	1.63	0.28
17-91-1 - 126	0.238	0.006	0.007	4.202	0.122	0.092	0.001	0.001	1376	33	36	1468	22	22	-5.0E+04	9.9E+04	-6.0E+02	9.2E+03	-1.0E+04	2.0E+04	1.38	0.02
17-91-1 - 127	0.185	0.021	0.021	5.405	0.614	0.093	0.009	0.009	1090	110	110	1400	190	190	1.0E+03	3.9E+04	5.0E+02	3.2E+03	1.1E+03	4.7E+03	3.74	0.95
17-91-1 - 128	0.323	0.016	0.017	3.096	0.163	0.138	0.004	0.004	1801	80	82	2191	54	54	4.3E+04	2.4E+04	6.3E+03	3.4E+03	1.2E+04	6.7E+03	0.90	0.12
17-91-1 - 129	0.215	0.018	0.018	4.651	0.389	0.114	0.010	0.010	1252	97	98	1790	180	180	4.7E+04	3.4E+04	4.3E+03	3.4E+03	5.3E+03	5.6E+03	6.10	3.40
17-91-1 - 130	0.184	0.014	0.014	5.435	0.414	0.081	0.003	0.003	1083	74	75	1193	81	81	-5.0E+03	2.3E+05	0.0E+00	1.9E+04	4.0E+04	6.1E+04	3.40	1.00
17-91-1 - 131	0.194	0.013	0.013	5.155	0.345	0.087	0.003	0.003	1141	70	71	1349	61	61	9.2E+04	8.7E+04	7.1E+03	7.4E+03	3.7E+04	4.0E+04	0.59	0.06
17-91-1 - 132	0.164	0.010	0.011	6.098	0.409	0.076	0.003	0.003	978	57	58	1071	77	77	-8.9E+04	9.6E+04	-6.7E+03	7.2E+03	-8.9E+03	9.2E+03	3.53	0.60
17-91-1 - 133	0.124	0.002	0.003	8.052	0.175	0.068	0.000	0.000	755	13	16	858	16	16	-2.0E+05	1.6E+05	-1.0E+04	1.0E+04	-8.0E+04	3.7E+04	1.26	0.06
17-91-1 - 134	0.152	0.016	0.016	6.579	0.693	0.085	0.003	0.003	908	91	92	1303	58	58	1.0E+05	1.9E+05	1.0E+03	1.7E+04	-4.0E+04	3.6E+04	4.30	1.00
17-91-1 - 135	0.140	0.007	0.007	7.148	0.353	0.070	0.001	0.001	843	37	39	918	28	28	-3.8E+04	6.4E+04	-2.8E+03	4.5E+03	-1.2E+03	5.6E+03	11.80	3.60
17-91-1 - 136	0.127	0.002	0.003	7.899	0.168	0.066	0.000	0.000	768	12	15	812	13	13	2.3E+04	4.6E+04	1.5E+03	3.0E+03	1.1E+03	3.0E+03	7.20	2.10
17-91-1 - 137	0.133	0.002	0.003	7.513	0.164	0.068	0.001	0.001	805	14	17	851	17	17	-7.2E+04	8.9E+04	-4.8E+03	5.9E+03	-3.8E+03	6.5E+03	3.19	0.52
17-91-1 - 138	0.163	0.008	0.008	6.143	0.309	0.106	0.007	0.007	971	44	45	1690	120	120	-8.0E+05	1.5E+05	-1.2E+04	2.1E+04	-1.3E+04	2.5E+04	1.61	0.04
17-91-1 - 139	0.169	0.004	0.005	5.917	0.158	0.079	0.001	0.001	1007	22	25	1161	24	24	2.6E+04	8.6E+04	2.0E+03	6.9E+03	2.0E+04	1.1E+04	2.86	0.14
17-91-1 - 140	0.123	0.004	0.004	8.117	0.277	0.068	0.001	0.001	749	22	24	866	31	31	1.0E+05	9.9E+04	6.9E+03	6.6E+03	8.0E+03	9.5E+03	4.30	1.10
17-91-1 - 141	0.215	0.013	0.013	4.651	0.281	0.087	0.002	0.002	1252	66	68	1357	50	50	8.7E+04	5.4E+04	7.4E+03	4.8E+03	1.3E+04	9.2E+03	2.17	0.53
17-91-1 - 142	0.201	0.005	0.006	4.983	0.149	0.086	0.001	0.001	1179	29	32	1345	28	28	7.5E+04	3.8E+04	6.5E+03	3.2E+03	1.3E+04	6.4E+03	1.68	0.06

17-91-1 - 143	0.141	0.006	0.006	7.077	0.301	0.075	0.002	0.002	852	32	34	1061	45	45	2.0E+05	1.1E+05	1.0E+03	7.9E+03	-1.0E+02	5.2E+03	6.90	1.50
17-91-1 - 144	0.103	0.005	0.005	9.681	0.487	0.071	0.002	0.002	633	30	31	947	57	57	8.0E+04	1.9E+04	6.0E+02	1.3E+03	7.0E+04	1.0E+04	1.33	0.09
17-91-1 - 145	0.096	0.007	0.007	10.460	0.777	0.080	0.006	0.006	588	41	42	1160	120	120	2.2E+04	6.4E+03	1.7E+03	4.3E+02	9.9E+03	2.4E+03	0.74	0.04
17-91-1 - 146	0.134	0.006	0.006	7.485	0.359	0.073	0.003	0.003	807	35	36	983	84	84	-5.0E+04	5.5E+04	-3.0E+02	3.8E+03	-9.0E+02	5.4E+03	3.50	1.00
17-91-1 - 147	0.121	0.004	0.004	8.251	0.300	0.067	0.001	0.001	737	24	26	852	27	27	1.7E+04	6.8E+04	1.1E+03	4.5E+03	-1.0E+02	1.2E+03	18.00	1.90
17-91-1 - 148	0.179	0.003	0.004	5.593	0.122	0.079	0.001	0.001	1060	17	21	1179	22	22	9.4E+04	8.9E+04	7.5E+03	7.0E+03	1.5E+04	1.5E+04	1.68	0.06
17-91-1 - 149	0.149	0.009	0.009	6.707	0.396	0.076	0.001	0.001	895	49	50	1083	35	35	-3.0E+05	1.4E+05	2.4E+03	6.1E+03	7.0E+04	2.2E+04	1.23	0.17
17-91-1 - 150	0.171	0.009	0.009	5.862	0.302	0.081	0.003	0.003	1014	47	48	1196	72	72	-1.9E+04	9.8E+04	-2.3E+03	8.3E+03	1.4E+03	7.3E+03	6.30	2.40
17-91-1 - 151	0.130	0.002	0.003	7.722	0.161	0.066	0.001	0.001	785	12	15	809	16	16	1.8E+04	4.6E+04	1.2E+03	3.0E+03	2.7E+03	8.2E+03	1.58	0.05
17-91-1 - 152	0.173	0.010	0.010	5.794	0.336	0.079	0.001	0.001	1024	55	56	1165	30	30	1.0E+05	5.4E+04	7.0E+02	4.3E+03	-1.0E+02	8.5E+03	2.73	0.63
17-91-1 - 153	0.125	0.005	0.006	8.032	0.361	0.075	0.002	0.002	756	31	32	1048	65	65	6.1E+04	2.8E+04	4.5E+03	2.0E+03	3.2E+03	1.8E+03	12.50	4.10
17-91-1 - 154	0.107	0.013	0.014	9.346	1.223	0.080	0.001	0.001	654	77	77	1187	29	29	1.8E+04	7.8E+03	1.4E+03	6.1E+02	1.6E+03	7.7E+02	7.50	1.90
17-91-1 - 155	0.228	0.003	0.004	4.380	0.079	0.090	0.001	0.001	1326	15	21	1434	12	12	-4.0E+05	1.8E+05	-4.0E+04	1.6E+04	-6.0E+04	2.2E+04	2.17	0.12
17-91-1 - 156	0.196	0.006	0.007	5.099	0.179	0.085	0.001	0.001	1153	35	37	1306	33	33	8.0E+04	6.5E+04	5.0E+02	5.4E+03	-3.0E+02	5.8E+03	3.54	0.78
17-91-1 - 157	0.118	0.003	0.003	8.453	0.243	0.068	0.001	0.001	720	18	20	849	32	32	4.1E+04	7.1E+04	2.8E+03	4.7E+03	1.4E+03	6.1E+03	2.56	0.14
17-91-1 - 158	0.151	0.001	0.002	6.645	0.102	0.069	0.000	0.000	903.9	7.8	13	903	11	11	2.9E+04	7.9E+04	2.0E+03	5.4E+03	5.9E+03	5.0E+03	3.21	0.73

Zircon trace element data tables

Measurements in ppm

Comments	Ti	Ti Int2SE	Y	Y Int2SE	Nb	Nb Int2SE	La	La Int2SE	Ce	Ce Int2SE	Nd	Nd Int2SE	Sm	Sm Int2SE	Eu	Eu Int2SE	Gd	Gd Int2SE	Dy	Dy Int2SE	Ho	Ho Int2SE	Er	Er Int2SE	Tm	Tm Int2SE	Yb	Yb Int2SE	Lu	Lu Int2SE	Hf	Hf Int2SE	Th	Th Int2SE	U	U Int2SE
17-37-1 - 1	18.5	2.8	820.0	110.0	1.1	0.1	0.1	0.1	6.0	1.0	1.3	0.3	3.1	0.4	0.3	0.1	15.5	1.7	76.0	10.0	27.7	3.9	130.0	19.0	26.2	3.9	247.0	38.0	49.5	7.5	1.1E+04	310.0	102.4	8.2	380.0	17.0
17-37-1 - 2	31.3	2.9	93.1	3.2	1.0	0.1	0.0	0.0	2.1	0.1	3.0	0.3	5.2	0.5	0.1	0.0	8.4	0.6	14.0	0.8	3.1	0.2	9.6	0.5	1.6	0.1	10.8	0.7	1.7	0.1	1.2E+04	300.0	104.5	2.5	432.0	10.0
17-37-1 - 3	23.7	2.4	103.2	4.3	0.9	0.1	0.0	0.0	2.2	0.1	3.3	0.3	5.0	0.4	0.1	0.0	8.4	0.6	15.1	0.9	3.4	0.2	11.1	0.9	1.7	0.2	12.4	1.4	2.2	0.3	1.2E+04	230.0	117.5	2.9	411.0	10.0
17-37-1 - 4	9.7	1.7	527.0	11.0	1.7	0.1	0.1	0.1	13.0	0.7	1.4	0.3	5.6	0.7	1.1	0.1	17.1	1.0	51.8	1.4	17.8	0.5	80.4	2.2	16.2	0.6	154.4	5.5	33.0	1.1	8.3E+03	370.0	93.1	4.7	191.0	34.0
17-37-1 - 5	8.7	1.5	114.8	2.5	0.8	0.1	0.3	0.1	1.5	0.1	2.9	0.3	11.5	0.8	0.6	0.1	17.2	0.9	20.5	0.8	3.9	0.2	11.4	0.4	1.6	0.1	12.1	0.6	2.0	0.1	1.2E+04	290.0	103.1	4.4	502.0	24.0
17-37-1 - 6	18.4	2.7	107.7	2.5	0.7	0.1	0.1	0.1	0.8	0.1	1.8	0.2	4.3	0.4	0.2	0.1	15.0	1.0	19.3	0.7	3.5	0.1	9.0	0.4	1.3	0.1	9.7	0.6	1.6	0.1	1.2E+04	300.0	71.5	3.3	357.9	7.1
17-37-1 - 7	20.6	2.0	162.9	4.2	0.7	0.1	0.0	0.0	1.0	0.1	1.2	0.2	4.5	0.3	0.2	0.0	12.7	0.7	24.3	0.8	5.2	0.2	16.9	0.6	2.6	0.1	19.6	0.8	3.2	0.1	1.1E+04	200.0	38.3	1.3	451.0	11.0
17-37-1 - 8	27.8	3.0	696.0	76.0	1.2	0.1	0.0	0.0	9.1	1.3	1.4	0.3	4.0	0.4	0.4	0.1	18.3	1.5	69.4	7.0	23.8	2.8	99.0	12.0	19.4	2.4	169.0	22.0	32.7	4.4	1.0E+04	280.0	110.6	9.5	308.0	14.0
17-37-1 - 9	25.2	3.3	403.0	50.0	1.5	0.2	0.6	0.3	30.3	6.0	2.0	0.3	4.2	0.5	0.8	0.2	14.0	1.0	40.2	3.8	12.8	1.6	57.5	7.9	12.5	1.8	123.0	18.0	27.2	4.1	1.0E+04	290.0	133.0	16.0	284.0	17.0
17-37-1 - 10	16.3	1.9	205.0	16.0	0.9	0.1	0.1	0.0	1.9	0.1	1.8	0.2	3.9	0.4	0.1	0.0	13.5	1.4	27.4	2.2	6.8	0.6	24.4	2.7	4.8	0.6	45.1	6.2	8.9	1.4	1.2E+04	270.0	113.0	3.3	458.0	17.0
17-37-1 - 11	9.2	1.4	94.8	2.6	0.8	0.1	0.5	0.1	1.8	0.1	2.8	0.3	6.1	0.5	0.3	0.1	11.2	0.8	15.8	0.9	3.1	0.2	8.7	0.4	1.4	0.1	9.5	0.6	1.5	0.1	1.2E+04	310.0	107.8	2.7	399.0	11.0
17-37-1 - 12	28.7	2.7	162.0	30.0	0.9	0.1	0.0	0.0	3.3	1.0	2.7	0.3	3.8	0.5	0.3	0.1	8.7	0.7	19.5	2.1	5.1	0.9	22.1	5.8	4.7	1.4	48.0	16.0	10.7	3.8	1.2E+04	330.0	108.9	5.1	334.0	12.0
17-37-1 - 13	23.3	2.2	137.6	3.6	0.8	0.1	0.0	0.0	1.2	0.1	1.8	0.3	5.6	0.5	0.2	0.0	11.2	0.7	20.1	0.6	4.8	0.2	14.4	0.5	2.2	0.1	16.5	0.6	2.7	0.1	1.1E+04	260.0	45.3	1.7	557.0	11.0
17-37-1 - 14	25.4	2.4	122.8	3.6	0.9	0.1	0.0	0.0	1.2	0.1	1.3	0.2	4.4	0.6	0.2	0.0	9.6	0.6	18.6	0.8	4.1	0.2	12.6	0.6	1.9	0.1	13.7	0.8	2.3	0.1	1.2E+04	290.0	41.3	1.1	466.0	12.0
17-37-1 - 15	19.5	2.0	359.0	18.0	1.9	0.1	0.1	0.0	3.9	0.3	1.4	0.3	3.1	0.4	0.3	0.1	10.9	1.1	35.0	1.8	12.5	0.6	53.8	3.1	11.3	0.6	105.4	6.2	20.8	1.3	1.0E+04	250.0	105.5	5.8	315.0	17.0
17-37-1 - 16	27.5	3.0	92.4	1.8	0.9	0.1	0.0	0.0	2.0	0.1	3.3	0.3	3.7	0.4	0.1	0.0	7.4	0.4	13.8	0.5	3.0	0.2	9.0	0.3	1.3	0.1	10.4	0.5	1.7	0.1	1.3E+04	280.0	126.5	2.7	378.2	9.7
17-37-1 - 17	12.4	1.7	171.0	24.0	0.8	0.1	0.1	0.0	0.9	0.1	1.5	0.3	3.9	0.5	0.2	0.0	11.4	0.7	25.6	2.3	5.6	0.8	18.2	3.6	3.4	0.9	31.1	9.6	5.6	1.9	1.2E+04	260.0	72.9	6.7	521.0	20.0
17-37-1 - 18	14.4	2.2	127.2	4.3	0.8	0.1	0.1	0.0	1.6	0.1	2.3	0.3	5.3	0.5	0.2	0.0	11.3	0.8	19.4	0.9	4.4	0.2	12.9	0.6	2.0	0.1	14.8	0.8	2.4	0.2	1.2E+04	280.0	83.9	2.8	571.0	14.0
17-37-1 - 19	18.0	2.6	325.0	94.0	0.9	0.2	0.0	0.0	1.9	0.8	0.9	0.2	2.8	0.5	0.1	0.1	14.2	1.0	40.8	8.0	11.0	3.3	41.0	15.0	7.3	2.9	68.0	29.0	13.2	5.6	1.2E+04	330.0	66.0	13.0	493.0	18.0
17-37-1 - 20	18.8	2.2	111.2	5.8	0.6	0.1	0.0	0.0	0.5	0.1	0.9	0.2	2.5	0.3	0.0	0.0	9.8	0.6	17.9	1.1	3.5	0.2	9.4	0.6	1.4	0.1	9.6	0.7	1.6	0.1	1.2E+04	290.0	44.2	3.6	333.2	9.9
17-37-1 - 21	27.1	2.5	125.8	8.6	0.9	0.1	0.0	0.0	2.6	0.2	2.5	0.3	3.7	0.3	0.2	0.0	7.3	0.5	15.8	1.0	4.1	0.3	15.7	1.8	3.5	0.5	33.1	5.4	7.1	1.4	1.2E+04	270.0	96.2	6.6	433.0	18.0
17-37-1 - 22	18.5	2.7	385.0	43.0	0.9	0.1	20.0	20.0	20.0	16.0	9.6	8.4	4.7	1.1	0.6	0.1	15.4	1.1	41.5	3.7	12.3	1.5	49.4	6.5	9.9	1.4	90.0	14.0	17.3	2.8	1.1E+04	330.0	95.0	10.0	410.0	17.0
17-37-1 - 23	13.7	2.0	134.4	7.6	0.7	0.1	0.1	0.1	0.8	0.1	1.5	0.2	4.4	0.5	0.1	0.0	13.3	0.6	22.4	1.1	4.3	0.2	11.5	0.8	1.8	0.2	12.5	1.2	2.0	0.2	1.2E+04	300.0	87.8	2.3	379.0	17.0
17-37-1 - 24	31.3	3.3	765.0	27.0	1.3	0.1	0.0	0.0	11.9	0.5	4.5	0.4	6.7	0.5	1.2	0.1	23.8	1.1	78.1	3.1	28.4	1.1	120.5	4.6	23.5	0.8	205.7	7.7	41.8	1.4	7.9E+03	240.0	96.5	3.4	154.0	11.0
17-37-1 - 25	21.4	2.7	351.0	24.0	1.5	0.2	0.0	0.0	7.6	0.8	0.9	0.2	3.9	0.4	0.4	0.1	10.9	0.8	33.0	1.8	11.2	0.8	52.3	4.0	11.7	1.0	117.9	9.8	25.2	2.3	1.2E+04	270.0	95.7	5.6	498.0	10.0
17-37-1 - 26	29.9	2.3	183.0	33.0	0.8	0.1	0.0	0.0	1.9	0.2	3.1	0.4	4.5	0.5	0.1	0.0	9.0	0.6	21.6	2.3	6.1	1.0	21.6	4.9	4.1	1.1	32.0	9.1	6.3	2.0	1.3E+04	220.0	110.5	9.6	421.0	18.0
17-37-1 - 27	15.1	1.7	159.0	17.0	0.8	0.1	0.1	0.0	1.3	0.1	2.1	0.3	3.3	0.3	0.1	0.0	9.7	0.6	20.7	1.6	5.1	0.6	18.0	2.8	3.5	0.7	31.2	6.8	6.0	1.4	1.2E+04	190.0	90.9	3.1	358.8	9.0
17-37-1 - 28	18.2	2.8	131.7	3.6	0.9	0.1	0.0	0.0	0.9	0.1	1.1	0.2	4.6	0.5	0.2	0.0	10.5	0.6	19.6	0.7	4.5	0.2	13.3	0.5	2.2	0.1	15.3	0.7	2.5	0.1	1.2E+04	350.0	39.0	0.8	453.8	9.4
17-37-1 - 29	12.8	1.4	979.0	86.0	1.6	0.1	0.1	0.0	7.5	0.7	1.4	0.3	3.8	0.6	1.2	0.2	20.5	1.9	88.8	7.9	33.7	2.8	150.0	12.0	31.4	2.6	290.0	23.0	59.2	4.6	7.8E+03	300.0	140.0	17.0	327.0	39.0
17-37-1 - 30	18.9	2.2	663.0	57.0	1.1	0.1	0.0	0.0	4.1	0.4	1.2	0.2	3.2	0.4	0.1	0.0	13.3	1.0	60.9	4.3	23.5	1.9	104.9	9.3	22.4	1.8	202.0	17.0	40.1	3.6	1.1E+04	230.0	100.9	3.1	239.0	15.0
17-37-1 - 31	24.8	2.6	157.0	26.0	0.8	0.1	0.0	0.0	1.2	0.2	1.8	0.3	3.2	0.3	0.4	0.1	7.8	0.5	19.5	2.4	5.2	0.9	19.3	4.0	3.8	0.9	32.8	8.2	5.8	1.6	1.2E+04	220.0	82.2	7.6	351.9	9.9
17-37-1 - 32	17.7	2.1	97.7	4.6	0.7	0.1	0.0	0.0	1.2	0.1	2.1	0.3	5.0	0.5	0.1	0.0	10.3	0.7	15.1	0.8	3.1	0.2	8.8	0.6	1.4	0.1	10.4	0.8	1.6	0.2	1.2E+04	280.0	89.4	3.3	331.0	12.0
17-37-1 - 33	16.3	1.9	614.0	30.0	2.2	0.4	0.3	0.1	20.7	3.6	0.9	0.2	3.2	0.4	0.5	0.1	11.7	1.2	53.3	2.6	20.5	1.0	94.3	4.3	21.4	1.0	201.8	9.4	38.7	2.2	1.1E+04	370.0	107.0	16.0	351.0	14.0
17-37-1 - 34	26.3	2.8	109.9	3.2	0.8	0.1	0.0	0.0	1.6	0.1	2.8	0.3	4.7	0.5	0.1	0.0	9.4	0.6	17.0	0.7	3.6	0.2	9.7	0.4	1.5	0.1	10.5	0.6	1.6	0.1	1.2E+04	290.0	114.0	2.9	340.9	8.8
17-37-1 - 35	26.2	2.5	97.3	2.2	0.8	0.1	0.0	0.0	2.2	0.1	3.2	0.4	4.9	0.6	0.1	0.0	8.0	0.5	14.0	0.5	3.3	0.1	9.7	0.5	1.5	0.1	11.4	0.6	1.7	0.1	1.3E+04	270.0	128.6	2.4	380.3	6.4
17-37-1 - 36	17.4	1.9	1642.0	97.0	1.6	0.1	0.1	0.1	4.2	0.4	2.0	0.4	5.5	0.6	0.8	0.2	27.8	2.1	140.3	8.6	54.8	3.2	244.0	12.0	51.3	2.5	468.0	21.0	92.4	4.4	1.1E+04	210.0	116.6	9.3	301.0	23.0

17-37-1 - 37	21.5	2.1	111.1	4.3	0.8	0.1	0.0	0.0	1.2	0.1	2.3	0.4	4.1	0.4	0.2	0.1	9.2	0.5	17.3	0.9	3.7	0.2	10.2	0.5	1.5	0.1	11.1	0.6	1.7	0.1	1.2E+04	300.0	76.8	4.5	424.0	17.0
17-37-1 - 38	24.6	3.0	129.3	3.7	0.7	0.1	0.1	0.1	0.9	0.1	1.8	0.3	3.6	0.3	0.3	0.1	11.7	0.8	21.3	0.9	4.1	0.2	11.3	0.5	1.8	0.1	12.4	0.7	1.9	0.1	1.2E+04	270.0	77.5	2.0	335.0	11.0
17-37-1 - 39	19.9	2.2	115.6	7.8	0.7	0.1	0.1	0.0	1.4	0.2	1.9	0.3	3.9	0.6	0.2	0.1	8.9	0.7	17.0	1.1	3.8	0.3	11.5	0.8	1.9	0.2	15.2	1.7	2.3	0.3	1.2E+04	290.0	73.7	3.7	430.0	17.0
17-37-1 - 40	14.1	1.4	1220.0	160.0	1.8	0.3	0.1	0.0	10.9	2.0	1.5	0.3	5.0	0.6	0.5	0.1	25.8	2.9	115.0	15.0	43.9	5.6	195.0	26.0	40.1	5.1	365.0	44.0	72.5	8.7	1.0E+04	250.0	199.0	19.0	397.0	29.0
17-37-2 - 1	19.8	2.3	381.0	87.0	0.7	0.1	0.0	0.0	0.5	0.1	1.2	0.3	3.2	0.4	0.1	0.0	12.6	1.0	39.1	7.5	12.6	3.0	53.0	14.0	11.4	3.2	109.0	31.0	20.3	5.8	1.1E+04	230.0	59.0	3.4	392.0	19.0
17-37-2 - 2	25.3	2.5	111.8	4.8	0.8	0.1	0.0	0.0	1.1	0.2	1.8	0.2	3.6	0.4	0.1	0.0	10.7	0.9	17.8	1.2	3.6	0.2	9.7	0.5	1.4	0.1	10.6	0.6	1.7	0.1	1.1E+04	260.0	74.3	2.8	337.0	16.0
17-37-2 - 3	27.1	2.7	86.5	2.4	0.9	0.1	0.0	0.0	2.1	0.1	2.9	0.4	3.6	0.4	0.1	0.0	6.3	0.5	12.6	0.5	3.0	0.2	8.9	0.5	1.3	0.1	10.2	0.6	1.6	0.1	1.1E+04	230.0	112.7	4.5	414.7	8.7
17-37-2 - 4	22.1	2.2	332.0	62.0	1.0	0.1	0.0	0.0	4.4	1.3	1.7	0.4	3.4	0.4	0.3	0.1	11.9	1.4	36.3	5.7	11.2	2.3	49.0	11.0	10.4	2.7	111.0	31.0	23.5	6.7	1.1E+04	290.0	85.0	12.0	430.0	25.0
17-37-2 - 5	400.0	150.0	893.0	74.0	1.5	0.2	0.1	0.0	1.9	0.2	1.9	0.4	4.6	0.8	0.5	0.1	21.8	1.6	85.3	6.0	30.6	2.5	130.0	12.0	25.3	2.4	236.0	23.0	44.8	4.8	9.8E+03	330.0	62.5	5.5	366.0	10.0
17-37-2 - 6	19.5	2.1	271.0	61.0	1.0	0.1	0.0	0.0	1.4	0.1	2.6	0.3	4.1	0.5	0.2	0.1	11.0	1.0	28.8	5.0	8.9	2.1	39.0	10.0	8.1	2.3	82.0	24.0	16.9	5.2	1.1E+04	240.0	110.0	4.9	458.0	28.0
17-37-2 - 7	25.4	2.7	1048.0	23.0	2.2	0.1	0.0	0.0	9.9	0.3	1.0	0.2	3.0	0.3	0.4	0.1	16.5	0.7	83.6	2.3	35.7	0.8	171.5	3.8	36.9	0.8	362.9	7.9	75.8	1.5	8.9E+03	180.0	159.2	3.2	328.0	11.0
17-37-2 - 8	18.3	2.2	517.0	62.0	1.7	0.3	0.1	0.0	31.4	7.4	4.3	0.9	6.4	1.1	1.5	0.3	19.0	2.4	56.8	6.8	17.4	2.1	72.4	8.4	15.4	1.8	148.0	17.0	29.6	3.3	1.0E+04	260.0	234.0	44.0	524.0	41.0
17-37-2 - 9	19.0	2.4	340.0	43.0	0.8	0.1	0.0	0.0	4.8	0.9	1.6	0.3	3.1	0.5	0.4	0.1	10.8	0.9	39.9	3.8	10.8	1.3	39.3	5.6	7.2	1.1	65.0	11.0	12.1	2.2	1.1E+04	280.0	79.4	8.1	552.0	30.0
17-37-2 - 10	27.0	2.6	131.1	7.9	0.9	0.1	0.0	0.0	2.2	0.2	2.4	0.3	4.0	0.4	0.1	0.0	8.8	0.6	17.9	0.9	4.3	0.2	13.7	0.8	2.3	0.2	18.6	1.8	3.1	0.3	1.2E+04	250.0	100.8	5.3	414.0	17.0
17-37-2 - 11	22.8	3.0	128.7	9.8	0.7	0.1	0.0	0.0	0.7	0.1	1.1	0.3	3.4	0.4	0.8	0.3	12.6	0.9	20.6	1.2	4.0	0.3	12.0	1.2	1.9	0.2	15.1	2.2	2.5	0.4	1.1E+04	310.0	61.2	2.4	371.0	11.0
17-37-2 - 12	33.8	2.7	103.1	2.8	1.1	0.1	0.0	0.0	2.3	0.1	4.1	0.4	6.3	0.6	0.1	0.0	11.9	0.7	17.5	0.7	3.5	0.1	8.7	0.5	1.2	0.1	8.5	0.5	1.2	0.1	1.2E+04	220.0	134.4	3.2	492.0	14.0
17-37-2 - 13	19.4	3.5	443.0	73.0	1.9	0.4	0.0	0.0	5.7	1.2	1.6	0.9	2.7	0.6	0.3	0.2	9.9	1.4	37.4	5.3	14.1	2.5	66.0	13.0	14.2	2.9	142.0	30.0	28.5	6.3	9.7E+03	420.0	115.0	14.0	362.0	15.0
17-37-2 - 14	22.5	2.4	123.3	8.4	0.7	0.1	0.0	0.0	1.4	0.1	2.0	0.3	3.5	0.4	0.2	0.1	9.3	0.6	17.6	1.2	3.8	0.3	11.0	0.8	1.5	0.2	12.0	1.1	1.9	0.2	1.1E+04	250.0	91.1	3.5	369.8	9.6
17-37-2 - 15	21.0	3.3	317.0	37.0	1.5	0.2	0.1	0.1	6.8	1.3	0.9	0.3	2.3	0.5	0.4	0.1	8.8	0.6	30.6	3.3	10.2	1.2	43.0	5.9	8.7	1.3	86.0	13.0	16.5	2.7	1.0E+04	270.0	87.0	5.6	340.0	28.0
17-37-2 - 16	25.8	3.1	437.0	38.0	1.4	0.1	0.0	0.0	8.8	1.0	1.1	0.2	2.3	0.3	0.4	0.1	9.8	0.6	39.4	2.7	14.1	1.4	65.8	6.7	14.3	1.5	144.0	16.0	30.3	3.5	9.7E+03	220.0	84.7	6.2	327.0	15.0
17-37-2 - 17	18.8	2.1	629.0	44.0	1.2	0.1	0.0	0.0	25.2	0.7	1.9	0.4	3.3	0.5	0.7	0.1	14.9	1.7	54.7	4.8	20.2	1.7	95.7	6.1	20.1	1.4	196.0	12.0	41.1	1.9	8.9E+03	200.0	147.0	16.0	184.0	18.0
17-37-2 - 18	23.9	2.9	127.9	7.2	0.8	0.1	0.0	0.0	0.7	0.1	1.4	0.3	3.8	0.4	0.1	0.0	12.0	0.9	19.4	1.0	4.2	0.3	11.8	0.9	1.8	0.2	12.4	1.0	2.1	0.2	1.1E+04	260.0	58.8	7.4	283.4	8.4
17-37-2 - 19	25.7	5.1	99.0	10.0	0.4	0.2	0.3	0.2	2.8	0.5	0.7	0.7	1.2	1.2	0.3	0.1	3.4	1.2	9.2	1.3	3.1	0.4	12.6	1.8	2.9	0.5	29.2	3.7	7.2	0.9	9.3E+03	340.0	34.0	2.5	121.0	15.0
17-37-2 - 20	20.5	3.0	103.3	7.2	0.9	0.1	0.0	0.0	2.2	0.2	2.5	0.4	3.9	0.5	0.1	0.0	7.3	0.5	13.8	0.7	3.5	0.2	11.0	1.3	1.8	0.3	15.4	2.5	2.7	0.6	1.2E+04	200.0	109.1	2.6	365.1	6.9
17-37-2 - 21	21.4	3.1	194.0	26.0	1.7	0.4	0.0	0.0	2.4	0.3	2.3	0.3	4.5	0.5	0.2	0.0	10.6	0.7	22.7	2.1	6.7	0.9	25.1	4.8	4.6	1.0	40.3	9.7	7.9	2.0	1.1E+04	290.0	76.8	5.8	456.0	14.0
17-37-2 - 22	27.5	3.4	710.0	170.0	1.3	0.2	0.0	0.0	5.1	1.0	2.6	0.3	5.3	0.5	0.6	0.1	17.9	2.6	66.0	14.0	24.4	5.8	104.0	26.0	20.3	5.2	184.0	48.0	36.2	9.5	1.0E+04	330.0	108.0	12.0	399.0	15.0
17-37-2 - 23	23.8	2.6	98.0	2.4	0.7	0.1	0.0	0.0	1.1	0.1	1.9	0.3	3.4	0.4	0.1	0.0	10.4	0.6	15.8	0.7	3.0	0.1	8.7	0.3	1.4	0.1	10.1	0.6	1.5	0.1	1.1E+04	230.0	79.4	1.9	392.0	21.0
17-37-2 - 24	36.9	4.5	948.0	49.0	1.5	0.1	0.1	0.0	10.0	0.4	2.3	0.3	4.8	0.4	1.5	0.2	23.1	1.5	90.9	5.1	32.2	1.7	141.4	7.4	28.1	1.2	241.0	13.0	48.3	2.2	8.7E+03	210.0	147.8	9.5	290.0	23.0
17-37-2 - 25	18.3	2.4	457.0	33.0	2.7	0.3	0.0	0.0	8.8	1.1	1.3	0.2	2.4	0.3	0.4	0.1	11.1	0.8	42.9	2.4	15.5	1.1	72.4	5.6	16.7	1.1	169.0	10.0	35.2	2.0	1.0E+04	240.0	80.0	5.9	371.0	42.0
17-37-2 - 26	23.1	3.5	100.7	3.4	0.8	0.1	0.0	0.0	1.4	0.2	2.5	0.4	4.5	0.5	0.2	0.1	8.9	0.8	14.9	0.7	3.2	0.2	8.8	0.5	1.4	0.1	9.9	0.6	1.7	0.1	1.1E+04	280.0	86.6	5.2	346.0	13.0
17-37-2 - 27	0.0	0.0	200.0	18.0	2.1	2.7	0.0	0.0	1.3	2.0	0.0	0.0	17.0	14.0	1.0	0.7	9.7	9.3	24.1	3.2	6.2	2.0	15.5	2.2	3.3	1.3	20.3	5.4	3.0	0.5	8.9E+03	920.0	43.4	7.1	486.0	35.0
17-37-2 - 28	18.5	2.8	422.0	28.0	1.9	0.2	0.0	0.0	5.0	0.6	1.2	0.3	2.8	0.4	0.3	0.1	9.6	0.9	38.4	2.1	14.2	0.9	67.4	4.3	14.4	0.9	142.0	11.0	29.5	2.5	1.0E+04	270.0	99.8	5.7	322.0	19.0
17-37-2 - 29	25.9	2.7	600.0	19.0	2.2	0.1	0.0	0.0	20.0	0.9	0.8	0.2	1.8	0.3	0.4	0.1	9.2	0.7	46.1	1.9	18.7	0.7	95.5	4.1	22.4	0.9	231.6	9.2	53.1	2.2	9.8E+03	210.0	87.9	4.5	189.0	11.0
17-37-2 - 30	13.8	6.2	427.0	41.0	0.7	0.2	0.2	0.3	1.1	0.3	2.5	0.7	6.9	2.1	1.2	0.6	23.8	2.6	50.8	6.1	13.3	1.7	50.5	5.8	9.1	1.2	84.0	10.0	14.6	2.2	9.9E+03	640.0	57.2	5.2	392.0	21.0
17-37-2 - 31	14.4	1.9	254.0	47.0	1.3	0.2	0.0	0.0	6.2	1.4	2.2	0.4	4.3	0.6	0.3	0.1	8.8	0.5	24.5	3.0	8.2	1.5	38.2	8.5	8.4	2.0	82.0	21.0	18.6	5.0	1.1E+04	310.0	108.0	4.3	378.0	28.0
17-37-2 - 32	19.3	2.1	409.0	53.0	1.1	0.1	0.0	0.0	1.9	0.2	1.7	0.3	4.6	0.6	0.4	0.1	14.0	1.1	43.2	4.7	13.6	1.8	54.7	8.5	10.8	1.8	94.0	17.0	18.3	3.3	1.1E+04	200.0	77.1	7.4	531.0	29.0
17-37-2 - 33	24.5	2.9	133.0	2.9	0.9	0.1	0.0	0.0	1.3	0.1	1.8	0.3	4.8	0.5	0.2	0.0	10.9	0.6	19.3	0.7	4.5	0.2	13.0	0.5	2.1	0.1	14.0	0.5	2.5	0.1	1.1E+04	250.0	52.1	1.2	489.0	11.0
17-37-2 - 34	25.5	3.0	145.0	11.0	0.8	0.1	0.0	0.0	1.3	0.2	2.2	0.3	4.1	0.5	0.2	0.1	11.5	0.8	20.8	1.3	4.5	0.4	15.3	2.0	2.8	0.5	23.7	4.8	4.2	1.0	1.1E+04	260.0	80.2	4.7	365.0	16.0
17-37-2 - 35	24.8	4.0	782.0	31.0	3.7	0.4	0.6	0.1	7.2	0.4	6.9	0.9	9.7	1.1	13.1	2.9	30.0	2.1	83.8	4.4	25.4	1.1	105.9	3.4	21.6	0.7	197.6	6.2	38.5	1.1	1.0E+04	190.0	167.1	9.4	735.0	20.0

| | | |

17-37-2-70	10.8	1.8	85.5	2.1	0.8	0.1	0.1	0.0	1.7	0.1	2.8	0.3	5.6	0.5	0.2	0.1	8.3	0.7	13.5	0.7	2.8	0.1	8.1	0.4	1.3	0.1	9.4	0.4	1.4	0.1	1.2E+04	240.0	126.5	3.3	399.2	9.6
17-37-2-71	380.0	230.0	451.0	75.0	1.4	0.4	0.3	0.1	4.5	1.3	3.4	0.8	4.5	1.0	4.2	1.0	16.6	1.9	49.1	6.8	14.4	2.4	59.0	13.0	12.6	2.7	133.0	27.0	27.0	5.6	1.0E+04	420.0	51.6	5.1	544.0	27.0
17-37-2-72	20.6	2.4	357.0	44.0	1.9	0.2	0.0	0.0	5.9	0.9	1.6	0.3	2.9	0.4	0.3	0.1	10.0	0.8	37.2	4.0	12.0	1.5	49.9	6.3	10.4	1.4	99.0	13.0	19.5	2.5	1.1E+04	280.0	103.6	3.7	415.0	13.0
17-37-2-73	19.9	2.7	237.0	32.0	0.9	0.1	0.0	0.0	0.9	0.1	1.0	0.2	2.1	0.3	0.1	0.0	9.9	0.7	32.3	2.4	7.7	1.0	24.3	4.0	4.3	0.7	36.8	6.7	6.7	1.2	1.1E+04	260.0	48.1	2.4	535.0	16.0
17-37-2-74	23.8	2.9	104.1	5.4	0.9	0.1	0.0	0.0	2.1	0.1	3.2	0.4	4.6	0.4	0.1	0.0	9.5	0.8	16.0	1.0	3.4	0.2	10.1	0.7	1.5	0.1	11.4	0.8	1.8	0.1	1.2E+04	280.0	113.6	6.1	426.0	14.0
17-37-2-75	23.2	2.5	108.0	13.0	1.0	0.1	0.0	0.0	1.9	0.1	2.5	0.4	3.7	0.4	0.2	0.1	7.0	0.5	14.1	1.2	3.5	0.4	11.9	1.7	2.0	0.3	15.6	2.8	2.6	0.5	1.2E+04	270.0	100.0	2.2	412.0	14.0
17-37-2-76	26.8	2.5	121.0	19.0	0.9	0.1	0.0	0.0	1.7	0.1	2.3	0.4	3.2	0.4	0.2	0.0	7.2	0.7	16.6	2.6	3.9	0.6	13.0	2.5	2.4	0.5	21.4	5.6	3.6	1.0	1.2E+04	260.0	105.3	9.2	388.5	9.8
17-37-2-77	39.0	18.0	102.0	4.9	0.8	0.1	0.1	0.0	1.6	0.2	2.3	0.3	4.3	0.4	0.2	0.0	10.4	0.8	16.9	1.1	3.3	0.2	9.3	0.6	1.3	0.1	10.8	0.7	1.6	0.1	1.1E+04	320.0	99.3	6.0	401.0	11.0
17-37-2-78	20.4	1.8	90.3	2.2	0.8	0.1	0.0	0.0	1.5	0.1	2.5	0.4	3.6	0.4	0.1	0.0	9.2	0.5	14.8	0.6	2.9	0.2	7.7	0.5	1.1	0.1	8.4	0.5	1.3	0.1	1.2E+04	200.0	108.8	3.6	379.0	13.0
17-37-2-79	22.1	2.4	106.7	4.2	0.6	0.1	0.0	0.0	0.4	0.1	0.8	0.2	2.5	0.4	0.0	0.0	12.2	1.0	21.4	1.3	3.5	0.2	8.0	0.5	1.1	0.1	8.0	0.6	1.2	0.1	1.1E+04	230.0	58.1	2.9	491.0	29.0
17-37-2-80	18.9	2.8	284.0	39.0	1.4	0.2	0.0	0.0	2.8	0.5	2.1	0.4	3.3	0.4	0.2	0.1	10.3	0.7	30.2	3.3	9.4	1.4	40.5	7.0	8.9	1.7	84.0	16.0	16.5	3.4	1.0E+04	300.0	66.0	2.4	337.0	21.0
17-37-2-81	21.3	2.2	590.0	14.0	0.9	0.1	0.1	0.0	2.3	0.2	1.6	0.3	3.6	0.5	0.4	0.1	13.6	0.9	57.0	1.6	19.1	0.5	84.1	2.5	17.6	0.7	172.5	6.8	33.5	1.6	1.1E+04	220.0	56.2	2.7	505.0	18.0
17-37-2-82	17.5	5.6	793.0	92.0	1.8	0.2	0.3	0.2	8.4	1.3	5.4	2.1	7.8	2.3	5.0	2.0	19.2	3.2	71.3	7.9	25.8	3.2	114.0	16.0	25.4	3.2	265.0	27.0	51.1	6.3	1.0E+04	480.0	106.0	14.0	716.0	58.0
17-37-2-83	38.7	9.6	194.0	22.0	0.7	0.1	0.1	0.0	0.8	0.1	1.2	0.4	3.5	0.7	0.2	0.1	15.7	1.2	27.5	2.1	6.2	0.7	21.3	3.3	4.2	0.8	38.3	8.2	7.3	1.5	1.1E+04	310.0	53.1	2.6	482.0	23.0
17-37-2-84	26.6	3.6	701.0	47.0	1.1	0.1	0.0	0.0	4.2	0.2	1.6	0.3	3.8	0.6	0.7	0.1	16.7	1.4	64.0	4.6	24.5	1.7	108.0	8.0	22.6	1.8	211.0	16.0	44.4	3.6	7.6E+03	260.0	81.2	5.5	216.0	21.0
17-37-2-85	29.2	4.4	470.0	32.0	0.9	0.1	0.1	0.1	3.4	0.3	2.1	0.5	3.9	0.7	2.9	0.4	13.1	1.4	46.7	3.4	14.3	1.1	59.1	4.5	11.8	0.9	108.6	8.4	21.7	1.7	1.0E+04	230.0	57.3	3.9	420.0	8.3
17-37-2-86	19.9	2.6	1260.0	110.0	1.9	0.2	240.0	190.0	680.0	530.0	400.0	320.0	80.0	63.0	1.7	0.5	52.0	25.0	111.0	12.0	40.1	3.5	189.0	16.0	40.0	3.4	384.0	31.0	81.9	6.8	9.0E+03	190.0	500.0	180.0	411.0	28.0
17-37-2-87	20.7	2.5	219.0	66.0	0.8	0.1	0.1	0.0	1.2	0.3	1.4	0.3	3.4	0.5	0.8	0.4	13.4	1.6	27.9	6.3	6.7	2.1	23.2	8.6	4.8	1.9	41.0	17.0	7.9	3.3	1.1E+04	280.0	75.3	6.2	368.0	21.0
17-37-2-88	26.1	3.1	450.0	20.0	1.3	0.1	0.1	0.0	5.6	0.8	0.9	0.2	1.6	0.2	0.3	0.1	8.8	0.5	44.9	2.6	14.7	0.8	63.3	4.2	13.8	1.1	131.0	11.0	26.5	2.2	1.0E+04	260.0	83.7	8.2	443.0	52.0
17-37-2-89	22.8	3.1	284.0	52.0	0.6	0.1	0.1	0.1	0.6	0.3	0.6	0.2	1.5	0.3	0.1	0.0	8.5	0.6	40.3	4.6	8.8	1.6	27.2	6.7	4.4	1.2	31.7	9.5	4.9	1.5	1.1E+04	200.0	23.2	2.4	655.0	24.0
17-37-2-90	22.1	2.7	1075.0	74.0	1.7	0.2	0.1	0.0	6.5	0.7	1.3	0.3	3.5	0.5	0.4	0.1	20.0	1.7	100.2	6.7	36.4	2.8	164.0	14.0	33.5	2.8	302.0	27.0	61.5	5.8	1.0E+04	200.0	102.9	9.3	374.0	46.0
17-37-2-91	27.2	3.8	1004.0	84.0	1.9	0.2	0.8	0.2	6.0	0.8	7.8	1.3	11.5	1.7	25.0	3.9	28.6	3.8	92.6	8.7	30.4	2.5	147.0	11.0	37.3	2.8	398.0	27.0	90.6	6.8	1.2E+04	290.0	106.0	10.0	856.0	48.0
17-37-2-92	18.4	2.1	442.0	13.0	1.9	0.1	0.0	0.0	5.7	0.4	2.0	0.3	3.4	0.5	1.0	0.3	11.3	0.6	42.0	1.4	14.7	0.6	64.4	2.0	13.1	0.4	116.4	5.5	23.8	1.0	8.8E+03	230.0	58.0	5.3	172.0	31.0
17-37-2-93	19.2	2.5	860.0	130.0	2.7	0.4	0.2	0.0	6.7	1.0	5.0	0.7	7.9	1.1	3.9	0.4	27.0	2.8	90.0	12.0	29.2	4.5	124.0	20.0	25.2	4.0	229.0	37.0	46.6	7.3	1.0E+04	330.0	186.0	26.0	668.0	49.0
17-37-2-94	32.2	3.8	610.0	100.0	1.2	0.2	0.4	0.1	8.8	2.3	2.9	0.5	4.5	0.7	11.5	3.2	16.5	1.7	61.5	7.3	17.5	2.8	66.0	12.0	13.1	2.7	117.0	25.0	23.5	5.3	1.1E+04	290.0	64.5	4.5	466.0	28.0
17-37-2-95	22.7	2.4	235.0	25.0	0.7	0.1	0.0	0.0	0.7	0.2	1.2	0.3	2.8	0.4	0.1	0.0	9.5	0.8	29.7	2.7	7.3	0.8	24.6	3.0	4.1	0.6	32.8	5.0	5.5	0.8	1.1E+04	290.0	51.7	6.9	523.0	20.0
17-37-2-96	22.9	2.5	156.0	13.0	0.8	0.1	0.0	0.0	1.2	0.2	2.1	0.4	6.9	0.6	0.2	0.1	14.4	1.3	24.7	2.2	5.4	0.5	15.7	1.4	2.5	0.2	16.5	1.5	2.7	0.2	1.1E+04	270.0	51.1	6.8	703.0	22.0
17-37-2-97	25.8	2.1	510.0	120.0	2.6	0.6	0.0	0.0	3.6	0.8	2.2	0.3	4.2	0.4	0.2	0.1	15.5	1.8	54.0	11.0	18.4	4.4	80.0	20.0	16.3	4.3	141.0	37.0	28.5	7.6	1.1E+04	260.0	131.0	12.0	397.0	26.0
17-37-2-98	21.7	2.7	135.0	11.0	1.1	0.1	0.0	0.0	1.3	0.2	2.4	0.3	3.5	0.5	0.1	0.0	12.0	0.7	19.7	1.0	4.3	0.4	14.0	1.9	2.7	0.5	25.7	6.2	5.2	1.3	1.1E+04	260.0	92.5	3.3	398.0	14.0
17-37-2-99	22.8	2.8	357.0	64.0	1.9	0.3	0.0	0.0	10.1	2.3	1.5	0.3	3.2	0.4	0.2	0.0	11.8	1.0	35.0	5.2	11.8	2.2	51.0	11.0	10.0	2.2	91.0	21.0	17.8	4.2	1.1E+04	430.0	166.0	18.0	294.0	11.0
17-37-2-100	25.2	2.4	98.4	2.3	0.8	0.1	0.0	0.0	2.0	0.2	3.0	0.4	4.0	0.4	0.1	0.0	8.1	0.7	14.9	0.6	3.3	0.2	9.7	0.5	1.5	0.1	10.9	0.6	1.7	0.1	1.2E+04	230.0	122.4	3.2	400.5	9.5
17-37-2-101	33.3	2.8	72.3	1.6	1.0	0.1	0.1	0.1	2.2	0.2	2.7	0.3	4.3	0.5	0.1	0.0	8.4	0.6	12.2	0.6	2.5	0.1	6.6	0.3	0.9	0.1	5.9	0.3	1.0	0.1	1.2E+04	290.0	97.5	3.0	482.0	12.0
17-37-2-102	34.1	2.6	75.6	1.7	1.2	0.1	0.0	0.0	2.2	0.2	2.7	0.3	4.6	0.4	0.1	0.0	9.1	0.6	13.1	0.7	2.6	0.1	6.7	0.3	1.0	0.1	6.3	0.4	1.0	0.1	1.2E+04	270.0	104.9	2.4	548.0	13.0
17-37-2-103	25.8	2.6	408.0	75.0	0.7	0.1	0.0	0.0	0.7	0.1	1.5	0.3	4.1	0.5	0.5	0.1	16.7	1.3	44.7	6.6	13.6	2.6	56.0	12.0	11.6	2.6	103.0	22.0	20.4	4.5	1.1E+04	220.0	57.5	3.4	394.0	17.0

17-37-2 - 104	41.2	4.8	1130.0	130.0	1.1	0.1	1.7	0.2	8.8	1.0	9.0	1.0	13.4	1.7	59.8	7.6	42.9	4.7	112.0	12.0	29.5	3.2	107.0	12.0	19.7	2.2	166.0	18.0	32.0	3.6	1.1E+04	240.0	96.0	6.0	561.0	34.0
17-37-2 - 105	74.0	60.0	1340.0	130.0	0.7	1.0	0.0	0.0	4.9	3.1	4.1	4.8	12.2	5.0	32.0	21.0	37.5	8.6	150.0	16.0	37.9	5.0	142.0	15.0	26.3	2.8	254.0	42.0	40.6	4.2	9.3E+03	690.0	62.7	6.8	550.0	41.0
17-37-2 - 106	17.7	2.6	1150.0	160.0	3.2	0.4	0.2	0.0	42.9	6.8	5.3	0.8	10.4	1.3	4.9	1.0	39.8	4.5	117.0	16.0	38.4	5.5	160.0	23.0	31.3	4.7	280.0	41.0	56.0	8.6	9.3E+03	260.0	265.0	37.0	449.0	14.0
17-37-2 - 107	23.3	2.2	375.0	63.0	0.9	0.1	0.1	0.0	9.2	1.9	2.5	0.4	5.4	0.7	1.8	0.7	20.0	2.4	46.1	6.3	12.2	2.0	47.7	8.2	8.9	1.6	75.0	13.0	15.2	2.8	1.0E+04	300.0	106.0	11.0	423.0	24.0
17-37-2 - 108	20.9	2.5	230.0	27.0	0.8	0.1	0.1	0.0	1.8	0.6	0.8	0.2	3.0	0.4	0.1	0.0	15.8	1.3	36.1	2.7	7.7	0.9	24.5	4.1	4.9	1.0	46.0	10.0	9.9	2.2	1.2E+04	280.0	48.3	7.1	706.0	25.0
17-37-2 - 109	31.0	3.1	100.4	2.2	0.8	0.1	0.0	0.0	2.0	0.1	3.4	0.4	4.1	0.4	0.1	0.0	9.0	0.5	14.6	0.6	3.4	0.1	9.7	0.4	1.4	0.1	10.5	0.5	1.7	0.1	1.2E+04	220.0	116.6	2.4	390.9	9.0
17-37-2 - 110	29.0	2.4	95.6	2.5	0.8	0.1	0.0	0.0	1.9	0.1	2.9	0.4	4.1	0.5	0.1	0.0	8.1	0.6	14.5	0.6	3.0	0.2	9.2	0.4	1.4	0.1	10.2	0.6	1.6	0.1	1.2E+04	290.0	113.5	2.4	386.9	8.0
17-37-2 - 111	9.1	1.5	124.2	4.8	0.8	0.1	0.3	0.1	1.0	0.1	1.7	0.3	6.1	0.5	0.3	0.1	19.0	1.0	23.6	1.2	4.1	0.2	10.5	0.6	1.6	0.1	11.6	1.0	1.9	0.2	1.1E+04	260.0	67.0	2.4	409.0	18.0
17-37-2 - 112	18.9	2.5	1182.0	49.0	1.1	0.3	0.1	0.0	1.1	0.1	1.8	0.3	4.6	0.4	0.6	0.2	23.7	1.5	107.7	5.6	39.4	1.8	179.7	6.1	36.3	1.1	327.4	9.6	63.8	1.6	1.0E+04	250.0	85.7	3.3	322.0	67.0
17-37-2 - 113	22.2	2.6	596.0	64.0	1.0	0.1	0.1	0.0	0.7	0.2	1.1	0.2	2.5	0.4	0.2	0.1	12.5	1.3	57.7	5.3	19.3	2.2	85.0	10.0	16.9	2.0	158.0	20.0	29.9	3.8	1.1E+04	250.0	44.6	4.2	517.0	31.0
17-37-2 - 114	27.1	3.0	102.4	2.7	0.8	0.1	0.0	0.0	0.6	0.1	1.4	0.3	3.6	0.4	0.1	0.0	10.7	0.6	16.9	0.8	3.1	0.1	8.4	0.4	1.3	0.1	9.1	0.5	1.5	0.1	1.1E+04	220.0	76.3	2.4	339.0	12.0
17-37-2 - 115	15.2	2.6	192.0	28.0	0.7	0.1	0.0	0.0	0.9	0.1	1.4	0.3	3.3	0.6	0.1	0.0	9.8	0.7	22.3	2.4	6.2	1.1	24.1	5.4	4.8	1.2	44.0	12.0	8.3	2.4	1.1E+04	290.0	71.4	3.7	363.0	14.0
17-37-2 - 116	16.9	2.2	310.0	18.0	1.2	0.1	0.1	0.0	2.5	0.2	3.7	0.4	5.1	0.5	3.2	0.4	13.3	0.8	34.4	1.9	9.9	0.5	40.9	2.9	9.6	0.8	101.7	8.2	21.8	2.1	1.1E+04	300.0	125.2	4.6	578.0	18.0
17-37-2 - 117	20.5	2.0	327.0	18.0	1.2	0.1	0.0	0.0	5.6	0.3	0.8	0.2	1.5	0.2	0.1	0.0	7.0	0.5	28.8	1.7	10.2	0.6	48.1	2.7	10.6	0.6	105.4	6.0	22.8	1.2	1.1E+04	320.0	89.3	3.4	472.0	17.0
17-37-2 - 118	205.0	98.0	129.6	7.8	0.8	0.1	0.0	0.0	0.5	0.1	1.4	0.3	4.8	0.6	0.3	0.1	19.1	1.4	25.9	1.9	4.2	0.3	10.6	0.7	1.6	0.1	10.4	0.7	1.8	0.1	1.1E+04	260.0	56.6	2.7	367.0	18.0
17-37-2 - 119	40.8	4.2	1123.0	57.0	1.4	0.1	0.1	0.0	40.0	1.5	8.4	0.8	10.5	0.6	3.5	0.2	38.5	2.4	115.0	6.3	38.5	2.0	157.6	8.3	31.1	1.5	276.0	13.0	55.2	2.5	7.0E+03	130.0	361.0	23.0	259.0	14.0
17-37-2 - 120	23.8	2.7	217.0	19.0	0.7	0.1	0.0	0.0	1.9	0.4	1.0	0.2	3.1	0.4	0.2	0.1	16.9	0.9	32.1	1.5	7.3	0.7	26.3	3.5	5.3	0.9	52.0	9.6	10.3	2.1	1.1E+04	230.0	42.4	1.8	615.0	21.0
17-37-2 - 121	21.0	2.6	407.0	40.0	1.4	0.1	0.1	0.0	8.0	1.2	1.2	0.3	2.7	0.4	0.4	0.1	9.7	0.7	39.7	3.3	13.3	1.4	57.5	6.5	12.1	1.4	116.0	14.0	23.0	2.7	1.0E+04	280.0	92.8	7.8	384.0	12.0
17-37-2 - 122	15.8	2.5	119.5	8.8	0.7	0.1	0.0	0.0	0.5	0.1	1.0	0.2	3.3	0.5	0.2	0.1	11.6	0.7	20.2	1.3	3.6	0.3	9.8	1.1	1.5	0.2	10.8	1.5	1.7	0.2	1.1E+04	220.0	56.7	2.9	404.0	11.0
17-37-2 - 123	13.0	10.0	118.8	3.1	0.9	0.3	0.0	0.0	2.0	0.4	1.8	1.3	7.4	2.3	0.5	0.2	14.1	1.7	19.6	1.6	3.7	0.3	11.4	0.9	1.7	0.2	12.2	1.0	1.9	0.2	1.1E+04	710.0	91.9	9.6	454.0	16.0
17-37-2 - 124	19.2	2.5	103.8	4.0	0.7	0.1	0.0	0.0	0.5	0.1	1.0	0.2	3.8	0.4	0.0	0.0	14.5	0.9	19.7	0.8	3.1	0.2	8.3	0.5	1.3	0.1	10.6	1.0	1.7	0.2	1.1E+04	290.0	67.9	2.2	321.0	8.2
17-37-2 - 125	24.4	2.4	87.0	3.3	0.9	0.1	0.0	0.0	0.7	0.1	1.5	0.2	3.5	0.4	0.0	0.0	12.2	0.9	15.4	0.9	2.7	0.1	6.7	0.5	0.9	0.1	7.0	0.6	1.0	0.1	1.1E+04	230.0	75.8	2.4	311.0	13.0
17-37-2 - 126	13.0	2.2	101.8	3.2	0.8	0.1	0.2	0.0	1.5	0.1	2.5	0.4	5.9	0.4	0.3	0.1	11.3	0.6	16.5	0.7	3.3	0.2	9.1	0.5	1.4	0.1	9.8	0.6	1.5	0.1	1.1E+04	220.0	104.5	6.8	341.0	11.0
17-37-2 - 127	12.3	1.5	409.0	72.0	0.7	0.1	0.1	0.0	1.0	0.1	1.6	0.3	4.0	0.4	0.2	0.0	14.3	0.9	40.8	5.5	14.2	2.6	66.0	14.0	14.6	3.2	151.0	34.0	31.0	7.0	1.1E+04	210.0	67.1	3.9	355.0	16.0
17-37-2 - 128	21.6	2.5	684.0	41.0	2.9	0.3	0.0	0.0	6.0	0.6	0.9	0.2	2.9	0.4	0.3	0.1	15.0	0.9	62.3	3.0	23.7	1.5	107.4	6.6	22.1	1.4	210.0	11.0	43.3	2.8	8.9E+03	320.0	90.7	8.0	341.0	14.0
17-37-2 - 129	21.7	2.0	95.1	2.8	0.8	0.1	0.0	0.0	2.1	0.1	3.0	0.4	4.5	0.5	0.1	0.0	8.4	0.6	14.2	0.6	3.2	0.2	9.6	0.5	1.6	0.2	12.3	1.3	1.9	0.2	1.1E+04	220.0	108.2	3.0	461.0	15.0
17-37-2 - 130	20.8	2.3	500.0	18.0	2.3	0.2	0.0	0.0	7.5	0.4	0.9	0.3	1.8	0.4	0.4	0.2	9.2	0.8	42.4	2.1	16.3	0.7	75.3	3.0	16.4	0.7	161.7	7.7	32.5	1.6	8.6E+03	220.0	110.5	4.8	297.0	25.0
17-37-2 - 131	13.3	1.7	760.0	110.0	2.6	0.3	0.1	0.0	20.3	3.5	1.8	0.4	3.7	0.6	0.6	0.1	19.2	1.8	70.6	8.8	24.7	3.7	120.0	20.0	26.1	4.3	263.0	42.0	55.4	8.9	1.1E+04	270.0	115.0	14.0	509.0	30.0
17-37-2 - 132	26.0	15.0	384.0	84.0	0.7	0.2	0.0	0.0	0.3	0.6	0.0	0.0	2.1	1.9	0.6	0.3	8.4	1.6	36.0	6.4	11.8	3.0	51.0	15.0	11.3	3.7	113.0	36.0	20.6	7.4	9.7E+03	910.0	49.8	4.3	400.0	44.0
17-37-2 - 133	23.1	2.1	165.0	20.0	0.8	0.1	0.0	0.0	2.0	0.2	2.9	0.3	4.6	0.5	0.2	0.1	10.3	0.9	23.2	2.3	5.5	0.7	18.4	2.8	3.1	0.6	29.1	6.3	5.4	1.4	1.1E+04	240.0	106.1	5.1	476.0	23.0
17-37-2 - 134	21.9	2.3	122.7	4.4	0.6	0.1	0.0	0.0	0.7	0.1	1.4	0.3	3.1	0.3	0.3	0.1	14.1	1.5	22.5	1.6	4.1	0.2	9.9	0.6	1.5	0.1	10.7	0.5	1.7	0.1	1.1E+04	220.0	62.7	3.2	437.0	20.0
17-37-2 - 135	26.2	3.1	1110.0	120.0	2.4	0.3	0.0	0.0	20.7	3.2	4.7	0.8	7.8	1.3	1.0	0.2	29.6	3.2	103.9	9.5	36.3	3.9	164.0	18.0	34.4	3.9	330.0	38.0	64.7	7.5	1.0E+04	260.0	321.0	46.0	536.0	27.0
17-37-2 - 136	22.8	3.1	98.1	2.3	0.8	0.1	0.0	0.0	1.0	0.2	1.9	0.3	3.6	0.4	0.1	0.0	9.7	0.7	16.5	0.7	3.1	0.1	8.2	0.5	1.1	0.1	9.0	0.6	1.4	0.1	1.1E+04	300.0	84.1	4.2	311.0	12.0
17-37-2 - 137	19.6	2.5	265.0	52.0	0.8	0.1	0.0	0.0	0.4	0.1	0.7	0.2	2.5	0.5	0.1	0.0	8.9	0.8	26.5	3.7	8.4	1.8	37.6	9.5	7.9	2.1	73.0	20.0	13.4	4.0	1.1E+04	260.0	53.8	5.7	430.0	21.0

17-37-2 - 138	21.2	2.8	516.0	75.0	2.5	0.3	0.0	0.0	5.5	0.7	2.1	0.3	3.9	0.5	0.2	0.0	13.5	1.2	50.3	6.5	18.3	2.8	82.0	12.0	15.5	2.4	142.0	22.0	27.5	4.4	1.1E+04	240.0	179.0	14.0	484.0	21.0
17-37-2 - 139	25.2	2.7	166.0	23.0	1.1	0.1	0.0	0.0	1.4	0.1	1.6	0.3	4.1	0.4	0.2	0.0	10.5	0.7	21.5	2.0	5.5	0.8	18.1	3.2	3.0	0.6	26.1	6.6	4.5	1.4	1.1E+04	240.0	51.6	1.3	529.0	12.0
17-37-2 - 140	24.4	2.7	477.0	76.0	1.4	0.2	0.0	0.0	9.2	1.9	1.8	0.3	3.3	0.5	0.2	0.1	13.6	0.9	46.9	6.0	16.1	2.7	69.0	13.0	13.7	2.7	132.0	27.0	26.2	5.5	1.1E+04	250.0	122.0	12.0	454.0	11.0
17-37-2 - 141	29.9	3.1	99.0	4.3	0.8	0.1	0.0	0.0	1.2	0.2	2.5	0.4	5.1	0.5	0.2	0.1	16.8	1.4	19.8	1.3	3.2	0.2	7.3	0.5	0.9	0.1	6.4	0.5	1.0	0.1	1.2E+04	230.0	95.8	4.7	410.7	9.0
17-37-2 - 142	32.2	3.2	72.5	1.6	1.3	0.1	0.1	0.0	2.2	0.1	2.9	0.3	4.1	0.4	0.1	0.0	8.0	0.6	12.4	0.6	2.4	0.1	6.3	0.3	0.9	0.1	6.3	0.4	0.9	0.1	1.2E+04	210.0	106.0	2.2	487.8	9.6
17-37-2 - 143	9.9	3.4	733.0	36.0	1.9	0.2	0.0	0.0	26.9	2.1	1.4	0.3	3.9	0.7	0.6	0.1	16.5	1.6	65.0	3.1	24.0	1.7	112.0	8.8	23.8	1.6	231.0	14.0	46.0	3.5	8.9E+03	320.0	95.7	5.1	196.0	23.0
17-59-1 - 1	14.1	1.9	326.0	67.0	0.7	0.0	0.4	0.1	1.2	0.1	1.9	0.4	4.0	0.6	2.2	0.6	13.2	1.5	22.9	2.5	5.0	0.7	13.7	2.0	2.4	0.4	22.4	3.2	4.4	0.7	1.2E+04	230.0	44.3	5.1	367.0	15.0
17-59-1 - 2	29.3	2.9	93.3	2.8	1.0	0.1	0.3	0.4	2.9	0.3	4.6	0.4	7.8	0.6	0.2	0.0	12.6	0.9	14.1	0.6	3.2	0.2	8.8	0.5	1.2	0.1	8.3	0.5	1.3	0.1	1.2E+04	300.0	100.7	3.8	361.0	9.0
17-59-1 - 3	35.9	3.3	57.3	1.4	1.3	0.1	0.0	0.0	2.7	0.2	3.3	0.4	5.0	0.4	0.1	0.0	7.2	0.5	8.9	0.5	1.8	0.1	4.7	0.2	0.7	0.1	5.1	0.3	0.7	0.0	1.2E+04	250.0	115.4	2.3	576.0	12.0
17-59-1 - 4	36.8	3.4	57.5	1.3	1.1	0.1	0.0	0.0	2.7	0.1	3.2	0.4	5.0	0.5	0.1	0.0	7.7	0.4	9.6	0.5	1.8	0.1	4.7	0.3	0.7	0.1	4.9	0.3	0.7	0.1	1.2E+04	260.0	109.3	3.1	574.1	7.4
17-59-1 - 5	26.3	2.5	55.3	2.0	0.8	0.1	0.0	0.0	1.9	0.1	2.2	0.3	5.2	0.6	0.2	0.0	11.2	0.8	11.3	0.5	1.8	0.1	4.1	0.3	0.5	0.1	3.9	0.4	0.6	0.1	1.2E+04	270.0	90.7	2.8	399.0	14.0
17-59-1 - 6	12.7	1.8	470.0	120.0	0.8	0.1	0.4	0.2	1.8	0.5	2.0	0.5	7.4	1.1	1.4	0.5	16.4	1.6	48.5	9.1	15.0	3.9	60.0	18.0	12.7	4.1	119.0	40.0	23.9	8.1	1.2E+04	310.0	40.8	6.0	446.0	36.0
17-59-1 - 7	18.1	2.5	56.1	1.3	1.1	0.1	0.0	0.0	2.7	0.1	2.6	0.3	4.5	0.4	0.1	0.0	6.6	0.4	8.8	0.4	1.7	0.1	4.9	0.2	0.7	0.1	5.4	0.4	0.8	0.1	1.2E+04	300.0	106.1	2.5	338.0	14.0
17-59-1 - 8	30.6	2.9	76.6	1.4	0.9	0.1	0.0	0.0	3.0	0.2	3.4	0.3	5.4	0.5	0.2	0.0	8.5	0.6	11.8	0.5	2.5	0.1	7.5	0.4	1.1	0.1	8.9	0.5	1.3	0.1	1.2E+04	230.0	100.5	2.2	273.0	6.6
17-59-1 - 9	34.6	2.6	65.9	1.6	1.0	0.1	0.0	0.0	2.7	0.1	2.8	0.3	4.7	0.5	0.2	0.0	7.3	0.4	10.1	0.5	2.2	0.1	6.1	0.3	1.0	0.1	7.0	0.3	1.1	0.1	1.2E+04	210.0	99.6	1.6	276.1	4.7
17-59-1 - 10	27.9	3.0	51.4	1.7	0.9	0.1	0.0	0.0	2.3	0.1	3.1	0.3	5.1	0.5	0.1	0.0	8.8	0.6	8.7	0.5	1.5	0.1	3.5	0.2	0.5	0.0	3.1	0.3	0.4	0.0	1.3E+04	240.0	100.7	2.6	433.0	11.0
17-59-1 - 11	26.2	2.6	61.9	1.7	0.9	0.1	0.0	0.0	2.6	0.1	3.7	0.4	5.9	0.6	0.1	0.0	9.0	0.5	10.7	0.5	1.9	0.1	4.5	0.3	0.6	0.1	4.3	0.3	0.6	0.1	1.3E+04	290.0	109.1	2.7	465.0	10.0
17-59-1 - 12	19.9	2.0	177.0	25.0	0.9	0.1	0.0	0.0	2.2	0.2	2.2	0.4	3.4	0.5	0.3	0.1	7.6	0.5	18.6	2.3	5.7	0.8	23.1	3.8	5.0	0.9	48.1	9.2	9.8	2.0	1.1E+04	230.0	78.8	5.6	323.0	17.0
17-59-1 - 13	23.2	2.3	869.0	41.0	0.8	0.1	0.1	0.0	5.7	0.3	4.2	0.5	7.7	0.8	0.2	0.0	29.1	2.3	92.4	5.2	30.9	1.5	121.3	6.1	23.0	1.0	194.2	7.4	37.0	1.5	9.7E+03	210.0	82.9	5.8	79.7	4.2
17-59-1 - 14	15.6	2.0	49.6	2.4	0.7	0.1	0.0	0.0	0.9	0.1	1.5	0.3	5.4	0.6	0.2	0.0	16.1	1.2	13.0	0.8	1.6	0.1	2.8	0.3	0.3	0.0	1.9	0.2	0.3	0.0	1.2E+04	280.0	77.6	2.5	508.0	16.0
17-59-1 - 15	18.2	2.3	524.0	12.0	0.8	0.1	0.0	0.0	16.2	0.6	2.1	0.3	4.7	0.5	0.9	0.1	16.5	0.9	51.3	1.5	17.7	0.4	75.0	1.8	15.4	0.4	143.4	3.9	29.2	0.8	8.7E+03	200.0	110.9	2.8	131.0	12.0
17-59-1 - 16	16.0	1.9	47.2	2.7	0.7	0.1	0.0	0.0	1.3	0.2	1.6	0.3	4.0	0.4	0.1	0.0	11.0	0.7	10.8	0.8	1.5	0.1	2.8	0.3	0.3	0.0	1.8	0.3	0.3	0.0	1.2E+04	240.0	65.4	5.7	334.4	8.9
17-59-1 - 17	15.2	1.9	524.0	36.0	0.9	0.1	1.0	0.2	10.1	0.7	4.2	0.6	7.2	0.7	5.4	0.7	17.2	1.3	40.3	2.2	13.0	0.9	55.1	4.3	11.5	1.0	113.9	9.6	25.4	2.3	9.5E+03	260.0	127.0	11.0	453.0	13.0
17-59-1 - 18	15.8	2.3	64.5	1.6	0.8	0.1	0.1	0.0	2.7	0.1	3.8	0.4	5.7	0.5	0.1	0.0	8.5	0.5	10.1	0.4	1.9	0.1	5.0	0.3	0.8	0.1	5.4	0.5	0.8	0.1	1.2E+04	250.0	102.6	2.4	487.0	13.0
17-59-1 - 19	22.1	2.1	65.9	3.2	0.8	0.1	0.0	0.0	2.3	0.1	3.5	0.3	5.0	0.4	0.1	0.0	8.8	0.6	10.5	0.4	1.9	0.1	4.9	0.4	0.7	0.1	5.4	0.7	0.9	0.1	1.3E+04	260.0	90.4	2.6	431.3	8.2
17-59-1 - 20	19.1	2.4	440.0	110.0	1.1	0.2	0.9	0.3	7.4	3.2	3.4	1.0	6.9	1.4	2.7	0.8	18.4	2.0	43.3	7.5	11.5	2.8	44.0	13.0	8.8	2.9	85.0	29.0	16.2	5.6	1.2E+04	290.0	49.0	10.0	419.0	25.0
17-59-1 - 21	22.4	2.1	913.0	37.0	5.1	0.4	0.0	0.0	13.1	0.5	1.0	0.2	2.8	0.4	0.6	0.1	17.1	2.0	85.3	6.0	32.1	1.5	146.0	4.2	31.2	0.9	297.0	9.6	59.9	2.3	1.1E+04	260.0	59.5	3.4	165.0	22.0
17-59-1 - 22	22.7	2.5	726.0	44.0	3.4	0.4	0.0	0.0	8.0	0.7	0.5	0.1	2.3	0.4	0.5	0.1	14.0	1.5	69.4	5.4	24.8	1.5	111.2	6.3	23.0	1.3	222.0	13.0	44.3	2.8	1.1E+04	280.0	44.7	2.1	325.0	25.0
17-59-1 - 23	19.5	3.0	429.0	67.0	2.2	0.2	1.4	0.5	7.1	1.0	6.5	2.2	8.4	2.7	3.5	1.3	13.3	3.3	34.2	5.8	11.8	1.5	51.1	5.0	10.7	1.1	104.0	10.0	20.8	2.0	9.5E+03	270.0	40.9	2.8	195.0	23.0
17-59-1 - 24	250.0	150.0	560.0	100.0	6.1	3.4	2.6	0.9	7.1	2.0	10.9	3.4	14.1	3.5	7.1	2.2	24.5	4.3	52.4	7.2	14.8	2.3	54.0	10.0	9.9	2.0	89.0	20.0	17.0	3.9	1.1E+04	310.0	37.6	5.9	378.0	22.0
17-59-1 - 25	21.2	2.7	325.0	31.0	1.0	0.1	0.5	0.2	4.6	0.8	1.1	0.2	2.3	0.4	0.2	0.0	8.6	0.6	32.9	2.5	10.6	1.1	43.1	5.4	8.5	1.1	84.0	11.0	17.5	2.4	1.1E+04	260.0	62.7	4.6	383.0	11.0
17-59-1 - 26	17.7	1.8	430.0	66.0	1.3	0.2	0.7	0.2	12.2	3.1	4.5	0.9	7.1	1.1	2.8	0.5	17.6	1.7	45.6	5.2	13.3	2.1	53.0	10.0	10.6	2.2	98.0	21.0	20.5	4.6	1.1E+04	310.0	85.0	15.0	372.0	15.0
17-59-1 - 27	209.0	35.0	7800.0	1300.0	1.6	0.2	59.0	11.0	110.0	22.0	254.0	49.0	313.0	60.0	279.0	51.0	462.0	79.0	590.0	100.0	138.0	24.0	380.0	69.0	51.5	9.5	327.0	60.0	52.2	9.6	1.2E+04	360.0	106.3	8.3	915.0	60.0
17-59-1 - 28	31.3	3.4	86.3	7.6	1.0	0.1	0.1	0.1	2.6	0.2	3.4	0.3	6.5	0.5	0.3	0.1	10.4	0.7	12.2	0.6	2.7	0.2	7.7	0.4	1.1	0.1	8.1	0.6	1.4	0.1	1.2E+04	270.0	82.5	2.0	427.0	19.0
17-59-1 - 29	26.0	2.6	1010.0	270.0	0.7	0.1	0.8	0.3	1.7	0.2	3.4	0.5	9.8	1.1	8.9	2.5	36.1	6.6	47.0	10.0	10.9	2.7	21.5	5.3	1.8	0.4	7.5	1.7	1.3	0.3	1.2E+04	300.0	58.8	3.4	427.0	15.0
17-59-1 - 30	22.1	2.4	54.1	3.0	0.7	0.1	0.0	0.0	1.9	0.2	2.5	0.4	5.3	0.6	0.2	0.0	11.6	0.9	11.2	0.6	1.8	0.1	3.8	0.5	0.5	0.1	3.4	0.6	0.5	0.1	1.2E+04	290.0	76.1	5.5	348.0	12.0
17-59-1 - 31	21.5	2.3	45.8	2.5	0.8	0.1	0.0	0.0	2.0	0.1	2.2	0.3	4.4	0.4	0.1	0.0	9.4	0.7	8.9	0.5	1.3	0.1	2.9	0.3	0.4	0.0	2.7	0.3	0.4	0.1	1.3E+04	250.0	79.0	2.8	356.2	9.7
17-59-1 - 32	19.9	3.0	690.0	110.0	2.1	0.5	2.1	0.5	11.6	2.7	12.8	2.4	17.7	3.2	5.8	1.3	32.1	4.7	69.0	12.0	19.3	3.7	69.0	16.0	12.2	3.1	106.0	29.0	20.8	5.9	1.2E+04	430.0	131.0	16.0	467.0	26.0
17-59-1 - 33	13.9	2.1	300.0	68.0	0.8	0.1	0.6	0.3	1.7	0.5	2.9	1.0	6.3	1.7	2.9	1.3	12.0	2.0	30.3	5.4	8.9	2.0	29.7	7.0	5.2	1.3	44.0	11.0	7.0	1.9	1.2E+04	270.0	35.5	3.5	574.0	34.0

17-59-1-34	14.6	2.3	30.0	1.1	0.8	0.1	0.1	0.1	1.7	0.1	2.0	0.3	3.7	0.4	0.1	0.0	7.8	0.5	6.5	0.4	0.9	0.1	1.8	0.2	0.2	0.0	1.3	0.2	0.2	0.0	1.2E+04	250.0	80.0	2.3	293.7	5.2
17-59-1-35	18.5	2.1	32.7	1.8	0.9	0.1	0.0	0.0	2.1	0.1	1.8	0.3	4.1	0.4	0.1	0.0	8.3	0.5	7.1	0.4	1.1	0.1	2.1	0.2	0.3	0.0	2.2	0.4	0.3	0.0	1.2E+04	290.0	91.2	3.2	366.9	9.3
17-59-1-36	15.9	2.0	44.9	1.2	0.7	0.1	0.1	0.1	1.6	0.1	2.0	0.3	5.6	0.4	0.2	0.0	14.3	0.7	11.3	0.5	1.5	0.1	2.4	0.2	0.3	0.0	2.0	0.3	0.3	0.0	1.2E+04	260.0	86.1	2.1	449.0	9.6
17-59-1-37	14.4	1.8	1240.0	110.0	1.8	0.1	0.2	0.1	23.3	1.3	6.5	1.2	10.3	1.3	1.1	0.1	35.3	3.1	119.0	9.6	41.4	3.6	170.0	15.0	30.9	2.5	266.0	21.0	50.7	3.8	8.8E+03	210.0	268.0	30.0	252.0	20.0
17-59-1-38	28.1	2.8	31.5	0.9	0.8	0.1	0.0	0.0	1.6	0.1	1.5	0.2	3.4	0.4	0.1	0.0	6.9	0.5	6.9	0.3	1.0	0.1	2.0	0.2	0.2	0.0	1.5	0.2	0.2	0.0	1.2E+04	260.0	60.4	2.7	357.0	13.0
17-59-1-39	20.7	2.0	88.1	3.0	1.0	0.1	0.1	0.0	3.1	0.1	3.9	0.3	6.9	0.5	0.1	0.0	10.6	0.6	13.6	0.7	2.9	0.2	8.6	0.4	1.2	0.1	9.3	0.5	1.4	0.1	1.2E+04	300.0	112.9	2.9	387.0	16.0
17-59-1-40	28.8	2.6	80.3	3.9	1.0	0.1	0.1	0.1	2.5	0.2	3.3	0.3	5.9	0.5	0.2	0.0	9.1	0.6	12.1	0.7	2.7	0.1	8.3	0.6	1.2	0.1	8.5	0.8	1.4	0.1	1.2E+04	320.0	86.9	2.1	565.0	13.0
17-59-1-41	15.0	2.3	50.2	1.4	0.7	0.1	0.0	0.0	1.8	0.1	2.3	0.3	5.4	0.6	0.2	0.0	11.3	0.8	10.1	0.5	1.6	0.1	2.9	0.2	0.4	0.1	2.6	0.3	0.4	0.1	1.2E+04	300.0	74.7	2.0	383.9	7.2
17-59-1-42	20.9	2.7	87.0	19.0	0.8	0.1	0.0	0.0	2.1	0.3	2.3	0.4	4.7	0.6	0.2	0.0	10.8	0.9	14.7	2.5	2.8	0.7	8.0	2.9	1.3	0.6	11.3	5.3	2.2	1.2	1.2E+04	250.0	65.3	7.1	370.0	13.0
17-59-1-43	34.4	2.2	78.6	3.1	1.1	0.1	0.0	0.0	2.5	0.1	3.7	0.3	6.7	0.6	0.3	0.1	10.2	0.7	11.5	0.5	2.3	0.1	6.4	0.2	0.9	0.1	6.0	0.4	0.9	0.1	1.2E+04	240.0	86.8	3.6	379.0	26.0
17-59-1-44	41.5	3.4	68.6	2.3	1.0	0.1	0.0	0.0	2.5	0.1	3.4	0.4	6.1	0.7	0.1	0.0	9.2	0.7	11.1	0.6	2.1	0.1	6.0	0.3	0.8	0.1	5.9	0.4	0.8	0.1	1.2E+04	280.0	79.3	3.3	320.0	18.0
17-59-1-45	16.6	2.4	502.0	74.0	1.2	0.1	34.0	24.0	23.0	13.0	8.9	4.7	6.5	1.4	0.7	0.2	14.9	1.5	53.4	6.4	17.1	2.5	73.0	13.0	14.5	2.6	141.0	27.0	28.7	5.6	1.1E+04	290.0	87.0	10.0	471.0	20.0
17-59-1-46	31.1	2.3	93.8	6.3	1.1	0.1	0.1	0.0	2.9	0.1	4.0	0.4	6.9	0.6	0.2	0.0	11.2	1.0	14.0	1.0	3.1	0.2	8.7	0.7	1.3	0.1	9.2	0.8	1.4	0.1	1.2E+04	220.0	98.9	3.5	423.0	14.0
17-59-1-47	24.2	2.8	94.1	5.2	1.0	0.1	0.0	0.0	2.9	0.2	4.6	0.4	7.8	0.6	0.2	0.0	12.9	0.9	15.1	1.0	2.8	0.2	6.7	0.5	1.0	0.1	7.2	0.4	0.9	0.1	1.2E+04	300.0	132.9	6.5	596.0	23.0
17-59-1-48	15.6	1.7	95.0	1.8	0.9	0.1	0.1	0.0	2.4	0.1	4.4	0.4	10.5	0.6	0.4	0.1	14.4	0.7	15.8	0.7	3.2	0.1	8.9	0.4	1.3	0.1	10.1	0.5	1.6	0.1	1.2E+04	280.0	108.8	2.2	380.9	7.7
17-59-1-49	25.4	3.7	821.0	48.0	1.3	0.1	2.8	0.5	11.5	1.1	15.2	2.2	21.6	2.7	9.2	1.0	33.1	2.8	75.4	3.6	23.3	1.1	94.5	4.0	18.5	0.9	171.7	8.6	35.2	1.7	1.0E+04	330.0	56.6	3.8	318.0	40.0
17-59-1-50	19.3	2.1	492.0	15.0	1.2	0.1	0.0	0.0	25.6	0.7	1.4	0.2	3.0	0.3	0.5	0.1	11.1	0.6	42.8	1.5	16.2	0.5	75.7	2.2	16.0	0.5	160.2	4.4	35.5	0.8	9.9E+03	250.0	161.1	7.4	211.8	7.6
17-59-1-51	10.1	1.6	627.0	29.0	2.0	0.1	0.2	0.1	3.6	0.3	1.4	0.2	28.2	3.4	1.0	0.1	45.2	4.1	66.1	3.5	21.2	1.0	97.6	4.6	21.1	1.0	209.0	8.3	44.5	1.9	9.1E+03	200.0	58.9	4.1	325.0	22.0
17-59-1-52	14.0	1.7	203.0	39.0	0.7	0.1	0.1	0.0	1.1	0.1	1.5	0.3	14.6	1.4	0.5	0.1	20.9	1.1	29.1	3.8	6.6	1.2	23.0	6.0	4.2	1.2	40.0	12.0	8.1	2.6	1.1E+04	250.0	44.4	6.5	353.9	8.1
17-59-1-53	23.2	2.5	852.0	46.0	1.7	0.1	0.1	0.1	16.7	1.1	1.4	0.2	3.7	0.4	0.5	0.1	19.6	1.3	81.1	4.1	29.4	1.6	127.6	6.6	24.1	1.5	218.0	11.0	44.6	2.5	9.2E+03	290.0	177.0	11.0	323.0	20.0
17-59-1-54	18.1	2.2	391.0	38.0	1.1	0.1	0.2	0.1	2.8	0.4	1.2	0.3	2.1	0.4	0.9	0.2	10.0	0.9	43.0	2.7	12.5	1.3	48.9	6.5	9.8	1.5	95.0	16.0	20.1	3.4	1.1E+04	260.0	53.3	6.4	541.0	43.0
17-59-1-55	57.0	29.0	114.0	30.0	0.8	0.1	2.6	1.8	2.5	1.0	2.0	0.5	3.8	0.6	0.2	0.0	11.6	0.8	19.3	3.4	3.6	1.0	10.6	3.9	1.6	0.7	15.1	7.3	2.6	1.3	1.2E+04	350.0	46.4	6.7	410.0	15.0
17-59-1-56	13.6	2.1	219.0	38.0	1.9	0.2	0.0	0.0	3.2	0.2	3.0	0.3	5.0	0.5	0.2	0.0	9.5	0.8	23.7	3.5	7.4	1.3	31.5	6.0	6.0	1.2	56.0	12.0	11.4	2.5	1.2E+04	250.0	105.8	4.5	367.0	14.0
17-59-1-57	47.7	6.1	2920.0	280.0	3.2	0.4	10.2	1.4	38.3	4.0	54.2	7.0	76.4	9.4	54.3	6.6	128.0	14.0	252.0	23.0	69.7	6.3	264.0	24.0	47.1	3.9	430.0	36.0	87.1	7.7	1.1E+04	250.0	192.0	16.0	633.0	31.0
17-59-1-58	22.3	2.7	66.4	1.6	1.1	0.1	0.0	0.0	2.7	0.2	3.3	0.3	5.2	0.5	0.1	0.0	8.3	0.6	10.6	0.5	2.2	0.1	5.9	0.3	0.8	0.1	5.8	0.3	0.8	0.1	1.2E+04	230.0	95.2	1.9	431.0	16.0
17-59-1-59	10.1	1.7	229.0	21.0	0.9	0.1	0.2	0.1	4.0	0.7	1.6	0.4	3.1	0.5	0.7	0.2	7.2	0.7	22.2	2.1	7.4	0.7	33.9	3.6	7.5	0.7	76.3	7.5	16.7	1.7	1.1E+04	270.0	51.7	7.1	369.0	15.0
17-59-1-60	22.8	3.2	241.0	51.0	1.0	0.1	0.0	0.0	2.0	0.3	2.3	0.5	3.8	0.7	0.2	0.0	7.1	0.6	22.9	3.9	7.5	1.6	32.8	7.9	6.9	1.8	70.0	18.0	14.1	3.9	1.2E+04	300.0	63.8	8.3	528.0	59.0
17-59-1-61	14.8	1.7	402.0	35.0	0.9	0.1	0.1	0.1	3.8	1.4	0.8	0.4	1.3	0.5	0.4	0.1	7.1	1.3	35.3	3.0	12.9	1.3	60.9	6.8	13.9	1.8	150.0	22.0	34.0	5.3	1.1E+04	260.0	54.0	17.0	356.0	19.0
17-59-1-62	19.4	2.0	48.7	1.4	0.8	0.1	0.0	0.0	2.1	0.2	2.8	0.4	5.1	0.6	0.1	0.0	11.5	0.9	10.0	0.5	1.4	0.1	3.0	0.3	0.4	0.0	2.7	0.3	0.4	0.0	1.2E+04	250.0	91.3	2.7	335.0	5.9
17-59-1-63	28.6	3.3	50.6	1.1	1.1	0.1	0.0	0.0	2.4	0.1	2.7	0.3	4.3	0.4	0.1	0.0	6.7	0.4	8.1	0.5	1.4	0.1	3.9	0.2	0.5	0.0	4.0	0.3	0.5	0.1	1.2E+04	290.0	94.4	2.0	465.0	8.4
17-59-1-64	29.8	2.4	106.3	4.9	1.2	0.1	0.0	0.0	3.0	0.2	5.5	0.5	8.8	0.8	0.3	0.0	16.1	1.2	17.6	1.1	3.4	0.2	8.8	0.6	1.2	0.1	8.9	0.8	1.4	0.1	1.2E+04	300.0	128.4	5.3	528.0	21.0
17-59-1-65	11.9	2.1	425.0	22.0	1.9	0.2	0.3	0.1	20.7	2.2	1.5	0.2	2.9	0.3	0.9	0.1	9.4	0.5	37.0	2.1	13.5	0.9	63.6	4.9	13.5	1.1	136.0	10.0	30.1	2.4	9.5E+03	340.0	56.9	3.3	147.0	24.0
17-59-1-66	20.4	2.5	52.4	2.5	0.9	0.1	0.0	0.0	2.3	0.2	2.6	0.3	3.9	0.4	0.2	0.0	7.3	0.4	8.3	0.5	1.7	0.1	4.4	0.4	0.6	0.1	4.3	0.5	0.7	0.1	1.2E+04	220.0	84.1	2.3	333.6	6.7
17-59-1-67	25.3	3.4	230.0	77.0	1.1	0.1	0.2	0.1	2.6	0.2	3.3	0.4	5.9	0.8	1.2	0.5	12.1	2.1	20.7	5.2	4.7	1.3	13.1	3.6	1.4	0.4	9.6	2.3	1.5	0.4	1.3E+04	300.0	99.0	2.6	502.0	17.0

17-59-1 - 68	22.5	2.6	41.3	2.1	0.8	0.1	0.0	0.0	1.5	0.2	1.9	0.3	3.8	0.5	0.1	0.0	8.7	0.6	8.5	0.4	1.2	0.1	2.7	0.3	0.3	0.0	2.3	0.3	0.3	0.0	1.2E+04	320.0	66.6	2.7	381.3	9.1
17-59-1 - 69	14.1	2.0	491.0	16.0	1.0	0.1	0.3	0.1	18.9	0.6	1.2	0.2	3.3	0.5	0.9	0.1	13.8	0.8	44.4	1.8	15.7	0.5	70.7	2.1	13.7	0.5	125.2	3.9	27.3	0.7	7.6E+03	210.0	81.2	2.0	118.2	2.8
17-59-1 - 70	10.5	1.7	625.0	31.0	0.9	0.1	0.1	0.0	17.2	0.5	1.7	0.2	5.2	0.5	1.1	0.1	18.7	1.5	58.4	3.5	20.4	1.2	90.6	4.5	17.7	0.9	162.7	6.9	34.9	1.6	7.6E+03	160.0	111.5	5.1	161.6	6.0
17-59-1 - 71	14.0	2.4	173.0	18.0	1.0	0.1	0.0	0.0	1.9	0.2	1.9	0.3	3.4	0.5	0.3	0.1	6.8	0.5	19.3	1.9	5.2	0.5	19.4	2.1	3.5	0.4	30.8	4.0	6.3	0.9	1.2E+04	320.0	59.9	4.6	413.0	27.0
17-59-1 - 72	11.6	1.8	287.0	37.0	2.2	0.5	0.1	0.0	2.6	0.5	3.2	0.9	5.5	1.3	0.3	0.1	13.1	1.8	31.8	3.4	9.4	1.2	36.5	6.1	7.2	1.2	66.0	13.0	13.8	3.0	1.1E+04	220.0	90.0	19.0	419.0	30.0
17-59-1 - 73	31.0	3.1	819.0	74.0	0.5	0.1	2.6	0.4	5.3	0.5	11.5	1.2	15.6	1.4	9.9	1.1	30.2	2.3	62.0	5.4	18.0	1.9	70.4	8.7	13.4	2.0	131.0	21.0	28.5	4.3	1.1E+04	400.0	74.7	5.0	424.0	44.0
17-59-1 - 74	10.3	1.5	891.0	73.0	2.6	0.1	0.5	0.2	4.5	0.2	2.2	0.7	4.7	1.0	3.5	0.9	20.4	2.0	75.7	3.9	27.9	1.2	123.6	4.6	23.7	0.8	214.1	6.4	45.0	1.2	7.5E+03	230.0	18.8	1.1	102.6	8.3
17-59-1 - 75	12.3	1.6	145.9	2.8	0.6	0.1	0.1	0.0	0.7	0.1	1.1	0.2	3.8	0.5	0.2	0.0	12.7	0.7	26.1	0.9	4.4	0.2	9.4	0.4	1.0	0.1	6.2	0.4	0.9	0.1	1.2E+04	270.0	31.5	3.0	329.0	7.3
17-59-1 - 76	25.5	4.4	670.0	140.0	1.5	0.1	2.6	0.6	10.4	1.7	14.1	3.2	17.4	3.2	8.4	2.0	31.4	5.4	53.7	9.8	14.4	2.7	50.9	9.0	8.7	1.5	81.0	13.0	16.2	2.6	1.2E+04	250.0	99.7	5.0	444.0	19.0
17-59-1 - 77	14.3	1.7	74.7	4.9	0.9	0.1	0.0	0.0	2.4	0.2	3.4	0.4	6.2	0.5	0.2	0.1	10.7	0.7	12.4	0.7	2.3	0.2	6.4	0.4	0.9	0.1	6.7	0.5	1.1	0.1	1.2E+04	280.0	95.0	2.4	323.6	7.1
17-59-1 - 78	14.4	1.7	274.0	19.0	0.7	0.1	0.0	0.0	0.3	0.1	0.3	0.1	0.8	0.2	0.2	0.1	5.9	0.7	29.8	2.7	8.2	0.5	27.1	2.7	4.5	0.6	35.7	5.4	7.1	1.3	1.1E+04	230.0	27.0	10.0	508.0	44.0
17-59-1 - 79	16.0	2.2	53.2	1.6	0.7	0.1	0.0	0.0	1.7	0.1	2.5	0.3	5.4	0.5	0.2	0.0	11.7	0.7	11.6	0.7	1.7	0.1	3.1	0.2	0.4	0.0	2.5	0.3	0.4	0.0	1.2E+04	310.0	77.2	2.3	412.0	14.0
17-59-1 - 80	30.6	2.9	201.0	61.0	0.9	0.1	0.1	0.1	2.7	0.1	4.7	0.5	7.0	0.7	1.0	0.4	13.7	2.0	20.2	3.4	4.4	0.9	11.7	2.3	1.6	0.3	10.1	1.6	1.6	0.2	1.2E+04	260.0	101.7	2.8	508.0	11.0
17-59-1 - 81	11.8	1.9	598.0	31.0	3.1	0.5	0.5	0.1	4.9	0.5	1.5	0.3	3.6	0.5	1.8	0.3	13.6	0.9	50.5	2.4	16.7	1.1	74.2	6.2	15.2	1.4	140.0	13.0	28.7	2.6	1.2E+04	250.0	92.4	7.7	397.0	14.0
17-59-1 - 82	13.4	2.4	422.0	61.0	1.7	0.3	0.8	0.2	2.8	0.6	4.0	1.0	5.6	1.3	2.5	0.7	14.5	1.6	41.2	4.8	12.0	1.6	48.0	6.9	9.4	1.4	88.0	14.0	17.4	2.8	1.2E+04	290.0	36.0	1.2	490.0	23.0
17-59-1 - 83	35.1	2.8	64.7	1.5	1.3	0.1	0.0	0.0	2.8	0.1	3.3	0.4	4.8	0.5	0.1	0.0	7.5	0.5	9.8	0.6	2.0	0.1	5.8	0.3	0.8	0.1	6.3	0.4	1.0	0.1	1.2E+04	250.0	102.9	2.3	291.7	6.6
17-59-1 - 84	32.0	2.7	57.8	1.5	1.3	0.1	0.0	0.0	2.7	0.1	2.8	0.3	4.2	0.4	0.1	0.0	6.9	0.5	8.7	0.4	1.9	0.1	5.2	0.3	0.8	0.1	5.3	0.3	0.8	0.1	1.2E+04	250.0	97.3	2.4	306.6	6.9
17-59-1 - 85	12.4	1.8	904.0	55.0	1.1	0.1	0.1	0.0	3.7	0.4	1.2	0.2	3.9	0.4	0.3	0.1	19.2	1.0	81.6	5.1	30.3	2.1	140.1	8.0	27.1	1.7	251.0	13.0	51.3	2.6	9.5E+03	320.0	91.2	6.4	219.0	21.0
17-59-1 - 86	15.3	2.2	1010.0	110.0	0.7	0.1	0.2	0.1	2.5	0.2	5.2	0.7	10.0	1.3	0.9	0.5	35.7	4.1	101.0	11.0	32.7	3.5	132.0	14.0	24.7	2.4	220.0	21.0	45.1	4.2	1.0E+04	290.0	144.0	19.0	317.0	73.0
17-59-1 - 87	10.7	2.0	632.0	37.0	2.9	0.3	0.5	0.2	4.0	0.5	2.7	0.8	5.3	1.1	1.8	0.7	16.0	1.6	59.5	3.7	21.7	1.5	96.5	6.5	19.7	1.3	181.0	11.0	37.3	2.4	1.0E+04	260.0	49.1	5.2	217.0	45.0
17-59-1 - 88	21.9	2.9	349.0	15.0	0.7	0.1	0.0	0.0	1.6	0.1	4.3	0.6	9.4	0.9	0.6	0.1	39.1	2.7	60.7	2.2	10.8	0.6	27.4	3.1	3.8	0.7	27.5	5.7	4.9	1.2	1.0E+04	280.0	87.0	5.2	285.5	8.1
17-59-1 - 89	18.5	2.6	758.0	72.0	1.8	0.3	6.8	1.9	13.9	1.8	8.9	1.3	13.0	1.9	7.2	1.3	23.9	3.2	67.2	6.3	21.1	1.7	91.6	6.7	19.4	1.5	195.0	17.0	41.0	3.7	1.1E+04	260.0	66.3	8.5	500.0	41.0
17-59-1 - 90	18.2	2.3	64.6	2.5	1.0	0.1	0.0	0.0	2.6	0.1	3.3	0.3	5.0	0.4	0.1	0.0	8.0	0.5	9.9	0.6	2.0	0.1	5.5	0.4	0.8	0.1	5.3	0.3	0.9	0.1	1.2E+04	260.0	95.8	2.1	342.1	7.0
17-59-1 - 91	28.1	2.8	71.6	6.7	0.9	0.1	0.0	0.0	1.6	0.2	2.6	0.5	5.1	0.6	0.2	0.0	13.1	0.9	14.2	1.0	2.2	0.2	5.8	1.1	0.9	0.2	7.1	2.0	1.4	0.4	1.2E+04	280.0	83.6	8.9	502.0	18.0
17-59-1 - 92	31.8	3.6	68.4	2.8	1.0	0.1	0.0	0.0	2.6	0.1	3.6	0.4	5.8	0.6	0.1	0.0	8.9	0.7	10.7	0.5	2.0	0.1	5.3	0.3	0.7	0.1	5.3	0.4	0.8	0.1	1.2E+04	280.0	100.1	2.0	519.0	10.0
17-59-1 - 93	31.5	2.9	78.9	1.9	0.9	0.1	0.1	0.0	2.7	0.1	3.5	0.4	5.1	0.3	0.2	0.0	9.3	0.6	12.8	0.6	2.5	0.1	7.3	0.4	1.1	0.1	8.8	0.4	1.4	0.1	1.2E+04	320.0	97.6	2.6	404.0	14.0
17-59-1 - 94	32.4	2.7	76.4	2.1	1.0	0.1	0.0	0.0	2.7	0.1	3.4	0.3	5.0	0.5	0.2	0.0	8.7	0.6	12.1	0.6	2.5	0.1	7.2	0.3	1.1	0.1	8.4	0.5	1.3	0.1	1.2E+04	270.0	101.8	3.2	408.0	20.0
17-59-1 - 95	16.6	2.0	473.0	24.0	2.0	0.2	0.0	0.0	14.6	0.6	0.9	0.2	3.0	0.3	0.4	0.1	11.7	0.9	45.5	2.6	15.7	0.9	67.7	3.8	13.7	0.8	123.5	5.3	23.9	1.2	9.6E+03	180.0	108.8	6.4	222.9	9.1
17-59-1 - 96	26.0	2.5	84.0	15.0	1.0	0.1	0.1	0.0	2.8	0.1	3.2	0.4	5.3	0.4	0.3	0.1	8.7	0.8	11.6	0.9	2.5	0.3	6.6	0.5	1.0	0.1	6.5	0.5	1.0	0.1	1.2E+04	270.0	88.8	2.2	288.3	5.0
17-59-1 - 97	49.0	29.0	1057.0	47.0	4.3	0.2	0.3	0.2	14.3	0.6	2.6	1.1	4.9	1.1	1.3	0.7	21.5	2.1	93.0	2.9	35.5	0.9	160.0	3.4	32.4	0.8	300.7	8.3	61.3	1.4	9.7E+03	220.0	168.4	4.5	343.4	7.8
17-59-1 - 98	28.3	3.0	78.0	1.5	1.1	0.1	0.0	0.0	2.4	0.1	3.1	0.3	5.4	0.4	0.2	0.0	9.2	0.5	12.2	0.5	2.5	0.1	7.4	0.4	1.0	0.1	7.3	0.4	1.2	0.1	1.2E+04	250.0	80.0	1.9	415.8	7.7
17-59-2 - 1	31.4	2.8	255.0	25.0	1.0	0.1	1.0	0.1	8.5	0.8	16.8	1.7	18.3	2.0	7.1	0.9	25.7	2.1	31.3	2.8	6.8	0.7	19.8	2.0	2.8	0.3	22.2	2.2	3.5	0.4	1.1E+04	290.0	77.8	6.2	380.9	8.9
17-59-2 - 2	16.1	2.0	363.0	24.0	0.6	0.1	0.1	0.0	0.6	0.1	1.5	0.3	4.3	0.4	1.9	0.4	22.3	1.6	43.5	2.0	10.0	0.5	34.1	2.6	6.2	0.5	57.1	4.8	10.3	0.8	1.1E+04	230.0	31.2	2.5	482.0	32.0
17-59-2 - 3	9.5	8.0	658.0	90.0	1.4	0.3	0.4	0.2	4.1	0.9	4.3	2.2	6.3	1.6	4.5	1.1	17.4	2.6	52.4	7.8	18.5	2.7	81.0	11.0	16.2	2.1	164.0	21.0	30.1	4.3	1.0E+04	470.0	71.0	15.0	385.0	36.0
17-59-2 - 4	18.3	2.2	576.0	52.0	2.0	0.2	0.0	0.0	27.0	2.6	1.1	0.2	2.3	0.3	0.5	0.1	10.6	0.6	43.0	3.0	18.2	1.7	92.0	9.5	21.2	2.2	238.0	26.0	55.0	6.0	9.5E+03	270.0	213.0	26.0	297.0	13.0
17-66-1 - 1	129.0	11.0	2560.0	200.0	4.5	0.3	34.2	3.0	95.3	5.7	85.1	8.3	67.3	6.5	219.0	20.0	163.0	15.0	235.0	19.0	59.7	4.3	196.0	13.0	31.7	1.8	249.0	12.0	47.1	2.2	1.0E+04	270.0	577.0	21.0	942.0	29.0
17-66-1 - 2	12.4	1.8	1610.0	110.0	1.6	0.2	192.0	85.0	224.0	83.0	109.0	40.0	28.6	7.7	6.8	1.0	56.4	3.4	167.0	10.0	54.2	3.7	218.0	15.0	42.1	2.9	369.0	24.0	69.0	4.9	1.1E+04	260.0	265.0	23.0	517.0	35.0
17-66-1 - 3	45.6	6.3	1080.0	120.0	2.0	0.2	3.4	0.9	37.1	2.1	17.6	3.0	23.1	4.0	25.1	6.7	59.2	9.4	120.0	15.0	35.4	3.5	129.0	11.0	22.9	1.6	194.0	12.0	36.6	2.1	9.4E+03	300.0	372.0	21.0	334.0	29.0
17-66-1 - 4	32.1	2.9	808.0	26.0	2.1	0.2	0.1	0.0	43.1	1.3	5.8	0.8	9.2	0.9	1.4	0.2	29.3	1.7	83.0	3.6	28.6	1.2	117.3	4.1	22.1	0.7	199.8	4.9	40.4	1.2	9.5E+03	280.0	525.0	22.0	371.0	10.0

17-66-1 - 5	19.0	2.5	382.8	8.2	1.7	0.1	0.0	0.0	15.6	0.5	0.3	0.1	0.9	0.2	0.1	0.0	6.2	0.4	30.6	1.1	12.6	0.4	57.8	1.4	12.8	0.4	123.1	2.8	25.5	0.7	1.1E+04	230.0	97.1	2.9	267.0	12.0
17-66-1 - 6	20.9	1.9	358.2	6.3	3.1	0.2	0.0	0.0	19.8	0.6	1.0	0.2	2.1	0.3	0.1	0.0	8.8	0.5	33.1	1.0	12.4	0.4	55.5	1.3	11.3	0.3	103.4	2.5	20.3	0.5	1.0E+04	210.0	168.1	3.1	224.5	4.9
17-66-1 - 7	17.2	2.5	246.0	25.0	1.5	0.2	0.0	0.0	6.6	1.4	0.6	0.2	1.5	0.2	0.2	0.0	8.6	0.5	28.5	2.0	8.4	0.9	29.9	3.7	5.9	0.8	51.2	8.0	10.0	1.6	1.1E+04	300.0	72.0	11.0	266.5	9.0
17-66-1 - 8	17.7	2.1	83.7	5.9	0.7	0.1	0.0	0.0	0.7	0.1	0.4	0.1	1.3	0.2	0.2	0.0	5.1	0.3	11.1	0.8	2.8	0.3	8.7	0.8	1.6	0.2	13.8	1.5	2.5	0.3	1.2E+04	250.0	29.2	1.0	254.2	6.1
17-66-1 - 9	33.9	5.5	1490.0	170.0	18.0	2.1	0.2	0.1	18.9	2.9	7.6	1.3	11.9	1.8	0.4	0.1	50.8	6.6	164.0	19.0	56.8	6.3	227.0	25.0	41.5	4.5	352.0	37.0	67.9	7.3	8.2E+03	390.0	226.0	36.0	226.0	18.0
17-66-1 - 10	23.1	2.7	791.0	50.0	8.1	1.5	0.1	0.0	4.0	1.2	0.7	0.3	2.1	0.6	0.2	0.1	13.9	2.3	73.5	5.3	26.6	1.8	106.6	7.8	20.5	1.9	169.0	17.0	31.1	3.5	1.1E+04	350.0	50.0	13.0	371.0	36.0
17-66-1 - 11	36.7	5.0	988.0	25.0	21.0	0.8	0.1	0.1	17.5	1.0	3.3	0.4	5.9	0.6	0.2	0.0	29.1	1.8	102.6	3.5	37.4	1.2	152.8	3.8	29.0	0.7	252.7	5.6	48.5	1.2	8.6E+03	370.0	154.4	6.7	185.7	5.9
17-66-1 - 12	25.2	2.3	791.0	18.0	5.8	0.3	1.0	0.2	51.7	1.4	5.7	0.7	8.0	0.6	7.1	1.1	26.4	1.3	78.0	2.7	27.5	1.0	114.0	3.4	22.2	0.8	201.9	7.6	38.1	1.2	9.4E+03	240.0	540.0	20.0	457.0	28.0
17-66-1 - 13	136.0	21.0	3260.0	320.0	1.6	0.1	15.2	3.3	53.5	6.2	54.3	9.2	69.9	9.8	146.0	31.0	219.0	25.0	343.0	37.0	91.3	8.7	289.0	27.0	43.1	3.6	327.0	27.0	58.0	4.7	9.0E+03	270.0	525.0	45.0	428.0	23.0
17-66-1 - 14	20.7	2.0	116.0	16.0	0.8	0.1	0.1	0.1	1.7	0.1	2.1	0.3	4.5	0.5	0.4	0.1	9.3	0.9	16.1	2.2	3.8	0.4	11.7	1.3	1.8	0.2	13.7	1.3	2.3	0.2	1.2E+04	270.0	64.0	2.5	664.0	18.0
17-66-1 - 15	107.0	13.0	1780.0	160.0	3.7	0.2	20.8	2.6	61.4	4.6	53.1	6.5	47.0	5.1	201.0	27.0	113.0	12.0	178.0	15.0	47.4	3.2	160.2	9.5	27.9	1.4	224.0	10.0	41.4	1.5	1.0E+04	250.0	488.8	9.6	943.0	23.0
17-66-1 - 16	13.8	2.6	377.0	14.0	1.8	0.1	130.0	81.0	110.0	57.0	46.0	27.0	15.6	8.5	0.6	0.1	14.6	3.2	36.4	1.8	12.9	0.6	54.8	2.2	11.0	0.4	106.4	4.1	21.0	0.8	9.1E+03	220.0	136.0	13.0	320.0	22.0
17-66-1 - 17	11.0	1.9	308.0	12.0	2.0	0.1	0.0	0.0	11.5	0.4	0.6	0.2	1.7	0.3	0.3	0.0	7.2	0.7	29.4	1.6	10.3	0.4	47.5	1.9	10.2	0.5	99.7	4.0	20.7	0.7	9.2E+03	240.0	109.8	4.8	291.0	14.0
17-66-1 - 18	29.5	4.9	2642.0	70.0	80.5	6.7	2.6	0.6	38.6	1.2	9.1	2.0	13.6	2.2	19.5	6.3	62.0	5.0	254.1	9.3	93.5	2.8	375.6	7.2	69.2	1.8	553.0	14.0	91.7	2.3	8.2E+03	200.0	461.0	34.0	768.0	22.0
17-66-1 - 19	18.3	2.3	276.0	30.0	1.7	0.2	0.0	0.0	3.6	0.5	0.5	0.2	1.4	0.3	0.1	0.0	7.9	0.5	28.3	2.2	9.4	1.1	39.4	5.4	8.0	1.1	76.0	11.0	15.2	2.3	1.1E+04	300.0	31.6	2.9	286.0	14.0
17-66-1 - 20	39.9	3.7	410.0	13.0	1.3	0.2	0.0	0.0	38.0	1.1	3.2	0.4	4.5	0.5	1.2	0.1	16.9	1.1	41.4	1.5	13.7	0.5	57.2	1.7	11.0	0.4	102.7	3.2	20.9	0.7	8.7E+03	200.0	321.0	16.0	225.0	13.0
17-66-1 - 21	29.9	3.0	269.0	15.0	1.2	0.1	0.0	0.0	30.8	1.9	1.2	0.2	2.5	0.3	0.5	0.1	9.6	0.7	25.7	1.7	9.1	0.5	38.5	2.0	7.8	0.5	71.1	3.7	15.3	0.6	9.1E+03	200.0	200.0	13.0	212.0	9.3
17-66-1 - 22	20.1	2.3	268.0	18.0	1.0	0.1	0.0	0.0	12.6	3.0	0.7	0.2	1.4	0.2	0.2	0.0	7.0	0.6	25.5	1.1	8.7	0.6	38.1	3.9	7.7	0.9	74.0	10.0	15.3	2.1	1.0E+04	360.0	80.0	15.0	286.0	26.0
17-66-1 - 23	35.9	3.5	330.0	33.0	1.6	0.2	0.0	0.0	9.5	1.1	0.6	0.1	1.0	0.2	0.1	0.0	5.8	0.5	28.4	3.0	11.0	1.1	49.2	4.5	10.3	0.8	95.8	7.5	18.0	0.9	1.1E+04	310.0	117.3	9.4	324.0	30.0
17-66-1 - 24	18.7	2.5	295.0	18.0	1.2	0.1	0.0	0.0	8.2	1.0	0.5	0.1	1.2	0.3	0.1	0.0	6.8	0.7	27.4	2.0	10.0	0.7	43.8	3.2	9.1	0.8	82.8	6.8	16.1	1.3	1.0E+04	280.0	96.1	8.7	231.0	22.0
17-66-1 - 25	13.5	2.0	778.0	17.0	0.6	0.1	0.1	0.0	0.6	0.1	1.6	0.3	3.9	0.5	0.5	0.2	24.9	1.2	88.8	2.5	27.6	0.8	101.1	2.6	18.5	0.6	160.7	6.4	29.9	1.0	1.1E+04	270.0	36.9	1.6	245.0	12.0
17-66-1 - 26	53.1	4.7	1229.0	54.0	1.4	0.1	5.3	0.6	17.4	1.4	20.1	2.2	21.5	2.8	42.9	4.0	53.6	6.0	122.4	8.0	39.4	1.7	164.8	5.6	32.9	0.9	292.2	8.1	56.0	1.3	1.0E+04	190.0	99.2	4.0	356.0	18.0
17-66-1 - 27	17.3	5.2	987.0	52.0	2.5	0.2	0.0	0.0	9.8	0.6	2.2	0.3	5.4	0.6	0.3	0.1	26.1	1.9	95.7	5.0	34.9	1.8	142.2	7.1	27.4	1.2	241.0	10.0	44.8	1.7	9.5E+03	280.0	206.0	14.0	420.0	21.0
17-66-1 - 28	8.8	1.6	980.0	85.0	2.5	0.2	0.0	0.0	9.9	0.4	2.1	0.3	5.4	0.5	0.4	0.1	25.5	2.3	95.1	7.8	34.6	2.6	143.0	10.0	27.1	1.9	234.0	15.0	45.2	2.8	9.8E+03	220.0	211.0	11.0	451.0	24.0
17-66-1 - 29	13.7	1.8	117.1	2.5	0.7	0.1	0.0	0.0	1.0	0.1	1.1	0.2	4.4	0.4	0.1	0.0	11.0	0.7	17.1	0.8	3.9	0.2	11.2	0.4	1.7	0.1	12.4	0.7	1.9	0.1	1.1E+04	250.0	40.8	3.6	685.0	25.0
17-66-1 - 30	21.7	2.2	77.9	5.0	0.8	0.1	0.0	0.0	2.0	0.1	2.0	0.3	4.3	0.4	0.2	0.0	8.1	0.6	11.4	0.8	2.5	0.2	6.9	0.7	1.1	0.1	7.2	0.7	1.1	0.1	1.2E+04	250.0	80.0	4.3	629.0	16.0
17-66-1 - 31	10.9	1.7	646.0	31.0	1.2	0.1	0.1	0.0	2.7	0.4	0.7	0.2	1.9	0.3	0.4	0.1	8.4	0.6	50.3	2.8	21.5	1.0	105.9	5.3	25.4	1.2	259.0	14.0	54.4	3.2	1.1E+04	210.0	40.4	3.8	401.0	23.0
17-66-1 - 32	45.3	9.9	1010.0	120.0	3.5	0.2	4.8	1.6	31.1	3.7	14.5	4.2	15.5	3.1	43.0	16.0	49.9	8.7	108.0	12.0	32.3	3.0	118.8	9.1	22.5	1.6	193.0	13.0	37.0	2.0	9.6E+03	230.0	362.0	24.0	626.0	11.0
17-66-1 - 33	11.8	1.9	467.0	85.0	1.2	0.1	0.1	0.1	0.9	0.1	0.7	0.2	2.5	0.4	0.2	0.0	10.9	0.8	44.9	7.2	15.9	2.9	72.0	14.0	15.5	3.0	150.0	29.0	30.5	6.0	1.2E+04	280.0	52.5	4.2	372.0	17.0
17-66-1 - 34	16.9	2.1	101.1	2.5	0.8	0.1	0.0	0.0	2.2	0.1	2.8	0.3	5.4	0.5	0.2	0.1	10.8	0.6	14.8	0.7	3.4	0.2	10.0	0.4	1.5	0.1	10.6	0.7	1.7	0.1	1.2E+04	230.0	90.2	1.9	856.0	18.0
17-66-1 - 35	14.5	1.7	765.0	15.0	2.1	0.1	0.7	0.1	25.1	0.8	2.6	0.4	4.4	0.5	1.2	0.2	18.7	1.0	70.1	2.2	25.7	0.6	117.0	2.6	24.7	0.6	236.5	5.2	49.5	1.4	9.0E+03	230.0	174.5	5.4	300.2	7.6
17-66-1 - 36	20.2	2.8	1113.0	79.0	2.2	0.2	1970.0	970.0	2500.0	1100.0	1210.0	550.0	199.0	83.0	5.2	1.3	84.0	25.0	113.0	10.0	36.9	2.5	160.2	9.5	33.3	1.7	311.0	16.0	63.7	2.9	8.6E+03	210.0	650.0	260.0	337.0	16.0
17-66-1 - 37	23.8	2.2	76.0	1.8	0.9	0.1	0.1	0.1	2.0	0.2	1.9	0.3	4.9	0.5	0.2	0.1	9.1	0.6	11.4	0.5	2.7	0.1	8.2	0.4	1.5	0.1	11.6	0.7	1.9	0.1	1.2E+04	270.0	64.9	1.4	743.0	15.0
17-66-1 - 38	24.4	3.6	1035.0	58.0	1.9	0.2	3.2	0.6	5.7	0.7	15.8	2.4	16.4	1.9	18.4	3.2	43.8	3.7	122.1	7.8	35.2	2.0	139.8	6.6	29.9	1.3	288.0	9.8	57.0	2.0	1.1E+04	260.0	80.4	3.9	798.0	25.0
17-66-1 - 39	11.9	1.7	734.0	72.0	1.0	0.1	0.3	0.1	22.6	3.3	4.9	0.7	9.7	1.4	2.8	0.5	29.2	3.4	74.1	7.5	23.8	2.4	102.0	11.0	21.5	2.3	206.0	22.0	40.7	4.4	1.0E+04	300.0	144.0	13.0	529.0	22.0
17-66-2 - 1	14.6	1.8	354.0	35.0	1.4	0.1	0.0	0.0	11.8	1.5	0.7	0.2	1.8	0.5	0.3	0.1	6.7	0.7	30.0	2.5	11.5	1.2	54.0	6.1	12.0	1.4	116.0	14.0	24.8	3.1	9.6E+03	280.0	52.1	3.1	238.0	55.0
17-66-2 - 2	11.0	1.5	382.0	49.0	1.1	0.1	0.0	0.0	3.2	0.8	1.5	0.3	2.8	0.5	0.7	0.1	12.7	1.1	45.6	4.9	12.4	1.7	48.8	7.8	10.0	1.8	98.0	18.0	19.1	3.6	1.1E+04	230.0	57.3	8.0	496.0	39.0
17-66-2 - 3	24.8	2.9	1012.0	70.0	1.4	0.1	0.6	0.1	11.0	1.2	8.7	0.9	10.9	1.1	10.4	1.1	34.6	2.6	100.3	7.3	31.6	2.4	133.0	11.0	26.4	2.1	244.0	17.0	55.6	3.8	9.2E+03	240.0	135.0	21.0	366.0	17.0
17-66-2 - 4	15.1	2.3	506.0	24.0	0.7	0.1	0.0	0.0	1.4	0.2	2.7	0.3	7.9	0.7	0.3	0.1	36.0	2.6	76.1	4.3	16.6	0.9	51.1	2.3	8.3	0.3	67.1	3.0	12.7	0.8	1.0E+04	220.0	72.8	3.5	318.0	10.0
17-66-2 - 5	17.5	3.2	1260.0	460.0	0.9	0.1	0.3	0.2	5.5	0.9	10.7	5.4	13.0	7.0	7.8	4.8	41.0	16.0	138.0	48.0	36.0	11.0	131.0	30.0	22.3	4.0	191.0	35.0	33.4	4.9	9.7E+03	470.0	72.0	11.0	286.0	20.0

17-66-2 - 6	15.3	2.3	114.0	18.0	0.8	0.1	0.0	0.0	0.9	0.1	0.8	0.2	2.9	0.3	0.2	0.0	10.2	0.8	16.9	1.6	3.8	0.6	12.3	2.8	2.2	0.6	21.7	6.7	4.3	1.4	1.1E+04	210.0	52.2	2.5	445.0	23.0
17-66-2 - 7	17.5	2.4	951.0	64.0	2.6	0.3	0.0	0.0	4.5	0.4	2.2	0.4	4.9	0.7	0.5	0.1	20.4	1.8	87.9	6.6	32.8	2.3	145.0	10.0	28.7	2.1	260.0	18.0	52.2	3.5	8.7E+03	300.0	98.0	12.0	206.0	29.0
17-66-2 - 8	13.5	2.6	161.0	13.0	0.6	0.1	0.0	0.0	0.9	0.2	0.8	0.4	2.4	0.7	0.3	0.1	8.6	0.8	23.2	2.1	4.9	0.5	14.8	1.4	2.6	0.3	21.2	2.6	4.0	0.6	1.1E+04	350.0	31.7	5.0	325.0	23.0
17-66-2 - 9	25.0	19.0	380.0	220.0	0.4	0.3	51000.0	41000.0	170000.0	130000.0	46000.0	37000.0	6200.0	4900.0	250.0	190.0	2300.0	1700.0	220.0	160.0	20.0	12.0	34.0	19.0	2.2	1.0	13.4	5.3	2.2	0.8	9.3E+03	750.0	18000.0	14000.0	910.0	520.0
17-66-2 - 10	0.0	0.0	2890.0	910.0	0.0	0.0	400000.0	150000.0	960000.0	350000.0	400000.0	140000.0	82000.0	22000.0	3080.0	640.0	19900.0	7000.0	1710.0	550.0	111.0	36.0	149.0	54.0	8.7	6.3	60.0	29.0	4.7	3.2	5.5E+03	1200.0	111000.0	47000.0	4500.0	1500.0
17-66-2 - 11	10.1	1.6	480.0	130.0	1.6	0.4	0.1	0.0	12.0	4.8	2.4	0.3	5.5	0.5	1.4	0.3	19.1	1.1	54.0	10.0	16.3	4.5	67.0	22.0	14.1	5.0	134.0	49.0	29.0	11.0	1.1E+04	290.0	120.0	20.0	481.0	24.0
17-66-2 - 12	12.2	2.0	460.3	7.2	4.2	0.2	0.0	0.0	10.8	0.3	0.7	0.2	1.7	0.3	0.1	0.0	9.1	0.5	40.2	1.1	15.2	0.4	70.0	1.6	14.6	0.4	135.6	2.4	27.1	0.6	9.7E+03	200.0	72.1	1.5	157.9	4.3
17-66-2 - 13	20.7	2.8	452.0	18.0	3.5	0.2	0.0	0.0	10.7	0.4	1.0	0.2	2.1	0.3	0.1	0.0	9.4	0.7	41.2	1.8	15.1	0.7	68.1	2.6	13.7	0.5	128.8	5.0	25.9	1.0	9.1E+03	160.0	68.8	1.8	128.3	4.1
17-66-2 - 14	14.9	1.4	233.0	12.0	0.7	0.1	0.0	0.0	0.2	0.0	0.3	0.1	1.5	0.2	0.3	0.1	12.5	0.6	41.1	2.1	7.5	0.4	16.5	0.9	1.9	0.1	12.6	0.7	1.8	0.1	1.1E+04	170.0	9.3	0.7	287.9	8.1
17-66-2 - 15	11.5	2.0	850.0	230.0	0.8	0.1	0.5	0.2	1.3	0.3	8.3	2.7	6.9	2.1	7.0	2.2	28.3	8.5	91.0	23.0	26.0	6.6	100.0	25.0	19.0	4.6	178.0	44.0	34.0	8.4	1.1E+04	230.0	12.4	1.3	352.0	15.0
17-66-2 - 16	17.0	2.1	704.0	58.0	1.8	0.2	0.2	0.1	17.7	1.8	5.2	0.8	8.7	0.9	2.3	0.3	25.9	2.5	76.1	6.8	23.2	2.1	94.5	8.5	19.1	1.7	177.0	16.0	35.5	3.3	8.9E+03	240.0	162.0	11.0	507.0	29.0
17-66-2 - 17	50.3	7.2	3040.0	440.0	2.5	0.3	0.1	0.0	40.9	6.1	15.6	2.5	25.7	3.9	12.8	2.0	99.0	14.0	305.0	45.0	103.0	15.0	420.0	63.0	78.0	12.0	700.0	110.0	137.0	21.0	7.6E+03	560.0	240.0	35.0	263.0	21.0
17-66-2 - 18	14.9	1.8	336.0	55.0	0.7	0.1	0.0	0.0	0.6	0.1	0.5	0.2	1.7	0.2	0.2	0.0	10.2	0.8	39.7	4.9	11.1	1.9	43.1	8.6	8.1	1.8	76.0	18.0	14.8	3.5	1.1E+04	230.0	25.9	2.5	355.0	13.0
17-66-2 - 19	NAN	NAN	NAN	NAN	NAN	NAN	NAN	NAN	NAN	NAN	NAN	NAN	NAN	NAN	NAN	NAN	NAN	NAN	NAN	NAN	NAN	NAN	NAN	NAN	NAN	NAN	NAN	NAN	NAN	NAN	NAN	NAN	NAN	NAN	NAN	NAN
17-66-2 - 20	14.5	1.9	108.2	7.6	0.8	0.1	0.0	0.0	1.2	0.2	1.5	0.3	2.9	0.4	0.3	0.1	10.9	1.0	18.9	1.6	3.5	0.3	8.8	0.6	1.1	0.1	8.4	0.8	1.2	0.1	1.1E+04	340.0	53.9	4.3	373.0	17.0
17-66-2 - 21	15.9	1.9	1387.0	50.0	9.6	0.6	0.2	0.1	21.0	1.1	5.8	0.7	8.8	0.6	1.8	0.7	34.7	1.9	132.7	5.6	47.3	2.1	205.9	8.3	40.3	1.7	362.0	13.0	71.4	2.7	9.9E+03	210.0	179.4	8.3	320.8	9.3
17-66-2 - 22	13.3	2.1	529.0	21.0	1.7	0.2	0.0	0.0	42.0	1.1	3.1	0.4	5.1	0.7	1.2	0.2	16.6	1.1	51.5	2.4	17.6	0.8	74.1	2.9	14.9	0.6	138.3	5.6	28.0	1.2	7.2E+03	190.0	148.1	8.5	119.0	10.0
17-66-2 - 23	17.0	2.3	645.0	54.0	1.3	0.2	1.0	0.4	7.0	1.9	12.1	3.9	10.9	3.2	13.8	5.1	22.4	4.0	70.9	7.7	21.5	2.0	92.7	7.5	20.8	1.6	223.0	16.0	45.6	3.5	1.1E+04	250.0	89.0	9.3	825.0	41.0
17-66-2 - 24	16.0	2.1	1770.0	190.0	0.7	0.1	0.6	0.1	2.8	0.5	9.1	1.3	11.4	1.4	6.0	0.8	48.0	5.1	176.0	18.0	53.5	6.2	206.0	27.0	37.8	5.3	335.0	47.0	63.8	9.3	1.0E+04	390.0	68.0	9.1	303.0	39.0
17-66-2 - 25	11.4	1.7	591.0	43.0	1.1	0.1	0.0	0.0	12.1	0.9	1.6	0.3	4.0	0.5	0.9	0.1	15.3	1.1	51.2	3.9	18.6	1.3	84.0	6.2	18.0	1.4	176.0	12.0	38.5	2.7	7.8E+03	230.0	162.0	19.0	256.0	20.0
17-66-2 - 26	10.6	1.7	253.0	26.0	0.8	0.1	0.0	0.0	0.5	0.1	0.7	0.2	1.4	0.2	0.3	0.1	8.4	0.5	32.5	2.2	8.0	0.9	28.2	4.4	5.5	1.1	56.0	12.0	11.5	2.7	1.1E+04	250.0	25.2	2.3	380.0	31.0
17-66-2 - 27	13.7	2.0	472.0	30.0	1.6	0.2	0.1	0.0	11.5	0.8	2.1	0.5	4.1	0.8	2.2	0.7	11.5	0.9	43.9	2.5	15.7	1.0	69.7	4.3	14.6	0.9	145.7	8.8	30.4	1.9	9.0E+03	270.0	105.1	5.5	394.0	14.0
17-66-2 - 28	13.5	2.1	542.0	22.0	2.0	0.1	0.0	0.0	13.2	0.6	1.0	0.2	2.5	0.4	0.2	0.0	11.8	0.9	48.8	2.5	18.3	0.9	80.9	3.5	16.1	0.7	152.9	6.2	29.8	1.0	8.1E+03	170.0	70.3	3.7	116.7	4.5
17-66-2 - 29	10.1	1.7	930.0	110.0	2.9	0.3	0.1	0.0	28.8	3.2	2.1	0.3	5.9	0.4	1.1	0.1	24.6	1.8	88.0	10.0	31.0	3.8	136.0	17.0	26.6	3.5	247.0	33.0	48.6	6.5	9.1E+03	300.0	205.0	22.0	483.0	15.0
17-66-2 - 30	18.0	1.9	256.0	34.0	2.0	0.2	0.0	0.0	11.7	2.6	1.0	0.3	2.0	0.5	0.5	0.1	7.5	1.6	22.5	3.6	7.8	1.2	35.7	4.6	7.7	0.8	84.6	7.8	20.1	1.7	1.1E+04	200.0	86.0	12.0	405.0	20.0
17-66-2 - 31	14.4	2.2	329.0	54.0	0.9	0.1	0.1	0.0	1.8	0.5	0.6	0.3	1.6	0.3	0.3	0.1	9.8	1.0	38.9	3.5	11.0	1.9	44.0	12.0	9.1	2.7	90.0	29.0	18.7	6.3	1.1E+04	200.0	32.3	8.6	353.0	38.0
17-66-2 - 32	17.4	2.1	1530.0	210.0	0.8	0.1	0.3	0.1	2.9	0.4	4.9	0.7	7.6	0.7	3.3	1.0	31.9	2.8	138.0	18.0	50.2	7.0	215.0	31.0	42.5	6.3	403.0	59.0	78.0	12.0	9.8E+03	270.0	117.0	9.2	345.0	28.0
17-66-2 - 33	16.3	3.5	1950.0	240.0	1.7	0.2	0.2	0.1	8.3	0.9	9.3	1.9	12.8	2.1	5.2	1.3	54.7	8.2	189.0	23.0	61.5	6.6	246.0	22.0	44.2	3.5	393.0	28.0	75.7	5.1	7.4E+03	260.0	168.0	22.0	263.0	31.0
17-66-2 - 34	19.9	4.3	1180.0	180.0	1.5	0.2	0.0	0.0	6.4	1.1	4.1	1.0	7.3	1.4	1.4	0.3	31.9	6.0	120.0	18.0	42.0	6.5	178.0	28.0	33.1	5.0	306.0	45.0	60.1	8.7	8.2E+03	510.0	129.0	25.0	266.0	33.0
17-66-2 - 35	19.5	2.1	1344.0	50.0	1.9	0.1	0.1	0.0	13.2	0.5	3.3	0.4	8.1	0.6	1.2	0.3	35.0	1.8	131.1	6.0	46.4	2.1	190.3	7.7	36.0	1.4	326.0	14.0	61.0	2.7	9.0E+03	170.0	474.0	23.0	619.0	17.0
17-66-2 - 36	17.4	3.0	927.0	91.0	1.7	0.2	0.3	0.1	31.1	4.1	5.3	1.2	7.2	0.9	5.7	1.7	24.4	1.9	86.5	8.2	31.9	3.3	144.0	15.0	28.8	3.1	284.0	31.0	59.1	6.7	8.2E+03	310.0	89.0	10.0	308.0	62.0
17-66-2 - 37	26.5	3.5	1496.0	50.0	2.7	0.1	6.1	3.5	53.0	10.0	19.9	9.1	12.3	2.6	1.9	0.2	36.5	2.1	137.5	5.6	51.5	1.9	229.5	8.1	45.0	1.6	434.0	16.0	87.1	3.1	9.1E+03	210.0	191.1	9.5	313.0	30.0
17-66-2 - 38	36.2	3.4	977.0	25.0	1.1	0.1	0.0	0.0	5.3	0.2	1.3	0.2	3.7	0.4	0.2	0.0	18.2	0.9	88.3	2.8	34.1	0.9	154.3	3.5	30.4	0.8	286.9	7.0	55.6	1.2	1.0E+04	200.0	143.6	5.7	323.6	7.6
17-66-2 - 39	14.9	2.0	472.0	15.0	4.6	0.2	0.0	0.0	15.9	0.6	1.2	0.2	2.8	0.3	0.1	0.0	11.1	0.6	44.0	1.5	15.9	0.6	72.1	2.4	14.4	0.6	136.6	4.9	26.7	1.0	8.8E+03	170.0	153.4	3.3	378.0	12.0
17-66-2 - 40	35.9	3.6	1189.0	40.0	1.1	0.1	0.8	0.3	9.5	1.5	8.0	2.4	10.2	2.0	19.8	6.9	32.5	3.5	110.7	3.7	39.7	1.9	168.8	9.8	32.7	2.2	302.0	21.0	58.2	4.2	1.0E+04	230.0	140.0	8.4	426.0	13.0
17-66-2 - 41	26.9	3.9	940.0	130.0	3.2	0.3	0.0	0.0	30.2	3.3	3.6	0.8	6.1	1.0	1.6	0.3	27.4	4.3	97.0	14.0	34.1	4.7	143.0	19.0	26.7	3.3	247.0	29.0	48.2	5.4	8.1E+03	190.0	120.0	21.0	69.9	7.4

17-66-2 - 42	18.9	2.4	379.0	10.0	2.2	0.1	0.0	0.0	14.0	0.4	0.9	0.2	1.4	0.2	0.4	0.1	8.0	0.5	35.1	1.1	13.4	0.4	59.6	1.8	11.7	0.4	118.2	3.3	23.7	0.6	8.2E+03	160.0	29.8	1.4	35.1	1.1
17-66-2 - 43	14.6	2.3	2157.0	88.0	1.7	0.1	0.3	0.1	3.7	0.4	4.6	0.9	6.4	1.0	3.5	0.8	31.0	2.4	184.4	8.7	69.1	3.0	303.0	13.0	61.5	2.5	588.0	24.0	111.6	4.5	1.2E+04	240.0	135.9	6.1	1018.0	52.0
17-72-1 - 1	26.8	4.6	879.0	28.0	2.5	0.2	1.8	0.3	12.1	1.3	6.6	0.6	8.1	0.8	5.1	0.4	30.6	1.9	97.7	4.2	28.5	0.9	125.8	4.4	28.0	1.5	286.0	20.0	59.8	4.8	1.1E+04	330.0	125.0	13.0	681.0	48.0
17-72-1 - 2	24.9	8.6	409.0	40.0	1.4	0.2	0.0	0.0	2.4	0.6	0.7	0.2	1.7	0.3	0.3	0.1	9.4	0.8	40.7	3.1	13.3	1.5	63.9	7.8	15.1	1.7	168.0	19.0	35.4	4.3	1.1E+04	250.0	35.4	6.0	533.0	46.0
17-72-1 - 3	13.3	2.3	215.4	8.5	0.6	0.1	0.1	0.0	0.4	0.1	1.4	0.3	3.7	0.4	1.0	0.4	15.7	0.9	33.0	1.4	7.0	0.3	20.5	1.1	3.1	0.2	22.8	1.5	3.5	0.2	1.1E+04	240.0	25.5	1.1	565.0	12.0
17-72-1 - 4	10.3	1.4	1194.0	55.0	1.8	0.1	0.0	0.0	16.8	1.0	2.0	0.3	4.5	0.5	0.5	0.1	24.4	1.8	109.0	5.3	41.7	2.0	187.7	8.4	38.7	1.8	356.0	16.0	72.9	3.1	9.2E+03	200.0	156.0	16.0	197.0	22.0
17-72-1 - 5	15.4	1.9	153.5	7.5	0.7	0.1	0.2	0.1	0.3	0.0	1.3	0.2	3.0	0.3	0.4	0.1	10.7	0.6	23.4	1.0	4.9	0.3	14.3	1.1	2.4	0.3	22.1	2.9	4.5	0.7	1.2E+04	300.0	30.6	1.4	447.0	16.0
17-72-1 - 6	10.7	1.8	123.0	6.6	0.6	0.0	0.0	0.0	0.2	0.0	0.7	0.2	2.2	0.3	0.0	0.0	9.5	0.6	20.8	0.7	3.8	0.2	10.5	1.0	1.8	0.2	14.5	2.4	2.4	0.4	1.2E+04	240.0	22.4	1.6	482.4	9.6
17-72-1 - 7	22.0	3.1	238.0	26.0	1.2	0.2	1.0	0.3	2.4	0.5	4.3	0.9	5.3	0.5	4.7	1.2	16.6	1.6	37.3	4.7	8.2	1.0	24.3	2.9	4.2	0.6	35.3	5.7	5.8	1.0	1.1E+04	240.0	27.3	1.6	643.0	36.0
17-72-1 - 8	14.9	2.1	1040.0	160.0	0.8	0.1	0.5	0.2	1.4	0.3	4.5	1.1	10.0	2.0	0.6	0.2	49.8	9.0	133.0	21.0	34.5	5.4	117.0	17.0	21.2	3.0	187.0	27.0	36.5	5.6	1.1E+04	290.0	89.0	19.0	278.0	40.0
17-72-1 - 9	15.4	2.1	1160.0	230.0	0.8	0.1	1.0	0.4	2.0	0.5	5.7	1.7	11.2	3.0	1.0	0.3	51.0	12.0	142.0	31.0	38.1	8.0	132.0	24.0	24.4	3.8	225.0	30.0	44.1	5.7	1.1E+04	340.0	102.0	29.0	277.0	25.0
17-72-1 - 10	14.1	2.3	683.0	46.0	2.3	0.1	17.0	9.9	19.0	8.5	8.9	4.6	6.2	1.5	1.2	0.3	21.4	3.2	72.5	6.2	23.9	1.8	100.5	6.6	21.3	1.2	198.0	11.0	39.7	2.0	1.1E+04	380.0	163.0	20.0	665.0	27.0
17-72-1 - 11	13.3	1.9	278.0	27.0	0.6	0.1	0.2	0.1	0.3	0.0	0.9	0.2	2.1	0.3	0.8	0.1	10.0	0.6	32.4	2.4	8.8	0.9	32.5	3.7	6.7	0.8	61.5	6.9	12.1	1.3	1.2E+04	260.0	18.4	1.3	513.0	13.0
17-72-1 - 12	11.5	1.9	527.0	53.0	2.1	0.2	1.1	0.2	2.3	0.4	2.7	0.4	2.7	0.4	1.3	0.2	12.3	1.0	51.0	5.0	16.4	1.7	75.4	7.6	18.6	1.9	209.0	21.0	45.2	4.5	1.2E+04	230.0	38.7	2.4	467.0	41.0
17-72-1 - 13	16.6	2.3	700.0	150.0	1.2	0.1	0.7	0.2	1.3	0.2	1.5	0.4	3.1	0.4	0.6	0.2	13.6	1.0	61.0	11.0	22.2	4.9	105.0	26.0	24.6	6.3	248.0	65.0	50.0	14.0	1.2E+04	270.0	36.3	1.2	620.0	37.0
17-72-1 - 14	8.3	1.6	163.9	4.0	0.5	0.1	0.2	0.1	0.3	0.0	1.1	0.2	3.3	0.4	0.1	0.0	14.8	0.9	29.8	1.3	5.6	0.2	12.8	0.5	1.7	0.1	11.6	0.6	1.7	0.1	1.2E+04	280.0	26.5	1.4	381.0	19.0
17-72-1 - 15	9.6	1.1	262.8	6.1	0.9	0.1	0.0	0.0	0.8	0.1	0.8	0.2	1.9	0.3	0.2	0.0	8.5	0.6	25.9	0.8	8.5	0.3	38.6	1.5	9.7	0.4	102.8	5.7	21.8	1.3	1.1E+04	270.0	37.7	1.2	467.0	16.0
17-72-1 - 16	12.9	1.9	128.0	4.2	0.7	0.1	0.1	0.0	0.2	0.0	0.7	0.2	2.7	0.4	0.1	0.0	11.6	0.6	19.7	0.9	4.2	0.2	12.5	0.7	1.9	0.1	13.8	0.8	2.2	0.1	1.1E+04	320.0	28.0	1.0	707.0	19.0
17-72-1 - 17	8.8	1.6	558.0	26.0	1.2	0.2	0.1	0.0	4.2	0.3	0.9	0.2	2.0	0.3	0.1	0.0	11.1	0.8	49.4	2.2	18.8	0.9	85.4	4.2	17.8	0.9	170.0	8.3	35.3	1.8	1.0E+04	250.0	80.4	4.6	258.0	35.0
17-72-1 - 18	16.9	3.0	1573.0	82.0	1.4	0.1	0.8	0.2	4.9	0.3	3.6	0.5	5.7	0.5	3.5	0.9	30.8	2.1	138.6	7.8	53.0	3.0	241.0	12.0	48.9	2.2	461.0	18.0	94.7	3.5	9.9E+03	220.0	98.8	5.6	277.0	24.0
17-72-1 - 19	15.6	2.2	1680.0	120.0	1.2	0.1	1.0	0.3	5.7	0.4	6.4	0.8	8.2	0.8	4.0	1.0	39.0	3.2	159.0	12.0	56.8	4.3	244.0	17.0	47.9	3.1	425.0	27.0	82.0	5.1	1.0E+04	260.0	250.0	33.0	462.0	33.0
17-72-1 - 20	10.8	1.8	477.0	81.0	1.2	0.1	0.0	0.0	25.9	2.6	1.5	0.5	3.0	0.8	0.9	0.3	12.3	2.9	44.0	8.3	16.7	3.0	72.0	12.0	15.1	2.4	142.0	21.0	29.3	4.0	9.1E+03	330.0	114.0	12.0	160.0	16.0
17-72-1 - 21	20.7	2.7	730.0	64.0	2.7	0.2	0.4	0.1	17.9	0.7	2.6	0.5	6.4	1.5	2.1	0.8	27.4	6.8	74.6	9.0	24.8	2.0	101.3	5.5	19.6	0.6	177.4	5.1	34.7	0.9	9.7E+03	230.0	317.0	13.0	392.0	19.0
17-72-1 - 22	10.0	1.9	120.2	2.4	0.5	0.1	0.0	0.0	0.1	0.0	0.7	0.2	2.0	0.3	0.0	0.0	11.0	0.6	25.4	1.0	4.3	0.2	8.1	0.4	1.0	0.1	6.5	0.6	0.9	0.1	1.2E+04	260.0	17.4	2.7	369.0	16.0
17-72-1 - 23	16.0	2.0	196.0	23.0	0.6	0.1	0.1	0.0	0.7	0.2	0.9	0.2	2.4	0.3	0.1	0.0	11.9	0.8	25.4	1.7	6.2	0.7	22.9	4.2	4.9	1.2	52.0	15.0	10.3	3.1	1.2E+04	260.0	34.2	3.7	536.0	21.0
17-72-1 - 24	17.3	2.1	159.9	3.5	0.7	0.1	0.2	0.1	0.4	0.1	0.9	0.2	3.5	0.4	0.2	0.1	13.9	0.8	23.8	0.8	5.4	0.2	15.7	0.5	2.4	0.1	16.6	0.7	2.6	0.1	1.1E+04	270.0	30.2	0.7	796.0	19.0
17-72-1 - 25	12.5	2.1	212.0	27.0	0.9	0.1	0.0	0.0	0.2	0.0	1.0	0.2	2.2	0.3	0.1	0.0	9.3	0.6	24.9	2.0	6.6	0.8	28.5	4.7	6.7	1.4	71.0	15.0	14.7	3.2	1.2E+04	280.0	36.7	2.6	569.0	24.0
17-72-1 - 26	14.6	2.9	1370.0	210.0	0.9	0.1	0.1	0.1	1.1	0.2	2.4	0.6	7.1	1.4	0.3	0.1	38.6	6.6	144.0	23.0	48.1	7.8	194.0	30.0	38.6	5.5	350.0	47.0	69.1	9.3	1.2E+04	390.0	77.0	13.0	468.0	27.0
17-72-1 - 27	39.3	5.1	744.0	78.0	1.6	0.1	1.4	0.2	28.6	1.3	9.2	1.5	12.3	1.8	9.6	1.4	43.1	6.5	81.5	9.9	23.4	2.4	82.3	6.0	15.2	1.0	125.8	6.3	24.0	1.2	8.4E+03	180.0	180.8	5.4	206.5	8.5
17-72-1 - 28	36.1	3.6	1000.0	120.0	1.6	0.1	1.3	0.2	22.1	1.2	7.8	1.1	13.3	1.9	11.8	1.4	55.0	7.1	112.0	14.0	30.8	3.4	108.0	10.0	18.7	1.8	153.0	12.0	28.2	2.2	8.6E+03	320.0	144.9	7.7	189.8	7.4
17-72-1 - 29	24.9	3.8	613.0	53.0	1.5	0.1	0.8	0.4	13.6	2.7	3.6	1.2	5.7	1.7	6.9	3.1	21.9	4.4	62.1	6.4	19.5	1.7	76.2	6.4	13.8	1.1	126.0	12.0	23.9	2.3	1.0E+04	440.0	119.0	22.0	449.0	53.0
17-72-1 - 30	22.2	2.8	576.0	35.0	1.7	0.1	0.3	0.2	22.6	2.7	2.2	0.7	4.3	0.7	1.8	1.1	17.0	1.4	56.3	3.3	19.6	1.1	78.4	4.4	15.2	0.8	135.3	7.5	26.4	1.7	9.4E+03	320.0	209.0	21.0	313.0	11.0
17-72-2 - 1	18.0	2.3	158.2	3.4	0.6	0.1	0.0	0.0	0.3	0.1	1.1	0.2	3.2	0.4	0.1	0.0	12.0	0.7	25.6	1.1	5.3	0.2	13.5	0.7	1.9	0.1	13.4	0.8	2.0	0.1	1.1E+04	300.0	30.3	2.1	514.0	18.0
17-72-2 - 2	9.0	1.5	361.0	27.0	0.7	0.1	0.0	0.0	1.6	0.4	0.6	0.2	1.2	0.3	0.2	0.1	7.6	0.8	32.4	1.7	10.7	0.8	51.7	4.8	12.4	1.3	132.0	14.0	27.1	3.1	1.1E+04	260.0	31.2	4.9	360.0	24.0
17-72-2 - 3	10.9	1.4	119.0	3.1	0.6	0.1	0.0	0.0	0.2	0.0	1.4	0.2	3.3	0.3	0.0	0.0	10.8	0.7	19.8	0.7	4.0	0.2	10.7	0.4	1.5	0.1	9.9	0.7	1.5	0.1	1.2E+04	290.0	46.5	1.4	619.0	16.0
17-72-2 - 4	12.2	1.9	691.0	76.0	1.7	0.2	0.0	0.0	10.5	1.3	1.0	0.3	2.9	0.5	0.4	0.1	14.5	1.8	62.6	6.8	23.5	2.7	110.0	13.0	23.2	2.7	227.0	25.0	47.8	5.3	9.5E+03	220.0	56.3	7.5	301.0	12.0
17-72-2 - 5	49.0	21.0	750.0	180.0	1.0	0.2	0.0	0.0	0.6	0.1	1.5	0.3	3.7	0.6	0.2	0.1	19.0	2.5	73.0	15.0	26.0	6.2	113.0	29.0	23.1	6.0	216.0	56.0	43.0	11.0	1.1E+04	260.0	47.1	5.6	656.0	27.0
17-72-2 - 6	14.9	2.2	158.7	8.8	0.6	0.1	0.0	0.0	0.2	0.0	1.0	0.2	3.3	0.5	0.1	0.0	12.2	0.8	22.7	1.2	5.3	0.4	15.5	1.0	2.3	0.2	16.8	1.2	2.6	0.2	1.1E+04	270.0	30.2	1.1	755.0	22.0
17-72-2 - 7	13.7	2.4	930.0	190.0	1.0	0.1	0.0	0.0	15.1	3.4	2.6	0.5	6.1	1.1	1.6	0.3	23.3	3.3	85.0	15.0	31.6	6.4	139.0	30.0	28.6	6.2	272.0	60.0	58.0	13.0	9.4E+03	390.0	81.0	12.0	404.0	59.0
17-72-2 - 8	16.2	2.3	129.0	3.9	0.6	0.1	0.0	0.0	0.2	0.0	0.8	0.2	2.4	0.4	0.2	0.1	9.9	0.9	21.2	0.7	4.1	0.2	10.7	0.8	1.5	0.1	10.5	1.0	1.7	0.2	1.1E+04	220.0	23.9	2.9	623.0	49.0
17-72-2 - 9	320.0	130.0	1055.0	42.0	4.7	0.6	0.4	0.1	67.4	5.6	6.2	0.9	8.7	0.8	6.6	1.5	33.9	1.8	102.8	3.9	34.0	1.4	148.9	6.6	30.9	1.3	298.0	12.0	62.5	2.8	8.9E+03	210.0	494.0	36.0	579.0	37.0
17-72-2 - 10	18.2	2.0	98.9	2.5	0.8	0.1	0.0	0.0	0.3	0.0	1.1	0.2	2.9	0.4	0.1	0.0	8.4	0.5	15.9	0.6	3.2	0.2	8.7	0.4	1.2	0.1	8.1	0.5	1.2	0.1	1.1E+04	230.0	43.3	1.3	552.0	16.0
17-72-2 - 11	17.6	2.1	138.4	7.9	0.7	0.1	0.0	0.0	0.2	0.1	0.7	0.2	2.5	0.4	0.0	0.0	9.4	0.8	20.4	1.2	4.7	0.3	13.1	0.9	2.3	0.2	18.6	2.4	3.4	0.5	1.1E+04	330.0	28.4	1.2	475.0	24.0
17-72-2 - 12	24.8	3.1	2350.0	290.0	2.3	0.2	0.6	0.2	4.5	0.6	4.5	0.7	8.1	1.0	4.9	1.1	44.8	4.6	216.0	25.0	79.0	10.0	349.0	45.0	69.1	8.9	630.0	83.0	123.0	16.0	1.0E+04	380.0	213.0	27.0	708.0	45.0

17-72-2 - 13	18.7	2.2	363.0	38.0	1.0	0.1	0.2	0.0	1.8	0.3	2.6	0.4	4.5	0.6	2.3	0.4	17.5	1.2	44.4	3.8	12.6	1.2	48.9	5.8	10.2	1.4	101.0	14.0	20.8	3.2	1.1E+04	230.0	36.6	2.3	615.0	25.0
17-72-2 - 14	16.0	31.0	166.0	12.0	0.3	0.5	0.0	0.9	1.0	0.8	0.8	2.7	2.8	2.6	0.6	0.3	13.9	2.2	24.1	2.1	6.0	1.5	16.0	0.9	2.0	0.3	22.9	7.9	2.4	0.3	9.8E+03	560.0	27.2	2.0	667.0	34.0
17-72-2 - 15	27.3	5.3	756.0	52.0	2.5	0.1	0.8	0.2	3.1	0.4	4.6	1.0	4.3	0.9	6.2	1.6	19.7	2.8	77.6	7.6	23.6	1.6	108.3	4.9	24.6	1.1	250.0	13.0	51.9	3.0	1.1E+04	260.0	52.6	2.1	519.0	19.0
17-72-2 - 16	12.8	2.1	137.2	5.8	0.7	0.1	0.0	0.0	0.2	0.0	0.9	0.2	3.0	0.4	0.1	0.0	10.8	0.7	21.0	1.1	4.7	0.2	13.4	0.7	1.8	0.1	13.4	0.8	2.0	0.1	1.1E+04	250.0	29.9	1.0	660.0	12.0
17-72-2 - 17	12.5	2.1	727.0	19.0	3.0	0.2	0.4	0.1	6.3	0.3	4.6	0.5	4.5	0.4	5.0	0.5	17.0	0.9	71.5	2.0	25.1	0.7	111.4	3.4	22.5	1.0	210.0	12.0	42.2	2.5	9.0E+03	250.0	86.2	3.3	275.8	7.1
17-72-2 - 18	13.4	2.5	641.0	71.0	1.3	0.2	22.2	8.3	55.0	20.0	40.0	13.0	12.2	2.8	7.6	1.4	27.6	3.2	73.7	7.1	21.5	2.3	87.0	10.0	16.6	1.9	148.0	17.0	28.6	3.2	1.0E+04	230.0	95.0	12.0	519.0	31.0
17-72-2 - 19	12.0	1.7	680.0	100.0	1.2	0.2	0.2	0.0	1.4	0.3	2.2	0.5	4.3	0.8	0.8	0.2	18.6	2.6	67.0	9.6	22.8	3.7	103.0	16.0	23.6	3.4	243.0	32.0	53.4	6.7	1.0E+04	360.0	68.0	11.0	488.0	28.0
17-72-2 - 20	13.1	2.4	132.8	5.1	0.5	0.1	0.1	0.0	0.4	0.1	1.0	0.3	2.2	0.4	0.4	0.1	13.3	1.0	27.7	1.2	4.6	0.2	9.8	0.8	1.2	0.2	7.7	1.0	1.2	0.2	1.1E+04	250.0	15.4	2.1	361.0	21.0
17-72-2 - 21	11.4	2.4	152.8	7.7	0.5	0.1	0.0	0.0	0.3	0.1	0.9	0.2	3.4	0.4	0.2	0.1	14.0	0.9	24.4	1.0	4.9	0.3	13.5	0.9	1.8	0.2	12.7	1.0	1.8	0.1	1.1E+04	270.0	28.9	1.6	470.0	13.0
17-72-2 - 22	14.0	1.7	188.0	29.0	0.7	0.1	0.1	0.0	1.7	0.7	1.0	0.2	3.0	0.4	0.3	0.1	13.6	1.0	27.3	2.7	6.6	1.1	24.2	5.2	5.0	1.2	54.0	13.0	11.3	3.0	1.1E+04	200.0	39.3	2.6	532.5	9.9
17-72-2 - 23	12.0	1.8	117.2	4.1	0.5	0.1	0.0	0.0	0.2	0.0	0.8	0.2	2.5	0.3	0.1	0.0	12.6	0.8	22.6	1.1	3.9	0.2	9.9	0.9	1.3	0.2	8.4	1.0	1.4	0.2	1.1E+04	240.0	28.6	1.8	581.0	38.0
17-72-2 - 24	19.3	2.0	252.0	22.0	0.8	0.1	0.1	0.0	1.3	0.3	0.8	0.2	1.6	0.3	0.2	0.1	9.3	1.0	29.6	1.1	7.9	0.7	31.9	4.7	7.0	1.3	72.0	16.0	14.9	3.6	1.1E+04	260.0	34.6	7.4	401.0	19.0
17-72-2 - 25	9.5	1.7	246.0	10.0	0.4	0.0	0.0	0.0	0.2	0.0	0.3	0.1	1.0	0.2	0.1	0.0	5.9	0.5	26.0	1.0	7.4	0.3	31.0	1.9	6.6	0.5	64.9	5.7	13.2	1.2	1.1E+04	230.0	10.3	1.2	360.0	15.0
17-72-2 - 26	8.6	1.6	422.0	68.0	1.1	0.1	0.0	0.0	7.4	2.0	1.0	0.2	2.5	0.4	0.4	0.1	13.2	1.6	44.5	6.4	14.6	2.6	63.0	12.0	13.5	2.7	130.0	27.0	26.3	5.6	1.1E+04	250.0	45.6	7.7	370.0	21.0
17-72-2 - 27	13.8	2.3	202.0	11.0	0.7	0.1	0.0	0.0	1.5	0.6	0.7	0.2	2.7	0.4	0.2	0.1	11.8	0.7	27.7	1.1	6.9	0.5	24.4	2.6	4.5	0.7	42.2	7.4	8.1	1.6	1.1E+04	230.0	26.4	2.1	523.0	16.0
17-72-2 - 28	10.6	1.6	389.0	41.0	0.9	0.1	0.1	0.1	0.6	0.3	0.5	0.2	1.0	0.3	0.2	0.0	7.0	0.8	35.1	2.9	13.2	1.5	64.7	8.8	16.3	2.3	182.0	26.0	40.0	5.9	1.1E+04	230.0	29.6	3.7	374.0	24.0
17-72-2 - 29	22.1	4.2	165.5	8.3	0.6	0.1	0.0	0.0	0.2	0.0	0.8	0.2	2.7	0.3	0.0	0.0	10.0	0.6	22.8	0.7	5.4	0.3	18.0	1.2	3.5	0.4	33.2	3.5	6.4	0.8	1.1E+04	230.0	26.7	1.1	475.0	19.0
17-72-2 - 30	11.0	1.9	694.0	71.0	1.4	0.1	480.0	290.0	1400.0	820.0	700.0	410.0	115.0	63.0	1.0	0.4	55.0	22.0	74.3	7.5	24.0	2.6	103.0	12.0	19.4	2.3	169.0	22.0	33.6	4.4	9.1E+03	310.0	510.0	230.0	330.0	54.0
17-72-2 - 31	7.2	1.4	640.0	64.0	1.3	0.1	0.0	0.0	22.7	1.8	1.8	0.3	3.7	0.6	0.8	0.1	16.4	1.9	61.0	6.9	21.8	2.3	100.2	9.5	19.8	1.8	186.0	15.0	37.8	2.9	9.4E+03	240.0	128.0	17.0	88.0	10.0
17-72-2 - 32	14.8	2.6	168.6	7.6	0.6	0.1	0.1	0.0	0.4	0.1	1.2	0.3	3.6	0.6	0.2	0.1	15.2	0.9	26.2	1.4	5.7	0.3	16.9	0.8	2.5	0.2	19.2	1.0	3.0	0.1	1.1E+04	320.0	27.6	1.1	621.0	19.0
17-72-2 - 33	15.8	3.4	472.0	75.0	1.1	0.1	0.4	0.2	2.9	1.0	1.9	0.5	4.0	0.6	0.9	0.2	15.8	1.4	49.8	6.5	14.6	2.3	61.0	10.0	13.0	2.2	133.0	24.0	25.0	4.4	1.1E+04	230.0	63.7	9.8	641.0	30.0
17-72-2 - 34	11.8	1.7	900.0	120.0	1.0	0.1	0.0	0.0	0.9	0.1	1.3	0.2	4.3	0.7	0.2	0.1	24.6	2.5	94.0	11.0	31.4	4.2	136.0	19.0	27.3	3.8	252.0	36.0	50.0	7.3	1.0E+04	230.0	85.0	11.0	586.0	19.0
17-72-2 - 35	10.5	1.5	495.0	36.0	1.8	0.3	4.7	4.9	24.0	21.0	5.3	4.6	2.4	1.0	0.4	0.1	8.9	1.3	45.6	2.7	16.5	1.3	77.3	7.2	18.2	1.8	191.0	20.0	39.9	4.8	1.1E+04	260.0	57.0	10.0	475.0	21.0
17-72-2 - 36	13.4	1.9	172.0	3.5	0.6	0.1	0.0	0.0	0.3	0.1	1.2	0.2	3.5	0.3	0.2	0.0	12.5	0.7	25.3	0.8	6.0	0.2	16.8	0.6	2.4	0.1	19.2	1.1	3.1	0.2	1.1E+04	250.0	33.6	1.0	602.0	16.0
17-72-2 - 37	13.4	2.8	335.0	38.0	1.2	0.2	0.0	0.0	3.4	0.5	1.8	0.6	2.7	0.6	0.4	0.1	10.4	1.5	30.9	3.1	10.5	1.3	47.7	6.8	10.5	1.7	107.0	18.0	22.2	4.1	9.2E+03	380.0	77.0	13.0	496.0	28.0
17-72-2 - 38	27.0	9.2	1000.0	170.0	1.5	0.2	0.3	0.1	2.5	0.5	2.7	0.5	4.6	0.8	1.3	0.3	23.2	3.3	92.0	15.0	32.6	5.6	150.0	25.0	31.4	5.2	318.0	48.0	60.4	9.5	1.0E+04	340.0	93.0	19.0	590.0	39.0
17-72-2 - 39	23.3	2.6	340.0	18.0	1.1	0.1	0.3	0.1	1.6	0.1	2.2	0.4	4.2	0.5	0.8	0.1	16.6	1.1	43.1	3.0	11.9	0.8	46.6	2.7	9.8	0.7	97.2	9.3	20.2	2.4	1.0E+04	250.0	41.6	2.4	609.0	36.0
17-72-2 - 40	9.7	1.5	425.0	23.0	1.3	0.1	240.0	180.0	810.0	580.0	420.0	300.0	74.0	52.0	1.0	0.3	34.0	18.0	41.1	4.0	13.8	0.8	67.3	3.5	15.1	0.8	153.0	6.1	33.4	1.2	9.9E+03	200.0	370.0	180.0	293.0	18.0
17-72-2 - 41	14.7	2.0	166.9	5.4	0.7	0.1	0.0	0.0	0.3	0.1	1.1	0.2	3.6	0.4	0.5	0.2	13.2	0.8	25.9	1.0	5.7	0.2	16.4	0.9	2.4	0.1	17.4	0.8	2.6	0.1	1.1E+04	220.0	29.3	0.8	715.0	18.0
17-72-2 - 42	22.5	6.8	634.0	92.0	1.4	0.3	0.1	0.0	10.0	2.3	2.3	0.5	4.1	0.8	0.9	0.2	17.8	3.1	61.9	9.5	21.2	3.2	95.0	14.0	20.2	2.6	200.0	25.0	41.0	4.7	9.3E+03	520.0	101.0	20.0	362.0	71.0
17-72-2 - 43	11.1	1.9	205.0	31.0	0.7	0.1	0.0	0.0	1.0	0.5	0.9	0.2	2.6	0.4	0.1	0.0	10.0	0.9	24.9	1.5	6.7	0.9	25.1	5.9	5.3	1.7	53.0	19.0	11.1	4.5	1.1E+04	240.0	34.2	2.1	586.0	24.0
17-72-2 - 44	16.6	2.5	782.0	95.0	1.4	0.2	0.5	0.1	4.7	0.7	3.2	0.6	4.5	0.5	3.4	0.6	18.3	1.6	79.4	8.6	27.8	3.3	127.0	16.0	27.0	3.4	262.0	33.0	53.9	6.8	9.8E+03	260.0	90.0	10.0	379.0	23.0
17-72-2 - 45	11.9	2.1	357.0	31.0	1.1	0.1	0.2	0.0	1.3	0.2	2.4	0.4	2.7	0.4	3.1	0.4	13.3	0.7	46.7	2.9	11.0	1.0	42.4	5.0	9.0	1.2	94.0	12.0	20.1	2.4	1.1E+04	250.0	14.0	1.6	414.0	16.0
17-72-2 - 46	11.2	2.1	481.6	9.4	1.5	0.1	0.1	0.0	20.1	0.6	1.1	0.2	2.3	0.2	0.7	0.1	10.0	0.6	38.4	1.4	15.0	0.4	76.6	2.3	17.6	0.5	191.7	4.7	45.3	1.1	8.7E+03	150.0	129.2	3.5	261.0	22.0

17-72-2 - 47	17.1	3.2	194.0	15.0	0.7	0.1	0.0	0.0	0.5	0.1	1.0	0.4	3.2	0.6	0.4	0.1	12.0	1.1	26.5	1.0	5.9	0.5	21.2	3.2	4.6	1.0	44.0	13.0	8.8	2.8	1.1E+04	250.0	28.3	2.7	500.0	39.0
17-72-2 - 48	340.0	110.0	790.0	26.0	3.4	0.3	0.5	0.1	4.0	0.4	3.0	0.5	4.6	0.4	1.8	0.2	19.7	0.9	79.8	3.2	26.2	1.0	118.8	3.8	26.4	0.8	267.2	9.5	55.8	1.8	9.5E+03	340.0	68.6	5.4	526.0	23.0
17-72-2 - 49	12.6	1.9	120.0	3.9	0.7	0.1	0.0	0.0	0.3	0.0	1.0	0.2	3.2	0.4	0.1	0.0	10.0	0.6	19.2	0.8	3.9	0.2	10.4	0.6	1.5	0.1	10.5	0.6	1.6	0.1	1.1E+04	240.0	39.1	1.7	707.0	17.0
17-72-2 - 50	11.9	2.0	187.6	6.7	0.6	0.1	0.1	0.0	0.4	0.1	0.9	0.2	3.1	0.4	0.2	0.1	11.5	0.9	25.6	1.1	6.0	0.3	20.5	1.2	3.9	0.3	35.7	2.6	6.6	0.6	1.1E+04	210.0	34.5	1.8	604.0	28.0
17-72-2 - 51	10.5	1.7	1885.0	72.0	4.4	0.2	0.0	0.0	21.2	1.0	3.7	0.3	8.4	0.6	0.6	0.1	41.6	1.5	171.1	7.0	64.4	2.8	284.0	11.0	56.8	1.7	485.0	20.0	98.2	3.1	8.9E+03	190.0	323.0	16.0	567.0	13.0
17-72-2 - 52	27.5	2.6	1793.0	74.0	1.1	0.1	0.0	0.0	3.8	0.2	1.9	0.3	5.7	0.6	0.2	0.0	28.9	1.6	157.4	8.1	60.7	3.1	273.0	12.0	54.7	2.4	482.0	24.0	93.4	4.0	9.9E+03	200.0	94.5	5.8	204.0	10.0
17-72-2 - 53	32.1	4.0	1909.0	96.0	1.3	0.1	0.7	0.3	9.0	1.6	7.5	2.1	14.5	2.2	17.8	8.5	59.7	5.4	183.0	12.0	62.3	3.2	260.0	14.0	50.3	2.4	439.0	19.0	85.8	3.4	9.5E+03	210.0	100.9	9.6	236.0	23.0
17-72-2 - 54	91.0	24.0	1186.0	45.0	1.0	0.1	10.9	3.6	13.4	2.9	9.2	1.9	12.0	1.5	12.9	2.1	35.5	2.8	116.9	4.2	38.5	1.4	175.1	8.1	34.8	1.6	305.0	15.0	59.6	3.1	1.0E+04	250.0	71.9	3.8	401.0	21.0
17-72-2 - 55	17.9	2.2	702.0	35.0	1.8	0.2	0.5	0.1	6.1	0.6	3.0	0.5	3.3	0.4	3.2	0.4	16.1	1.2	70.2	4.3	22.5	1.3	98.4	4.7	21.6	1.2	204.0	11.0	41.1	2.6	1.0E+04	260.0	93.9	5.3	426.0	32.0
17-72-2 - 56	19.6	3.8	1490.0	190.0	1.1	0.2	0.0	0.0	3.2	0.4	3.6	0.6	8.9	0.9	0.5	0.1	41.2	3.8	150.0	18.0	50.2	6.6	213.0	31.0	40.8	6.0	350.0	53.0	69.0	11.0	9.4E+03	250.0	215.0	28.0	431.0	14.0
17-72-2 - 57	18.6	2.7	1480.0	190.0	1.2	0.1	0.0	0.0	3.2	0.4	3.5	0.5	9.4	1.0	0.6	0.1	43.4	4.0	151.0	18.0	50.2	6.7	213.0	30.0	41.2	5.8	352.0	51.0	68.0	10.0	9.8E+03	270.0	224.0	28.0	500.0	13.0
17-72-2 - 58	19.8	3.8	1660.0	150.0	1.3	0.2	0.0	0.0	3.8	0.3	4.1	0.5	9.5	0.8	0.6	0.1	43.7	2.3	157.0	12.0	56.3	5.5	239.0	25.0	46.6	5.2	405.0	44.0	80.6	9.3	9.0E+03	240.0	225.0	19.0	419.0	16.0
17-72-2 - 59	9.2	2.6	368.0	52.0	1.6	0.3	0.4	0.3	5.2	1.2	1.5	0.4	2.6	0.6	0.3	0.1	9.9	1.1	34.5	3.9	12.3	1.8	56.0	10.0	13.7	2.8	147.0	31.0	30.8	6.7	1.0E+04	410.0	70.0	11.0	509.0	31.0
17-72-2 - 60	22.3	3.3	558.0	32.0	3.6	0.4	0.7	0.1	6.1	0.5	6.6	0.7	6.2	0.9	6.1	0.5	23.0	1.8	67.1	4.2	18.2	1.0	74.5	4.8	16.4	1.1	168.0	11.0	34.9	2.6	1.0E+04	230.0	78.0	6.0	736.0	33.0
17-72-2 - 61	16.5	1.8	156.1	7.9	0.8	0.1	0.0	0.0	0.2	0.0	1.0	0.2	3.4	0.4	0.1	0.0	12.4	0.8	23.7	1.3	5.2	0.3	15.0	0.9	2.2	0.2	14.3	0.9	2.3	0.2	1.1E+04	260.0	32.8	0.9	821.0	18.0
17-72-2 - 62	18.9	1.7	161.8	8.4	0.8	0.1	0.0	0.0	0.2	0.0	1.0	0.2	3.6	0.4	0.1	0.0	12.4	0.8	23.5	1.2	5.2	0.3	15.4	0.9	2.2	0.2	15.6	1.0	2.5	0.2	1.1E+04	260.0	32.4	0.8	841.0	15.0
17-72-2 - 63	11.0	1.9	1530.0	180.0	1.3	0.2	0.0	0.0	0.8	0.1	1.0	0.2	3.5	0.5	0.2	0.0	22.5	1.7	127.0	13.0	48.4	5.7	232.0	28.0	50.6	6.2	467.0	59.0	96.0	12.0	1.1E+04	200.0	61.9	5.3	543.0	31.0
17-72-2 - 64	12.6	1.4	115.6	3.7	0.7	0.1	0.0	0.0	0.2	0.0	0.8	0.2	3.1	0.3	0.0	0.0	9.6	0.6	18.1	0.9	3.8	0.2	10.5	0.6	1.5	0.1	11.1	0.7	1.8	0.1	1.1E+04	240.0	31.3	0.7	622.0	16.0
17-72-2 - 65	17.4	2.3	495.0	30.0	1.9	0.2	0.6	0.1	9.0	0.8	2.6	0.4	3.0	0.4	1.6	0.2	12.2	0.8	47.5	3.1	15.8	1.0	73.4	4.5	17.1	1.2	178.0	13.0	37.3	2.9	9.4E+03	300.0	63.6	3.1	423.0	32.0
17-72-2 - 66	11.0	2.1	338.0	32.0	1.3	0.2	0.2	0.1	1.5	0.4	1.8	0.3	2.4	0.3	0.5	0.1	11.8	0.8	41.7	3.3	10.4	1.0	44.5	5.3	10.4	1.4	110.0	15.0	23.8	3.3	1.1E+04	210.0	35.2	3.9	580.0	34.0
17-72-2 - 67	11.1	1.8	270.0	39.0	1.0	0.1	0.0	0.0	2.1	0.5	1.0	0.2	2.8	0.4	0.5	0.1	12.1	0.8	32.4	2.9	8.6	1.3	34.6	6.5	7.6	1.6	74.0	17.0	16.0	3.8	1.1E+04	260.0	32.1	1.8	544.0	26.0
17-72-2 - 68	38.0	18.0	399.0	47.0	1.7	0.3	0.0	0.0	7.0	1.5	0.5	0.1	1.5	0.3	0.3	0.1	8.0	0.6	36.9	3.0	12.6	1.5	64.6	9.0	16.7	2.6	184.0	29.0	40.9	6.4	1.0E+04	220.0	45.4	6.4	570.0	47.0
17-72-2 - 69	14.9	1.8	152.4	4.5	0.6	0.1	0.0	0.0	0.2	0.0	0.7	0.2	2.8	0.3	0.1	0.0	12.9	0.8	28.0	1.8	5.0	0.2	10.7	0.7	1.4	0.1	10.0	1.0	1.6	0.2	1.1E+04	250.0	22.0	2.5	415.0	29.0
17-72-2 - 70	12.6	1.9	1356.0	54.0	2.6	0.2	0.0	0.0	48.0	2.2	3.3	0.4	6.2	0.6	1.7	0.2	24.6	1.5	105.5	5.0	42.1	1.9	203.1	9.3	45.4	2.0	435.0	20.0	98.8	4.7	7.3E+03	130.0	367.0	16.0	308.0	10.0
17-78-1 - 1	16.9	2.1	517.0	38.0	1.3	0.1	0.5	0.3	9.4	0.7	1.3	0.3	2.1	0.3	0.2	0.0	10.4	1.1	43.1	3.4	17.9	1.4	92.0	6.2	20.9	1.3	213.0	13.0	45.6	2.9	1.1E+04	260.0	56.6	4.0	30.7	2.7
17-78-1 - 2	9.4	1.7	13.6	1.9	0.8	0.1	0.0	0.0	27.3	0.8	2.4	0.4	4.0	0.6	0.3	0.1	5.4	0.7	3.1	0.5	0.5	0.1	0.9	0.2	0.1	0.0	0.8	0.1	0.2	0.0	1.2E+04	310.0	68.0	18.0	91.8	2.8
17-78-1 - 3	13.5	2.3	347.0	80.0	1.0	0.1	0.5	0.3	17.9	2.3	1.8	0.3	2.7	0.3	0.4	0.1	6.5	0.8	27.5	6.2	11.9	2.7	60.0	14.0	13.4	3.0	134.0	29.0	28.5	6.3	1.1E+04	290.0	29.1	7.5	137.0	20.0
17-78-1 - 4	18.1	2.2	911.0	40.0	1.7	0.1	0.1	0.1	9.1	0.3	1.0	0.2	3.5	0.4	0.5	0.1	19.4	1.0	95.2	4.5	32.0	1.4	116.8	5.1	18.5	1.0	135.9	6.6	23.1	1.0	1.1E+04	230.0	37.9	1.2	80.7	1.8
17-78-1 - 5	16.1	2.1	1214.0	46.0	2.7	0.2	10.0	3.4	62.0	10.0	19.0	5.9	8.8	1.4	3.8	1.1	25.0	1.2	107.9	5.2	43.1	1.9	204.1	8.6	45.2	1.6	453.0	13.0	94.5	2.8	9.9E+03	230.0	152.0	11.0	329.0	44.0
17-78-1 - 6	19.8	2.3	349.0	25.0	1.2	0.1	0.0	0.0	16.0	0.5	2.3	0.3	5.8	0.4	0.4	0.0	13.7	0.9	31.8	1.7	11.8	0.8	57.6	4.7	12.9	1.1	125.0	12.0	25.5	2.3	1.1E+04	240.0	124.9	6.7	59.7	2.0
17-78-1 - 7	17.6	2.3	1225.0	89.0	2.2	0.2	3.5	1.2	64.1	7.1	24.0	5.2	21.8	2.7	6.9	0.9	51.3	5.8	128.0	11.0	42.9	3.4	173.0	13.0	32.7	2.6	291.0	24.0	56.9	4.9	9.1E+03	380.0	399.0	64.0	288.0	36.0
17-78-1 - 8	18.9	1.6	814.0	23.0	1.3	0.1	0.5	0.2	8.0	0.6	2.5	0.9	2.9	0.6	1.0	0.2	12.6	0.6	74.1	1.8	28.0	0.9	117.2	3.9	21.0	0.9	179.8	9.8	34.1	1.9	1.1E+04	240.0	23.2	1.0	175.0	11.0
17-78-1 - 9	20.4	2.3	1006.0	17.0	4.4	0.2	0.0	0.0	8.2	0.2	0.4	0.1	0.9	0.2	0.1	0.0	6.4	0.5	59.9	1.9	34.7	0.8	214.1	5.3	55.3	1.9	600.0	25.0	139.3	5.9	1.1E+04	180.0	60.1	1.7	33.5	4.0
17-78-1 - 10	17.7	2.1	264.0	40.0	1.4	0.2	0.1	0.0	20.7	1.3	2.9	0.5	4.2	0.7	0.4	0.1	6.3	0.5	16.0	1.7	7.9	1.1	53.7	8.6	15.5	2.6	182.0	29.0	44.9	7.5	1.1E+04	230.0	102.1	7.1	99.0	14.0
17-78-1 - 11	28.2	3.0	582.0	65.0	0.9	0.1	33.1	4.0	113.0	14.0	91.0	13.0	35.6	4.7	19.5	2.5	28.7	3.0	64.3	5.0	21.1	2.2	98.0	14.0	23.2	3.8	247.0	43.0	57.0	10.0	1.1E+04	270.0	55.4	9.3	637.0	56.0
17-78-1 - 12	14.4	1.7	797.0	85.0	1.5	0.1	2.1	0.7	12.0	1.9	4.1	1.0	3.1	0.5	1.2	0.2	10.2	0.8	61.8	6.3	27.0	2.9	146.0	17.0	36.1	4.5	397.0	52.0	88.0	12.0	1.1E+04	260.0	30.8	5.9	255.0	46.0
17-78-1 - 13	12.7	1.4	97.5.0	85.0	1.9	0.1	2.6	0.7	10.5	0.9	3.4	0.7	3.5	0.5	0.8	0.2	11.6	0.6	72.4	5.7	33.1	2.9	182.0	17.0	45.3	4.5	495.0	50.0	110.0	11.0	1.1E+04	200.0	35.9	8.6	227.0	16.0
17-78-1 - 14	16.6	2.2	697.0	32.0	1.8	0.1	0.2	0.2	8.7	0.9	1.2	0.3	3.5	0.6	0.3	0.0	12.6	1.2	55.2	2.9	23.7	1.1	121.7	6.1	28.4	1.5	284.0	17.0	64.5	4.4	1.1E+04	280.0	77.0	10.0	127.1	5.7
17-78-1 - 15	12.0	2.1	1709.0	39.0	1.5	0.1	14.4	3.5	22.3	4.4	11.4	2.5	3.9	0.6	0.5	0.1	12.4	0.5	118.3	3.4	58.7	1.5	357.0	10.0	95.8	2.5	1083.0	25.0	231.2	5.3	1.1E+04	290.0	9.0	0.5	123.7	3.9

| | | |

17-78-2-10	144.0	48.0	1063.0	75.0	1.9	0.2	33.1	7.8	210.0	48.0	163.0	35.0	86.0	18.0	38.3	8.2	66.0	12.0	122.0	17.0	38.5	3.4	173.0	10.0	41.7	1.6	450.0	14.0	99.0	2.7	1.1E+04	230.0	72.4	7.2	1145.0	69.0
17-78-2-11	19.1	4.3	740.0	110.0	1.7	0.2	0.1	0.1	10.6	2.2	1.5	0.7	3.3	0.6	0.5	0.1	14.8	1.6	65.4	9.4	24.4	3.7	109.0	17.0	22.4	3.4	200.0	28.0	40.5	6.0	1.0E+04	420.0	52.0	10.0	165.0	22.0
17-78-2-12	9.3	1.8	1097.0	34.0	1.8	0.1	4.9	1.7	16.4	2.4	3.1	0.5	4.6	0.5	0.4	0.1	22.6	1.3	100.0	3.9	38.7	1.6	171.7	6.3	34.9	1.3	333.0	13.0	71.0	2.7	1.0E+04	200.0	98.9	4.7	47.2	2.0
17-78-2-13	12.2	1.7	753.0	53.0	1.3	0.1	2.7	0.8	12.3	1.2	2.5	0.5	3.5	0.4	0.3	0.1	15.3	1.1	64.8	5.3	25.6	2.1	116.6	8.2	24.9	1.8	240.0	15.0	52.6	3.4	1.1E+04	330.0	68.3	3.4	53.4	3.2
17-78-2-14	23.2	2.6	569.0	17.0	1.4	0.1	0.5	0.2	11.9	0.4	2.1	0.3	3.2	0.3	0.6	0.1	12.3	0.7	47.7	1.5	19.2	0.7	88.8	2.8	18.4	0.7	165.0	5.8	34.4	1.4	1.1E+04	200.0	51.5	1.3	120.4	4.0
17-78-2-15	20.8	2.7	1245.0	84.0	1.8	0.1	0.0	0.0	7.6	0.5	1.4	0.2	3.4	0.5	0.3	0.1	16.8	1.0	99.4	6.7	41.2	2.8	199.0	15.0	43.5	3.2	426.0	32.0	89.9	6.9	1.0E+04	230.0	56.6	3.8	109.4	9.4
17-78-2-16	31.6	3.7	1080.0	160.0	1.4	0.2	45.0	12.0	159.0	40.0	144.0	35.0	59.0	14.0	26.7	6.1	56.0	11.0	118.0	19.0	38.0	5.8	173.0	21.0	40.6	4.6	412.0	39.0	90.7	8.4	1.0E+04	270.0	176.0	42.0	570.0	81.0
17-78-2-17	19.8	1.9	992.0	28.0	1.4	0.1	0.2	0.1	6.4	0.4	1.0	0.2	2.9	0.3	0.6	0.1	15.5	0.8	92.8	2.4	33.6	1.0	139.7	5.1	25.9	1.1	214.2	9.5	40.9	2.4	1.1E+04	220.0	31.4	2.7	172.0	12.0
17-78-2-18	22.5	2.3	903.0	62.0	1.6	0.2	0.3	0.1	6.8	0.4	1.9	0.3	3.0	0.4	1.0	0.1	8.9	1.1	67.1	4.9	30.3	2.0	168.0	11.0	42.4	2.9	462.0	32.0	102.7	7.5	1.1E+04	220.0	24.1	1.3	491.0	37.0
17-78-2-19	20.5	2.4	600.0	49.0	1.3	0.1	0.1	0.0	6.3	0.6	1.2	0.3	2.6	0.4	0.7	0.1	12.5	1.1	60.0	5.6	20.7	1.8	83.4	7.1	14.9	1.4	122.0	13.0	25.1	3.2	1.1E+04	230.0	27.2	5.1	185.0	27.0
17-78-2-20	31.4	3.9	684.0	54.0	1.1	0.1	15.7	2.5	96.0	14.0	53.4	8.1	22.3	3.6	12.1	1.9	28.9	3.8	69.7	6.0	23.5	1.9	103.9	8.0	23.4	2.0	241.0	22.0	51.5	4.9	1.0E+04	210.0	51.8	3.4	425.0	30.0
17-78-2-21	16.5	3.1	151.0	39.0	0.8	0.1	0.4	0.3	22.6	0.8	3.7	0.6	4.6	0.6	0.6	0.1	8.6	0.7	16.5	3.4	5.2	1.4	19.7	6.1	3.8	1.2	32.0	11.0	6.5	2.1	1.0E+04	290.0	117.9	6.1	33.0	5.9
17-78-2-22	20.7	2.4	352.0	59.0	0.9	0.1	0.0	0.0	12.9	1.2	2.2	0.4	5.1	0.7	0.4	0.1	11.3	0.8	32.5	4.6	11.9	2.1	54.0	10.0	11.5	2.4	108.0	24.0	22.8	5.2	1.0E+04	200.0	104.0	13.0	34.5	1.5
17-78-2-23	18.1	2.1	117.0	23.0	0.8	0.1	0.0	0.0	17.3	0.6	3.3	0.4	7.8	0.7	0.6	0.1	13.8	0.9	16.0	2.0	4.3	0.8	13.8	3.4	2.3	0.7	18.6	5.8	3.6	1.2	1.0E+04	240.0	173.3	5.6	38.0	2.7
17-78-2-24	17.1	1.8	995.0	41.0	1.7	0.1	0.6	0.2	6.1	0.4	1.4	0.3	2.4	0.3	0.6	0.1	12.1	0.8	82.7	4.0	32.5	1.3	149.0	4.3	31.6	0.9	289.0	10.0	57.7	3.0	1.1E+04	240.0	20.1	0.8	266.0	12.0
17-78-2-25	14.8	6.7	31.3	2.9	1.0	0.3	0.1	0.1	19.1	1.0	4.8	2.1	7.5	1.7	1.1	0.5	11.2	2.6	6.8	0.9	1.1	0.2	2.5	0.4	0.2	0.1	1.5	0.3	0.3	0.1	8.8E+03	750.0	138.1	9.6	21.9	1.3
17-78-2-26	13.3	4.3	1511.0	42.0	2.8	0.2	0.6	0.4	8.4	0.8	2.2	0.8	2.7	0.4	0.6	0.1	11.6	0.7	100.6	2.6	48.2	1.7	266.0	11.0	63.9	3.5	641.0	39.0	137.2	9.3	1.1E+04	290.0	33.3	1.4	318.0	13.0
17-78-2-27	15.1	1.8	67.0	70.0	1.1	0.1	0.9	0.4	8.6	1.0	1.4	0.3	2.0	0.4	0.4	0.1	7.2	0.6	46.7	4.7	22.4	2.3	129.0	15.0	35.7	4.6	415.0	58.0	94.0	13.0	1.1E+04	230.0	49.1	8.7	275.0	42.0
17-78-2-28	21.3	3.0	809.0	21.0	1.6	0.1	38.0	12.0	98.0	25.0	93.0	18.0	36.3	6.1	18.6	3.0	23.5	2.9	63.8	2.9	27.1	0.9	147.9	4.0	38.5	1.0	457.0	14.0	105.8	3.7	1.1E+04	270.0	55.1	2.3	1216.0	71.0
17-78-2-29	8.5	1.4	1190.0	200.0	1.6	0.2	15.4	6.0	43.0	12.0	31.1	8.9	12.7	2.3	1.1	0.2	15.6	2.1	88.0	15.0	41.3	6.9	229.0	38.0	56.7	9.2	603.0	96.0	131.0	21.0	1.1E+04	290.0	26.8	5.6	106.7	8.2
17-78-2-30	11.5	1.9	603.0	14.0	1.4	0.1	0.0	0.0	8.9	0.5	1.6	0.2	3.2	0.3	0.5	0.1	16.1	0.8	64.8	1.9	21.6	0.6	84.4	2.5	16.7	0.8	152.0	11.0	31.9	2.6	1.0E+04	200.0	51.8	3.9	84.0	14.0
17-78-2-31	17.1	2.2	973.0	50.0	2.3	0.1	0.0	0.0	7.1	0.2	0.7	0.1	2.2	0.3	0.4	0.1	13.3	0.9	81.7	4.3	34.1	1.7	160.4	8.5	32.3	1.9	295.0	18.0	62.8	4.1	1.1E+04	220.0	41.0	1.7	76.1	1.9
17-78-2-32	17.3	3.0	102.0	8.6	0.5	0.1	0.0	0.0	6.4	0.8	1.1	0.2	3.0	0.4	0.9	0.1	15.7	1.8	19.7	1.8	3.6	0.3	9.8	1.6	1.6	0.4	15.2	4.8	3.2	1.0	1.0E+04	230.0	32.5	3.9	59.7	4.1
17-78-2-33	17.3	2.1	134.6	6.5	0.6	0.1	0.0	0.0	4.5	0.2	1.0	0.2	4.0	0.5	1.2	0.1	20.7	1.6	29.0	1.9	4.7	0.3	10.4	1.0	1.5	0.2	11.1	2.4	2.3	0.6	1.0E+04	240.0	23.2	0.8	65.5	1.8
17-78-2-34	8.6	2.0	573.0	37.0	1.4	0.1	0.1	0.0	8.4	0.5	1.0	0.2	2.1	0.4	0.4	0.1	7.9	0.6	42.8	3.0	18.7	1.3	100.9	7.2	23.8	1.9	243.0	19.0	53.6	4.5	1.0E+04	260.0	50.6	3.1	77.0	5.0
17-78-2-35	22.1	2.6	1063.0	25.0	1.4	0.1	0.0	0.0	6.3	0.2	0.7	0.2	2.1	0.3	0.5	0.1	14.0	0.8	94.8	3.0	36.2	0.9	155.0	3.6	29.9	0.8	256.6	9.4	48.0	2.2	1.1E+04	210.0	25.8	1.0	253.0	12.0
17-78-2-36	14.9	2.0	45.1	2.5	0.7	0.0	0.2	0.1	16.5	0.6	2.7	0.3	5.0	0.5	0.8	0.1	13.8	1.1	11.0	0.8	1.7	0.1	3.1	0.3	0.3	0.0	1.8	0.2	0.3	0.0	1.0E+04	220.0	101.7	4.6	40.6	2.0
17-78-2-37	22.6	2.8	113.7	7.9	0.8	0.1	0.0	0.0	21.6	0.6	4.6	0.4	11.9	0.9	0.8	0.1	20.0	0.9	19.3	1.1	3.9	0.3	11.5	1.4	2.0	0.4	19.1	4.3	3.7	0.9	1.0E+04	220.0	207.8	5.0	38.8	2.1
17-78-2-38	26.4	2.3	37.6	2.3	0.8	0.1	0.1	0.0	21.6	0.6	4.5	0.5	8.2	0.6	0.7	0.1	12.8	1.0	8.1	0.6	1.3	0.1	2.6	0.2	0.3	0.0	1.9	0.2	0.4	0.0	1.0E+04	230.0	204.3	8.7	65.4	1.7
17-78-2-39	29.3	2.0	116.6	3.7	1.0	0.1	0.0	0.0	18.8	0.4	3.7	0.4	10.8	0.7	0.6	0.1	25.0	1.0	23.9	0.9	4.3	0.2	9.6	0.5	1.1	0.1	7.4	0.4	1.4	0.1	1.1E+04	210.0	241.5	5.0	53.4	1.3
17-78-2-40	16.5	2.0	290.0	50.0	1.2	0.1	0.0	0.0	15.2	1.6	1.5	0.3	2.8	0.4	0.5	0.1	10.0	0.8	31.2	4.8	9.8	1.7	40.4	7.4	8.2	1.6	79.0	16.0	17.0	3.5	1.0E+04	240.0	59.2	6.2	78.0	14.0
17-78-2-41	21.4	2.2	27.4	1.6	0.8	0.1	0.0	0.0	25.3	0.6	2.8	0.4	3.3	0.4	0.4	0.1	5.4	0.6	5.2	0.4	1.1	0.1	2.6	0.2	0.3	0.0	1.6	0.3	0.3	0.1	1.0E+04	220.0	100.5	2.2	10.5	0.7
17-78-2-42	12.8	2.1	592.0	86.0	1.6	0.2	0.1	0.1	11.6	1.6	2.4	0.8	2.6	0.6	0.6	0.1	9.6	0.9	48.1	6.8	20.0	3.0	96.0	14.0	19.5	2.9	177.0	25.0	35.9	5.3	1.0E+04	290.0	73.1	9.0	95.6	6.4
17-78-2-43	NAN	NAN	NAN	NAN	NAN	NAN	NAN	NAN	NAN	NAN	NAN	NAN	NAN	NAN	NAN	NAN	NAN	NAN	NAN	NAN	NAN	NAN	NAN	NAN	NAN	NAN	NAN	NAN	NAN	NAN	NAN	NAN	NAN	NAN	NAN	NAN

17-78-2 - 44	19.5	2.3	266.0	67.0	1.2	0.2	0.0	0.0	19.3	0.5	2.8	0.3	5.2	0.5	0.4	0.1	11.8	0.6	25.9	5.5	9.4	2.4	41.0	12.0	9.2	2.7	92.0	28.0	18.2	5.4	1.1E+04	250.0	127.6	4.6	65.0	17.0
17-78-2 - 45	23.6	2.4	910.0	150.0	1.8	0.2	0.3	0.1	13.1	1.6	2.6	0.6	3.8	0.6	0.8	0.1	15.9	1.4	77.0	12.0	30.3	5.1	137.0	23.0	27.0	4.4	231.0	37.0	46.1	7.3	1.1E+04	260.0	99.0	14.0	95.0	8.6
17-78-2 - 46	20.1	4.1	927.0	80.0	1.7	0.2	3.0	1.9	27.0	13.0	18.0	12.0	8.1	3.7	3.7	2.0	18.6	4.2	79.3	4.2	31.7	2.8	152.0	19.0	34.0	5.3	344.0	63.0	73.0	14.0	1.1E+04	230.0	29.3	0.8	316.0	27.0
17-78-2 - 47	17.0	2.1	657.0	15.0	1.1	0.1	0.5	0.4	7.4	0.6	1.5	0.3	2.6	0.4	0.5	0.1	11.8	0.7	62.5	1.9	21.6	0.7	82.6	2.3	13.8	0.5	101.9	4.0	17.4	0.9	1.1E+04	210.0	25.8	1.6	406.0	11.0
17-78-2 - 48	20.4	2.3	1440.0	140.0	1.9	0.1	0.1	0.0	6.1	0.4	0.9	0.2	2.2	0.4	0.4	0.1	16.1	1.1	114.7	9.5	47.8	4.7	246.0	34.0	55.2	8.9	550.0	100.0	115.0	22.0	1.0E+04	230.0	30.4	2.7	299.0	19.0
17-78-2 - 49	24.6	3.0	281.0	47.0	1.3	0.2	0.0	0.0	8.7	2.4	1.1	0.3	1.4	0.4	0.3	0.1	3.9	0.6	20.2	3.1	9.6	1.6	60.0	11.0	17.7	3.2	212.0	39.0	49.2	9.3	1.1E+04	270.0	41.0	12.0	161.0	32.0
17-78-2 - 50	12.2	1.7	1187.0	95.0	1.4	0.1	18.2	3.4	41.6	5.6	22.7	3.2	11.1	0.7	2.1	0.3	19.2	0.9	94.5	6.9	40.0	3.1	223.0	18.0	57.3	4.6	622.0	49.0	137.0	11.0	1.0E+04	210.0	48.3	9.7	58.3	2.8
17-78-2 - 51	22.5	2.6	1550.0	150.0	3.1	0.3	0.9	0.5	9.8	1.5	2.5	0.7	2.3	0.3	0.6	0.1	12.0	0.8	99.6	9.1	47.5	4.8	285.0	30.0	76.0	8.4	822.0	93.0	177.0	21.0	1.1E+04	220.0	23.6	2.5	363.0	40.0
17-78-2 - 52	18.7	2.3	626.0	74.0	1.4	0.1	0.7	0.3	13.0	2.1	2.3	0.6	2.8	0.6	0.5	0.1	9.1	0.6	48.1	5.0	20.0	2.4	109.0	14.0	26.9	3.6	302.0	43.0	65.0	9.4	1.0E+04	220.0	67.0	12.0	252.0	22.0
17-78-2 - 53	11.3	2.3	970.0	230.0	1.8	0.3	0.8	0.7	7.2	2.8	2.7	1.9	3.6	1.1	1.3	0.9	12.5	2.8	74.0	17.0	34.8	8.1	200.0	46.0	53.0	12.0	600.0	140.0	131.0	29.0	1.1E+04	280.0	24.8	5.0	137.0	21.0
17-78-2 - 54	40.0	21.0	660.0	170.0	1.2	0.2	10.7	7.7	25.0	10.0	4.1	1.5	4.9	1.6	3.1	1.8	12.6	1.0	50.1	9.7	20.2	5.1	109.0	31.0	29.1	9.2	330.0	110.0	70.0	22.0	9.9E+03	310.0	59.4	9.9	168.0	31.0
17-78-2 - 55	20.8	2.3	1179.0	37.0	2.0	0.1	1.7	0.4	7.7	0.6	1.7	0.2	1.8	0.2	0.4	0.1	10.8	0.7	86.9	3.4	38.7	1.4	214.7	6.6	56.8	1.8	647.0	20.0	141.3	4.0	1.1E+04	260.0	22.3	1.0	470.0	14.0
17-78-2 - 56	15.8	2.1	86.5	5.7	0.6	0.1	0.0	0.0	5.2	0.4	0.9	0.2	3.5	0.4	0.9	0.1	16.2	1.2	20.9	1.6	3.1	0.3	5.8	0.5	0.4	0.0	2.2	0.3	0.3	0.0	1.0E+04	190.0	26.3	1.4	66.9	2.9
17-78-2 - 57	15.0	2.2	74.2	3.0	0.5	0.0	0.0	0.0	5.1	0.3	0.8	0.2	3.4	0.4	1.0	0.1	15.6	1.0	18.8	0.9	2.7	0.2	4.7	0.3	0.4	0.0	1.9	0.2	0.3	0.0	1.0E+04	250.0	25.3	1.4	63.6	1.9
17-78-2 - 58	17.1	2.2	1137.0	28.0	1.7	0.1	1.8	0.7	7.3	0.9	1.0	0.3	1.9	0.3	0.4	0.1	12.9	0.7	96.9	2.4	36.9	0.9	163.3	3.4	31.5	0.8	268.3	6.8	50.0	1.6	1.1E+04	220.0	18.7	0.7	379.2	8.6
17-78-2 - 59	22.1	2.7	1270.0	110.0	2.6	0.2	0.0	0.0	9.3	0.5	0.9	0.2	2.7	0.3	0.4	0.1	18.2	0.9	115.2	7.2	42.5	3.4	172.0	17.0	31.0	3.6	256.0	30.0	46.7	5.7	1.1E+04	230.0	51.5	3.1	152.2	7.3
17-78-2 - 60	23.0	2.4	1235.0	38.0	2.9	0.2	0.0	0.0	9.3	0.3	0.9	0.2	2.3	0.4	0.4	0.1	14.6	0.8	103.7	3.6	41.3	1.3	184.8	4.4	37.0	1.2	335.0	11.0	64.8	1.8	1.0E+04	240.0	52.4	1.5	102.7	6.4
17-78-2 - 61	13.4	2.6	960.0	180.0	1.8	0.2	0.1	0.1	14.5	0.8	2.3	0.7	4.2	0.5	0.4	0.1	16.3	1.7	74.0	13.0	30.5	5.8	156.0	31.0	36.9	7.3	373.0	72.0	79.0	16.0	1.0E+04	260.0	87.2	3.5	92.0	13.0
17-78-2 - 62	20.1	2.2	1177.0	33.0	1.8	0.1	0.7	0.2	7.2	0.4	1.8	0.4	3.1	0.4	0.9	0.2	15.6	1.0	101.9	4.0	38.8	1.2	180.1	5.2	36.9	0.9	345.0	12.0	69.0	2.7	1.1E+04	270.0	25.1	1.0	432.0	13.0
17-78-2 - 63	31.3	6.5	1089.0	46.0	1.5	0.1	17.8	5.8	120.0	40.0	81.0	28.0	36.0	12.0	27.4	9.3	37.0	8.7	108.1	8.9	38.0	1.8	169.9	6.9	37.9	2.0	386.0	26.0	78.5	5.9	1.1E+04	240.0	21.1	1.1	522.0	70.0
17-78-2 - 64	16.4	2.4	1221.0	31.0	2.0	0.1	0.6	0.3	12.2	0.8	1.9	0.4	3.4	0.4	0.5	0.1	17.8	0.7	97.4	2.4	39.1	1.0	199.7	4.8	45.4	1.1	460.0	10.0	97.2	2.0	1.0E+04	210.0	53.6	1.7	134.7	8.4
17-78-2 - 65	22.1	2.6	223.0	44.0	1.0	0.1	0.0	0.0	14.8	0.6	2.6	0.3	6.0	0.6	0.5	0.1	13.1	0.7	22.4	2.9	7.4	1.5	35.1	8.6	7.6	2.1	79.0	24.0	16.1	5.0	1.0E+04	240.0	125.6	5.6	51.0	11.0
17-78-2 - 66	21.0	2.0	1308.0	69.0	3.3	0.3	0.0	0.0	6.1	0.2	0.6	0.1	2.0	0.3	0.4	0.1	12.2	0.9	92.8	5.9	41.8	2.5	226.0	14.0	54.3	3.6	577.0	40.0	125.8	9.0	1.1E+04	170.0	23.1	0.7	287.0	33.0
17-78-2 - 67	12.7	1.7	1483.0	80.0	1.3	0.1	11.1	4.9	31.0	12.0	9.6	3.2	4.5	0.7	0.7	0.1	18.4	1.4	113.7	5.4	50.1	2.7	260.0	14.0	61.3	3.5	637.0	36.0	136.3	8.0	9.9E+03	180.0	25.1	1.2	90.0	18.0
17-78-2 - 68	17.7	2.3	1588.0	59.0	2.5	0.1	1.7	0.9	10.5	1.3	3.0	0.8	3.0	0.4	0.8	0.2	14.8	0.9	106.0	3.6	50.8	1.8	301.0	8.1	81.5	2.5	982.0	37.0	230.2	7.4	1.0E+04	210.0	42.8	1.8	251.0	10.0
17-91-1 - 1	51.2	9.4	700.0	140.0	1.2	0.3	2.3	1.0	12.4	2.9	10.5	3.8	11.1	3.4	28.0	12.0	30.1	7.2	71.0	14.0	21.6	4.0	89.0	16.0	15.9	2.8	140.0	25.0	27.9	5.0	1.0E+04	320.0	102.0	12.0	284.0	40.0
17-91-1 - 2	33.6	4.5	630.0	120.0	1.0	0.1	2.0	0.6	7.3	1.7	9.1	2.0	9.3	1.8	20.4	5.1	27.2	4.5	71.0	11.0	19.3	3.5	70.0	16.0	12.5	3.1	101.0	26.0	19.6	5.4	1.1E+04	260.0	47.9	6.1	439.0	21.0
17-91-1 - 3	35.6	2.9	872.0	53.0	1.1	0.1	0.2	0.2	5.5	0.7	1.7	0.6	3.6	0.7	2.0	1.7	17.3	2.0	76.8	4.7	28.9	1.4	137.0	7.2	28.0	1.6	249.0	15.0	50.4	2.6	1.0E+04	230.0	98.9	5.6	254.4	9.9
17-91-1 - 4	29.7	2.9	610.0	93.0	1.0	0.2	0.8	0.2	4.5	0.9	4.4	0.9	6.3	1.0	8.3	2.2	23.4	2.5	66.9	7.4	19.5	2.9	75.0	14.0	13.7	2.9	117.0	27.0	22.2	5.3	1.1E+04	260.0	51.9	7.6	279.0	14.0
17-91-1 - 5	27.5	3.5	1601.0	89.0	19.4	0.8	5.3	3.7	21.2	4.0	4.7	1.7	6.8	0.8	0.2	0.0	35.6	1.8	153.7	6.8	56.1	2.6	244.0	11.0	44.6	2.1	373.0	15.0	70.9	3.0	1.0E+04	210.0	206.3	8.7	331.0	18.0
17-91-1 - 6	182.0	54.0	952.0	21.0	28.3	0.9	0.0	0.0	13.4	0.5	1.3	0.2	3.6	0.4	0.1	0.0	19.6	0.9	90.9	2.4	34.7	1.1	154.7	3.7	29.6	0.8	249.5	6.1	47.9	1.0	1.1E+04	210.0	166.6	5.8	285.2	6.3
17-91-1 - 7	28.2	3.0	259.5	5.9	0.7	0.1	0.0	0.0	2.0	0.2	0.4	0.1	1.1	0.2	0.3	0.0	6.4	0.6	25.2	1.7	8.2	0.3	34.7	1.1	7.0	0.3	69.2	3.4	15.1	0.9	8.9E+03	230.0	13.7	0.8	141.0	24.0
17-91-1 - 8	19.1	2.2	224.0	12.0	1.0	0.1	0.0	0.0	1.0	0.1	0.3	0.1	1.0	0.2	0.1	0.0	6.8	0.6	27.0	2.0	7.0	0.4	24.0	1.1	3.9	0.2	35.0	1.5	6.8	0.4	1.1E+04	220.0	16.8	1.6	264.0	15.0
17-91-1 - 9	31.3	5.2	1870.0	170.0	2.6	0.4	2.6	0.6	10.2	1.7	15.0	2.4	15.3	2.1	33.1	7.9	48.1	3.7	162.0	13.0	58.0	6.7	275.0	40.0	57.3	9.2	526.0	88.0	111.0	19.0	1.1E+04	290.0	143.0	22.0	582.0	40.0
17-91-1 - 10	44.0	9.1	1339.0	89.0	4.3	0.3	0.9	0.4	7.7	0.8	7.7	1.2	10.2	1.1	11.2	4.0	40.1	2.7	135.7	9.4	47.5	2.9	207.0	14.0	39.2	2.2	345.0	17.0	70.4	3.3	8.1E+03	230.0	139.0	21.0	254.0	40.0
17-91-1 - 11	25.5	3.8	1150.0	150.0	2.3	0.3	1.8	0.3	10.6	0.7	12.3	1.5	19.4	2.8	23.0	3.3	68.0	10.0	119.0	14.0	31.0	3.2	104.6	8.3	16.9	1.1	140.2	8.9	26.9	1.8	9.8E+03	300.0	67.4	2.7	213.0	14.0
17-91-1 - 12	24.2	2.7	79.9	2.7	0.4	0.0	0.0	0.0	3.0	0.1	4.2	0.4	4.4	0.4	0.1	0.0	8.0	0.6	11.9	0.7	2.7	0.2	8.2	0.4	1.2	0.1	8.8	0.6	1.4	0.1	1.1E+04	250.0	118.4	7.5	288.0	16.0
17-91-1 - 13	38.9	3.5	961.0	21.0	1.0	0.1	0.1	0.0	3.8	0.2	1.2	0.2	2.7	0.3	0.3	0.2	15.9	0.9	81.0	2.2	31.7	0.8	146.8	3.0	30.5	0.7	272.8	5.9	55.0	1.2	1.1E+04	220.0	101.2	3.3	293.7	7.0
17-91-1 - 14	17.5	2.4	670.0	110.0	1.1	0.2	0.2	0.1	2.7	0.3	1.7	0.3	3.7	0.4	1.9	0.6	14.2	1.4	62.1	9.5	22.8	3.9	108.0	20.0	22.6	4.1	203.0	37.0	40.8	7.6	1.0E+04	230.0	83.1	5.4	326.0	26.0

17-91-1-15	38.7	3.5	569.0	65.0	0.4	0.1	1.0	0.2	5.7	1.1	10.0	1.5	14.8	1.9	12.7	2.6	44.8	5.6	75.7	8.9	16.7	1.9	44.5	4.9	5.9	0.7	35.8	4.3	5.4	0.6	1.1E+04	230.0	58.4	4.0	218.0	20.0
17-91-1-16	251.0	59.0	2090.0	190.0	28.7	1.4	1.3	0.9	25.8	2.7	15.0	7.1	15.4	5.0	13.7	9.4	56.0	11.0	206.0	20.0	71.6	5.0	293.0	15.0	54.0	3.0	444.0	22.0	81.6	3.4	7.2E+03	170.0	297.7	7.5	367.0	18.0
17-91-1-17	97.0	24.0	1620.0	470.0	1.5	0.4	9.3	3.3	28.3	9.6	43.0	14.0	45.0	13.0	94.0	32.0	112.0	33.0	186.0	51.0	44.0	12.0	132.0	38.0	18.4	5.4	131.0	40.0	21.8	6.7	1.1E+04	230.0	48.2	5.1	463.0	63.0
17-91-1-18	33.7	2.9	76.0	2.1	0.3	0.0	0.0	0.0	1.8	0.1	1.8	0.3	4.4	0.4	0.2	0.0	13.9	0.7	15.5	0.7	2.8	0.1	6.4	0.4	0.8	0.1	5.9	0.3	1.2	0.1	1.1E+04	240.0	89.5	1.8	407.0	16.0
17-91-1-19	41.4	3.9	76.6	2.9	0.2	0.0	0.0	0.0	1.6	0.1	1.4	0.2	3.1	0.4	0.2	0.0	11.2	0.6	14.0	0.6	2.6	0.1	6.8	0.4	1.0	0.1	7.8	0.5	1.6	0.1	1.1E+04	260.0	72.8	2.4	267.2	6.5
17-91-1-20	26.0	3.4	1339.0	56.0	6.2	0.3	0.2	0.0	8.0	0.4	5.8	0.5	8.5	0.6	0.8	0.1	37.8	1.7	136.5	5.5	46.8	1.8	199.5	8.2	37.4	1.5	309.0	13.0	60.8	2.3	7.2E+03	130.0	143.7	8.1	146.5	4.9
17-91-1-21	21.8	2.4	874.0	75.0	1.1	0.1	0.0	0.0	8.3	0.6	1.8	0.4	4.3	0.7	0.4	0.2	19.3	2.2	81.6	7.5	30.2	2.7	134.0	12.0	25.5	2.0	225.0	16.0	43.4	3.1	9.0E+03	250.0	231.0	22.0	345.0	23.0
17-91-1-22	24.2	3.3	867.0	86.0	1.1	0.1	1.5	0.4	9.6	0.8	8.4	2.1	11.1	2.3	17.3	4.4	32.2	6.1	91.0	11.0	27.9	2.6	117.3	8.4	23.0	1.7	207.0	13.0	38.7	2.4	9.8E+03	200.0	107.6	6.0	276.0	18.0
17-91-1-23	18.4	2.2	703.0	19.0	1.0	0.1	0.3	0.1	7.0	0.5	2.7	0.6	4.0	0.5	2.9	1.1	15.8	1.1	65.8	2.3	23.6	0.6	107.3	2.4	21.5	0.6	195.3	4.5	37.8	0.8	9.9E+03	230.0	123.3	4.0	242.3	8.4
17-91-1-24	480.0	110.0	1315.0	26.0	40.6	1.4	0.4	0.1	15.6	0.5	3.4	0.4	6.1	0.5	3.3	0.4	30.9	1.1	137.2	3.4	48.3	1.2	206.9	5.3	37.8	0.9	316.3	7.8	58.2	1.7	9.2E+03	210.0	191.4	6.4	327.0	10.0
17-91-1-25	96.0	19.0	2179.0	76.0	31.8	1.9	0.6	0.1	18.1	1.0	7.3	0.5	12.3	0.8	5.1	0.6	57.9	2.6	221.7	8.5	78.1	3.7	324.0	14.0	59.4	2.4	496.0	18.0	93.4	3.8	8.6E+03	300.0	352.0	27.0	458.0	12.0
17-91-1-26	33.6	4.9	692.0	48.0	2.2	0.2	1930.0	970.0	2200.0	1100.0	910.0	480.0	106.0	48.0	3.0	0.8	51.0	12.0	77.4	5.4	23.8	1.7	97.6	6.7	17.9	1.1	159.0	9.1	30.7	1.7	8.2E+03	130.0	670.0	260.0	172.0	12.0
17-91-1-27	34.4	3.1	395.0	17.0	2.4	0.1	0.0	0.0	41.7	1.7	2.0	0.3	2.9	0.3	0.8	0.1	11.6	0.9	39.8	1.9	13.4	0.7	56.8	2.6	11.3	0.4	104.6	3.9	20.8	0.8	8.5E+03	230.0	92.3	4.5	97.7	2.7
17-91-1-28	31.0	2.8	950.0	30.0	1.0	0.1	0.0	0.0	5.8	0.2	1.5	0.3	3.0	0.4	0.1	0.0	18.1	0.8	86.7	2.3	32.5	0.9	144.0	4.5	29.2	0.9	260.9	7.5	51.7	1.4	9.9E+03	200.0	140.7	4.1	272.4	7.0
17-91-1-29	22.0	2.7	738.0	23.0	1.1	0.1	0.4	0.2	3.4	0.4	1.8	0.6	3.2	0.7	3.9	1.9	13.9	1.5	64.8	2.1	24.5	0.8	112.4	4.4	23.2	0.9	216.6	8.5	42.3	2.0	1.1E+04	320.0	64.3	5.6	335.0	21.0
17-91-1-30	28.5	3.3	1283.0	60.0	1.8	0.1	2.2	0.4	16.0	1.0	10.9	1.8	12.7	1.7	21.5	3.7	40.1	3.3	126.4	6.6	43.1	1.7	182.9	7.0	35.0	1.2	307.0	11.0	58.8	1.8	1.0E+04	220.0	296.0	14.0	493.0	18.0
17-91-1-31	19.7	2.4	1350.0	120.0	1.8	0.1	0.2	0.1	14.0	0.7	2.5	0.4	6.3	0.8	1.5	0.5	31.1	3.1	136.0	13.0	48.2	4.7	208.0	18.0	39.8	3.1	351.0	27.0	66.0	4.7	1.0E+04	210.0	424.0	42.0	541.0	35.0
17-91-1-32	26.2	2.6	686.0	52.0	1.8	0.2	0.0	0.0	9.0	0.7	1.0	0.2	2.4	0.3	0.1	0.0	13.0	1.6	62.2	5.2	23.5	1.9	108.4	8.6	22.2	1.5	205.0	12.0	41.1	2.4	1.1E+04	240.0	180.0	19.0	371.0	24.0
17-91-1-33	17.2	1.9	1640.0	120.0	2.3	0.1	0.5	0.3	10.4	0.4	2.4	0.3	6.5	0.8	0.4	0.1	32.8	3.1	153.0	13.0	56.0	4.5	244.0	20.0	47.0	3.6	419.0	30.0	79.9	5.8	9.8E+03	210.0	229.0	16.0	364.0	23.0
17-91-1-34	42.8	9.8	940.0	150.0	1.5	0.2	3.3	1.0	14.4	3.4	15.6	4.4	16.6	4.3	43.0	13.0	39.8	9.3	103.0	17.0	29.3	4.3	110.0	15.0	20.0	2.8	174.0	25.0	31.8	4.4	1.0E+04	270.0	102.0	14.0	392.0	33.0
17-91-1-35	18.8	2.5	740.0	25.0	1.3	0.1	0.5	0.3	8.4	0.7	3.4	1.2	4.5	1.0	6.5	3.2	18.0	1.8	70.6	3.3	25.4	1.0	111.4	3.5	21.7	0.6	196.8	5.1	38.2	0.8	1.0E+04	230.0	157.5	6.0	323.0	15.0
17-91-1-36	3050.0	560.0	1755.0	74.0	17.7	2.1	6.8	0.5	27.5	1.2	34.3	2.5	35.7	2.4	64.0	4.1	81.4	4.4	208.0	10.0	61.4	3.2	235.0	12.0	44.0	2.3	387.0	21.0	69.9	3.6	8.1E+03	200.0	148.0	11.0	339.0	22.0
17-91-1-37	20.0	2.6	602.0	66.0	3.4	0.5	0.1	0.1	7.3	1.0	2.4	0.5	4.3	0.7	1.6	0.6	17.0	1.6	65.6	6.4	21.8	2.5	87.0	11.0	16.7	2.2	148.0	19.0	28.3	3.7	9.4E+03	390.0	99.5	9.9	207.0	20.0
17-91-1-38	35.8	6.7	1640.0	170.0	1.4	0.1	3.6	1.0	13.3	1.7	13.2	2.9	27.7	4.6	38.0	14.0	98.0	13.0	195.0	21.0	53.5	4.8	191.0	15.0	33.8	2.2	278.0	17.0	49.2	2.1	1.1E+04	250.0	130.2	4.4	481.0	53.0
17-91-1-39	28.6	2.6	504.0	62.0	1.8	0.2	0.2	0.1	21.0	4.3	1.8	0.5	3.9	1.0	2.8	0.9	16.2	2.9	54.6	6.7	16.7	2.1	64.6	8.2	12.2	1.5	108.0	13.0	20.3	2.4	1.0E+04	360.0	195.0	35.0	355.0	17.0
17-91-1-40	16.3	2.2	357.6	6.6	2.4	0.2	0.3	0.1	27.5	1.3	1.3	0.3	2.5	0.3	0.4	0.1	7.9	0.6	31.9	1.0	11.7	0.3	55.9	1.5	12.7	0.6	127.7	5.8	27.0	1.4	9.8E+03	230.0	213.5	7.6	377.0	26.0
17-91-1-41	34.9	3.7	217.0	16.0	1.7	0.1	0.1	0.0	17.1	0.6	0.8	0.2	1.7	0.4	0.8	0.3	6.5	1.3	21.3	2.6	7.3	0.6	32.1	2.3	7.2	0.4	73.8	3.3	17.8	0.7	1.2E+04	280.0	128.9	4.8	449.0	13.0
17-91-1-42	16.9	2.0	366.0	41.0	2.4	0.1	0.1	0.0	25.3	0.9	1.1	0.3	2.7	0.7	1.0	0.4	11.4	3.2	35.0	5.7	11.4	1.1	48.8	3.5	10.2	0.7	93.1	4.7	18.7	0.8	1.0E+04	250.0	198.0	10.0	288.5	9.7
17-91-1-43	12.5	1.3	126.5	6.1	0.3	0.0	0.0	0.0	2.2	0.1	1.9	0.2	4.3	0.5	0.2	0.1	13.7	1.0	20.9	1.1	4.3	0.2	11.5	0.7	1.7	0.1	11.5	0.8	1.9	0.1	1.1E+04	280.0	87.6	2.7	193.1	5.1
17-91-1-44	13.2	1.7	109.0	12.0	0.6	0.2	0.0	0.0	2.1	0.2	1.5	0.2	2.7	0.3	0.2	0.0	9.2	0.5	16.6	1.2	3.7	0.5	10.9	1.7	1.8	0.4	16.6	4.8	2.8	1.0	1.1E+04	240.0	64.0	4.3	220.0	13.0
17-91-1-45	93.0	30.0	2430.0	110.0	85.2	7.6	1.9	0.4	33.1	2.5	14.9	2.0	24.2	2.8	17.9	3.8	81.6	7.7	256.0	13.0	83.8	3.5	335.0	14.0	59.7	2.3	482.0	21.0	80.1	3.4	8.4E+03	210.0	231.0	19.0	486.0	38.0
17-91-1-46	14.7	2.0	163.0	25.0	0.6	0.1	0.0	0.0	2.1	0.2	2.1	0.3	3.0	0.4	0.1	0.0	6.0	0.5	17.3	1.8	5.1	0.7	17.2	2.8	2.8	0.5	21.9	3.8	3.6	0.7	1.1E+04	270.0	79.7	6.3	355.0	31.0
17-91-1-47	24.2	2.3	167.7	3.9	0.3	0.0	0.0	0.0	2.1	0.1	2.5	0.3	5.0	0.4	0.4	0.0	16.9	0.7	27.3	0.9	5.7	0.2	16.1	0.6	2.3	0.1	16.3	0.5	2.6	0.1	1.1E+04	230.0	88.3	2.1	205.9	4.2
17-91-1-48	28.3	2.6	70.3	1.1	0.3	0.0	0.0	0.0	2.9	0.1	3.4	0.3	4.8	0.4	0.2	0.0	7.6	0.4	10.9	0.5	2.5	0.1	7.0	0.3	1.2	0.1	7.3	0.4	1.1	0.1	1.1E+04	270.0	80.8	1.9	298.2	6.4

17-91-1 - 49	25.4	3.1	482.0	15.0	1.0	0.1	0.0	0.0	8.5	0.5	1.3	0.3	2.8	0.4	0.2	0.0	11.9	0.5	46.4	1.2	16.1	0.5	73.9	2.7	15.4	0.6	147.3	6.1	30.2	1.2	8.6E+03	310.0	67.0	4.2	134.7	9.8
17-91-1 - 50	56.0	18.0	720.0	260.0	0.9	0.2	7.2	3.4	20.4	8.8	26.0	12.0	22.9	9.0	48.0	22.0	49.0	17.0	93.0	30.0	22.3	7.6	70.0	25.0	11.4	4.2	94.0	35.0	16.1	6.1	1.1E+04	270.0	48.6	8.0	401.0	66.0
17-91-1 - 51	24.7	2.5	697.0	17.0	2.0	0.1	0.1	0.0	24.6	0.7	2.5	0.3	5.5	0.4	1.4	0.3	19.8	0.9	70.1	2.0	24.9	0.8	105.8	2.9	21.2	0.7	189.0	4.7	36.9	1.1	8.3E+03	180.0	541.0	25.0	544.0	18.0
17-91-1 - 52	15.0	1.8	715.0	55.0	2.4	0.1	0.3	0.1	26.3	0.9	2.4	0.6	5.3	1.0	1.8	0.6	21.5	3.2	73.3	6.8	24.5	2.0	104.5	7.3	20.6	1.3	186.0	11.0	36.9	2.0	1.0E+04	200.0	374.0	24.0	527.0	23.0
17-91-1 - 53	33.9	5.2	1740.0	280.0	14.7	2.9	0.1	0.0	10.5	2.3	3.4	0.8	7.3	1.5	0.3	0.1	41.0	6.7	198.0	32.0	68.0	11.0	279.0	47.0	50.2	8.3	416.0	69.0	72.0	12.0	8.7E+03	560.0	106.0	17.0	410.0	19.0
17-91-1 - 54	59.0	9.1	2110.0	340.0	18.6	3.7	0.2	0.1	16.7	3.6	5.3	0.8	10.9	1.8	0.8	0.3	53.9	8.4	245.0	40.0	84.0	14.0	342.0	57.0	60.8	9.9	485.0	76.0	82.0	13.0	7.4E+03	730.0	126.0	18.0	327.0	33.0
17-91-1 - 55	21.9	2.6	1640.0	300.0	11.8	2.5	0.0	0.0	9.7	2.0	2.7	0.6	7.4	1.2	0.3	0.1	42.0	7.1	192.0	34.0	66.0	12.0	264.0	50.0	46.9	8.9	361.0	69.0	59.0	11.0	8.0E+03	720.0	98.0	13.0	262.7	6.5
17-91-1 - 56	28.1	2.5	138.1	8.3	0.4	0.1	0.0	0.0	2.3	0.1	2.1	0.3	4.5	0.4	0.2	0.0	14.8	1.0	22.5	1.3	4.7	0.3	12.4	0.8	1.8	0.1	12.8	1.0	2.0	0.1	1.1E+04	270.0	88.7	1.9	201.6	4.2
17-91-1 - 57	22.5	2.1	125.8	2.7	0.4	0.0	0.0	0.0	2.2	0.1	2.7	0.3	4.9	0.3	0.3	0.1	15.0	0.8	21.1	0.7	4.2	0.2	10.9	0.5	1.6	0.1	10.5	0.4	1.6	0.1	1.1E+04	210.0	80.8	1.5	182.4	3.3
17-91-1 - 58	151.0	19.0	3140.0	200.0	2.4	0.1	73.0	29.0	72.0	11.0	73.0	11.0	62.8	8.1	224.0	27.0	147.0	14.0	311.0	20.0	90.2	4.6	343.0	14.0	62.2	2.4	502.0	16.0	92.9	2.6	9.7E+03	240.0	588.0	26.0	823.0	26.0
17-91-1 - 59	32.9	8.6	1460.0	93.0	2.2	0.1	2.3	1.3	18.5	2.2	8.3	3.5	12.4	3.6	33.0	18.0	41.0	6.5	145.6	9.4	49.9	2.3	211.9	8.7	40.9	1.5	349.0	10.0	66.0	2.2	1.0E+04	220.0	408.0	24.0	565.0	20.0
17-91-1 - 60	424.0	73.0	1730.0	140.0	4.3	0.2	1.1	0.2	12.5	0.7	11.8	1.6	21.7	3.0	8.6	1.5	83.0	11.0	199.0	17.0	58.9	4.5	220.0	15.0	39.3	2.2	320.0	17.0	58.5	2.9	7.8E+03	190.0	137.0	10.0	119.8	7.0
17-91-1 - 61	97.0	29.0	916.0	56.0	1.3	0.1	0.0	0.0	16.5	0.6	1.4	0.3	3.8	0.4	0.7	0.1	20.2	1.4	87.3	5.5	31.5	1.9	136.8	7.8	27.1	1.5	241.0	12.0	46.8	2.1	8.9E+03	190.0	69.3	5.4	76.0	3.8
17-91-1 - 62	64.4	9.1	1740.0	190.0	1.6	0.2	7.3	1.0	18.4	2.2	31.4	3.6	33.7	4.1	63.8	8.9	89.0	14.0	171.0	21.0	49.0	4.7	189.0	13.0	34.8	1.8	289.0	11.0	53.3	2.2	1.2E+04	290.0	25.8	2.2	518.0	17.0
17-91-1 - 63	16.2	1.9	940.0	160.0	1.3	0.3	0.0	0.0	13.4	3.0	1.3	0.2	2.9	0.3	0.6	0.1	15.9	1.9	82.0	13.0	32.3	5.6	150.0	27.0	30.9	5.9	295.0	57.0	58.0	10.0	1.0E+04	260.0	63.4	7.8	84.0	13.0
17-91-1 - 64	20.7	1.9	137.8	9.6	0.2	0.0	0.0	0.0	1.7	0.1	2.1	0.3	5.4	0.5	0.7	0.2	15.1	0.8	22.0	1.2	4.4	0.3	12.2	0.6	1.7	0.1	11.9	0.6	1.9	0.1	1.0E+04	240.0	62.9	1.5	260.6	6.1
17-91-1 - 65	25.7	3.8	363.0	22.0	1.0	0.1	1.3	0.4	12.3	1.1	5.2	1.3	5.8	1.0	13.2	3.7	16.6	2.1	40.4	2.8	11.4	0.7	39.9	2.7	7.2	0.6	62.6	5.3	11.8	1.0	1.1E+04	260.0	134.0	19.0	420.0	17.0
17-91-1 - 66	63.4	6.1	2980.0	240.0	1.8	0.1	6.2	0.7	16.4	1.7	22.2	2.2	27.4	3.5	72.0	8.2	98.0	15.0	275.0	29.0	89.8	7.5	388.0	26.0	75.2	4.3	674.0	30.0	135.8	6.2	1.1E+04	260.0	78.3	4.5	374.0	12.0
17-91-1 - 67	31.5	3.0	350.0	11.0	1.5	0.1	0.0	0.0	15.4	0.5	1.2	0.2	1.9	0.3	0.1	0.0	8.7	0.6	34.2	1.2	12.2	0.5	53.2	2.0	11.0	0.4	98.9	3.4	19.9	0.8	9.1E+03	200.0	163.6	7.1	167.8	7.2
17-91-1 - 68	32.6	3.2	845.0	31.0	1.1	0.1	0.1	0.0	8.3	0.3	2.0	0.3	4.0	0.3	0.6	0.2	19.3	1.0	82.5	3.1	29.6	1.0	130.7	4.4	25.5	0.9	224.3	6.2	43.2	1.2	9.7E+03	240.0	195.1	8.2	312.0	10.0
17-91-1 - 69	24.3	2.6	730.0	36.0	1.1	0.1	0.0	0.0	7.4	0.4	1.5	0.3	3.2	0.5	0.1	0.0	15.0	1.2	69.5	4.2	24.9	1.3	111.9	5.3	22.2	1.1	197.6	8.2	38.7	1.7	9.6E+03	190.0	163.0	10.0	298.9	7.1
17-91-1 - 70	31.5	3.4	930.0	80.0	1.8	0.1	2.3	0.5	11.8	0.9	8.4	1.7	10.4	1.8	16.9	3.4	34.5	5.2	98.0	10.0	31.2	2.7	131.0	9.4	25.5	1.5	222.0	11.0	42.2	2.0	9.9E+03	180.0	164.7	8.4	333.0	14.0
17-91-1 - 71	22.0	2.6	409.0	10.0	1.6	0.1	0.0	0.0	13.6	0.4	0.8	0.2	1.6	0.2	0.1	0.0	8.6	0.6	37.7	1.3	13.8	0.4	61.7	1.7	12.4	0.4	112.8	3.3	21.7	0.5	9.7E+03	240.0	175.0	5.5	314.6	6.8
17-91-1 - 72	37.9	3.6	604.0	23.0	1.4	0.1	0.0	0.0	7.5	0.8	0.8	0.2	1.7	0.3	0.1	0.0	9.1	0.7	51.6	1.5	20.0	0.6	96.8	3.6	20.5	1.0	185.5	8.8	37.5	1.8	1.0E+04	230.0	114.0	11.0	336.0	37.0
17-91-1 - 73	30.3	3.3	734.0	38.0	1.3	0.1	0.0	0.0	10.3	0.5	1.3	0.3	3.0	0.3	0.1	0.0	14.7	1.2	67.9	4.1	25.0	1.6	114.0	5.7	23.0	1.1	207.0	10.0	40.4	1.7	9.8E+03	240.0	198.0	15.0	296.0	11.0
17-91-1 - 74	25.5	3.0	269.0	14.0	0.8	0.1	0.6	0.3	3.4	0.3	5.4	0.6	9.5	0.9	0.5	0.1	23.7	1.5	37.3	1.4	8.5	0.5	30.1	2.9	5.6	0.8	54.6	9.5	11.5	2.2	1.1E+04	250.0	155.9	7.1	367.8	7.9
17-91-1 - 75	33.1	3.2	135.0	6.0	0.3	0.0	0.0	0.0	1.9	0.1	2.6	0.3	5.3	0.4	0.3	0.0	14.5	0.7	22.3	0.8	4.5	0.2	12.1	0.8	1.9	0.2	13.8	1.4	2.3	0.3	1.1E+04	220.0	80.2	2.4	271.6	5.8
17-91-1 - 76	26.9	2.9	444.0	39.0	1.4	0.1	0.4	0.2	13.9	1.0	2.4	0.9	3.2	0.6	2.7	1.8	11.6	1.7	42.6	4.2	15.0	1.2	65.1	4.5	13.5	1.0	119.4	7.0	23.7	1.2	9.9E+03	280.0	103.6	8.5	137.6	9.7
17-91-1 - 77	40.5	4.2	926.0	39.0	1.8	0.2	2.2	0.5	6.5	0.8	7.3	1.5	7.3	1.3	17.8	3.0	26.3	2.9	84.0	4.2	29.2	1.0	135.7	3.3	29.2	0.8	285.0	9.3	58.9	2.3	1.2E+04	300.0	69.8	2.1	587.0	42.0
17-91-1 - 78	41.7	5.5	1034.0	27.0	1.5	0.1	0.4	0.1	16.7	0.6	5.2	0.5	8.4	0.6	0.8	0.1	31.7	1.3	109.6	2.8	36.5	1.1	151.2	3.6	27.7	0.7	239.8	6.0	45.2	1.1	8.5E+03	240.0	215.0	10.0	140.8	8.1
17-91-1 - 79	12.8	1.8	449.0	59.0	1.4	0.1	0.0	0.0	12.0	0.4	1.2	0.3	2.6	0.5	0.2	0.1	11.1	1.9	42.8	6.6	15.3	2.1	68.9	8.7	13.9	1.5	127.0	12.0	25.0	2.2	9.9E+03	370.0	178.2	6.7	247.0	30.0
17-91-1 - 80	27.3	3.5	1734.0	94.0	2.7	0.1	3.2	0.8	10.6	1.9	10.2	2.6	11.9	2.5	25.7	6.6	35.2	4.8	146.3	8.9	55.5	2.4	263.1	8.5	55.4	1.5	530.0	14.0	106.3	2.3	1.1E+04	210.0	163.6	7.8	637.0	23.0
17-91-1 - 81	60.7	7.2	2960.0	170.0	2.6	0.1	12.6	1.5	34.5	3.7	40.4	4.8	44.0	5.2	122.0	15.0	103.0	11.0	262.0	18.0	84.6	4.0	360.0	11.0	71.3	1.7	649.0	18.0	127.8	2.9	1.1E+04	260.0	208.2	6.7	797.0	23.0
17-91-1 - 82	74.0	9.5	2170.0	100.0	8.1	0.5	3.5	0.7	24.8	2.4	22.2	2.2	24.5	2.1	0.4	0.1	77.5	5.6	247.0	15.0	81.1	4.5	338.0	18.0	62.9	3.2	535.0	26.0	103.4	4.7	5.4E+03	150.0	250.0	17.0	232.0	10.0

17-91-1-83	17.2	3.0	1025.0	59.0	4.2	0.3	0.1	0.0	5.4	0.3	2.9	0.3	5.3	0.4	0.2	0.0	24.7	1.1	102.0	5.1	37.5	2.2	170.0	11.0	33.3	2.2	288.0	20.0	56.4	4.0	7.9E+03	320.0	112.0	4.1	297.6	7.4
17-91-1-84	15.0	2.0	1107.0	88.0	0.9	0.1	0.7	0.7	4.0	0.5	5.0	0.8	8.6	1.0	0.7	0.3	35.3	2.9	118.4	9.1	39.1	3.3	159.0	14.0	29.4	2.5	253.0	22.0	48.7	4.3	9.9E+03	360.0	206.0	21.0	305.0	42.0
17-91-1-85	13.7	1.7	218.0	24.0	0.4	0.1	0.3	0.1	2.1	0.3	2.6	0.5	4.4	0.5	2.3	0.8	13.0	1.2	27.8	2.4	6.7	0.6	24.0	3.0	4.2	0.7	37.1	6.9	6.7	1.3	1.1E+04	220.0	61.3	4.6	268.0	11.0
17-91-1-86	40.8	5.3	1114.0	37.0	4.0	0.2	0.0	0.0	11.2	0.5	3.4	0.5	6.6	0.6	0.4	0.1	28.5	1.6	112.6	4.2	38.8	1.5	166.2	5.4	31.7	1.0	271.0	7.8	52.0	1.8	8.6E+03	230.0	150.7	6.4	148.1	7.3
17-91-1-87	28.4	2.2	220.0	33.0	0.3	0.0	0.5	0.1	3.4	0.4	5.3	0.7	7.2	0.9	3.2	0.7	21.0	2.7	31.1	4.2	6.4	0.9	17.1	2.4	2.2	0.3	14.6	1.7	2.2	0.3	1.1E+04	190.0	81.9	7.5	197.1	6.0
17-91-1-88	51.4	3.9	2216.0	86.0	36.6	3.2	0.0	0.0	18.7	1.1	3.4	0.4	8.4	0.7	0.2	0.1	46.0	1.9	213.9	8.0	77.4	2.8	332.0	12.0	59.9	2.2	481.0	18.0	86.7	3.2	8.5E+03	170.0	345.0	16.0	440.0	15.0
17-91-1-89	32.0	2.9	870.0	100.0	1.0	0.1	0.0	0.0	6.3	0.7	1.0	0.2	2.5	0.3	0.1	0.0	13.6	1.3	76.1	8.9	29.4	3.6	138.0	17.0	28.4	3.4	257.0	30.0	50.5	5.8	1.0E+04	260.0	96.9	7.3	221.4	5.9
17-91-1-90	32.9	2.8	886.0	70.0	1.2	0.1	0.0	0.0	5.2	0.3	0.9	0.2	2.2	0.4	0.2	0.0	14.2	1.2	77.3	6.3	29.1	2.4	139.0	12.0	27.6	2.2	253.0	21.0	49.6	4.2	1.0E+04	280.0	87.8	4.3	277.0	30.0
17-91-1-91	35.3	3.0	557.0	19.0	0.8	0.1	0.0	0.0	6.5	0.2	1.1	0.2	2.4	0.3	0.1	0.0	10.6	0.7	50.6	1.8	18.8	0.8	87.1	3.4	17.4	0.7	156.2	5.6	31.4	1.3	9.6E+03	210.0	99.9	4.8	194.4	9.6
17-91-1-92	33.1	2.8	518.0	12.0	1.2	0.1	0.0	0.0	3.3	0.3	0.6	0.1	1.5	0.3	0.1	0.0	7.8	0.6	45.2	1.3	17.0	0.5	76.0	2.6	15.5	0.5	135.8	4.7	26.7	1.0	1.1E+04	260.0	63.0	3.6	323.0	19.0
17-91-1-93	29.5	2.6	619.0	33.0	0.9	0.1	0.0	0.0	5.6	0.5	1.5	0.2	2.9	0.4	0.1	0.0	13.1	0.7	57.4	2.8	20.6	1.0	93.8	5.1	18.5	1.0	170.6	7.0	33.7	1.4	9.7E+03	220.0	108.1	6.3	252.0	21.0
17-91-1-94	19.6	2.2	824.0	36.0	1.2	0.1	0.0	0.0	6.1	0.4	1.2	0.2	3.3	0.4	0.1	0.0	15.5	1.1	75.5	3.7	27.5	1.4	129.1	5.5	26.2	1.0	234.5	8.5	47.1	1.8	1.0E+04	260.0	139.0	11.0	320.0	13.0
17-91-1-95	35.3	3.3	1160.0	240.0	1.2	0.1	1.1	0.3	23.0	1.9	8.1	1.8	21.6	5.1	11.7	3.0	82.0	20.0	139.0	30.0	34.4	7.0	113.0	20.0	17.3	2.8	132.0	18.0	22.8	2.7	8.8E+03	330.0	142.0	14.0	148.0	23.0
17-91-1-96	19.4	1.9	552.0	75.0	1.6	0.2	0.4	0.2	8.5	1.4	2.4	0.4	4.4	0.5	3.2	1.2	15.5	1.0	51.4	6.2	18.8	2.7	86.0	13.0	17.5	2.5	158.0	22.0	31.8	4.5	1.0E+04	280.0	160.0	21.0	398.0	25.0
17-91-1-97	11.4	1.5	793.0	20.0	3.5	0.2	0.0	0.0	7.1	0.3	1.9	0.3	4.6	0.4	0.4	0.1	21.5	1.1	79.5	2.3	28.3	0.9	119.0	3.0	22.4	0.7	195.6	4.9	39.3	1.2	8.1E+03	160.0	85.6	3.8	86.5	4.3
17-91-1-98	29.3	3.2	1020.0	150.0	2.0	0.3	2.0	0.4	9.3	0.6	11.0	1.2	17.0	2.0	15.5	2.2	54.9	8.1	117.0	17.0	33.0	4.8	120.0	17.0	20.4	2.9	162.0	23.0	30.3	4.1	9.4E+03	260.0	111.2	3.8	196.0	14.0
17-91-1-99	17.0	2.3	1290.0	120.0	1.1	0.1	0.2	0.2	5.6	0.3	1.9	0.3	4.5	0.7	0.2	0.0	23.4	2.2	118.0	11.0	44.2	4.1	203.0	18.0	40.9	3.4	356.0	30.0	71.1	5.9	1.0E+04	230.0	103.6	5.8	175.1	5.7
17-91-1-100	14.4	2.1	306.7	5.9	5.0	0.2	0.1	0.0	8.5	0.3	0.6	0.2	1.2	0.2	0.1	0.0	5.9	0.4	28.5	0.9	10.6	0.3	50.6	1.1	10.6	0.3	98.4	2.7	20.3	0.5	1.0E+04	260.0	61.6	2.2	122.1	6.0
17-91-1-101	28.7	3.3	458.0	49.0	2.0	0.1	1.8	0.6	13.3	1.4	7.1	2.1	7.9	2.0	13.5	4.4	22.2	4.5	48.9	6.7	14.3	1.3	59.3	4.6	12.5	0.8	115.9	6.0	24.5	1.0	1.1E+04	280.0	146.4	9.1	552.0	16.0
17-91-1-102	10.8	1.9	536.0	24.0	1.4	0.1	0.0	0.0	34.1	1.2	5.1	0.5	7.1	0.6	1.6	0.2	23.0	1.6	56.6	3.1	17.7	0.9	73.3	3.5	14.1	0.6	127.4	5.5	26.6	1.1	8.4E+03	200.0	306.0	19.0	231.0	10.0
17-91-1-103	14.1	2.0	250.0	10.0	1.3	0.1	0.0	0.0	20.6	0.7	1.0	0.2	1.6	0.2	0.4	0.1	6.2	0.7	22.5	1.4	7.9	0.4	36.7	1.7	7.9	0.4	77.3	3.3	16.9	0.8	1.0E+04	220.0	151.2	7.2	354.0	15.0
17-91-1-104	25.2	2.7	1083.0	20.0	1.6	0.1	0.1	0.0	56.2	1.2	7.6	0.6	14.5	0.8	2.9	0.3	44.1	1.8	118.7	3.0	36.1	0.8	146.5	3.1	27.4	0.7	237.7	5.9	47.3	1.2	9.1E+03	200.0	831.0	21.0	440.0	12.0
17-91-1-105	30.2	3.0	125.0	22.0	0.3	0.0	0.5	0.2	4.6	0.6	5.7	1.0	6.4	1.1	3.3	1.3	11.5	1.8	16.3	2.5	3.7	0.6	10.8	1.7	1.6	0.2	11.2	1.5	1.8	0.3	1.2E+04	310.0	125.9	3.2	229.0	11.0
17-91-1-106	25.7	3.7	745.0	42.0	2.1	0.1	5.6	1.7	17.0	1.1	5.6	1.1	6.9	1.1	6.6	1.6	20.6	1.9	70.8	4.3	25.1	1.4	107.3	4.9	21.4	1.0	195.1	9.8	39.8	2.0	9.0E+03	230.0	231.0	13.0	369.0	16.0
17-91-1-107	13.2	2.2	1050.0	110.0	1.2	0.1	0.7	0.3	16.3	1.4	5.1	1.1	10.6	1.8	6.1	2.6	36.4	5.5	107.0	11.0	34.2	3.4	136.0	11.0	25.5	2.2	211.0	16.0	41.5	2.8	9.9E+03	260.0	329.0	25.0	486.0	17.0
17-91-1-108	56.7	7.2	970.0	180.0	1.7	0.3	7.1	1.6	17.3	3.4	18.0	4.0	21.7	4.7	65.0	15.0	53.0	10.0	105.0	18.0	26.9	4.7	97.0	16.0	18.7	3.0	177.0	29.0	37.5	6.2	1.1E+04	350.0	48.2	5.8	507.0	39.0
17-91-1-109	18.5	2.3	306.0	10.0	2.3	0.1	0.0	0.0	2.8	0.1	1.1	0.2	1.7	0.3	0.2	0.0	7.9	0.6	31.0	1.4	11.0	0.4	46.6	1.5	9.4	0.4	86.0	3.3	17.6	0.6	6.4E+03	190.0	23.9	1.6	45.4	6.5
17-91-1-110	24.1	3.9	651.0	37.0	1.9	0.1	0.1	0.0	2.8	0.3	2.8	0.5	4.2	0.6	0.4	0.1	16.3	1.5	65.9	4.1	23.0	1.4	100.1	5.8	19.4	1.2	173.0	11.0	35.3	2.2	7.8E+03	490.0	32.1	3.0	169.0	39.0
17-91-1-111	16.6	2.0	567.0	17.0	2.7	0.1	0.2	0.1	29.0	1.0	1.3	0.3	3.0	0.4	1.1	0.3	12.2	0.8	49.9	2.0	18.7	0.7	87.1	3.0	17.4	0.8	159.2	5.3	32.1	1.1	9.8E+03	240.0	394.0	13.0	670.0	26.0
17-91-1-112	86.8	8.7	1720.0	140.0	2.3	0.2	15.8	2.2	43.7	3.5	43.0	5.1	41.0	4.1	140.0	18.0	96.0	10.0	187.0	17.0	51.3	4.7	189.0	16.0	33.8	2.6	286.0	22.0	53.7	4.1	1.0E+04	250.0	286.0	13.0	719.0	38.0
17-91-1-113	20.6	2.3	680.0	29.0	2.2	0.1	0.1	0.0	10.1	0.8	0.8	0.2	2.3	0.3	0.3	0.1	11.5	0.7	59.5	2.7	22.4	0.9	104.3	4.2	20.8	0.9	187.9	8.8	37.1	1.4	1.0E+04	180.0	193.0	15.0	415.0	14.0
17-91-1-114	23.5	2.5	971.0	82.0	1.9	0.2	0.8	0.2	15.0	1.4	5.3	1.2	10.2	1.8	9.2	2.4	37.7	6.0	98.8	8.8	30.3	1.9	122.0	6.3	23.4	1.0	204.7	8.5	38.5	1.9	1.0E+04	270.0	250.0	36.0	529.0	17.0
17-91-1-115	3200.0	1300.0	1255.0	78.0	6.6	0.6	0.7	0.2	8.3	0.4	1.9	0.3	5.5	0.8	1.6	0.8	24.6	1.7	111.6	7.0	42.3	2.7	201.0	14.0	39.2	2.5	356.0	23.0	71.5	4.4	8.9E+03	280.0	244.0	25.0	405.0	24.0
17-91-1-116	25.1	2.7	131.5	6.1	0.3	0.0	0.0	0.0	2.4	0.1	1.8	0.3	5.0	0.5	0.3	0.0	15.2	0.9	21.6	1.1	4.5	0.2	12.0	0.7	1.7	0.1	11.0	0.8	1.8	0.1	1.1E+04	200.0	92.9	5.2	209.2	9.2

D.5 | Tera-Wasserburg concordia diagrams, shaded for alpha dose (α-dose) events/mg x10³, calculated for the upper-intercept ages of discords for metamorphic zircon from samples 17-37, -59, -72 and -91.